Dissertation zur Erlangung des Doktorgrades
der Fakultät für Chemie und Pharmazie
der Ludwig-Maximilians-Universität München

Azobenzene photoswitches: synthetic methodology and biological applications

Adrian Peter Müller-Deku
aus
Tokio, Japan

2022

Erklärung

Diese Dissertation wurde im Sinne von § 7 der Promotionsordnung vom 28. November 2011 von Herrn Dr. Oliver Thorn-Seshold betreut.

Eidesstattliche Versicherung

Diese Dissertation wurde eigenständig und ohne unerlaubte Hilfe erarbeitet.

München, 13.06.2022

Adrian Peter Müller-Deku

.....

Dissertation eingereicht am	21.06.2022
1. Gutachter:	Dr. Oliver Thorn-Seshold
2. Gutachter:	Dr. Dorian Didier
Mündliche Prüfung am	09.08.2022

Part of this work has been published in peer reviewed journals:

Adrian Müller-Deku, Joyce C. M. Meiring, Kristina Loy, Yvonne Kraus, Constanze Heise, Rebekkah Bingham, Klara I. Jansen, Xiaoyi Qu, Francesca Bartolini, Lukas C. Kapitein, Anna Akhmanova, Julia Ahlfeld, Dirk Trauner & Oliver Thorn-Seshold;

Photoswitchable paclitaxel-based microtubule stabilisers allow optical control over the microtubule cytoskeleton.

Nature Communications **2020**, 11, 4640. https://doi.org/doi: 10.1038/s41467-020-18389-6

Martina F. Ober, Adrian Müller-Deku, Anna Baptist, Benjamin Ajanović, Heinz Amenitsch, Oliver Thorn-Seshold, Bert Nickel;

SAXS measurements of azobenzene lipid vesicles reveal buffer-dependent photoswitching and quantitative *Z*→*E* isomerisation by X-rays.

Nanophotonics **2022**, 11, 2361–2368. https://doi.org/10.1515/nanoph-2022-0053

Part of this work has been deposited on a preprint server and is currently in review:

Adrian Müller-Deku, Oliver Thorn-Seshold;

Exhaustive catalytic *ortho*-alkoxylation of azobenzenes: flexible access to functionally diverse yellow-light-responsive photoswitches.

ChemRxiv **2022**, 10.26434/chemrxiv-2022-vpq96 (in review)

Other manuscripts arising from this PhD:

Li Gao, Joyce C. M. Meiring, Constanze Heise, Ankit Rai, Adrian Müller-Deku, Anna Akhmanova, Julia Thorn-Seshold, Oliver Thorn-Seshold;

Photoswitchable Epothilone-Based Microtubule Stabilisers Allow GFP-Imaging-Compatible, Optical Control over the Microtubule Cytoskeleton.

Angewandte Chemie International Edition, **2022**, 61, e202114614; https://doi.org/10.1002/anie.202114614

Angewandte Chemie **2022**, 134, e202114614.

***Manuscripts in preparation*:**

Adrian Müller-Deku, Dominik Lonken, Maximilian Wranik, Tobias Weinert, Michel Steinmetz, Oliver Thorn-Seshold;

Photoswitchably covalent-reactive microtubule-disrupting agents.

Benedikt Winkler, Adrian Müller-Deku, Robert Mayr, Florian Steiner, Martin Reynders, Christoph Gross, Armin Ofial, Philip Tinnefeld, Viktorija Glembockyte, Oliver Thorn-Seshold;

Quantitative, NIR *cis→trans* photoisomerization of azobenzenes without substituent tuning, by photostable singlet-manifold photoredox

1 Abstract

1.1 Azobenzenes: new aspects for this "Swiss Army knife of photoswitches"

Photoswitches are molecular motifs that can be reversibly photoisomerised between two isomeric forms. First explored as pigments, they are now finding broader applications in materials sciences, as molecular machines, and in chemical biology. In this thesis I present three topics working towards extending the applications and improving the usability of azobenzene photoswitches.

(1) The microtubule cytoskeleton is a centrepiece in the organisation and motility of the eukaryotic cell. It plays an important role in cell division, and small molecules disturbing the delicate balance of microtubule dynamics are used extensively in cancer therapy. However, as research tools, small molecule inhibitors do not provide adequately spatiotemporally controlled inhibition. Photoswitchable inhibitors can help to solve this problem, by using light to direct their bioactivity to selected cells or regions at specific times. We reported the first photoswitchable microtubule stabiliser (AzTax) based on the natural product paclitaxel.

I rationally designed and optimized the AzTax structure; derivative **AzTax3MP** was selected as the best-performing compound. Light-dependent stabilization of microtubules by **AzTax3MP** was demonstrated in cell-free and cellular assays. FACS analysis showed that **AzTax3MP** also provides optical control over cell cycle progression; live cell imaging showed that it can be used to reversibly inhibit microtubule dynamics in live cells over several cycles with single-cell resolution. In primary hippocampal neurons extracted from rats, **AzTax3MP** could even block microtubule polymerisation with subcellular resolution – a scale that has been exceptionally difficult to achieve for freely diffusing photopharmaceuticals.

(2) The utility of azobenzenes as photoswitches depends intimately on their photochemistry; tuning their switching yield and light response to improve their biological performance and applicability is a major challenge. For example, their maximum possible bioactivity differential depends on the isomer ratios that can be obtained by irradiations. Furthermore, photoresponse at wavelengths between 400-800 nm (the biological transparency window) may be crucial for addressing biological systems noninvasively, as light outside this range can cause photodamage and cannot penetrate deeply into samples. Both these properties of azobenzenes are controlled by their substitution pattern.

Tetra-*ortho*-substitutions are an approach that combines visible light addressability with good switching efficiency, thanks to a combination of electronic effects and steric repulsion that separates the n→π* absorption bands of the two isomers. However, the systematic study and use of tetra-*ortho*-substitution patterns has sometimes been complicated or blocked by the need for intolerant, multistep synthetic routes.

I developed a new method for the synthesis of tetra-*ortho*-alkoxy azobenzenes, by combining a known C-H activation strategy and a known mono-alkoxylation procedure with catalyst reoxidation, then optimizing conditions and scope, to deliver exhaustive alkoxylation. With this new method I prepared a wide scope of per-*ortho*-alkoxylated products using simple alcohols as alkoxy sources. Notably, mixed tetra-*ortho*-(difluoro-dimethoxy) substitutions proved to have particularly good switching efficiency; and alkoxylation with 1,3-propanediol increased water solubility. All in all, this tetra-*ortho*-alkoxylation method now allows access to azobenzenes with unusual substitution patterns and novel properties in acceptable yields.

(3) Maximising switching yield is one of the great conceptual goals of the photoswitching community; although in some settings, even measuring switching yield has remained problematic. However, light is not the only stimulus capable of isomerizing azobenzenes. A recent field of research concerns the *Z*→*E* isomerisation of azobenzenes via electron or hole catalysis (catalytic reduction or oxidation). This brings several advantages, including that isomerisation to the thermodynamically more stable isomer is complete on a bulk population level; but this principle has found few applications so far.

SAXS (Small Angle X-ray Scattering) can be used to measure membrane thickness in lipid bilayer vesicles prepared from **AzoPC** (a phosphatidyl choline derivative that carries a modified azobenzene instead of one fatty acid). I developed a new method to correlate SAXS bilayer thickness with the *Z*/*E*-ratio in the membrane, giving a readout for switching yield that is independent of UV-Vis absorption. Using the new correlation method, we found differences in isomerisation behaviour in the artificial membranes compared to azobenzene isomerisation in solution. However, we also observed that photoisomerisation efficiency in the membrane varies depending on the ionic strength of the surrounding aqueous media, which cannot be expected from this model. Lastly, it was found that X-rays can be non-innocent in the switching process: irradiation of mostly-*Z*-**AzoPC** vesicles with 8 keV (soft) X-rays led to a dramatic increase in membrane thickness, reaching that of an all-*E* membrane. It was hypothesized that soft X-ray radiation creates hydroxy radicals that catalytically oxidize and isomerize the azobenzene from the *Z* to the *E*-isomer. The latter two unexpected findings await further investigation and exploitation.

This thesis thus presents (1) azobenzene derivatives that light-dependently control the stabilization of microtubules, (2) a new synthetic methodology for the synthesis of tetra-*ortho*-alkoxy azobenzenes, and (3) the unexpected photoproperties and X-ray sensitivity of azobenzene-containing lipid bilayer membranes: showing how chemical development can variously be directed towards the biological utility, synthetic access, and biophysical performance of azobenzene: a truly multifunctional, "Swiss army knife" photoswitchable motif.

1.2 Azobenzole: das schweizer Taschenmesser der lichtschaltbaren Moleküle

Lichtschaltbare Moleküle lassen sich durch einen Lichtimpuls reversibel zwischen zwei isomerischen Zuständen hin und her schalten. Zuerst wurden diese Moleküle nur als Farbstoffe eingesetzt, in letzter Zeit finden sie allerding immer breitere Anwendung in den Materialwissenschaften, als molekulare Maschinen und in der chemischen Biologie. In dieser Arbeit stelle ich drei separate Themen vor, die das gemeinsame Ziel haben, Azobenzole für ein breites Spektrum an Anwendungen leichter herstellbar und besser nutzbar zu machen.

(1) Mikrotubuli sind ein zentrales Element im Zytoskelett der eukaryotischen Zelle und leisten einen wichtigen Beitrag im Bereich der Organisation und Beweglichkeit der Zelle. Des Weiteren spielen sie eine wichtige Rolle bei der Zellteilung, deshalb werden kleine Moleküle, die das empfindliche Gleichgewicht der Mikrotubulidynamik stören, häufig in der Krebstherapien eingesetzt. Als Forschungsinstrument mangelt es jedoch vielen dieser Moleküle an Spezifität und sie bieten keine ausreichend kontrollierbare Aktivität. Mit Hilfe von lichtschaltbaren molekularen Werkzeugen kann dieses Problem gelöst werden. Bislang gab es jedoch keine lichtschaltbaren Mikrotubuli-Stabilisatoren, wir haben nun auf Basis des Naturstoffs Paclitaxel den ersten lichtschaltbaren Mikrotubulistabilisator (AzTax) entwickelt.

Die AzTax-Struktur wurde optimiert und aus den synthetisierten Molekülen **AzTax3MP** als das Molekül mit der am besten lichtschaltbaren Aktivität ausgewählt. Die lichtabhängige Stabilisierung von Mikrotubuli wurde *in vitro* und in Zellkultur bestätigt und FACS-Analysen zeigten, dass **AzTax3MP** auch Kontrolle über den Zellzyklus ermöglicht. Außerdem kann das dynamische Gleichgewicht der Mikrotubuli auch in lebenden Zellen mit zellulärer Auflösung gesteuert werden. Die Inhibition kann über mehrere Zyklen aktiviert und wieder deaktiviert werden. In, von Ratten entnommenen, primären Hippocampus-Neuronen-Zellen, konnte **AzTax3MP** sogar mit subzellulärer Auflösung aktiviert werden – eine räumlich Präzision in dieser Größenordnung ist für frei diffundierende Photopharmazeutika eine besondere Herausforderung.

(2) Für das Benutzen von Azobenzolen sind die Beleuchtungseigentschaften von entscheidender Bedeutung. Das Optimieren der Effizienz des Schaltprozesses und der Reaktion auf Licht ist eine große Herausforderung bei der Anwendung in einem biologischen Kontext. Bei der Beleuchtung von Azobenzolen entsteht ein bestimmtes Isomerenverhältnis welches von den Eigenschaften des jeweiligen Moleküls abhängt. Diese Isomerenverhältnis hängt eng mit dem Aktivitätsunterschied zusammen, den man zwischen einer beleuchteten Probe und einer nicht beleuchten Probe erhält. Zusätzlich ist in biologische Systeme eine Lichtaktivierung zwischen 400-800 nm, dem so genannten biologischen Fenster, vorteilhaft andernfalls kann das Licht erhebliche Schäden verursachen oder nicht tief genug in die Probe

eindringen. Die Eigenschaften von Azobenzolen werden durch ihr Substitutionsmuster bestimmt.

Bei der Tetra-*ortho*-substitution werden elektronische Effekte mit sterischer Abstoßung kombiniert, um eine Trennung der n→π*-Absorptionsbanden zwischen den Isomeren zu bewirken. Die häufig mehrstufigen Synthesen erschweren die systematische Untersuchung solcher Substitutionsmuster.

Wir haben eine neue Methode für die Synthese von Tetra-*ortho*-alkoxyazobenzolen entwickelt. Ausgehend von einem bekannten Pd-katalysierten C-H-Aktivierungsverfahren und einer bekannten Azobenzol-mono-alkoxylierung, haben wir die Bedingungen durch Reoxidierung des Katalysators optimiert, um das tetra-*ortho*-alkoxylierte Produkt zu erhalten. Mit unserer neuen Methode haben wir diverse Derivate synthetisiert, wobei wir simple Alkohole als Reagenz verwenden konnten. Gemischte Methoxy- und Fluorosubstitution wiesen besonders interessante Eigenschaften auf. Die Substitution mit 1,3-Propandiol erhöhte die Wasserlöslichkeit des Azobenzolderivats. Alles in allem haben wir eine Tetra-*ortho*--Alkoxylierungsmethode entwickelt, die die Synthese von Azobenzolen mit ungewöhnlichen Substitutionsmustern und Eigenschaften in akzeptablen Ausbeuten ermöglicht.

(3) Lichtschalbare Moleküle möglichst vollständig von einem Zustand in den anderen zu schalten ist eines der am längsten bestehenden Forschungsziele aller damit befassten Wisschaftler*innen. Licht ist nicht der einzige Stimulus, der Azobenzole isomerisieren kann. Ein Bereich, in dem in den letzten Jahren einige Fortschritte erzielt wurden, ist die *Z*→*E*-Isomerisierung durch Elektron-Loch-Katalyse (Oxidation/Reduktion). Zu den Vorteilen der Katalyse mit einem Elektron/Loch-Paar gehört die vollständige Rückkehr zum thermodynamisch stabileren Isomer in der gesamten molekularen Population. Allerdings hat dieses Prinzip bisher noch wenige Anwendungen gefunden.

In künstlichen Vesikeln, aus AzoPC (einem Phosphatidylcholinderivat, welches anstelle einer Fettsäure ein modifiziertes Azobenzol trägt), wurden mit SAXS (Small angle X-ray Scattering) die Membrandicke gemessen. Wir haben eine neue Methode entwickelt, um die Membrandicke mit dem *Z*/*E*-Verhältnis in der Membran zu korrelieren, unabhängig von direkten UV/Vis-Messungen. Bei der Anwendung unserer neuen Methode stellten wir Unterschiede im Isomerisierungsverhalten in den künstlichen Membranen im Vergleich zur Isomerisierung von Azobenzol in Lösung und abhängig von der ionenstärke des umgebenden Mediums fest. Außerdem wurde beobachtet, dass durch das Bestrahlen der Membrane mit 8 keV Rötgenstrahlung die Membrandicke sich wieder dem Equilibriumszustand annähert. Es wurde die Hypothese aufgestellt, dass die Röntgenstrahlung Hydroxylradikale erzeugt, die

das Azobenzol oxidieren. Das Azobenzol isomerisiert dann vom *Z* zum E-Isomer. Diese interessanten Ergebnisse müssen noch weiter untersucht werden

Insgesamt wurden verschiedene Projekte vorgestellt, die sich um die Optimierung von Azobenzol als lichtschaltbares Werkzeug für biologische Forschung drehen. Ich habe gezeigt, dass Azobenzole (1) lichtabhängig Mikrotubuli stabilisieren können, (2) eine neue Synthesemethode für Tetra-*ortho*-alkoxyazobenzole und (3) eine Studie über azobenzolhaltige Membranen und ihre exotischen Reaktionen auf Licht und Röntgenstrahlung: Azobenzole lassen sich wirklich verwenden, wie ein schweizer Taschenmesser.

2 Introduction

2.1 Photoswitches

2.1.1 Natural and artificial light-absorbing molecules

Light is one of the most important external factors for life on Earth. It is an important source of energy and a stimulus that triggers a myriad of processes. When some organic molecules absorb light, they photoswitch: they reversibly change their structure, often with accompanying changes in chemical properties such as polarity or solubility, which has a fundamental impact on their surrounding environment. One of the most prominent examples is retinal,[1] a chemical chromophore bound to the G protein coupled receptor (GPCR) rhodopsin in the eye, that reacts to light. When light hits the eye, *Z*-retinal is isomerized to *E*-retinal and the receptor is activated (Fig 1a). The downstream effects of the isomerisation generate a neuronal signal that can be processed and be perceived as vision.[2]

The diverse structures and functions of natural light-absorbing small molecules have also served as blueprints for artificial light-responsive molecules. Research in this area has been motivated because light is a stimulus that can be applied with great precision in research, giving experimenters fine control over molecular photoresponses which in turn control desired functions. Photoswitches, photocages and molecular machines are all families of photoresponsive compounds that have found applications for high-precision functional control. Photocages can only be activated by light once, by which a light-responsive part of the molecule is irreversibly cleaved, releasing the part that was "caged" previously.[3] A molecular machine is a system that performs work while changing reversibly between different states. For this purpose, the motion during change must have a defined direction that stays the same over several activation cycles (e.g., a motif that rotates clockwise as often as it turns counter-clockwise does not perform work).[4] A photoswitch is a system that also can reversibly change between multiple states, although without any restrictions on the direction of motion (Fig 1b).[5]

Photoswitches are often designed so that not only individual molecules but also bulk populations can be isomerised with good yield between two (or more) isomeric states. Typically, a photoswitch features a thermodynamic isomer and a metastable isomer, each of which can absorb a photon from their electronic ground states and then relax into an electronic ground state of the other isomer. Depending on energetics, a metastable isomer can typically also relax thermally to the thermodynamic isomer. If the metastable state has different light absorbing properties compared to the ground state – e.g., different absorption maxima, different extinction coefficients, and/or different quantum yields for isomerisation at the same wavelength – it can be possible to selectively excite one rather than the other isomer, and so to use light to shift the population distribution more towards one or the other isomer.

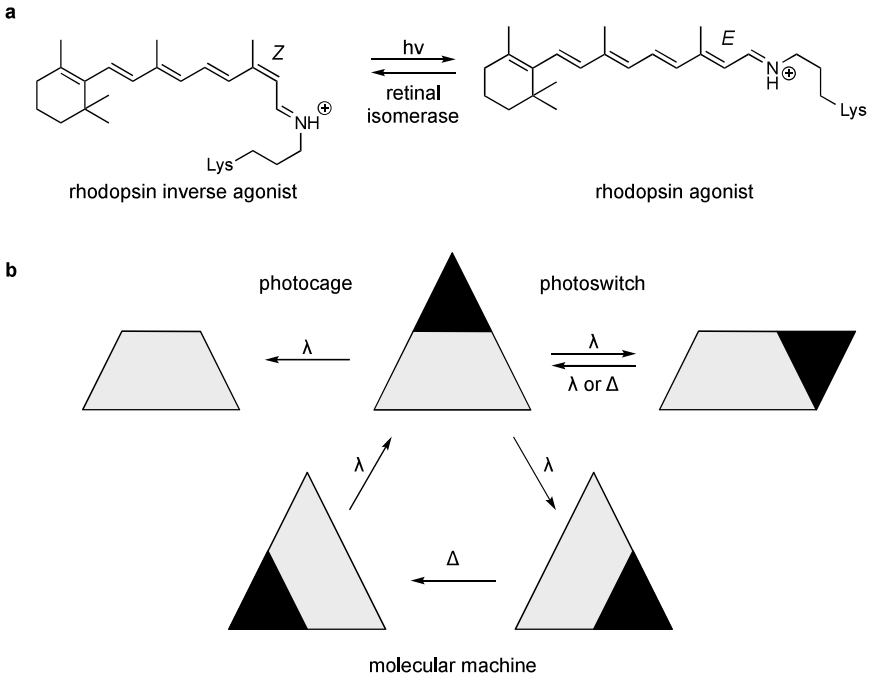

Figure 1: **(a)** The covalently bound retinal can be photoisomerised from the *Z*-isomer to the *E*-isomer, turning it from an inverse agonist of rhodopsin into an antagonist. The retinal is bound covalently via a lysine residue. The retinal can be returned to the *Z*-isomer with the help of retinal isomerase **(b)** Schematic comparison of photocages, photoswitches and molecular machine. The black triangle represents the molecular change upon irradiation. It either is cleaved (photocage), changes the overall shape of the geometric figure (photoswitch) or the position in space changes unidirectionally (molecular machine).

The concept of using chemical photoswitching to control properties and functions has already found applications in fields from materials sciences[5] to biology[6] and is even being developed for disease therapy[7].

2.1.2 A diversity of photoswitchable scaffolds

Many molecules are capable of photoswitching and new ones are continuously developed. However, most photoswitches can be categorised in that their photochromism is either based on double bond isomerisation, or on 6π-electrocyclisation (Fig 2).

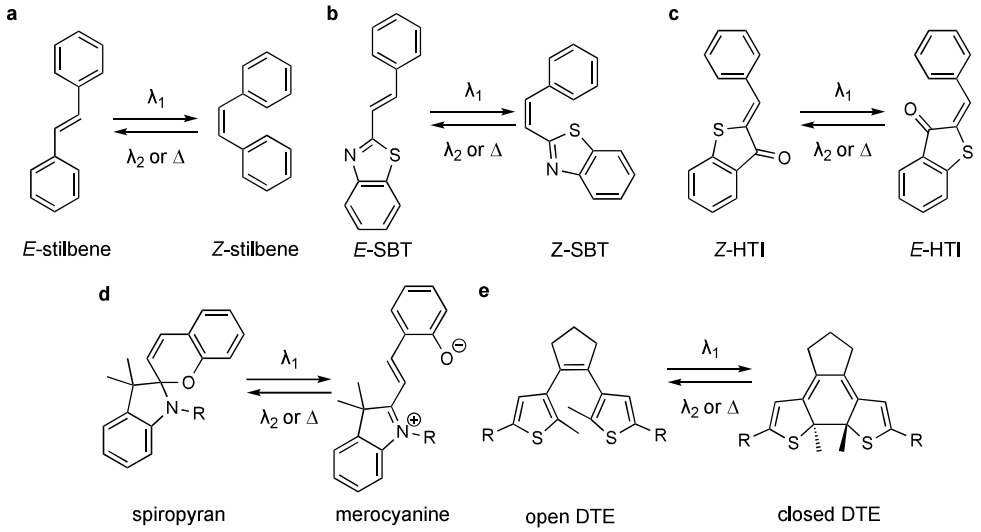

Figure 2: Selection of photoswitches and their respective states **(a)** Stilbenes isomerize *E*→*Z* with 300-350 nm light. The return *E*→*Z* isomerisation can be achieved with 250 nm light **(b)** SBTs are isomerised with λ_1 = 350-400 nm and λ_2 = 250 nm **(c)** HTIs show isomerisation with λ_1 = ~400 nm and λ_2 = ~500 nm **(d)** Spiropyran is opened using 320-350 nm irradiation. The back reaction merocyanine to spiropyran is mainly thermal but can be accelerated with 550-600 nm light. **(e)** Dithienylethene can be ring closed with λ_1 = ~250 nm and ring opened with λ_2 = ~400 nm.

Stilbenes (Fig 2a) are the classic photoswitch relying on double bond isomerisation. Stilbene populations are isomerised primarily in the *E*→*Z* direction under illumination with light of 300-350 nm (lower UV-A). The "back-isomerisation" to return the thermodynamic *E* isomer is more difficult to achieve. The thermal activation barrier is high, and there are several challenges involved in photoisomerisation. The *E* and *Z*-isomers' absorbances overlap, and the *Z*-isomer typically has smaller extinction coefficients (except around 250 nm), so that selective excitation of the *Z*-isomer is difficult. Even excitation at 250 nm only partially leads to the desired *Z*→*E* isomerisation, as it can also trigger a reversible intramolecular 6π electrocyclisation to dihydrophenanthrene, that can oxidise irreversibly to phenanthrene - so locking it in the cyclized state, and decreasing the stilbene's utility as a reversible photoswitch.[8] However, engineered stilbenes such as stiff-stilbenes and overcrowded alkenes have found many uses[9], most notably as molecular machines, recognized with the 2016 Nobel prize.[10] Alternatively, heteroarylstilbenes - most notably styrylbenzothiazoles (SBTs, Fig 2b) - have gained more attention as photoswitches in recent years. The SBT *E*→*Z* isomerisation wavelength is shifted usefully towards the visible (360-410 nm), and their metabolic stability makes them a good match for applications in cell biology.[11,12] Nevertheless, *Z*→*E* photoisomerisation remains a challenge requiring high energy UV-A light that can lead to 2+2 cycloadditions.

Hemithioindigos are very photostable photoswitches that are somewhat analogous to stilbenes, which have also emerged in recent years (HTIs, Fig 2c).[13] HTIs allow for visible light bulk photoisomerization in both directions (*E*→*Z* >400 nm, *Z*→*E* ~500 nm). Despite their

smaller overall geometric difference between their two isomers they have shown great promise in photopharmaceutical applications[14–16] as well as in molecular machines.[17] HTI-derived photoswitches that substitute the stilbenoid C=C double bond with heteroatoms, among them hydrazones[18] and iminothioindoxyls, are also reported.[19]

Spiropyrans (SPs, Fig 3d) open to form merocyanines (MCs) upon irradiation with UV light (320-350 nm). MCs are fromally heteroaryl stilbene, but their switching behaviour is however not solely based on the isomerisation of the double bond. Instead, the spiro C-O bond on the SP is cleaved by light irradiation and the *Z*-double bond isomerises thermally to give the *trans*-MC when no longer fixed in place. The closed SP form is thermodynamically more stable, and the MC relaxes back either thermally or with visible light (550-600 nm). The open and closed forms differ strongly in polarity due to the charge carried by the open form.[20] SPMC show significant photoinstability and are not very hydrolytically stable in water, but they are frequently used in material science[21] and have been developed towards imaging applications.[20]

6π-electrocyclisation processes are used in a separate category of photoswitches. The undesired 6π-electrocyclisation side reaction of stilbenes is harnessed as the switching mechanism of diarylethenes, using methyl substituents to block the irreversible oxidation. The most widely used aryl group is thiophene (DTE, Fig 3e), as it bears the smallest energy penalty for losing aromaticity upon cyclisation. The cyclisation of open-DTE to closed-DTE creates a larger conjugated π-system that greatly redshifts its absorption.[22,23] The small geometric change make diarylethenes ideal for applications in materials, and their high fatigue resistance[22] and strong electronic changes recommend them for use in memories.[22] Fulgides[24] and pyrenes[25] work along the same principles.

2.1.3 Azobenzenes

Azobenzenes are arguably the most thoroughly investigated photoswitch.[26] The azobenzene motif looks back on a long history. Discovered in the 1830s,[27] Hartley was the first to describe their light driven *E*→*Z* isomerisation, in 1937.[28] The two isomers vary not only in geometry, but also in e.g. dipole moment and total length - the *Z*-isomer has a dipole moment of 3 Debye[26] and a ~3.5 Å shorter end to end distance (Fig 3a) than the *E*-isomer (0 Debye).[29] Such differences between the two isomers can translated into changes of microscopic or macroscopic properties upon isomerisation; and indeed, azobenzenes have moved from their original uses as dyes towards application in neuroscience[7], chemical biology[26] and materials sciences.[30]

Azobenzenes (or azoheteroarenes) consist of two aryl rings that are connected by a diazene bridge. The diazene, rather than C=C bridge, gives azobenzene unique properties and advantages compared to stilbenes. For this thesis, the most important is that the diazene

substantially addresses the problems for *Z*→*E* photoisomerisation caused by spectral overlap of *Z*- and *E*-stilbene isomers. The difference of the two compound classes can be best understood when looking at the UV-spectra and the molecular orbital theory (MO) diagram depiction of the unsubstituted azobenzene (Fig 3).

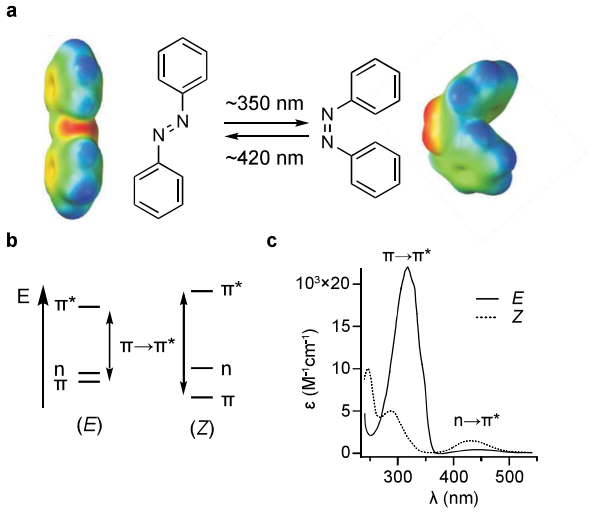

Figure 3: **(a)** Unsubstituted azobenzenes switches *E*→*Z* with ~350 nm light. The return *E*→*Z* isomerisation can be achieved with 420 nm light. The electron density distribution of azobenzene in *E* and *Z*-isomer showcases the different properties of the two isomers. Red areas indicate high electron density, blue low electron density. The *Z*-isomer has a higher dipole moment compared to the *E*-isomer and a lower end to end distance. **(b)** MO-scheme comparing both isomers. *E*-isomer hast lower π→π* distance and higher n→π* distance. The general position of orbitals on the energy scale is ca. between -2 to -6 eV. **(c)** UV/Vis spectrum of azobenzene in ethanol, showcasing the difference in absorbance between the two isomers. (adapted from Wooley and Beharry[26] and Hecht[31])

There are two distinct absorption bands in the UV-A to Vis region of azobenzene that are important to the isomerisation. The π→π* transition corresponds to the excitation of an electron in the binding π-orbital (HOMO-1) to its antibonding orbital. It has its absorption maximum at ~315 nm for the *E*-isomer and at ~280 nm for the *Z*-isomer. Due to the twisting of the two aryl rings out of plane by 56° in the *Z*-isomer, to avoid the steric clash between the *ortho* H atoms (similarly to stilbene), the planar and better-conjugated *E* isomer has stronger π→π* band intensity .[32,33] The n→π* transition is the excitation of an electron in a nonbonding orbital (n-orbital) that could also be described as a lone pair on the nitrogen, into the π*-orbital; this transition is unique to azobenzene. This transition is symmetry forbidden and thereby has lower intensity than the π→π*. The n→π* band for both isomers has its maximum around 440 nm but is generally bathochromically shifted for the *Z*-isomer, and it is distinctly stronger for the *Z* due to symmetry breaking. The combination of these two bands allows for the reversible photoisomerisation of azobenzene: since the π→π* band can be used to excite mainly the *E* isomer so giving a *Z*-rich population, and the n→π* band to excite mainly the *Z* isomer so giving an *E*-rich population. However, the spectral overlap, and the *E*→*Z* isomerisation in the UV-region, leave room for improvement (Fig 3b,c).

2.1.4 Controlling photochemical properties by substitution

In application as photoswitches, azobenzenes should influence their targeted environment differently depending on which isomeric state they are in. The superficially simple aim - to use *E*/*Z* isomers as "on" and "off" states on a single-molecule level - requires high efficiency of isomerisation to exert bulk on/off effects in practice. However, unsubstituted azobenzene in solution switches to only ~80% *Z*-isomer when irradiated with 340 nm light, and to ~70% *E*-isomer when irradiated with 440 nm light. Such ratios of isomers obtained under saturating illumination at a certain wavelength (i.e. at the equilibrium of photoisomerisation rates in each direction) are called photostationary states (PSS). PSS depend on the ratio of the extinction coefficients for the isomers, and the quantum yields of isomerisation. The efficiency and completeness of *E*⇄Z isomerisations are also limited in practical applications by other parameters. Azobenzene *Z*-isomers are typically metastable, so depending on the operating temperature and the energetic barrier between the two states, thermal relaxation to their *E* isomers must also be taken into consideration for their practical performance.[34] Even applying illumination to samples may be complex: absorption and scattering may prevent the precise administration of saturating light intensities; and not all environments tolerate irradiation, especially with UV light, without taking significant photodamage. Taken together, strategies to tune the isomers' absorption properties (and PSS), and the thermal half-life of the metastable isomer, are required in order to improve the completeness of control over azobenzene's performance as a photoswitch. The most straightforward is to modify the substitution pattern of an azobenzene, with the most effective modifications being *para* and *ortho* substitutions, since they communicate electronically most directly with the diazene bridge (Fig 4).[33–35]

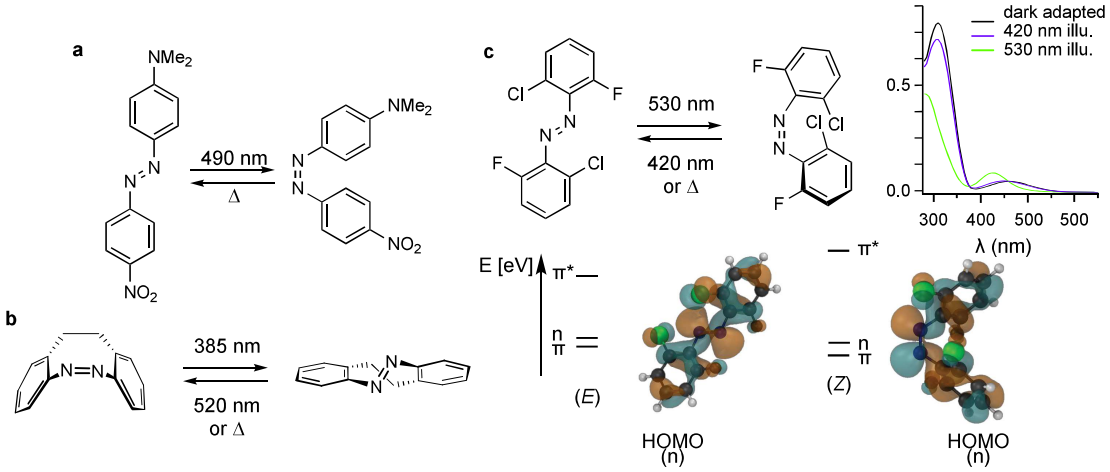

Figure 4: **(a)** A "push-pull" azobenzene with dimethylamine as the push substituent and a nitro group as the pull substituents. The π→π* band is shifted to ~500 nm, depending strongly on the solvent.[36] **(b)** Cyclic azobenzenes with inverse thermodynamic stability. **(c)** Tetra-*ortho*-subsitutued azobenzenes that can be photoisomerised with visible light and very good switching efficiency. The visible part of the spectrum shows the large separation particularly of the n→π* band for the two isomers. The *ortho* substitutions distort the geometry compared to parent

azobenzene, and lead to a change in MO-scheme structure that changes the photoproperties significantly. (Part of this figure was adapted from Konrad[37]).

A widely used strategy for shifting absorption maxima to lower energy is the substitution with an electron donating and an electron withdrawing group at opposing *para* positions ("push-pull"-azobenzenes; Fig 4a).[26] In these compounds the $\pi \rightarrow \pi^*$ gap is reduced compared to unsubstituted azobenzene. This allows for strong $\pi \rightarrow \pi^*$ excitation even towards 550 nm (*E* $\rightarrow$*Z*); however, the $\pi \rightarrow \pi^*$ absorption band now almost overlaps with the weaker $n \rightarrow \pi^*$, preventing selective *Z* $\rightarrow$ *E* photoisomerisation. The thermal isomerisation in the thermodynamically favoured direction of "push-pull" azobenzenes (typically *Z*$\rightarrow$*E*) is on the timescale of milliseconds to seconds.[38] This fast relaxation makes it difficult to know the ratio of *Z/E*-isomer actually established in a sample - usually it remains mostly *E*-isomer.[33,35]

An interesting strategy for red shifting the absorption bands without them overlapping was published by Herges *et al.*[39] Azobenzenes that are connected not only by the diazene bridge but also by a C2 linker in *ortho*-position display an extraordinary set of properties (Fig 4b). First, the strain of the 8-membered ring makes the *Z* isomer the thermodynamically more stable isomer, not *E*. Second, the cyclic diazene can be isomerised from *Z*$\rightarrow$*E* to a PSS of >90% *E* with 370-400 nm light, and back to the *Z*-isomer with 480-550 nm to a PSS of close to 100% *Z*. Modifications were published by Herges *et al.*[40] and Woolley *et al.*[41] The efficient synthesis published by Trauner *et al.* gave the opportunity to investigate this scaffold more deeply and tune the photoproperties with different substituents.[42] However, low extinction coefficients and slow isomerisation make the cyclic azobenzene scaffold difficult to apply.

As seen in the cyclic azobenzenes, *ortho* substitutions can change not only the electronic structure, but also the geometric orientation of the two aryl rings relative to each other. Tetra-*ortho*-alkyl substitution was first reported by Zerner *et al.*[43] The concept was investigated further by Woolley *et al.* who introduced tetra-*ortho*-methoxy substitution.[44] The steric and electronic repulsion surrounding the diazene manifests itself in substantial changes in photoproperties. The isomerisation in both directions can be entirely driven by excitation of the $n \rightarrow \pi^*$ transition, as this absorption band is well separated between the two isomers.

For the *E*-isomer of tetra-*ortho*-methoxy azobenzenes the $n \rightarrow \pi^*$ band is redshifted compared to unsubstituted azobenzenes: typically, switching *E*$\rightarrow$Z with ~530 nm light reaches a PSS of 80% *Z*.[44] This red-shifting is most likely due to a destabilization of the n-orbital by the electronic repulsion between the free electron pairs on the oxygen of the methoxy groups and on the diazene bridge.[31,44,45] In the *Z*-isomer the repulsion is reduced and the $n \rightarrow \pi^*$ transition is blue shifted due to the decrease in destabilisation of the n-orbital: thus the *Z*-isomer is converted from *Z*$\rightarrow$*E* with ~440 nm irradiation giving a PSS of 85% *E*-isomer.[44] . Because of the steric constriction around the diazenes the energetic barrier for *Z*$\rightarrow$*E*

isomerisation is significantly elevated and tetra-*ortho*-methoxy azobenzenes show half-lives of hours to days.[44,46]

The approach separating the n→π* between the isomers was developed further by Hecht *et al.*[31] reporting the tetra-*ortho*-fluoro substitution pattern. The fluoro substituents lead to an even further separation of the n→π* transitions of the two isomers. In the *E*-isomer the smaller distortion caused by tetra-*ortho*-fluoro substitution compared to tetra-*ortho*-methoxy substitution leads to a comparative stabilisation of the π*-orbital. That leads to a bathochromic shift in the n→π* transition. The distortion in *Z*-isomer on the other hand remains high and the π*-orbital is destabilised - blueshifting the n→π* absorption band. With substituted tetra-*ortho*-fluoro azobenzenes a very high bidirectional switching completeness of up to 97% for Z→E and 90% for *E*→*Z* can be obtained. *Z*-tetra-*ortho*-fluoro azobenzenes are exceptionally stable with thermal half-lives of up to 2 years at ambient temperature in DMSO.[47] Mixed fluoro/chloro tetra-*ortho*-substitution introduced by Konrad *et al.* have shown exceptional band separation and MO profile similar to tetrafluoro substitution (Fig 4c).[37]

Other tetra-*ortho*-substitution patterns that were investigated include tetra-*ortho*-chloro,[46] tetra-*ortho*-bromo[46] and tetra-*ortho*-thio[48] substituted azobenzenes. These derivatives showed similar properties as their lighter analogues.

Chapter 6 will present a new synthetic method for azobenzene tetra-*ortho*-alkoxylation.

2.1.5 Indirect photoswitching of azobenzenes

Azobenzenes as photoswitches need to combine many different properties. As discussed above they need certain photoproperties (switching yield, addressable by a suitable wavelength, tuned half-life etc.) but they also need to act on their environment in a way that fits the requirements of the system (fit to a protein binding site, metabolic stability, solubility etc.). A modular approach, that splits these two sets of features into "activity" and "photoproperties" components that can be installed separately into an overall structure, could improve the practicality of azobenzene-based photocontrol. A conceptually simple idea could be to combine an azobenzene as the "active" component with a different light absorbing motif to control photoproperties; however, a typical energy transfer from a light absorbing motif to azobenzene would require the absorbing motif to absorb light at a higher energy wavelength than typical photoisomerisation energies for the azobenezene, which is not desirable.

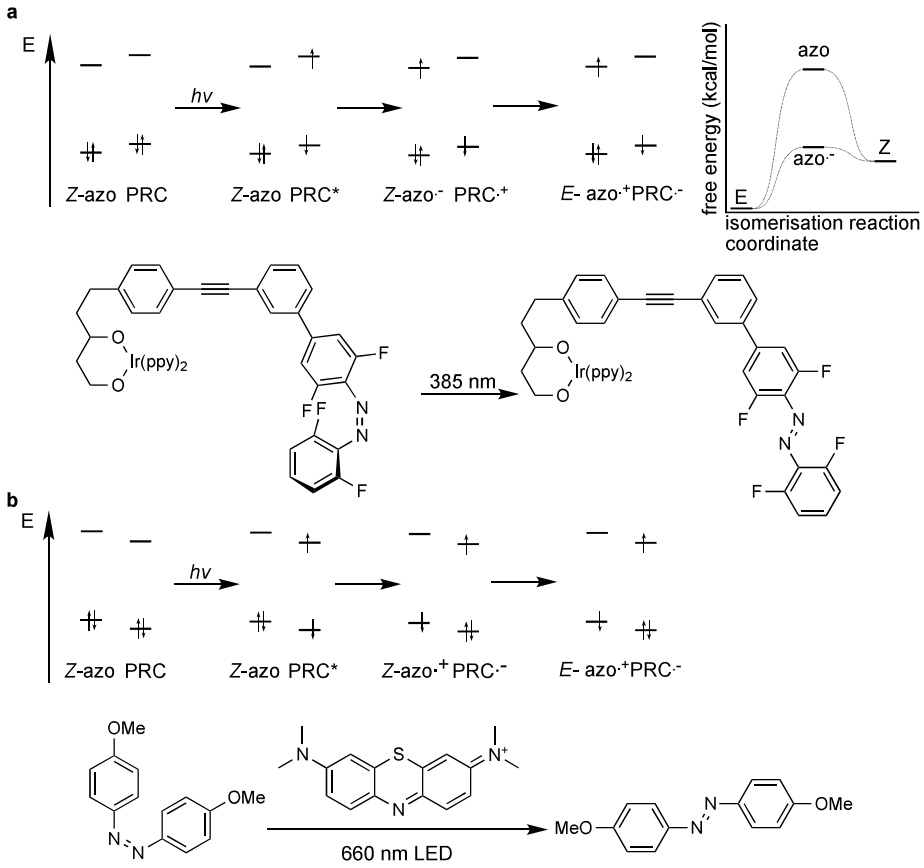

Figure 5: **(a)** The photoredox catalyst (PRC) is excited. The excited electron is transferred to the *Z*-azobenzene and a *Z*-azobenzene radical anion is formed. The energy barrier for the isomerization to the *E*-isomer is drastically reduced by the reduction and the radical anion isomerizes. An example is the Ir-complex tetra-*ortho*-fluoro conjugate (ppy = 2-phenylpyridine). **(b)** The PRC is excited and the *Z*-azobenzene transfers an electron into the hole left by the excited electron. A *Z*-azobenzene radical cation is formed. The radical cation rapidly isomerizes to the *E*-isomer. An example is the combination of 4,4'-methoxy azobenzene and methylene blue.

At the end of the 1970s it was discovered that azobenzene can be electrochemically *Z*→*E* isomerised by reduction.[49,50] Hecht *et al*. elaborated on that discovery by systematically investigating isomerisation by electrochemical reduction.[51] The reduction of *Z*-azobenzene to the radical anion of azobenzene leads to a decrease of the double bond character in the diazene and rapid relaxation to the more stable *E*-isomer, followed by radical recombination or oxidation back to the uncharged, *E*-azobenzene. The mechanism allows the isomerisation to be triggered catalytically and leads to quantitative isomerisation – something that cannot be achieved for azobenzenes with light. However the process is highly sensitive to oxygen.[50]

An electric current is not the only source of electrons that can be used for this process. Hecht *et al*. published a tetra-*ortho*-fluoro azobenzene that is covalently attached to a ligand that coordinates a photoredox active Ir^{III}-complex. The excited state oxidation potential of the iridium complex is sufficient to reduce the azobenzene, allowing for isomerisation to the *E*-isomer when the complex is irradiated with 380 nm, where the iridium complex (as well as the azobenzene) absorbs. However, when the authors compared the PSS of the complex with the

PSS of the pure azobenzene they observed significantly improved switching yield. A drawback of the switching mechanism is its sensitivity. The reduction mechanism can go via a triplet state that is quenched by oxygen and photobleaches the iridium complex (Fig. 5a).[52]

Durandin *et al.* published a modular approach towards switching based on triplet sensitisation by a palladium porphyrin complex in non-covalent mixtures with azobenzenes. Upon excitation the porphyrin complex functions as a triplet sensitizer and can isomerise the azobenzene from *Z*→*E*. The complex has an absorption peak at 712 nm and can be excited up to ~750 nm; whereas azobenzenes allowing direct excitation in this region could not yet be used for photoswitching applications due to their very short thermal half-lives. Triplet sensitization leads to a photostationary state so the switching is not quantitative as for the redox pathway.[53] Another triplet sensitization approach published by Durandin *et al.* utilizes the combination of iodine and oxygen for isomerisation.[54]

A cationic redox pathway towards *Z*→*E* isomerisation can also be envisaged. To address the light triggered oxidation of *Z*-azobenzenes, the catalyst's excited state reduction potential must match the oxidation potential of the azobenzenes. Hecht *et al.* investigated methylene blue as photocatalyst and found that when the oxidation potentials of azobenzene and dye match, the yield of photoisomerisation is 100% *E* isomer. Quantum yields >1 indicate that the isomerisation by oxidation must be catalytic. The methylene blue is excited with 660 nm. The excitation leaves a hole in the ground state that is filled by oxidation of the azobenzene. The resulting *Z*-azobenzene radical cation rapidly isomerises to the *E*-isomer and is reduced by another azobenzene, propagating the reaction (Fig 5b). The cationic mechanism does not seem to be influenced by the presence of oxygen, however methylene blue does generate singlet oxygen and degrades under illumination.[55] This completeness of isomerisation that can be obtained via photoredox chemistry is difficult to obtain by other methods.

2.2 Using light to control biology

2.2.1 Photopharmacology

The field of photopharmacology uses small molecule photoswitches to control biological systems. Most photopharmaceuticals are targeted towards a specific protein of interest (POI). Upon irradiation such photopharmaceuticals should undergo a geometric or electronic change that influences the interaction between protein and molecule: e.g. the affinity to a binding site increases significantly; and it should subsequently be possible to decrease the affinity again by returning to the previous state, either by irradiation or thermal relaxation (Fig 6).[56]

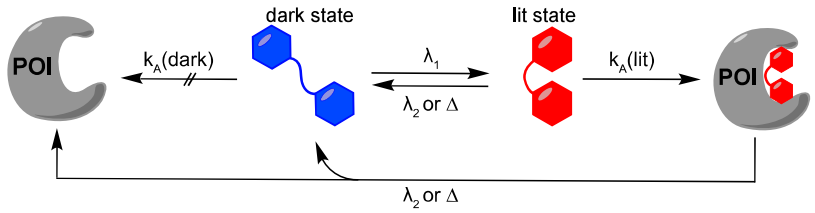

Figure 6: Schematic example of a lit active photoswitch. The dark state does not bind the POI. However, upon irradiation with λ_1 the binding affinity increases. The photoswitch binds the POI. Thermal relaxation or irradiation with λ_2 leads to the release of the photopharmaceutical from the binding site. For the repeated binding the photoswitch needs to be irradiated again with λ_1.

Photopharmacology has expanded massively in recent years to address many new systems - including ion channels and GPCRs,[7] the cytoskeleton,[57,58] antibiotics,[59] lipid membranes[60] etc. The photoswitchable scaffold most used in photopharmacology is azobenzene, due to its strong geometric change that can change its interaction with a binding pocket. However, designing an effective photopharmaceutical is a non-trivial challenge.

Generally, a known ligand for the desired target is chosen and modified to be photoswitchable. Popular strategies include “azologisation”, “azoextension” or controlling the linker structure by incorporation of an azobenzene. Azologisation incorporates the azobenzene structure into the inherent structure of the chosen ligand. Structural motifs that can be substituted with an azobenzenes include stilbenes, *N*-phenyl benzamides, benzyl phenyl ethers, benzyl anilines or biaryls etc.[61] Azoextension on the other hand is based more on identifying a suitable attachment site for the azobenzene by identifying a position in the binding site that would tolerate the addition but still reacts to the difference in geometry or dipole moment upon isomerisation.

As examples, both approaches were demonstrated on the appetite suppressant Rimonabant® by Decker *et al.*[62] The authors incorporated an azobenzene in *Z*-geometry as a near isostere to a biaryl or extended the azobenzene from a tolerant side chain. In this example the higher binding difference between the isomers was reported for the compound obtained by azoextension (Fig 7).

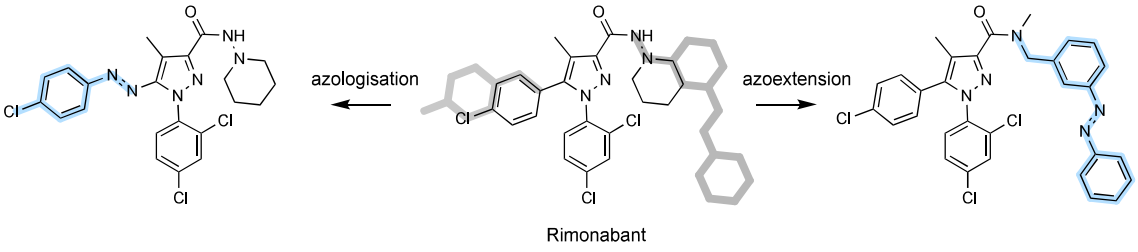

Figure 7: Different strategies for making Rimonabant photoswitchable. In the azologisation strategy the biaryl is converted to an azobenzene. In the azoextension approach an azobenzene is extended off the amide.

A different setup for photocontrol was demonstrated by Trauner *et al.* for an ionotropic glutamate receptor. A glutamate ligand was covalently tethered to the receptor *via* a linker, which was modified with an azobenzene. When isomerised to the *E*-isomer the linker was

shortened and the glutamate could no longer bind the receptor.[63,64] A mixed approach combining linker based photopharmacology and binding affinity switching was also used for photoswitching the activity of PROTACs.[65,66]

2.2.2 Microtubules and photopharmacology

The microtubule (MT) cytoskeleton is a particularly rewarding target for photopharmaceutical control. MTs are involved in a wide variety of different cell functions. They are crucial for cell motility and intracellular transport. Their central role in cell division makes them a prominent target for cancer therapy. However, because of their many different and survival-critical roles it is difficult to inhibit MTs with small molecule drugs without doing significant damage to the complete cell and generating complex cellular effects that cannot be understood in terms of single MT-dependent circuits. Photopharmaceuticals can address this problem by being spatiotemporally targetable and minimising unwanted overall toxicity.

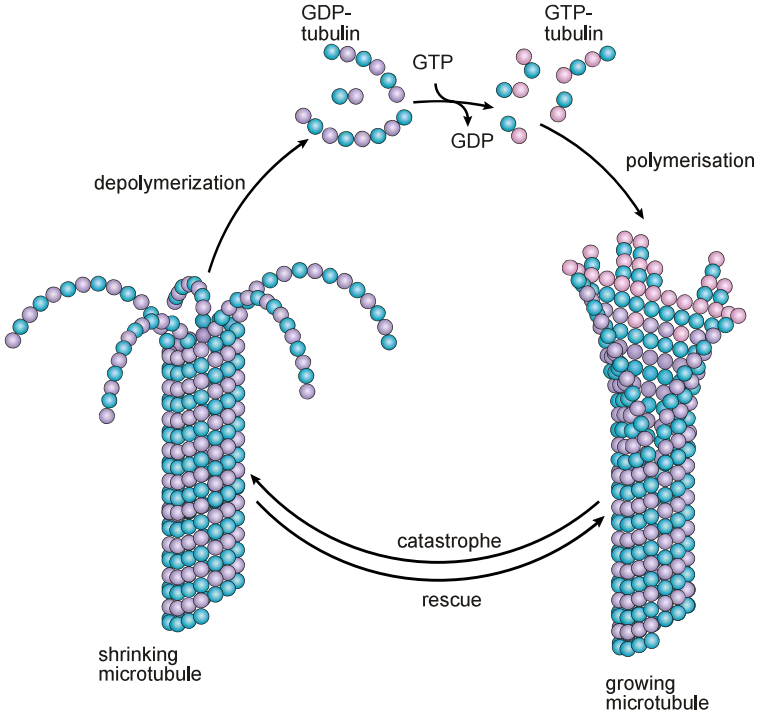

Figure 8: Schematic representation of the growing and shrinking of a MT. From the top: Tubulin monomers build from α-subunit (blue sphere) and GDP bound β-subunit (purple spheres) exchange the GDP for GTP at the β-subunit (pink sphere). The tubulin can then be incorporated into the MT. In the MT the GTP is hydrolysed. When hydrolysis reaches the tip of the MT the MT starts to shrink (catastrophe). The shrinking can be reversed (rescue). MT dynamics are dependent on many different factors (figure is adapted from Steinmetz[67]).

MTs are dynamic polymer structures (Fig 8) that are comprised of tubulin monomers - a dimeric protein that is built from an α and a β-tubulin subunit. Each subunit has a GTP binding site but only the GTP on β-tubulin can be hydrolysed to GDP. Tubulin monomers polymerise by aligning in a head-to-tail fashion into single stranded protofilaments; these assemble in

parallel forming a MT as a ca. 25 nm diameter hollow tube, usually of 13 protofilaments.[68] The lateral interactions between the protofilaments stabilise the MT tube.[69]

MTs are polarized structures; the two ends are differentiated into a growing *plus* (+) and a slower growing/shrinking *minus* (-) end. At the growing end of the tube new tubulin monomers are attached, which involves a whole machinery of accessory proteins.[70] Only monomers in which both subunits are bound to GTP can be incorporated into a MT, since only in the GTP-bound state is the tubulin dimer straight and capable of forming stable lateral contacts. When incorporated into the MT, the β-subunit GTP slowly hydrolyses to GDP.[71] The lateral contacts stay intact as long the tubulin dimer is surrounded by other tubulin units.[72] However, if hydrolysis occurs up to the (+)-end, the MT can start to disintegrate rapidly. This process is termed catastrophe; its stoppage and the restarting of MT polymerisation is termed rescue (Fig. 8).

MT dynamics are controlled by a complex interplay of regulatory proteins,[71] posttranslational modifications,[68] and local GTP-monomer concentration. The delicate balance of polymerisation and depolymerisation can be strongly influenced with small molecule inhibitors. These inhibitors are generally grouped into microtubule destabilisers and microtubule stabiliser.[73]

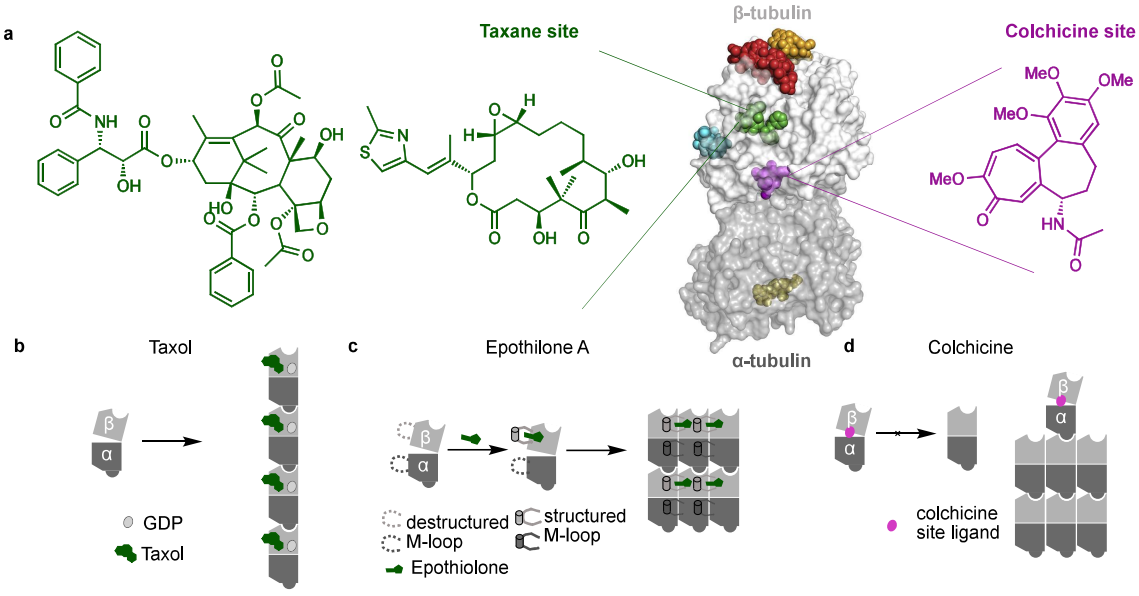

Figure 9: **(a)** The taxane binding site is located on β-tubulin (green). Two well-known taxane site binders are taxol, and the epothilones. All taxane site binders are microtubule stabilising agents. Colchicine - a microtubule destabiliser - has its own binding site at the interface between α and β tubulin (purple). Other binding sites are color coded: maytansine site (orange), vinca site (red), laulimalide site (blue), pironetin site (yellow). **(b)** Taxol strengthens the longitudinal tubulin contacts along protofilaments so much that it can even cause GDP-bound tubulin to polymerise into MTs. **(c)** Epothilone A structures the tubulin M-loop into a short helix, which strengthens the lateral contracts between protofilaments, so stabilizing MTs by a different mechanism. **(d)** The colchicine binding site is located at the interface between α and β tubulin. Colchicine binders inhibit the curved to straight transition of tubulin, so that incorporation of a tubulin monomer that is bound by a colchicine site ligand inhibits the further growth of MTs (parts of the figure are adapted from Steinmetz[67]).

The structurally diverse group of colchicine site binders are all microtubule destabilisers. The binding site is named after the toxic natural product colchicine that can be isolated from the autumn crocus *Colchicum autumnale*. The binding site is at the interface between the α and the β tubulin subunits. A binder prevents the straightening of tubulin that is needed for good lateral interactions to stabilise the MT, and curves the MT tip: which slows or stops its further polymerisation (i.e. the addition of new tubulin monomers) (Fig 9b).[67]

The most famous microtubule binding agent is probably the MT stabiliser paclitaxel (Taxol). This highly complex natural product was isolated in 1971[74] after discovering the high toxicity of plant extracts collected from the pacific yew *Taxus brevifolia* in the mid 1960s.[75] In the following years its mode of action was elucidated by Horwitz *et al.*[76] and in December 1992 paclitaxel was approved by the FDA for use in ovarian cancer.[77]

The binding site for taxol is on the luminal face of the MT at the β-subunit. The Taxol binding site is a versatile binding site: on the binder, MTs are stabilized by different mechanisms. Paclitaxel binding seems to have an influence of the curvature of tubulin protofilaments, by straightening them even in the GDP bound state (Fig 9b).[78] Other Taxol site binders like epothilone A stabilise the adjacent M-loop, increasing lateral stabilisation within MTs, again in a GDP/GTP-independent manner (Fig 9c).[67]

Small molecule MT inhibitors play crucial roles as clinical therapeutics[67,79,80] and contribute broadly as tools for cytoskeleton studies and cell biology.[81] However, their high toxicity can hamper the use of MT-targeting agents as research reagents.[82,83] To cleanly study a dynamic anisotropic system, dynamic tools that can be spatio-temporally controlled are needed.

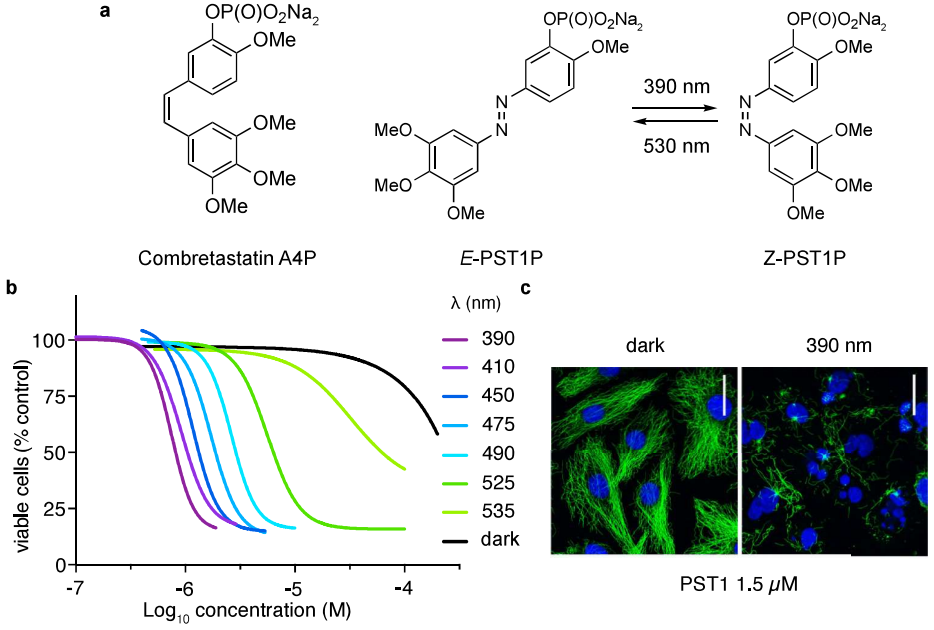

Figure 10: **(a)** PST1P is modelled after combretastatin CA4P that is only active as its *Z*-isomer. PST1P isomerizes *E*→*Z* with 390 nm (90% *Z*) and *Z*→*E* with 530 nm (85% *E*). **(b)** Antiproliferation assay dose response curves as a function of the wavelength of irradiation, in HeLa cells. Wavelengths with highest *E*→*Z* conversions (eg 390 nm) give the highest antiproliferative activity. **(c)** Immunofluorescence staining of HeLa cells treated with

PST1 shows its light-dependent influence on the MT cytoskeleton, as cells irradiated with 390 nm light show only residual MTs and have multiple nuclei (MTs in green; nuclei in blue; Figure adapted from Trauner and Thorn-Seshold[57]).

There are several approaches to increase the spatiotemporal precision of control over MT structure and function.[84,85] Trauner and Thorn-Seshold *et al*. published the photoswitchable MT depolymerising agent (PST1) derived from CA4 – a colchicine site binder. By substituting the CA4 stilbene core with the isosteric azobenzene the authors created a photoswitchable CA4 analogue. PST1 was phosphorylated for solubility (PST1P) (Fig. 10a). The *Z*-PST was > 200-fold more potent than its *E*-isomer in antiproliferation assays, and wavelengths could be varied to tune the toxic effect: demonstrating its dependence on the isomeric ratio at PSS (Fig. 10b). PST1P could be used as a non-invasive, reversible tool compound that controls MT structure (Fig. 10c) and MT dynamics with cellular resolution.[57] PST1P was then applied across a range of animal models; e.g. Plachta *et al.* used PST1P to investigate the organisation of MTs in early mouse embryos;[86] and several other photoswitchable colchicine site binders have since emerged.[12,16] Photocontrollable microtubule stabilisers had, however, remained unexplored; and even though several groups have published photocaged paclitaxels, the compounds suffered from low solubility[87,88] and after 2003 they were removed from the market by their manufacturer Molecular Probes.[89]

Chapter 5 will present research into the first photoswitchable microtubule stabilisers.

2.3 Using light to control photoswitchable lipid membranes

2.3.1 Membranes and Lipids

The cell membrane is integral to all life. It surrounds cells, defining their borders and maintaining chemical gradients against the extracellular environment. Inside eukaryotic cells, compartmentalisation by internal lipid membranes is used to regulate cell functions and localise cellular machineries - approximately 30% of cellular proteins are membrane-associated.

Biological membranes are typically bilayers of amphiphilic lipids that have hydrophilic head groups and hydrophobic tails. The most abundant membrane lipids are phospholipids, having a phosphate in combination with a choline or serine as the polar head group. The hydrophobic tails are mostly saturated or unsaturated fatty acid chains with chain length between 14-24 carbons. The polar and unpolar parts of lipids are connected by either glycerol or sphingosine (Fig 11b). Lipids self-organise into bilayers in aqueous environments, with the hydrophobic tails oriented towards themselves and the polar headgroups presented to the aqueous surrounding (Fig 11a).[90]

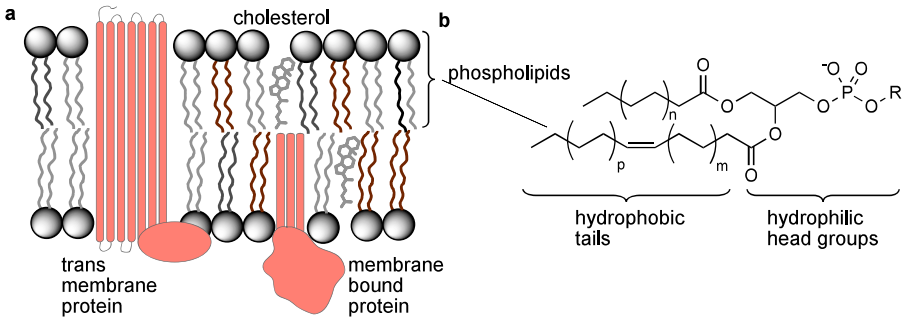

Figure 11: **(a)** Schematic view of a biological lipid membrane. The membrane is a bilayer of amphiphilic lipid molecules that present their polar headgroup to the aqueous surrounding while their fatty acid tails are oriented towards each other. The two other major components of biological membranes are proteins – that can either span the membrane or just be localized to it – and cholesterol, which influences the properties of a membrane. **(b)** Phospholipids and glycolipids are the most common groups of lipids; a phospholipid was chosen as an example. The saturated and unsaturated fatty acids have a chain length between C14-24 (n,m,p ≈ 0-10). A fatty acid can contain more than one double bond. There is a wide variety of fatty acid combinations. The hydrophilic head group is a phosphate in combination with mostly a choline or serine (R: choline, serine, ethanolamine, glycoside etc.)

The properties of the membrane have strong influence on the function of the membrane proteins.[91] Many factors contribute to properties of the lipid bilayer, eg. additives like cholesterol or the abundance of fatty acid tails with various degrees of saturation. Cellular membranes are also diverse and dynamic structures, and local compositions may not reflect the overall composition of the membrane.[92]

Dynamically controlling the properties of cellular membranes remains a challenge, since most reagents induce permanent or slowly-reversible changes in properties. However, lipids modified with azobenzenes have been valuable tools in reversibly controlling membrane properties by light irradiation.[93,94]

2.3.2 Photoswitchable lipids in application

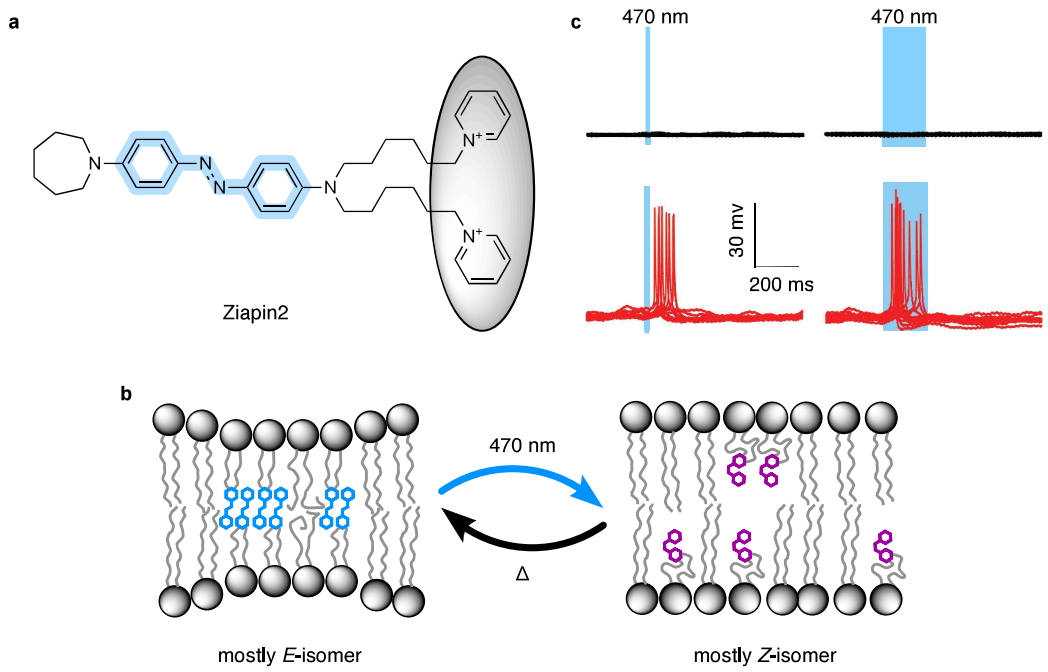

Figure 12: **(a)** Ziapin2, an artificial lipid mimic with two pyridinum rings as polar head groups and a diamino azobeneze as the fatty acid equivalent. **(b)** In the *E*-isomer, azobenzenes anchored in opposing leaflets dimerize. This dimerization pulls the pyridinium head groups closer together leading to thinner membranes in areas that contain *E*-Ziapin2. When irradiated with 470 nm light the azobenzenes isomerize to the *Z*-isomer, that no longer dimerizes, and membrane thickness returns to standard value. Thermal relaxation returns the azobenzene groups to the *E*-isomer. **(c)** Action potential recordings from primary hippocampal neurons silenced with synaptic blockers and optionally treated with Ziapin2, under controlled irradiation with 470 nm light (blue squares). Light alone does not trigger action potentials (black curves). With Ziapin2, action potentials fire upon irradiation (red curves).

Photoswitchable membrane dopants have been used to control several biological responses, including neuronal cell firing. Lanzani *et al*.[95] published Ziapin2 – a short lipid-like azobenzene derivative attached to two pyridinium cations that function as a polar head group (Fig. 11a). Due to the double *para*-amino substitution, the azobenzene can be isomerized from the *E* to the *Z* isomer with 470 nm light. The authors observed an increase of membrane capacitance upon incorporation of Ziapin2 into a membrane. They attribute the change to dimerization of *E*-azobenzenes that are anchored in the opposing leaflets of the membrane, by π-stacking. Being shorter than conventional lipids, stacking pulls the polar headgroups closer together than in typical membranes, with the positive charge of the Ziapin2 headgroup entraining the negatively charged phosphates in the surrounding membrane and locally thinning it. When isomerised to the *Z*-isomer the stacking is interrupted, and the membranes return to their native thickness (Fig 11b). The light impulses were used to control the firing rate of primary hippocampal neurons with light, presumably due to VGIC (voltage gated ion channels) triggered by the capacitance change associated with changes in membrane thickness. The neurons were first silenced with synaptic blockers and then reactivated by irradiation with 470 nm light, leading to rapid successions of action potentials (Fig 11c).[95]

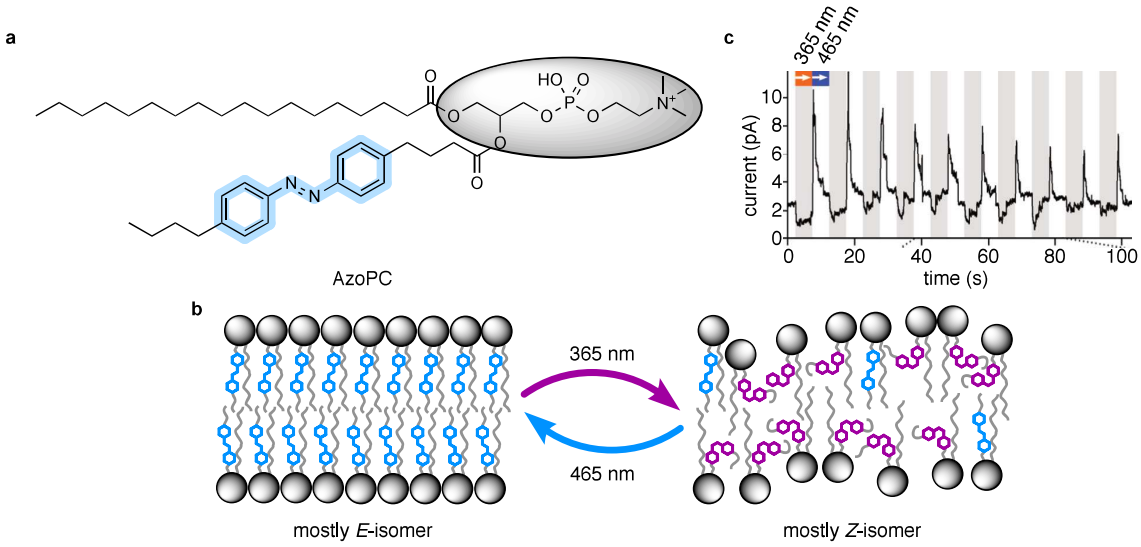

Figure 13: **(a)** AzoPC is based on phosphatidylcholine, with one lipid tail substituted by a modified azobenzene. **(b)** In the mostly-*E* conformation the membrane is more ordered. Upon irradiation with 365 nm the azobenzene isomerizes to mostly-*Z*. This mimics the effect of unsaturated lipids with a *Z*-double bond: the membrane becomes less ordered, and head to head distances shrink. **(c)** In a patch clamp set-up an azoPC membrane was constructed between two electrodes and the absolute current across the membrane was measured. The discreet stepwise change in current indicates that the observed absolute current is a combination of displacement and ion currents. Upon switching from the mostly *Z*-state to the mostly *E*-state a sharp increase in current was observed. The authors claim that the sharp onset of ion currents is due to transient pore formation caused by a reorganisation of the membrane during the switch from a photolipid conformation with larger to a smaller area cross section. The readout is repeatable over several cycles.

Artificial membranes have been valuable tools in investigating the influence of membranes on protein function.[96] Amphiphilic azobenzene derivatives form relatively stable aggregates in water[97] but generally have to be incorporated into an existing membrane.[98] However, AzoPC, a compound published by Trauner *et al.*,[99] has been used extensively to form membrane vesicles that can be manipulated in many of their key properties. AzoPC is a phosphatidylcholine lipid with one of the lipid tails modified with an azobenzene (Fig 13a). The *E*→*Z* isomerisation decreases the order of packing in the membrane. The reversibly introduced *Z*-double bond acts similarly to an unsaturated hydrocarbon chain in the changes it brings to the properties of the membrane.[100] Photoisomerisation not only controls membrane thickness, but it also allows for light activated pore formation (Fig. 13b), and the sudden increase in permeability can trigger an electric signal in artificial membrane setups (Fig 13c).[101] Other interesting properties have been investigated eg. fluidity,[100] budding[99] and phase transitions.[60] However, the incomplete switching of AzoPC, and its need for isomerisation in the UV (365 nm) and blue (465 nm) can limit the range of control in many applications.

Chapter 7 will present research into the nature of AzoPC membrane switching, including a role for redox-based switching related to the mechanisms discussed in section 2.1.5.

3 Aims of this thesis

Azobenzenes have been the most-used photoswitch in photopharmacology for many years. Their reversible switching, their synthetic accessibility, and their tuneable properties make azobenzenes a versatile option. Their rapidly reversible switching allows for the control of highly dynamic and sensitive systems (chapter 1.2) and their lipophilicity makes them well suited for applications targeted at membranes and membrane bound proteins (chapter 1.3). The aims of this thesis are to find ways of improving azobenzenes as tools in chemical biology: either by developing new synthetic routes, or by elaborating on alternative switching mechanisms, and towards harnessing these discoveries in applications that most benefit from the use of photoswitchable tools.

(1) The microtubule skeleton is a dynamic system that is difficult to address with conventional small molecule probes. Photoswitchable microtubule disrupting agents have proven to be powerful research tools.[86] However, photoswitchable microtubule stabilisers, that offer alternative biological activity and which could potentially *facilitate* rather than block processes relying on stable microtubules, have not yet been addressed. I develop the first photoswitchable MT stabilizing agent (MSA), **AzTax** (chapter 5).

(2) The azobenzene scaffold is used in a plethora of applications, but it still struggles with many shortcomings. In biological applications, for example, its relative metabolic instability, its switching wavelengths that lie outside the biological transparency window, and its incomplete photoswitching are all major problems. Tetra-*ortho*-substitution has opened new perspectives for near-complete bidirectional all-visible light switching. However, the steric constriction around the diazene make them synthetically more difficult to access, and the absence of convenient late-stage synthetic methods hinders investigation. Therefore, I have pursued the development of new synthetic methods to broaden their applications (chapter 6).

(3) Lipid membranes are the most common barriers used for maintaining gradients, localising species and compartmentalising processes, and photoswitchable artificial lipid membranes are important tools for investigating membrane physical properties. Small angle X-ray scattering (SAXS) is a technique to measure changes in membrane thickness; we calibrate these changes against azobenzene isomerisation, then use SAXS to study in-membrane azobenzene isomerization (chapter 7).

These aims are detailed in the following chapters.

4 Author contributions

Over the course of my PhD research, I have been in exchange with many people. With some of them I had the good fortune to collaborate in a way that led to publishable results; with others I have exchanged ideas and discussed progress. I am deeply grateful to all of them, since almost no scientific result can be reached alone. In this paragraph I identify the tasks that were explicitly done be me, so as to not take away credit that is due to all the wonderful people I have worked with.

4.1.1 Chapter 5: Photoswitchable taxane

I designed the synthesis and prepared all the iterations of azobenzenes as well as their water-soluble derivatives for photoswitching. I synthesized or resynthesized the AzTax compounds, and performed the photocharacterizations and chemical data assembly. I contributed to the manuscript preparation - mainly written by Oliver Thorn-Seshold.

4.1.2 Chapter 6: Exhaustive azobenzene *ortho*-alkoxylation

I optimized the method and developed the screening method. I prepared all starting materials and synthesised all final compounds. I designed the lipophilicity study and performed photocharacterization of all compounds. I assembled all data and contributed to the manuscript preparation - mainly written by Oliver Thorn-Seshold.

4.1.3 Chapter 7: AzoPC membrane studies

I performed the resynthesis of AzoPC and synthesis of FAzoM. I designed the concept for the UVVis/HPLC/SAXS calibration of Z/E ratio measurements, performed the measurements of calibration curves and calculations.

5 The first photoswitchable tool for microtubule stabilization

In the following work we rationally designed, tested and demonstrated the utility of the first ever reported photoswitchable microtubule stabilizer. Our probe allows for precise spatio-temporal control of microtubule dynamics while retaining microtubule density.

We chose paclitaxel as the inhibitor scaffold for our probes. The highly complex natural product shows enough flexibility in SAR studies to allow for modification with an azobenzene in certain positions. Among them, the benzamide in the sidechain 3'-position can be substituted with hydrophobic residues, however, the binding site is still well enough defined that isomerization might lead to a difference in binding affinity.

For ease of synthesis, we started from docetaxel, where the 3'-nitrogen is Boc protected, and can be deprotected and acylated following established procedures. We prepared a set of AzTax, docetaxel derivatives acylated with azobenzenes. The orientation of azobenzene was varied by permutating the position of the amide relative to the diazene bridge, and the substitution pattern of the distal ring was also varied. The derivatives were tested for light-dependant antiproliferative activity against HeLa cells, with the difference between the toxicity under illumination and that without light used as the most important metric for selecting a lead for further investigation. The toxicity of most AzTax compounds was indeed light-dependant, with the *Z*-isomers typically more toxic than the *E*-isomers (a useful situation, as bioactivity can be "photoswitched on" by selectively illuminating less active, thermodynamically stable *E*-isomer); **AzTax3MP** was identified as the most promising structure.

To test if **AzTax3MP** retains the mode of action of docetaxel we characterised its light-dependant effects on MTs *in vitro* and *in cellulo*. Immunofluorescence staining showed the light-dependent interruption of mitosis, with cells treated under 360 nm featuring multiple nuclei and an arrested spindle apparatus. FACS cell cycle analysis supported this qualitative analysis by quantifying light-dependent G2/M arrest.

In live cells **AzTax3MP** could be used to control microtubule dynamics with high spatio-temporal resolution. Single cell spatial resolution was obtained by precise irradiation with a 405 nm laser, and the disruption of the microtubule dynamics could be repeated several times. The residual toxicity of *E*-**AzTax3MP** was minimal; only a small reduction in microtubule velocity, and none in microtubule density, were observed.

Light as a stimulus provides excellent temporal control and can easily be applied. However, the greater challenge for small molecule photopharmacology is to provide subcellular spatial resolution, as intracellular diffusion counteracts photoactivations within subcellular areas. We investigated **AzTax3MP** in hippocampal neurons cells, where cell shape probably limits diffusion; they allowed for very precise control of the MT dynamics in specified dendrites.

AzTax3MP is a first in class reagent for photoswitching-based control over microtubule stabilization, and its subcellular resolution of blocking MT dynamics is outstanding for a small molecule probe. Its spatiotemporal precision may provide access to new insights into the role of the cytoskeleton in cellular transport mechanisms.

nature COMMUNICATIONS

ARTICLE

https://doi.org/10.1038/s41467-020-18389-6 OPEN

Photoswitchable paclitaxel-based microtubule stabilisers allow optical control over the microtubule cytoskeleton

Adrian Müller-Deku[1], Joyce C. M. Meiring[2], Kristina Loy[1], Yvonne Kraus[1], Constanze Heise[1], Rebekkah Bingham[1], Klara I. Jansen[2], Xiaoyi Qu[3], Francesca Bartolini[3], Lukas C. Kapitein[2], Anna Akhmanova[2], Julia Ahlfeld[1], Dirk Trauner[4,5] & Oliver Thorn-Seshold[1,5]✉

Small molecule inhibitors are prime reagents for studies in microtubule cytoskeleton research, being applicable across a range of biological models and not requiring genetic engineering. However, traditional chemical inhibitors cannot be experimentally applied with spatiotemporal precision suiting the length and time scales inherent to microtubule-dependent cellular processes. We have synthesised photoswitchable paclitaxel-based microtubule stabilisers, whose binding is induced by photoisomerisation to their metastable state. Photoisomerising these reagents in living cells allows optical control over microtubule network integrity and dynamics, cell division and survival, with biological response on the timescale of seconds and spatial precision to the level of individual cells within a population. In primary neurons, they enable regulation of microtubule dynamics resolved to subcellular regions within individual neurites. These azobenzene-based microtubule stabilisers thus enable non-invasive, spatiotemporally precise modulation of the microtubule cytoskeleton in living cells, and promise new possibilities for studying intracellular transport, cell motility, and neuronal physiology.

[1] Department of Pharmacy, Ludwig-Maximilians University, Butenandtstrasse 5-13, Munich 81377, Germany. [2] Cell Biology, Neurobiology and Biophysics, Department of Biology, Faculty of Science, Utrecht University, Padualaan 8, 3584 Utrecht, The Netherlands. [3] Department of Pathology & Cell Biology, Columbia University Medical Center, New York, NY 10032, USA. [4] Department of Chemistry, New York University, 100 Washington Square East, New York, NY 10003, USA. [5] These authors jointly supervised this work: Dirk Trauner, Oliver Thorn-Seshold. ✉email: oliver.thorn-seshold@cup.lmu.de

The cytoskeleton serves as the scaffold for critical biological processes ranging from signalling and cargo trafficking, to cell shape maintenance and cell division. Most of the cytoskeleton's myriad of biological roles are inherently spatially and temporally differentiated, although they all rely on the same protein scaffold structures. Studying these cytoskeleton-dependent processes with the spatiotemporal resolution necessary to understand and exploit these individual biological functions is an important challenge. Accordingly, in recent years, a number of approaches towards photocontrol over cytoskeletal or cytoskeleton-associated proteins have been made, aiming to allow their spatiotemporally precise optical manipulation[1–3]. Nevertheless, much remains to be done before generally applicable tool systems can be developed.

We here focus on the microtubule (MT) cytoskeleton. MTs play particularly important roles in intracellular transport, cell motility and morphological plasticity, and there is a conspicuous need to achieve a better understanding of how these many functions are implemented and regulated[4,5]. The role of MT dynamics during cell proliferation has also made them a major anticancer target, for which several outstanding drugs (taxanes, epothilones and vinca alkaloids) have been developed[6–8]. These drugs and other small molecule modulators (e.g., nocodazole, combretastatin and peloruside) remain the most general tools for MT cytoskeleton research. However, these inhibitors simultaneously suppress all MT-dependent functions spatially indiscriminately. Therefore, they do not allow spatiotemporally precise MT inhibition on the length or time scales appropriate for selectively studying MT-dependent processes. This restricts their scope of applications and their utility for selective research into MT cytoskeleton biology[9].

Deeper insights could be gained from inhibitors that allow spatiotemporally specific MT manipulation. In this regard, optogenetic approaches to MT regulation have advanced greatly in recent years. In one example, a photo-inactivatable variant of the MT plus tip adaptor protein EB1 was engineered, which upon illumination lost its ability to bind other plus-end-tracking proteins, thus optically inhibiting MT growth and allowing spatiotemporally resolved modulation of directional cell migration[10]. Another domain of research has focused on optogenetic switches tethered to kinesins and compartment identity markers, to manipulate the transport of vesicles and organelles. With such methods, it is possible to photomodulate the association of motor proteins to cargos, to investigate the role of MTs in specific transport processes[11,12].

However, while optogenetics has succeeded in providing motors and scaffold-associated proteins that are responsive to externally controlled stimuli, no optogenetic variants of the basic cytoskeleton scaffold proteins actin and tubulin have been achieved. An exogenously controllable system for directly patterning cytoskeleton scaffold dynamics and structure with spatiotemporal resolution would however be highly desirable, since it would allow researchers to modulate any of the cytoskeleton-dependent functions. For this purpose, pharmacological interventions that directly address the stability and dynamics of the cytoskeleton scaffold remain the methods of choice. For example, photouncageable versions of MT inhibitors, particularly of the blockbuster drug paclitaxel, have been used for localised photoactivatable inhibition of MT dynamics in several studies[13,14]. Yet despite their ability to modulate the cytoskeleton directly, photouncaging approaches suffer disadvantages, such as irreversibility of inhibition, the intense and phototoxic mid-UV illumination typically needed for uncaging, the often slow and rate-limiting intermediate hydrolysis that diminishes their precision of temporal control, their release of nonspecifically toxic and also phototoxic photouncaging byproducts, background activity through enzymatic hydrolysis, and increased molecular weight that can cause biodistribution problems[15].

Against this background, photopharmaceuticals—photoswitchably potent exogenous small molecule inhibitors—have been extensively developed in recent years[16–19]. Photopharmaceuticals conceptually enable studies not otherwise accessible to biology, marrying the spatiotemporal precision of light application known from optogenetics, to the flexibility and system-independence of exogenous small molecule inhibitors. This combination is favourable for non-invasive studies of temporally regulated, spatially anisotropic biological systems—such as the MT cytoskeleton[16,19,20]. Photopharmaceuticals have succeeded in delivering a measure of optical control over a broad range of biochemical and biological phenomena, with early cell-free studies now supplanted by applications in cultured cells and recently in vivo in embryonic and adult animals[21–24].

In the cytoskeleton field, several photopharmaceutical MT destabilisers were recently developed, to begin addressing the need for spatiotemporally precise MT cytoskeleton studies. The azobenzene-based Photostatins (**PST**s), which can be reversibly photoswitched by low-intensity visible light between their biologically inactive *E*-isomers and their MT-destabilising colchicine-like *Z*-isomers, were first developed in 2014[16,25–27]. MT-destabilising photopharmaceuticals based on two different families of molecular photoswitch—styrylbenzothiazoles (**SBTubs**)[28] and hemithioindigos (bi-active **HOTubs**[29] and dark-active **HITubs**[30])—have since been developed, delivering increased metabolic robustness in the intracellular environment and alternative optical switching profiles (all-visible switching with hemithioindigos, GFP-orthogonal switching with **SBTubs**). All three reagent families have enabled spatiotemporally precise optical control over endogenous MT network integrity, MT polymerisation dynamics, cell division and cell death. **PST**s have already been used in animals to tackle unsolved questions in mammalian development[21,22] and neuroscience[31]. These applications illustrate the power of photopharmacology to enable previously inaccessible studies of spatiotemporally anisotropic cytoskeletal processes without genetic engineering.

With the optically precise destabilisation of MTs addressed by a range of agents, we desired to develop photopharmaceutical MT stabilisers as conceptually novel tools with an alternative spectrum of biological research applications. While both MT destabilisers and MT stabilisers can be used to suppress MT polymerisation dynamics in cell culture, stabilisers have enabled a variety of research and human therapeutic applications which are inaccessible to destabilisers[14,32,33], due to their differing pharmacology, stoichiometry and spectrum of biological effects. Since the biological functions of the MT cytoskeleton are primarily dependent on the localisation of stabilised or growing MTs themselves, we reasoned that optically controlled tools modulating MT network stability could allow spatiotemporally precise stimulation of a range of these MT-dependent functions, in ways not otherwise amenable to control.

We therefore chose to develop light-responsive paclitaxel analogues as optically controlled MT stabilisers for in situ spatiotemporally precise photocontrol of cellular MT network architecture, dynamics and MT-dependent functions. We now report our development of these reagents.

Results

Design and synthesis. We chose the azobenzene photoswitch for installing photoswitchable potency onto the taxane core. This photoswitch offers a substantial geometric change upon isomerisation, which we hoped would differentiate the isomers' binding constants, and it allows reliable, high-quantum-yield,

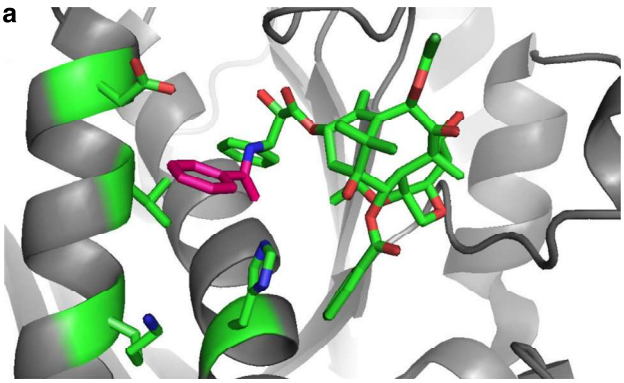

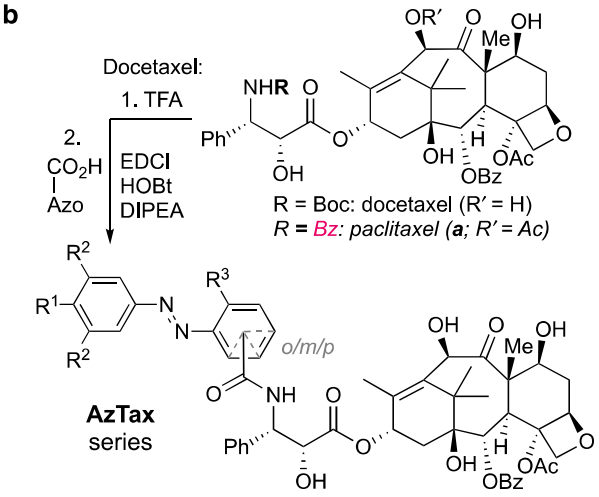

c

Compound	Diazene	R^1	R^2	R^3
AzTax4H	*para*	H	H	H
AzTax3H	*meta*	H	H	H
AzTax4MP	*para*	OMe	H	H
AzTax3MP	*meta*	OMe	H	H
AzTax2MP	*ortho*	OMe	H	H
AzTax3TM	*meta*	OMe	OMe	H
AzTax3MTM	*meta*	OMe	OMe	OMe
AzTax4DMA	*para*	NMe_2	H	H
AzTax3DMA	*meta*	NMe_2	H	H
AzTax3DEA	*meta*	$N(C_2H_4OH)_2$	H	H

Fig. 1 Design and synthesis of AzTax. a Paclitaxel:tubulin structure (PDB: 3J6G[36]) with the benzamide indicated in pink. **b** Synthesis of **AzTax** from docetaxel. **c** Panel of **AzTax** examined in this study.

near-UV/visible-light-mediated, highly robust *E*↔*Z* photoisomerisability, which enables repeated photoswitching in situ in living cells. Taxanes feature a number of chemically modifiable positions; we chose to focus on sites where substituents can be tolerated, but where their geometric changes might impact binding potency through steric interactions or by modulating the orientation of key interacting groups nearby. Potent taxanes feature a side-chain 3′-amine acylatedsubstituted with mid-size hydrophobic groups (e.g., Boc group in docetaxel and Bz in paclitaxel)[8,34] which abut the tubulin protein surface yet are projected away from the protein interior (Fig. 1a, highlighted in pink); the other side-chain positions (e.g., the 3′-phenyl or 2′-hydroxyl) offer less tolerance for substitution as they project into the protein[8]. The 3′-amine also tolerates the attachment of somewhat polar cargos such as the large silarhodamine fluorophore, as long as they are attached via a long spacer, with only moderate potency loss[35], making it desirable for photopharmaceutical tuning as it might tolerate azobenzenes with a range of structural characteristics. However, we anticipated that attenuating the high potency of paclitaxel itself (low nM range) might be required, in order that the relatively small structural change of a *E*/*Z* isomerisation at the molecular periphery could substantially modify the overall potency.

We accordingly designed a panel of 3′-azobenzamide-taxanes (**AzTax**) for biological testing. As taxanes have famously poor aqueous solubility (still worsened by attaching an azobenzene), we initially determined to focus on compounds displaying satisfactory potency at concentrations substantially below their solubility limit. This avoids the case that the compounds' apparent potencies would be dictated by solubility effects, and so should enable robust use as reagents across a variety of systems and settings. Theorising that the sterics around the azobenzene phenyl ring proximal to the taxane core would be the greatest potency-affecting factor, we first focussed on testing which orientations of photoswitch would be best tolerated. We therefore scanned orientations of the diazene in *ortho*, *meta* and *para* relative to the amide (**AzTax2**/**3**/**4** compound sets, Fig. 1b, c), and when early cellular testing showed that the **AzTax2** set had the lowest potency, we abandoned it at this stage.

Next, examination of the published tubulin:paclitaxel cryo-EM structures (Fig. 1a)[36,37] indicated that the azobenzene's distal ring can project freely away from the protein. Therefore, we hypothesised that steric variation to the distal ring would not greatly impact binding potency of either isomer, but could be used orthogonally to tune their photochemical properties, by substitutions in *para* to the diazene that chiefly mesomerically affect the photochemistry of the N=N double bond. We accordingly synthesised unsubstituted ("H"), *para*-methoxy ("MP") and *para*-dimethylamino ("DMA") derivatives of the **AzTax3**/**4** sets. These were chosen to vary the photochemical properties of most relevance to photopharmacology: the completeness of the *E*→*Z* and the *Z*→*E* photoisomerisations at fixed wavelengths, which dictate the dynamic range of isomer photoswitchability, and τ (the halflife of the spontaneous unidirectional *Z*→*E* relaxation). Lastly, when the **AzTax3** set proved promising in early studies, we also examined installing an electron-donating 3,4,5-trimethoxy motif on the distal ring (**AzTax3TM**) as well as an additional R^3 methoxy group to reduce the rotatability of the proximal ring in case this could amplify the difference between isomer potencies (**AzTax3MTM**), and we controlled for solubility effects by exchanging the dimethylamino substituent for a more soluble diethanolamino ("DEA") group (**AzTax3DEA**). The target **AzTax** were synthesised by degradation of commercial docetaxel followed by amide couplings to various azobenzenecarboxylic acids in moderate yields (Fig. 1b, c and Supplementary Note 1).

Photochemical characterisation. The **AzTax** all displayed robust and repeatable *E*↔*Z* photoswitching under near-UV/visible illuminations, as expected from the literature[19] (Supplementary Fig. 1). Since their protein target is located in the cytosol, we first wished to evaluate their photoswitching in physiological aqueous media. Since taxanes are too poorly water-soluble to perform reliable photoswitching studies easily by UV–Vis spectroscopy, we synthesised fully water-soluble diethanolamides of all the azobenzenecarboxylic acids and used them in aqueous photoswitching tests (see Supplementary Note 2). The photochemical properties within each substituent set were similar. The unsubstituted (H) compounds displayed a 3-fold dynamic range of *Z*-isomer photoswitchability between the photostationary states (PSSs) at 375 nm (80% *Z*) and 410 nm (26% *Z*), and had

substantially slower relaxation than biological timescales (τ ca. 50 days). The methoxylated compounds (MP, TM and MTM) had been chosen to improve the dynamic range of isomer photoswitching by relative shifting of the isomers' absorption bands[16] (Supplementary Fig. 2). Indeed, they delivered a ca. 9-fold dynamic range of *Z*-isomer photoswitchability (375 nm: 96% *Z*; 530 nm: 11% *Z*), and their relaxation remained substantially slower than biological timescales (τ ca. 24 h).

Advantageously for practical work, the metastable *Z*-isomers of all **AzTaxs** could be quantitatively relaxed to *E* by warming DMSO stocks to 60 °C overnight (which increases the practical ease-of-use of these reagents as compared to irreversibly photouncaged reagents). The *para*-amino (DMA and DEA) compounds featured τ values too small to observe bulk photoswitching in aqueous media under biologically applicable conditions. Yet, since less water-solvated environments such as lipid vesicles, membranes, or protein-adsorbed states are likely intracellular localisations for hydrophobic taxane conjugates, we then determined their photochemistry in moderately polar aprotic media (EtOAc). Here, they were easily bulk-switchable (τ ca. 11 min), giving a 4-fold dynamic range of *Z*-isomer photoswitchability (410 nm: 91% *Z*; 530 nm: 21% *Z*) (further detail in Supplementary Note 2). As the **AzTax** reagents were intended for use with microscopy, we also examined photoswitching of all compounds over a broader range of wavelengths, to determine what dynamic range of isomer photoswitchability would be accessible in practice, with standard (405, 488 and 514 nm) or more exotic (380, 440 and 532 nm) microscopy laser wavelengths (Fig. 2a, Supplementary Fig. 2 and Supplementary Table 1).

We then proceeded to explore the biological applicability of **AzTax** as photoswitchable MT stabilisers in living cells. Since near-UV illumination gave PSSs with high-*Z* populations for all photoswitches, while thermal relaxation and maintenance in the dark returned the *E*-isomer quantitatively, we began by comparing all-*E* "dark" conditions (all-*E* stock applied, then maintained dark) with mostly *Z* "360 nm" lit conditions (all-*E* stock applied, then photoisomerised *in situ* by pulsed illuminations with low-power 360 nm LED light, giving a mostly-*Z* PSS), to determine which structures allowed the highest fold difference of bioactivity.

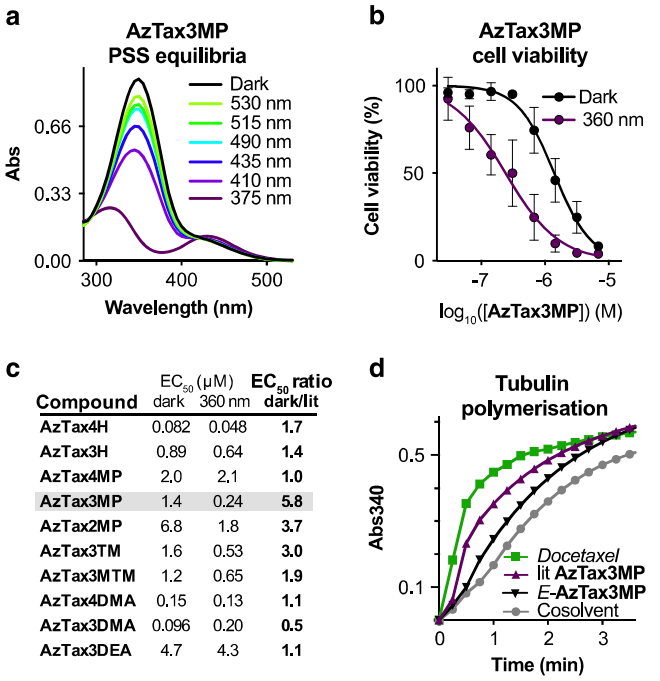

Fig. 2 Photoswitchable performance of AzTax. a Photostationary state UV–Vis absorption spectra of **AzTax3MP** under a range of cell-compatible wavelengths similar to microscopy laser lines. **b, c** Resazurin antiproliferation assays of **AzTax** highlight their structure- and light-dependent cell cytotoxicity. HeLa cells, 40 h incubation in dark conditions (all-*E*) or under pulsed illuminations with low-power LEDs (75 ms per 15 s near-UV at < 1 mW cm^{-2}; lit = ~80% Z) (dose-response curves are fitted to the means (shown with s.d.) of 3 independent biological experiments). **d** A cell-free assay for polymerisation of purified tubulin comparing the MT stabilisation activity of docetaxel, all-*E*- and 360 nm-lit-**AzTax3MP** (all 10 μM) shows light-specific promotion of polymerisation by *Z*-**AzTax3MP**, matching the trend observed in cellular assays.

AzTax display photocontrolled bioactivity in living cells. Since stabilisation of MTs in cells over a prolonged period blocks cell proliferation and ultimately causes cell death[8], we first assayed the **AzTax** for light-dependent cellular activity by the resazurin cell proliferation/viability assay. Viability dose-response curves under dark or UV conditions were assessed in the HeLa cervical cancer cell line (Fig. 2b, c). All compounds displayed dose-response curves with similar Hill coefficients as the parent drug docetaxel (Supplementary Fig. 3), which is in line with the conjecture that they act through the same mechanism, albeit with different potency. All compounds except the fast-relaxing **AzTax3DMA** had *Z*-isomers that were more potent, or else equipotent, to the *E*-isomers, suggesting that this trend in isomer-dependent cellular bioactivity across several photoswitch types has robust significance. *E*-**AzTax2MP** had the poorest overall potency (EC_{50} ca. 7 μM, all-*E*), which we took as indicating the unsuitability of *ortho* substitutions that likely project the azobenzene into solution (c.f. Fig. 1a) where its hydrophobicity could interfere with binding stability. By contrast, the **AzTax4** set featured compounds up to 100 times more potent, and structure-dependently covered a 40-fold potency range. However, despite the good isomeric photoswitchability of e.g., **AzTax4MP**, none of the **AzTax4** set displayed substantial *photoswitchability of bioactivity* (fold difference between the 360 nm and the dark bioactivity). We interpreted this substitution-independent result as an indication that the distal ring may project too far from the protein contact surface, in both *E*- and *Z*-isomers, for the **AzTax4** isomer state to substantially affect binding.

In contrast, members of the **AzTax3** series all showed photoswitchability of bioactivity. **AzTax3MP** featured a nearly 6-fold difference between the more-toxic *Z* and less-toxic *E*-isomers' bioactivity, over the 48 h experimental time course (Fig. 2b). Adding more methoxy groups to the scaffold decreased the *Z*-isomer's cytotoxicity without greatly affecting that of the *E*-isomer (**AzTax3TM**, **AzTax3MTM**), and deleting the methoxy group also decreased the *Z*-isomer's cytotoxicity (**AzTax3H**), which we took as a sign that balancing the polarity of the photoswitch was important for maximising bioactivity. In line with this interpretation, the potencies of **AzTax3DMA** were similar to **AzTax4DMA** while the more hydrophilic **AzTax3DEA** showed a 40-fold loss of potency. Despite the potential for photoswitching the *para*-amino **AzTax** inside lipid environments, they should only reach their cytosolic target tubulin as the *E*-isomers due to fast aqueous relaxation. Surprisingly, **AzTax3DMA** appeared slightly more bioactive as the unilluminated *E*-isomer, although as expected **AzTax4DMA** and **AzTax3DEA** both showed no illumination-dependency of bioactivity; and controls under 410 nm illumination (to establish the optimum PSS for the *para*-amino compounds) showed no different result to those obtained with UV illumination (Fig. 2). The apparent cytotoxicity differential seen for **AzTax3DMA** might reflect reduced availability to the cytosol rather than

differential binding of the isomers[30] although these results do not allow further conjecture.

To continue the study, we therefore selected **AzTax3MP**, due to its photoswitchability of bioactivity (6-fold when under optimum illumination conditions), satisfactory potency (EC_{50} = 0.24 µM when UV illuminated), bidirectional photoswitchability (optimum 9-fold-change of concentration of the more bioactive *Z*-isomer), and reproducibly photoswitchable cellular performance across assays with different illumination conditions, to proceed with further mechanistic biological evaluations.

Photocontrol of tubulin polymerisation and cell cycle. To examine the molecular mechanism of **AzTax** isomer-dependent cellular bioactivity, we first assayed the potency of **AzTax3MP** for promoting tubulin polymerisation in cell-free assays using purified tubulin. The majority-*Z* 360 nm-lit state gave a ca. 60% enhancement of polymerisation over control (benchmarked to docetaxel at 100%), while all-*E*-**AzTax3MP** gave only ca. 30% polymerisation enhancement (Fig. 2d and Supplementary Note 2). Note that the enhancements seen in this cell-free assay are not predictive of the relative cellular potencies, but it clarifies the mechanism of action of **AzTax** as MT stabilisers, like their parent taxanes. We next studied the direct effects of in situ-photoisomerised **AzTax** upon cellular MT organisation and MT-dependent processes. Immunofluorescence imaging of cells after 24 h of exposure revealed that **AzTax3MP** light-dependently disrupts MT network architecture. As **AzTax** concentration increases, MTs first become disorganised, then mitotic spindle defects that result in multinucleated cells are seen, and finally mitotically arrested and early apoptotic cells with fragmented nuclei dominate; the effective concentrations needed to achieve these effects are substantially lower for lit **AzTax** than under all-*E* dark conditions (Fig. 3, further detail in Supplementary Note 4). The best window for visualising this isomer-dependent bioactivity lay around 0.3–1 µM. Both the mitotic arrest, and the nuclear defects of cells that escape arrest, are hallmarks of MT stabiliser treatment[38], arguing that the isomer-dependent cytotoxicity of **AzTax3MP** arises from MT stabilisation preferentially by its *Z*-isomer.

The presence of multinucleated cells indicated that **AzTax** also inhibit MT-dependent functions such as successful completion of mitosis. To quantify this we examined cell-cycle repartition after **AzTax** treatment by flow cytometry, expecting to observe G_2/M-phase cell-cycle arrest[39]. G_2/M-arrest was observed with approximate EC_{50} around 1.5 µM after 24 h incubation with the lit **AzTax3MP**. This was twice as potent as *E*-**AzTax** (Fig. 4a–c) and mimicked the effect of docetaxel although with lower potency (Supplementary Fig. 4). As a control for illumination/photoswitch-dependent off-target effects, we also examined the non-photoswitchably bioactive but potent **AzTax4DMA**, which reproduced the effects of docetaxel independent of illumination conditions indicating no significant assay complications (Supplementary Fig. 4). This further supported the notion that **AzTax3MP** acts across a range of assays and readouts as a light-modulated taxane, with reproducible photocontrol over the isomers' bioactivity, allowing effective inhibition both of MTs and of MT-dependent processes.

AzTax enable spatiotemporally specific MT control in cells. With their photoisomerisation-dependent bioactivity shown in long-term experiments (days), we next tested one of the key conceptual advantages that photoswitchable MT stabilisers should enable: real-time in situ optical control of the MT cytoskeleton with single-cell spatial specificity and high temporal precision.

We transfected HeLa cells to express the EB3-tdTomato fluorescent reporter, that selectively labels GTP:tubulin-rich regions of MTs. In ordinary conditions this is a marker for the GTP cap region of polymerising MTs, thus selectively revealing polymerising MTs as comets moving towards the cell periphery[40]. As taxane treatment suppresses MT polymerisation dynamics[41], we imaged EB3-tdTomato dynamics using live cell confocal microscopy, as a spatiotemporally resolved readout for MT inhibition by **AzTax**.

We applied **AzTax3MP** globally to these cells at 1 µM, and targeted single cells with low-intensity illuminations at 405 nm, hoping to achieve precisely temporally resolved control of MT dynamics in those single cells only, by selectively isomerising **AzTax3MP** inside them. In targeted cells, EB3 comet counts were halved upon 405 nm illuminations, recovering almost completely within 80 s after 405 nm illumination was stopped (Fig. 5a), while surrounding cells as well as non-treated controls were unaffected (Fig. 5b); and the process could be repeated over several cycles (Supplementary Movies 1 and 2, Supplementary Note 4 and Supplementary Discussion). Thus, **AzTax** can indeed be used to reversibly inhibit MT dynamics of target cells with temporal precision on the scale of seconds and spatial precision on the level of tens of microns. To examine *E*-**AzTax3MP** (dark state) for residual effects on MT dynamics, we also quantified other parameters of EB3 motility. *E*-**AzTax3MP** caused only a slight decrease in EB3 comet velocities (Fig. 5c), and an insignificant decrease in EB3 comet density (Fig. 5d). By comparison, in photoswitched cells, so few comets remain that meaningful velocity quantification was not possible (Fig. 5c, d). It can be concluded that working concentrations can be appropriately chosen such that **AzTax3MP** does not hinder MT polymerisation in the absence of illumination, but does so strongly when illuminated.

Finally, to study the entire cellular MT population and not only the actively polymerising fraction of MTs, HeLa cells transfected to express mCherry-α-tubulin were imaged to quantify total MT density under **AzTax3MP** treatment (Supplementary Movies 3 and 4). No change in MT density was observed during treatment or photoswitching (Supplementary Fig. 5). Taken together, this argues that, as expected, **AzTax** do not act by reducing the overall number of MTs, but rather by suppressing MT polymerisation dynamics.

AzTax allow subcellular photocontrol of neuronal MT dynamics. Having demonstrated MT control with spatial resolution to single cells, we now wished to examine the performance of **AzTax** as applied to subcellular resolution. Small molecule inhibitors diffuse rapidly within cells, so using them to achieve sustained subcellular patterning of biological effects is challenging. Yet, for potential applications in neurobiology, the highly polarised, elongated neuronal cell shape should restrict diffusion and favour subcellular resolution. We used mature cultured rat hippocampal neurons with well-developed dendrites, and transfected these cells with EB3-tdTomato for imaging. For each neuron, we selected equal-sized areas along independent processes, and monitored their EB3 dynamics before and during **AzTax3MP** treatment, with ROI-localised 405 nm application to one area (Fig. 6 and Supplementary Movies 5–8).

Kymographs of these areas reveal localised reductions in MT polymerisation dynamics in 405 nm-illuminated ROIs in the presence of **AzTax3MP**, while no significant changes are seen in other dendritic processes; and internal controls before/after **AzTax** application confirmed that no significant photobleaching is caused by 405 nm illumination before **AzTax** application (Fig. 6a). The induction of inhibition in the ROI was typically

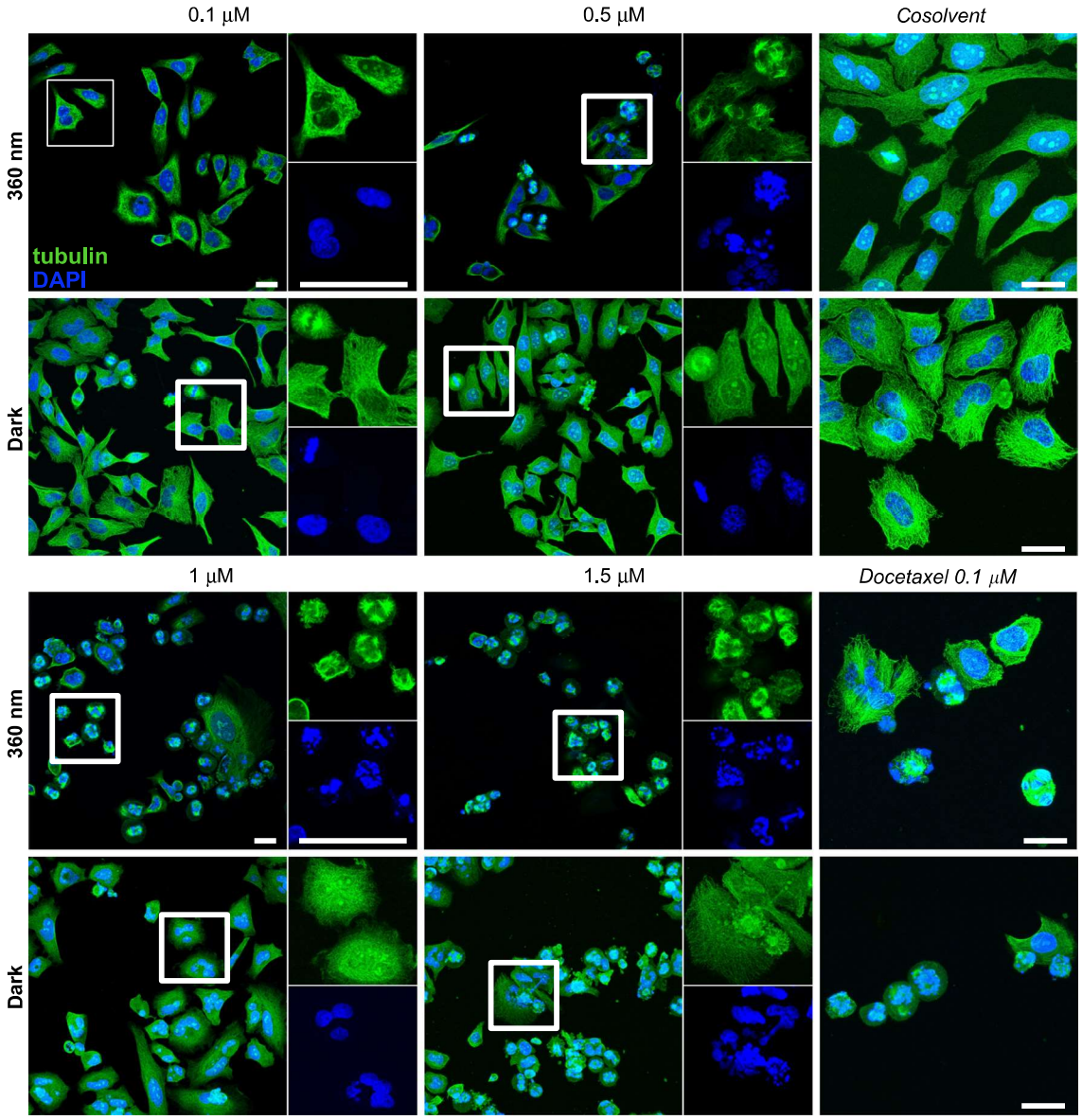

Fig. 3 AzTax3MP light-dependently disrupts MTs in cultured cells. Immunofluorescence staining indicates dose- and light-dependent disruption of MT organisation, mitotic completion, and cell viability. HeLa cells treated with **AzTax3MP**, docetaxel, or DMSO cosolvent only for 24 h; α-tubulin in green, DNA in blue; docetaxel positive control at 0.1 μM; DMSO cosolvent at 1% in all conditions; scale bars 25 μm (staining was repeated twice after two independent experiments and evaluated each time by at least two scientists independently).

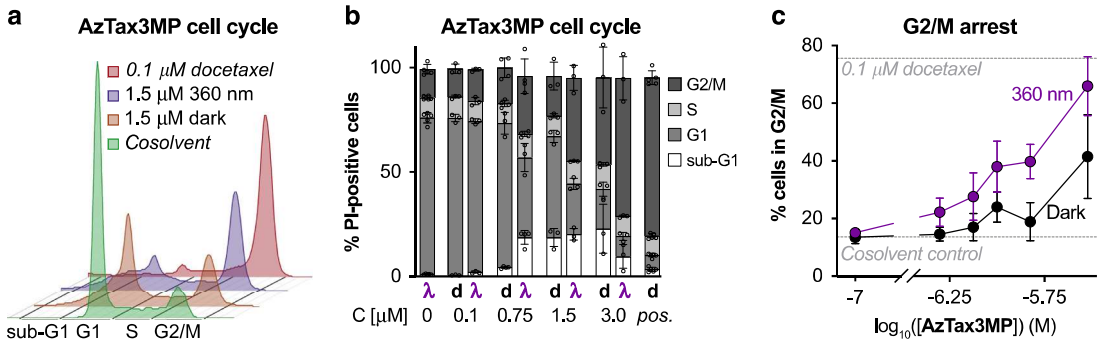

Fig. 4 AzTax3MP leads to dose- and light-dependent cell-cycle arrest. a Flow cytometry analysis of cell-cycle repartition shows that **AzTax3MP** leads to a light-dependent shift of living cells towards G_2/M phase. **b**, **c** The cell-cycle distribution of **AzTax**-treated cells approaches that of docetaxel-treated cells in a dose- and light-dependent manner. HeLa cells treated under light/dark conditions for 24 h (**d** indicates dark and **λ** indicates lit conditions; *pos.* indicates docetaxel control at 0.1 μM; $n = 3$ biologically independent experiments, except $n = 4$ for 0.75 μM **AzTax3MP** and $n = 5$ for cosolvent and docetaxel controls; data shown as mean with s.d.).

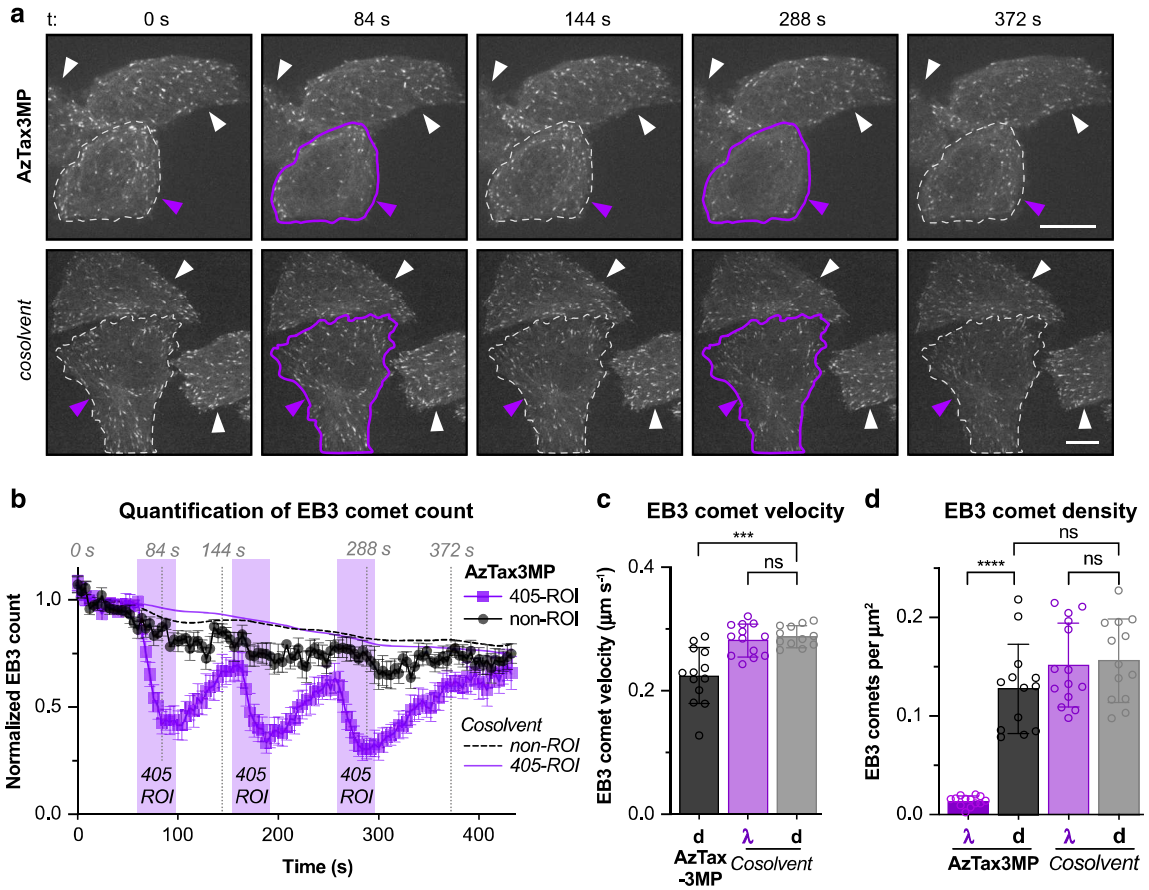

Fig. 5 AzTax photoswitching allows cell-precise, temporally reversible inhibition of MT polymerisation dynamics. Data related to Supplementary Movies 1 and 2. HeLa cells transfected with EB3-tdTomato treated with 1% DMSO cosolvent with or without 1 µM **AzTax3MP**. **a, b** Target cells (violet arrowheads) were selectively illuminated with 405 nm in bursts, and EB3 tracking in defined regions of interest (ROIs) performed. **a** Target ROIs in frames acquired immediately after 405 nm illumination are outlined in violet, target ROIs in t_0 and post-recovery frames (ca. 80 s after 405 nm illumination periods) are outlined in dotted white; nontarget cells are indicated with white arrowheads; scale bars indicate 10 µm. **b** Quantification of EB3 comet counts (averages over $n = 7$ cells per treatment group across 3 experiments, each cell's EB3 comet count time course was normalised to the average of the first ten frames) in target ROI and in non-illuminated cells. Periods of ROI illumination with 405 nm are shaded in violet; times of frames from the representative movies shown in **(a)** are indicated with dotted lines annotated with the times, data shown as group-average of EB3 comet count time course (normalised to initial count) with s.e.m. For clarity, data for cosolvent-only areas are shown with LOWESS fits. **c, d** HeLa cells transfected with EB3-tdTomato were treated with either 1 µM **AzTax3MP** or DMSO cosolvent only, and imaged directly after drug application for 2.4 min with 405 nm illumination (signified by "λ") or without (signified by "d"). Supplementary Movies were analysed for **c** EB3 comet velocity ($n = 12$ cells for **AzTax3MP**; $n = 13$ cells for cosolvent conditions), and **d** EB3 comet counts, normalised to cell surface area ($n = 13$ cells for **AzTax3MP** lit and both cosolvent conditions; $n = 14$ cells for **AzTax3MP** dark condition). EB3 comet velocity could not be meaningfully analysed in **AzTax3MP**-treated cells under 405 nm illumination due to the strong loss of EB3 comets and is therefore not represented. Data are shown as mean with s.d. Unpaired, two-tailed t test: $^{***}P = 0.001$ (95% CI 0.035–0.093), $^{****}P < 0.0001$ (95% CI 0.089–0.14), ns denotes not significant, no adjustments for multiple comparisons.

clear within ca. 1–3 min, which is approximately one order of magnitude slower than in the whole-cell photoswitching experiments of Fig. 5, and which may partially reflect the lower **AzTax** concentration that was selected to avoid complications with the more sensitive neurons. Statistics collected over multiple cells highlighted the reproducibility of using ROI-localised **AzTax3MP** illumination to deliver subcellularly localised MT polymerisation inhibition in this system (Fig. 6b).

Collectively, these results demonstrate the use of **AzTax3MP** as a powerful tool to directly optically modulate endogenous MT network architecture, polymerisation dynamics and MT-dependent functions in live cells with excellent spatiotemporal control.

Discussion

Photocontrol over protein function is an attractive method to study anisotropic, multifunctional cellular systems, since it can deliver the spatiotemporal specificity required to focus on specific roles or aspects within these complex biological systems. Small molecule photopharmaceuticals have already proven valuable photocontrol tools because of their ability to address such targets that are not directly accessible to optogenetics, such as the MT cytoskeleton (for which a range of photoswitchable depolymerising agents have recently been reported[16,28,30]). Here we have expanded the scope of photopharmaceutical MT reagents to demonstrate the first photoswitchable MT stabilising agents. Through structure-photochemistry/activity-relationship studies, we have selected a lead compound **AzTax3MP** that gives robust, in situ photoswitchable MT stabilising activity in cell-free and cellular assays, and can light-dependently reproduce key direct as well as downstream biological effects of the taxanes but with excellent spatiotemporal control down to the subcellular level. While this is a promising starting point for further reagent optimisation, we believe that **AzTax3MP** itself will already find a

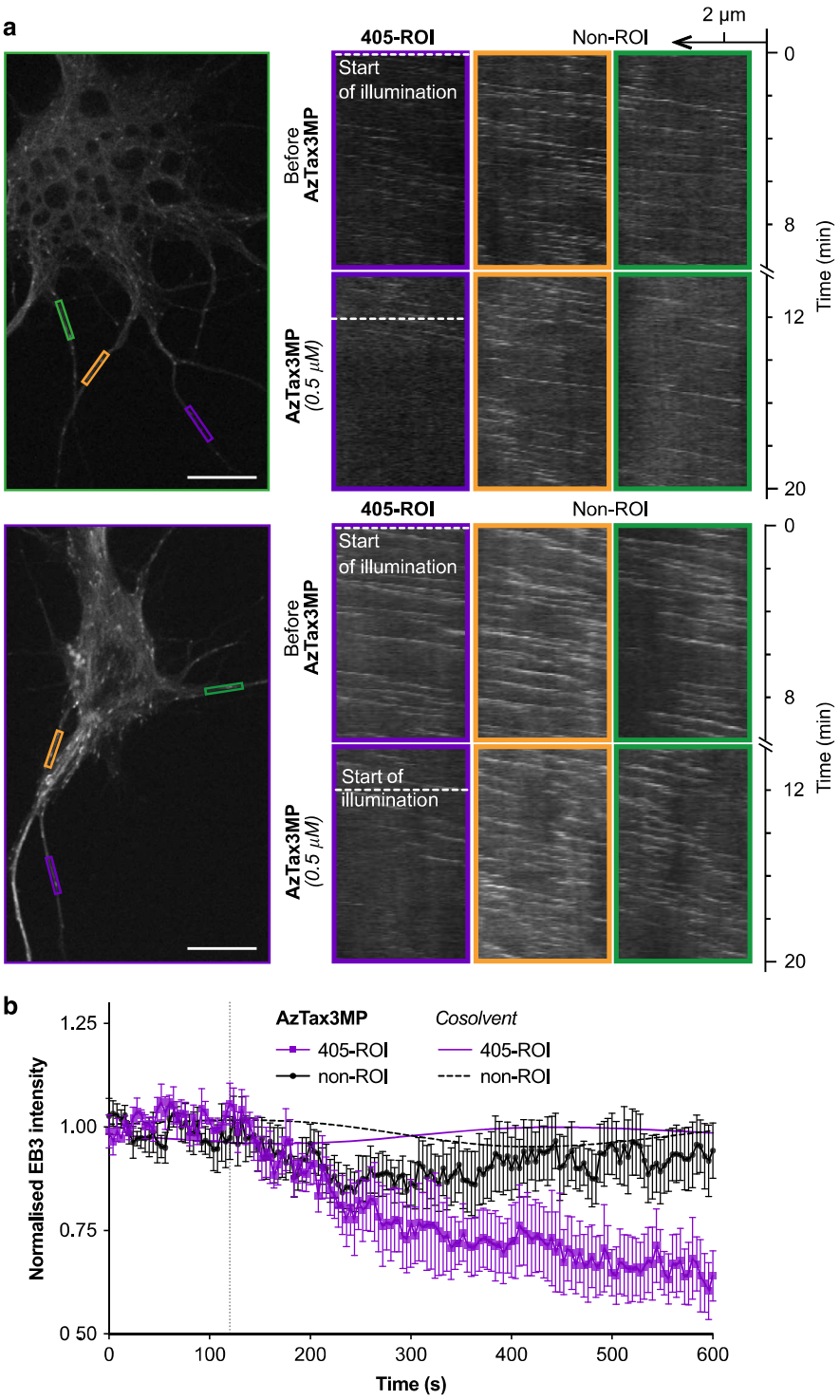

Fig. 6 Manipulation of MT polymerisation dynamics in subcellular ROIs of rat primary hippocampal neurons using AzTax3MP. Data related to Supplementary Movies 5–8. **a**, **b** Cultured primary neurons (9 days in vitro) transfected with EB3-tdTomato treated with 1% DMSO were initially imaged for EB3 for 10 min while a ROI (violet box) was pulsed with 405 nm light, establishing baselines for EB3 activity in the cell and in the ROI, which were demonstrated to be light-independent. The same neurons were then exposed to 0.5 µM **AzTax3MP** and immediately imaged for another 10 min; during this time the same ROI (violet box) was pulsed with 405 nm light beginning at 2 min into the acquisition (indicated by dotted lines). **a** Cell images with areas marked, and corresponding kymographs of these areas. The ROI pulsed with 405 nm is boxed in violet, the non-ROI areas (not pulsed with 405 nm) are boxed in orange and green. Scale bars indicate 10 µm. **b** Normalised area-average pixel EB3 intensities (with s.e.m.), for areas treated with or without **AzTax3MP** and 405 nm pulsing ($n = 4$ cells). For clarity, data for cosolvent-only areas are shown as spline fits; see Supplementary Note 4 for further details.

range of applications particularly in embryology, neuroscience and studies of cell motility and polarity, where its spatiotemporally specific bioactivity will enable studies not previously possible.

Liu et al. also recently reported photoswitchable MT stabilisation, using a photoswitchable supramolecular host-guest system intended to crosslink cellular MTs[42]. However, these effects were also reproduced when the tubulin stabilisation motif was deleted[43], and it remains unclear if the host-guest system could perform specific tubulin binding[44]. The druglike reagents developed in this work, offering robust and structurally rationalisable performance, may therefore be valuable to address still-unmet needs.

If **AzTax** reagents with still greater bioactivity differentials could be accessed, this would improve reagent performance with respect to several limitations of the current best candidate **AzTax3MP**. This reagent's dynamic range of bioactivity photoswitching is between two- and six-fold, depending on the assay readout. Thus, relatively precise concentration tuning is needed to find the best working concentration, and background activity before photoactivation may be observed depending on the assay and conditions. Determining the sources of the differential bioactivity between **AzTax** isomers in living cells is therefore key for reagent optimisation. Since modifying polarity at a distal site that should not clash sterically with the protein gave a 40-fold change of apparent potency (**AzTax3DEA** compared to **AzTax3DMA**), we believe that the sterics of the **AzTax** isomers are not necessarily the sole determinant of cellular bioactivity. Yet, polarity-dependent cellular biolocalisation or penetration cannot entirely explain the photoswitchable activity of **AzTax3MP** since it shows isomer-dependent activity in cell-free assays also, so the azobenzene must significantly impact protein-ligand affinity. Therefore, we conclude that maximising the bioactivity difference between isomers will require photoswitches with isomer-dependency both of sterics and of polarity. We note too that the completeness of the *E*→*Z* photoswitchability of the azobenzene was not correlated to the photoswitchability of biological activity (c.f. **AzTax3MTM**, **AzTax4MP**). Since the *Z*-**AzTax** were typically the more-active isomers, we conclude that further defavouring the binding of the *E*-isomer while allowing the *Z*-isomer to retain bioactivity, e.g. by tuning sterics and polarity, is likely the best way to maximise the photocontrol over inhibition. Research in these directions is underway.

Reducing the halflife of spontaneous relaxation of an **AzTax** to its less-binding isomer, could also offer perspectives for improving the ease of cellularly or subcellularly specific photocontrol. Faster relaxation could reduce the biological effects of a photoactivated isomer diffusing away from a desired spatial and temporal locality, and so improve spatiotemporal precision. However, if relaxation becomes too fast, the requirements for repeated localised illuminations may become the limiting factor for compound utility. We estimate that relaxation on the scale of seconds, or hundreds of microseconds, would best address most desirable short-term assays. While the relaxation speed of **AzTax3MP** was in this respect too slow, and that of **AzTax3DMA** was too fast, it is likely that by electronic tuning of the azobenzene's distal phenyl ring, more useful derivatives with intermediate relaxation rates can be obtained. Research in this direction is ongoing.

Photopharmacology studies often assume that increasing the dynamic range of isomeric photoswitchability under a freely available choice of illumination conditions, and red-shifting overall absorption wavelengths, are required for improved biological performance. However, in the case of the current or any potentially tuned future **AzTax** stabilisers, as elsewhere, probably neither is true:

First, after *Z*-**AzTax** induces increased MT rescues, which alter MT dynamics and network architecture, the downstream MT-dependent biology probably cannot be rapidly returned to its usual state even if the stabiliser would be totally removed (e.g., by complete back-isomerisation to a hypothetically non-binding state). This is because any **AzTax**-stabilised MTs are likely to be organised abnormally, and will presumably require time to break down and return tubulin monomer to the cytoplasmic pool so that a functional, directional MT network can be rebuilt. Therefore, there is probably a limit to the temporal resolution of *true* biological reversibility that any photoswitchable stabiliser can display, even if selected readouts (such as speed of polymerisation of individual MTs) recover more quickly. With this consideration in mind, we do not believe that improving the completeness of bidirectional isomeric photoswitchability[45] will be as important for **AzTax** development as for other classes of inhibitors that can feature instantaneous downstream biological response.

Second, red-shifting photoswitch absorption wavelengths is also likely to be counterproductive for microscopy, since there are few fluorescent proteins with significant excitation efficiency at laser lines above 561 nm (typically the next wavelength available is 647 nm). Therefore, maintaining orthogonality to the widest possible range of imaging wavelengths by blue-shifting is in our opinion and experience more advantageous, since it can keep other imaging channels vacant for multiparameter, photo-orthogonal studies[28]. However, a key property that should be readily tunable to the advantage of this system is the *E*→*Z* photoisomerisation efficiency at 405 nm, which is usually the only microscopy laser available in the 350–440 nm range. Here we consider that improved performance for **AzTax**-like reagents will depend on optimising photoconversion at the wavelength/s that will in practice be used for their photocontrol. Developing a set of standard photoswitches with better 405 nm *E*→*Z* photoconversion than these *para*-alkoxyazobenzenes (~46% *Z*) yet with similar polarity and substantial stability against thermal relaxation, is a nontrivial goal of our ongoing research.

From a biological perspective, while **AzTax** have reproduced the effects expected for taxanes across these studies, comparing their mechanism more deeply remains to be addressed. Given the structural overlap of the binding pharmacophores (Fig. 1; ca. 215 Å^2 of paclitaxel's total polar surface area (221 Å^2) overlaps with that of **AzTax3MP** (249 Å^2)) we consider it likely that their effects will prove similar in a variety of settings. This would open up possibilities towards e.g., time-resolved studies of the effects of taxane binding relying on these photoswitchable analogues.

The **AzTax** photoswitchable MT stabilisers can be used in conjunction with long term, in situ photoswitching in live cells to control critical biology from cytoskeleton architecture to cell survival. In short-term experiments, they can reliably apply cell-specific and temporally reversible MT inhibition under straightforward optical control, and have allowed subcellularly resolved inhibition in primary cells with unusual geometry. By complementing the existing MT-depolymerising photopharmaceuticals, the development of **AzTax** now brings both principal modes of pharmacological MT modulation under optical control.

AzTax reagents open up a multitude of possibilities for high-precision biological studies not possible with previous methods. They may contribute to studies across a variety of settings where temporally, cell- or subcellularly specific roles of MTs either are unclear, or else determine downstream biology that is itself of interest. For example, cell specific, temporally precise modulation of MT stability and dynamics may be particularly useful for studies of rapid coordinated processes such as mitotic progression, transport, migration and immune cell response, even in complex environments. **AzTax** may also find particular utility in

neurobiology, for example in exploring the recently discovered important roles of MTs in developing and regenerating neurons. Although MT stabilisation during development was shown to determine axonal identity and remodelling, MT stabilisation in mature neurons seems to promote axonal regeneration by reducing the formation of retraction bulbs and modulating glial scar formation after spinal cord injury[14,32,46–48]. However, the temporal characteristics of these phenomena are unclear, and the roles of MT stabilisation in surrounding glia and immune cells rather than in damaged neurons themselves have not yet been resolved. Photopharmaceutical stabilisers could shed new light on this field by stimulating the phenomena with high enough spatiotemporal resolution to clarify the primary processes responsible[32,33].

In the field of pharmacology, it is still to a large degree unclear[38] how the blockbuster taxane drugs exert their cellular/tissue-level effects in vivo. This provides enormous clinically driven interest in increasing the understanding of taxane pharmacology: both towards improved paclitaxel-site antimitotic therapeutics, and towards designing better combination treatment regimens involving these broad-spectrum cancer chemotherapeutics. Against this backdrop too, **AzTax** offer an intriguing method for precise studies, that may clarify the spatiotemporal dependency of biological action of the parent taxanes.

Beyond the first generation of **AzTax** reagents, we have also identified perspectives for further improving **AzTax**'s photocontrol of biological function through structure-photochemistry/activity-relationship studies. This opens up several avenues for applying fundamental research in the rapidly evolving field of chemical photoswitches to generate specialty MT stabiliser photopharmaceuticals for cell-free mechanistic studies, cell biology, and towards in vivo use. More broadly, this work will also guide and encourage further photopharmaceutical reagent development for other proteins inaccessible to direct optogenetics, including the actin cytoskeleton.

In conclusion, we believe that the **AzTax** will prove useful in studies from intracellular transport, cell division and cell motility, to neurobiology; and that this first demonstration of photoswitchable MT stabilisers is a substantial step towards high-spatiotemporal-precision studies of a range of critical processes in cell biology.

Methods

Full and detailed experimental protocols can be found in the Supplementary Information.

Compound synthesis and characterisation. Reactions and characterisations were performed by default with non-degassed solvents and reagents (Sigma-Aldrich, TCI Europe, Fisher Scientific), used as obtained, under closed air atmosphere without special precautions. Manual flash column chromatography was performed on Merck silica gel Si-60 (40–63 μm). MPLC flash column chromatography was performed on a Biotage Isolera Spektra, using Biotage prepacked silica cartridges. Thin-layer chromatography was run on 0.25 mm Merck silica gel plates (60, F-254), with UV light (254 and 365 nm) for visualisation. NMR characterisation was performed on Bruker 400 or 500 MHz spectrometers. HRMS was performed by electron impact at 70 eV with Thermo Finnigan MAT 95 or Jeol GCmate II spectrometers; or by electrospray ionisation with a Thermo Finnigan LTQ FT Ultra Fourier Transform Ion Cyclotron resonance spectrometer. Analytical HPLC-MS was performed on an Agilent 1100 SL HPLC with H_2O:MeCN eluent gradients, a Thermo Scientific Hypersil GOLD™ C18 column (1.9 μm; 3 × 50 mm) maintained at 25 °C, detected on an Agilent 1100 series diode array detector (DAD) and a Bruker Daltonics HCT-Ultra mass spectrometer.

Photocharacterisation. UV–Vis-based studies (determination of absorption spectra, photostationary states, reversibility of photoisomerisation, and *Z* to *E* relaxation) were performed on a Varian CaryScan 60 (1 cm pathlength) at room temperature with model photoswitches that were water-soluble analogues of the **AzTax** species, since reliable UV–Vis studies require compound concentrations around 25–50 μM, while the **AzTax** compounds are only reliably molecularly soluble at such concentrations with high cosolvent percentages (e.g., 50% DMSO) that do not reflect the intracellular environment and also alter the isomers' spectra, quantum yields, and relaxation times. We synthesised and used di(2-ethanol)amine carboxamides as water-soluble analogues of the taxane carboxamide **AzTax** (see Supplementary Information) enabling measurements in PBS at pH ~7.4 with only 1% of DMSO as cosolvent, thus matching the intracellular environment around the **AzTax**' protein target, tubulin. Star model 3W LEDs (360–530 nm, each FWHM ~25 nm, Roithner Lasertechnik) were used for photoisomerisations in cuvette that were thus predictive of what would be obtained in the cytosol during LED-illuminated cell culture. Spectra of pure *E*- and *Z*-isomers were acquired from the HPLC's inline Agilent 1100 series DAD over the range 200–550 nm, manually baselining across each elution peak of interest to correct for eluent composition.

Tubulin polymerisation in vitro. In total, 99% purity tubulin from porcine brain was obtained from Cytoskeleton Inc. (cat. #T240) and polymerisation assays run according to manufacturer's instructions. Tubulin was incubated at 37 °C with lit- or dark-**AzTax** (10 μM) in buffer (with 3% DMSO, 10% glycerol) and GTP (1 mM), and the change in absorbance at 340 nm was monitored over 15 min at 37 °C[49].

Standard cell culture. HeLa (ATCC CCL-2) and COS-7 (ATCC CRL-1651) cells were maintained under standard cell culture conditions in Dulbecco's modified Eagle's medium supplemented with 10% foetal calf serum (FCS), 100 U mL^{-1} penicillin and 100 μg mL^{-1} streptomycin, at 37 °C in a 5% CO_2 atmosphere (see also Supplementary Information for protocols for other cell types). For long-term assays under photoswitching, HeLa cells were transferred to phenol red free medium prior to assays. Compounds (in the all-*E* state) and cosolvent (DMSO; 1% final concentration) were added via a D300e digital dispenser (Tecan). Treated cells were then incubated under dark (light excluded) or lit conditions (where 75 ms illumination pulses were applied to microtiter plates every 15 s by self-built wavelength-specific multi-LED arrays, to create and maintain the wavelength-dependent photostationary state isomer ratios throughout the experiment[16]).

Antiproliferation assay. As a proxy readout for viable cells, mitochondrial diaphorase activity in HeLa cell line was quantified by measuring the reduction of resazurin (7-hydroxy-3*H*-phenoxazin-3-one 10-oxide) to resorufin. 5000 cells per well were seeded on 96-well plates. After 24 h, cells were treated with *E*-**AzTax**, shielded from ambient light with light-proof boxes, and exposed to the appropriate light regimes. Following 48 h of treatment, cells were incubated with 20 μL of 0.15 mg mL^{-1} resazurin per well for 3 h at 37 °C. The resorufin fluorescence (excitation 544 nm, emission 590 nm) was measured using a FLUOstar Omega microplate reader (BMG Labtech). Results are represented as percent of DMSO-treated control (reading zero was assumed to correspond to zero viable cells) and represented as mean of at least three independent experiments with s.d.

Cell-cycle analysis. *E*-**AzTax** were added to HeLa cells in 6-well plates (seeding density: 300,000 cells per well) and incubated under dark or lit conditions for 24 h. Cells were harvested and fixed in ice-cold 70% ethanol then stained with propidium iodide (PI, 200 μg mL^{-1} in 0.1% Triton X-100 containing 200 μg mL^{-1} DNase-free RNase (Thermo Fischer Scientific EN0531) for 30 min at 37 °C. Following PI staining, cells were analysed by flow cytometry using an LSR Fortessa (Becton Dickinson) run by BD FACSDiva 8.0.1 software. The cell-cycle analysis was subsequently performed using FlowJo-V10 software (Tree Star Inc.). Cells were sorted into sub-G1, G1, S and G_2/M phase according to DNA content (PI signal). Quantification from gating on the respective histograms is shown as percent of live/singlet/PI-positive parent population per cell-cycle phase across different concentrations of the compound. Every experiment was performed in technical triplicates, at least three times independently, with a minimum of 10,000 (mean: 14,000) PI-positive singlet cells analysed per replicate.

Immunofluorescence staining. HeLa cells seeded on glass coverslips in 24-well plates (50,000 cells per well) were left to adhere for 24 h then treated for 24 h with **AzTax** under dark or lit conditions. Cover slips were washed then fixed with 0.5% glutaraldehyde, quenched with 0.1% $NaBH_4$, blocked with PBS + 10% FCS, treated with rabbit alpha-tubulin primary antibody (ab18251, abcam), washed, and incubated with donkey-anti-rabbit Alexa fluor 488 secondary antibody (A-21206, Invitrogen). After washing with PBS, coverslips were mounted onto glass slides using Roti-Mount FluorCare DAPI (Roth) and imaged with a Leica SP8 confocal microscope with a 63 × glycerol objective (DAPI: 405 nm, tubulin: 488 nm). Z-stacks (step size: 0.33 μm) were projected using Fiji and gamma values adjusted for visualisation.

EB3 imaging with cell-specific photoisomerisation. HeLa cells were transiently transfected with EB3-tdTomato (gift from Erik Dent; Addgene #50708) using FuGENE 6 (Promega) according to manufacturer's instructions (see Supplementary Information for all other imaging protocols). Cells were imaged on a Nikon Eclipse Ti microscope equipped with a perfect focus system (Nikon), a spinning disk-based confocal scanner unit (CSU-X1-A1, Yokogawa) and an Evolve 512 EMCCD camera (Photometrics) with a stage top incubator INUBG2E-ZILCS

(Tokai Hit) and lens heating calibrated for incubation at 37 °C with 5% CO_2. Cells were incubated in standard cell culture medium with 0.5% DMSO cosolvent, with or without *E*-**AzTax3MP**, for 10 min before microscope image acquisition using MetaMorph 7.7 was begun, with EB3-tdTomato imaging performed at 561 nm (0.17 mW, 300 ms every 4 s). Periods of intracellular-ROI-localised 405 nm illuminations (10 µW, 1 scan every 4 s during 24 s periods) were applied during imaging. Acquisition used a Plan Apo VC 60 × NA 1.4 oil objective. Comet count analysis was performed in ImageJ using the ComDet plugin (E. Katrukha, University of Utrecht, https://github.com/ekatrukha/ComDet).

Subcellular MT manipulation in primary hippocampal neurons. Mouse primary hippocampal neurons were derived from hippocampi of embryonic day 18 pups and plated on poly-L-lysine (Sigma-Aldrich) and laminin (Roche) coated coverslips. Primary neurons were cultured in Neurobasal medium (NB) supplemented with 2% B27 (Gibco), 0.5 mM glutamine (Gibco), 15.6 µM glutamate (Sigma-Aldrich) and 1% penicillin/streptomycin (Gibco) at 37 °C and 5% CO_2. Neurons were transfected with EB3-tdTomato on the 7th day in vitro (DIV 7) using Lipofectamine 2000 (Invitrogen) and were imaged at DIV 9. Neurons were imaged on the same system used for cell-specific-photoisomerisation experiments (described above). Neurons were first immersed in conditioned NB with 1% DMSO. EB3-tdTomato was imaged at 561 nm (0.1 mW, 400 ms every 4 s), while a ROI (violet box) was pulsed with 405 nm light (0.2 mW, 8 ms per trace) tracing over the ROI four times every 4 s with imaging frames interleaved. The same neurons were then immersed in conditioned NB with 1% DMSO and 0.5 µM AzTax3MP and immediately imaged for another 10 min; during this time the same ROI (violet box) was pulsed with 405 nm light (same protocol) starting 2 min into the acquisition.

Statistics. If not indicated otherwise all statistical analyses are unpaired, two-tailed Student's *t* test conducted with GraphPad Prism for Mac 8.4. *P* values below 0.05 were considered significant.

Reporting summary. Further information on research design is available in the Nature Research Reporting Summary linked to this article.

Data availability

All data generated or analysed during this study are included in this published article and its Supplementary Information files, including the Source Data file provided (raw data for Figs. 2–5 and Supplementary Figs. 1–5). This and all data of the study can also be obtained from the authors upon request. None of these datasets are resources of public interest and therefore are not archived publicly in other forms. All materials are available from the Corresponding Author upon request. Source data are provided with this paper.

Received: 14 November 2019; Accepted: 19 August 2020;
Published online: 15 September 2020

References

1. Wu, Y. I. et al. A genetically encoded photoactivatable Rac controls the motility of living cells. *Nature* **461**, 104–108 (2009).
2. Tas, R. P. et al. Guided by light: optical control of microtubule gliding assays. *Nano Lett.* **18**, 7524–7528 (2018).
3. Adikes, R. C., Hallett, R. A., Saway, B. F., Kuhlman, B. & Slep, K. C. Control of microtubule dynamics using an optogenetic microtubule plus end–F-actin cross-linker. *J. Cell Biol.* **217**, 779–793 (2018).
4. Bruce, A. et al. *Molecular Biology of the Cell*. (Garland Science, 2007).
5. Kopf, A. et al. Microtubules control cellular shape and coherence in amoeboid migrating cells. *J. Cell Biol.* **219**, e201907154 (2020).
6. Dumontet, C. & Jordan, M. A. Microtubule-binding agents: a dynamic field of cancer therapeutics. *Nat. Rev. Drug Discov.* **9**, 790–803 (2010).
7. Peterson, J. R. & Mitchison, T. J. Small molecules, big impact: a history of chemical inhibitors and the cytoskeleton. *Chem. Biol.* **9**, 1275–1285 (2002).
8. Kingston, D. G. I.Taxol, a molecule for all seasons. *Chem. Commun*. 867–880. https://doi.org/10.1039/b100070p (2001).
9. Castle, B. T. & Odde, D. J. Optical control of microtubule dynamics in time and space. *Cell* **162**, 243–245 (2015).
10. van Haren, J. et al. Local control of intracellular microtubule dynamics by EB1 photodissociation. *Nat. Cell Biol.* **20**, 252–261 (2018).
11. Nijenhuis, W., van Grinsven, M. M. P. & Kapitein, L. C. An optimized toolbox for the optogenetic control of intracellular transport. *J. Cell Biol.* **219**, e201907149 (2020).
12. van Bergeijk, P., Adrian, M., Hoogenraad, C. C. & Kapitein, L. C. Optogenetic control of organelle transport and positioning. *Nature* **518**, 111–114 (2015).
13. Buck, K. B. & Zheng, J. Q. Growth cone turning induced by direct local modification of microtubule dynamics. *J. Neurosci.* **22**, 9358–9367 (2002).
14. Witte, H., Neukirchen, D. & Bradke, F. Microtubule stabilization specifies initial neuronal polarization. *J. Cell Biol.* **180**, 619–632 (2008).
15. Klán, P. et al. Photoremovable protecting groups in chemistry and biology: reaction mechanisms and efficacy. *Chem. Rev.* **113**, 119–191 (2013).
16. Borowiak, M. et al. Photoswitchable inhibitors of microtubule dynamics optically control mitosis and cell death. *Cell* **162**, 403–411 (2015).
17. Rastogi, S. K. et al. Photoresponsive azo-combretastatin A-4 analogues. *Eur. J. Med. Chem.* **143**, 1–7 (2018).
18. Borowiak, M. et al. Optical manipulation of F-actin with photoswitchable small molecules. *J. Am. Chem. Soc.* **142**, 9240–9249 (2020).
19. Hüll, K., Morstein, J. & Trauner, D. In vivo photopharmacology. *Chem. Rev.* **118**, 10710–10747 (2018).
20. Zenker, J. et al. Expanding actin rings zipper the mouse embryo for blastocyst formation. *Cell* **173**, 776–791 (2018).
21. Zenker, J. et al. A microtubule-organizing center directing intracellular transport in the early mouse embryo. *Science* **357**, 925–928 (2017).
22. Singh, A. et al. Polarized microtubule dynamics directs cell mechanics and coordinates forces during epithelial morphogenesis. *Nat. Cell Biol.* **20**, 1126–1133 (2018).
23. Morstein, J. et al. Optical control of sphingosine-1-phosphate formation and function. *Nat. Chem. Biol.* **15**, 623–631 (2019).
24. Laprell, L. et al. Photopharmacological control of bipolar cells restores visual function in blind mice. *J. Clin. Investig.* **127**, 2598–2611 (2017).
25. Thorn-Seshold, O., Borowiak, M., Trauner, D. & Hasserodt, J. Azoaryls as reversibly modulatable tubulin inhibitors. WO2015166295A1. https://worldwide.espacenet.com/patent/search/family/051263438/publication/WO2015166295A1?q=pn%3DWO2015166295A1 (2014).
26. Engdahl, A. J. et al. Synthesis, characterization, and bioactivity of the photoisomerizable tubulin polymerization inhibitor azo-combretastatin A4. *Org. Lett.* **17**, 4546–4549 (2015).
27. Sheldon, J. E., Dcona, M. M., Lyons, C. E., Hackett, J. C. & Hartman, M. C. T. Photoswitchable anticancer activity via trans-cis isomerization of a combretastatin A-4 analog. *Org. Biomol. Chem.* **14**, 40–49 (2016).
28. Gao, L. et al. Photoswitchable microtubule inhibitors enabling robust, GFP-orthogonal optical control over the tubulin cytoskeleton. Preprint at https://www.biorxiv.org/content/10.1101/716233v1 (2019).
29. Sailer, A. et al. Hemithioindigos as desymmetrised molecular switch scaffolds: design control over the isomer-dependency of potent photoswitchable antimitotic bioactivity in cellulo. *ChemBioChem* **20**, 1305–1314 (2019).
30. Sailer, A. et al. Potent hemithioindigo-based antimitotics photocontrol the microtubule cytoskeleton in cellulo. *Beilstein J. Org. Chem.* **16**, 125–134 (2020).
31. Vandestadt, C. et al. Early migration of precursor neurons initiates cellular and functional regeneration after spinal cord injury in zebrafish. Preprint at https://www.biorxiv.org/content/10.1101/539940v1 (2019).
32. Hellal, F. et al. Microtubule stabilization reduces scarring and causes axon regeneration after spinal cord injury. *Science* **331**, 928–931 (2011).
33. Sengottuvel, V., Leibinger, M., Pfreimer, M., Andreadaki, A. & Fischer, D. Taxol facilitates axon regeneration in the mature CNS. *J. Neurosci.* **31**, 2688–2699 (2011).
34. Kingston, D. G. I. The chemistry of taxol. *Pharmacol. Therapeutics* **52**, 1–34 (1991).
35. Lukinavicius, G. et al. Fluorogenic probes for live-cell imaging of the cytoskeleton. *Nat. Meth* **11**, 731–733 (2014).
36. Alushin, G. M. et al. High-resolution microtubule structures reveal the structural transitions in αβ-tubulin upon GTP hydrolysis. *Cell* **157**, 1117–1129 (2014).
37. Löwe, J., Li, H., Downing, K. H. & Nogales, E. Refined structure of αβ-tubulin at 3.5 Å resolution. *J. Mol. Biol.* **313**, 1045–1057 (2001).
38. Mitchison, T. J. The proliferation rate paradox in antimitotic chemotherapy. *Mol. Biol. Cell* **23**, 1–6 (2012).
39. Das, G. C., Holiday, D., Gallardo, R. & Haas, C. Taxol-induced cell cycle arrest and apoptosis: dose-response relationship in lung cancer cells of different wild-type p53 status and under isogenic condition. *Cancer Lett.* **165**, 147–153 (2001).
40. Merriam, E. B. et al. Synaptic regulation of microtubule dynamics in dendritic spines by calcium, F-actin, and drebrin. *J. Neurosci.* **33**, 16471–16482 (2013).
41. Gonçalves, A. et al. Resistance to taxol in lung cancer cells associated with increased microtubule dynamics. *Proc. Natl Acad. Sci. USA* **98**, 11737–11742 (2001).
42. Zhang, Y.-M., Zhang, N.-Y., Xiao, K., Yu, Q. & Liu, Y. Photo-controlled reversible microtubule assembly mediated by paclitaxel-modified cyclodextrin. *Angew. Chem. Int. Ed.* **57**, 8649–8653 (2018).
43. Zhang, Y.-M., Liu, J.-H., Yu, Q., Wen, X. & Liu, Y. Targeted polypeptide–microtubule aggregation with cucurbit[8]uril for enhanced cell apoptosis. *Angew. Chem. Int. Ed.* **58**, 10553–10557 (2019).

44. Thorn-Seshold, O. Comment on "Photo-Controlled Reversible Microtubule Assembly Mediated by Paclitaxel-Modified Cyclodextrin". *Angew. Chem. Int. Ed.* **59**, 7652–7654 (2020).
45. Weston, C. E., Richardson, R. D., Haycock, P. R., White, A. J. P. & Fuchter, M. J. Arylazopyrazoles: azoheteroarene photoswitches offering quantitative isomerization and long thermal half-lives. *J. Am. Chem. Soc.* **136**, 11878–11881 (2014).
46. Brill, M. S. et al. Branch-specific microtubule destabilization mediates axon branch loss during neuromuscular synapse elimination. *Neuron* **92**, 845–856 (2016).
47. Ertürk, A., Hellal, F., Enes, J. & Bradke, F. Disorganized microtubules underlie the formation of retraction bulbs and the failure of axonal regeneration. *J. Neurosci.* **27**, 9169–9180 (2007).
48. Ruschel, J. et al. Axonal regeneration. Systemic administration of epothilone B promotes axon regeneration after spinal cord injury. *Science* **348**, 347–352 (2015).
49. Lin, C. M. et al. Interactions of tubulin with potent natural and synthetic analogs of the antimitotic agent combretastatin: a structure-activity study. *Mol. Pharmacol.* **34**, 200–208 (1988).

Acknowledgements

This research was supported by funds from the German Research Foundation (DFG: SFB1032 Nanoagents for Spatiotemporal Control project B09 to D.T. and O.T.-S.; SFB TRR 152 project P24 number 239283807, Emmy Noether grant TH2231/1-1, and SPP 1926 project number 426018126 to O.T.-S.); the NIH (Grant R01GM126228 to D.T.; RO1AG050658 to F.B.); and the Thompson Family Foundation (TFFI to F.B.). We thank P.A.S. (LMU) for initial synthesis, F. Ermer and M. Borowiak (LMU) for initial MTT viability assays, H. Harz for microscopy access (LMU microscopy platform CALM), and CeNS (LMU) for support. We thank Natalia Marahori and Thomas Misgeld for valuable experimental feedback on **AzTax3MP**; and Maximilian Wranik, Michel Steinmetz, and the members of the Steinmetz group for work towards obtaining crystal structures of **AzTax**s bound to tubulin. We are indebted to Tim Mitchison for his contributions to small molecule inhibitors in MT research.

Author contributions

A.M.-D. performed synthesis, photocharacterisation, and coordinated chemical data assembly. J.C.M.M. performed temporally reversible live cell imaging studies. K.L. and Y.K. performed cell biology. C.H. performed flow cytometry. R.B. performed in vitro tubulin polymerisation assays. K.I.J. and L.C.K. performed primary neuron isolation and culture. X.Q. and F.B. conducted early cell experimentation. A.A. supervised temporally reversible cell studies. J.A. performed and supervised cell biology, and coordinated biological data assembly. D.T. designed the concept and supervised initial synthesis. O.T.-S. designed the study, performed and supervised synthesis, supervised all other experiments, coordinated data assembly and wrote the paper with input from all authors.

Funding

Open Access funding provided by Projekt DEAL.

Competing interests

The authors declare no competing interests.

Additional information

Supplementary information is available for this paper at https://doi.org/10.1038/s41467-020-18389-6.

Correspondence and requests for materials should be addressed to O.T.-S.

Peer review information *Nature Communications* thanks Craig Streu and the other, anonymous, reviewer(s) for their contribution to the peer review of this work. Peer reviewer reports are available.

Reprints and permission information is available at http://www.nature.com/reprints

Publisher's note Springer Nature remains neutral with regard to jurisdictional claims in published maps and institutional affiliations.

Supplementary Information

Photoswitchable paclitaxel-based microtubule stabilisers allow optical control over the microtubule cytoskeleton

Müller-Deku *et al.*

Supplementary Information to:

Photoswitchable paclitaxel-based microtubule stabilisers allow optical control over the microtubule cytoskeleton

Adrian Müller-Deku[1], Joyce C.M. Meiring[2], Kristina Loy[1], Yvonne Kraus[1], Constanze Heise[1], Rebekkah Bingham[1], Klara I. Jansen[2], Xiaoyi Qu[3], Francesca Bartolini[3], Lukas C. Kapitein[2], Anna Akhmanova[2], Julia Ahlfeld[1], Dirk Trauner[4,*], Oliver Thorn-Seshold[1,*,#]

1: Department of Pharmacy, Ludwig-Maximilians University, Butenandtstrasse 7, Munich 81377, Germany; 2: Cell Biology, Neurobiology and Biophysics, Department of Biology, Faculty of Science, Utrecht University, Padualaan 8, 3584 Utrecht, the Netherlands; 3: Department of Pathology & Cell Biology, Columbia University Medical Center, New York, NY 10032, USA; 4: Department of Chemistry, New York University, 100 Washington Square East, New York, NY 10003, USA.

* Senior Authors

Correspondence and requests for materials to O.T.-S. (oliver.thorn-seshold@cup.lmu.de)

ORCIDs: A.M-D. 0000-0001-6050-2545; J.A. 0000-0002-4879-4159; D.T. 0000-0002-6782-6056; O.T.-S. 0000-0003-3981-651X

Table of Contents

Supplementary Note 1: Chemistry

Conventions

Abbreviations:

The following abbreviations are used: Boc: *tert*-butoxycarbonyl; brsm: based on recovered starting material; DCM: dichloromethane; DIPEA: diisopropylethylamine; DMF: dimethylformamide; DMSO: dimethylsulfoxide; EA: ethyl acetate; EDCI: 1-Ethyl-3-(3-dimethylaminopropyl)carbodiimide; IHex: distilled isohexane; HOBt: 1-hydroxybenzotriazole; Me: methyl; TFA: trifluoroacetic acid; PBS: phosphate buffered saline; T3P: propylphosphonic anhydride; wt%: percentage by weight.

Safety Hazards:

No remarkable safety hazards were encountered.

Reagents and Conditions:

Unless stated otherwise, (1) all reactions and characterisations were performed with unpurified, undried, non-degassed solvents and reagents, used as obtained, under closed air atmosphere without special precautions; (2) “hexane” used for chromatography was distilled from commercial crude isohexane fraction by rotary evaporation; (3) “column” and “chromatography” refer to manual flash column chromatography on Merck silica gel Si-60 (40–63 µm) unless otherwise specified; (4) procedures and yields are unoptimised; (5) yields refer to isolated chromatographically and spectroscopically pure materials; (6) all eluent and solvent mixtures are given as volume ratios unless otherwise specified, thus “1:1 iHex:EA” indicates a 1:1 mixture (by volume) of hexanes and ethyl acetate; (7) chromatography eluents e.g. “3:1 → 1:1” indicate a stepwise or continual gradient of eluent composition.

Thin-layer chromatography (TLC):

TLC was run on 0.25 mm Merck silica gel plates (60, F-254), typically with iHex:EA eluents. All compounds carrying an azobenzene need no visualization on the TLC-plate but are clearly visible as colored spots (color range yellow to red). The presence of an azobenzene can be verified by exposure of the colored spot to TFA vapors, which transiently changes the color to shades of purple according to basicity. For further visualization UV light (254 nm) was used. TLC characterizations are abbreviated as $\mathbf{R}_f = 0.64$ (UV 254 nm, iHex:EA = 1:1).

Nuclear magnetic resonance spectroscopy (NMR):

Standard NMR characterisation was by ^{1}H- and ^{13}C-NMR spectra on an Avance III HD 400 MHz Bruker BioSpin or Bruker Ascend 400, or Avance III HD 500 MHz Bruker BioSpin (1H: 400 MHz and 500 MHz, 13C: 101 MHz and 126 MHz). Chemical shifts (δ) are reported in ppm calibrated to residual non-perdeuterated solvent as an internal reference[1]. Peak descriptions singlet (s), doublet (d), triplet (t), quartet (q), multiplet (m) and broad (br) are used. Apparent multiplicities (resolved by 2D experiments or determined by complete spectral

assignment) are denoted by a tilde, eg. “appears as a triplet with apparent coupling constant *J* = 3 Hz” is denoted (~t, 3 Hz). NMR spectra are given in Supplementary Note 5.

High resolution mass spectrometry (HRMS):

HRMS was performed by electron impact (EI) at 70 eV with a Thermo Finnigan MAT 95 or a Jeol GCmate II spectrometer; or electrospray ionization (ESI) with a Thermo Finnigan LTQ FT Ultra Fourier Transform Ion Cyclotron resonance mass spectrometer; as specified.

High-performance liquid chromatography coupled to mass spectrometry (LCMS):

Analytical high-performance liquid chromatography (HPLC) was performed on an Agilent 1100 SL coupled HPLC system with (a) a binary pump to deliver H_2O:MeCN eluent mixtures containing 0.1% formic acid at a 0.4 mL/min flow rate, (b) Thermo Scientific Hypersil GOLD™ C18 column (1.9 µm; 3 × 50 mm) maintained at 25°C, whereby the solvent front eluted at t_{ret} = 0.5 min, (c) an Agilent 1100 series diode array detector, (d) a Bruker HCT Ultra mass spectrometer. Typical run conditions were a linear gradient of H_2O:MeCN eluent composition from 90:10 through to 1:99, applied during the separation phase (first 5 min), then 0:100 for 2 min for flushing; the column was (re)equilibrated with 90:10 eluent mixture for 2 min before each run. Ion peaks from (positive/negative mode) are reported as (+/-) with units Th (m/z). Thus “LCMS(+): t_{ret} = 5.60 & 5.82 min, each 419 Th = $[MH]^+$” indicates LCMS under the standard run conditions with ESI ionisation giving two positive ion peaks eluting at 5.60 and 5.82 min retention times, each at m/z = 419 Th, attributed as the protonated molecular ion. Unless stated otherwise, all reported peaks in the positive mode were $[MH]^+$ peaks.

Text
Text

Standard Procedures

Where Standard Procedures were used in synthesis, unless stated otherwise, the amounts of reactants/reagents employed were implicitly adjusted to maintain the same molar ratios as in the given Procedure, and no other alterations from the Standard Procedure (eg. reaction time, extraction solvent, temperature) were made, unless stated otherwise.

Standard Procedure A: Azo coupling with a phenol partner

A flask was charged with the aniline coupling partner (1.0 eq) and MeOH (3 mL/mmol). Aqueous HCl (2 M, 6.0 eq) was added. The reaction mixture was cooled to 0°C and a 2 M aqueous of solution of $NaNO_2$ (1.1 eq) was added dropwise. It was allowed to stir for 30 min. A solution of the phenol coupling partner (1.1 eq) in MeOH (4 mL/mmol) and 0.5 M aqueous K_2HPO4 (4 mL/mmol) was prepared at 0°C. The diazonium solution was added dropwise onto the phenol mixture. The pH was maintained between 9-10 by adding aq. KOH (1 M). Upon completion of the addition the reaction mixture was allowed to stir for 1 h in the cold. The reaction progress was monitored by LCMS/TLC analysis. The reaction was quenched by the adjustment of the pH to pH 4-6 with 2 M aqueous HCl and extracted with EA (3 × 20 mL/mmol). The combined organic phases were dried with Na_2SO_4, filtrated and concentrated. The crude product was purified by flash chromatography using a iHex:EA gradient.

Standard Procedure B: Azo coupling with a dialkylaniline partner

A flask was charged with the aniline coupling partner (1.0 eq) and MeOH (3 mL/mmol). Aqueous HCl (2 M, 6.0 eq) was added. The reaction mixture was cooled to 0°C and a 2 M aqueous of solution of $NaNO_2$ (1.1 eq) was added dropwise. It was allowed to stir for 30 min. Acetic acid (3 mL/mmol) followed by the dialkylaniline coupling partner (1.5 eq) were added neat. Sodium acetate (10.0 eq) was added portionwise. Upon completion of the addition the reaction mixture was allowed to stir for 1 h in the cold. The reaction progress was monitored by LCMS/TLC analysis. The reaction was quenched by neutralization with KOH solution (1 M) and extracted with EA (3 × 20 mL/mmol). The combined organic phases were dried with Na_2SO_4, filtrated and concentrated. The crude product was purified by flash chromatography using a IHex:EA gradient.

Standard Procedure C: Methylation of a *para*-hydroxy azobenzene

A flask was charged with the respective azobenzene compound and acetone (5 mL/mmol) was added. Potassium carbonate (5.0 eq) was added. Iodomethane (3.00 eq) was added dropwise. The reaction mixture was heated to 50°C for typically 5 h. The reaction progress was monitored by LCMS/TLC analysis. The reaction was quenched by the addition of water (20 mL/mmol) and extracted with EA (3 × 20 mL/mmol). The combined organic phases were dried with Na_2SO_4, filtrated and concentrated. The crude product was purified by flash chromatography on silica using a iHex:EA gradient.

Standard Procedure D: Hydrolysis of an azobenzenecarboxylate ester

A flask was charged with the respective azobenzenecarboxylate ester and MeOH (5 mL/mmol) was added. Potassium hydroxide (5.0 eq) was added neat. The reaction mixture was heated to 65°C for 12 h. The reaction progress was monitored by LCMS/TLC analysis. Upon completion the reaction was quenched with water (20 mL/mmol), neutralized with 2 M aqueous KOH and extracted with EA (3 × 20 mL/mmol). The combined organic phases were dried with Na_2SO_4, filtrated and concentrated. Typically, no further purification was needed.

Standard Procedure E: Docetaxel deprotection and amide coupling

A flask was charged with docetaxel (16 mg, 20 μmol, 1.0 eq) and DCM (2 mL) and the solution stirred at 0°C for 2 min. TFA (2 mL) was added and the mixture stirred at 0°C for 1 hour. The solution was added into rapidly stirred sat. aq. $NaHCO_3$ (15 mL). Solid $NaHCO_3$ was added until all TFA was neutralized. The mixture was extracted with DCM (3 × 10 mL). The combined organic layers were washed with sat. aq. $NaHCO_3$ (10 mL), brine (10 mL), dried on Na_2SO_4, filtered and concentrated to a colourless crude foam (typically 10 mg, 15 μmol, 71%; LCMS(+): t_{ret} = 4.71 min, 708 Th = $[MH]^+$). The crude was dissolved in HPLC-grade DMF (2 mL). The azobenzene carboxylic acid (1.2 eq.) was dissolved in HPLC-grade DMF (1 mL), HOBt·H_2O (2.5 eq) and EDCI (2.25 eq) were added and the solution stirred at room temperature for 5 min. A DMF (1 mL) solution of DIPEA (4.0 eq) was added dropwise and stirring continued for 10 min. The solution of crude deprotected docetaxel was added and the solution stirred for

12 h at room temperature, then poured into 10% aq. $NaHCO_3$ (20 mL) and extracted with DCM (3 × 10 mL). The combined organic layers were washed with sat. aq. $NaHCO_3$ (10 mL), sat. aq. LiCl (10 mL), brine (10 mL), dried on Na_2SO_4, filtered and concentrated to a yellow solid. Chromatography on silica with a iHex:EA= 7:3→1:1 then DCM:MeOH= 1:0→9:1 gradient couple typically separated the product fractions. These were combined, concentrated, and dried under high vacuum.

Standard Procedure F: Preparation of soluable azo derivatives for photocharacterization

A flask was charged with the azobenzene carboxylic acid (1.0 eq) and DMF (25 mL/mmol) was added. Triethylamine (10.0 eq) was added. Diethanolamine (2.0 eq) dissolved in DMF (0.65 mL/mmol) was added to the reaction mixture. T3P (2.0 eq, ≥50 wt. % in EA) was added and the resulting solution was allowed to stir for 16 h at 25°C. Progress of the reaction was monitored by LCMS. Upon completion the DMF was removed *in vacuo* and the crude product was purified by flash chromatography on silica using a DCM:MeOH gradient.

Azobenzene carboxylic acids

4-(phenyldiazenyl)benzoic acid (4H-CO_2H)

Commercially available (CAS 1562-93-2).

4-((4-(dimethylamino)phenyl)diazenyl)benzoic acid (4DMA-CO_2H)

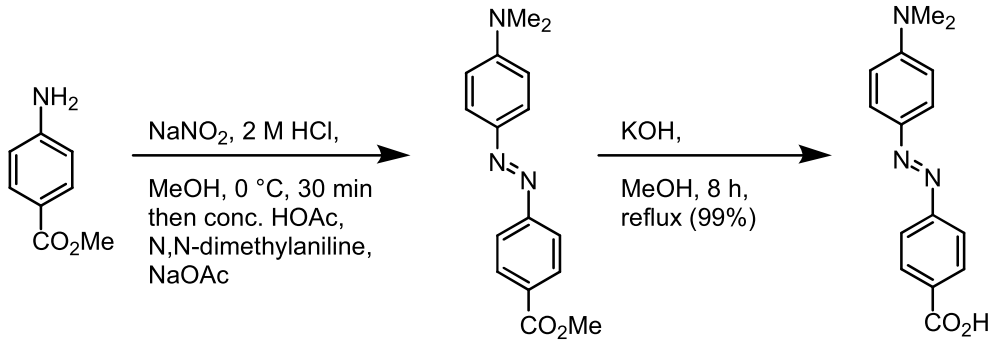

S1 **4DMA-CO_2H**

By standard procedure B, commercially available methyl 4-aminobenzoate (302 mg, 2.0 mmol, 1.0 eq) was reacted with dimethyaniline (364 mg, 3.0 mmol, 1.5 eq). After purification by flash chromatography (EA:iHex, 9:1 → 8:2) the desired product **methyl 4-((4-(dimethylamino)phenyl)diazenyl)benzoate** (**S1**) (224 mg, 0.80 mmol, 40%) was obtained as a red solid. Spectral data matches literature[2]: **^{1}H NMR** (400 MHz, chloroform-*d*) δ (ppm) = 8.19 – 8.10 (m, 2H), 7.96 – 7.82 (m, 4H), 6.79 – 6.73 (m, 2H), 3.94 (s, 3H), 3.11 (s, 6H). **^{13}C NMR** (101 MHz, chloroform-*d*) δ (ppm) = 167.1, 156.3, 153.2, 144.0, 130.8, 130.4, 125.8, 122.3, 111.7, 52.5, 40.6. **LCMS(+)**: t_{ret} = 4.7 min, 284 Th = $[MH]^+$**. HRMS (EI):** calc. for $[C_{16}H_{17}O_2N_3]^+ = [M]^+$: 283.1321; found: 283.1314.

By standard procedure D, **S1** (100 mg, 0.35 mmol, 1.0 eq) was reacted to the desired product **4DMA-CO_2H** (93 mg, 0.40 mmol, 98%) which was obtained as a red solid. Spectral data

matches literature[2]: **^{1}H NMR** (400 MHz, DMSO-d6) δ (ppm) = 8.13 – 8.02 (m, 2H), 7.89 – 7.78 (m, 4H), 6.92 – 6.79 (m, 2H), 3.08 (s, 6H). **^{13}C NMR** (101 MHz, DMSO) δ (ppm) = 166.9, 155.1, 153.0, 142.7, 130.9, 130.5, 125.3, 121.7, 111.6, 39.8. **LCMS(+):** t_{ret} = 4.7 min, 270 Th = $[MH]^+$. **HRMS (EI):** calc. for $[C_{15}H_{15}O_2N_3]^+ = [M]^+$: 269.1164; found: 269.1158.

4-((4-methoxyphenyl)diazenyl)benzoic acid (4MP-CO_2H)

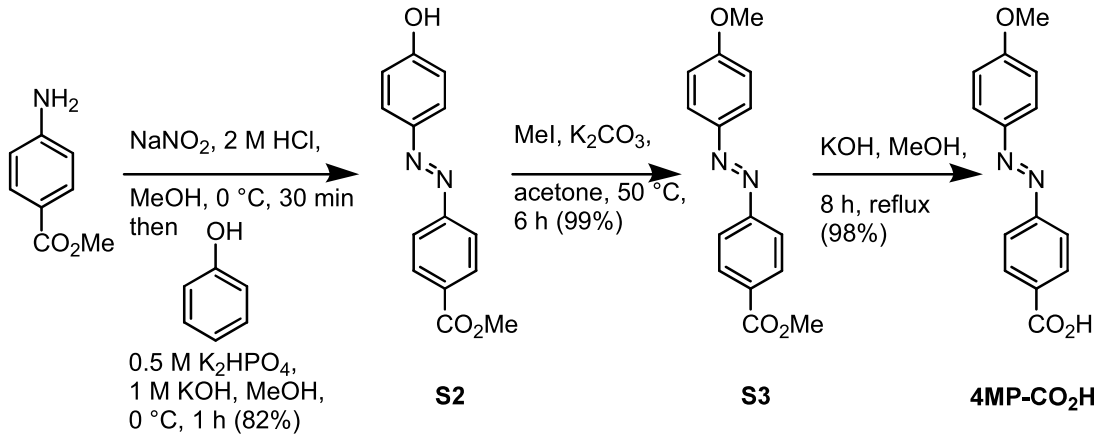

By standard procedure A, commercially available methyl 4-amino benzoate (302 mg, 2.0 mmol, 1.0 eq) was reacted with phenol (207 mg, 2.2 mmol, 1.1 eq). After purification by means of flash chromatography (EA:iHex, 8:2 → 1:1) the desired product **methyl 4-((4-hydroxyphenyl)diazenyl)benzoate** (**S2**) (421 mg, 1.6 mmol, 82%) was obtained as an orange solid. Spectral data matches literature[3]: **^{1}H NMR** (400 MHz, DMSO-d_6) δ (ppm) = 8.17 – 8.08 (m, 2H), 7.93 – 7.88 (m, 2H), 7.88 – 7.80 (m, 2H), 7.00 – 6.93 (m, 2H), 3.89 (s, 3H). **^{13}C NMR** (101 MHz, DMSO-d_6) δ (ppm) = 165.7, 161.8, 154.8, 145.3, 130.6, 130.5, 125.4, 122.3, 116.1, 52.4. **LCMS(+):** t_{ret} = 5.0 min, 257 Th = $[MH]^+$. **HRMS (EI):** calc. for $[C_{16}H_{17}O_2N_3]^+ = [M]^+$: 256.0848; found: 256.0843.

By standard procedure C, **S2** (410 mg, 1.6 mmol, 1.0 eq) was reacted with methyl iodide (681 mg, 4.8 mmol, 3.0 eq). After purification by means of flash chromatography (EA:iHex, 9:1 → 7:3) the desired product **methyl 4-((4-methoxyphenyl)diazenyl)benzoate** (**S3**) (431 mg, 1.6 mmol, 99%) was obtained as an orange solid. Spectral data matches literature[4,5]: **^{1}H NMR** (400 MHz, chloroform-*d*) δ (ppm) = 8.21 – 8.14 (m, 2H), 7.95 (d, *J* = 9.0 Hz, 2H), 7.91 (d, *J* = 8.7 Hz, 2H), 7.03 (d, *J* = 9.0 Hz, 2H), 3.95 (s, 3H), 3.91 (s, 3H). **^{13}C NMR** (101 MHz, chloroform-*d*) δ (ppm) = 166.8, 162.8, 155.5, 147.2, 131.3, 130.7, 125.3, 122.5, 114.5, 55.8, 52.4.. **LCMS(+):** t_{ret} = 6.0 min, 271 Th = $[MH]^+$**. HRMS (EI):** calc. for $[C_{15}H_{14}N_2O_3]^+ = [M]^+$: 270.1004; found: 270.0998.

By standard procedure D, **S3** (100 mg, 0.35 mmol, 1.0 eq) was reacted to the desired product **4-((4-(dimethylamino)phenyl)diazenyl)benzoic acid** (**4MP-CO_2H**) (93 mg, 0.40 mmol, 98%) was obtained as an orange solid. Spectral data matches literature[6]: **^{1}H NMR** (400 MHz, DMSO-d_6) δ (ppm)= 8.03 (d, J = 8.4 Hz, 2H), 7.91 (d, J = 9.0 Hz, 2H), 7.79 (d, J = 8.4 Hz, 2H), 7.14 (d, J = 9.0 Hz, 2H), 3.87 (s, 3H). **^{13}C NMR** (101 MHz, DMSO) δ (ppm) = 166.8, 162.6,

154.4, 146.2, 132.2, 130.6, 125.0, 122.2, 114.8, 55.7. **LCMS(+):** t_{ret} = 5.0 min, 257 Th = $[MH]^+$. **HRMS (EI):** calc. for $C_{14}H_{12}O_3N_2^+$ $[M]^+$: 256.0848; found: 256.0838.

3-(phenyldiazenyl)benzoic acid (3H-CO_2H)

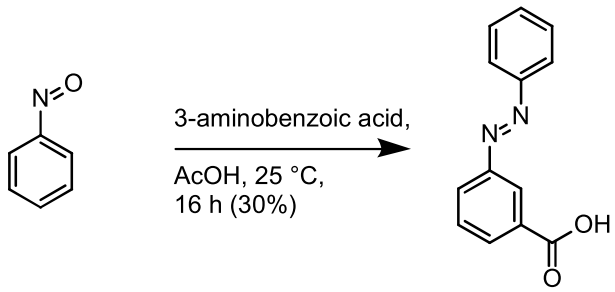

3H-CO_2H

Prepared according to literature[7]. A flask was charged with nitrosobenzene (214 mg, 2.0 mmol, 1.0 eq) and 5 mL AcOH was added. 3-aminobenzoic acid (274 mg, 2.0 mmol, 1.0 eq) was added and the reaction mixture was allowed to stir for 24 h at 25°C. LCMS indicated completion. The reaction was quenched with water (30 mL) and the aqueous phase was extracted with EA (3 × 50 mL). The combined organic phases were dried with Na_2SO_4, filtrated and concentrated. After purification by means of flash chromatography (DCM:MeOH, 98:2 → 94:6) the desired product **3-(phenyldiazenyl)benzoic acid** (**3H-CO_2H**) (134 mg, 0.59 mmol, 30%) was obtained as an orange solid. Spectral data matches literature[7]: **^{1}H NMR** (500 MHz, DMSO-d_6) δ (ppm) = 13.33 (s, 1H), 8.38 (t, *J* = 1.9 Hz, 1H), 8.14 (ddt, *J* = 13.7, 7.7, 1.4 Hz, 2H), 7.95 (dd, *J* = 8.0, 1.8 Hz, 2H), 7.75 (t, *J* = 7.8 Hz, 1H), 7.67 – 7.57 (m, 3H). **^{13}C NMR** (126 MHz, DMSO-d_6) δ (ppm) = 166.7, 151.9, 151.8, 132.2, 132.0, 131.8, 130.0, 129.5, 127.4, 122.7, 122.2. **LCMS(+):** t_{ret} = 4.9 min, 227 Th = $[MH]^+$.

3-((4-methoxyphenyl)diazenyl)benzoic acid (3MP-CO_2H)

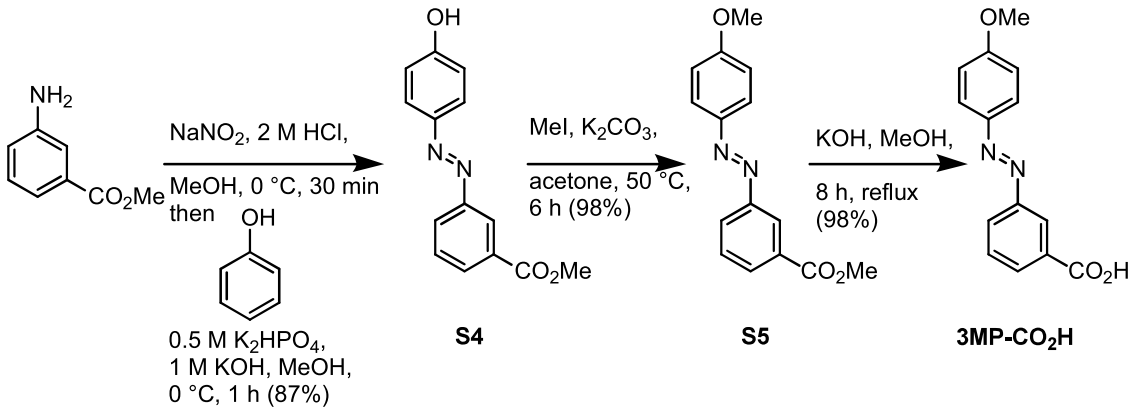

By standard procedure A, commercial methyl 3-amino benzoate (302 mg, 2.0 mmol, 1.0 eq) was reacted with phenol (207 mg, 2.2 mmol, 1.1 eq). After purification by flash chromatography (EA:iHex, 9:1 → 7:3), the desired product **methyl 3-((4-hydroxyphenyl)-diazenyl)benzoate** (**S4**) (445 mg, 1.6 mmol, 87%) was obtained as an orange solid. **^{1}H NMR** (400 MHz, chloroform-*d*) δ (ppm) = 8.53 (t, *J* = 1.9 Hz, 1H), 8.12 (dt, *J* = 7.8, 1.4 Hz, 1H), 8.07

(ddd, *J* = 8.0, 2.0, 1.1 Hz, 1H), 7.94 – 7.88 (m, 2H), 7.58 (t, *J* = 7.8 Hz, 1H), 7.01 – 6.94 (m, 2H), 3.97 (s, 3H). **^{13}C NMR** (101 MHz, chloroform-*d*) δ (ppm) = 166.9, 158.9, 152.8, 147.2, 131.4, 131.3, 129.3, 126.9, 125.5, 123.9, 116.0, 77.4, 52.5. **LCMS(+):** t_{ret} = 5.0 min, 257 Th = $[MH]^+$, **HRMS (EI):** calc. for $[C_{14}H_{12}O_3N_2]^+ = [M]^+$: 256.0848; found: 256.0850.

By standard procedure C, **S4** (440 mg, 1.7 mmol, 1.0 eq) was reacted with methyl iodide (731 mg, 5.2 mmol, 3.0 eq). After purification by means of flash chromatography (EA:iHex, 9:1 → 7:3) the desired product **methyl 3-((4-methoxyphenyl)diazenyl)benzoate** (**S5**) (454 mg, 1.7 mmol, 98%) was obtained as an orange solid. **^{1}H NMR** (400 MHz, chloroform-*d*) δ (ppm) = 8.56 – 8.50 (m, 1H), 8.11 (ddd, *J* = 7.7, 1.7, 1.2 Hz, 1H), 8.06 (ddd, *J* = 8.0, 2.1, 1.2 Hz, 1H), 8.00 – 7.91 (m, 2H), 7.58 (td, *J* = 7.8, 0.5 Hz, 1H), 7.07 – 6.98 (m, 2H), 3.97 (s, 3H), 3.90 (s, 3H). **^{13}C NMR** (101 MHz, chloroform-*d*) δ (ppm) = 166.7, 162.4, 152.8, 146.9, 131.2, 131.1, 129.1, 126.8, 125.0, 123.7, 114.3, 55.6, 52.3. **LCMS(+):** t_{ret} = 5.9 min, 271 Th = $[MH]^+$**. HRMS (EI):** calc. for $[C_{15}H_{14}N_2O_3]^+ = [M]^+$: 270.1004; found: 270.0998.

By standard procedure D, **S5** (430 mg,1.6 mmol, 1.0 eq) was reacted to the desired product **3-((4-methoxyphenyl)diazenyl)benzoic acid** (**3MP-CO$_2$H**) (399 mg, 1.6 mmol, 98%), obtained as an orange solid. **^{1}H NMR** (400 MHz, methanol-d_4) δ (ppm) = 10.02 (t, *J* = 1.8 Hz, 1H), 9.67 (dt, *J* = 7.7, 1.4 Hz, 1H), 9.63 (ddd, *J* = 8.0, 2.1, 1.2 Hz, 1H), 9.53 – 9.47 (m, 2H), 9.19 (t, *J* = 7.8 Hz, 1H), 8.67 – 8.62 (m, 2H), 5.46 (s, 3H). **^{13}C NMR** (101 MHz, methanol-d_4) δ (ppm) = 167.79, 162.82, 152.72, 146.72, 131.84, 130.89, 129.00, 126.32, 124.62, 123.06, 114.04, 54.76. **LCMS(+):** t_{ret} = 5.2 min, 257 Th = $[MH]^+$**.** **HRMS (EI):** calc. for $[C_{14}H_{12}O_3N_2]^+ = [M]^+$: 256.0848; found: 256.0842.

3-((4-(dimethylamino)phenyl)diazenyl)benzoic acid (3DMA-CO$_2$H)

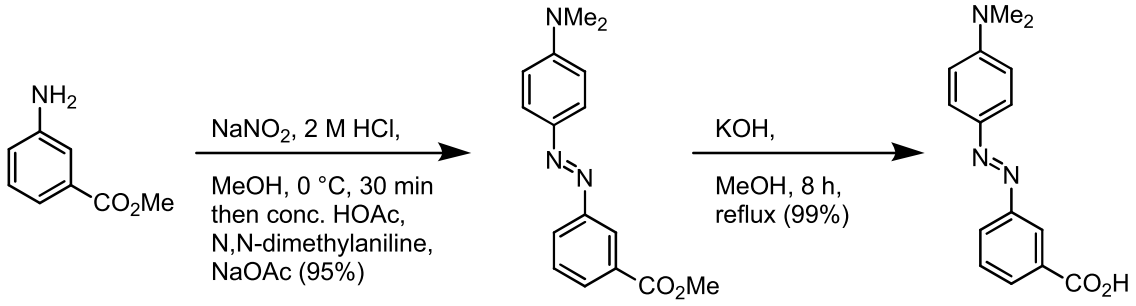

S6 **3DMA-CO$_2$H**

By standard procedure B, commercially available methyl 3-amino benzoate (302 mg, 2.0 mmol, 1.00 eq) was reacted with dimethyaniline (364 mg, 3.0 mmol, 1.5 eq). After purification by means of flash chromatography (EA:iHex, 9:1 → 8:2) the desired product **methyl 3-((4-(dimethylamino)phenyl)diazenyl)benzoate** (**S6**) (539 mg, 1.9 mmol, 95%) was obtained as a red solid. Spectral data matches literature[8]: **^{1}H NMR** (500 MHz, chloroform-*d*) δ (ppm) = 8.49 (t, *J* = 1.8 Hz, 1H), 8.04 (tdd, *J* = 7.3, 2.4, 1.2 Hz, 2H), 7.92 (d, *J* = 9.1 Hz, 2H), 7.54 (t, *J* = 7.8 Hz, 1H), 6.78 (d, *J* = 9.0 Hz, 2H), 3.96 (s, 3H), 3.11 (s, 6H).**^{13}C NMR** (126 MHz, chloroform-*d*) δ (ppm) = 166.9, 153.1, 152.7, 143.5, 131.1, 130.1, 129.0, 126.4, 125.4,

123.4, 111.7, 52.3, 40.4. **LCMS(+):** t_{ret} = 6.0 min, 284 Th = $[MH]^+$. **HRMS (EI):** calc. for $[C_{16}H_{17}O_2N_3]^+ = [M]^+$: 283.1321; found: 283.1315.

By standard procedure D, **S6** (100 mg, 0.35 mmol, 1.0 eq) was reacted to the desired product **3-((4-(dimethylamino)phenyl)diazenyl)benzoic acid** (**3DMA-CO_2H**) (93 mg, 0.35 mmol, 98%), obtained as red solid. Spectral data matches literature[9]: **^{1}H NMR** (500 MHz, methanol-d_4) δ (ppm) = 8.41 (t, *J* = 1.8 Hz, 1H), 8.04 (dt, *J* = 7.7, 1.4 Hz, 1H), 8.02 – 7.99 (m, 1H), 7.89 – 7.84 (m, 2H), 7.59 (t, *J* = 7.8 Hz, 1H), 6.87 – 6.82 (m, 2H), 3.10 (s, 6H). **^{13}C NMR** (126 MHz, methanol-d_4) δ (ppm) = 169.6, 154.8, 154.7, 144.8, 133.3, 131.4, 130.4, 127.5, 126.4, 124.2, 112.8, 40.5. **LCMS(+):** t_{ret} = 6.2 min, 270 Th = $[MH]^+$. **HRMS (EI):** calc. for $[C_{16}H_{17}O_2N_3]^+ = [M]^+$: 269.1164; found: 269.1159.

4-methoxy-3-((3,4,5-trimethoxyphenyl)diazenyl)benzoic acid (3MTM-CO_2H)

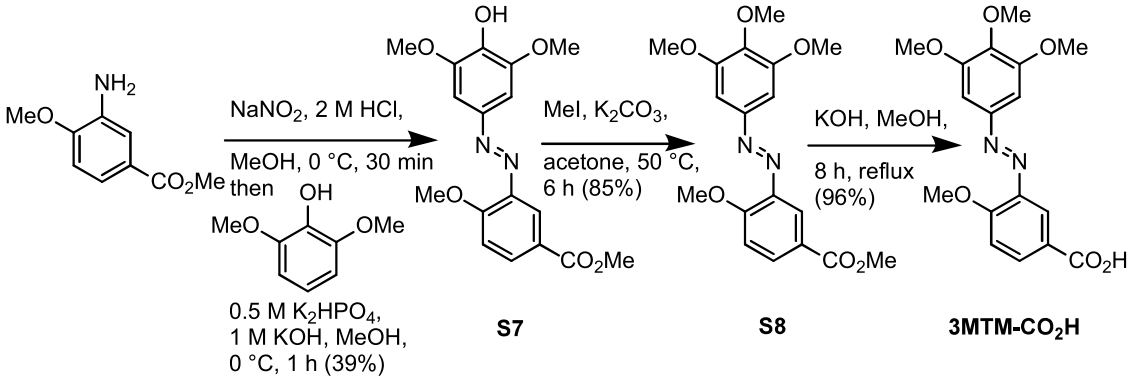

By standard procedure A, commercial methyl 3-amino 4-methoxybenzoate (181 mg, 1.0 mmol, 1.0 eq) was reacted with 2,6-dimethoxyphenol (185 mg, 1.2 mmol, 1.2 eq). Purification by flash chromatography (EA:iHex, 9:1 → 1:1) gave the desired product **methyl 3-((4-hydroxy-3,5-dimethoxyphenyl)diazenyl)-4-methoxybenzoate** (**S7**) (136 mg, 0.39 mmol, 39%) as a yellow solid. **^{1}H NMR** (400 MHz, chloroform-*d*) δ (ppm) = 8.28 (d, J = 2.2 Hz, 1H), 8.12 (dd, J = 8.7, 2.2 Hz, 1H), 7.32 (s, 2H), 7.12 (d, J = 8.7 Hz, 1H), 5.88 (s, 1H), 4.08 (s, 3H), 4.01 (s, 6H), 3.92 (s, 3H). **^{13}C NMR** (101 MHz, chloroform-*d*) δ (ppm) = 166.8, 159.9, 147.4, 146.2, 142.0, 138.4, 133.2, 123.1, 119.0, 112.2, 101.1, 56.7, 56.6, 52.3. **LCMS(+):** t_{ret} =4.5 min, 347 Th = $[MH]^+$. **HRMS (EI):** calc. for $[C_{17}H_{18}N_2O_6]^+ = [M]^+$: 346.1165; found: 346.1160.

By standard procedure C, **S7** (136 mg, 0.39 mmol, 1.0 eq) was reacted with methyl iodide (111 mg, 0.79 mmol, 2.0 eq). After purification by means of flash chromatography (EA:iHex, 9:1 → 1:1) the desired product **methyl 4-methoxy-3-((3,4,5-trimethoxyphenyl)diazenyl)-benzoate** (**S8**) (120 mg, 0.33 mmol, 85%) was obtained as an orange solid. **^{1}H NMR** (400 MHz, chloroform-*d*) δ (ppm) = 8.27 (d, *J* = 2.2 Hz, 1H), 8.14 (dd, *J* = 8.7, 2.2 Hz, 1H), 7.27 (s, 2H), 7.12 (d, *J* = 8.8 Hz, 1H), 4.08 (s, 3H), 3.97 (s, 6H), 3.94 (s, 3H), 3.92 (s, 3H). **^{13}C NMR** (101 MHz, chloroform-*d*) δ (ppm) = 166.6, 159.9, 153.5, 148.9, 141.8, 141.0, 133.4, 122.9, 118.8, 112.1, 100.8, 61.1, 56.4, 56.3, 52.1. **LCMS(+):** t_{ret} = 4.9 min, 361 Th = $[MH]^+$. **HRMS (EI):** calc. for $[C_{18}H_{20}N_2O_6]^+ = [M]^+$:360.1321; found: 360.1314.

By standard procedure D, **S9** (110 mg,0.32 mmol, 1.0 eq) was reacted to the desired product **4-methoxy-3-((3,4,5-trimethoxyphenyl)diazenyl)benzoic acid** (**3MTM-CO_2H**) (102 mg, 0.30 mmol, 96%), obtained as a yellow solid.

^{1}H NMR (400 MHz, DMSO-d_6) δ (ppm) = 8.11 – 8.05 (m, 2H), 7.38 (d, J = 9.4 Hz, 1H), 7.26 (s, 2H), 4.04 (s, 3H), 3.89 (s, 6H), 3.77 (s, 3H). **^{13}C NMR** (101 MHz, DMSO-d_6) δ (ppm) = 167.2, 160.1, 153.8, 148.6, 141.2, 140.9, 134.8, 134.0, 123.5, 118.1, 113.8, 101.0, 60.8, 57.0, 56.5. **LCMS(+):** t_{ret} = 4.3 min, 347 Th = $[MH]^+$. **HRMS (EI):** calc. for $[C_{18}H_{20}N_2O_6]^+$ = $[M]^+$:346.1165; found: 346.1157.

3-((3,4,5-trimethoxyphenyl)diazenyl)benzoic acid (3TM-CO_2H)

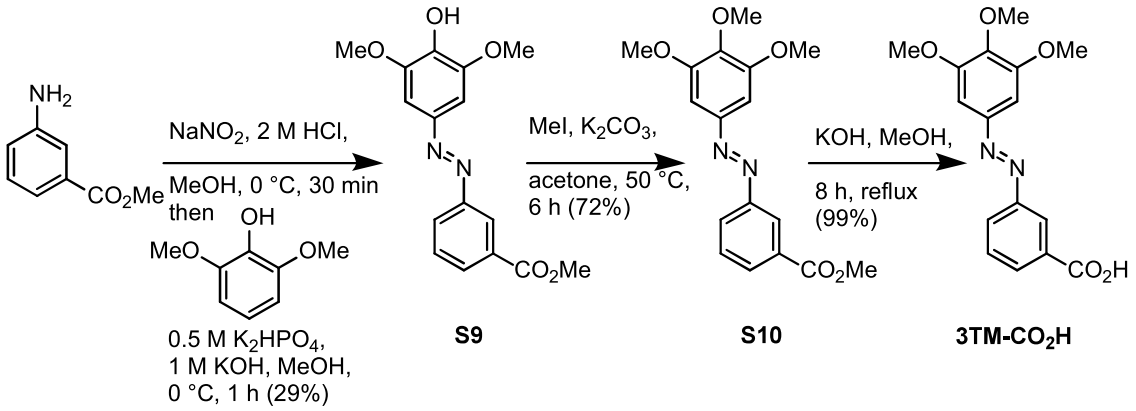

By standard procedure A, commercial methyl 3-amino benzoate (151 mg, 1 mmol, 1.00 eq) was reacted with 2,6-dimethoxyphenol (185 mg, 1.1 mmol, 1.1 eq). After purification by flash chromatography (EA:iHex, 9:1 → 6:4), the desired product **methyl 3-((4-hydroxy-3,5-dimethoxyphenyl)diazenyl)benzoate** (**S9**) (229 mg, 0.72 mmol, 73%) was obtained as an orange solid.**^{1}H NMR** (400 MHz, chloroform-d) δ (ppm) = 8.46 (t, J = 1.7 Hz, 1H), 8.05 (ddd, J = 7.7, 1.7, 1.2 Hz, 1H), 7.99 (ddd, J = 8.0, 2.1, 1.2 Hz, 1H), 7.51 (td, J = 7.8, 0.5 Hz, 1H), 7.18 (s, 1H), 5.81 (s, 1H), 3.94 (s, 6H), 3.90 (s, 3H).**^{13}C NMR** (101 MHz, chloroform-d) δ (ppm) = 166.8, 152.8, 147.4, 138.5, 131.5, 131.3, 129.3, 126.9, 123.9, 100.9, 56.6, 52.5. **LCMS(+):** t_{ret} = 4.9 min, 317 Th = $[MH]^+$. **HRMS (EI):** calc. for $[C_{16}H_{16}O_5N_2]^+$ = $[M]^+$: 316.1059; found: 316.1050.

By standard procedure C, **S9** (221 mg, 0.70 mmol, 1.0 eq) was reacted with methyl iodide (198 mg, 1.4 mmol, 2.0 eq). After purification by means of flash chromatography (EA:iHex, 9:1 → 7:3) the desired product **methyl 3-((3,4,5-trimethoxyphenyl)diazenyl)benzoate** (**S10**) (174 mg, 0.53 mmol, 72%) was obtained as a yellow solid. **^{1}H NMR** (400 MHz, chloroform-*d*) δ (ppm) = 8.55 (t, J = 1.6 Hz, 1H), 8.14 (ddd, J = 7.7, 1.7, 1.2 Hz, 1H), 8.09 (ddd, J = 7.9, 2.1, 1.2 Hz, 1H), 7.60 (td, J = 7.8, 0.5 Hz, 1H), 7.29 (s, 2H), 3.98 (s, 6H), 3.98 (s, 3H) 3.95 (s, 3H). **^{13}C NMR** (101 MHz, chloroform-*d*) δ (ppm) = 166.7, 153.7, 152.7, 148.5, 141.2, 131.6, 131.5, 129.4, 127.0, 124.1, 100.8, 61.2, 56.4, 52.5. **LCMS(+):** t_{ret} = 5.7 min, 331 Th = $[MH]^+$. **HRMS (EI):** calc. for $[C_{17}H_{18}O_5N_2]^+$ = $[M]^+$: 330.1216; found: 330.1206.

By standard procedure D, **S10** (174 mg,0.53 mmol, 1.0 eq) was reacted to the desired product **3-((3,4,5-trimethoxyphenyl)diazenyl)benzoic acid** (**3TM-CO_2H**) (167 mg, 0.53 mmol, 99%),

obtained as yellow solid. **^{1}H NMR** (500 MHz, methanol-d_4) δ (ppm) = 8.53 (t, J = 1.8 Hz, 1H), 8.17 (dt, J = 7.7, 1.4 Hz, 1H), 8.13 (ddd, J = 7.9, 2.1, 1.2 Hz, 1H), 7.67 (t, J = 7.8 Hz, 1H), 7.38 (s, 2H), 3.98 (s, 6H), 3.89 (s, 3H). **^{13}C NMR (126 MHz,** methanol-d_4**)** δ (ppm) = 168.3, 153.6, 152.4, 148.4, 140.9, 132.8, 131.4, 129.0, 126.3, 123.2, 100.4, 59.9, 55.3, 55.2. **LCMS(+):** t_{ret} = 4.6 min, 317 Th = $[MH]^+$. **HRMS (EI):** calc. for $[C_{16}H_{16}O_5N_2]^+ = [M]^+$: 316.1043; found: 316.1059.

3-((4-(bis(2-hydroxyethyl)amino)phenyl)diazenyl)benzoic acid (3DEA-CO_2H)

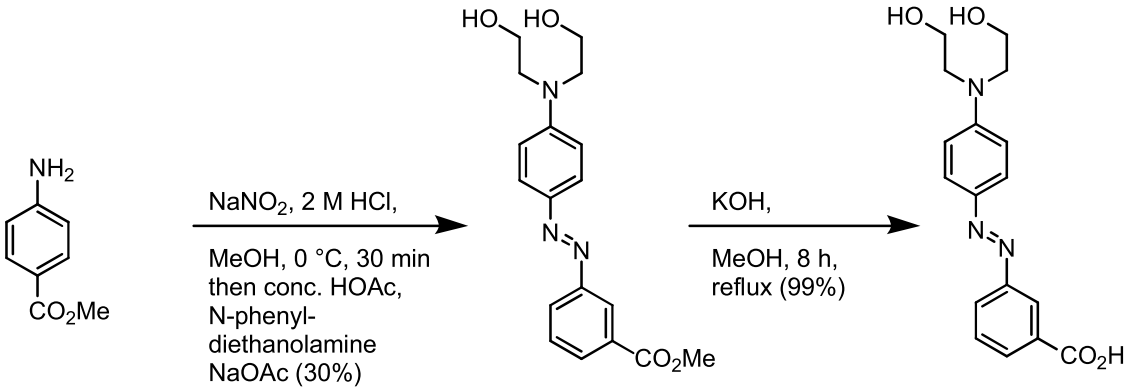

S11 **3DEA-CO_2H**

By standard procedure B, commercial methyl 3-amino benzoate (302 mg, 2 mmol, 1.00 eq) was reacted with *N*-phenyldiethanolamine (544 mg, 3 mmol, 1.50 eq). After purification by flash chromatography (DCM:MeOH, 95:5), the desired product **methyl 3-((4-(bis(2-hydroxyethyl)amino)phenyl)diazenyl)benzoate** (**S11**) (200 mg, 0.58 mmol, 29%) was obtained as a red solid. **^{1}H NMR** (400 MHz, chloroform-d) δ 8.49 (t, J = 1.8 Hz, 1H), 8.04 (tdd, J = 7.9, 2.4, 1.2 Hz, 2H), 7.89 (d, J = 8.7 Hz, 2H), 7.54 (t, J = 7.9 Hz, 1H), 6.80 (d, J = 8.9 Hz, 2H), 3.95 (d, J = 4.3 Hz, 7H), 3.82 (d, J = 18.8 Hz, 2H), 3.73 (t, J = 4.9 Hz, 4H). **^{13}C NMR** (101 MHz, MeOD-d_4) δ (ppm) = 168.3, 152.9, 132.6, 131.1, 130.6, 127.8, 126.7, 123.8, 113.0, 60.4, 55.2, 53.0. **LCMS(+):** t_{ret} = 4.3 min, 344 Th = $[MH]^+$. **HRMS (EI)**: calc. for $[C_{18}H_{21}N_3O_4]^+ = [M]^+$: 343.1532; found: 343.1529.

By standard procedure D, **S11** (200 mg,0.58 mmol, 1.0 eq) was reacted to the desired product **3-((4-(bis(2-hydroxyethyl)amino)phenyl)diazenyl)benzoic acid** (**3DEA-CO_2H**) (154 mg, 0.47 mmol, 80%), obtained as a yellow solid. The compound has been reported[10] but no spectral data for comparison was available, so we report it here: **^{1}H NMR** (400 MHz, DMSO-d_6) δ (ppm) = 7.95 – 7.89 (m, 4H), 7.61 (dt, J = 6.4, 1.9 Hz, 5H), 4.83 (d, J = 21.9 Hz, 2H), 3.64 (s, 2H), 3.56 (d, J = 6.0 Hz, 2H), 3.47 (s, 3H). **^{13}C NMR** (101 MHz, DMSO-d_6) δ 170.3, 151.9, 151.7, 140.0, 131.8, 130.7, 129.6, 128.1, 122.7, 122.5, 58.5, 58.5, 51.6, 47.4. **LCMS(+):** t_{ret} = 3.6 min, 330 Th = $[MH]^+$. **HRMS (EI)**: calc. for $[C_{17}H_{19}N_3O_4]^+$ **=** $[M]^+$: 329.1576; found: 329.1362.

2-((4-methoxyphenyl)diazenyl)benzoic acid (2MP-CO_2H)

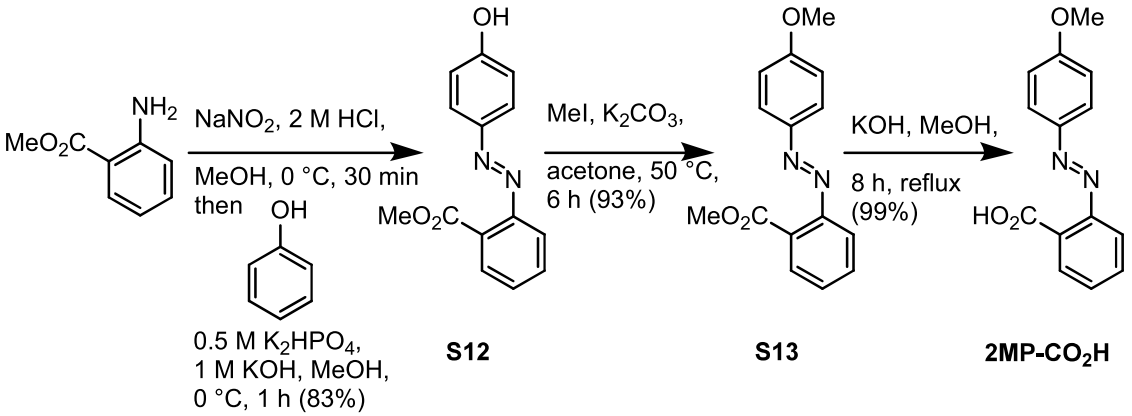

By standard procedure A, commercially available methyl 2-amino benzoate (302 mg, 2.0 mmol, 1.0 eq) was reacted with phenol (207 mg, 2.2 mmol, 1.1 eq). After purification by means of flash chromatography (EA:iHex, 9:1 → 7:3) the desired product **methyl 2-((4-hydroxyphenyl)diazenyl)benzoate** (**S12**) (423 mg, 1.8 mmol, 83%) was obtained as an orange solid. The compound has been reported but no spectral data for comparison were available so these are given here[11]: **^{1}H NMR** (400 MHz, DMSO-d_6) δ 7.79 – 7.75 (m, 2H), 7.74 (dd, *J* = 7.5, 1.4 Hz, 1H), 7.69 (ddd, *J* = 8.6, 7.1, 1.5 Hz, 1H), 7.63 (dd, *J* = 8.1, 1.4 Hz, 1H), 7.56 (td, *J* = 7.3, 1.5 Hz, 1H), 7.01 – 6.92 (m, 2H), 3.81 (s, 3H). **^{13}C NMR** (101 MHz, DMSO-d_6) δ (ppm) = 168.2, 161.9, 151.2, 145.7, 132.4, 130.1, 129.6, 128.8, 125.6, 119.8, 116.5, 52.7. **LCMS(+):** t_{ret} =4.5 min, 257 Th = $[MH]^+$. **HRMS (EI):** calc. for $[C_{14}H_{12}N_2O_3]^+$ = $[M]^+$: 256.0848; found: 256.0838.

By standard procedure C, **S12** (402 mg, 1.57 mmol, 1.0 eq) was reacted with methyl iodide (668 mg, 4.7 mmol, 3.0 eq). After purification by means of flash chromatography (EA:iHex, 8:2) the desired product **methyl 2-((4-methoxyphenyl)diazenyl)benzoate** (**S13)** (394 mg, 0.53 mmol, 93%) was obtained as a yellow solid. The compound has been reported but no spectral data for comparison were available so these are given here: **^{1}H NMR** (400 MHz, chloroform-*d*) δ (ppm) = 7.97 – 7.87 (m, 2H), 7.80 (ddd, *J* = 7.7, 1.4, 0.5 Hz, 1H), 7.64 – 7.54 (m, 2H), 7.45 (ddd, *J* = 7.7, 7.0, 1.6 Hz, 1H), 7.05 – 6.98 (m, 2H), 3.90 (d, *J* = 2.3 Hz, 6H).**^{13}C NMR** (101 MHz, chloroform-*d*) δ (ppm) = 168.2, 162.5, 152.1, 147.1, 131.9, 129.7, 129.2, 128.4, 125.2, 119.0, 114.3, 55.6, 52.3. **LCMS(+):** t_{ret} = 5.4 min, 271 Th = $[MH]^+$. **HRMS (EI):** calc. for $[C_{15}H_{14}N_2O_3]^+$ = $[M]^+$: 270.1004; found: 270.1003.

By standard procedure D, **S15** (385 mg,0.53 mmol, 1.0 eq) was reacted to the desired product **2-((4-methoxyphenyl)diazenyl)benzoic acid** (**2MP-CO_2H**) (363 mg, 0.53 mmol, 99%) was obtained as a yellow solid. Spectral data matches literature[12]: **^{1}H NMR** (400 MHz, methanol-d_4) δ (ppm) = 7.93 – 7.89 (m, 2H), 7.88 (dd, *J* = 7.7, 1.5 Hz, 1H), 7.71 (dd, *J* = 8.0, 1.3 Hz, 1H), 7.66 – 7.59 (m, 1H), 7.54 (td, *J* = 7.5, 1.3 Hz, 1H), 7.12 – 7.07 (m, 2H), 3.90 (s, 3H). **^{13}C NMR** (101 MHz, methanol-d_4) δ (ppm) = 170.0, 163.2, 150.9, 146.7, 131.6, 130.1, 129.7, 129.5, 125.0, 117.3, 114.2, 54.8. **LCMS(+):** t_{ret} =4.9 min, 257 Th = $[MH]^+$. **HRMS (EI):** calc. for $[C_{14}H_{12}O_3N_2]^+$ = $[M]^+$: 256.0848; found: 256.0847.

AzTaxs

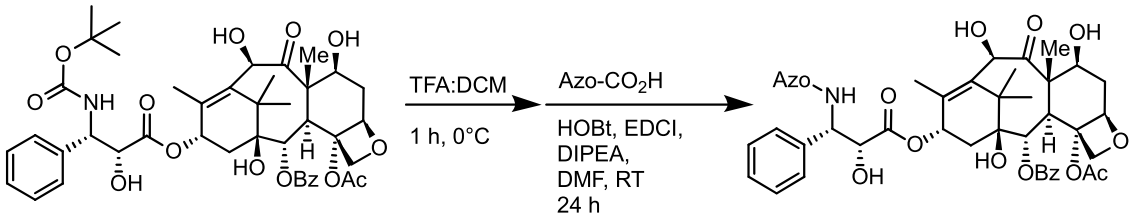

(2aR,4S,4aS,6R,9S,11S,12S,12aR,12bS)-12b-acetoxy-4,6,11-trihydroxy-9-(((2R,3S)-2-hydroxy-3-phenyl-3-(4-(phenyldiazenyl)benzamido)propanoyl)oxy)-4a,8,13,13-tetramethyl-5-oxo-2a,3,4,4a,5,6,9,10,11,12,12a,12b-dodecahydro-1H-7,11-methanocyclodeca[3,4]benzo[1,2-b]oxet-12-yl benzoate (AzTax4H)

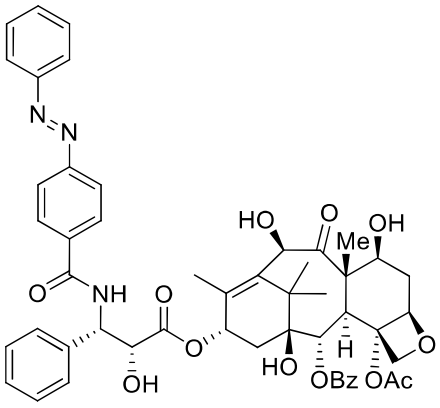

AzTax4H

By Standard Procedure E, docetaxel (25 mg, 31 µmol) was deprotected with TFA-DCM and the crude foam reacted with **4H-CO_2H** (7.5 mg, 33 µmol), DIPEA (11 mg, 86 µmol), EDCI (10.7 mg, 56 µmol), and HOBt.H_2O (6.5 mg, 42 µmol) to yield a yellow crude solid. Chromatography on 5:1:0→1:1:0→1:1:0.2 iHex:EA:MeOH returned **AzTax4H** as a yellow solid (22 mg, 24 µmol, 76 %). **^{1}H NMR** (400 MHz, chloroform-*d*) δ (ppm) = 8.16 – 8.09 (m, 2H), 7.95 – 7.91 (m, 2H), 7.68 – 7.31 (m, 14H), 7.28 (s, 1H), 6.24 – 6.17 (m, 1H), 5.79 (dd, *J* = 8.9, 2.8 Hz, 1H), 5.67 (d, *J* = 6.9 Hz, 1H), 5.18 (d, *J* = 4.9 Hz, 1H), 4.93 (dd, *J* = 9.6, 2.2 Hz, 1H), 4.80 (d, *J* = 2.9 Hz, 1H), 4.31 (d, *J* = 8.4 Hz, 1H), 4.24 – 4.16 (m, 2H), 3.89 (d, *J* = 7.2 Hz, 1H), 2.61 – 2.50 (m, 1H), 2.38 (s, 3H), 2.29 (dd, *J* = 9.0, 3.9 Hz, 2H), 1.89 – 1.79 (m, 2H), 1.78 – 1.73 (m, 6H), 1.72 – 1.68 (m, 1H), 1.20 (s, 3H), 1.11 (s, 3H). **^{13}C NMR** (101 MHz, chloroform-*d*) δ (ppm) = 211.2, 172.5, 170.5, 167.0, 166.3, 154.5, 152.5, 138.1, 137.8, 136.1, 135.3, 133.8, 131.7, 130.2, 129.2, 129.1, 129.0, 128.8, 128.4, 128.1, 127.1, 123.1, 123.0, 84.1, 81.1, 78.7, 77.2, 74.7, 74.5, 73.2, 72.4, 72.0, 57.7, 55.2, 46.5, 43.0, 37.0, 35.9, 26.6, 22.6, 20.6, 14.4, 9.9. **LCMS(+):** t_{ret} = 7.26 & 8.25 min, each 916 Th = $[MH]^+$, *Z* & *E* isomers respectively. **HRMS (ESI+)** calcd for $[C_{51}H_{54}N_3O_{13}]^+ = [MH]^+$: m/z 916.36566, found 916.36715.

(2aR,4S,4aS,6R,9S,11S,12S,12aR,12bS)-12b-acetoxy-9-(((2R,3S)-3-(4-((4-(dimethylamino)phenyl)diazenyl)benzamido)-2-hydroxy-3-phenylpropanoyl)oxy)-4,6,11-trihydroxy-4a,8,13,13-tetramethyl-5-oxo-2a,3,4,4a,5,6,9,10,11,12,12a,12b-dodecahydro-1H-7,11-methanocyclodeca[3,4]benzo[1,2-b]oxet-12-yl benzoate (AzTax4DMA)

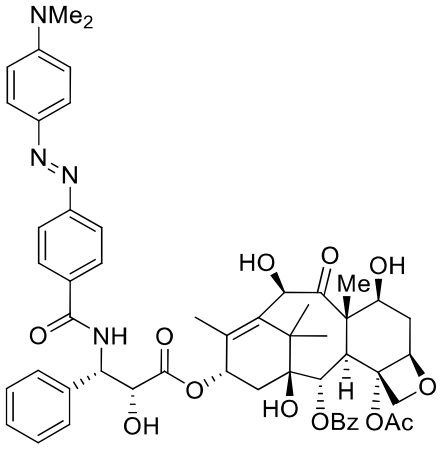

AzTax4DMA

By Standard Procedure E, docetaxel (23 mg, 28 µmol) was deprotected with TFA-DCM and the crude foam (20 mg) reacted with **4DMA-CO_2H** (11 mg, 41 µmol), Hünig base (11.1 mg, 85 µmol), EDCI (8.6 mg, 45 µmol), and HOBt·H_2O (6.9 mg, 45 µmol) to yield a yellow crude solid. Chromatography on 5:1:0→1:1:0→1:1:0.08 iHex:EA:MeOH returned **AzTax4DMA** as a yellow solid (13.8 mg, 14.4 μmol, 51%). **^{1}H NMR** (400 MHz, chloroform-*d*) δ (ppm) = 9.07 (d, *J* = 8.4 Hz, 1H), 8.05 (d, *J* = 8.6 Hz, 2H), 7.97 (d, *J* = 7.5 Hz, 2H), 7.86 (d, *J* = 8.4 Hz, 2H), 7.84 (d, *J* = 9.0 Hz, 2H), 7.78 – 7.68 (m, 1H), 7.69 – 7.59 (m ~t, *J* = 7.7 Hz, 2H), 7.46 – 7.41 (m, 2H), 7.43 – 7.38 (m, 2H), 7.23 (tt, *J* = 5.7, 2.9 Hz, 1H), 6.85 (d, *J* = 9.3 Hz, 2H), 6.23 (d, *J* = 7.8 Hz, 1H), 5.91 (t, *J* = 9.0 Hz, 1H), 5.39 (t, *J* = 8.6 Hz, 1H), 5.39 (d, *J* = 6.5 Hz), 5.09 (d, *J* = 2.6 Hz), 5.03 (d, *J* = 7.2 Hz, 1H), 4.98 (d, *J* = 2.4 Hz, 1H), 4.92 (dd, *J* = 9.7, 2.2 Hz, 1H), 4.57 (s, 1H), 4.59 (~t, *J* = 7.8 Hz, 1H), 4.11 – 3.96 (m, 3H, H10), 3.67 (d, *J* = 7.1 Hz, 1H), 3.09 (s, 6H), 2.35 – 2.25 (m, 1H), 2.23 (s, 3H), 1.90 – 1.81 (m, 1H), 1.73 – 1.65 (m, 1H), 1.74 (s, 3H), 1.72 – 1.63 (m, 1H), 1.53 (s, 3H), 1.01 (s, 3H). **^{13}C NMR** (101 MHz, chloroform-*d*) δ (ppm) = 209.7, 173.2, 170.2, 166.1, 165.7, 154.6, 153.3, 143.1, 139.7, 137.3, 136.2, 135.1, 133.9, 130.5, 130.0, 129.2, 129.0, 128.8, 128.0, 127.9, 125.6, 122.0, 112.0, 84.2, 80.7, 77.3, 75.9, 75.2, 74.2, 74.1, 71.3, 70.2, 57.4, 57.1, 46.4, 43.4, 40.6, 36.9, 35.4, 23.0, 21.5, 14.1, 10.3. **LCMS(+):** t_{ret} = 8.39 min, 959 Th = $[MH]^+$, E isomer only. **HRMS (ESI+)** calcd for $[C_{53}H_{59}N_4O_{13}]^+$ = $[MH]^+$: m/z 959.40786, found 959.40758**.**

(2aR,4S,4aS,6R,9S,11S,12S,12aR,12bS)-12b-acetoxy-4,6,11-trihydroxy-9-(((2R,3S)-2-hydroxy-3-(4-(4-methoxyphenyl)diazenyl)benzamido)-3-phenylpropanoyl)oxy)-4a,8,13,13-tetramethyl-5-oxo-2a,3,4,4a,5,6,9,10,11,12,12a,12b-dodecahydro-1H-7,11-methanocyclodeca[3,4]benzo[1,2-b]oxet-12-yl benzoate (AzTax4MP)

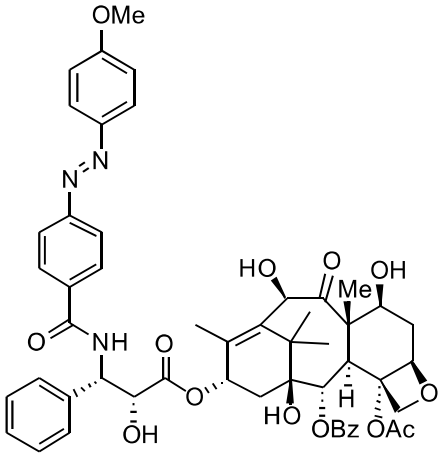

AzTax4MP

By Standard Procedure E, docetaxel (20 mg, 24 µmol) was deprotected with TFA-DCM and the crude foam (17 mg) reacted with **4MP-CO_2H** (8 mg, 28 µmol, 1.2 eq), Hünig base (12 mg, 96 µmol, 4.0 eq), EDCI (7 mg, 36 µmol), and HOBt·H_2O (7 mg, 85 %wt, 39 µmol, 1.6 eq) to yield a yellow crude solid. Chromatography on (iHex:EA 7:3→1:1; DCM:MeOH 99:1→95:5) returned **AzTax4MP** as a yellow solid (10 mg, 10.4 μmol, 41%). **^{1}H NMR** (400 MHz, chloroform-*d*) δ (ppm) = 8.09 – 8.03 (m, 2H), 7.89 – 7.83 (m, 2H), 7.81 (d, *J* = 1.3 Hz, 3H), 7.58 – 7.51 (m, 1H), 7.49 – 7.39 (m, 4H), 7.39 – 7.32 (m, 2H), 7.32 – 7.25 (m, 1H), 7.12 (d, *J* = 9.0 Hz, 1H), 6.98 – 6.91 (m, 2H), 6.19 – 6.08 (m, 1H), 5.73 (dd, *J* = 9.0, 2.8 Hz, 1H), 5.61 (d, *J* = 7.0 Hz, 1H), 5.11 (d, *J* = 1.6 Hz, 1H), 4.91 – 4.83 (m, 1H), 4.73 (dd, *J* = 5.1, 2.8 Hz, 1H), 4.25 (d, *J* = 8.5 Hz, 1H), 4.19 – 4.10 (m, 3H), 3.83 (s, 4H), 3.55 (d, *J* = 5.3 Hz, 1H), 2.51 (ddd, *J* = 14.3, 9.6, 6.5 Hz, 1H), 2.32 (s, 3H), 2.23 (dd, *J* = 8.9, 5.1 Hz, 2H), 1.83 – 1.66 (m, 8H), 1.14 (s, 3H), 1.05 (s, 3H). **^{13}C NMR** (101 MHz, chloroform-*d*) δ (ppm) = 211.4, 172.7, 170.6, 167.1, 166.6, 162.8, 154.9, 147.1, 138.2, 138.0, 136.3, 134.8, 133.9, 130.3, 129.3, 129.2, 128.9, 128.5, 128.2, 127.2, 125.3, 122.9, 114.5, 84.3, 81.3, 78.9, 74.9, 74.7, 73.4, 72.6, 72.2, 57.8, 55.8, 55.3, 46.6, 43.2, 37.2, 36.1, 26.7, 22.7, 20.7, 14.5, 10.0. **LCMS(+):** tret =8.4 min, 946 Th = $[MH]^+$ **HRMS (ESI+)** calcd for $[C_{52}H_{56}N_3O_{14}]^+$ = $[MH]^+$: m/z 946.37568, found 946.37796**.**

(2aR,4S,4aS,6R,9S,11S,12S,12aR,12bS)-12b-acetoxy-4,6,11-trihydroxy-9-(((2R,3S)-2-hydroxy-3-phenyl-3-(3-(phenyldiazenyl)benzamido)propanoyl)oxy)-4a,8,13,13-tetramethyl-5-oxo-2a,3,4,4a,5,6,9,10,11,12,12a,12b-dodecahydro-1H-7,11-methanocyclodeca[3,4]benzo[1,2-b]oxet-12-yl benzoate (AzTax3H)

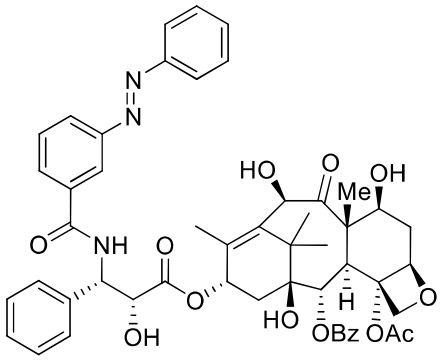

3H

By Standard Procedure E, docetaxel (40 mg, 50 µmol) was deprotected with TFA-DCM and the crude foam (32 mg) reacted with **3H-CO_2H** (5.3 mg, 23 µmol), Hünig base (6.3 mg, 49 µmol), EDCI (5.1 mg, 26 µmol), and HOBt·H_2O (4.1 mg, 27 µmol) to yield a yellow crude solid (31 mg). Chromatography on 5:1:0→1:1:0→1:1:0.1 iHex:EA:MeOH returned **AzTax3H** as a yellow solid (12.2 mg, 13.3 *µ*mol, 58%). **^{1}H NMR** (400 MHz, DMSO-d_6) δ (ppm) = 9.24 (d, *J* = 8.5 Hz, 1H), 8.44 (t, *J* = 1.9 Hz, 1H), 8.08 (t, J = 7.1 Hz, 2H), 8.00 – 7.92 (m, 4H), 7.77 – 7.69 (m, 2H), 7.64 (ddd, *J* = 7.9, 6.2, 2.1 Hz, 5H), 7.44 – 7.39 (m, 3H), 6.91 – 6.83 (m, 1H), 6.26 (d, *J* = 7.7 Hz, 1H), 5.96 – 5.88 (m, 1H), 5.45 – 5.38 (m, 2H), 5.09 (s, 1H), 5.05 – 4.94 (m, 2H), 4.91 (dd, *J* = 9.7, 2.2 Hz, 2H), 4.57 (d, *J* = 2.3 Hz, 1H), 4.08 – 3.95 (m, 4H), 3.72 – 3.62 (m, 1H), 2.21 (s, 3H), 2.09 (s, 1H), 1.75 (d, *J* = 1.4 Hz, 3H), 1.53 (s, 3H). **^{13}C NMR** (101 MHz, DMSO-d_6) δ (ppm) = 209.7, 173.2, 170.2, 165.9, 165.7, 153.8, 153.8, 152.3, 152.2, 139.5, 137.3, 136.2, 136.2, 133.9, 132.4, 130.8, 130.5, 130.1, 130.1, 130.0, 129.4, 129.1, 128.8, 128.0, 125.2, 123.1, 122.3, 120.4, 84.2, 83.4, 83.0, 80.9, 80.7, 77.3, 75.2, 74.2, 74.1, 71.3, 70.2, 57.4, 43.4, 41.2, 33.9, 28.7, 24.6, 21.5, 17.9, 17.2, 15.1, 14.1, 10.3, 8.3.**LCMS(+):** t_{ret} = 8.5 & 8.7 min, each 916 Th = $[MH]^+$, *Z* & *E* isomers respectively.**HRMS (ESI+)** calcd for $[C_{51}H_{54}N_3O_{13}]^+$ = $[MH]^+$: m/z 916.36566, found 916.36526.

(2aR,4S,4aS,6R,9S,11S,12S,12aR,12bS)-12b-acetoxy-9-(((2R,3S)-3-(3-((4-(dimethylamino)phenyl)diazenyl)benzamido)-2-hydroxy-3-phenylpropanoyl)oxy)-4,6,11-trihydroxy-4a,8,13,13-tetramethyl-5-oxo-2a,3,4,4a,5,6,9,10,11,12,12a,12b-dodecahydro-1H-7,11-methanocyclodeca[3,4]benzo[1,2-b]oxet-12-yl benzoate (AzTax3DMA)

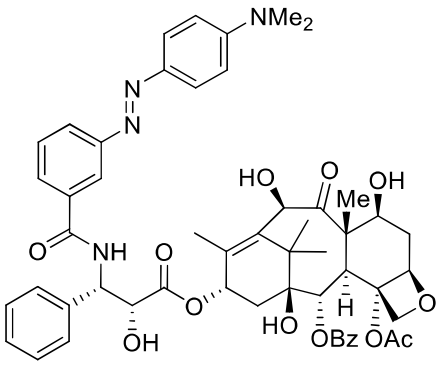

AzTax3DMA

By Standard Procedure E, docetaxel (20 mg, 24 µmol) was deprotected with TFA-DCM and the crude foam (17 mg) reacted with **3DMA-CO_2H** (8 mg, 28 µmol, 1.2 eq), Hünig base (12 mg, 96 µmol, 4.0 eq), EDCI (7 mg, 36 µmol), and HOBt·H_2O (7 mg, 85 %wt, 39 µmol, 1.6 eq) to yield a yellow crude solid. Chromatography on (iHex:EA 7:3→1:1; DCM:MeOH 99:1→95:5) returned **AzTax3DMA** as a yellow solid (8 mg, 8.3 *µ*mol, 35%).

^{1}H NMR (400 MHz, chloroform-*d*) δ (ppm) = 8.17 – 8.10 (m, 3H), 7.98 – 7.92 (m, 1H), 7.89 – 7.82 (m, 2H), 7.79 (dt, J = 8.0, 1.3 Hz, 1H), 7.62 – 7.55 (m, 1H), 7.54 – 7.46 (m, 5H), 7.46 – 7.39 (m, 2H), 7.38 – 7.33 (m, 1H), 7.18 (d, J = 9.0 Hz, 1H), 6.79 – 6.71 (m, 2H), 6.23 (t, J = 8.9 Hz, 1H), 5.85 – 5.79 (m, 1H), 5.69 (d, J = 7.1 Hz, 1H), 5.17 (s, 1H), 4.97 – 4.90 (m, 1H), 4.80 (s, 1H), 4.31 (d, J = 8.5 Hz, 1H), 4.27 – 4.14 (m, 3H), 3.91 (d, J = 7.1 Hz, 1H), 3.65 (s, 1H), 3.10 (s, 6H), 2.57 (ddd, J = 15.2, 9.6, 6.5 Hz, 1H), 2.40 (s, 3H), 2.37 – 2.23 (m, 2H), 1.91 – 1.83 (m, 1H), 1.80 (d, J = 1.4 Hz, 3H), 1.76 (s, 3H), 1.58 (s, 1H), 1.22 (s, 3H), 1.12 (s, 3H). **^{13}C NMR** (101 MHz, chloroform-*d*) δ (ppm) = 211.4, 172.6, 170.5, 167.0, 166.8, 153.2, 152.8, 143.4, 138.2, 137.9, 136.1, 134.5, 133.7, 130.2, 129.5, 129.2, 129.0, 128.8, 128.4, 128.0, 127.1, 125.5, 125.3, 120.4, 111.5, 84.1, 81.1, 78.8, 74.8, 74.5, 73.3, 72.5, 72.0, 57.7, 55.1, 46.5, 43.1, 40.3, 37.1, 36.0, 26.6, 22.6, 20.6, 14.4, 9.9. **LCMS(+):** t_{ret} =8.7 min, 959 Th = $[M]^+$. **HRMS (ESI+)** calcd for $[C_{53}H_{59}N_4O_{13}]^+$ = $[MH]^+$: m/z 959.40731, found 959.40885**.**

(2a*R*,4*S*,4a*S*,6*R*,9*S*,11*S*,12*S*,12a*R*,12b*S*)-12b-acetoxy-4,6,11-trihydroxy-9-(((2*R*,3*S*)-2-hydroxy-3-(3-((*E*)-(4-methoxyphenyl)diazenyl)benzamido)-3-phenylpropanoyl)oxy)-4a,8,13,13-tetramethyl-5-oxo-2a,3,4,4a,5,6,9,10,11,12,12a,12b-dodecahydro-1*H*-7,11-methanocyclodeca[3,4]benzo[1,2-*b*]oxet-12-yl benzoate (AzTax3MP)

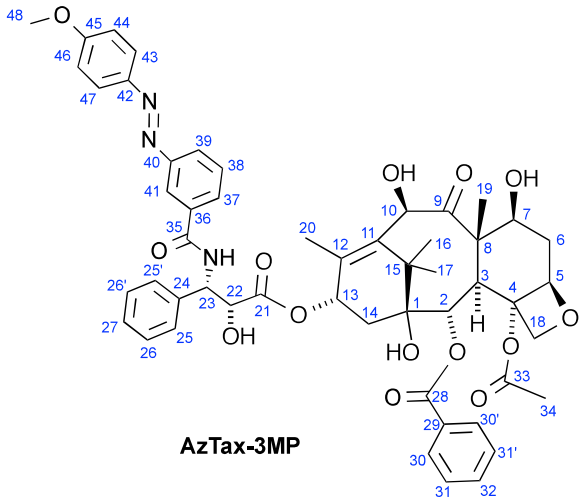

AzTax-3MP

By Standard Procedure E, docetaxel (21 mg, 26 µmol) was deprotected with TFA-DCM and the crude foam reacted with **3MP-CO$_2$H** (7.3 mg, 28 µmol), Hünig base (9.4 mg, 73 µmol), EDCI (7.1 mg, 37 µmol), and HOBt·H$_2$O (5.5 mg, 36 µmol) to yield a yellow crude solid. Chromatography on 5:1:0→1:1:0→1:1:0.2 iHex:EA:MeOH returned **AzTax3MP** as a yellow solid (20 mg, 21 μmol, 81%).

^{1}H NMR (400 MHz, DMSO-d_6) δ (ppm) = 8.13 (~t, J = 1.8 Hz, 1H), 8.05 (d, J = 7.8 Hz, 2H), 7.92 (d, J = 7.0 Hz, 1H), 7.83 (d, J = 9.0 Hz, 2H), 7.77 (d, J = 7.7 Hz, 1H), 7.51 (~t, J = 7.5 Hz, 1H), 7.45 (t, J = 7.6 Hz, 1H), 7.48 – 7.34 (m, 2H), 7.43 – 7.39 (m, 2H), 7.35 (~t, J = 7.5 Hz, 2H), 7.27 (t, J = 7.4 Hz, 1H), 6.94 (d, J = 9.0 Hz, 2H), 6.15 (t, J = 8.7 Hz, 1H), 5.75 (dd, J = 8.9, 2.8 Hz, 1H), 5.61 (d, J = 7.0 Hz, 1H), 5.11 (s, 1H), 4.86 (~d, J = 9.5 Hz, 1H), 4.73 (d, J = 2.8 Hz, 1H), 4.24 (d, J = 8.5 Hz, 1H), 4.16-4.09 (m, 2H), 3.82 (s, 3H), 3.85 – 3.80 (m overlapped, 1H), 2.56 – 2.43 (m, 1H), 2.32 (s, 3H), 2.27 – 2.19 (m, 1H), 1.89 – 1.72 (m, 1H), 1.72 – 1.64 (m, 1H), 1.71 (s, 3H), 1.68 (s, 3H, 3H19), 1.13 (s, 3H,), 1.04 (s, 3H). **^{13}C NMR** (101 MHz, DMSO-d_6) δ (ppm) = 211.3 (C9), 172.6 (C21), 170.5 (C33), 166.9 (C35), 166.6 (C28), 162.5 (C45), 152.7 (C40), 146.7 (C42), 138.1 (C12), 137.9 (C11), 136.1 (C36), 134.7 (C24), 133.7 (C32), 130.2 (C30 & C30'), 129.5 (C29), 129.1 (C37), 129.0 (C31 & C31'), 128.9 (C38), 128.7 (C26 & C26'), 128.4 (C27), 127.1 (25 & 25'), 125.8 (C39), 125.1 (C43 & C47), 121.0 (C41), 114.3 (C44 & C46), 84.2 (C5), 81.1 (C4), 78.7 (C1), 77.2 (C18), 74.8 (C2), 74.5 (C7), 73.2 (C22), 72.4 (C10), 72.0 (C13), 57.7 (C48), 55.6 (C23), 55.2 (C8), 46.5 (C3), 43.0 (C15), 37.0 (C6), 36.0 (C14), 26.6 (C34), 22.6 (C16), 20.6 (C17), 14.4 (C20), 9.9 (C19). **LCMS(+):** t_{ret} = 7.20 & 8.21 min, each 946 Th = $[MH]^+$, Z & E isomers respectively. **HRMS (ESI+)** calcd for $[C_{52}H_{56}N_3O_{14}]^+ = [MH]^+$: m/z 946.37623, found 946.37733**.**

(2aR,4S,4aS,6R,9S,11S,12S,12aR,12bS)-12b-acetoxy-4,6,11-trihydroxy-9-(((2R,3S)-2-hydroxy-3-(4-methoxy-3-((3,4,5-trimethoxyphenyl)diazenyl)benzamido)-3-phenylpropanoyl)oxy)-4a,8,13,13-tetramethyl-5-oxo-2a,3,4,4a,5,6,9,10,11,12,12a,12b-dodecahydro-1H-7,11-methanocyclodeca[3,4]benzo[1,2-b]oxet-12-yl benzoate (AzTax3MTM)

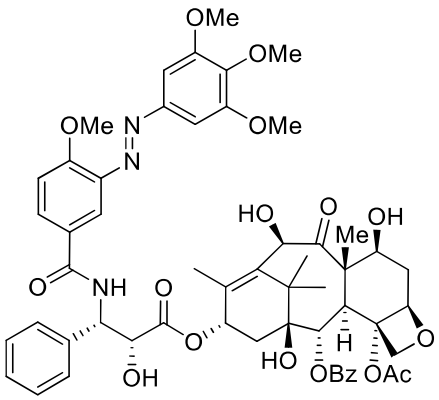

AzTax3MTM

By Standard Procedure E, docetaxel (20 mg, 24 µmol) was deprotected with TFA-DCM and the crude foam (17 mg) reacted with **3MTM-CO_2H** (8 mg, 28 µmol, 1.2 eq), Hünig base (12 mg, 96 µmol, 4.0 eq), EDCI (7 mg, 36 µmol), and HOBt·H_2O (7 mg, 85 %wt, 39 µmol, 1.6 eq) to yield a yellow crude solid. Chromatography on (iHex:EA 7:3→1:1; DCM:MeOH 99:1→95:5) returned **AzTax3MTM** as a yellow solid (8 mg, 8.3 *µ*mol, 35%).

^{1}H NMR (400 MHz, chloroform-*d*) δ (ppm) = 8.14 – 8.06 (m, 3H), 7.94 – 7.87 (m, 2H), 7.58 – 7.52 (m, 1H), 7.48 (td, *J* = 8.6, 8.1, 1.6 Hz, 4H), 7.43 (t, *J* = 1.7 Hz, 1H), 7.42 – 7.39 (m, 2H), 7.39 – 7.32 (m, 2H), 7.19 (s, 2H), 7.13 – 7.09 (m, 1H), 7.07 (d, *J* = 8.7 Hz, 1H), 6.26 – 6.18 (m, 1H), 5.82 (dd, *J* = 9.0, 2.7 Hz, 1H), 5.69 (d, *J* = 7.0 Hz, 1H), 5.17 (s, 1H), 4.92 (d, *J* = 8.8 Hz, 1H), 4.81 (d, *J* = 2.6 Hz, 1H), 4.30 (d, *J* = 8.4 Hz, 1H), 4.24 – 4.19 (m, 3H), 4.03 (s, 3H), 3.97 (q, *J* = 2.2, 1.6 Hz, 2H), 3.94 (s, 6H), 3.93 (s, 3H), 2.56 (ddd, *J* = 14.2, 9.5, 6.6 Hz, 2H), 2.40 (s, 3H), 2.29 – 2.19 (m, 2H), 1.89 – 1.84 (m, 3H), 1.80 (d, *J* = 1.4 Hz, 3H), 1.76 (s, 3H), 1.21 (s, 3H), 1.11 (s, 3H). **^{13}C NMR** (101 MHz, $CDCl_3$) δ (ppm) = 211.4, 172.7, 170.7, 167.0, 166.3, 162.8, 159.3, 153.6, 148.9, 141.8, 141.2, 138.2, 138.1, 136.2, 133.8, 131.2, 130.3, 129.3, 129.1, 128.8, 128.4, 127.2, 126.1, 116.0, 112.6, 101.0, 84.3, 81.2, 78.8, 75.0, 74.6, 73.4, 72.6, 72.1, 61.2, 57.8, 56.6, 56.4, 55.2, 46.6, 43.2, 37.1, 36.7, 36.3, 31.6, 29.8, 26.7, 22.7, 20.8, 14.5, 10.0. **HRMS (ESI+)** calcd for $[C_{55}H_{62}N_3O_{17}]^+$ = $[MH]^+$: m/z 1036.40737, found 1036.40818.

(2aR,4S,4aS,6R,9S,11S,12S,12aR,12bS)-12b-acetoxy-4,6,11-trihydroxy-9-(((2R,3S)-2-hydroxy-3-phenyl-3-(3-((3,4,5-trimethoxyphenyl)diazenyl)benzamido)propanoyl)oxy)-4a,8,13,13-tetramethyl-5-oxo-2a,3,4,4a,5,6,9,10,11,12,12a,12b-dodecahydro-1H-7,11-methanocyclodeca[3,4]benzo[1,2-b]oxet-12-yl benzoate (AzTax3TM)

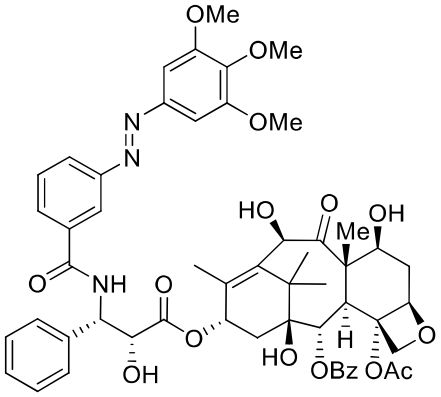

AzTax3TM

By Standard Procedure E, docetaxel (20 mg, 24 µmol) was deprotected with TFA-DCM and the crude foam (17 mg) reacted with **3TM-CO_2H** (10 mg, 29 µmol, 1.2 eq), Hünig base (12 mg, 96 µmol, 4.0 eq), EDCI (7 mg, 36 µmol), and HOBt·H_2O (7 mg, 85 %wt, 39 µmol, 1.6 eq) to yield a yellow crude solid. Chromatography on (iHex:EA 7:3→1:1; DCM:MeOH 99:1→96:4) returned **AzTax3TM** as a yellow solid (9 mg, 9.0 μmol, 37%).

^{1}H NMR (400 MHz, chloroform-d) δ (ppm) = 8.22 (t, J = 1.9 Hz, 1H), 8.15 – 8.10 (m, 2H), 8.04 – 7.99 (m, 1H), 7.87 (dt, J = 7.9, 1.3 Hz, 1H), 7.62 – 7.54 (m, 2H), 7.54 – 7.48 (m, 4H), 7.47 – 7.44 (m, 1H), 7.44 – 7.39 (m, 2H), 7.39 – 7.35 (m, 1H), 7.24 (s, 2H), 7.20 (dd, J = 8.7, 3.9 Hz, 1H), 6.26 – 6.20 (m, 1H), 5.84 (dd, J = 9.0, 2.6 Hz, 1H), 5.69 (d, J = 7.1 Hz, 1H), 5.17 (d, J = 4.7 Hz, 1H), 4.97 – 4.90 (m, 1H), 4.82 (s, 1H), 4.31 (d, J = 8.5 Hz, 1H), 4.22 (d, J = 8.2 Hz, 3H), 3.96 (s, 6H), 3.94 (s, 3H), 3.93 – 3.87 (m, 2H), 3.69 – 3.60 (m, 2H), 3.58 (s, 1H), 2.57 (ddd, J = 15.7, 9.7, 6.5 Hz, 1H), 2.40 (s, 3H), 2.37 – 2.21 (m, 3H), 1.86 (d, J = 12.4 Hz, 2H), 1.80 (d, J = 1.4 Hz, 2H), 1.76 (s, 3H), 1.21 (s, 4H), 1.12 (s, 3H). **^{13}C NMR** (101 MHz, chloroform-d) δ (ppm) = 211.3, 172.6, 170.5, 167.0, 166.4, 152.5, 148.2, 141.2, 138.1, 137.9, 136.2, 134.7, 133.7, 130.2, 129.6, 129.2, 129.2, 129.1, 128.7, 128.4, 127.1, 126.0, 121.0, 100.8, 84.1, 81.1, 78.8, 74.8, 74.5, 73.1, 72.5, 72.0, 61.1, 57.7, 56.3, 55.1, 46.5, 43.1, 37.0, 36.0, 29.7, 26.6, 22.6, 20.6, 14.4, 9.9. **LCMS(+):** t_{ret} =8.2 min, 1006 Th = $[M]^+$. **HRMS (ESI+)** calcd for $[C_{55}H_{63}N_4O_{15}]^+$ = $[MH]^+$: m/z 1006.39681, found 1006.39929.

(2aR,4S,4aS,6R,9S,11S,12S,12aR,12bS)-12b-acetoxy-9-(((2R,3S)-3-(3-((4-(bis(2-hydroxyethyl)amino)phenyl)diazenyl)benzamido)-2-hydroxy-3-phenylpropanoyl)oxy)-4,6,11-trihydroxy-4a,8,13,13-tetramethyl-5-oxo-2a,3,4,4a,5,6,9,10,11,12,12a,12b-dodecahydro-1H-7,11-methanocyclodeca[3,4]benzo[1,2-b]oxet-12-yl benzoate (AzTax3DEA)

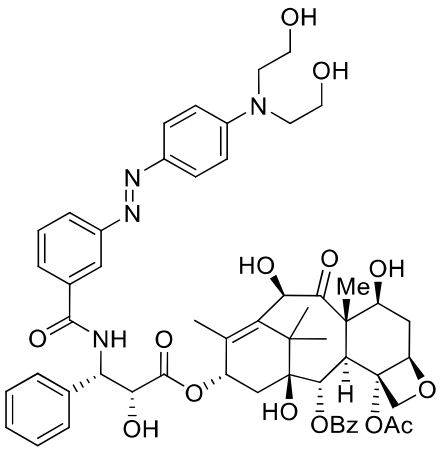

AzTax3DEA

By Standard Procedure E, docetaxel (20 mg, 24 µmol) was deprotected with TFA-DCM and the crude foam (17 mg) reacted with **3DEA-CO_2H** (10 mg, 29 µmol, 1.2 eq), Hünig base (12 mg, 96 µmol, 4.0 eq), EDCI (7 mg, 36 µmol), and HOBt·H_2O (7 mg, 85 %wt, 39 µmol, 1.6 eq) to yield a yellow crude solid. Chromatography on (DCM:MeOH 98:2→92:8) returned **AzTax3DEA** as a yellow solid (12 mg, 11.8 *µ*mol, 49%).

^{1}H NMR (400 MHz, methanol-d_4) δ (ppm) = 8.29 (t, *J* = 1.8 Hz, 1H), 8.12 (d, *J* = 1.2 Hz, 1H), 8.10 (d, *J* = 1.5 Hz, 1H), 7.96 (ddd, *J* = 8.0, 2.0, 1.1 Hz, 1H), 7.89 (dt, *J* = 7.8, 1.4 Hz, 1H), 7.85 – 7.81 (m, 2H), 7.68 – 7.62 (m, 1H), 7.61 – 7.55 (m, 3H), 7.55 – 7.52 (m, 1H), 7.50 (d, *J* = 1.2 Hz, 1H), 7.43 (t, *J* = 7.8 Hz, 2H), 7.33 – 7.27 (m, 1H), 6.89 (d, *J* = 9.3 Hz, 2H), 6.27 – 6.17 (m, 1H), 5.69 (d, *J* = 5.3 Hz, 1H), 5.64 (d, *J* = 7.2 Hz, 1H), 5.25 (s, 1H), 4.99 – 4.94 (m, 1H), 4.76 (d, *J* = 5.4 Hz, 1H), 4.58 (s, 1H), 4.20 (td, *J* = 8.6, 5.9 Hz, 3H), 3.88 (d, *J* = 7.2 Hz, 1H), 3.79 (t, *J* = 5.9 Hz, 4H), 3.68 (t, *J* = 5.9 Hz, 4H), 2.48 – 2.40 (m, 1H), 2.39 (s, 3H), 2.30 – 2.18 (m, 2H), 1.96 (dd, *J* = 15.5, 8.8 Hz, 1H), 1.89 (d, *J* = 1.4 Hz, 3H), 1.82 (td, *J* = 12.6, 11.3, 2.6 Hz, 1H), 1.69 (s, 3H), 1.16 (s, 3H), 1.11 (s, 3H). **^{13}C NMR** (101 MHz, methanol-d_4) δ (ppm) = 209.7, 173.1, 170.5, 170.0, 168.3, 166.3, 153.2, 151.2, 143.3, 137.8, 136.6, 130.1, 129.8, 129.0, 128.4, 128.3, 127.8, 127.6, 127.1, 125.0, 120.5, 111.4, 84.6, 80.9, 77.8, 76.2, 75.1, 74.2, 73.6, 71.2, 71.1, 58.9, 57.5, 56.5, 53.6, 46.4, 43.1, 36.1, 35.5, 25.6, 21.9, 13.0, 9.1. **LCMS(+):** t_{ret} =7.3 min, 1019 Th = $[M]^+$. **HRMS (ESI+)** calcd for $[C_{55}H_{59}N_3O_{16}]^+ = [MH]^+$: m/z 1019.42844, found 1019.42877

(2aR,4S,4aS,6R,9S,11S,12S,12aR,12bS)-12b-acetoxy-4,6,11-trihydroxy-9-(((2R,3S)-2-hydroxy-3-(2-((4-methoxyphenyl)diazenyl)benzamido)-3-phenylpropanoyl)oxy)-4a,8,13,13-tetramethyl-5-oxo-2a,3,4,4a,5,6,9,10,11,12,12a,12b-dodecahydro-1H-7,11-methanocyclodeca[3,4]benzo[1,2-b]oxet-12-yl benzoate (AzTax2MP)

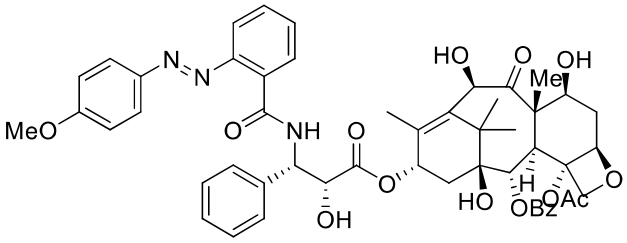

AzTax2MP

By Standard Procedure E, docetaxel (20 mg, 24 µmol) was deprotected with TFA-DCM and the crude foam (17 mg) was dissolved in 2 mL DMF. **4MP-CO_2H** (8 mg, 28 µmol, 1.2 eq) was added to the reaction mixture. Triethylamine (24 mg, 240 *µ*mol, 10 eq) was added. T3P (26 mg, 50 wt% in EA, 40 *µ*M, 1.7 eq) was added. The resulting organic solution was stirred at room temperature for 16 h. Upon completion the DMF was removed *in* vacuo and the resulting yellow crude product was purified by means of flash chromatography on silica (iHex:EA 7:3→1:1; DCM:MeOH 99:1→95:5). **AzTax2MP** was obtained as a yellow solid (10 mg, 10.4 *µ*mol, 41%).

^{1}H NMR (400 MHz, chloroform-*d*) δ (ppm) = 9.69 (d, *J* = 8.6 Hz, 1H), 8.28 (dd, *J* = 7.9, 1.6 Hz, 1H), 8.20 – 8.12 (m, 2H), 7.85 – 7.80 (m, 2H), 7.78 (dd, *J* = 8.2, 1.3 Hz, 1H), 7.66 – 7.60 (m, 1H), 7.56 – 7.47 (m, 5H), 7.42 (td, *J* = 7.6, 1.3 Hz, 1H), 7.38 – 7.30 (m, 3H), 6.96 (d, *J* = 9.0 Hz, 2H), 6.22 (d, *J* = 8.8 Hz, 1H), 5.95 (dd, *J* = 8.7, 2.5 Hz, 1H), 5.68 (d, *J* = 7.0 Hz, 1H), 5.16 – 5.12 (m, 1H), 4.94 (d, *J* = 9.4 Hz, 1H), 4.77 (dd, *J* = 4.9, 2.5 Hz, 1H), 4.33 (d, *J* = 8.5 Hz, 1H), 4.25 – 4.16 (m, 3H), 3.89 (s, 4H), 3.69 (d, *J* = 7.6 Hz, 2H), 2.58 (t, *J* = 15.2 Hz, 2H), 2.42 (s, 3H), 2.40 – 2.22 (m, 3H), 1.86 (d, *J* = 14.3 Hz, 2H), 1.80 (d, *J* = 1.4 Hz, 3H), 1.77 (d, *J* = 5.5 Hz, 3H), 1.51 (s, 2H), 1.19 (s, 3H), 1.11 (s, 3H).

^{13}C NMR (101 MHz, chloroform-*d*) δ (ppm) = 172.5, 170.5, 167.0, 165.9, 163.2, 150.1, 146.7, 138.7, 138.5, 135.9, 133.7, 132.2, 131.9, 130.7, 130.3, 129.4, 129.3, 128.9, 128.8, 128.3, 128.3, 128.0, 127.2, 126.8, 125.8, 116.1, 114.6, 84.1, 81.1, 78.8, 74.8, 74.6, 73.8, 72.3, 72.1, 57.7, 55.7, 46.5, 43.0, 37.0, 36.0, 29.7, 26.5, 22.7, 20.6, 14.6, 9.9. **LCMS(+):** t_{ret} =8.7 min, 946 Th = $[MH]^+$, **HRMS (ESI+)** calcd for $[C_{52}H_{55}N_3O_{14}]^+ = [MH]^+$: m/z 946.37740, found 946.37568.

Water-soluble model photoswitch carboxamides

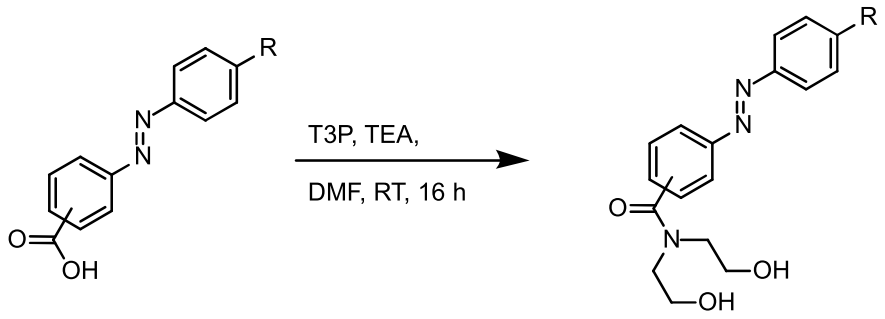

para, R: H, **4H**
meta, R:OMe, **3MP**
meta, R: NMe_2, **3DMA**

***N,N*-bis(2-hydroxyethyl)-4-(phenyldiazenyl)benzamide (4H)**

By standard procedure F, commercial **4H-CO_2H** (20 mg, 0.089 mmol, 1.0 eq) was reacted with diethanolamine (19 mg, 0.18 mmol, 2.0 eq). After purification by flash chromatography (DCM:MeOH, 100:0→98:2) the desired product ***N,N*-bis(2-hydroxyethyl)-4-(phenyldiazenyl)benzamide** (**4H**) (18 mg, 0.057 mmol, 65%) was obtained as a orange solid. **^{1}H NMR** (400 MHz, methanol-d_4) δ (ppm) = 8.01 – 7.97 (m, 2H), 7.97 – 7.92 (m, 2H), 7.68 – 7.63 (m, 2H), 7.60 – 7.51 (m, 3H), 3.87 (t, *J* = 5.5 Hz, 2H), 3.74 (t, *J* = 5.6 Hz, 2H), 3.64 (t, *J* = 5.6 Hz, 2H), 3.54 (t, *J* = 5.7 Hz, 2H). **^{13}C NMR** (101 MHz, DMSO-d_6) δ (ppm) = 170.3, 151.9, 151.7, 140.0, 131.8, 130.7, 129.6, 128.1, 122.7, 122.5, 58.5, 58.5, 51.6, 47.4. **LCMS(+):** t_{ret} = 3.8 min, 314 Th = $[MH]^+$. **HRMS (EI):** calc. for $C_{17}H_{19}N_3O_3^+$ $[M]^+$: 313.1426; found: 313.1409.

3-((4-(dimethylamino)phenyl)diazenyl)-*N,N*-bis(2-hydroxyethyl)benzamide (3DMA)

By standard procedure F, **3DMA-CO_2H** (20 mg, 0.074 mmol, 1.0 eq) was reacted with diethanolamine (16 mg, 0.15 mmol, 2.0 eq). After purification by flash chromatography (DCM:MeOH, 98:2→96:4) the desired product **3-((4-(dimethylamino)phenyl)diazenyl)-N,N-bis(2-hydroxyethyl)benzamide** (**3DMA**) (16 mg, 0.045 mmol, 60%) was obtained as a yellow solid. **^{1}H NMR** (500 MHz, methanol-d_4) δ (ppm) = 7.92 – 7.81 (m, 4H), 7.57 (dd, *J* = 8.5, 7.6 Hz, 1H), 7.48 (dt, *J* = 7.5, 1.4 Hz, 1H), 6.86 – 6.81 (m, 2H), 3.88 (t, *J* = 5.7 Hz, 2H), 3.74 (t, *J* = 5.7 Hz, 2H), 3.64 (t, *J* = 5.8 Hz, 2H), 3.54 (t, *J* = 5.7 Hz, 2H), 3.10 (s, 6H). **^{13}C NMR** (126 MHz, methanol-d_4) δ (ppm) = 173.1, 165.0, 153.1, 153.0, 143.3, 137.5, 129.0, 127.2, 124.8, 123.0, 119.8, 111.2, 59.2, 59.0, 52.3, 39.0. **LCMS(+):** t_{ret} = 4.0 min, 357 Th = $[MH]^+$. **HRMS (EI):** calc. for $C_{14}H_{12}O_3N_2^+$ $[M]^+$: 356.1848; found: 356.1839.

***N,N*-bis(2-hydroxyethyl)-3-((4-methoxyphenyl)diazenyl)benzamide (3MP)**

By standard procedure F, **3MP-CO_2H** (20 mg, 0.078 mmol, 1.0 eq) was reacted with diethanolamine (16 mg, 0.16 mmol, 2.0 eq). After purification by flash chromatography (DCM:MeOH, 98:2→95:5) the desired product **N,N-bis(2-hydroxyethyl)-3-((4-methoxyphenyl)diazenyl)benzamide** (**3MP**) (17 mg, 0.050 mmol, 64%) was obtained as a yellow solid. **^{1}H NMR** (400 MHz, methanol-d_4) δ (ppm) = 7.97 – 7.90 (m, 4H), 7.64 – 7.58 (m,

1H), 7.56 (dt, J = 7.6, 1.5 Hz, 1H), 7.12 – 7.04 (m, 2H), 3.89 (s, 5H), 3.74 (t, J = 5.7 Hz, 2H), 3.64 (t, J = 5.7 Hz, 2H), 3.53 (t, J = 5.7 Hz, 2H). **^{13}C NMR** (101 MHz, methanol-*d*$_4$) δ (ppm) = 172.1, 162.0, 151.7, 145.9, 136.8, 128.4, 127.6, 123.8, 122.6, 119.5, 113.2, 58.4, 58.1, 54.0, 51.5. **LCMS(+):** t_{ret} = 3.6 min, 344 Th = $[MH]^+$. **HRMS (EI):** calc. for $C_{14}H_{12}O_3N_2^+$ $[M]^+$: 343.1532; found: 343.1522.

Supplementary Note 2: Photocharacterisation *in vitro*

Materials and Methods

HPLC for UV-Vis spectroscopy on separated isomers

During HPLC (as in Supplementary Note 1), the diode array detector was used to acquire peak spectra of separated photoswitch isomers over the range 200–550 nm, manually baselining across each elution peak of interest to correct for eluent composition effects.

UV-Vis spectrophotometry to monitor photoswitching and relaxation in bulk samples

Absorption spectra in cuvette ("UV-Vis") were acquired on a Varian CaryScan 60 (1 cm pathlength). For photoisomerisation measurements, Hellma microcuvettes (108-002-10-40) taking 500 μL volume to top of optical window were used with test solution such that the vertical pathlength of the isomerization light is less than 7 mm to the bottom of the cuvette, with the default test solution concentrations of 25 μM. Measurements on soluble photoswitches were performed by default in PBS at pH ~7.4 with 1% of DMSO to better mimic the intracellular environment during cell culture conditions (with 1% DMSO). Photoisomerisations and relaxation rate measurements were performed at room temperature. "Star" LEDs (3W H2A1-models spanning 360–590 nm from Roithner Lasertechnik) were used for photoisomerisations in the cuvette that were also predictive of what would be obtained in LED-illuminated cell culture.

The **AzTaxs** were not reliably soluble enough to be assayed in physiologically relevant aqueous media (~1% DMSO max, aqueous buffer) at ~50 μM as is necessary for long-term UV-Vis based studies on our setup. Therefore, the spectra of the excellently water-soluble diethanolamide model photoswitches were instead acquired, in physiologically relevant aqueous media (PBS with <1% DMSO), to give the closest approximation of the PSSs to be expected in cell assays with the cognate series of **AzTax**s. Their absorption spectra at the photostationary states (PSSs) under illumination at different biocompatible and photoswitching-relevant wavelengths, were measured. Note that "dark" represents a solution quantitatively relaxed to all-*E* by warming overnight to 60°C.

Thermally reversible and photoreversible photoisomerisation

Azobenzenes photoswitches featuring *para*-dialkylamino groups (**3DMA**, **3DEA**, **4DMA**) did not appear to undergo bulk photoisomerisation in homogeneous aqueous physiological media (1 cm UV-Vis cuvette measurement, 25 μM, PBS pH ~7.4, <1% DMSO, 37°C, detection limit for photoisomerisation is to maintain ca. >2% *Z* isomer) which literature suggests is caused by fast (halflife < ms range) spontaneous ("thermal"), quantitative, unidirectional $Z \rightarrow E$ relaxation in this media.[13] All other azobenzenes were photoreversibly isomerisable in this homogeneous aqueous physiological media, which literature supports for azobenzenes not featuring strong resonance donor groups in *para* to the diazene[14]; results are shown for representative photoswitch **3MP** (Supplementary Figure 1).

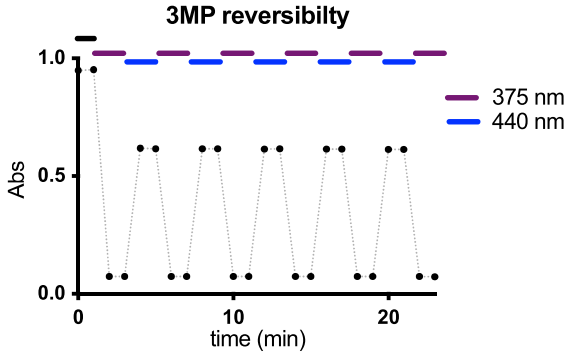

Supplementary Figure 1: Photoisomerisations in homogeneous aqueous physiological media (PBS pH ~7.4, <1% DMSO, 37°C) are perfectly photoreversible over many cycles, with no signs of degradation, implying robust and reproducible photoswitching can be possible under biological conditions (Source Data are provided in the Source Data file).

We have previously observed however that non-azobenzene photoswitches that were not bulk-photoswitchable in homogeneous aqueous physiological media, can reliably display photoswitchability of bioactivity when used in the heterogeneous context of cell biology.[15] There are also reports of light-dependent activity for very fast-relaxing azobenzene photopharmaceuticals intended to address intracellular protein targets located in aqueous environments[16]; although, as far as we are aware, those fast-relaxing azobenzenes required illumination with such high photon flux to trigger irreversible bioactivity, that it is conceivable (given e.g. the mismatch between the *trans*-active structure-activity relationship expected, and the experimental *cis*-active result, as well as non-photoreversibility of biological effect) that transient photoisomerisation could to some extent be followed by glutathione (GSH) degradation of the more GSH-sensitive *cis*-azobenzene isomer[17], yielding a range of undefined, non-photoswitchable byproducts presumably including the diazene scission product aniline, several of which could be expected to be potent, photoirreversible, and biologically essentially irreversible enzyme-inhibiting species. In this work we therefore determined that biological evaluations for fast-relaxing **AzTax** conjugates would proceed with very limited photon flux, applied from short and low-intensity LED pulses, which we estimate to be insufficient[18–20] to give confounding results. Assuming that biological photoswitchability for these species can only arise by their biolocalisation in relatively water-excluded environments (membranes, lipid vesicles, adsorbed onto proteins) which allow greater thermal stability of the metastable isomer, we therefore measured all photoproperties of the *para*-dialkylaminoazobenzenes in ethyl acetate solution, which we consider to be a reasonable mimic of an aprotic, moderately polar environment. We observed that this allowed **3DMA** to exhibit fully photoreversible isomerisations (Supplementary Figure 2) which gave hope that *para*-dialkylaminoazobenzene **AzTax**s might prove to display photoswitchable bioactivity *in cellulo*.

We also monitored the rate of spontaneous ("thermal"), quantitative, unidirectional $Z \rightarrow E$ relaxation of all azobenzenes. The photoswitches used in this study could be split in two groups according to their performance as relevant to conditions for biological use: (1) The *para*-dialkaylamino switches had *cis*-halflife $t_{1/2} \sim 11$ min in EtOAc (although no switching was

observed in water); whereas (2) *para*-alkoxy and *para*-unsubstituted azobenzenes showed relaxation that is much slower (in PBS with < 1% DMSO at 37°C) than the typical 1-to-60 min timescale that biological assays would require for delivering functional reversibility; these would therefore require active *Z*→*E* photoisomerisation and/or diffusion-based reduction of localised *Z* isomer concentration in order to display biological reversibility. *Para*-alkoxy compounds displayed $t_{1/2}$ (halflife) values on the order of 10 h - 5 days (representative **3MP** had $t_{1/2} \sim 24$ h); unsubstituted compounds displayed $t_{1/2}$ values substantially above 1 day (representative **4H** had $t_{1/2}$ estimated by exponential decay fit to be ca. 50 days). Note however that it is not important for this reagent development research to know precisely the values of the switches' halflives in homogeneous media *in cuvette*: they should be determined to be either far below, or else far above, the biological timescale, and then be handled accordingly.

Photostationary state (PSS) equilibria

PSSs were measured. Results for three compounds representative of the three electronic classes of azobenzenes (**3MP** for *p*-OMe, **3DMA** for *p*-NR_2, **4H** for *p*-unsubstituted switches) are shown in Supplementary Figure 2.

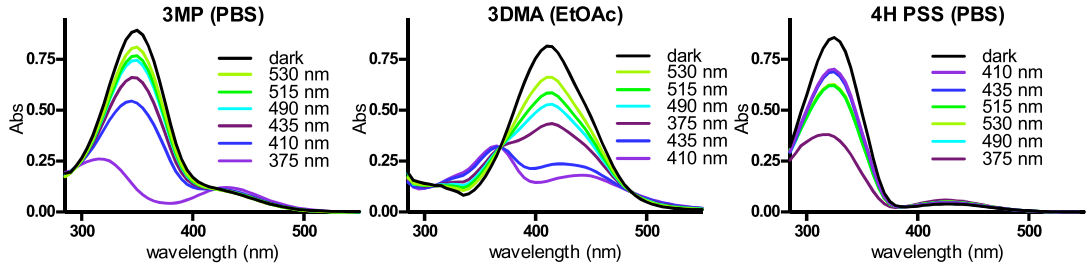

Supplementary Figure 2: PSS spectra for photoswitches representative of the three structural classes explored in this work (Source Data are provided in the Source Data file).

PSS analysis

For photopharmaceutical assays in biology it is helpful to anticipate the *E*/*Z* ratio at any wavelength's photostationary state (PSS), to choose optimal wavelengths for illumination during biological assays or to understand the limits of what is possible on a given setup: e.g. on a microscope with laser lines 405 nm, 488 nm and 515 nm, what dynamic range of photoswitchability is possible by establishing localised PSSs (inside a single cell) that alternate between 405 nm and 515 nm? Ideally, 405 nm would establish a PSS with 100% of one isomer (e.g. *Z*), and 515 nm would establish a PSS with 100% of the other isomer, implying a 100% dynamic range of isomer photoswitchability; and ideally, one isomer (e.g. *Z*) would be bioactive while the other isomer would be entirely biologically inactive, therefore that 405 nm / 515 nm photoswitching would also allow 100% dynamic range of biological photoswitchability. However, no azobenzenes have ever been shown to enable 100% dynamic range of isomer photoswitchability, and anyway as far as we are aware only **PSTs**[20] feature one isomer that is entirely biologically inactive. Therefore it is impossible that any azobenzene-based photopharmaceutical according to current designs features 100%

dynamic range of biological photoswitchability. Analysing PSS ratios *in cuvette* can extract the isomer photoswitchability, and analysing bioactivity determinations under those same PSSs in light of the isomer photoswitchabilities can determine the isomer *bioactivity differentials*; both analyses are needed to be able to gauge the dynamic range of biological photoswitchability that is theoretically obtainable under any arbitrary wavelength.

We have previously published a workflow[17] to estimate PSS at any wavelength in biological media, based on acquiring separated *E* and *Z* isomer spectra by LCMS-UV, and relying on isosbestic point determination in physiological media. In brief, to determine the ratios of *E* and *Z* isomers in PSS equilibria, the UV/Vis spectra of the HPLC-separated isomers are measured by inline DAD, extracted, scaled relative to each other using the isosbestic point determined from UV-Vis studies in biological media, then fitted as a linear combination to the measured PSS absorption spectra, with the linear combination coefficients then being the PSS fractions of each isomer.

However, in this research, the isolated E and Z spectra of the amides in LCMS eluent did not match up to their dark (all-*E*) and illuminated (mostly-*Z*) spectra as recorded in PBS buffer. The n→π* band notably showed lower intensity in the LCMS spectra which we attribute to influence of solvent, as the acidic acetonitrile/water eluent provides a different environment for the azobenzene than the neutral aqueous PBS buffer. We decided that results from measurements in PBS buffer however provide far more useful information for biology, than would performing PSS measurements in the HPLC solvent system, so we changed to a different "envelope" method that establishes entirely robust and assumption-free upper and lower bounds for the true PSS ratios. Since these bounds are often remarkably close to each other the method can allow remarkably precise, assumption-free estimation of the PSS isomer ratios in biological media, and also gives a maximum possible error of that PSS which it is useful to know.

Envelope Method

(0) The absorption spectrum of a fully-relaxed sample (60°C overnight relaxation) is acquired and assumed to be the all-*E* spectrum. This step can also be checked by NMR (in contrast, we consider that establishing illuminated PSSs by NMR is not a straightforward approach due to (a) Lambert-Beer shielding at relatively high concentrations plus high reflection from the tube surface making establishment of many PSSs in many NMR tubes a very timeconsuming process; and (b) need for deuterated biological buffers).

(1) *Upper Bounds:* The *relative completeness* of photoreversions towards the all-*trans* state under different illuminations was examined first. For each PSS wavelength, the "relative completeness fraction" RCF(λ) calculated as the ratio [[P(λ)-MC(λ)]/[D(λ)-MC(λ)]], where P(λ) is the PSS absorption spectrum being evaluated, MC(λ) is the PSS absorption spectrum under the wavelength giving the most-*cis*-containing PSS, and D(λ) is the all-*trans* absorption spectrum, was calculated. This “relative completeness fraction” was calculated across the data range where the variation in absorbances with different PSSs is strongest (typically 370-420 nm), then the data were averaged to give the mean, and their standard deviation

determined as a measure of the error in this fitting method. These completeness fraction values are, by definition, lower bounds for the PSS values of *E*-content, so **[1-RCF(λ)] determines robust upper bounds** for the PSS values of *Z*-content.

(2) *Lower Bounds:* **Lower bounds** for the PSS *Z*-content values may separately be obtained by assuming the absorption of the *cis* isomer is zero at a single wavelength λ_{strong} (the wavelength with the largest fold differential of extinction coefficients between *cis* and *trans* forms) and then tabulating $A(\lambda_{strong,\ PSS})/A(\lambda_{strong,\ all\text{-}trans})$. Typically, λ_{strong} is approx. 385 nm.

(3) *Envelope:* The interval from lower to upper bound is an assumption-free bounded range for the true PSS at any measured wavelength. This will be seen to be more than sufficient to give a PSS range with typically only ±5-10% possible error at the wavelengths of most interest to this study. We here represent the envelope midpoint as the fitted "PSS %Z", and give the half-width of the envelope (100% CI) as the possible error "± %" (Table S1).

λ (nm)	3MP		4H		3DMA (in EA)	
	PSS %Z	+/- %	PSS %Z	+/- %	PSS %Z	+/- %
375	96%	4%	80%	20%	53%	5%
410	44%	2%	26%	6%	91%	9%
435	29%	1%	28%	7%	80%	8%
490	18%	1%	39%	10%	39%	4%
515	16%	1%	39%	9%	32%	3%
530	11%	1%	38%	9%	21%	2%

Supplementary Table 1 - Estimated PSSs from the envelope method and maximum error in the estimated PSSs, for the three different families of azobenzene photoswitches used in this study (*p*-OMe, *p*-unsubstituted, *p*-NR_2).

Supplementary Note 3: Biochemistry: tubulin polymerisation *in vitro*

99% tubulin from porcine brain was obtained from Cytoskeleton Inc. (cat. #T240). The polymerisation reaction was performed at 5 mg/mL tubulin, in polymerisation buffer BRB80 (80 mM piperazine-N,N′-bis(2-ethanesulfonic acid) (PIPES) pH = 6.9; 0.5 mM EGTA; 2 mM $MgCl_2$), in a cuvette (120 µL final volume, 1 cm path length) in a Varian CaryScan 60 with Peltier cell temperature control unit maintained at 37°C; with glycerol (10 µL). Tubulin was incubated at 37°C with “pre-lit”- [360 nm-pre-illuminated; mostly-*Z*-] or dark- [all-*E*] **AzTax3MP**, or docetaxel (final inhibitor concentration 10 µM), or without inhibitor ("cosolvent" control), in buffer with 3% DMSO and 1 mM GTP, and the change in absorbance at 340 nm was monitored, scanning at 15 s intervals[21]. Docetaxel showed the strongest microtubule hyperpolymerisation effect; pre-lit **AzTax3MP** had ca. 2/3 of docetaxel's hyperpolymerising potency compared to cosolvent-only control; all-*E* **AzTax3MP** had had ca. 1/3 of docetaxel's potency (Fig 2d). Note however that this is a highly nonlinear experiment in a non-cellular setting; these results neither imply that the potency of *Z*-**AzTax3MP** is 2/3 of that of docetaxel, nor that the potency of *E*-**AzTax3MP** is half of that of *Z*-**AzTax3MP**.

Supplementary Note 4: Cell Biology

Cell assay methods

General cell culture

HeLa and COS-7 cells were maintained under standard cell culture conditions in Dulbecco's modified Eagle's medium (DMEM; PAN-Biotech: P04-035550) supplemented with 10% fetal calf serum (FCS), 100 U/mL penicillin and 100 μg/mL streptomycin. Cells were grown and incubated at 37°C in a 5% CO_2 atmosphere. Cells were cultured in phenol red free medium prior to assays (DMEM; PAN-Biotech: P04-03591). Compounds and cosolvent (DMSO; 1% final concentration) were added *via* a D300e digital dispenser (Tecan); all photoswitches were added in their all-*E* state (thermal relaxation of the DMSO stocks at 60°C overnight, applied under light exclusion conditions). Cells were either incubated under "lit" or "dark" conditions; "lit" indicates a pulsed illumination protocol applied by multi-LED arrays to create, *in situ* in cells, the wavelength-dependent PSS isomer ratio of the compounds, and then maintain it throughout the experiment, as described previously.[17,19] Typical "lit" timing conditions were 75 ms pulses applied every 15 s. "Dark" indicates that compounds were applied while working, sterile, under red-light conditions, and cells were then incubated in light-proof boxes to shield them from ambient light, so maintaining an all-*E*-isomer population throughout the experiment.

Resazurin antiproliferation assay

Cells were seeded in 96-well plates at 5,000 cells/well and left to adhere for 24 h before treating with various concentrations of different compounds. *E*-**AzTax** were added and incubated under the indicated lighting conditions for 48 h (final well volume 100 μL, 1% DMSO; three technical replicates); the "cosolvent control" ("ctrl") indicates treatment with DMSO only. Cell viability was measured by addition of resazurin, which is reduced to resorufin under metabolic activity in live cells. Fluorescence of the resorufin product was measured using a FLUOstar Omega microplate reader (BMG Labtech) at 544/590 nm (ex/em). Fluorescence data was averaged over technical replicates, then normalized to viable cell count from cosolvent control cells (%control) as 100%, where 0% viability was assumed to correspond to zero. Three independent experiments were performed and data is shown as mean+/-SD; data were plotted against the log of **AzTax** concentration ($\log_{10}$([**AzTax**]) (M)).

Cell cycle analysis

HeLas were seeded in 6 well plates (300,000/well) 24 h prior to treatment. **AzTax3MP** and **AzTax4DMA** were added to the wells and cells were incubated either under "dark" or "lit" regimens. 0.1 μM Docetaxel served as positive control and 1% DMSO as cosolvent control. Cells were harvested 24 h later and fixed overnight in 70% ice cold ethanol. After 12 h, cells were washed and re-hydrated for 15 min in PBS before staining with propidium iodide ("PI", 200 μg/mL in 0.1 % Triton X-100 containing 200μg/mL DNase-free RNase (Thermo Fischer Scientific EN0531) for 30 min at RT. Flow cytometry was done with an LSR Fortessa (BD Biosciences) run by BD FACSDiva 8.0.1 software and at least 10,000 individual PI-positive

cells per condition were collected. FlowJo software (BD Biosciences) was used for gating, first selecting alive cells, then single cells and then setting gates in the PI channel that correspond to less than two sets of chromosomes (subG1), two sets of chromosomes (G1), more than two and less than four (S) and four sets of chromosomes (G2/M). Results plotted as % of parent gate and are given as the mean±SD of at least three biological replicates.

Immunofluorescence staining

For visualization of polymerized tubulin and DNA cells were seeded on glass coverslips in 24 well plates (50,000 cells/well) 24 h prior to treatment. **AzTax3MP**, DMSO or 0.1 μM docetaxel was applied the next day (concentration range **AzTax3MP**: 0.1 μM-3 μM, all wells with 1% DMSO) and cells were incubated either in the dark or with the regular illumination protocol. The next day medium was removed, Cells were washed with pre-warmed (37°C) MTSB buffer (80 mM PIPES, pH 6.8; 1 mM $MgCl_2$, 5 mM ethylene glycol tetraacetic acid (EGTA) dipotassium salt; 0.5% Triton X-100) for 30 s to remove tubulin monomers then fixed with 0.5% glutaraldehyde for 10 min. After quenching with 0.1% $NaBH_4$ cells were blocked for 30 min in PBS containing 30% FCS before incubation with anti-α-tubulin primary antibody (1:400 rabbit Abcam ab18251) for 1 h. Secondary antibody was donkey-anti-rabbit Alexa488 (Thermo Fisher Scientific A21206; 1:400 in PBS + 10% FCS). Coverslips were then mounted on slides with Roti-Mount FluorCare DAPI (Carl Roth) and left to dry. Confocal images were acquired on a Leica SP8 with a 405 nm laser and a white light laser, using a 63× glycerol objective. Confocal stacks (0.33 μm step size) were z-projected and gamma adjusted for better visualization in Fiji/ImageJ.

Live cell EB3 imaging (common protocols)

For Movies 1-2 and Movies 9-14, HeLa cells were transfected with EB3-tagRFP-T or EB3-tdTomato using FuGENE 6 (Promega) according to manufacturer's instructions. For Movies 3-4, COS-7 cells were transfected with mCherry-α-tubulin[22] using FuGENE 6 according to manufacturer's instructions. Cells were incubated for 5 min with 1% DMSO cosolvent, optionally including *E*-**AzTax3MP** at the stated concentration, then, without washout, imaged on a Nikon Eclipse Ti microscope equipped with perfect focus system (Nikon) and Evolve 512 EMCCD camera (Photometrics) with INUBG2E-ZILCS stage top incubator (Tokai Hit) and lens heating calibrated for incubation at 37°C with 5% CO_2. Microscope image acquisition was controlled using MetaMorph 7.7. Comet count analysis was performed in ImageJ using the ComDet plugin (E. Katrukha, University of Utrecht, https://github.com/ekatrukha/ComDet). EB3 comet velocities were quantified in Image J using the MTrackJ plugin.[23] EB3-tdTomato was a gift from Erik Dent (Addgene #50708); EB3-tagRFP-T was a gift from Y. Mimori-Kiyosue. EB3-mCherry dynamics crosschecks (data not shown) were performed with similar transfection and treatment, imaged on a GE DeltaVision OMX SR; the mCherry-EB3-C-20 plasmid was a gift from Michael Davidson (Addgene #55038).

Live Cell Imaging 1: EB3 imaging during cell-specific 405 nm illumination

For Movies 1-2, HeLa cells expressing EB3-tdTomato were imaged with a spinning disk-based confocal scanner unit (CSU-X1-A1, Yokogawa) at 561 nm (0.17 mW, 300 ms every 4 s) while periods of 405 nm single-cell-ROI-localised illuminations were applied (10 μW, 1 scan every 4 s during each 24 s period, Movies 1-2, see Fig 5a for cell ROI example) to isomerise **AzTax3MP** if present (1 μM). Images were acquired using a Plan Apo VC 100× NA 1.4 oil objective.

Live Cell Imaging 2: α-tubulin imaging during full-frame 405 nm illumination

For Movies 3-4, COS-7 cells expressing mCherry-α-tubulin were imaged with a spinning disk-based confocal scanner unit (CSU-X1-A1, Yokogawa) at 561 nm (0.2 mW, 1000 ms, once every minute) and from 3 minutes into the experiment onwards, 405 nm illuminations in full frame mode were applied (20 μW, 1000 ms every 6 s) to isomerise **AzTax3MP** if present (4 μM). Images were acquired using a Plan Apo VC 100× NA 1.4 oil objective.

Live Cell Imaging 3: EB3 imaging during full-frame 405 nm illumination

For Movies 9-10, HeLa cells expressing EB3-tagRFP-T were imaged with a spinning disk-based confocal scanner unit (CSU-X1-A1, Yokogawa) at 561 nm (0.17 mW, 500 ms every 2 s) while periods of 405 nm illuminations in full frame mode were applied (22 μW, 1200 ms every 2 s during each 20 s period) to isomerise **AzTax3MP** if present (0.6 μM). Images were acquired using a Plan Apo VC 100× NA 1.4 oil objective.

Live Cell Imaging 4: EB3 imaging during full-frame TIRF live cell imaging

For Movies 11-14, TIRF imaging of HeLa cells expressing EB3-tagRFP-T was performed a TIRF-E motorized TIRF illuminator modified by Roper Scientific/PICTIBiSA (Institut Curie). EB3-tagRFP-T was imaged at 561 nm using a 100 mW Jive (Cobolt) laser (200 ms every 2 s), while periods of full-field 405 nm illumination were performed using a 100 mW Vortran Stradus 405 nm laser (1200 ms every 2 s for a period of 20 s) to isomerise **AzTax3MP** (1 μM). Images were acquired using a Nikon CFI Apo TIRF 100×, 1.49 N.A. oil objective (Nikon).

Live Cell Imaging 5: EB3 imaging in primary neuronal cultures

Animals

All animal experiments were performed in accordance with Dutch law (Wet op de Dierproeven, 1996) and European regulations (Directive 2010/63/EU). All animal experiments were approved by the Dutch Animal Experiments Committee (DEC, Dier Experimenten Commissie) (license number AVD1080020173404) and were in line with the institutional guidelines of Utrecht University. Pregnant Wistar rats (Janvier), which were at least 10 weeks of age and not involved in any previous experiments, were used in this study.

Primary neuronal cultures and transfections

Primary hippocampal neurons were derived from hippocampi of embryonic day 18 pups (male and female). Hippocampi were dissociated into single cells by a combination of enzymatic and

mechanical dissociation, as described.[24] After dissociation, neurons were plated in 12-well plates at a density of 100,000 cells per well on coverslips coated with poly-L-lysine (37.5 μg/mL, Sigma-Aldrich) and laminin (1.25 μg/mL, Roche). The primary hippocampal cultures were kept at 37°C and 5% CO_2 in Neurobasal medium (NB, Gibco) supplemented with 2% B27 (Gibco), 0.5 mM glutamine (Gibco), 15.6 μM glutamate (Sigma-Aldrich) and 1% penicillin/streptomycin (Gibco).

Neurons were transfected at the 7th day *in vitro* (DIV 7) using Lipofectamine 2000 (Invitrogen) and were imaged at DIV 9. Briefly, for the transfection of each coverslip, 1.8 μg of plasmid DNA was mixed with 3.3 μL of Lipofectamine 2000 in 200 μL non-supplemented NB and incubated for 30 min at 20°C. Before the DNA/Lipofectamine mix was added to the neurons, half of the volume of supplemented NB in which the neurons had been growing (conditioned NB) was transferred to a new 12-well plate and replaced by NB supplemented with 0.5 mM glutamine. Then, the DNA/Lipofectamine mix was added to the neurons and incubated for 1 hour at 37°C and 5% CO_2. After transfection, neurons were rinsed by dipping the coverslips into pre-warmed, non-supplemented NB and placed back in conditioned NB that was mixed 50/50 with fresh, supplemented NB.

Live neuronal imaging

For Movies 5-8, neurons were immersed in conditioned NB with 1% DMSO cosolvent. Cells were imaged on the Nikon Eclipse Ti system used for cell-specific photoisomerisation assays with similar conditions, except in that tdTomato was imaged at 561 nm (0.1 mW, 400 ms every 4 s). Neurons were initially imaged for EB3 for 10 min while a ROI (purple box) was pulsed with 405 nm light, establishing baselines for EB3 activity in the cell and in the ROI (areas not pulsed with 405 nm but analysed in kymographs are boxed in orange and green); the ROI-pulsing protocol was to illuminate the ROI with 405 nm (0.2 mW, 8 ms per trace) tracing over the ROI four times every 4 s with imaging frames interleaved. The same neurons were then immersed in conditioned NB with 1% DMSO and 0.5 μM AzTax3MP and immediately imaged for another 10 min; during this time the same ROI (purple box) was pulsed with 405 nm light (same pulsing protocol) starting 2 min into the acquisition.

Resazurin viability assay results for all compounds

Results for all compounds are shown in Supplementary Figure 3. The results of the resazurin assays can be correlated with the compounds' structures. The important parameters are the general potency of the compound (roughly, the average IC_{50} of the lit and dark states) and the dynamic range (fold difference of IC_{50} between dark and lit conditions).

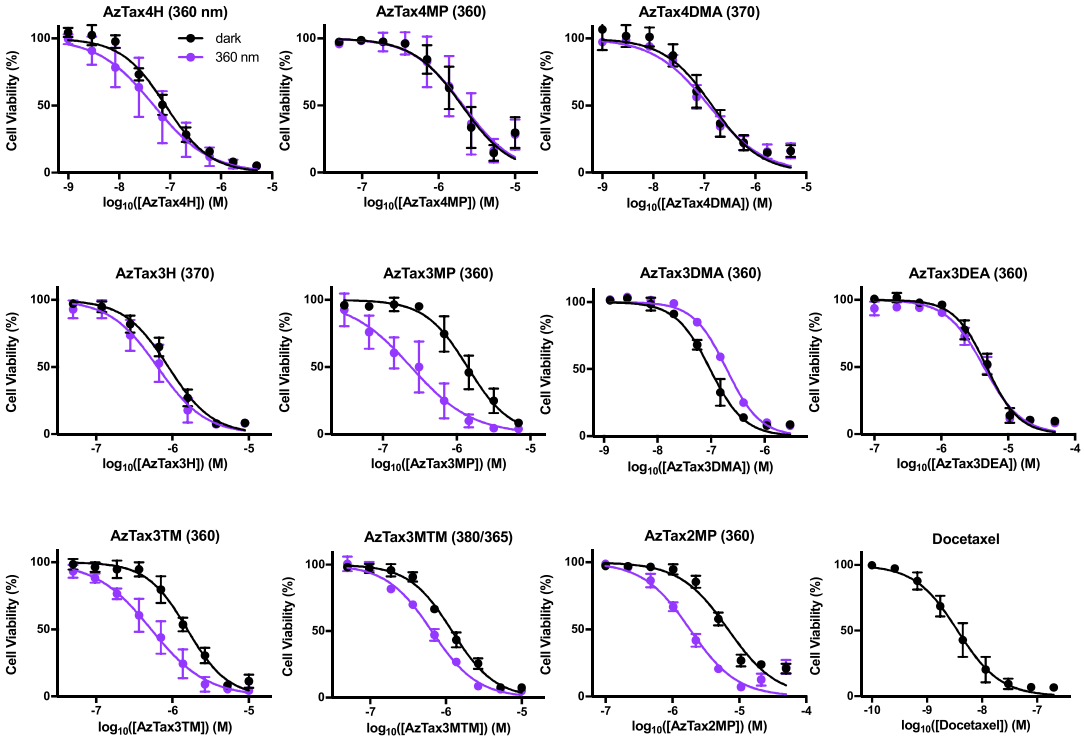

Supplementary Figure 3: resazurin viability assay results for all compounds. The wavelength/s (in nm) used for the "lit" experiments (shown as purple curves) are given in brackets after each graph title, as different wavelengths were used for the assays. The “dark” experiments are depicted in black. The error bars for 360-lit **AzTax3DMA** are not missing but were in all cases too small to be visible (< 3.1%). (n = 3 biologically independent experiments; error bars correspond to s.d.) (Source Data are provided in the Source Data file).

The first structural element to be examined is the attachment point of the azobenzene to the taxane scaffold. The number in the compound name specifies the attachment relative to the diazene bridge (2 = *ortho*, 3 = *meta*, 4 = *para*). It can be generalized that no *para* connected compound showed significant lit vs. dark difference of IC_{50}. *Meta* connected compounds show the highest dynamic range, and attachment in *ortho* reduced the overall potency significantly.

The second structural element examined is the substitution on the azobenzenes. Unsubstituted compounds **AzTax4H** and **AzTax3H** show no significant toxicity change upon illumination, although **AzTax4H** is an order of magnitude more toxic than **AzTax3H**. Alkylated *para*-amino compounds with fast relaxation times also show no strong difference between dark and lit experiments; **AzTax4DMA** and **AzTax3DMA** are approximately equally toxic and **AzTax3DMA** is the only compound that appears to show a higher toxicity under dark conditions, while more polar **AzTax3DEA** shows substantially lower toxicity than either dimethylamino compound. The last group of **AzTax** compounds are variously methoxylated. **AzTax4MP** shows no difference in IC_{50} upon irradiation. The meta connected **AzTax3MP** shows the highest dynamic range as well as satisfactory toxicity. The two derivatives **AzTax3TM** and **AzTax3MTM** have roughly the same cytotoxicities but more moderate dynamic range. **AzTax2MP** shows a drop in toxicity while displaying higher toxicity under illuminated conditions.

FACS cell cycle analysis

Results of cell cycle analysis for **AzTax3MP** were shown in Fig 3b-c. Docetaxel and DMSO and lighting controls are shown in Supplementary Figure 4a; results for non-photoswitchable yet cytotoxic control compound **AzTax4DMA** are shown in Supplementary Figure 4b; and gating strategy is depicted in Supplementary Figure 4c. Lighting and cosolvent cause no change to cell cycle repartition; **AzTax4DMA** (whose short aqueous *cis*-halflife should prevent any light-dependent bioactivity being visible) shows no light-dependent effects, and it also dose-dependently recapitulates the cell cycle repartition seen for positive control docetaxel.

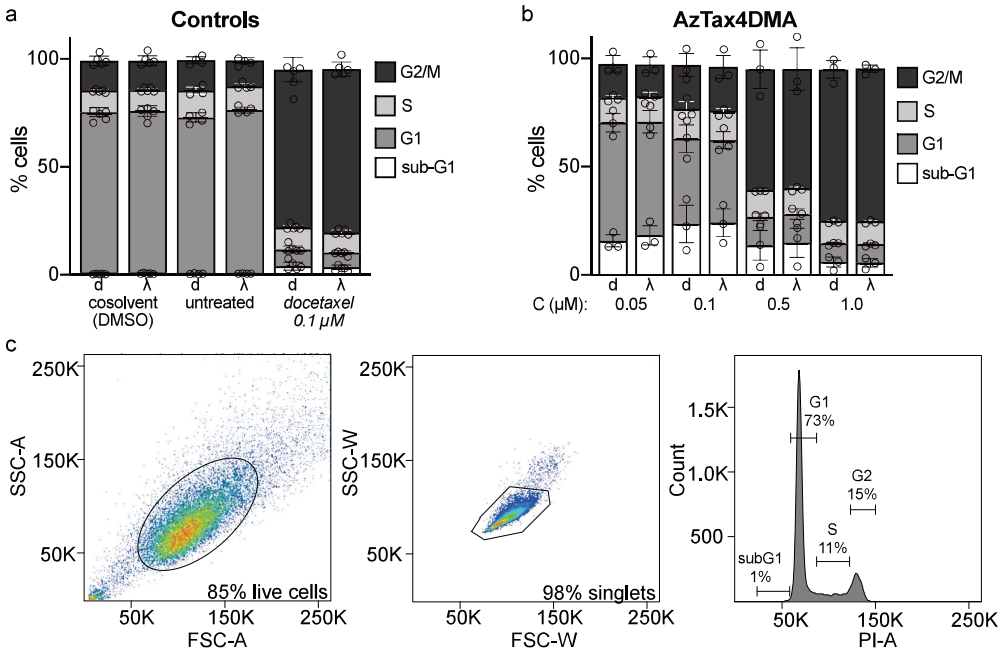

Supplementary Figure 4: Controls for cell cycle repartition. **a** Controls without ("untreated") and with ("DMSO") cosolvent show no cosolvent-induced change of cell cycle repartition; positive control docetaxel gives strong G2/M arrest; and none of these controls show light-dependency of cell cycle repartition (n = 4 independent experiments for untreated, n = 5 independent experiments for docetaxel and cosolvent conditions; mean with s.d.). **b** Non-photoswitchable **AzTax4DMA** shows no light-dependency of cell cycle repartition, but does show dose-dependent G2/M arrest (compare Fig 4b; n = 3 independent experiments; mean with s.d.). **c** Gating strategy for the FACS cell cycle analyses used in Fig 4 (Source Data are provided in the Source Data file).

Immunofluorescence imaging of microtubule network structure

AzTax3MP caused light- and dose-dependent disruption of microtubule organisation, as well as cell toxicity (visible as the density of cells) (Fig 3). At 0.1 μM, slight disorganisation of the MT network can be observed under lit conditions while cell that were kept under dark conditions show no alterations compared to cosolvent controls under lit or dark conditions. At 0.5 μM under lit conditions, **AzTax3MP** causes extensive mitotic arrest and spindle malformations such as multi-spindled cells (top right of inset) and unstructured MT formations (other cells in inset) while under dark conditions, cells are adherent, MT network organisation and progression through mitosis comparable to the cosolvent control as shown by typical microtubule organisation of cells in metaphase (lower left of inset). At 1 μM, under lit conditions only a minor population of adherent cells persist, of which the majority show some MT

organisational defects and multinucleation. Mitotic spindle defects are evident, while under dark conditions cells predominantly escape complete mitotic arrest and re-attach to the plate, albeit with nuclear defects resulting from disorganised MT-dependent processes during cell division. Cells exposed to 1.5 μM **AzTax3MP** under lit conditions display fragmented nuclei, condensed DNA, multipolar of spindles and disrupted microtubule organisation; some cells appear to have no remaining microtubule structures. This can be due to the washing away of non-microtubular tubulin aggregates expected at high doses of MT stabiliser (as seen in the cell-free polymerisation assay) during the wash steps of the staining process, or due to cellular degradation of non-MT tubulin aggregates treated as damaged material, similar to what has been observed under tubulin alkylation. Comparable phenomena are observed in the docetaxel positive control. In the dark, nuclear and MT network disorganisation become severe although phenotypically distinct.

Live cell microscopy assays: detailed quantification

Z-**AzTax3MP** was expected, like other taxanes, to induce curved microtubules. Due to the high cellular density of microtubules, this induced curvature makes it difficult to analyze and quantify cellular microtubule dynamics by studying labelled tubulin, since it becomes impossible to distinguish growth/shortening episodes from lateral MT displacements. We thus chose to use fluorescently labelled EB3, a microtubule plus tip marker that associates with the GTP cap of polymerizing microtubules, to analyze the impact of **AzTax3MP** on microtubule dynamics.[25] EB3 comet velocities cannot be accurately quantified for **AzTax3MP** under blue light due to the lack of any EB3 comets to track, however 1 μM *E*-**AzTax3MP** without blue light activation was found to slow EB3 comet velocities by 20% (Fig 5c). While blue light alone or 1 μM *E*-**AzTax3MP** alone did not significantly reduce EB3 comets, blue light illumination of cells treated with 1 μM **AzTax3MP** caused a striking 89% reduction in the number of EB3 comets compared to the **AzTax3MP** without light (Fig 5d). This indicates that within seconds after isomerisation to to *Z*-**AzTax3MP**, microtubule polymerisation dynamics are either suppresed, as expected for taxanes, or else microtubules themselves are depolymerized, which is not expected for taxanes on this timescale.[26]

To determine whether blue light activated **AzTax3MP** stabilized microtubules or induced microtubule catastrophes, microtubule density was quantified in live COS-7 cells, a cell type with a relatively low microtubule density compared to HeLa, to allow for more accurate quantification. Cells were transfected with mCherry-α-tubulin and treated with **AzTax3MP** or cosolvent DMSO only, before and after blue light activation (compare to Movies 3-4). We found that even with a higher dose of **AzTax3MP**, drug activation had no impact on microtubule density (Supplementary Figure 5). These data are consistent with **AzTax3MP** being a potently photoactivatable microtubule stabilizing agent.

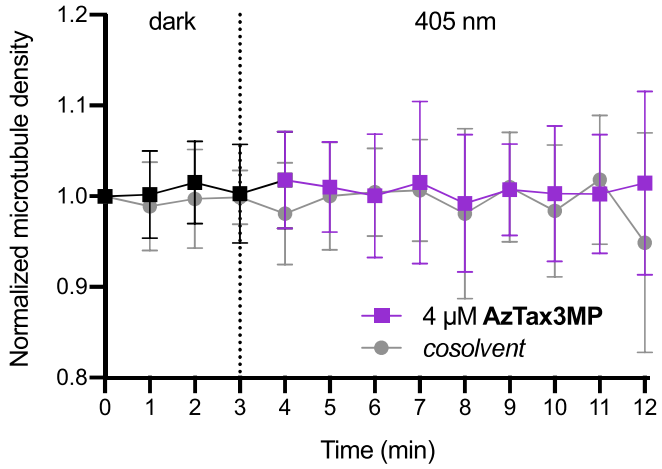

Supplementary Figure 5: AzTax3MP does not alter microtubule density in live cells. COS-7 cells were transfected with mCherry-α-tubulin, treated with 4 μM **AzTax3MP** or 1% DMSO cosolvent alone, and illuminated with a 405 nm laser from 3 min into imaging onwards. Microtubule density was quantified by determining the area fraction with microtubules in a cell for all 13 time points, normalized to time zero (results averaged over n = 9 cells per treatment). Graph shows mean with standard deviation (Source Data are provided in the Source Data file).

Supplementary Discusion: live cell microscopy assays

(1) In EB3 assays we noted that *trans*-**AzTax3MP** at 1 μM already reduces microtubule dynamics even without activation with light; concentrations can be tuned to minimise this if needed. (2) When **AzTax3MP** was illuminated throughout the sample volume with higher photon flux (Movies 11-12), a distinct decrease in EB3-tagRFP-T comets was observed, comparable to that seen with EB3-tdTomato (Movies 1-2). EB3 typically only localises to the growing microtubule tips and microtubules typically grow in relatively straight lines. However after illumination of **AzTax3MP**-treated samples, EB3 comets slowed and/or disappeared as seen previously and the EB3-tagRFP-T now began to label the microtubule lattice which curled and contorted, while cosolvent controls were unaffected (Movies 13-14). Increased flexibility in taxane-stabilized MTs has been reported previously[27–29] which could explain the curliness we observed after high intensity, full-field illumination, although the change of marker from tdTomato to tagRFP-T may also play a role in this observation. The same observation was also shown via confocal microscopy (Movies 9-10). When repeating the entire-sample illumination protocol with cells transfected with mCherry-α-tubulin as a structural marker of the entire microtubule (Movies 3-4), increased curvature on this timescale was not as striking. The interpretation of this difference is tempting but beyond the scope of this paper.

Supplementary Note 5: NMR Spectra

methyl 4-((4-(dimethylamino)phenyl)diazenyl)benzoate (S1): ^{1}H-NMR

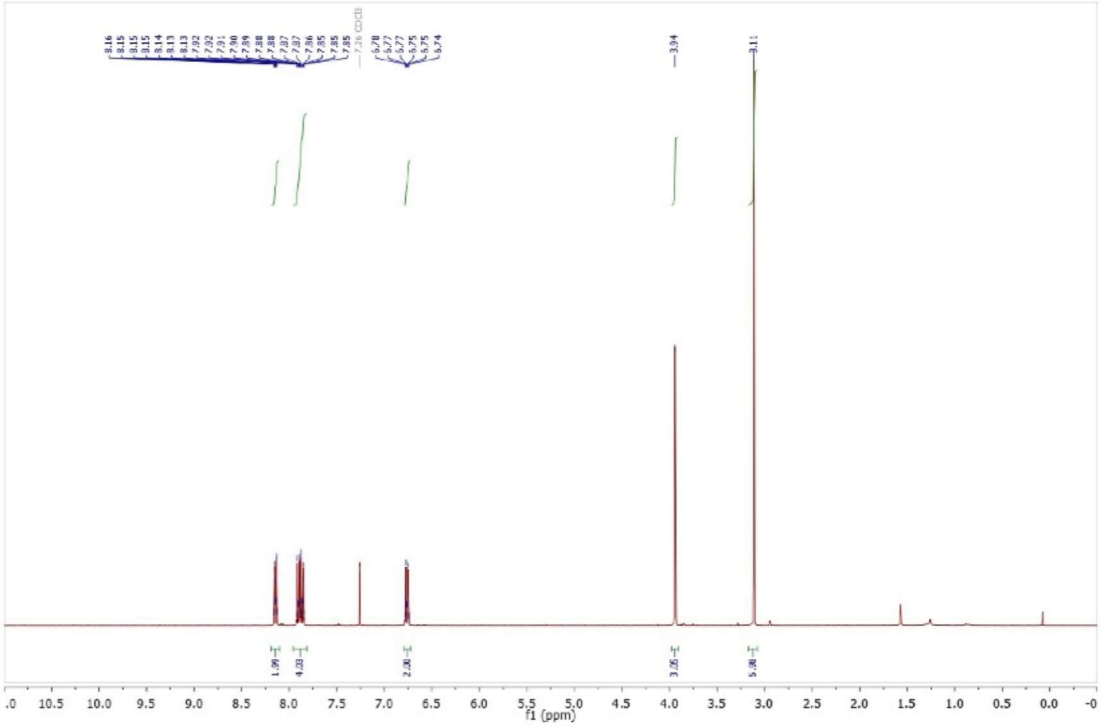

^{13}C-NMR

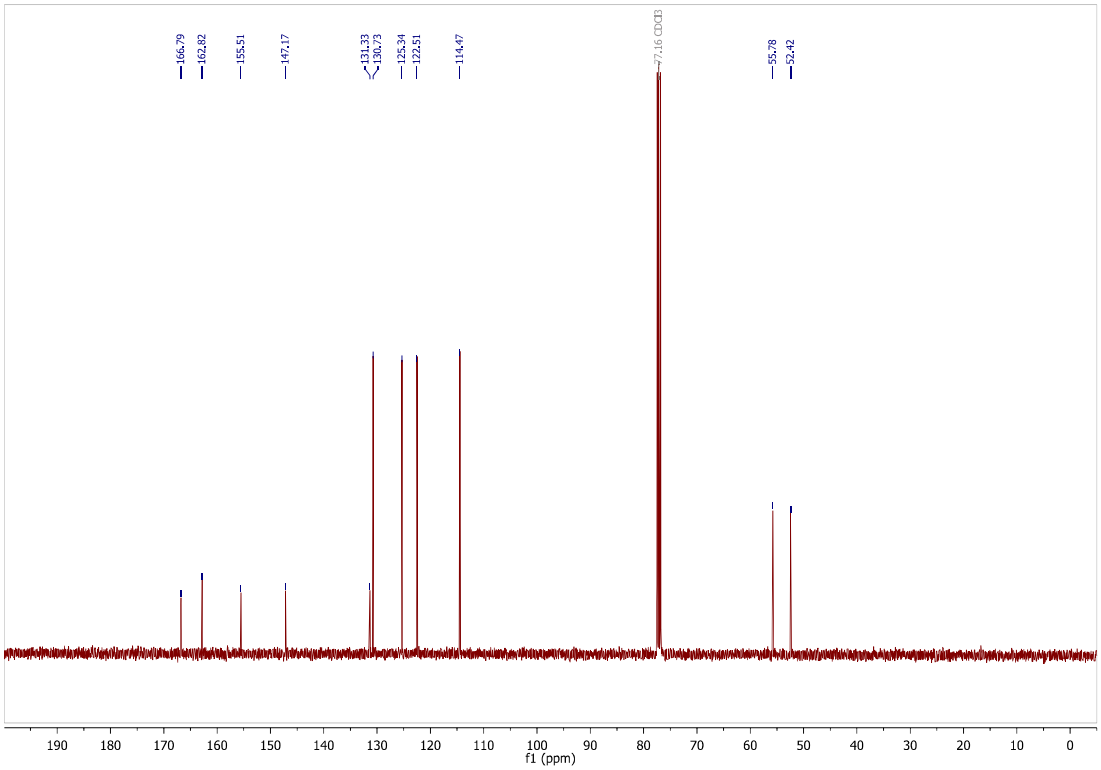

4-((4-(dimethylamino)phenyl)diazenyl)benzoic acid (4DMA-CO_2H): ^{1}H-NMR

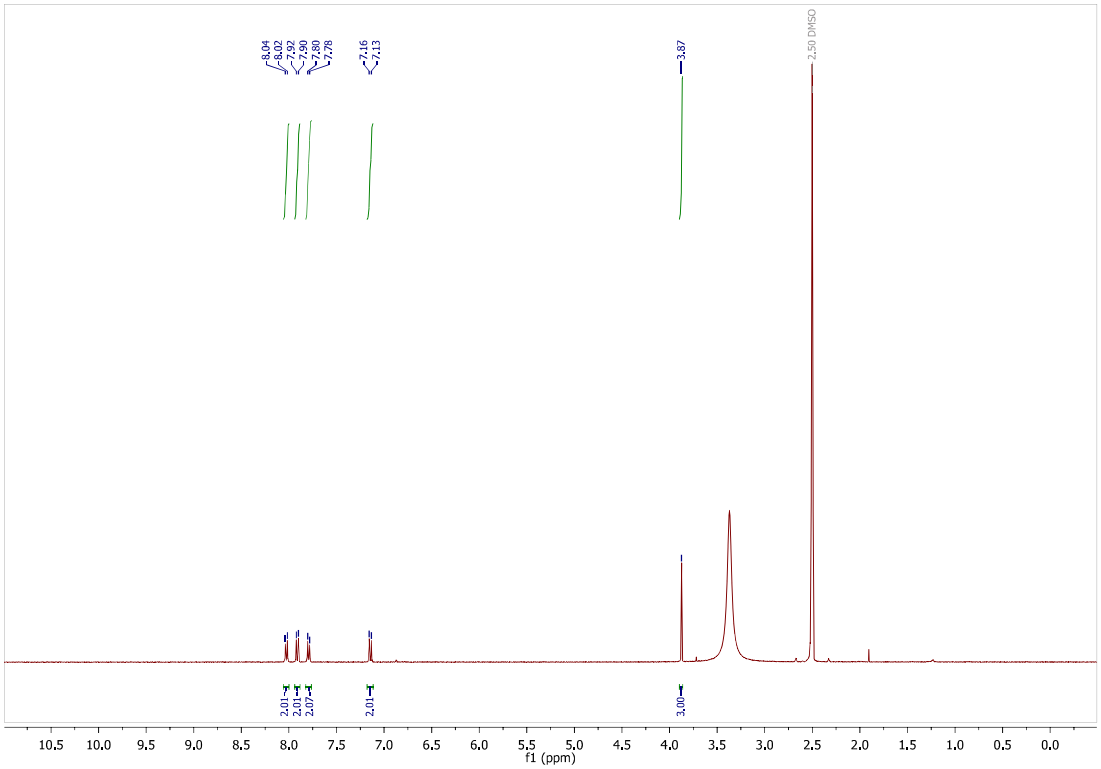

^{13}C-NMR

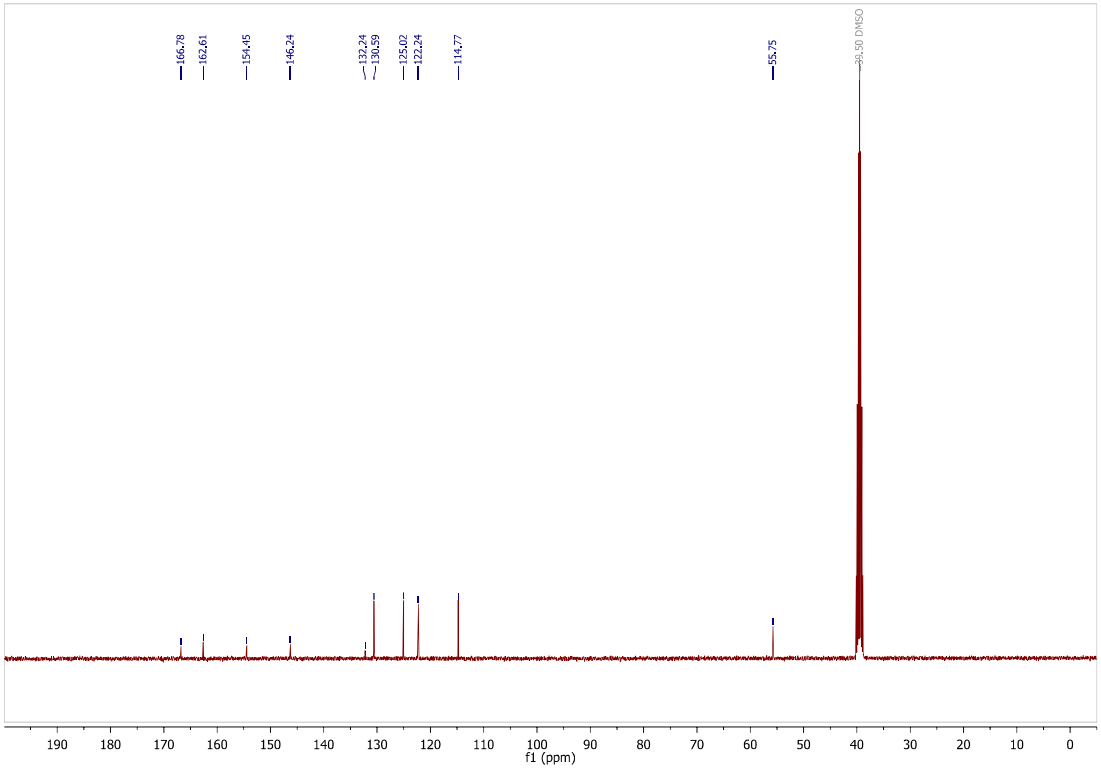

methyl 4-((4-hydroxyphenyl)diazenyl)benzoate (S2): ^{1}H-NMR

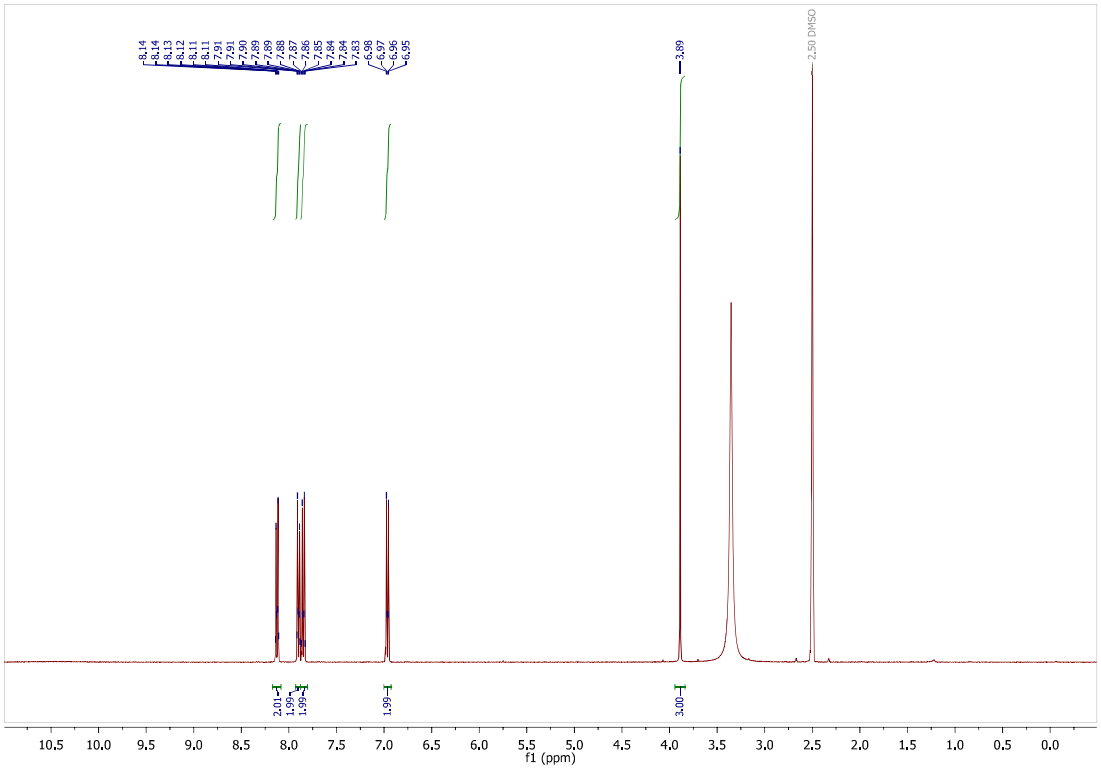

^{13}C-NMR

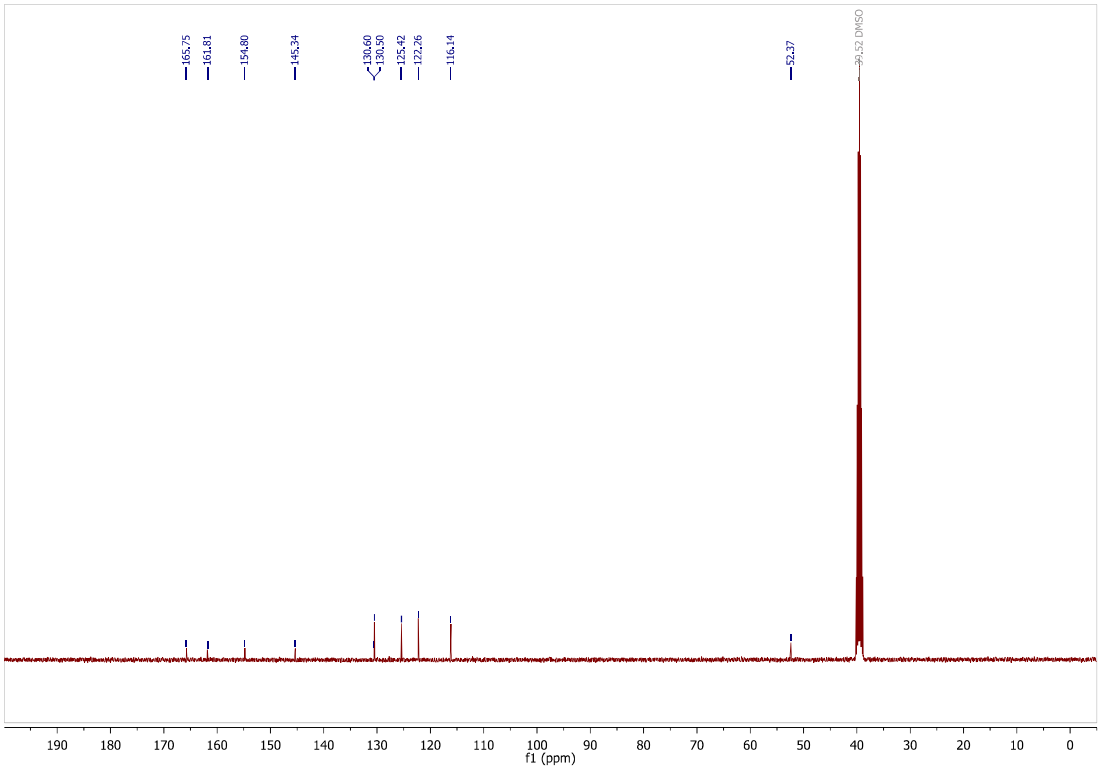

methyl 4-((4-methoxyphenyl)diazenyl)benzoate (S3): ^{1}H-NMR

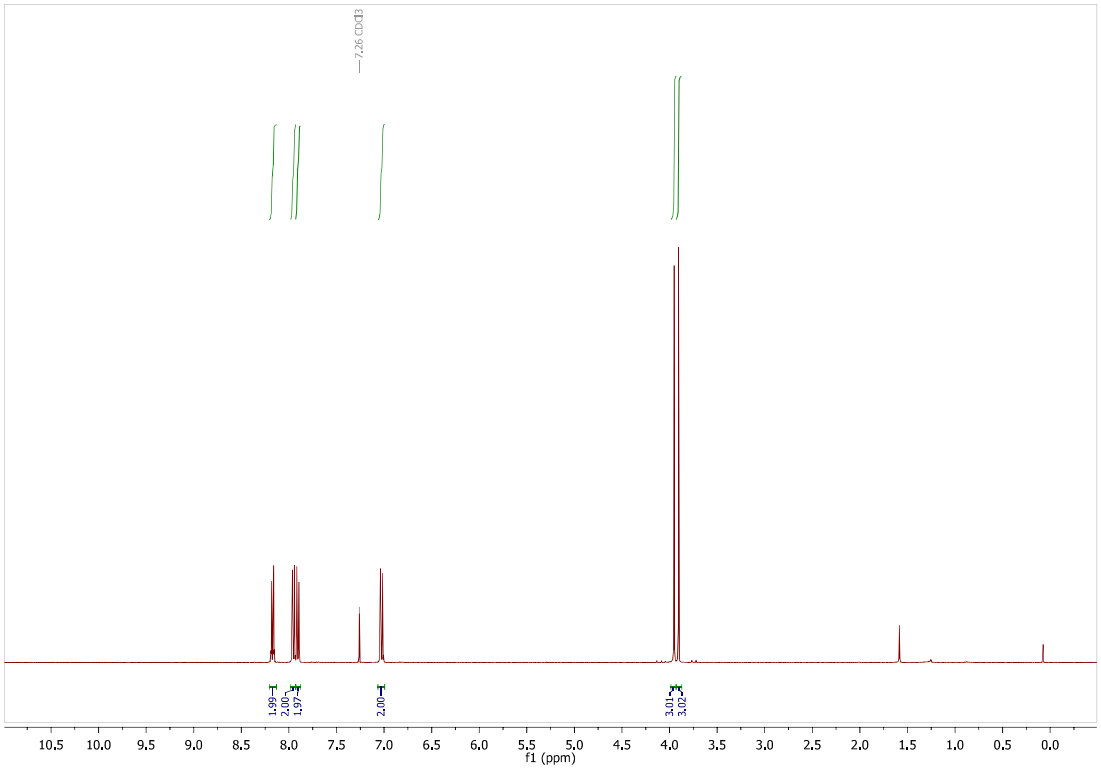

^{13}C-NMR

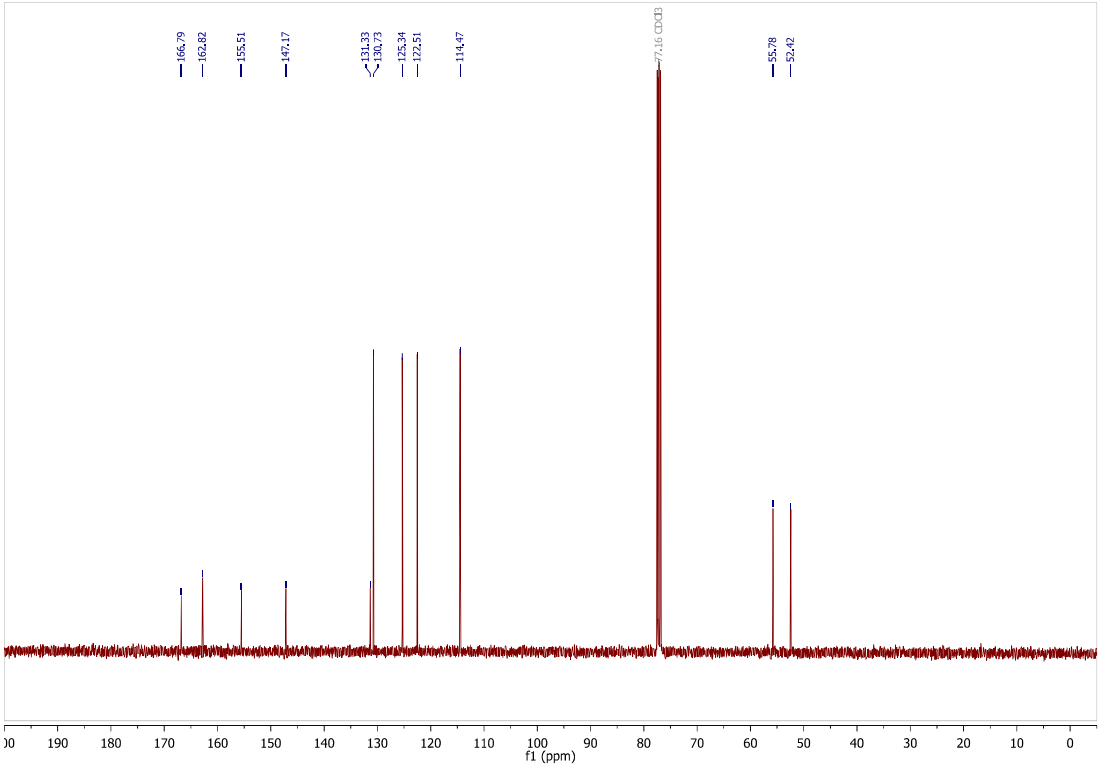

4-((4-methoxyphenyl)diazenyl)benzoic acid (4MP-CO_2H): ^{1}H-NMR

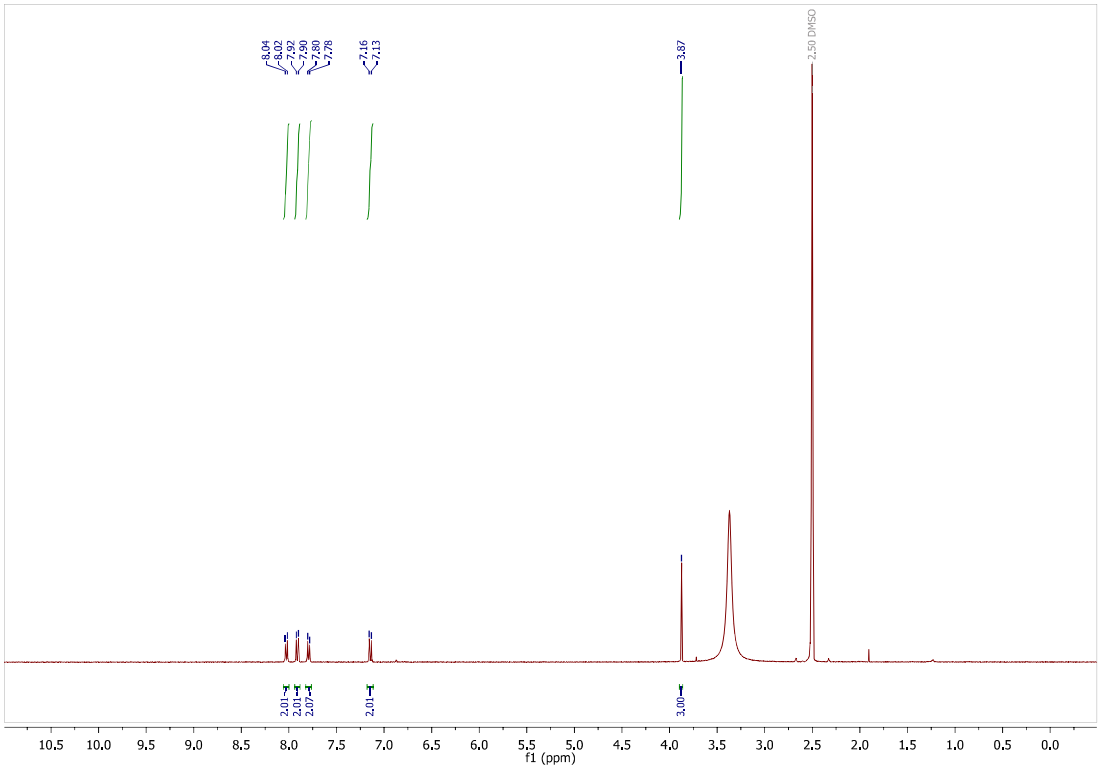

^{13}C-NMR

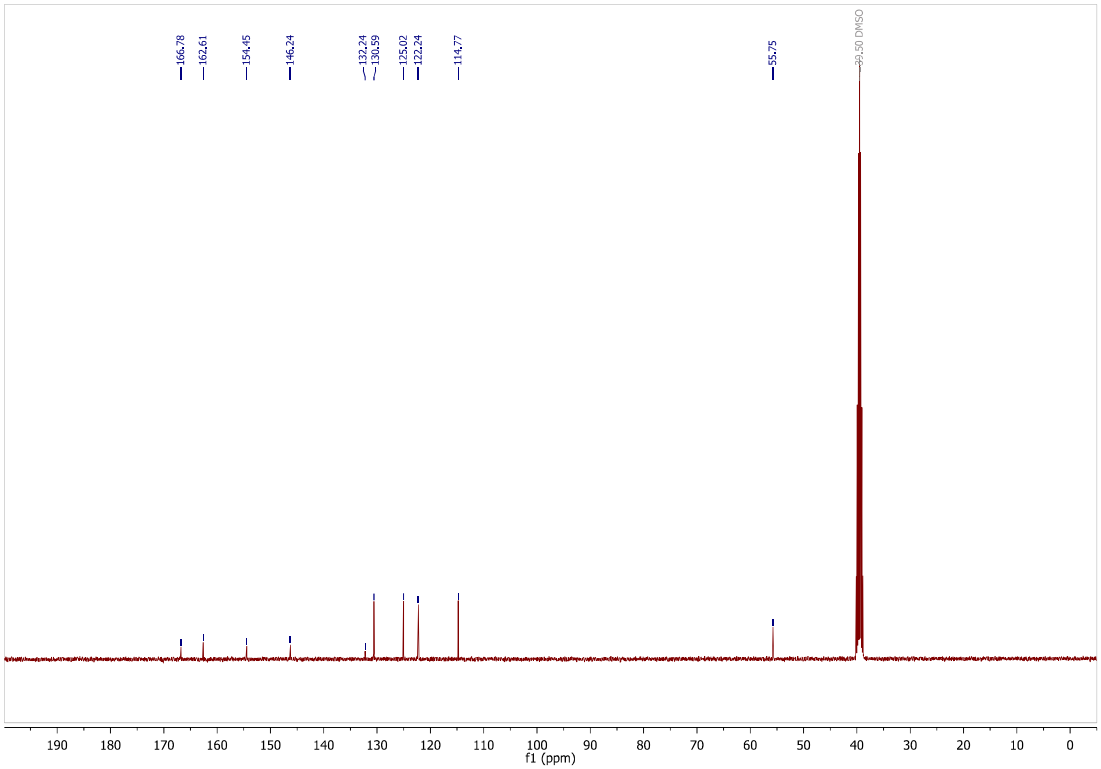

3-(phenyldiazenyl)benzoic acid (3H-CO_2H): ^{1}H-NMR

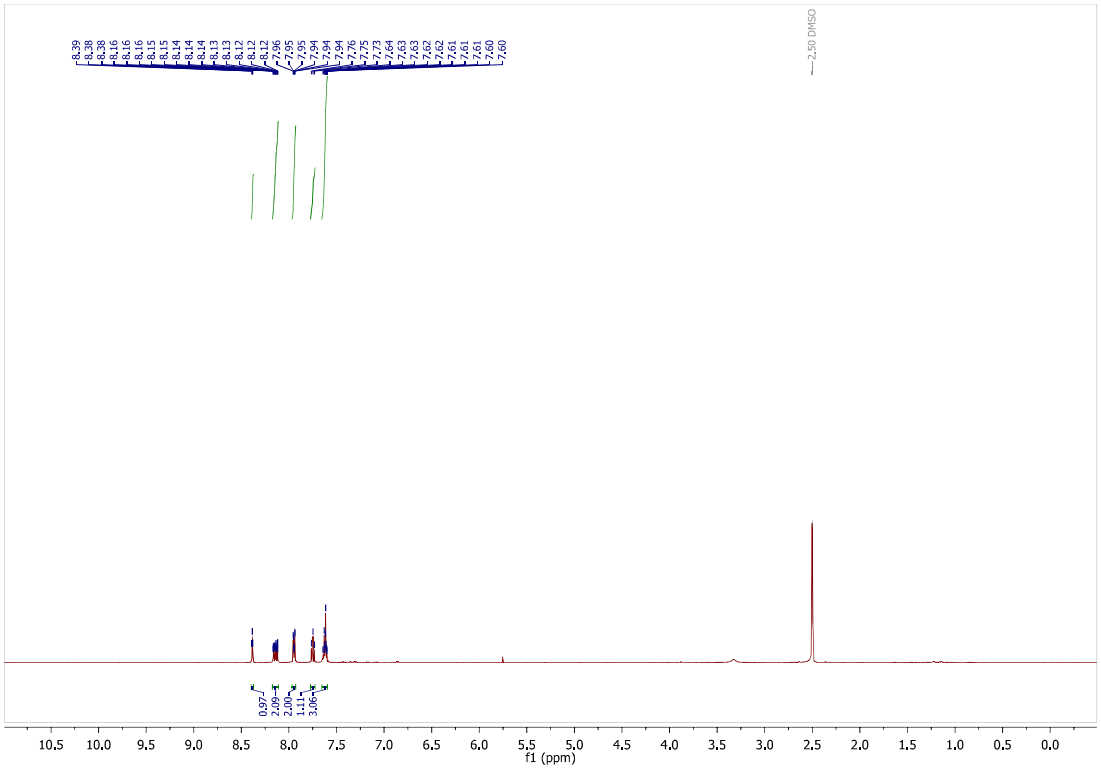

^{13}C-NMR

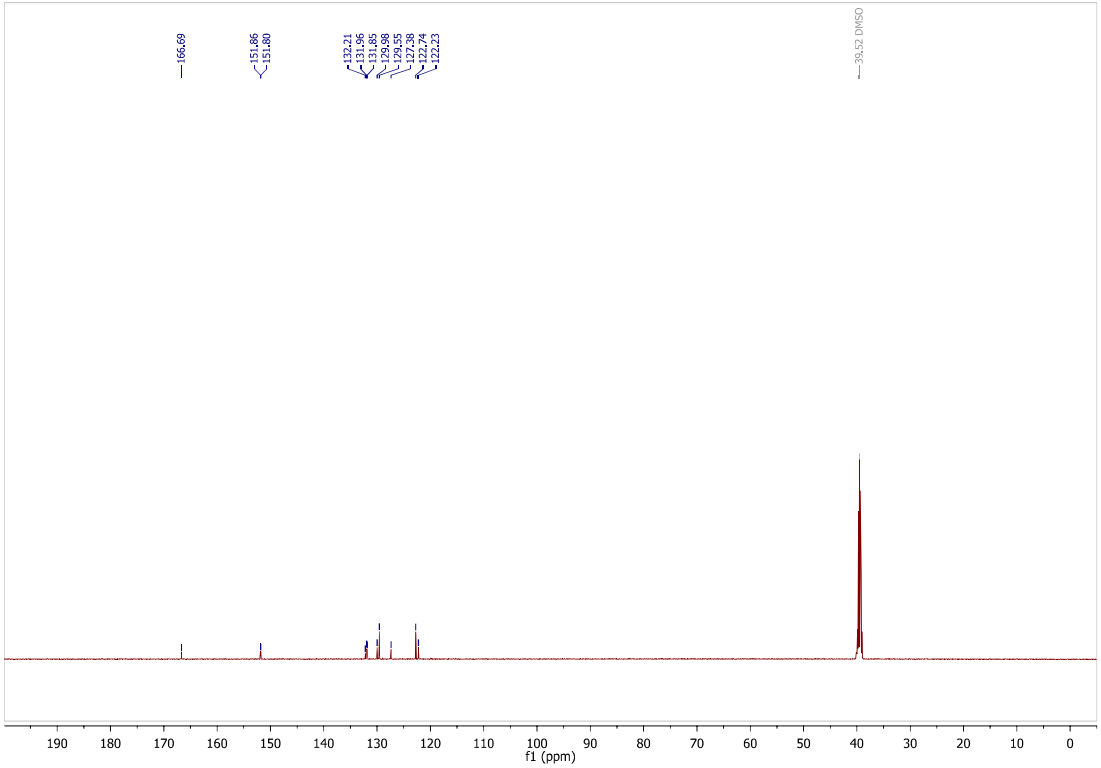

methyl 3-((4-hydroxyphenyl)diazenyl)benzoate (S4): ^{1}H-NMR

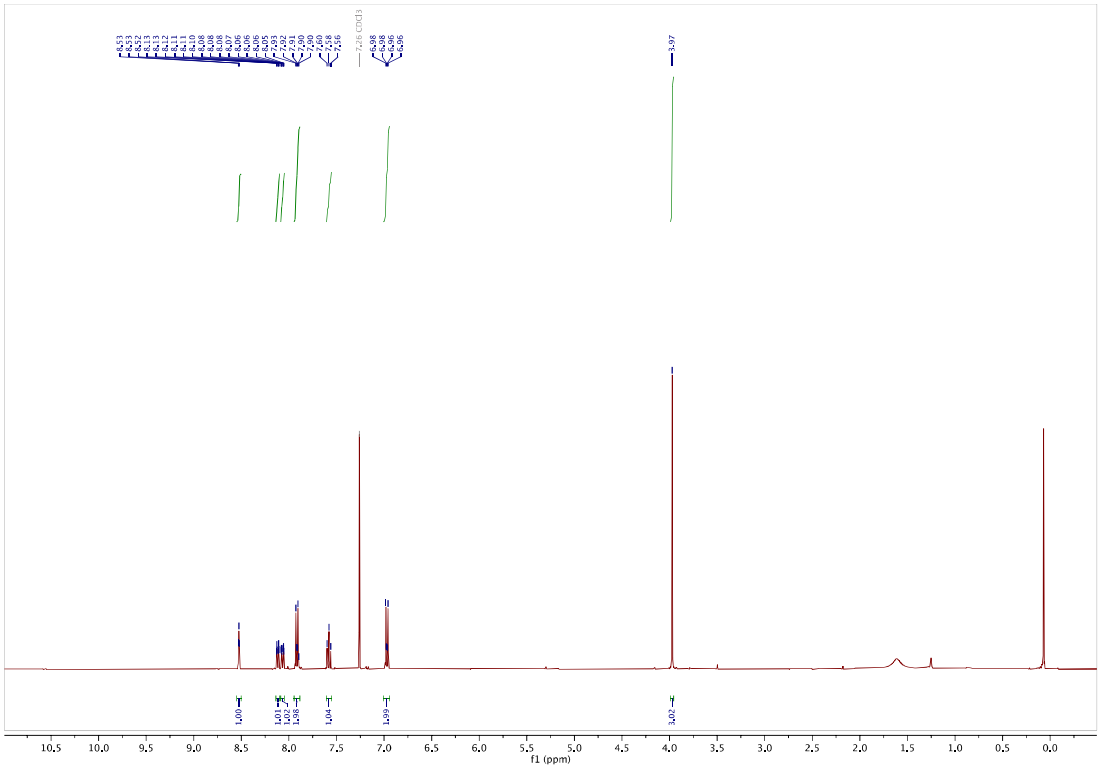

^{13}C-NMR

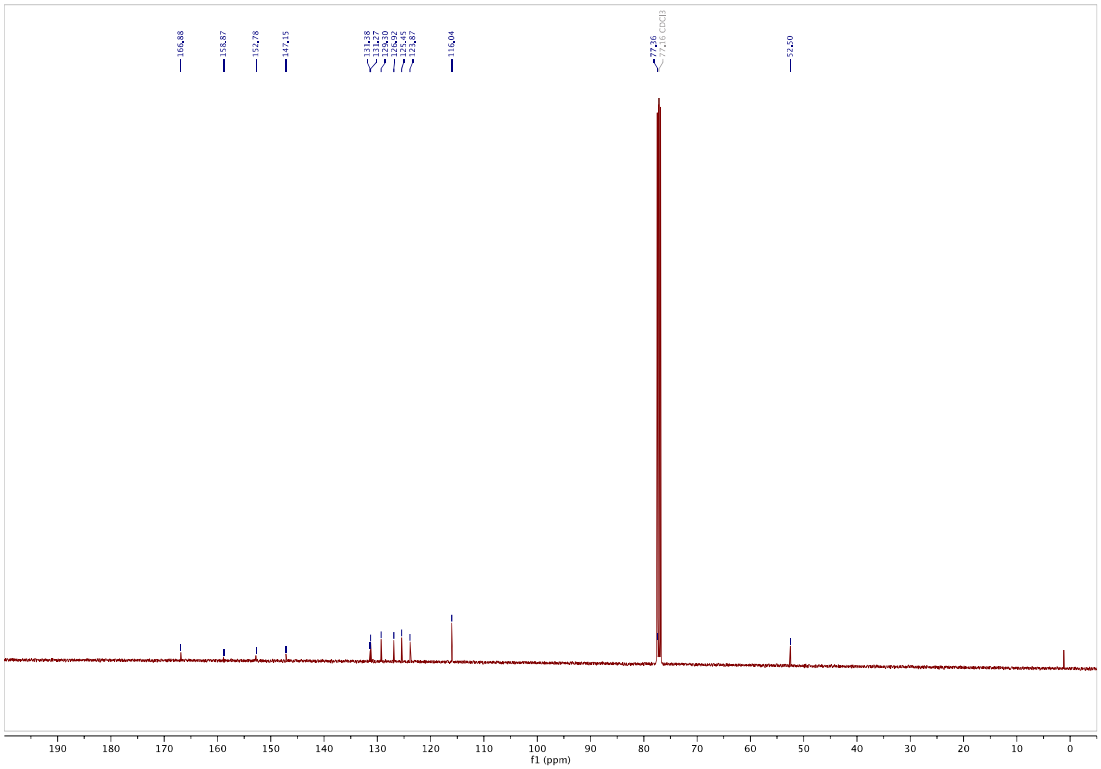

methyl 3-((4-methoxyphenyl)diazenyl)benzoate (S5): ^{1}H-NMR

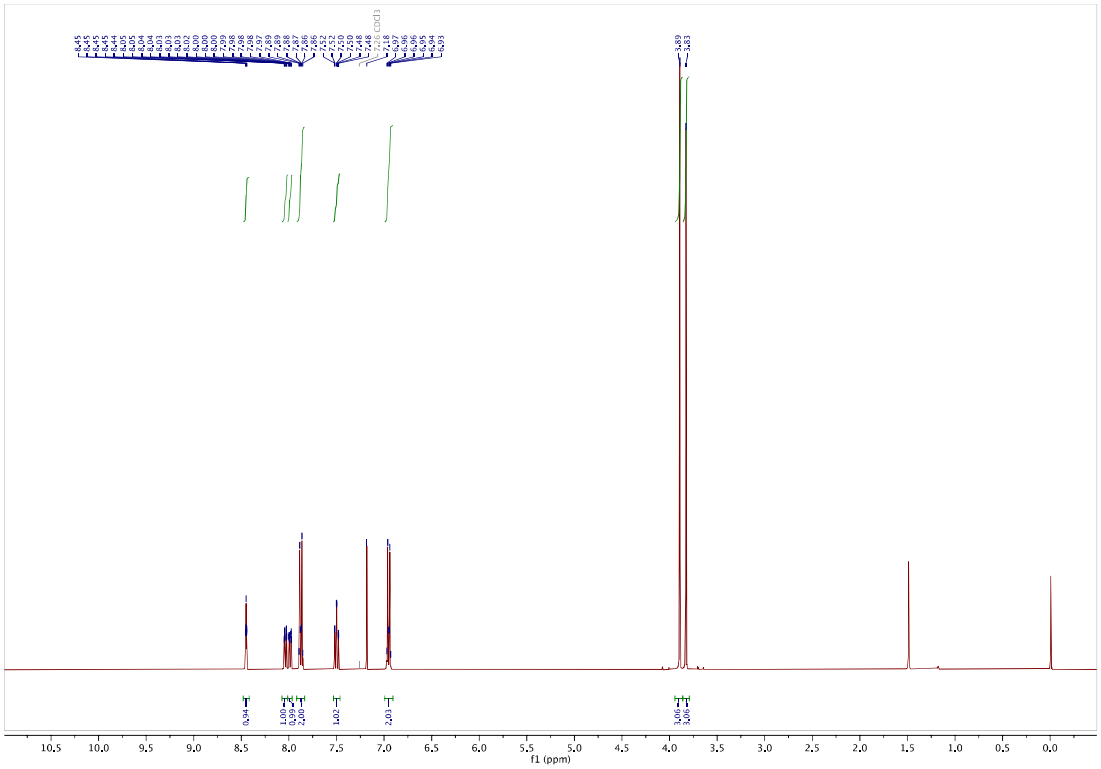

^{13}C-NMR

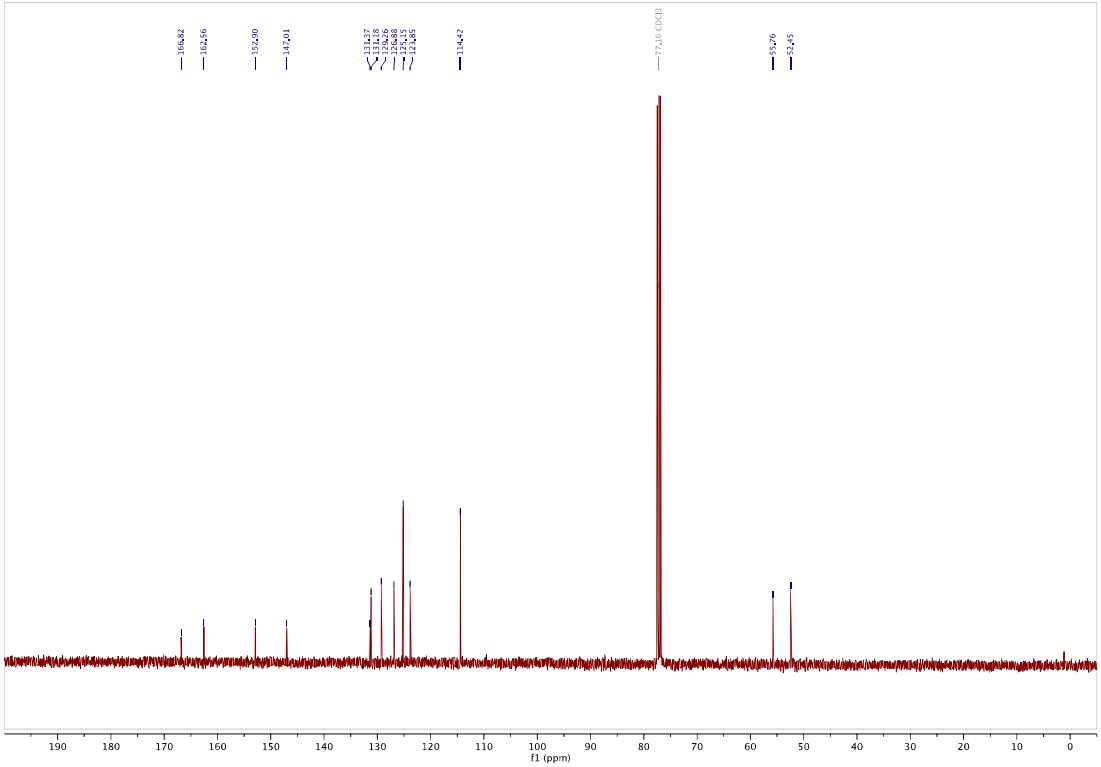

3-((4-methoxyphenyl)diazenyl)benzoic acid (3MP-CO_2H): ^{1}H-NMR

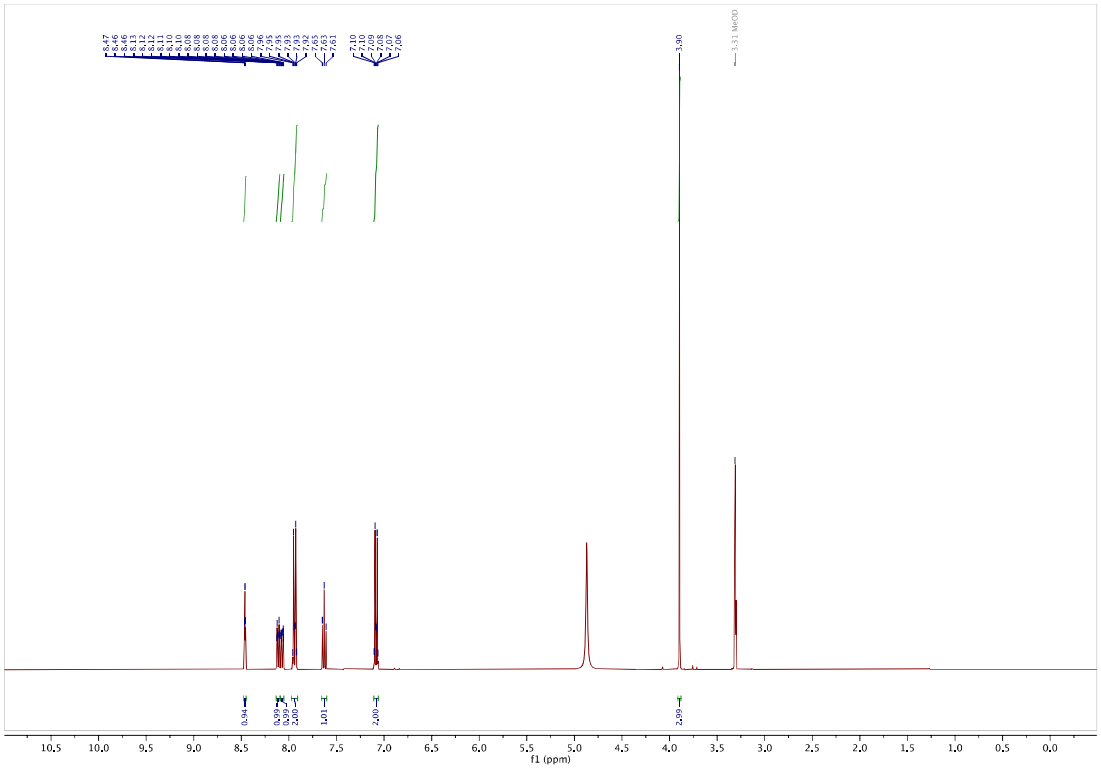

^{13}C-NMR

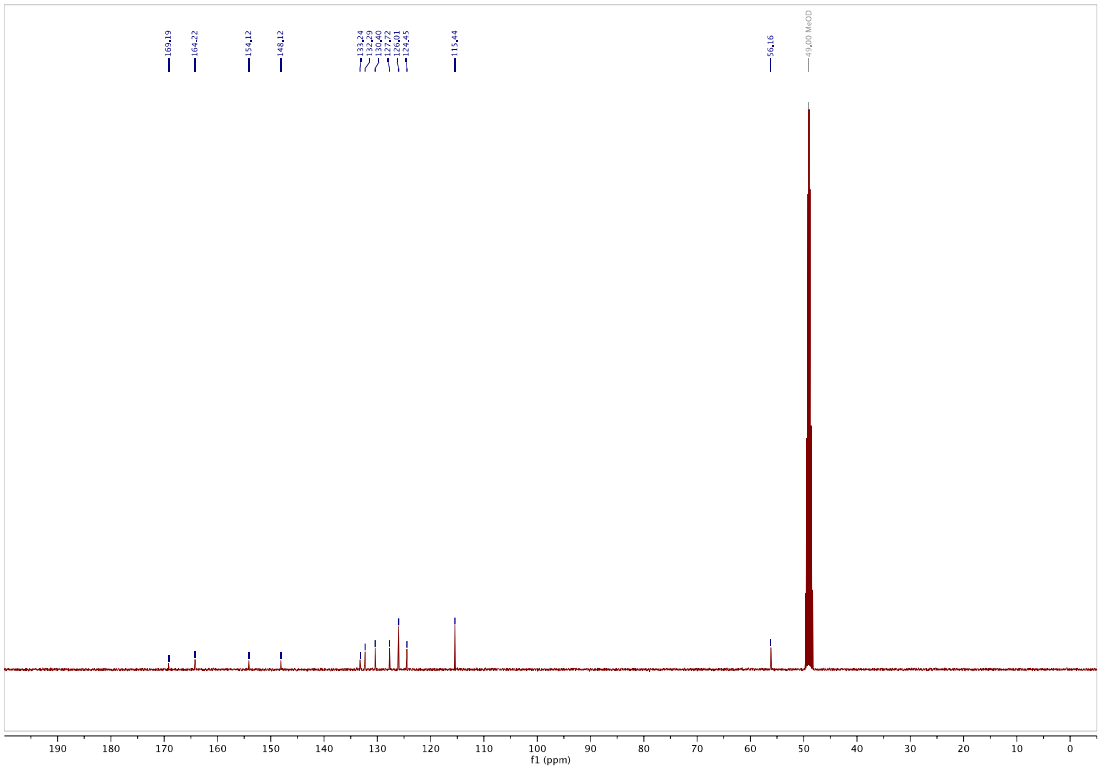

methyl 3-((4-(dimethylamino)phenyl)diazenyl)benzoate (S6): ^{1}H-NMR

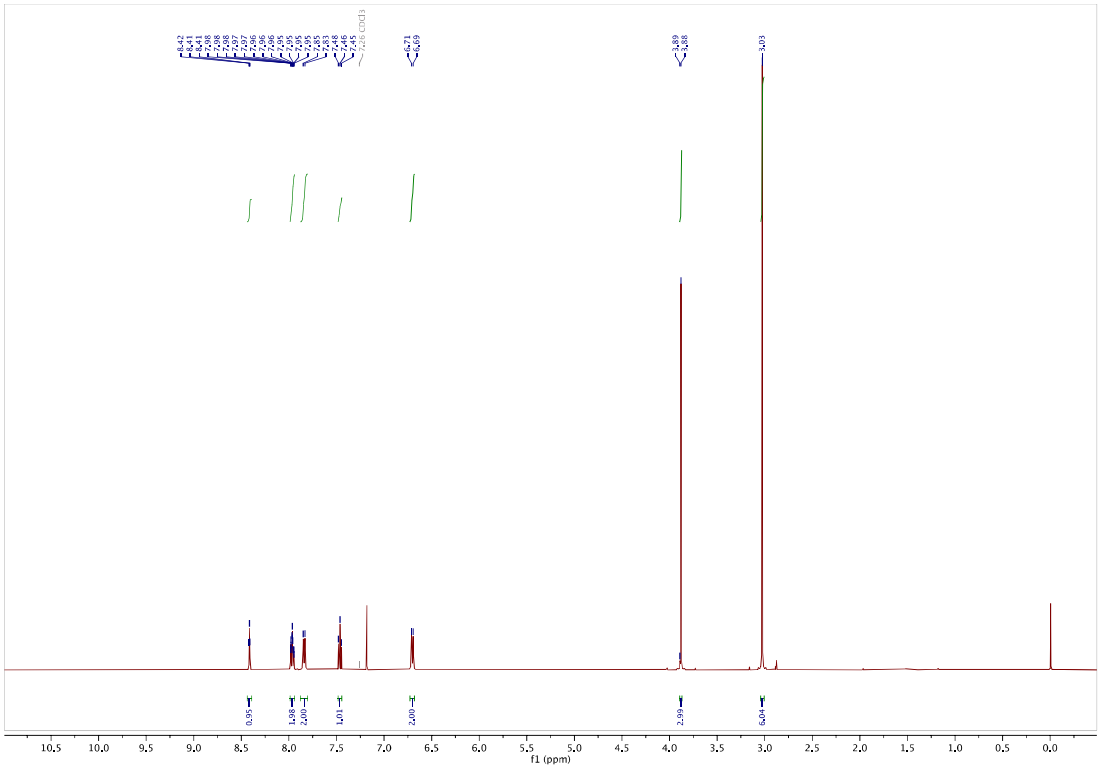

^{13}C-NMR

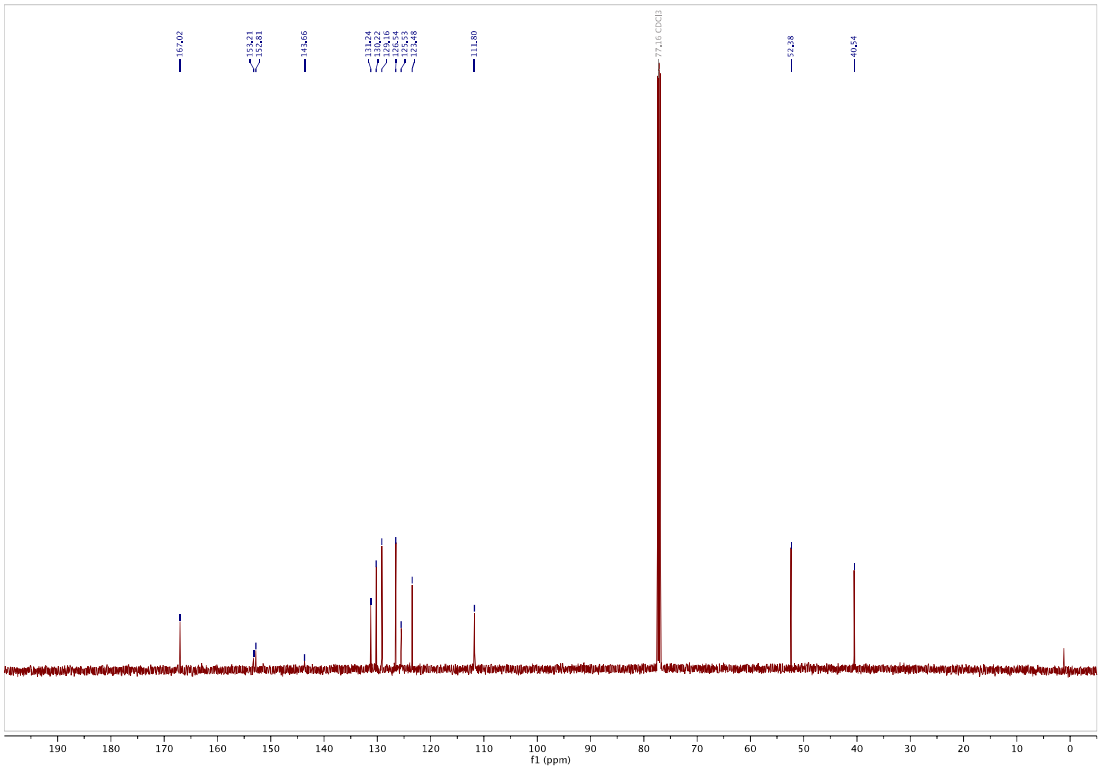

3-((4-(dimethylamino)phenyl)diazenyl)benzoic acid (3DMA-CO_2H): ^{1}H-NMR

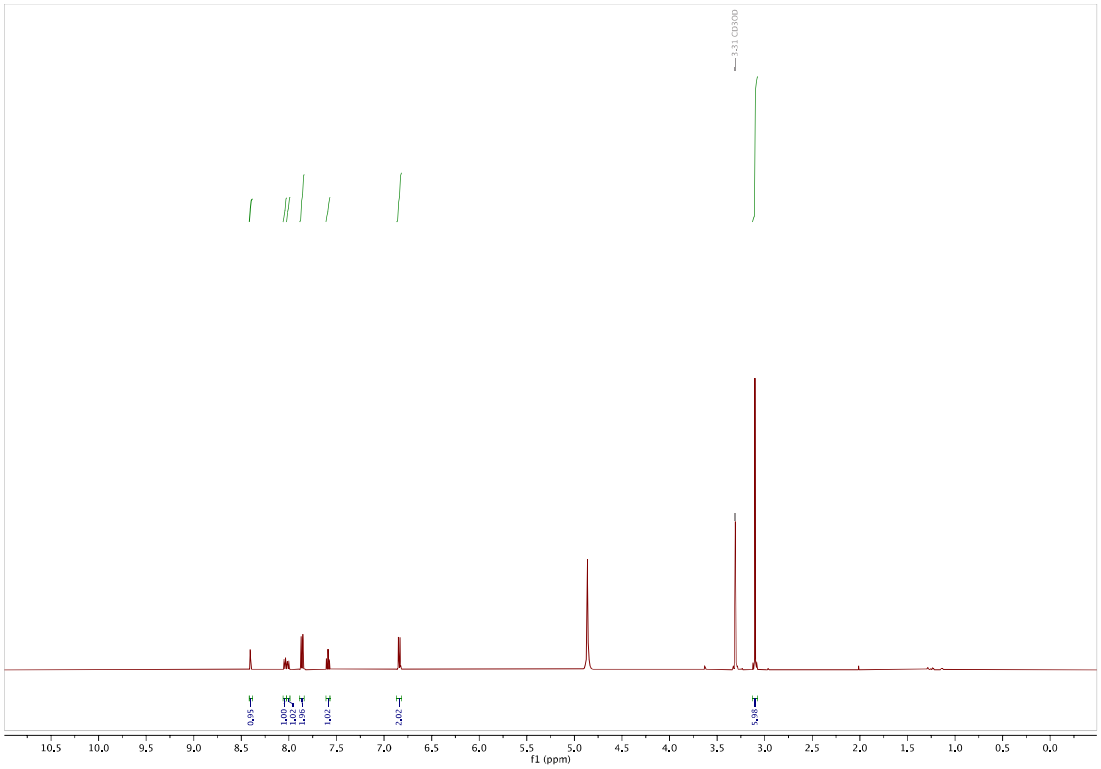

^{13}C-NMR

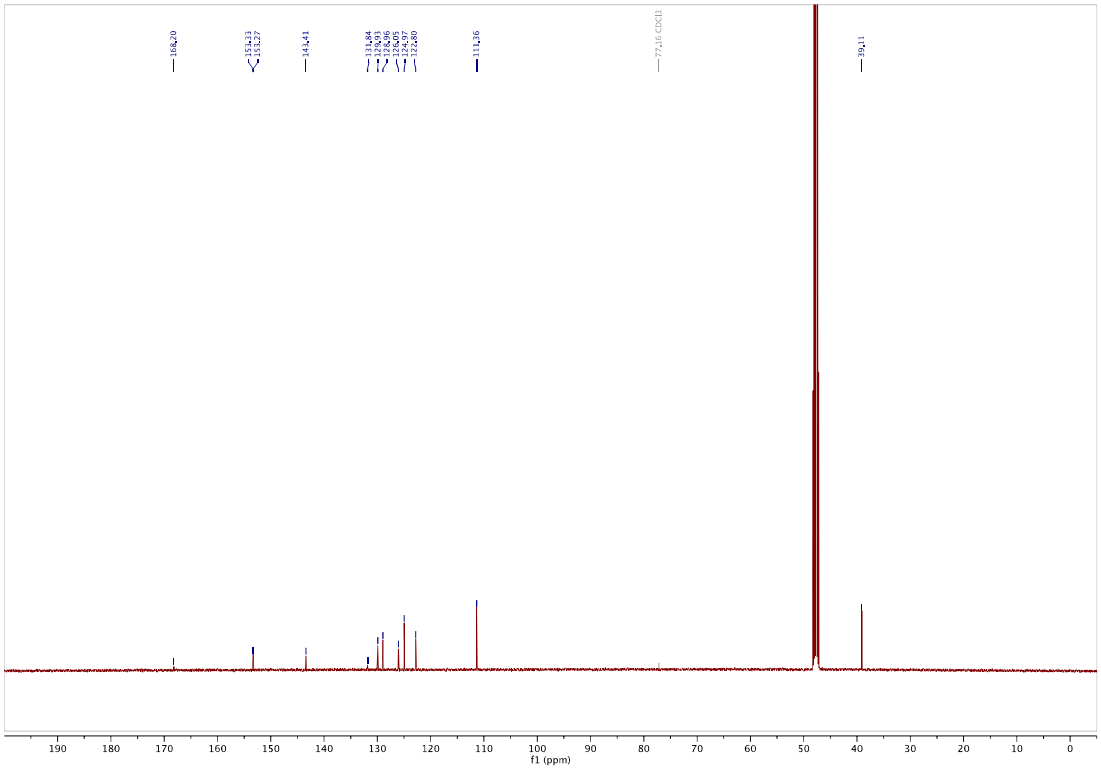

methyl 3-((4-hydroxy-3,5-dimethoxyphenyl)diazenyl)-4-methoxybenzoate (S7): ^{1}H-NMR

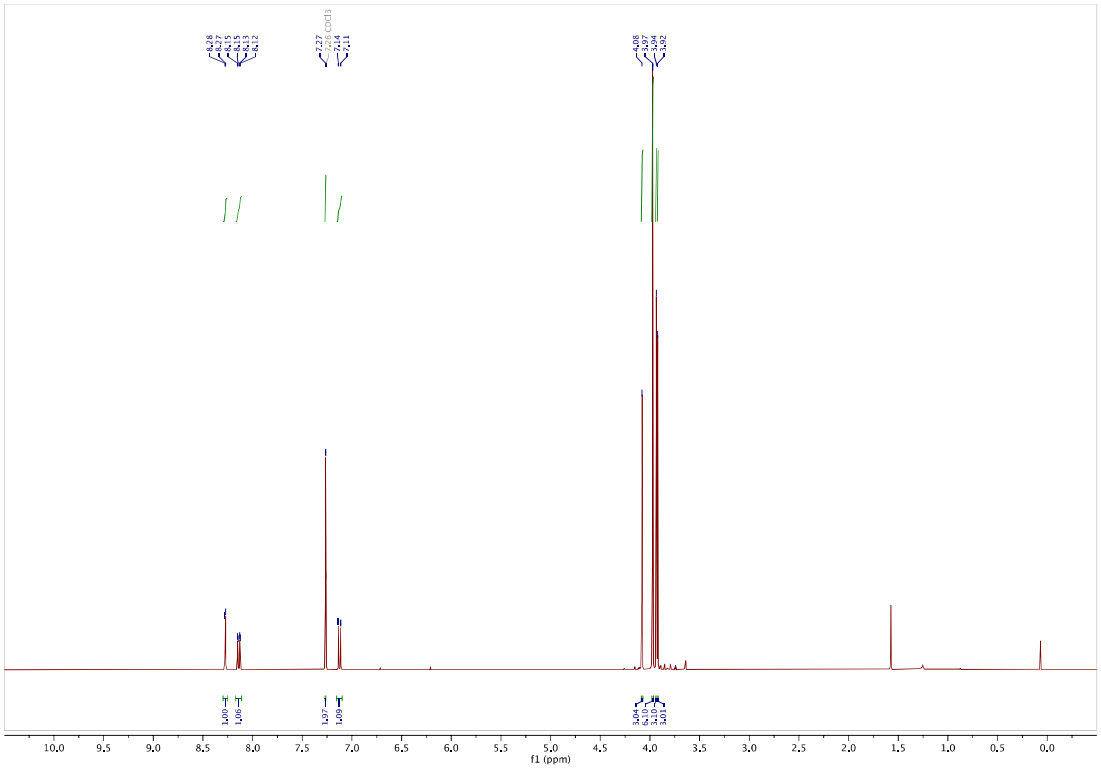

^{13}C-NMR

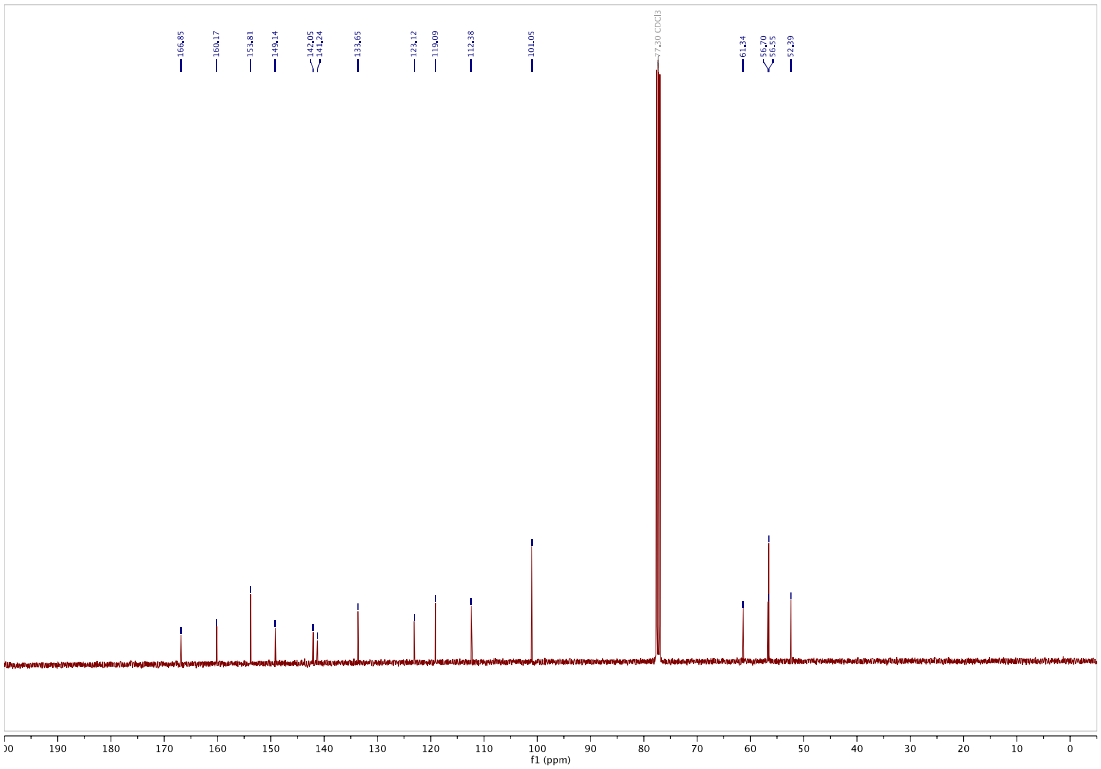

methyl 4-methoxy-3-((3,4,5-trimethoxyphenyl)diazenyl)benzoate (S8): ^{1}H-NMR

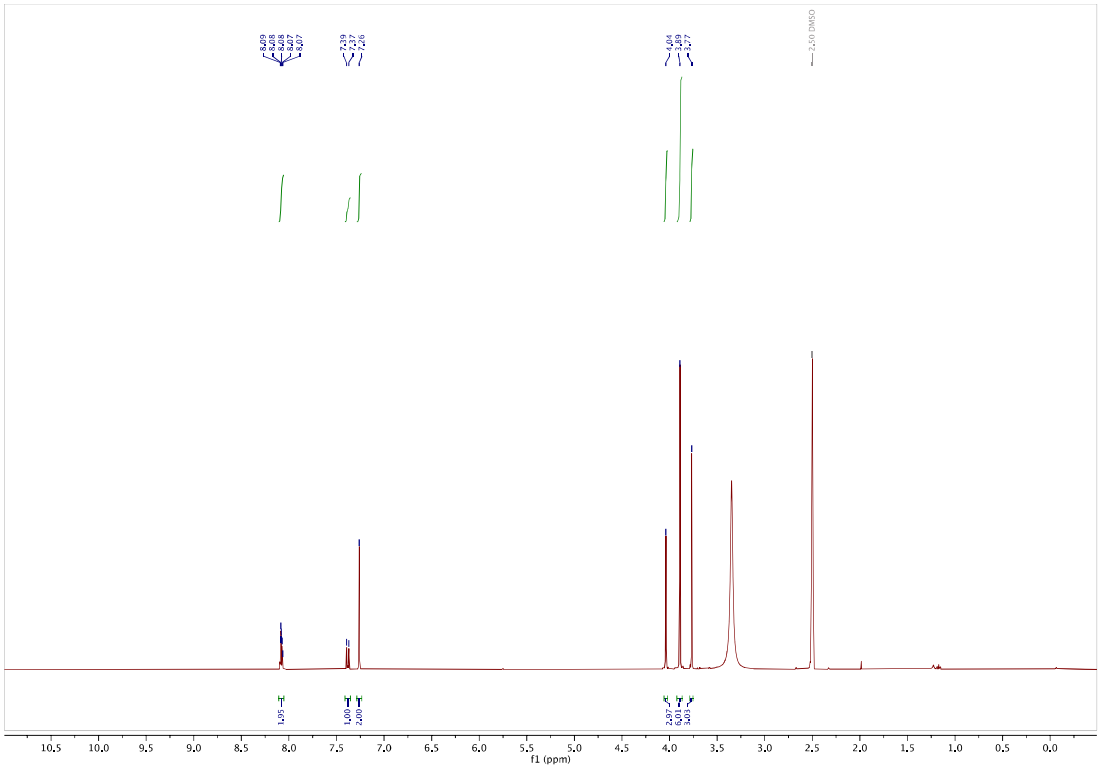

^{13}C-NMR

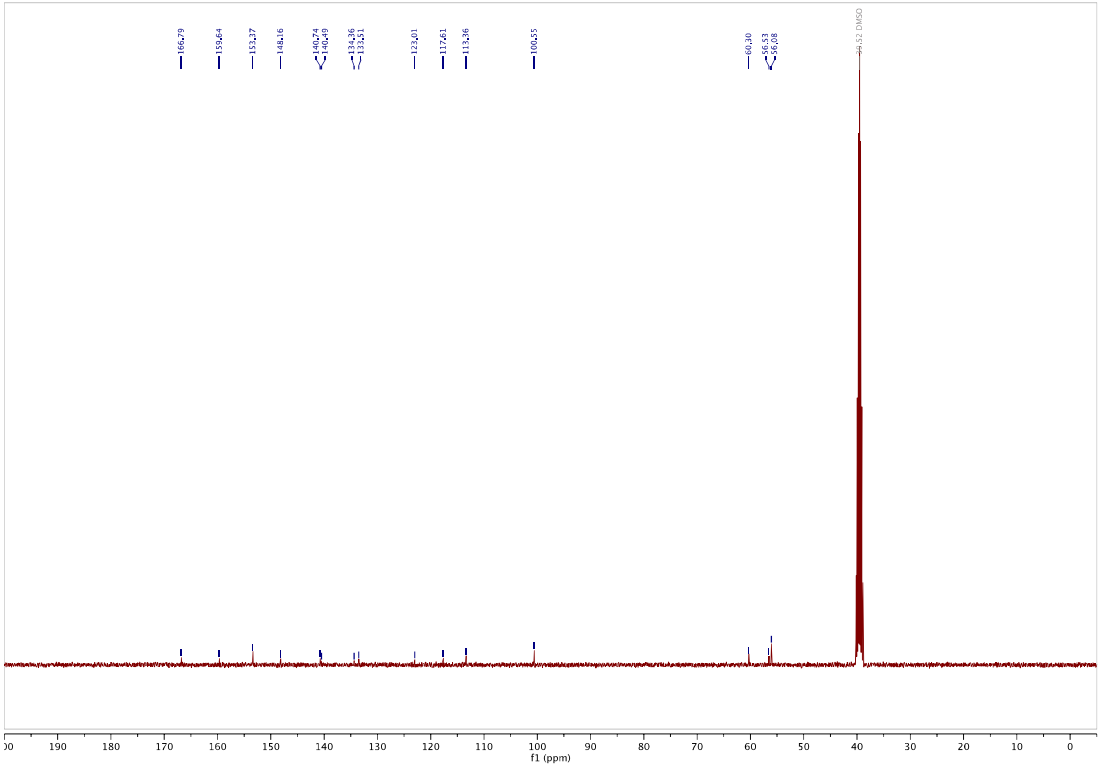

4-methoxy-3-((3,4,5-trimethoxyphenyl)diazenyl)benzoic acid (3MTM-CO_2H): ^{1}H-NMR

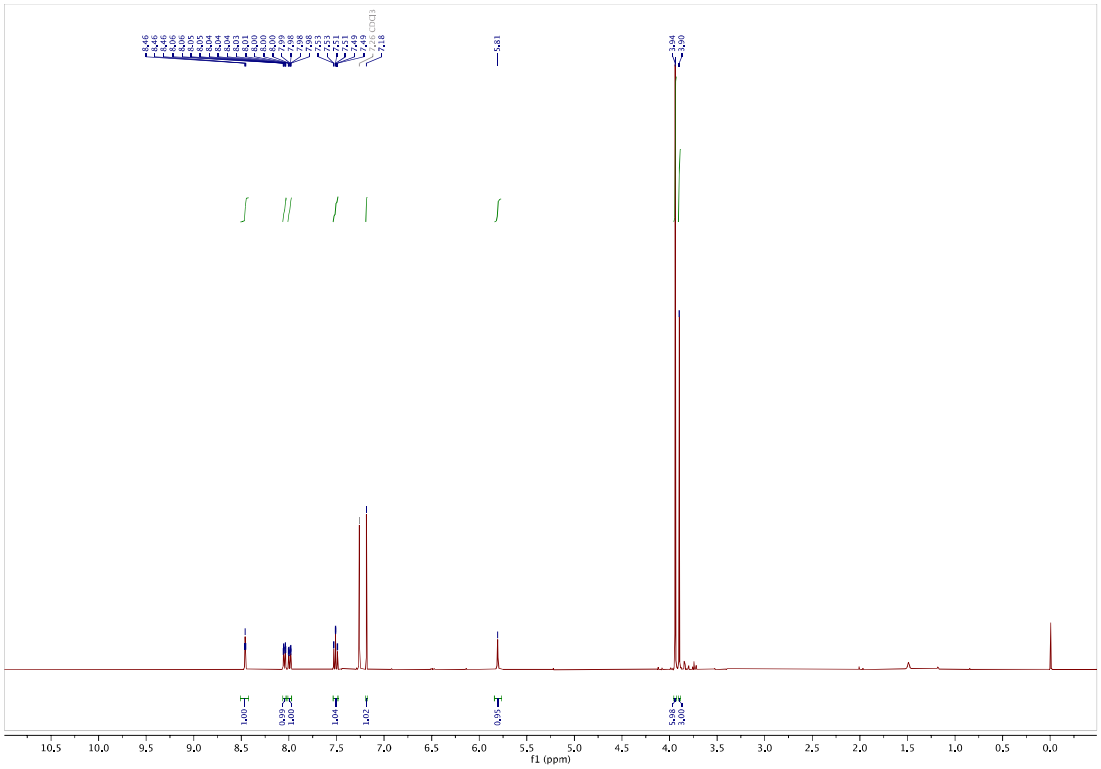

^{13}C-NMR

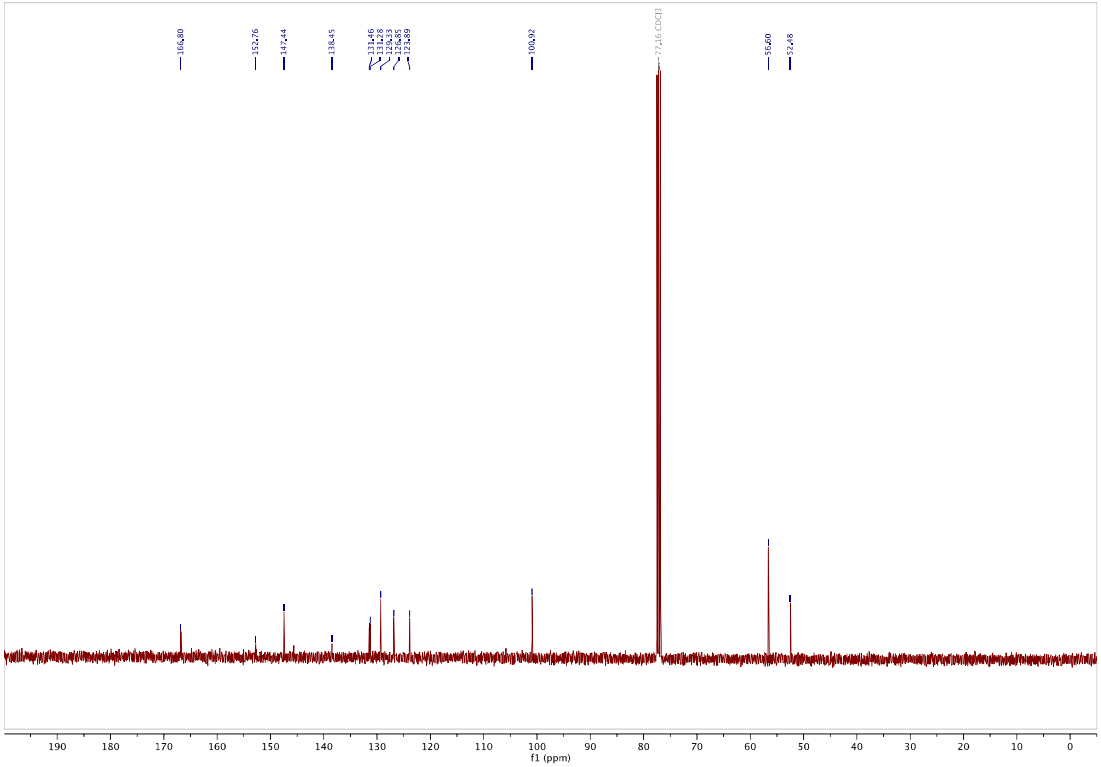

Methyl 3-((4-hydroxy-3,5-dimethoxyphenyl)diazenyl)benzoate (S9): ^{1}H-NMR

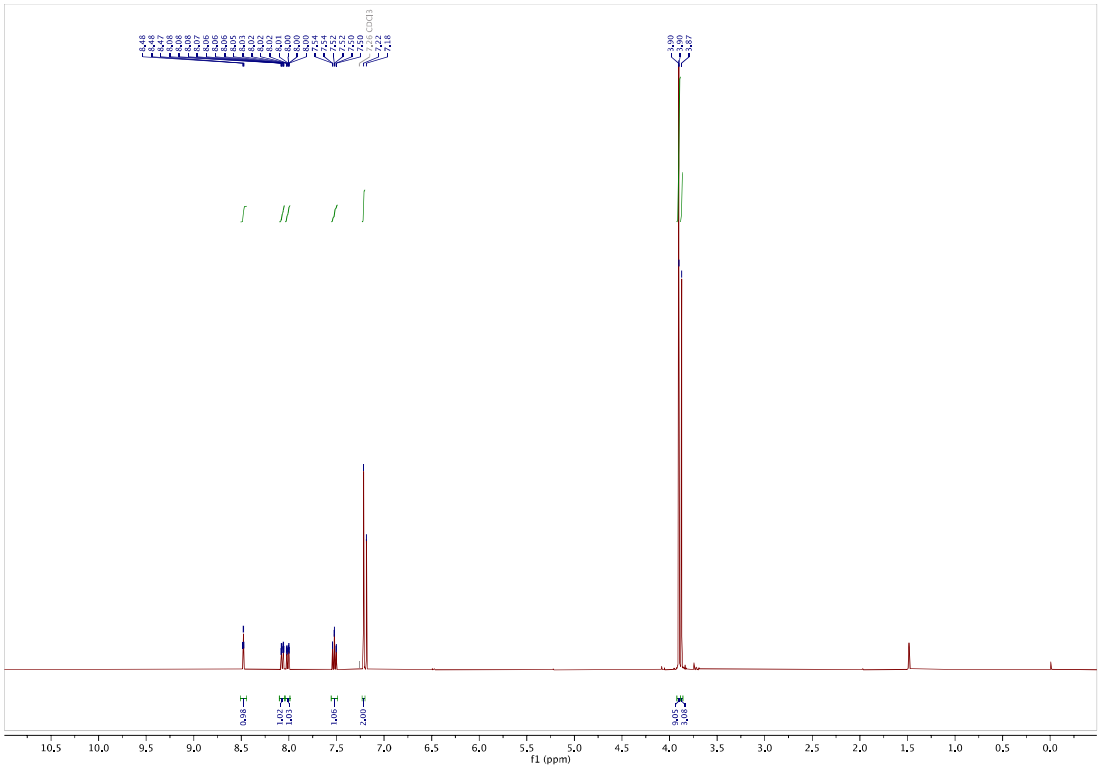

^{13}C-NMR

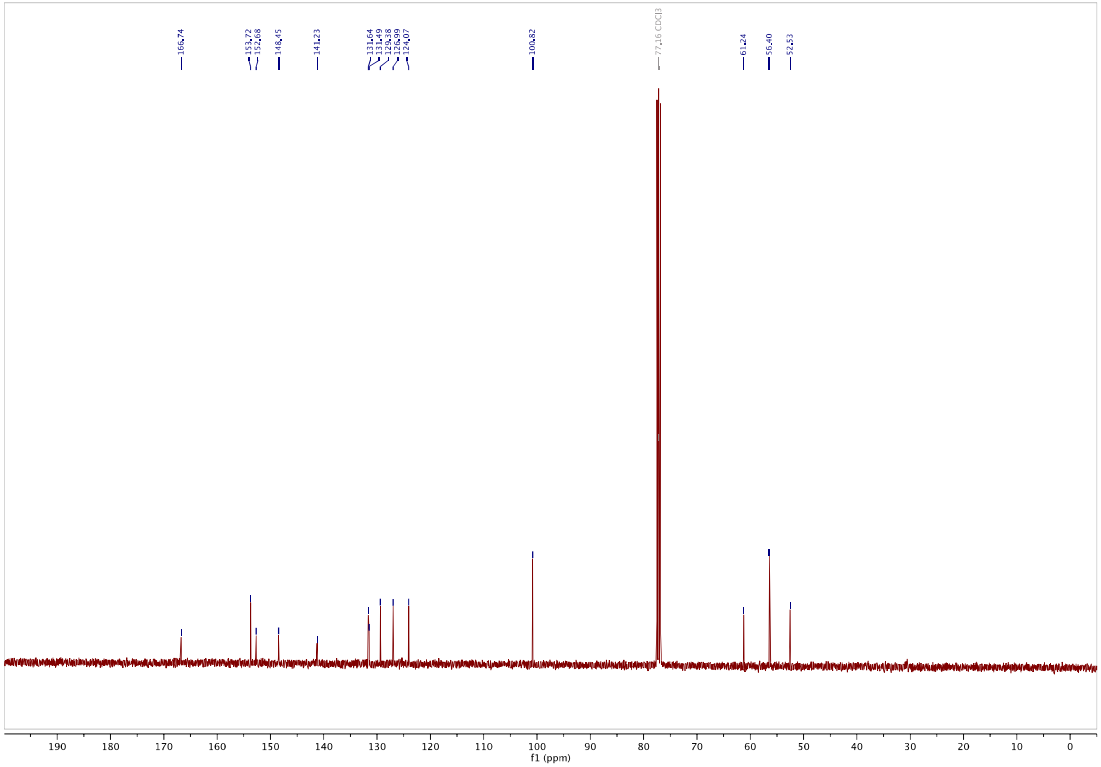

methyl 3-((3,4,5-trimethoxyphenyl)diazenyl)benzoate (S10): ^{1}H-NMR

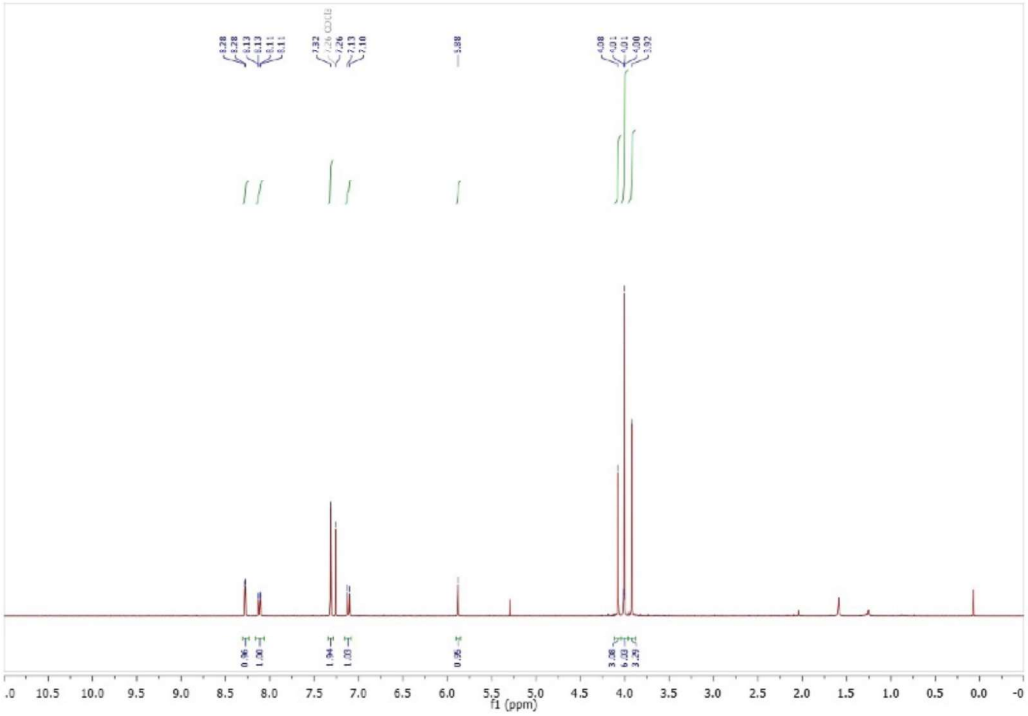

^{13}C-NMR

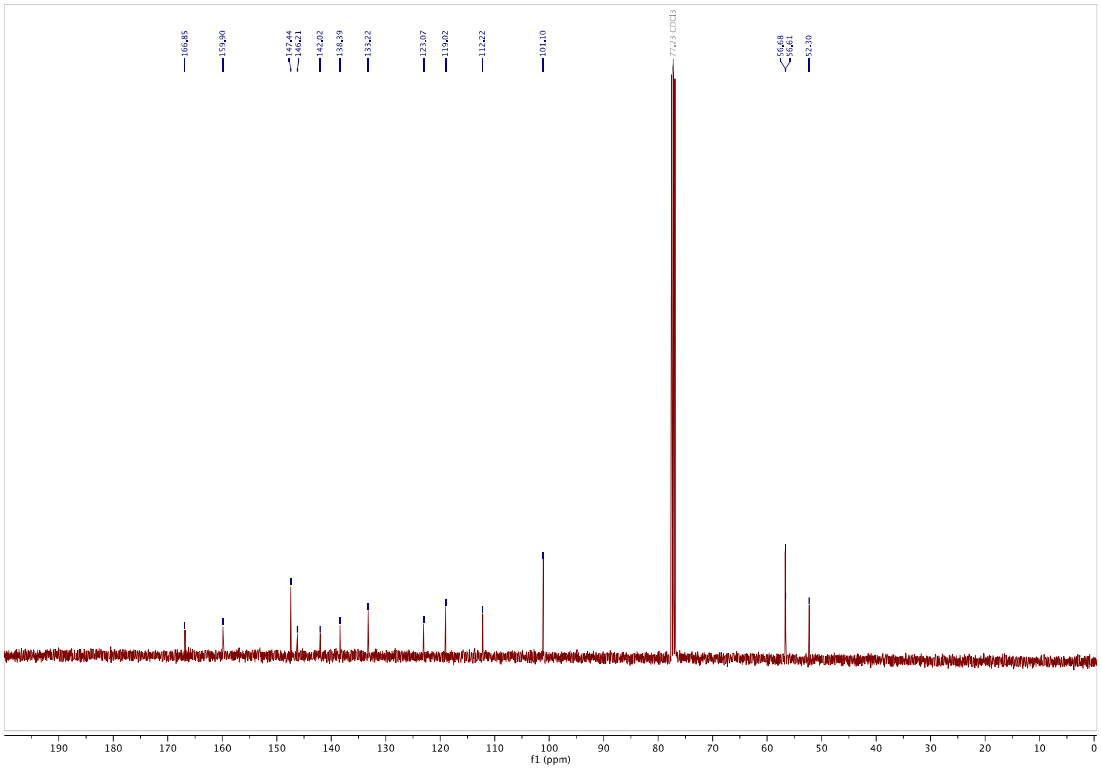

3-((3,4,5-trimethoxyphenyl)diazenyl)benzoic acid (3TM-CO_2H): ^{1}H-NMR

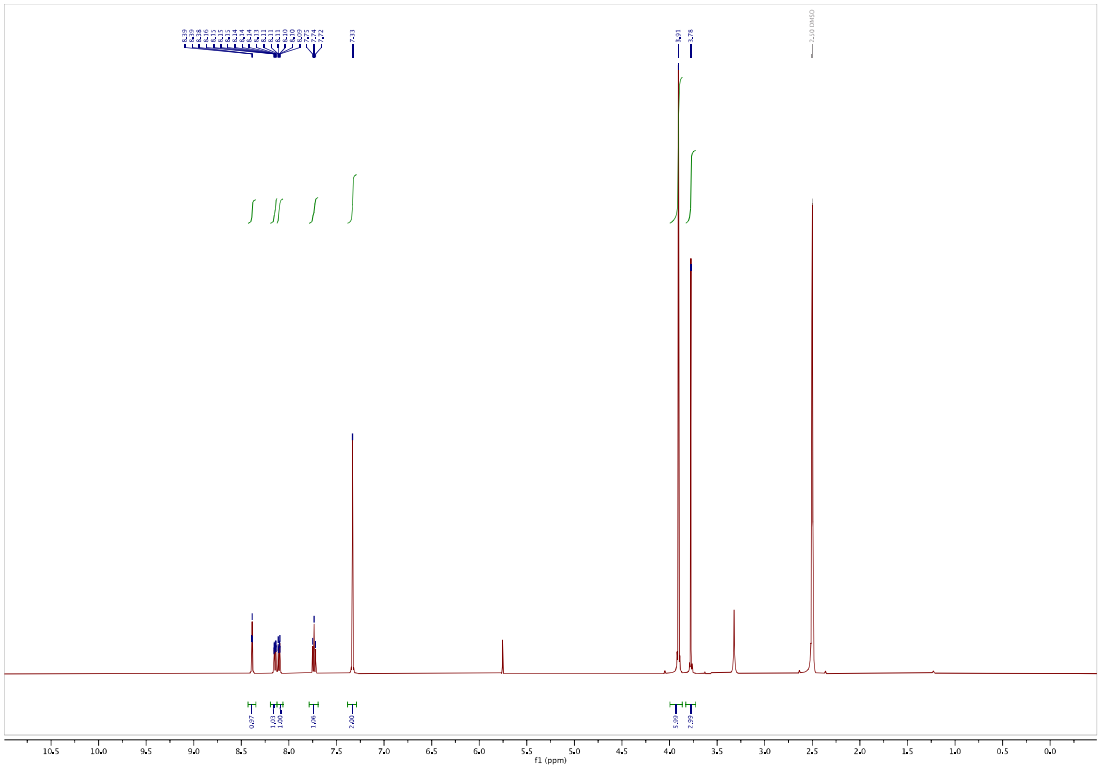

^{13}C-NMR

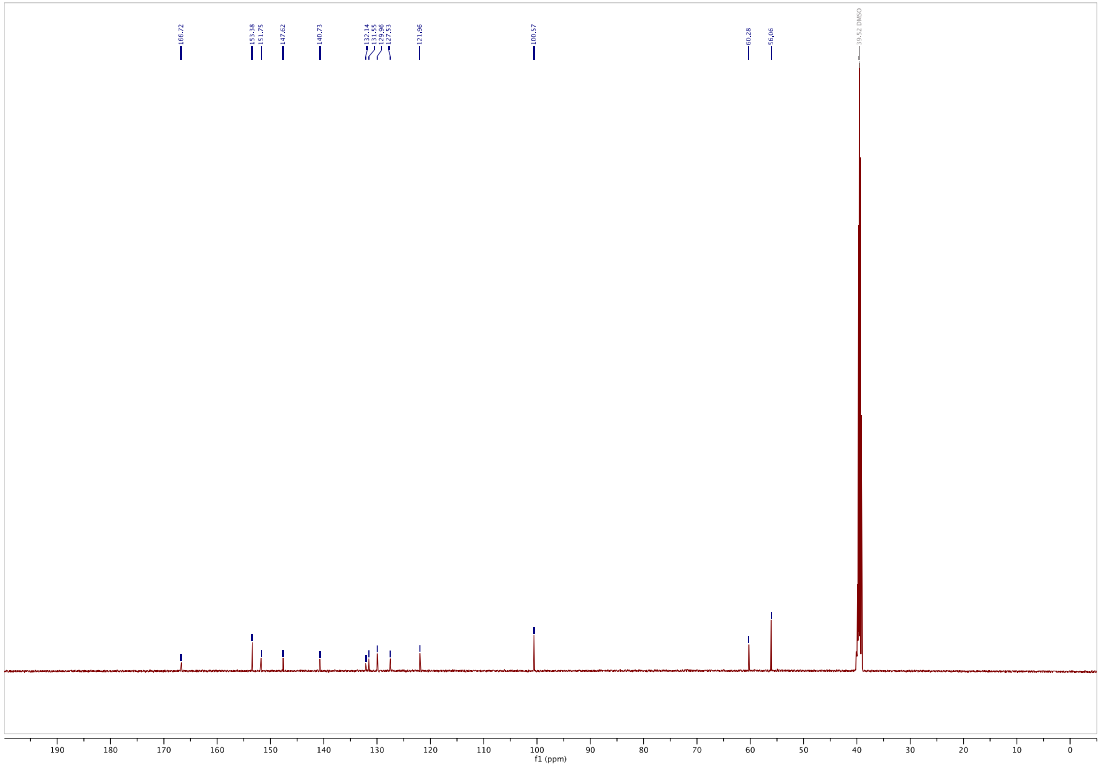

methyl 3-((4-(bis(2-hydroxyethyl)amino)phenyl)diazenyl)benzoate (S11): ^{1}H-NMR

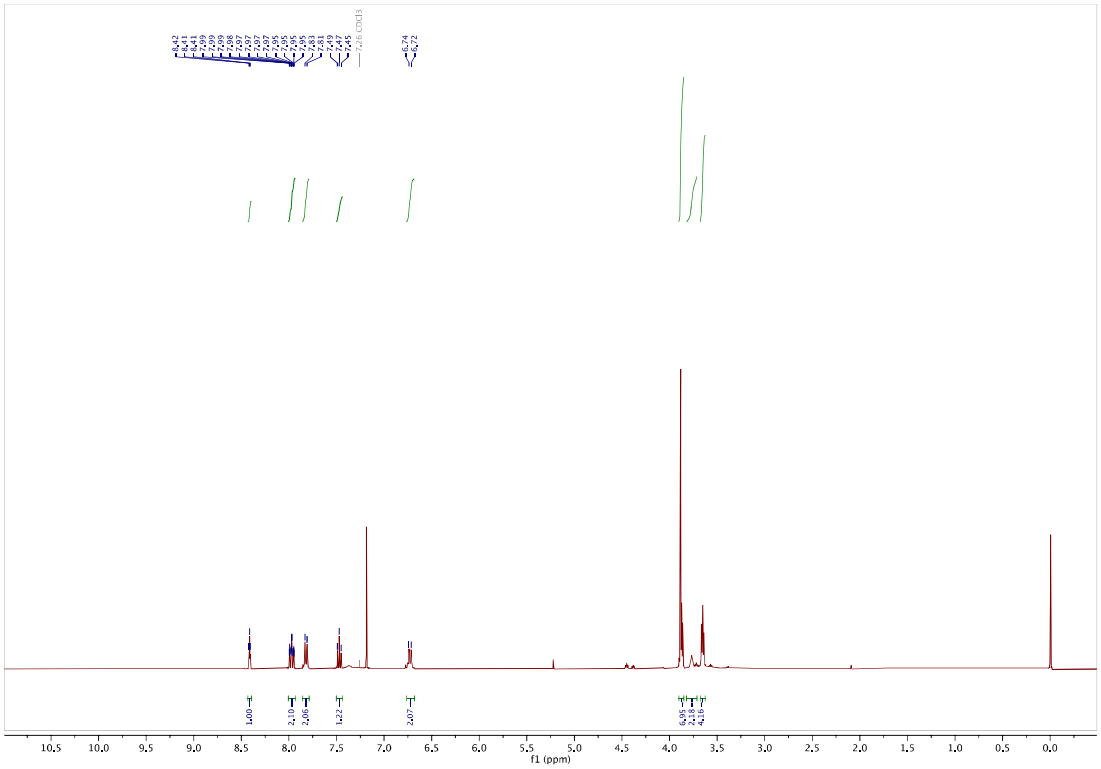

^{13}C-NMR

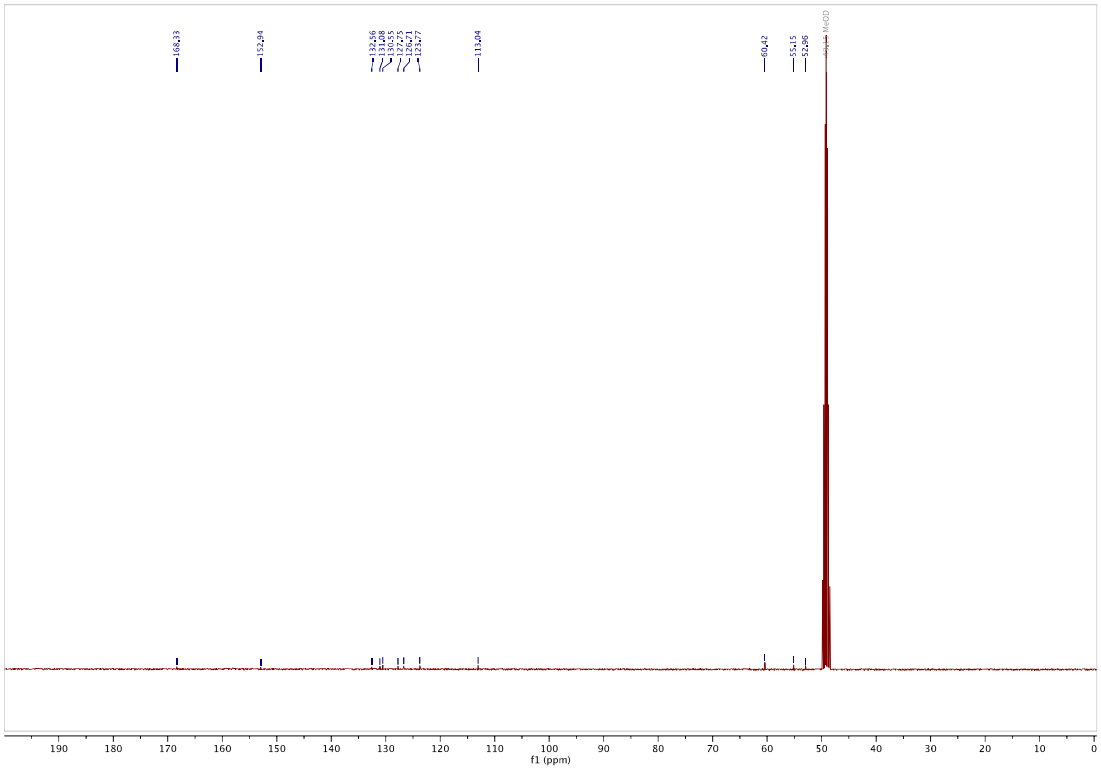

3-((4-(bis(2-hydroxyethyl)amino)phenyl)diazenyl)benzoic acid (3DEA-CO_2H): ^{1}H-NMR

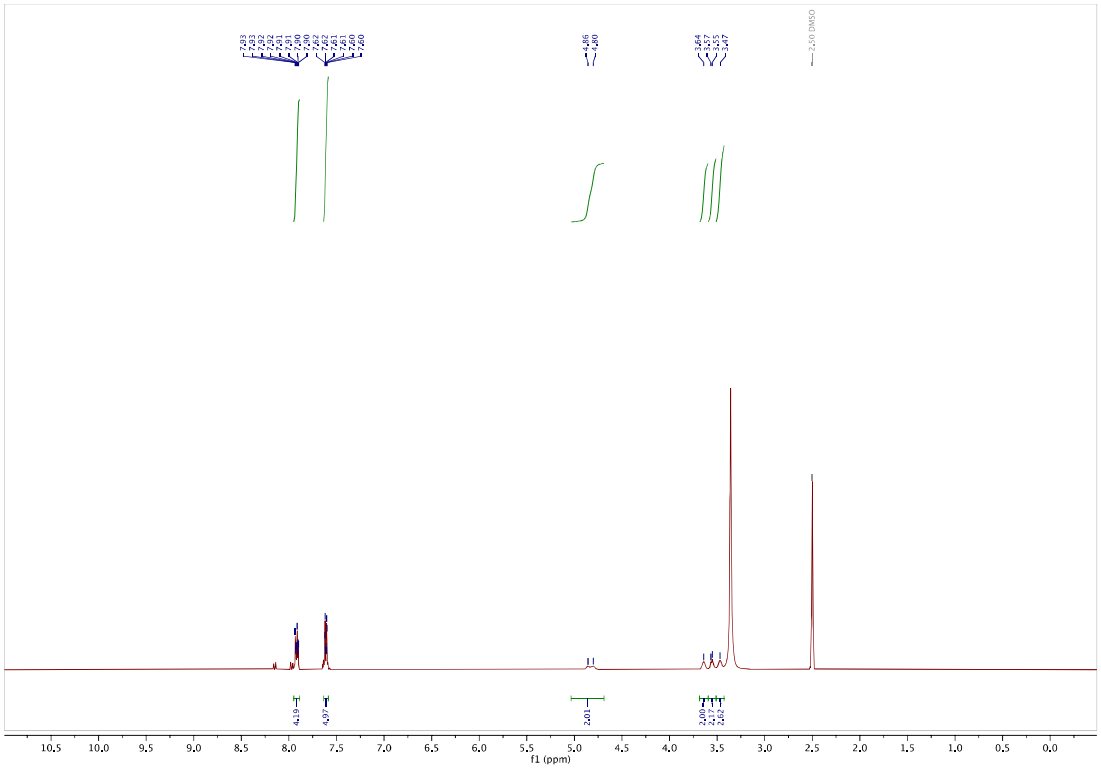

^{13}C-NMR

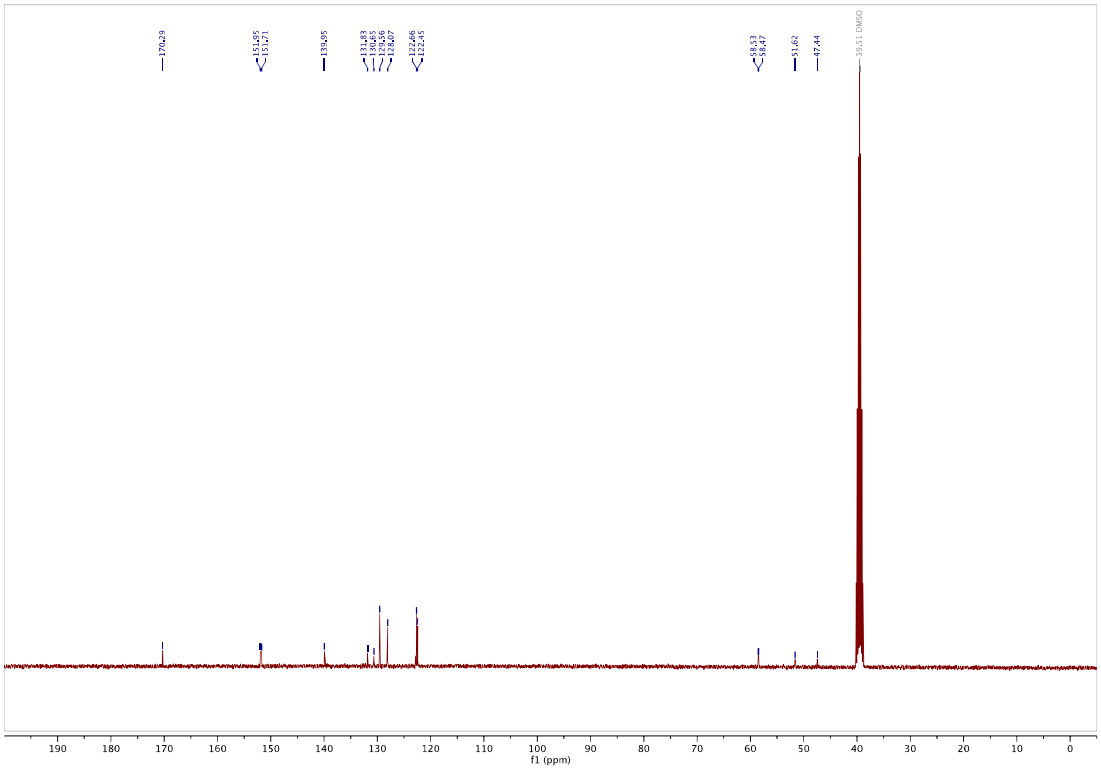

methyl 2-((4-hydroxyphenyl)diazenyl)benzoate (S12): ^{1}H-NMR

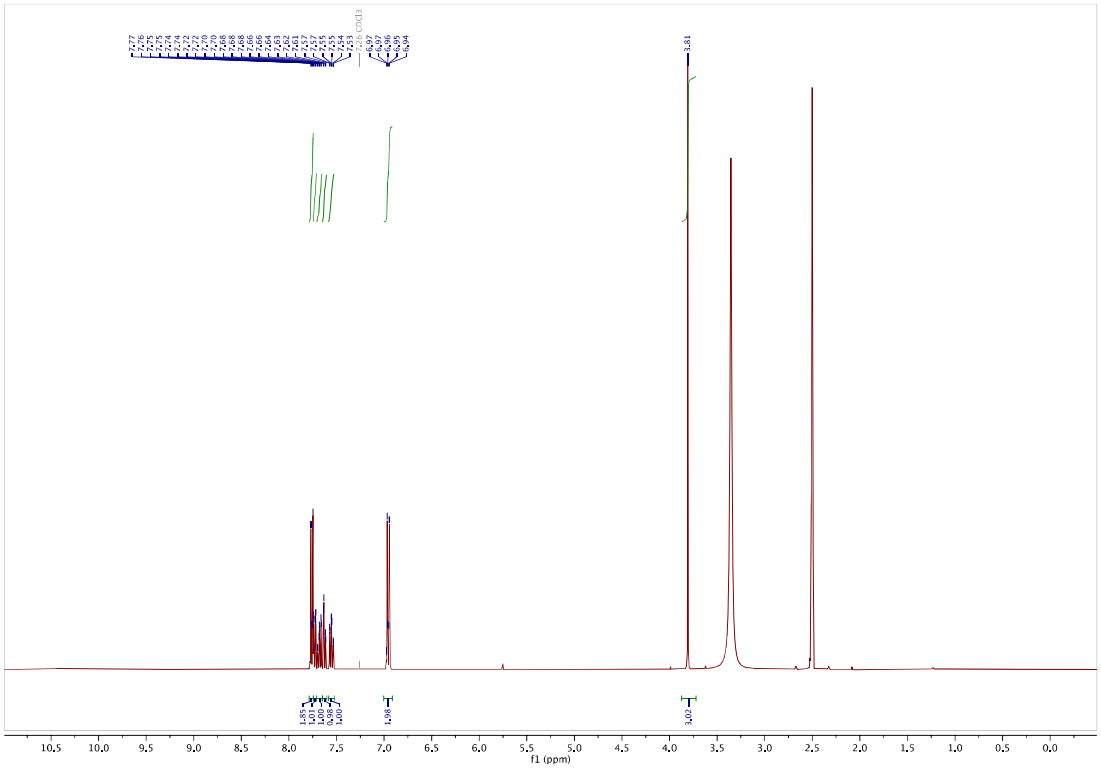

^{13}C-NMR

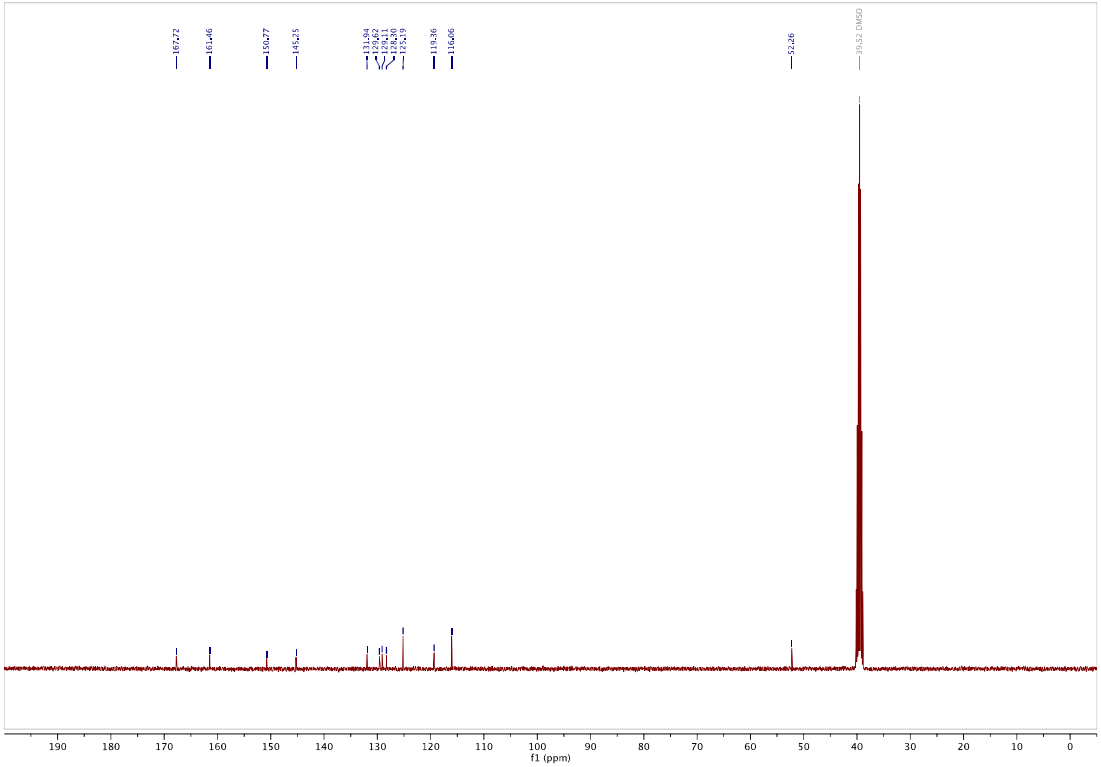

methyl 2-((4-methoxyphenyl)diazenyl)benzoate (S13): ^{1}H-NMR

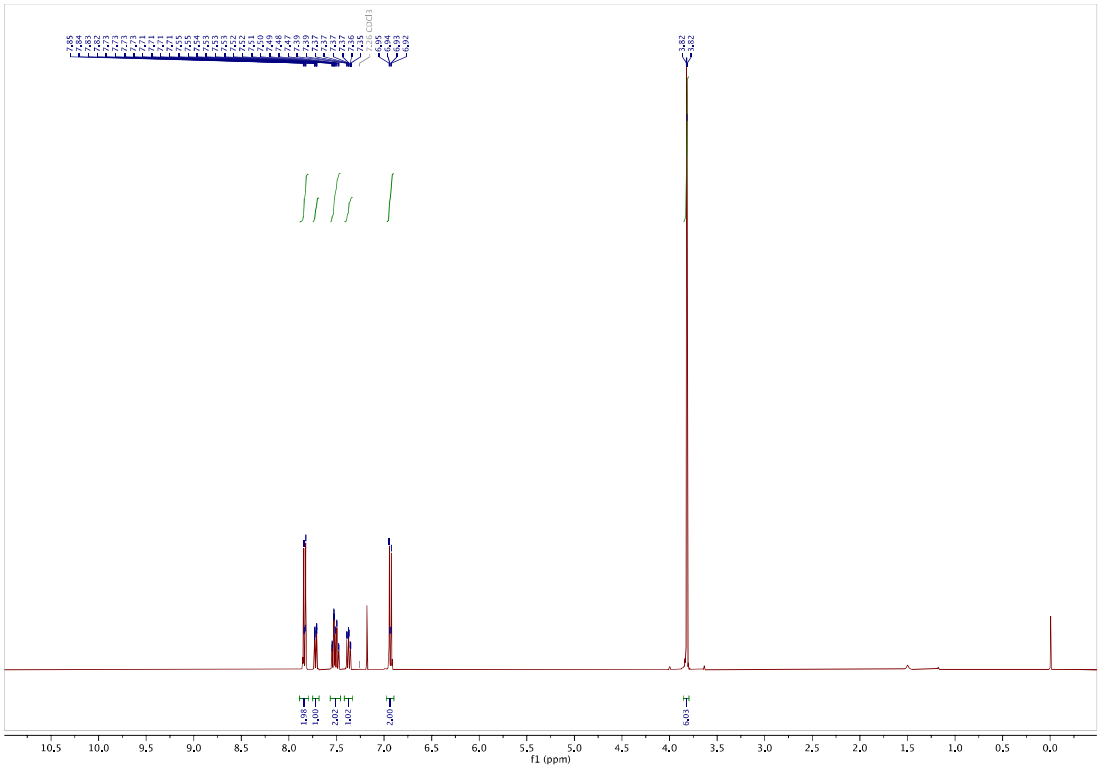

^{13}C-NMR

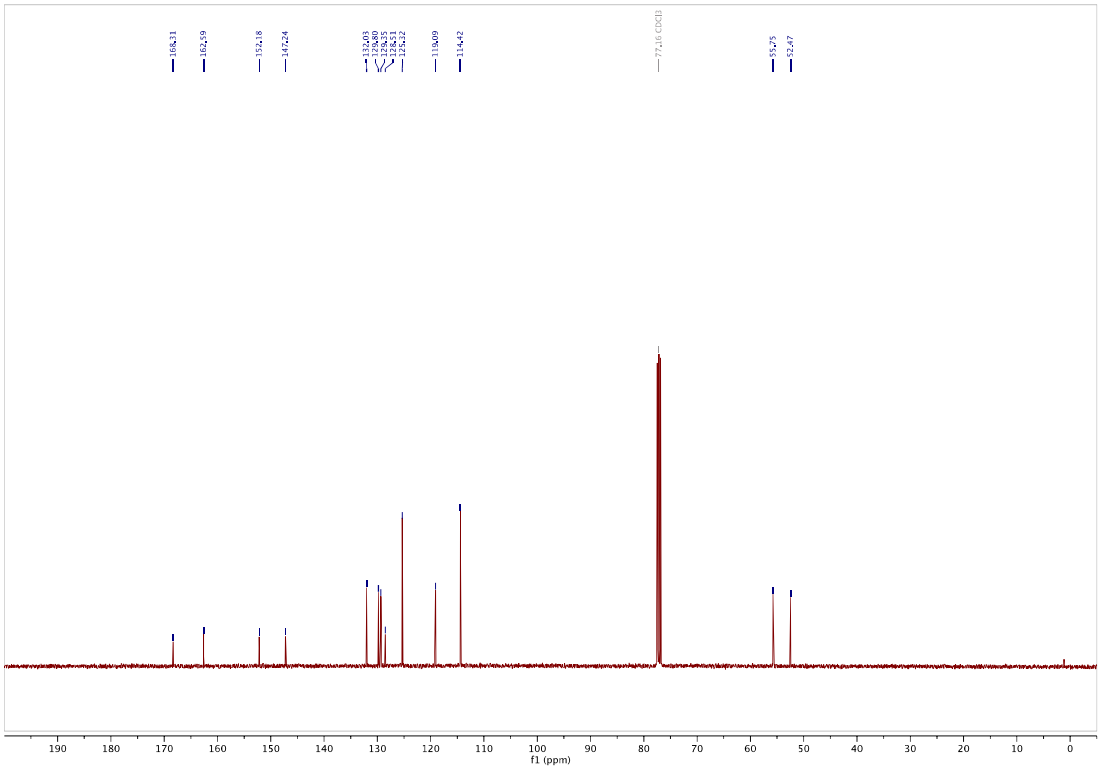

2-((4-methoxyphenyl)diazenyl)benzoic acid (2MP-CO_2H): ^{1}H-NMR

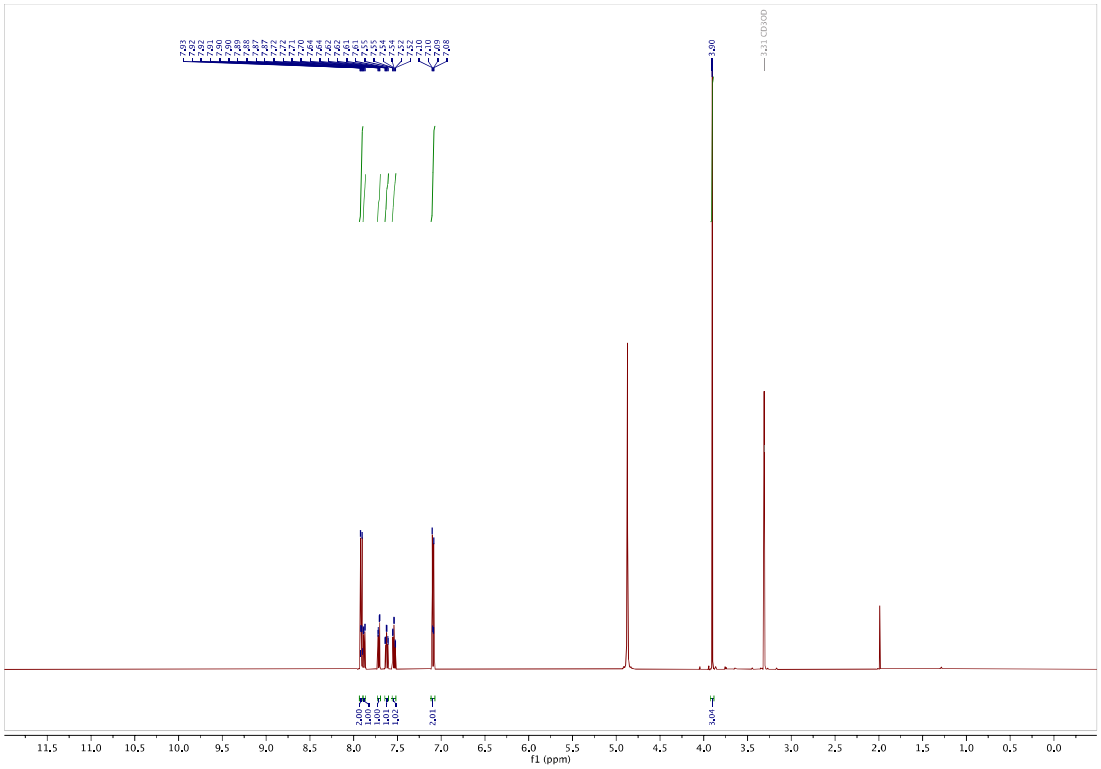

^{13}C-NMR

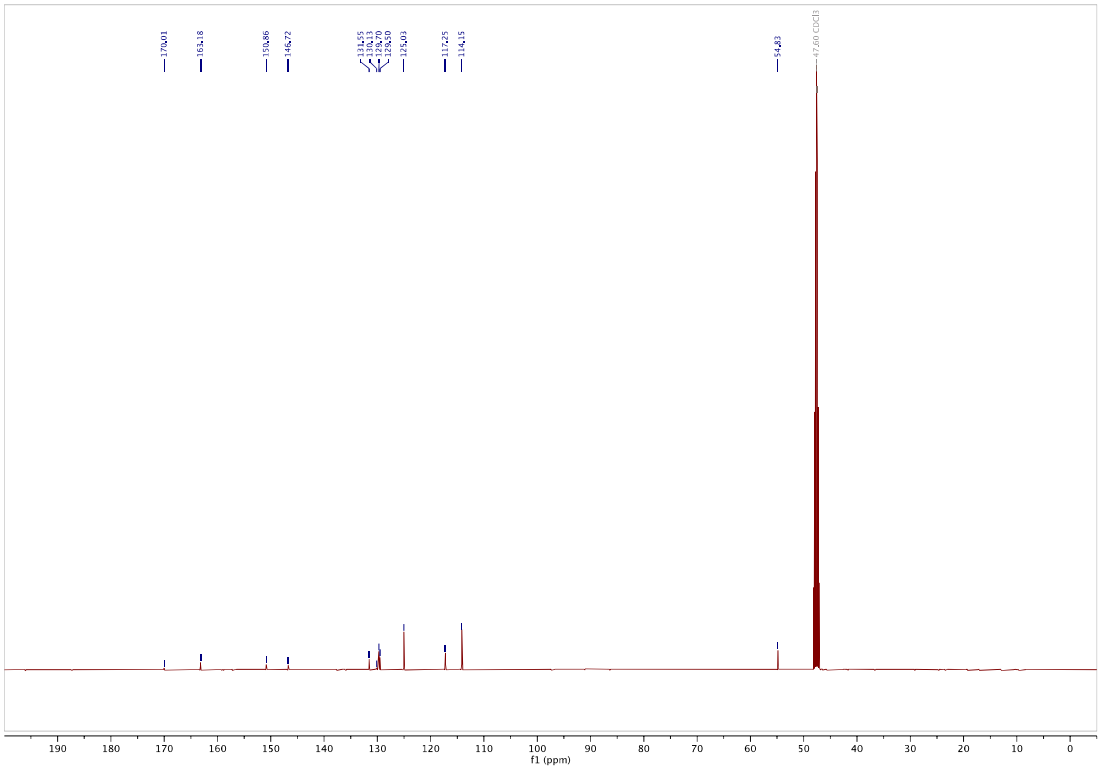

AzTax4H: **^{1}H-NMR**

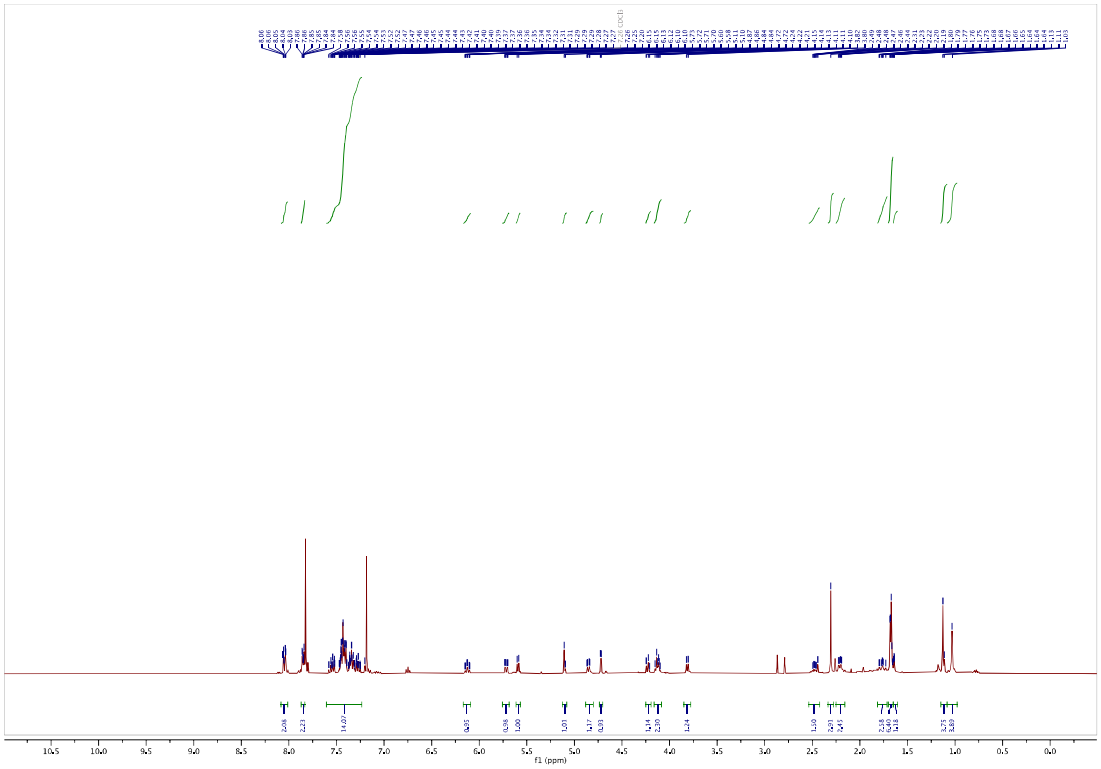

^{13}C-NMR

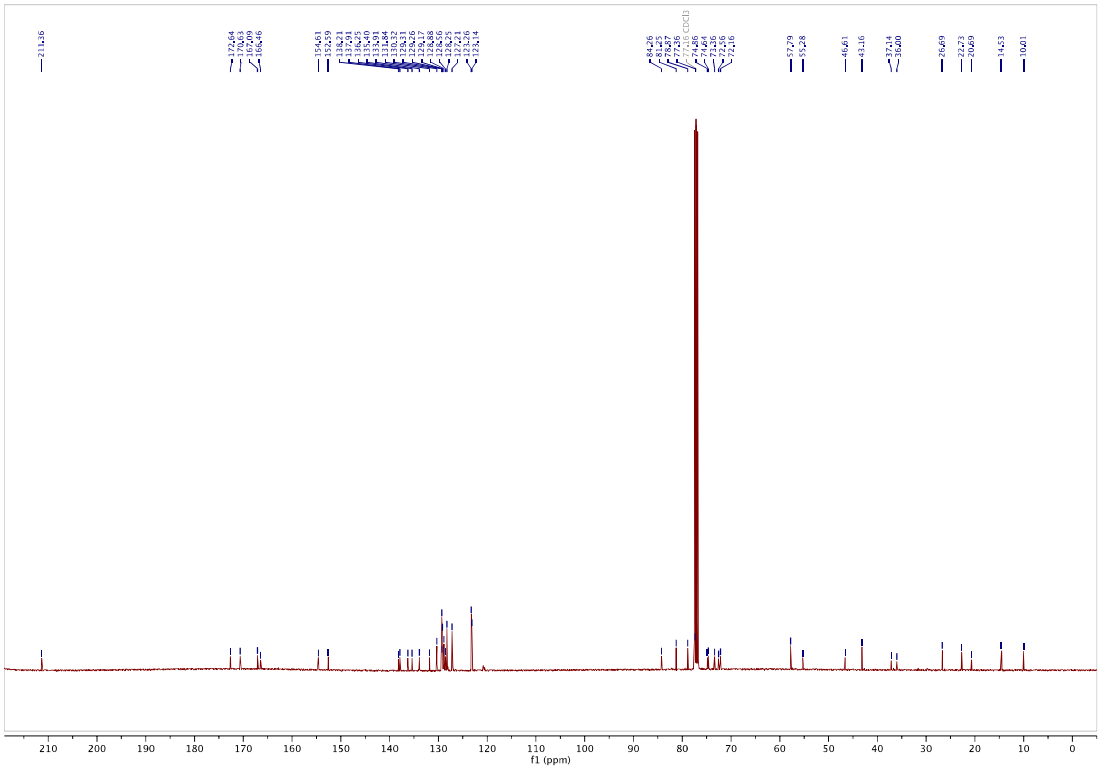

AzTax4DMA: **^{1}H-NMR**

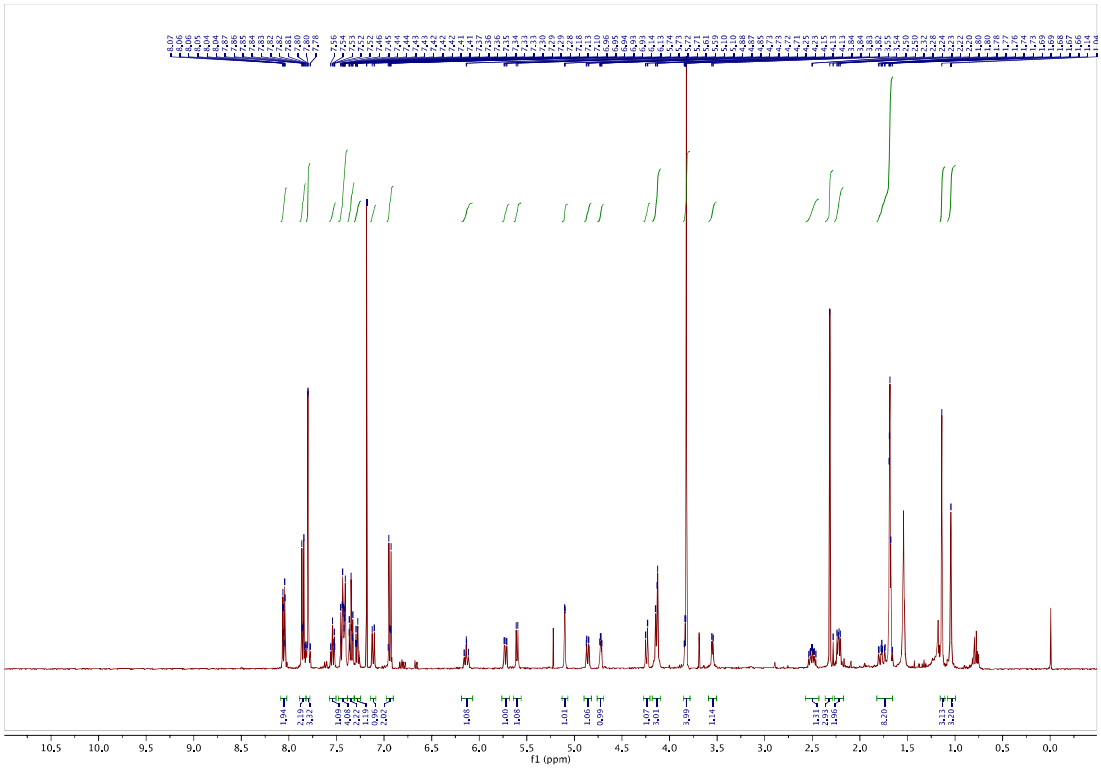

^{13}C-NMR

Text
Text

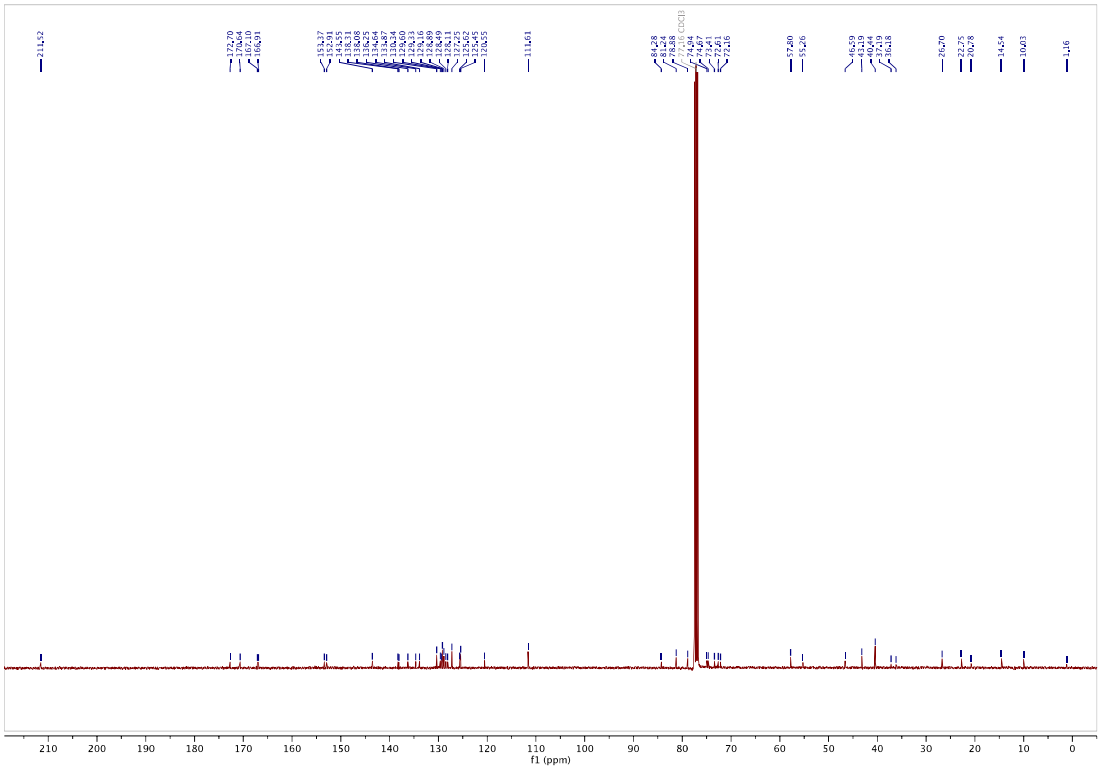

AzTax4MP: **^{1}H-NMR**

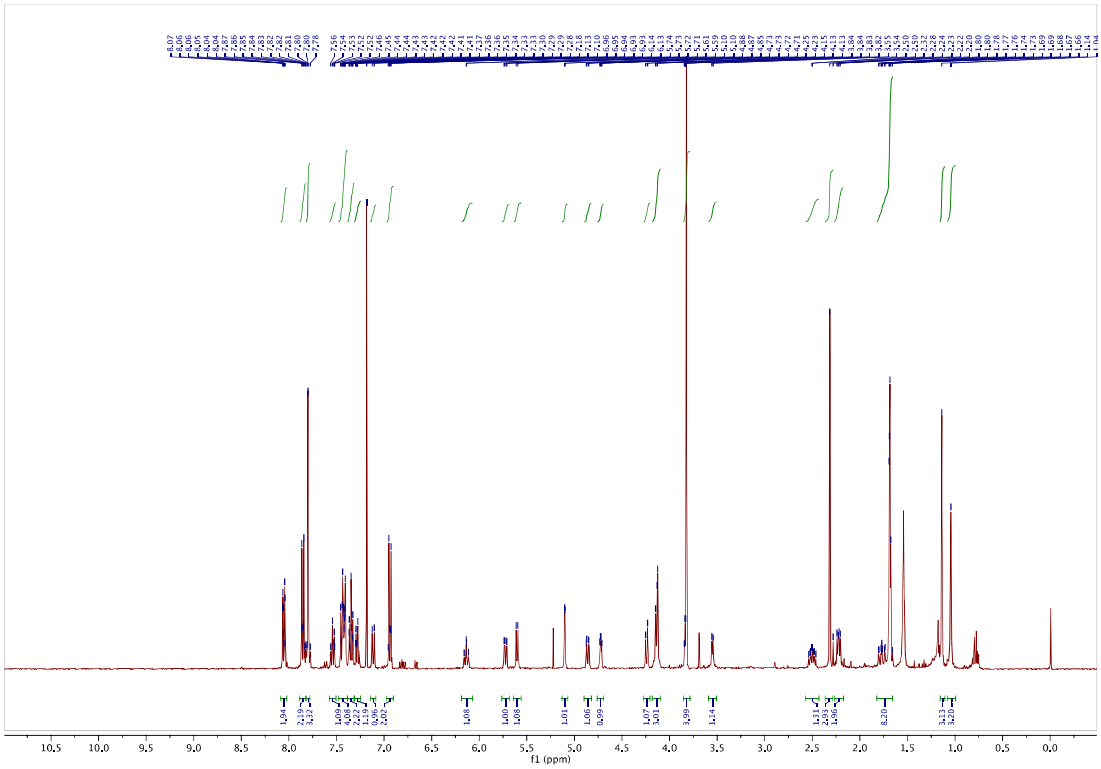

^{13}C-NMR

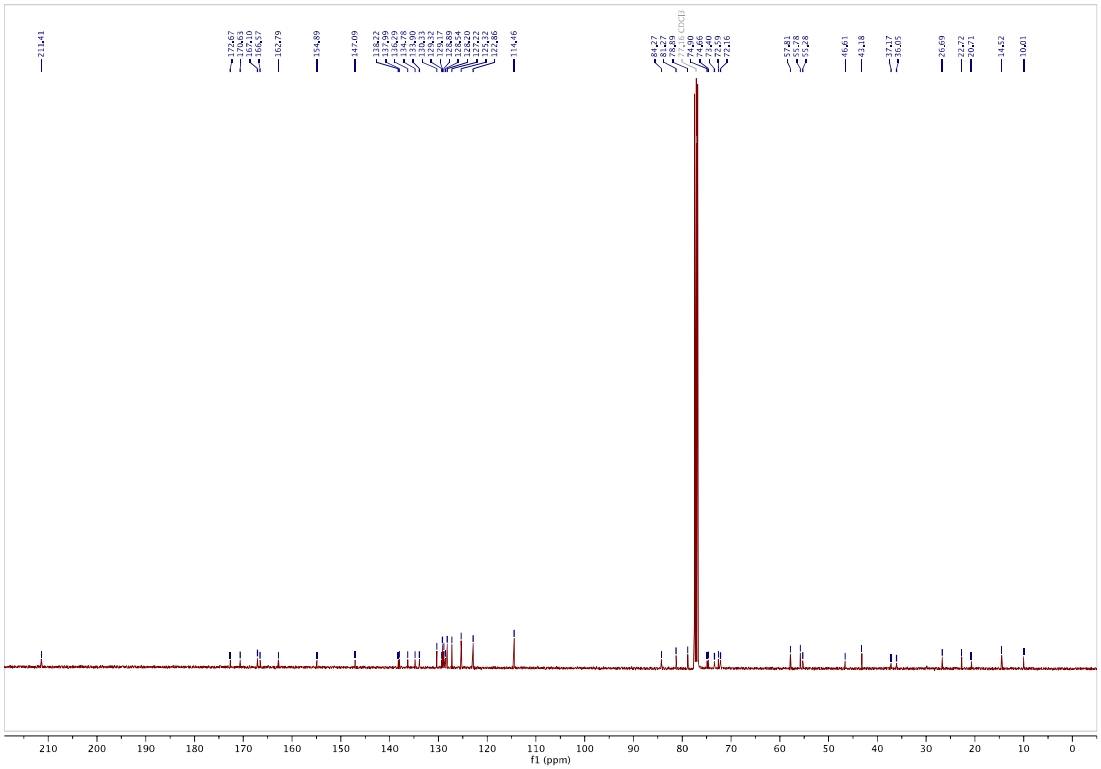

AzTax3H: **^{1}H-NMR**

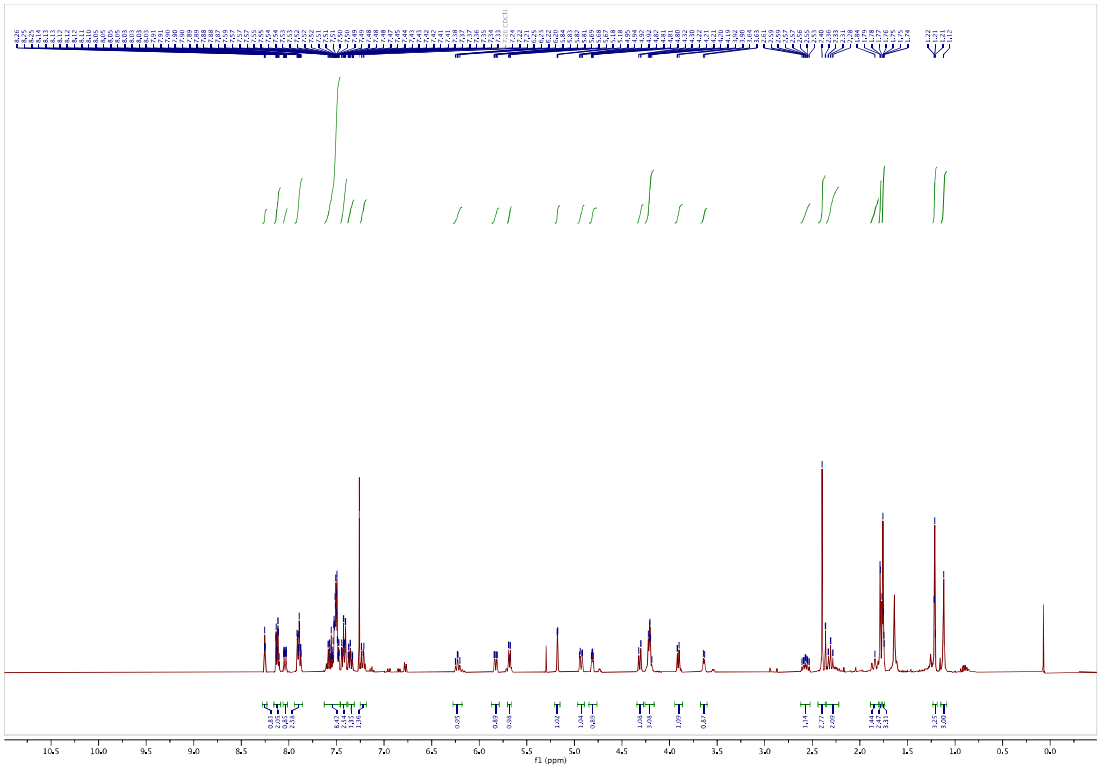

^{13}C-NMR

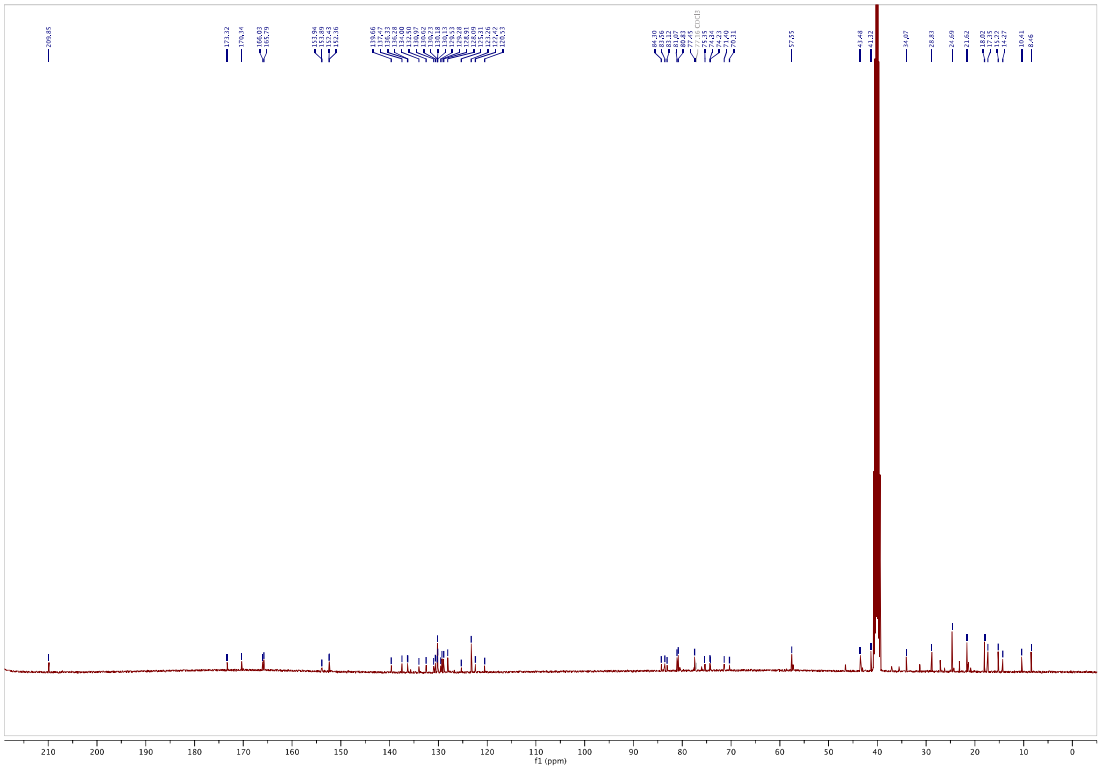

AzTax3DMA: **^{1}H-NMR**

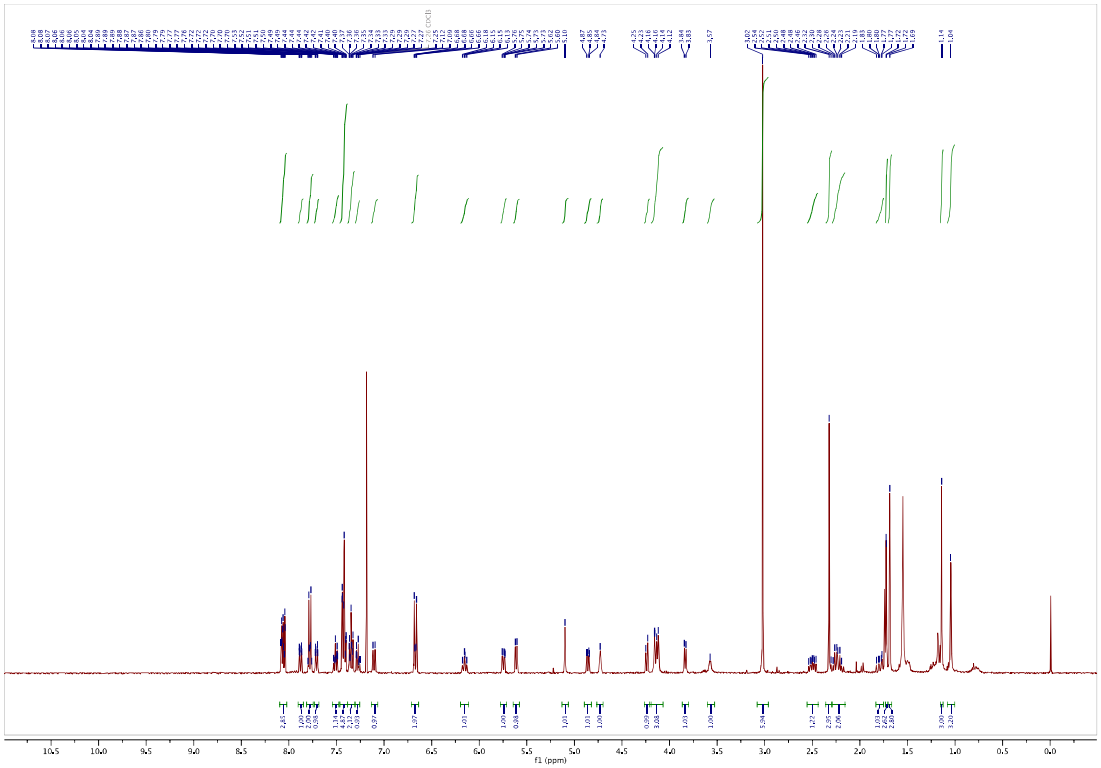

^{13}C-NMR

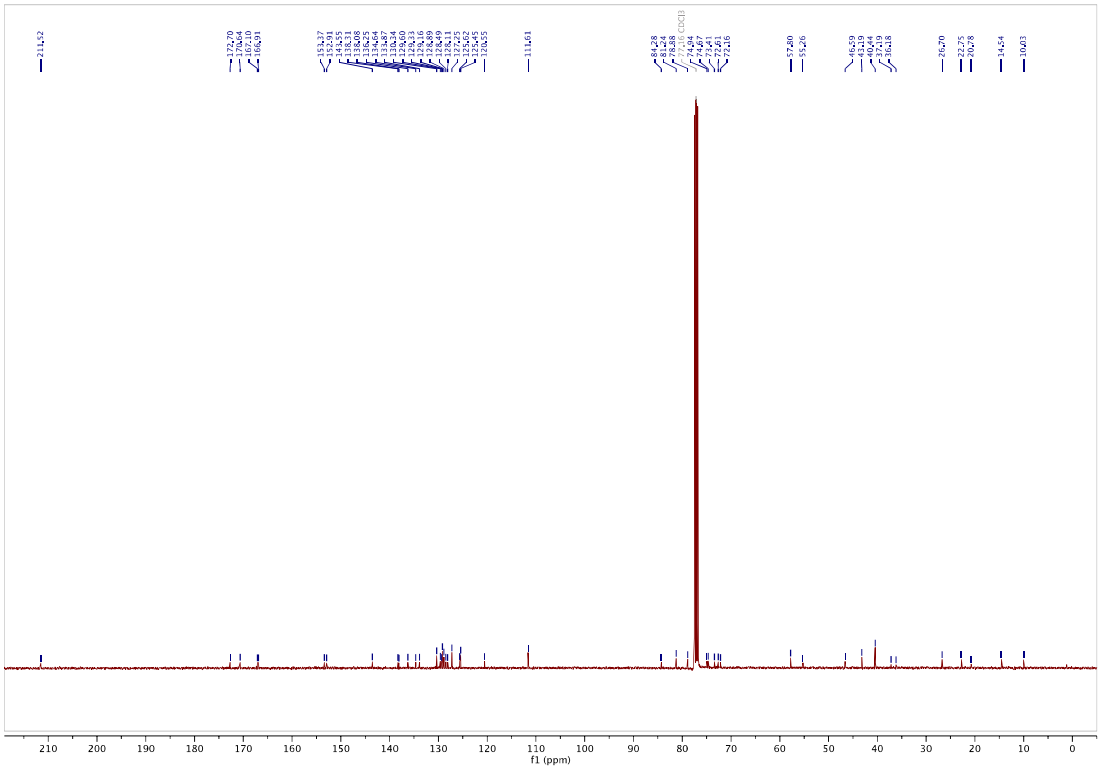

AzTax3MP: **^{1}H-NMR**

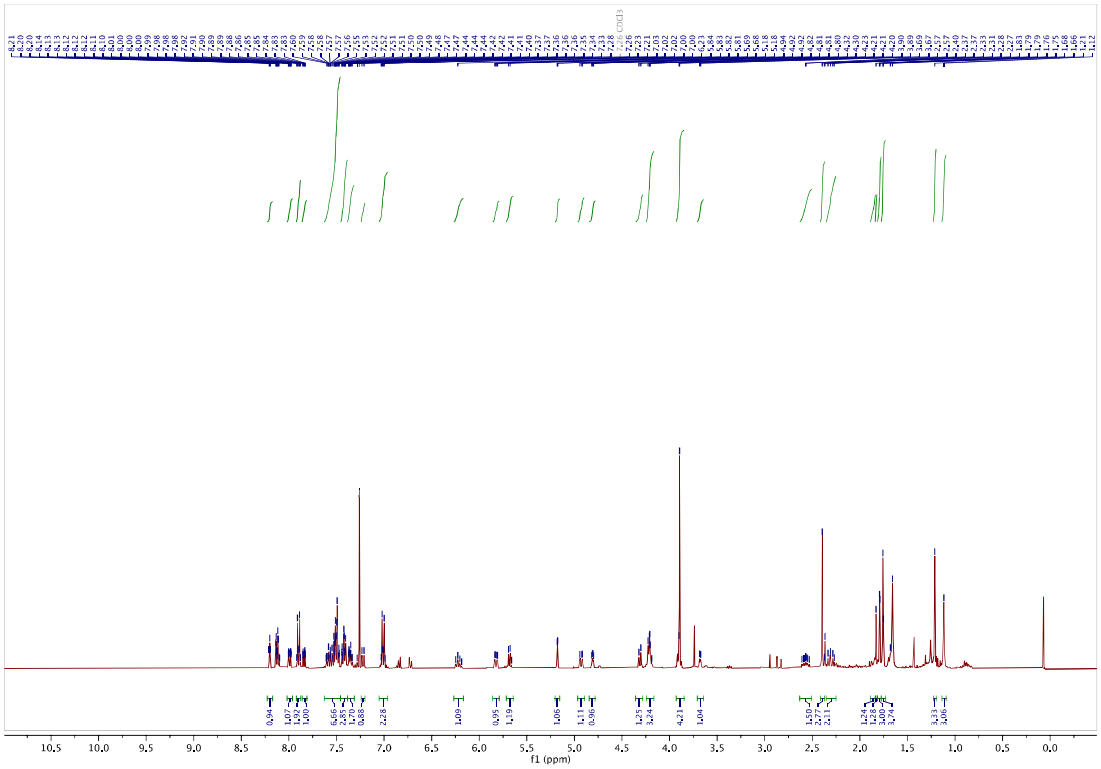

^{13}C-NMR

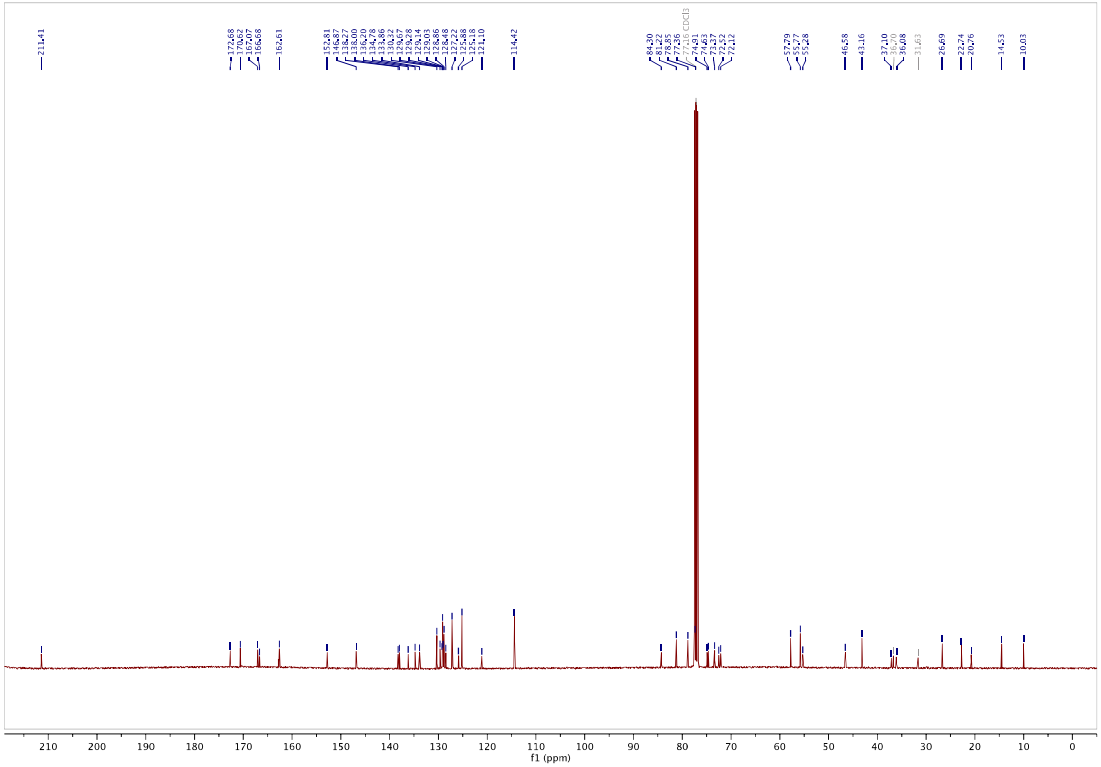

AzTax3MTM: **^{1}H-NMR**

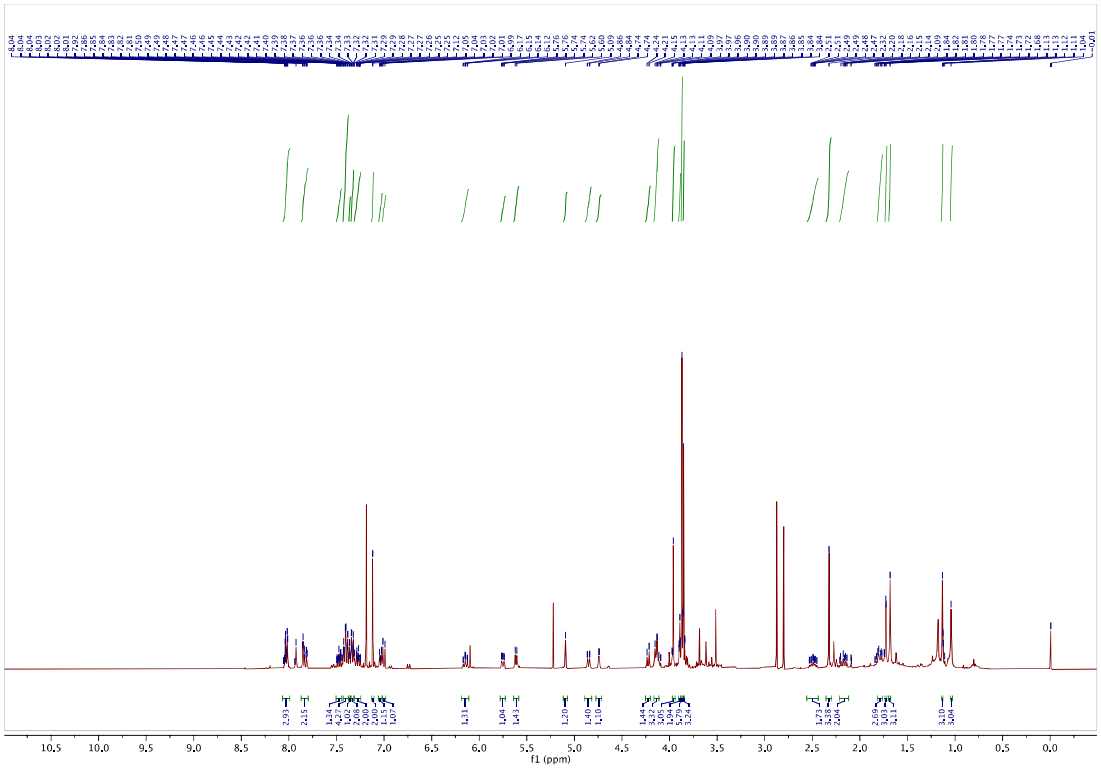

^{13}C-NMR

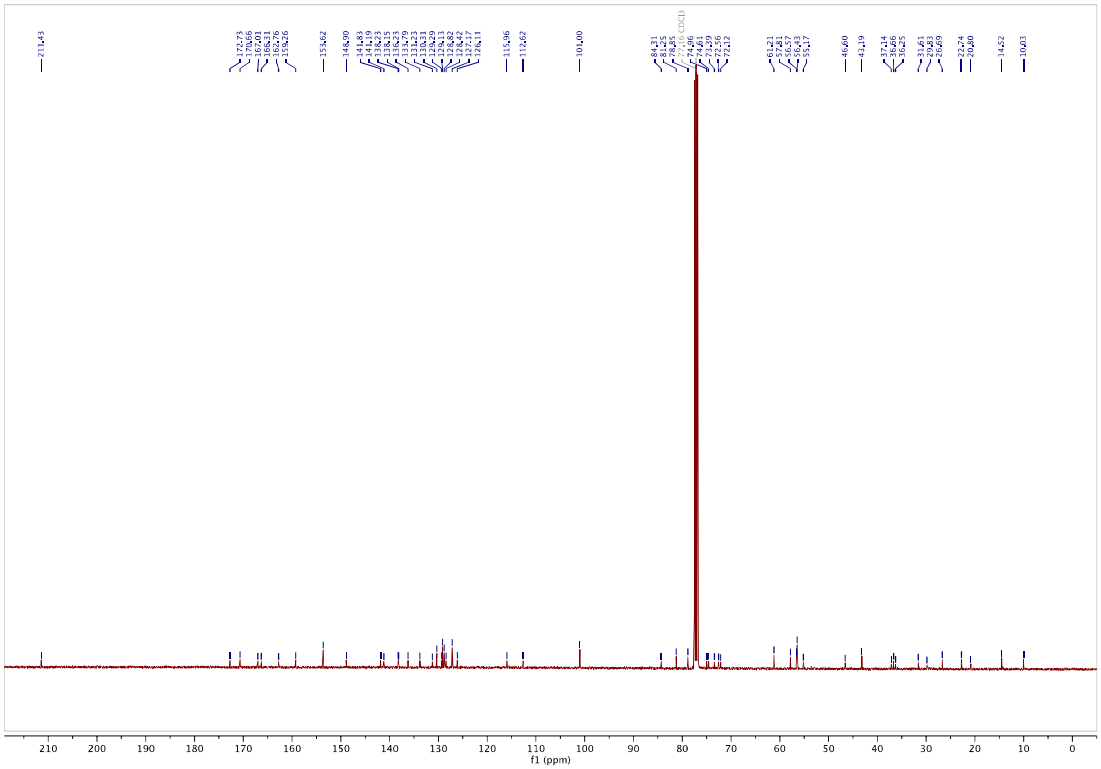

AzTax3TM: ^{1}H-NMR

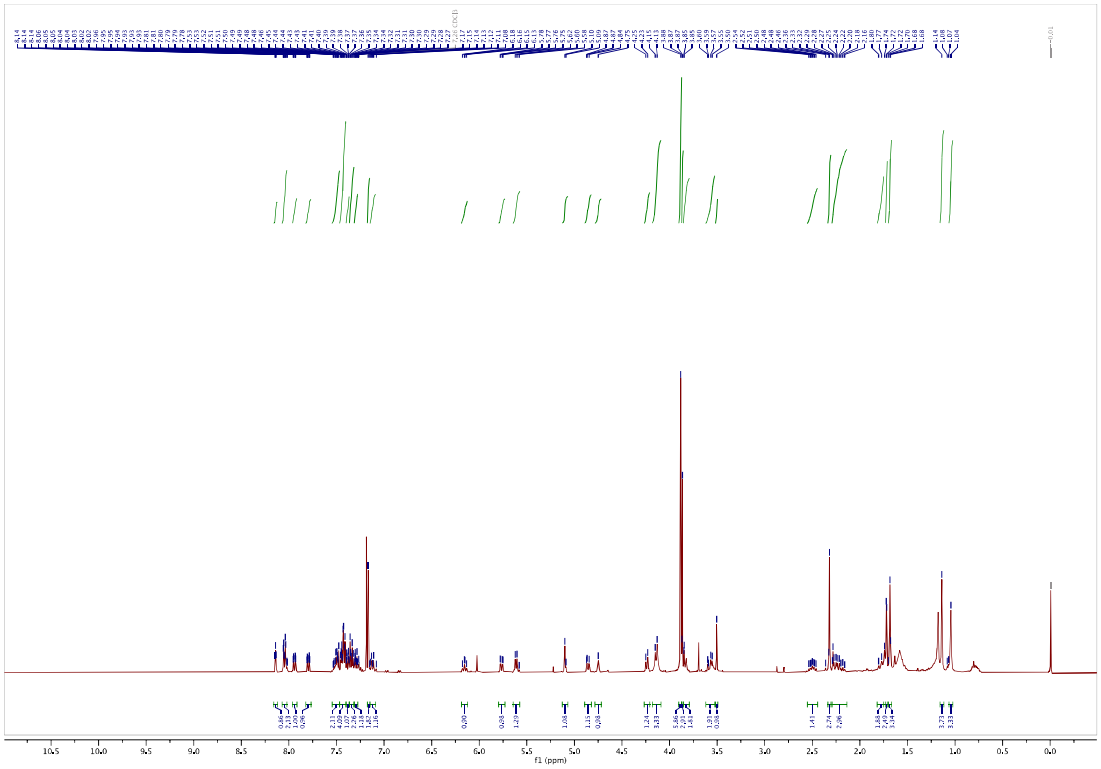

^{13}C-NMR

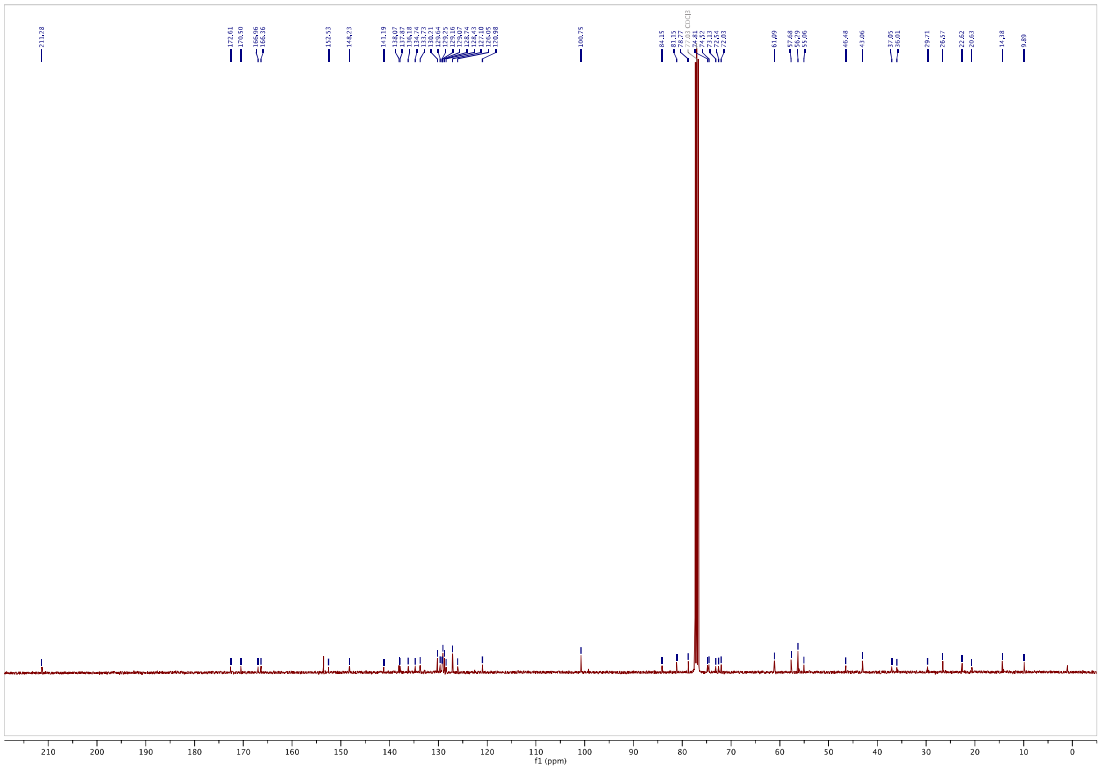

AzTax3DEA: **^{1}H-NMR**

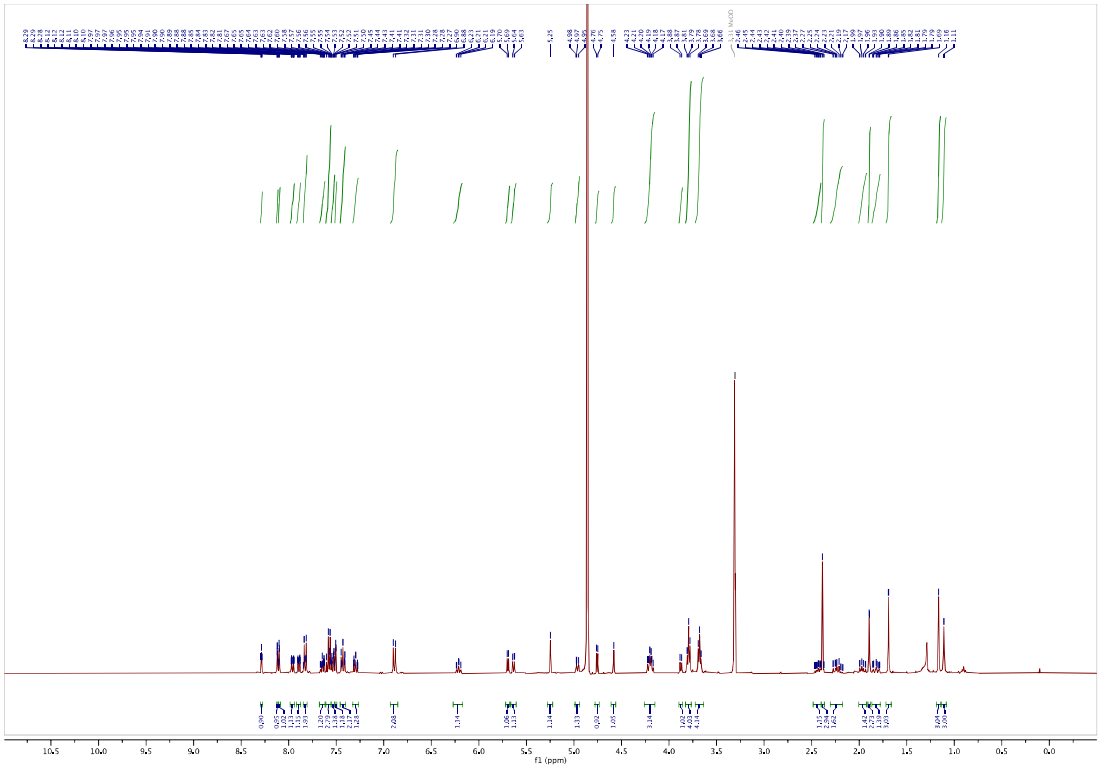

^{13}C-NMR

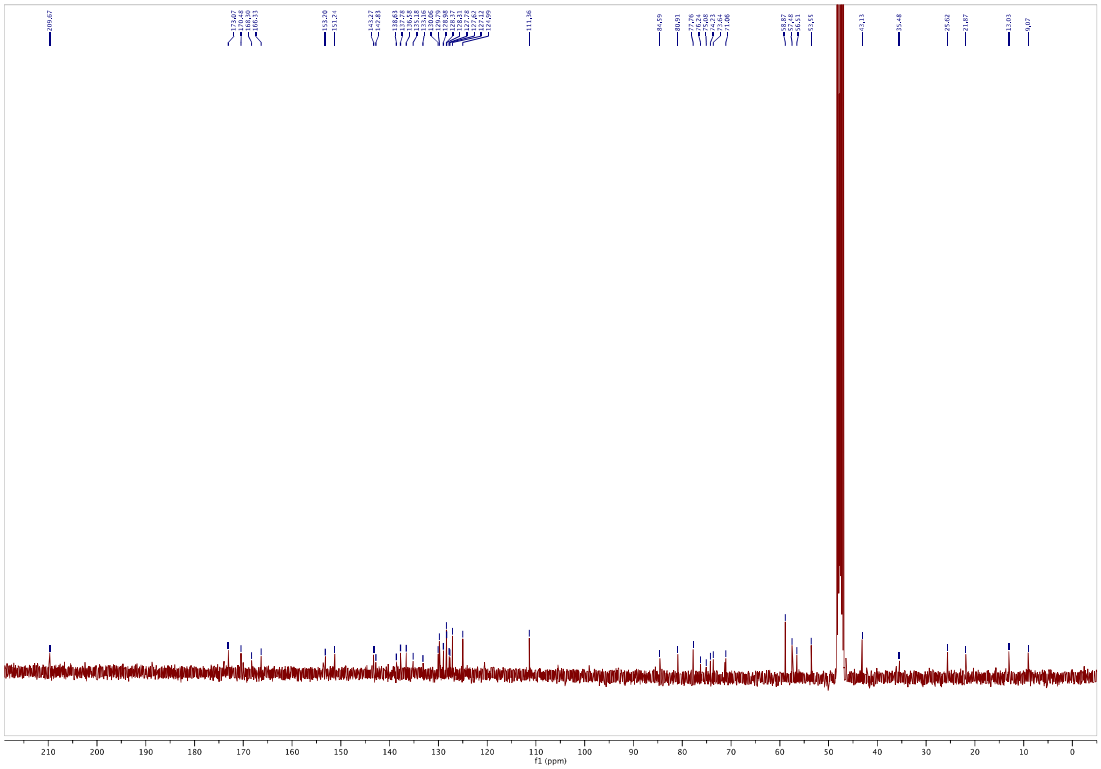

AzTax2MP: **^{1}H-NMR**

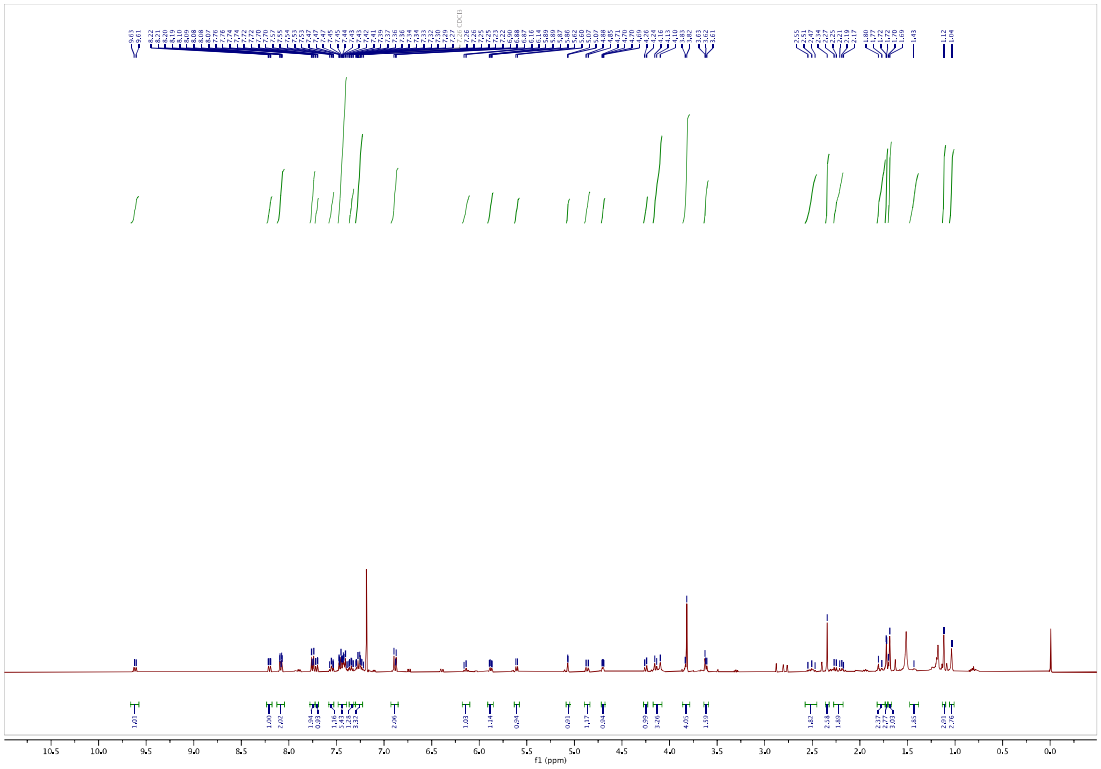

^{13}C-NMR

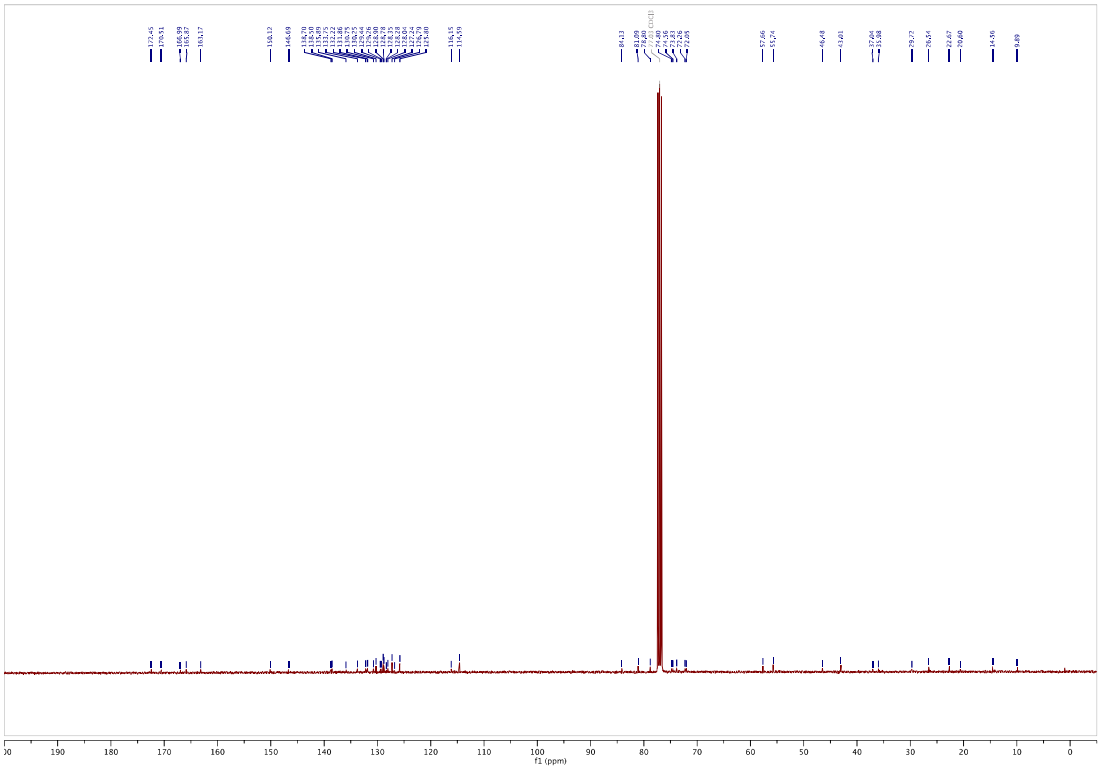

N,N-bis(2-hydroxyethyl)-4-(phenyldiazenyl)benzamide (4H): ^{1}H-NMR

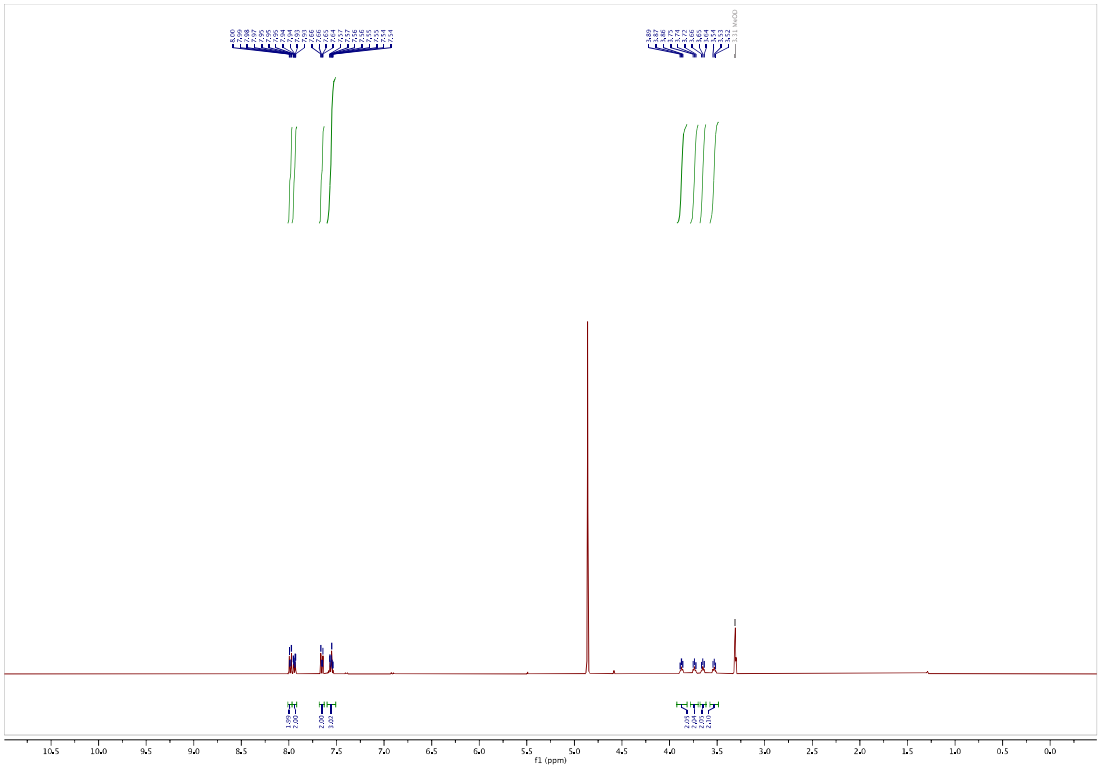

^{13}C-NMR

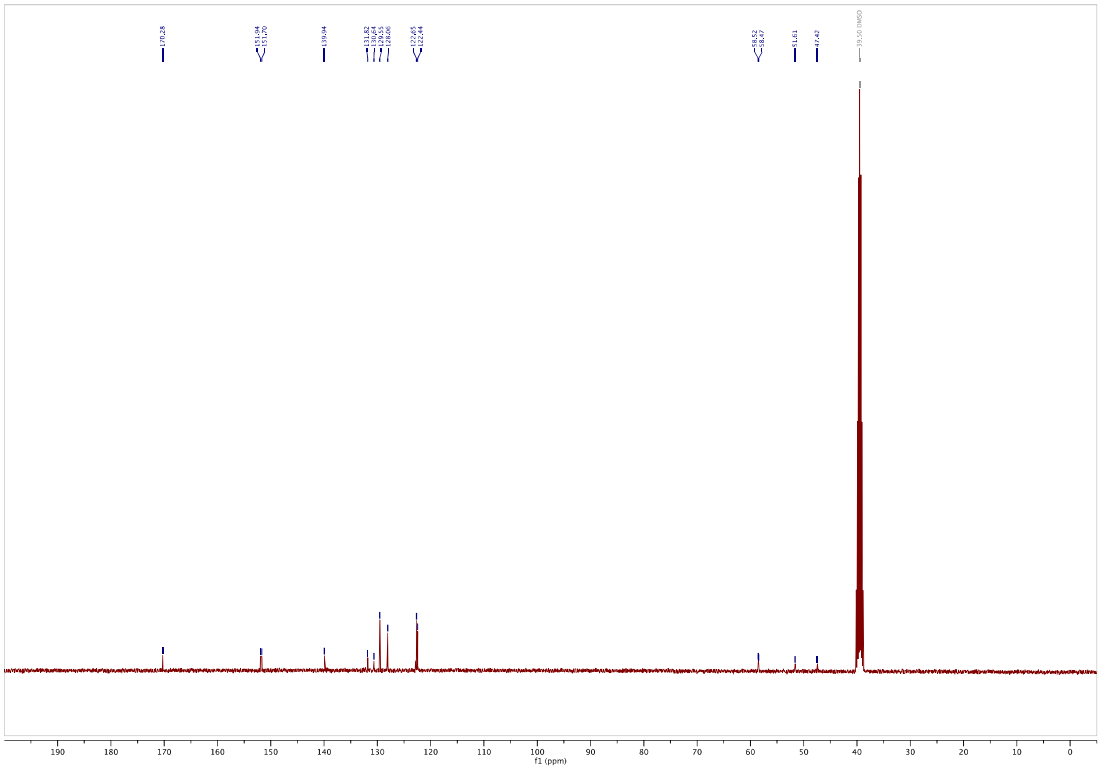

3-((4-(dimethylamino)phenyl)diazenyl)-*N,N*-bis(2-hydroxyethyl)benzamide (3DMA):

^{1}H NMR

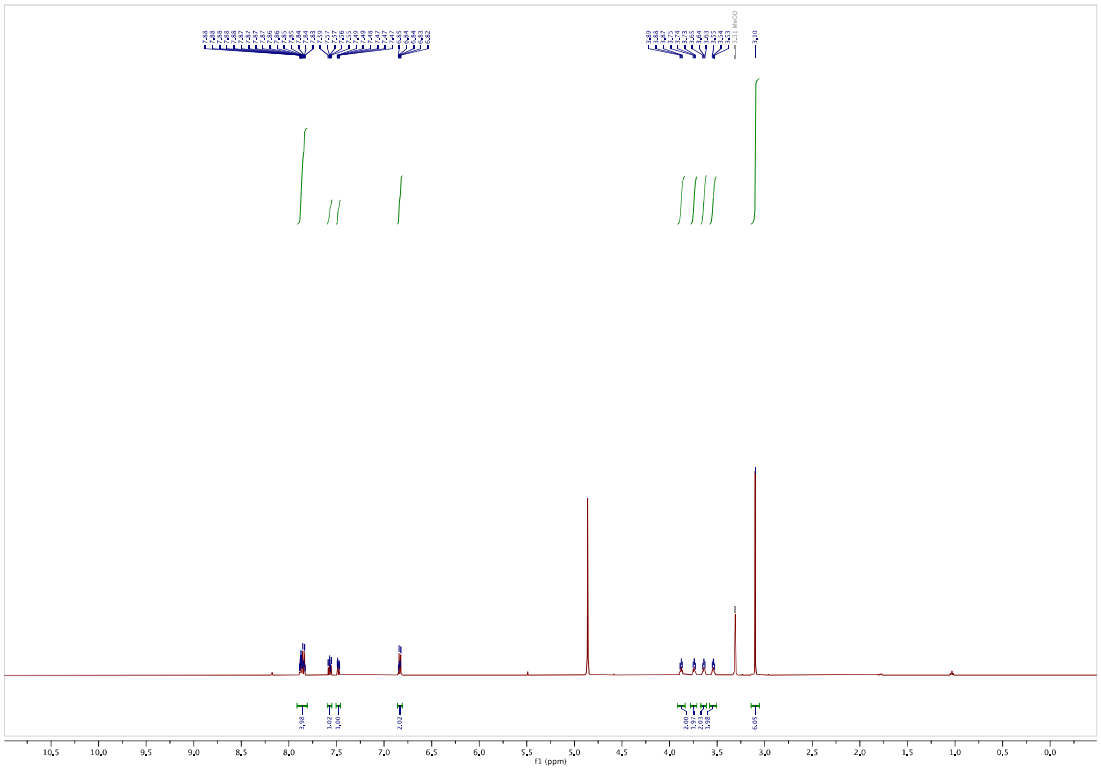

^{13}C-NMR

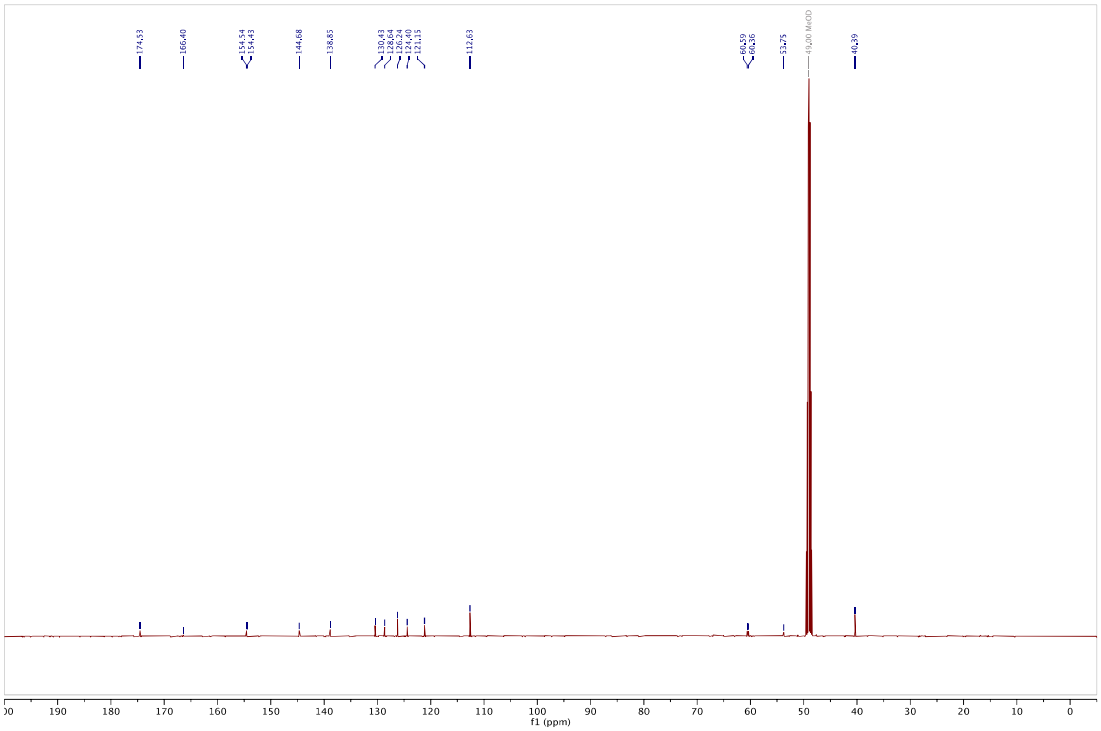

N,N-bis(2-hydroxyethyl)-3-((4-methoxyphenyl)diazenyl)benzamide (3MP): ^{1}H-NMR

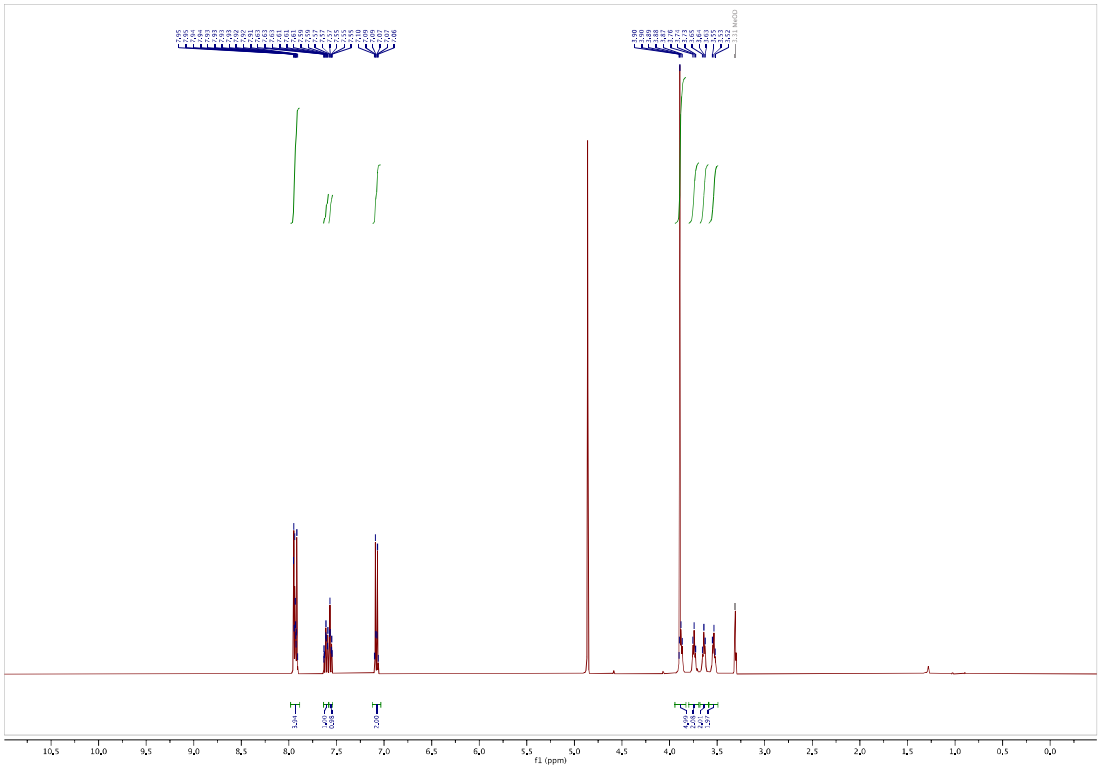

^{13}C-NMR

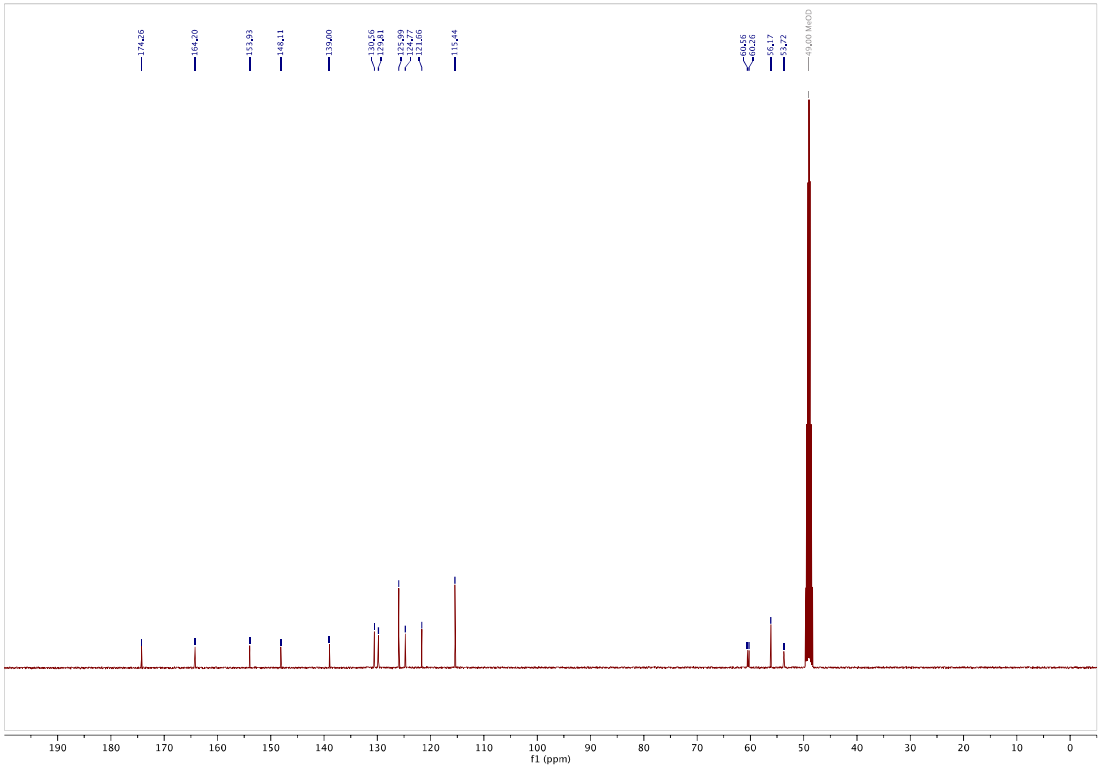

Supplementary References

(1) Gottlieb, H. E.; Kotlyar, V.; Nudelman, A. NMR Chemical Shifts of Common Laboratory Solvents as Trace Impurities. *J. Org. Chem.* **1997**, *62* (21), 7512–7515. https://doi.org/10.1021/jo971176v.

(2) McNamara, W. R.; Milot, R. L.; Song, H.; Snoeberger III, R. C.; Batista, V. S.; Schmuttenmaer, C. A.; Brudvig, G. W.; Crabtree, R. H. Water-Stable, Hydroxamate Anchors for Functionalization of TiO2 Surfaces with Ultrafast Interfacial Electron Transfer. *Energy Environ. Sci.* **2010**, *3* (7), 917–923. https://doi.org/10.1039/C001065K.

(3) Palmer, L. C.; Leung, C.-Y.; Kewalramani, S.; Kumthekar, R.; Newcomb, C. J.; Olvera de la Cruz, M.; Bedzyk, M. J.; Stupp, S. I. Long-Range Ordering of Highly Charged Self-Assembled Nanofilaments. *J. Am. Chem. Soc.* **2014**, *136* (41), 14377–14380. https://doi.org/10.1021/ja5082519.

(4) Lim, Y.-K.; Lee, K.-S.; Cho, C.-G. Novel Route to Azobenzenes via Pd-Catalyzed Coupling Reactions of Aryl Hydrazides with Aryl Halides, Followed by Direct Oxidations. *Org. Lett.* **2003**, *5* (7), 979–982. https://doi.org/10.1021/ol027311u.

(5) Davey, M. H.; Lee, V. Y.; Miller, R. D.; Marks, T. J. Synthesis of Aryl Nitroso Derivatives by Tert-Butyl Hypochlorite Oxidation in Homogeneous Media. Intermediates for the Preparation of High-Hyperpolarizability Chromophore Skeletons. *J. Org. Chem.* **1999**, *64* (13), 4976–4979. https://doi.org/10.1021/jo990235x.

(6) Kreger, K.; Wolfer, P.; Audorff, H.; Kador, L.; Stingelin-Stutzmann, N.; Smith, P.; Schmidt, H.-W. Stable Holographic Gratings with Small-Molecular Trisazobenzene Derivatives. *J. Am. Chem. Soc.* **2010**, *132* (2), 509–516. https://doi.org/10.1021/ja9091038.

(7) Fatás, P.; Longo, E.; Rastrelli, F.; Crisma, M.; Toniolo, C.; Jiménez, A. I.; Cativiela, C.; Moretto, A. Bis(Azobenzene)-Based Photoswitchable, Prochiral, Cα-Tetrasubstituted α-Amino Acids for Nanomaterials Applications. *Chemistry – A European Journal* **2011**, *17* (45), 12606–12611. https://doi.org/10.1002/chem.201102609.

(8) Stawski, P.; Sumser, M.; Trauner, D. A Photochromic Agonist of AMPA Receptors. *Angewandte Chemie International Edition* **2012**, *51* (23), 5748–5751. https://doi.org/10.1002/anie.201109265.

(9) Wang, Y.-T.; Zhang, Y.; Gong, H.; Sun, R.; Mao, W.; Wang, D.-H.; Chen, Y. A Colorimetric Pb^{2+} Chemosensor: Rapid Naked-Eye Detection, High Selectivity, Theoretical Insights, and Applications. *Journal of Photochemistry and Photobiology A: Chemistry* **2018**, *355*, 101–108. https://doi.org/10.1016/j.jphotochem.2017.10.027.

(10) Šťastná, M.; Trávníček, M.; Šlais, K. New Azo Dyes as Colored Isoelectric Point Markers for Isoelectric Focusing in Acidic PH Region. *Electrophoresis* **2005**, *26* (1), 53–59. https://doi.org/10.1002/elps.200406088.

(11) Leriche, G.; Budin, G.; Brino, L.; Wagner, A. Optimization of the Azobenzene Scaffold for Reductive Cleavage by Dithionite; Development of an Azobenzene Cleavable Linker for Proteomic Applications. *European Journal of Organic Chemistry* **2010**, *2010* (23), 4360–4364. https://doi.org/10.1002/ejoc.201000546.

(12) Farrera, J.-A.; Canal, I.; Hidalgo-Fernández, P.; Pérez-García, M. L.; Huertas, O.; Luque, F. J. Towards a Tunable Tautomeric Switch in Azobenzene Biomimetics: Implications for the Binding Affinity of 2-(4′-Hydroxyphenylazo)Benzoic Acid to Streptavidin. *Chemistry – A European Journal* **2008**, *14* (7), 2277–2285. https://doi.org/10.1002/chem.200701407.

(13) Dunn, N. J.; Humphries, W. H.; Offenbacher, A. R.; King, T. L.; Gray, J. A. pH-Dependent Cis → Trans Isomerization Rates for Azobenzene Dyes in Aqueous Solution. *J. Phys. Chem. A* **2009**, *113* (47), 13144–13151. https://doi.org/10.1021/jp903102u.

(14) Hüll, K.; Morstein, J.; Trauner, D. In Vivo Photopharmacology. *Chemical Reviews* **2018**, *118* (21), 10710–10747. https://doi.org/10.1021/acs.chemrev.8b00037.

(15) Sailer, A.; Ermer, F.; Kraus, Y.; Bingham, R.; Lutter, F. H.; Ahlfeld, J.; Thorn-Seshold, O. Potent Hemithioindigo-Based Antimitotics Photocontrol the Microtubule Cytoskeleton in Cellulo. *Beilstein Journal of Organic Chemistry* **2020**, *16*, 125–134. https://doi.org/10.3762/bjoc.16.14.

(16) Reis, S. A.; Ghosh, B.; Hendricks, J. A.; Szantai-Kis, D. M.; Törk, L.; Ross, K. N.; Lamb, J.; Read-Button, W.; Zheng, B.; Wang, H.; Salthouse, C.; Haggarty, S. J.; Mazitschek, R. Light-Controlled Modulation of Gene Expression by Chemical Optoepigenetic Probes. *Nature Chemical Biology* **2016**, *12*, 317. https://doi.org/10.1038/nchembio.2042.

(17) Gao, L.; Kraus, Y.; Wranik, M.; Weinert, T.; Pritzl, S. D.; Meiring, J. C. M.; Bingham, R.; Olieric, N.; Akhmanova, A.; Lohmüller, T.; Steinmetz, M. O.; Thorn-Seshold, O. Photoswitchable Microtubule Inhibitors Enabling Robust, GFP-Orthogonal Optical Control over the Tubulin Cytoskeleton. *bioRxiv* **2019**, 716233. https://doi.org/10.1101/716233.

(18) Kopf, A.; Renkawitz, J.; Hauschild, R.; Girkontaite, I.; Tedford, K.; Merrin, J.; Thorn-Seshold, O.; Trauner, D.; Häcker, H.; Fischer, K.-D.; Kiermaier, E.; Sixt, M. Microtubules Control Cellular Shape and Coherence in Amoeboid Migrating Cells. *bioRxiv* **2019**, 609420. https://doi.org/10.1101/609420.

(19) Sailer, A.; Ermer, F.; Kraus, Y.; Lutter, F.; Donau, C.; Bremerich, M.; Ahlfeld, J.; Thorn-Seshold, O. Hemithioindigos as Desymmetrised Molecular Switch Scaffolds: Design Control over the Isomer-Dependency of Potent Photoswitchable Antimitotic Bioactivity in Cellulo. *ChemBioChem* **2019**, *20*, 1305–1314. https://doi.org/10.1002/cbic.201800752.

(20) Borowiak, M.; Nahaboo, W.; Reynders, M.; Nekolla, K.; Jalinot, P.; Hasserodt, J.; Rehberg, M.; Delattre, M.; Zahler, S.; Vollmar, A.; Trauner, D.; Thorn-Seshold, O. Photoswitchable Inhibitors of Microtubule Dynamics Optically Control Mitosis and Cell Death. *Cell* **2015**, *162* (2), 403–411. https://doi.org/10.1016/j.cell.2015.06.049.

(21) Lin, C. M.; Singh, S. B.; Chu, P. S.; Dempcy, R. O.; Schmidt, J. M.; Pettit, G. R.; Hamel, E. Interactions of Tubulin with Potent Natural and Synthetic Analogs of the Antimitotic Agent Combretastatin: A Structure-Activity Study. *Molecular Pharmacology* **1988**, *34* (2), 200–208.

(22) Shaner, N. C.; Campbell, R. E.; Steinbach, P. A.; Giepmans, B. N. G.; Palmer, A. E.; Tsien, R. Y. Improved Monomeric Red, Orange and Yellow Fluorescent Proteins Derived from Discosoma Sp. Red Fluorescent Protein. *Nat Biotechnol* **2004**, *22* (12), 1567–1572. https://doi.org/10.1038/nbt1037.

(23) Meijering, E.; Dzyubachyk, O.; Smal, I. Chapter Nine - Methods for Cell and Particle Tracking. In *Methods in Enzymology*; conn, P. M., Ed.; Imaging and Spectroscopic Analysis of Living Cells; Academic Press, 2012; Vol. 504, pp 183–200. https://doi.org/10.1016/B978-0-12-391857-4.00009-4.

(24) Kapitein, L. C.; Yau, K. W.; Hoogenraad, C. C. Microtubule Dynamics in Dendritic Spines. *Methods Cell Biol* **2010**, *97*, 111–132. https://doi.org/10.1016/S0091-679X(10)97007-6.

(25) Merriam, E. B.; Millette, M.; Lumbard, D. C.; Saengsawang, W.; Fothergill, T.; Hu, X.; Ferhat, L.; Dent, E. W. Synaptic Regulation of Microtubule Dynamics in Dendritic Spines by Calcium, F-Actin, and Drebrin. *J. Neurosci.* **2013**, *33* (42), 16471. https://doi.org/10.1523/JNEUROSCI.0661-13.2013.

(26) Yvon, A.-M. C.; Wadsworth, P.; Jordan, M. A. Taxol Suppresses Dynamics of Individual Microtubules in Living Human Tumor Cells. *MBoC* **1999**, *10* (4), 947–959. https://doi.org/10.1091/mbc.10.4.947.

(27) Kikumoto, M.; Kurachi, M.; Tosa, V.; Tashiro, H. Flexural Rigidity of Individual Microtubules Measured by a Buckling Force with Optical Traps. *Biophysical Journal* **2006**, *90* (5), 1687–1696. https://doi.org/10.1529/biophysj.104.055483.

(28) Bechstedt, S.; Lu, K.; Brouhard, G. J. Doublecortin Recognizes the Longitudinal Curvature of the Microtubule End and Lattice. *Current Biology* **2014**, *24* (20), 2366–2375. https://doi.org/10.1016/j.cub.2014.08.039.

(29) Dye, R. B.; Fink, S. P.; Williams, R. C. Taxol-Induced Flexibility of Microtubules and Its Reversal by MAP-2 and Tau. *Journal of Biological Chemistry* **1993**, *268* (10), 6847–6850.

6 Exhaustive *ortho*-alkoxylation of azobenzenes to create diverse substitution patterns

Unsubstituted azobenzene can be isomerised *E*→*Z* with ~310 nm and *Z*→*E* with ~440 nm light. The light absorption properties of an azobenzene are strongly dependant on its substitution pattern. For biological applications it is desirable to have the highest separation of absorbance bands between the two isomers, as well as having absorptions shifted towards the longer wavelength region of the visible spectrum. A strategy to separate the absorption bands of the isomers, while making the azobenzene completely visible light addressable, is tetra-*ortho*-substitution. There are several examples of tetra-*ortho*-substitution in literature - most prominently tetrafluoro[31], tertrachloro[102] and tetramethoxy[44]; however, the synthetic access to these molecules can be challenging.

In this paper we present a method for the preparation of tetra-*ortho*-alkoxylated azobenzenes via exhaustive palladium-catalysed C-H activation. We present our efforts to optimize the reaction between azobenzene and primary alcohols. We observed that contrary to the usual C-H activation protocols, a decrease in temperature lead to an increase in product formed, as a decrease in temperature increases the lifetime of the catalyst and slows down the formation of palladium black. The reaction temperature was reduced to 40 °C for the best yield of exhaustively alkoxylated product. Other screened reaction conditions (solvent, catalyst loading, additives) did not strongly improve the reaction outcome.

With optimised conditions in hand, we examined the scope of our transformation with *para* and *meta* substituents. The reaction tolerates several functional groups (esters, nitro groups, halogens) but struggles with electron-donating groups. Weakly electron-donating groups decrease the yield significantly in *para*-position (alkyl); strongly donating groups (methoxy) are only tolerated in *meta*-position. However, different primary alcohols can be used in the reaction – eg methanol, ethanol, propanol etc. Depending on the azobenzene used as starting material, different substitution patterns can be introduced. The strategic introduction of tetra-*ortho*-alkoxy substitution allowed us to conduct a systematic test of the influence of differently bulky and hydrophobic alkoxy groups in *ortho* positions on the photoproperties of the azobenzene.

We also prepared compounds that carry a mixture of fluoro and methoxy substituents. They show well separated absorption spectra of *E* and *Z*-isomers and allow for an almost quantitative isomerisation to the *Z* isomer (95%).

Notably too, we prepared a water soluble azobenzene by introducing 1,3-propandiol in the ortho positions. The modification could help solubilise notoriously insoluble photopharmaceutical agents in a late state transformation.

Finally, we were able to access d_{12} azobenzenes by cheaply installing deuterated methoxy groups in the *ortho* position. Given that photopharmaceuticals are being pushed towards *in vivo* applications, such labelling could be useful for deeper investigations into the metabolic pathways of azobenzenes.

In conclusion, we present a new method for the preparation of per-*ortho*-alkoxylated azobenzenes and demonstrate the power of our newfound method by exploring its limits in substrate scope, allowing us the prepare new azobenzenes with thus far unexplored *ortho*-substitution patterns.

Exhaustive catalytic *ortho*-alkoxylation of azobenzenes: flexible access to functionally diverse yellow-light-responsive photoswitches

Adrian Müller-Deku[1], Oliver Thorn-Seshold[1,*]

1: Department of Pharmacy, Ludwig-Maximilians University, Butenandtstrasse 5-13, Munich 81377, Germany.
ORCIDs: A.M-D. 0000-0001-6050-2545; O.T.-S. 0000-0003-3981-651X
* Correspondence to O.T.-S. (oliver.thorn-seshold@cup.lmu.de)

Keywords: azobenzene, C-H activation, photoswitch, photopharmacology, catalysis.

ABSTRACT: We develop the first method for catalytic, exhaustive *ortho*-alkoxylation of azobenzene photoswitches. Alkoxylation is known to improve the photoswitch properties that control azobenzenes' success in chemical biology or materials sciences: e.g. better completeness of both *E*→*Z* and *Z*→*E* photoisomerisations, and >100 nm red-shifting of photoresponse. Our method enables straightforward late-stage diversification of photoswitches with interesting functional handles. We showcase four applications, using it to rationally tune lipophilicity, prepare isotopic tracers for metabolism studies, install full water solubility without ionic charges, and efficiently access previously difficult mixed-substituent photoswitches. We also identified a previously unstudied mixed-substituent tetra-*ortho*-family, difluoro-dialkoxy-azobenzenes, whose photoresponse can outperform previous 'gold standard' tetrafluoro-, dichloro-difluoro-, and tetrachloro-azobenzenes in significant ways. We thus expect that both the scaffolds we showcase and the method we develop will impact broadly on photochemistry and photopharmacology.

INTRODUCTION

Reversible *E*→*Z* and *Z*→*E* isomerisations of azobenzenes can be effected with UV/visible light[1], as well as with redox reactions following photocatalysis[2], electrocatalysis[3], or X-ray illumination[4]. The high spatiotemporal precision, non-invasiveness, and rapidity with which bulk populations of azobenzenes can be photoisomerised in both *E*→*Z* and *Z*→*E* directions has made azobenzene photoswitching a powerful tool for manipulating the physical and optical properties of solid materials[5], the electronic and dynamic properties of soft matter[6], and for controlling protein functions and downstream cascades in biochemistry, cell biology, and in adult animals.[7–12]

Azobenzene photoresponse and isomerisation completeness are critical for all these applications. Alkylazobenzenes respond efficiently to light only up to ca. 500 nm. They are often best photoisomerised around 360 nm (giving photostationary states (PSSs) of ca. 20:80 *E*:*Z*), and around 450 nm (PSSs ca. 80:20 *E*:*Z*).[13,14]

Several azobenzene substitution patterns have been developed to tune the isomers' spectra, and thus the photoresponsiveness and completion of photoisomerisations.[15] Tetra-*ortho*-substitutions particularly improve photoswitch performance, without necessarily compromising function (as most azobenzene photopharmaceuticals are "azo-extension" or "azo-linker" designs[16] where only the 4,4' positions determine bioactivity).[17–20] Hecht's tetra-*ortho*-fluoro pattern gives excellent *E*→*Z* isomerisation at 500 nm and *Z*→*E* at 400 nm.[21] Woolley's sterically congested tetra-*ortho*-methoxy,[22] -thioalkyl[23], and -chloro[24] azobenzenes improved on older tetra-*ortho*-alkyl azobenzenes,[25,26] with still better *E*→*Z* isomerisation at 550 nm (for good biocompatibility and depth penetration) making them alluring for photopharmacology *in vivo*;[12] *Z*→*E* isomerisation is most complete at 400 nm (see **Supporting Note 1**).[21,22] However, most tetra-*ortho* syntheses are inflexible, needing *ortho*-substituents to be introduced early and carried through synthesis;[24,27] the only exhaustive late-stage *ortho*-derivatisations reported are tetra-*ortho*-chlorination (**Fig 1a**)[20,28] and a similar method for tetra-*ortho*-bromination[28].

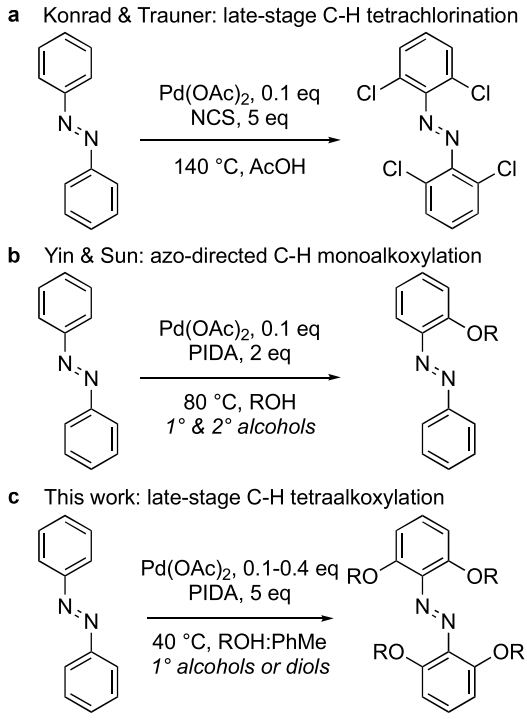

Figure 1. Towards per-*ortho*-alkoxylation. (a) Konrad and Trauner's per-*ortho*-chlorination.[20] (b) Yin and Sun's mono-*ortho*-alkoxylation.[29] (c) Pd-catalysed per-*ortho*-alkoxylation reported here.

The particular allure of the tetra-*ortho*-alkoxy pattern is that, unlike tetra-halides, it offers four ideal sites for functional diversification (as the alkyl part should not affect photoresponse). Yet, lacking a modular tetra-*ortho*-alkoxylation method, essentially no scope of functional *ortho*-substituents has been explored: e.g. these positions have never been exploited for solubilisation, isotopic labelling, or rational logD tuning. Continuing our interest in polyalkoxylated photopharmaceuticals,[9,30,31] but aiming to avoid polyphenol alkylations (see **Supporting Note 1**), we here aimed to develop a flexible, late-stage, exhaustive *ortho*-alkoxylation procedure for azobenzenes.

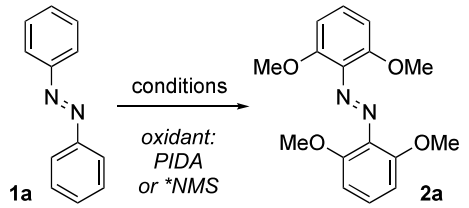

entry	T [°C]	solvent / OMe eq.	$Pd(OAc)_2$ [eq.]	isol. yield [%]
1	140	AcOH / NMS*	0.10	**-**
2	80	MeOH	0.10	**6**
3	60	MeOH	0.10	**9**
4	40	MeOH	0.10	**21**
5	40	MeOH:PhMe 1:1	0.10	**28**
6	40	MeOH:PhMe 1:1	0.20	**33**
7	40	MeOH:PhMe 1:1	0.40	**38**

Figure 2. Initial optimisation for temperature, cosolvent, and catalyst loading [NMS: *N*-methoxysuccinimide].

Results

Catalytic tetra-*ortho*-methoxylation of azobenzene

Palladium-catalysed CH-oxidation using the diazene as an *ortho*-directing group was developed from a stoichiometric into a catalytic, exhaustive *ortho*-chlorination method by Konrad and Trauner,[20] with *N*-chlorosuccinimide (NCS) acting as both oxidant and chlorine source (**Fig 1a**). We first tested if alkoxy analogues of NCS, e.g. *N*-methoxysuccinimide [NMS], could likewise function as both oxidant and alkoxy source, but saw no conversion (**Fig 2, entry 1**).

We then moved to alcohols as straightforward alkoxy sources, seeking tandem oxidation by another reagent to complete the turnover. Yin and Sun have made the only report of oxidative azobenzene *ortho*-alkoxylation, isolating mono-*ortho*-alkoxyazobenzenes in up to 77% yield by reacting a variety of non-, mono-*meta*-, and bis-*meta*-substituted azobenzenes with $Pd(OAc)_2$ (10 mol%), alcohol, and $PhI(OAc)_2$ [PIDA] oxidant (1-2 eq.) at 80°C (**Fig 1b**, mechanism in **Scheme S2**).[29] However, despite superstoichiometric oxidant, no polyalkoxylation was reported. Clean oxidative per-alkoxylation is anyway a challenging prospect, as each alkoxylation step will increase the substrate's electron density, so raising the chances of non-regiospecific or undesired oxidations (**Scheme S2**).

Aiming to achieve up to four CH-oxidations per azobenzene for clean per-*ortho*-alkoxylation (**Fig 1c**), we began our quest at Yin and Sun's mono-methoxylation conditions, raising oxidant loading to 5 mol. eq. (**Table S1**). HPLC-MS analysis revealed a low but encouraging 6% yield (**Fig 2, entry 2**). Residual substrate and monomethoxy intermediate were the major impurities isolated, with di- and trimethoxylated intermediates as trace products only, matching the expectation of increasing reactivity per alkoxylation step.

However, we observed rapid formation of palladium black during heating, as expected for reduction of $Pd(OAc)_2$ by methanol,[32] likely blocking reaction progress. As reduction was slower at lower temperatures, we screened down to 40°C under strict temperature control, increasing the tetra-substitution yield to 28% (**Fig 2, entries 3-4**). This is unusual for CH activations, that are generally favoured by high temperatures. As nitrogen ligands can stabilise $Pd(OAc)_2$ against reduction, we tested pyridine and 1,1'-bipyridine; while these prevented formation of palladium black, they also blocked alkoxylation (**Table S1, entries 8-10**).

Cosolvent, oxidant, additives, and catalyst loading

We next screened cosolvents to methanol (**Table S1, entries 11-25**); toluene improved yields, with good results at 1:1 MeOH:PhMe (**Fig 2, entry 5**). We also screened diluted conditions, since the solubility of PIDA is only moderate: but these lowered isolated yields greatly (**Table S1, entry 26**), coherent with the role of a dimeric intermediate (**Scheme S2**). PIDA was however superior to PIFA, oxone, or $K_2S_2O_8$ as the oxidant, and increasing its loading (10 eq.) only reduced yields (**Table S1, entries 27-32**). This is coherent with expectations that excess or stronger oxidants drive parasitic oxidations of the increasingly electron-rich intermediates/product. Acidic, basic, or dehydrating additives also did not give improvements (**Table S1, entries 33-40**). Instead, reaction yields improved when $Pd(OAc)_2$ loading was raised (**Fig 2, entries 6-7**).

Taken together, this screening had improved isolated yields of tetra-*ortho*-methoxylation to reach nearly 40% (**Fig 2, entry 7**), corresponding to ca. 75% yield per CH activation/C-O formation, which matches pleasingly to the single-step yields of Yin and Sun.[29]

Scope for azobenzene substituents

To study this method's substrate preference, we applied the conditions optimised for unsubstituted **1a** to a set of mono-substituted azobenzenes (**Fig 3**). Electron-donating groups in *para* gave poor (alkyl **2b**) to negligible (oxyether) yields, but were better tolerated in *meta* (**2c**-**2d**) (discussion at **Scheme S2**). Electron-poor *para*-substituents were successful (ester **2e**, halogens **2f-2g**, nitro **2h**). These patterns, which offer flexible derivatisation by reduction/acylation (nitro), esterification/amidation (ester), or cross-coupling (halide), can now be accessed by an easier and more tolerant route than previously possible with e.g. lithium base[27] methods.

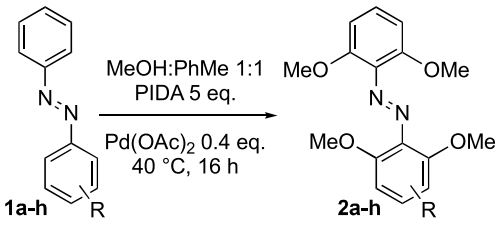

compound	position	R	yield [%]
2a	-	-	38
2b	*para*	Me	6
2c	*meta*	Me	28
2d	*meta*	OMe	4
2e	*para*	CO_2Me	18
2f	*para*	F	16
2g	*para*	Cl	15
2h	*para*	NO_2	23

Figure 3. Substituent effects on tetra-methoxylation [isolated yields].

ortho-alkoxylation as a functional handle

To explore the scope for exhaustive alkoxylation to products other than tetramethoxy species, we tested alcohols other than methanol, and performed reactions on partially-*ortho*-substituted substrates (**Fig 4**). Secondary alcohols (*i*PrOH) gave only traces of tetraalkoxylation, and tertiary alcohols (*t*BuOH) gave no conversion, which is understandable due to sterics. Though electron-poor primary alcohols (CF_3CH_2OH) were unreactive, we found good scope for primary alcohols, which enables tackling four novel applications:

(1) Lipophilicity is a key property for cellular pharmacology, impacting apparent on-target affinity, off-target binding, subcellular localisation, bioavailability, and membrane permeation.[33] Late-stage per-alkoxylations could give diversified sets of spectrally identical photopharmaceuticals, with rationally tuned logD values according to the alkoxy residues attached: for convenient validation of their mechanism of action, or for potency optimisation. Per-alkoxylation with OMe, OEt and OPr groups on mono-, di- and tri-alkoxy substrates (**3a-3j**) gave respectable yields (ca. 55% per substitution).

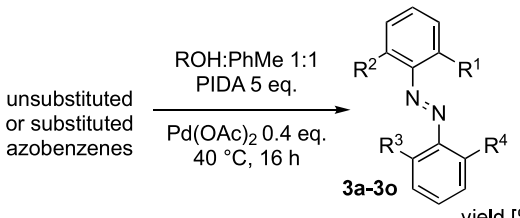

compound	R^1	R^2	R^3	R^4	yield [% per substitution]
Lipophilicity Tuning					
3a	**OMe**	**OMe**	**OMe**	(OEt)	54
3b	(OMe)	**OEt**	(OMe)	**OEt**	40
3c	(OMe)	(OMe)	**OEt**	**OEt**	67
3d	(OMe)	**OEt**	**OEt**	**OEt**	54
3e	**OEt**	**OEt**	**OEt**	**OEt**	58
3f	(OMe)	**OPr**	(OMe)	**OPr**	53
3g	(OMe)	(OMe)	**OPr**	**OPr**	88
3h	(OMe)	**OPr**	**OPr**	**OPr**	63
3i	(OEt)	**OPr**	**OPr**	**OPr**	43
3j	**OPr**	**OPr**	**OPr**	**OPr**	47
Mixed Substituents					
3k	**OMe**	**OMe**	**OMe**	(F)	55
3l	**OMe**	(F)	**OMe**	(F)	33
3m	**OMe**	**OMe**	(F)	(F)	22
Isotopic Labelling					
3n	**OCD_3**	**OCD_3**	**OCD_3**	**OCD_3**	70
Water Solubility					
3o	**OPrOH**	**OPrOH**	**OPrOH**	**OPrOH**	45

Figure 4. Per-*ortho*-alkoxylations of a range of azobenzenes giving otherwise difficult to access or unreported substituent patterns. Bracketed residues, e.g. (OMe), were present in the starting materials; bold residues were introduced by the reaction [isolated yields].

(2) Asymmetry: The optical properties of symmetric tetra-*ortho*-substituted azobenzenes have been explored (see **Introduction**). However, only a few asymmetric tetra-*ortho* azobenzenes (where substituents differ from each other) have been studied, and these only recently: yet strong performance enhancements were already found.[19] Exhaustive alkoxylation of partially *ortho*-substituted substrates offers a convenient synthetic access to otherwise time-intensive mixed-substituent patterns that have not yet been systematically explored. Pleasingly, mixed fluoro/alkoxy tetra-*ortho* azobenzenes **3k-3m** were all accessed with moderate yields, for later study.

(3) Metabolism: As photopharmacology moves towards applications in adult animals,[10–12] monitoring the metabolism of yellow/red-light responsive photoswitches will become increasingly urgent. We know of no reports preparing isotopically-labelled photopharmaceuticals for unbiased MS-based metabolite studies, which typically require light/heavy drug pairs with >M+5 for the heavy drug:[34] but reasoned that exhaustive *ortho*-alkoxylation is an attractive method to do so. Using CH_3OH/CD_3OD provides up to M+12 difference in light/heavy masses of scaffold-intact metabolites, M+6 difference of the principal hypothesised azobenzene metabolites (N=N scission products), or M+9 difference of mono-*ortho*-demethylated species: all of which are sufficient for unbiased metabolite detection, and which may reveal the *in vivo* fate of photopharmaceuticals. Yields of tetra-*ortho*-(OCD_3) derivatisation were good (**3n**).

(4) Solubility: Like most photoswitches (typically, flat aromatics), azobenzenes have very poor water solubility and tend to aggregate; this complicates their photoswitching and spectra,[13,35] and hampers applications from materials sciences through to biology.[36] Exhaustive alkoxylation with diols could be a late-stage solubilising method that also provides beneficial tetra-*ortho* photoresponse, without crowding the *para*-positions needed for "azo-extension" and "azo-linker" photopharmacology,[8] and without charges that complicate bioactivity. Tetra-alkoxylation with propylene glycol gave good isolated yields of water-soluble tetrol **3o** (45% per substitution): the first example we know of such solubilisation in photoswitching.

Photoswitching performance

The tetra-*ortho*-alkoxyazobenzenes' optical properties matched Woolley's reports[22,24]. They absorb well in the visible, with substantial separation between the isomers' band maxima giving ca. 80% *Z* at PSS under 550 nm, and ca. 85% *E* at PSS under 405 nm (**Fig 5a-b**, **3i**/**3o**). Bulk photoswitching with blue and green light was efficient; and despite low absorption coefficients above 550 nm they can be isomerised by yellow light up to 600 nm (**Fig 5c**, **Fig S2**). The spontaneous *Z*→*E* relaxation of all derivatives was slow on relevant timescales (halflives > 7 days; **Fig S2a**). Bidirectional photoswitching was fully reversible without detectable losses over tens of cycles (**Fig S2b**). Water-soluble tetrol **3o** was assayed in all-aqueous buffer, supporting the utility of this approach for biology (**Fig 5, Fig S2**).

This straightforward access to per-*ortho*-alkoxylated azobenzenes can now drive systematic investigations, identifying promising new switches. For example, difluoro-dialkoxy-azobenzenes were only accessed once before,[27] though their photoswitching was not investigated and they have not been practically applied. We saw that both asymmetric and symmetric difluoro-dialkoxy **3m** and **3l** had ca. 20 nm more separation between the $n\rightarrow\pi^*$ bands of their *E*- and *Z*-isomers than tetra-alkoxy derivatives (**Fig S2c**). This greater separation drives excellent completeness of *E*→*Z* photoswitching under green light (only 4-5% *E* remaining, **Fig 5a**), which outperforms tetra-*ortho*-alkoxy- (20%) and even difluoro-dichloro-azobenzenes[19] (15%) by several fold, while all have comparable *Z*→*E* conversion. Symmetric **3l** also has a ca. 20 nm red-shift of *E*→*Z* photoresponse compared to popular tetra-*ortho*-fluoro[21] species (asymmetric **3m** has a 30 nm blue-shift); and both enjoy the benefits of the flexible alkoxy handles. This performance and access recommend them for adoption, and should more broadly motivate studies of mixed substitution patterns to refine the photochemistry, biophysical properties, and functions accessible for photopharmacology.

a

PSS %Z	405	435	470	490	525	550	λ (nm)
3i	**11**	**16**	43	55	78	81	
3m	**18**	23	66	90	**94**	**95**	
3l	22	34	80	87	**95**	**96**	
3o	**16**	18	44	57	76	80	

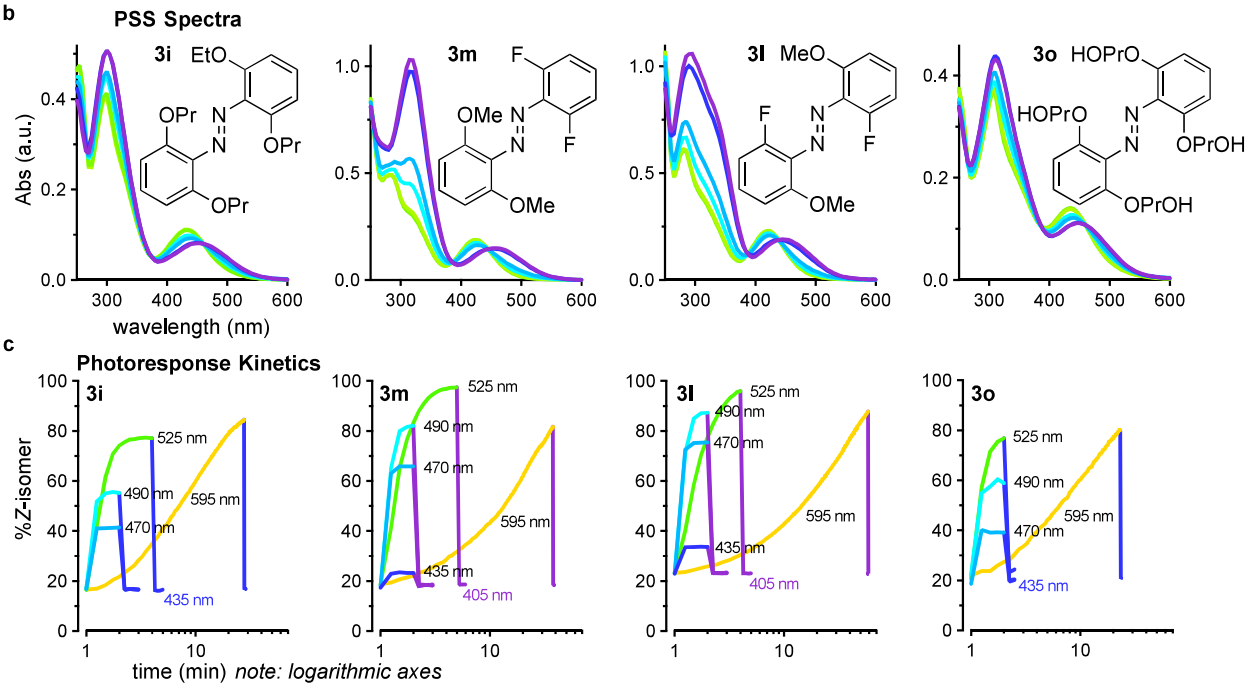

Figure 5. Optical properties. **(a-b)** Photostationary state (PSS) *E*:*Z* proportions (by HPLC) and corresponding UV-Vis absorption spectra. **(c)** *E*⇌*Z* photoisomerisation timecourses illustrating variations of photoresponse speed and completeness with wavelength. *E*→*Z* photoswitching was performed with the annotated test wavelengths starting at t=1 min; at the end of each test, *Z*→*E* back-switching was performed at 435 nm or 405 nm to verify photoreversibility (LED sources, see discussion at **Fig S2-S3**). Spectra measured in MeCN (**3i**, **3m**, **3l**) or in deionised water (**3o**).

Conclusion

Tetra-*ortho*-alkoxyazobenzenes feature all-visible-light bidirectional photoswitching that is substantially complete in both *E*→*Z* and *Z*→*E* directions.[22] Unlike bridging[37,38] or tetra-*ortho*-halogenation[19,21] approaches to redshift azobenzene photoresponses, per-*ortho*-alkoxylation offers up to four flexible handles for installing functionality, potentially without compromising bioactivity or *Z*-isomer stability.

Building mainly on the works of Konrad and Trauner[20] and of Yin and Sun[29], we here present the first method for exhaustive *ortho*-alkoxylation of electron-poor to electron-neutral azobenzenes with primary alcohols, giving isolated yields around 50-75% per alkoxylation. The congested structures accessible by this method are not easily accessible otherwise. It both enables late-stage diversification, and also simplifies synthesis in general by avoiding the need to install alkoxy substituents before azobenzene formation.

We also present method applications that may extensively impact photopharmacology (**Fig 4**): stepwise tuning of lipophilicity in a spectrally identical series of derivatives; poly-deuteration for unbiased metabolism studies; conversion to water-soluble uncharged polyols; and new access to hitherto poorly-studied switches. The latter led us to identify difluoro-dialkoxy-azobenzenes as highly performant photoswitches (**Fig 5**). Since the greater sensitivity of tetra-*ortho*-alkoxy-azobenzenes to bithiol-mediated degradation (as compared to their tetra-*ortho*-halo counterparts) is a concern for long-term biological studies,[24] this method towards new difluoro-dialkoxy switches may prove particularly valuable for chemical biology: by finally combining the biological stability of halogenation with the functional flexibility of alkoxylation (on top of the general photophysical benefits of tetra-*ortho*-substitution patterns).

This straightforward and flexible method for functional photoswitch tuning can therefore promote access to a range of efficiently and bidirectionally visible-light responsive, metabolically traceable, solubilised, and rationally tunable azobenzene photoswitches, with particular applications to materials sciences and chemical biology.

ASSOCIATED CONTENT

Supporting Information

The Supporting Information is available free of charge on the ACS Publications website.

PDF containing synthetic protocols; photocharacterisation; and NMR spectra.

Datafile (XLSX) with *E*/*Z* and PSS spectra of selected compounds.

AUTHOR INFORMATION

Corresponding Author

* Correspondence to O.T.-S. (oliver.thorn-seshold@cup.lmu.de)

Author Contributions

A.M.-D. performed all synthesis, characterisation, and data assembly. O.T.-S. designed the study, supervised experiments, and wrote the manuscript.

Funding Sources

This research was supported by funds from the German Research Foundation (DFG: SFB1032 Nanoagents for Spatiotemporal Control project B09 number 201269156; SFB TRR 152 project P24 number 239283807, Emmy Noether grant TH2231/1-1 number 400324123, and SPP 1926 project number 426018126).

ACKNOWLEDGMENT

We thank Nurunnisa Özyürek and Nesrin Hamou (LMU) for synthesis, Dr. Lars Allmendinger (Zentral Analytik, LMU) for NMR, and Martin Maier (LMU) for manuscript feedback.

ABBREVIATIONS

NMS: *N*-methoxysuccinimide; PIDA, phenyliodine(III) diacetate; PIFA, phenyliodine(III) bis(trifluoroacetate); PBS, phosphate-buffered saline.

REFERENCES

(1) Jerca, F. A.; Jerca, V. V.; Hoogenboom, R. Advances and Opportunities in the Exciting World of Azobenzenes. *Nature Reviews Chemistry* **2021**, 1–19. https://doi.org/10.1038/s41570-021-00334-w.

(2) Goulet-Hanssens, A.; Rietze, C.; Titov, E.; Abdullahu, L.; Grubert, L.; Saalfrank, P.; Hecht, S. Hole Catalysis as a General Mechanism for Efficient and Wavelength-Independent Z → E Azobenzene Isomerization. *Chem* **2018**, *4* (7), 1740–1755. https://doi.org/10.1016/j.chempr.2018.06.002.

(3) Greenfield, J. L.; Gerkman, M. A.; Gibson, R. S. L.; Han, G. G. D.; Fuchter, M. J. Efficient Electrocatalytic Switching of Azoheteroarenes in the Condensed Phases. *JACS* **2021**, *143* (37), 15250–15257. https://doi.org/10.1021/jacs.1c06359.

(4) Ober, M. F.; Müller-Deku, A.; Baptist, A.; Amenitsch, H.; Thorn-Seshold, O.; Nickel, B. SAXS Measurements of Azobenzene Lipid Vesicles Reveal Buffer-Dependent Photoswitching and Quantitative Z->E Isomerisation by X-Rays. *ArXiv211112570 Cond-Mat Physicsphysics* **2021**.

(5) Russew, M.-M.; Hecht, S. Photoswitches: From Molecules to Materials. *Advanced Materials* **2010**, *22* (31), 3348–3360. https://doi.org/10.1002/adma.200904102.

(6) Boelke, J.; Hecht, S. Designing Molecular Photoswitches for Soft Materials Applications. *Advanced Optical Materials* **2019**, *7* (16), 1900404. https://doi.org/10.1002/adom.201900404.

(7) Beharry, A. A.; Woolley, G. A. Azobenzene Photoswitches for Biomolecules. *Chem Soc Rev* **2011**, *40* (8), 4422–4437. https://doi.org/10.1039/C1CS15023E.

(8) Hüll, K.; Morstein, J.; Trauner, D. In Vivo Photopharmacology. *Chemical Reviews* **2018**, *118* (21), 10710–10747. https://doi.org/10.1021/acs.chemrev.8b00037.

(9) Borowiak, M.; Nahaboo, W.; Reynders, M.; Nekolla, K.; Jalinot, P.; Hasserodt, J.; Rehberg, M.; Delattre, M.; Zahler, S.; Vollmar, A.; Trauner, D.; Thorn-Seshold, O. Photoswitchable Inhibitors of Microtubule Dynamics Optically Control Mitosis and Cell Death. *Cell* **2015**, *162* (2), 403–411. https://doi.org/10.1016/j.cell.2015.06.049.

(10) Gómez-Santacana, X.; Pittolo, S.; Rovira, X.; Lopez, M.; Zussy, C.; Dalton, J. A. R.; Faucherre, A.; Jopling, C.; Pin, J.-P.; Ciruela, F.; Goudet, C.; Giraldo, J.; Gorostiza, P.; Llebaria, A. Illuminating Phenylazopyridines To Photoswitch Metabotropic Glutamate Receptors: From the Flask to the Animals. *ACS-CS* **2017**, *3* (1), 81–91. https://doi.org/10.1021/acscentsci.6b00353.

(11) Hüll, K.; Fernández-Dueñas, V.; Schönberger, M.; López-Cano, M.; Trauner, D.; Ciruela, F. Optical Control of Adenosine-Mediated Pain Modulation. *Bioconj Chem* **2021**, *32* (9), 1979–1983. https://doi.org/10.1021/acs.bioconjchem.1c00387.

(12) Frank, J. A.; Antonini, M.-J.; Chiang, P.-H.; Canales, A.; Konrad, D. B.; Garwood, I. C.; Rajic, G.; Koehler, F.; Fink, Y.; Anikeeva, P. In Vivo Photopharmacology Enabled by Multifunctional Fibers. *ACS-ChemNeurosci* **2020**, *11* (22), 3802–3813. https://doi.org/10.1021/acschemneuro.0c00577.

(13) Urban, P.; Pritzl, S. D.; Konrad, D. B.; Frank, J. A.; Pernpeintner, C.; Roeske, C. R.; Trauner, D.; Lohmüller, T. Light-Controlled Lipid Interaction and Membrane Organization in Photolipid Bilayer Vesicles. *Langmuir* **2018**, *34* (44), 13368–13374. https://doi.org/10.1021/acs.langmuir.8b03241.

(14) Frank, J. A.; Moroni, M.; Moshourab, R.; Sumser, M.; Lewin, G. R.; Trauner, D. Photoswitchable Fatty Acids Enable Optical Control of TRPV1. *NComm* **2015**, *6*, 7118. https://doi.org/10.1038/ncomms8118 https://www.nature.com/articles/ncomms8118#supplementary-information.

(15) Küllmer, F.; Gregor, L.; Arndt, H.-D. Property-Selected Asymmetric Azobenzenes for Photoswitchable Ligands. *ChemRxiv* **2022**. https://doi.org/10.26434/chemrxiv-2022-fd950.

(16) Müller-Deku, A.; Meiring, J. C. M.; Loy, K.; Kraus, Y.; Heise, C.; Bingham, R.; Jansen, K. I.; Qu, X.; Bartolini, F.; Kapitein, L. C.; Akhmanova, A.; Ahlfeld, J.; Trauner, D.; Thorn-Seshold, O. Photoswitchable Paclitaxel-Based Microtubule Stabilisers Allow Optical Control over the Microtubule Cytoskeleton. *NComm* **2020**, *11* (1), 4640. https://doi.org/10.1038/s41467-020-18389-6.

(17) Volgraf, M.; Gorostiza, P.; Numano, R.; Kramer, R. H.; Isacoff, E. Y.; Trauner, D. Allosteric Control of an Ionotropic Glutamate Receptor with an Optical Switch. *NChB* **2006**, *2* (1), 47–52. https://doi.org/10.1038/nchembio756.

(18) Wegener, M.; Hansen, M. J.; Driessen, A. J. M.; Szymanski, W.; Feringa, B. L. Photocontrol of Antibacterial Activity: Shifting from UV to Red Light Activation. *JACS* **2017**, *139* (49), 17979–17986. https://doi.org/10.1021/jacs.7b09281.

(19) Konrad, D. B.; Savasci, G.; Allmendinger, L.; Trauner, D.; Ochsenfeld, C.; Ali, A. M. Computational Design and Synthesis of a Deeply Red-Shifted and Bistable Azobenzene. *JACS* **2020**, *142* (14), 6538–6547. https://doi.org/10.1021/jacs.9b10430.

(20) Konrad, D. B.; Frank, J. A.; Trauner, D. Synthesis of Redshifted Azobenzene Photoswitches by Late-Stage Functionalization. *Chemistry* **2016**, *22* (13), 4364–4368. https://doi.org/10.1002/chem.201505061.

(21) Bléger, D.; Schwarz, J.; Brouwer, A. M.; Hecht, S. O-Fluoroazobenzenes as Readily Synthesized Photoswitches Offering Nearly Quantitative Two-Way Isomerization with Visible Light. *JACS* **2012**, *134* (51), 20597–20600. https://doi.org/10.1021/ja310323y.

(22) Beharry, A. A.; Sadovski, O.; Woolley, G. A. Azobenzene Photoswitching without Ultraviolet Light. *JACS* **2011**, *133* (49), 19684–19687. https://doi.org/10.1021/ja209239m.

(23) Samanta, S.; McCormick, T. M.; Schmidt, S. K.; Seferos, D. S.; Woolley, G. A. Robust Visible Light Photoswitching with Ortho-Thiol Substituted Azobenzenes. *Chemical Communications* **2013**, *49* (87), 10314–10316. https://doi.org/10.1039/C3CC46045B.

(24) Samanta, S.; Beharry, A. A.; Sadovski, O.; McCormick, T. M.; Babalhavaeji, A.; Tropepe, V.; Woolley, G. A. Photoswitching Azo Compounds in Vivo with Red Light. *JACS* **2013**, *135* (26), 9777–9784. https://doi.org/10.1021/ja402220t.

(25) Forber, C. L.; Kelusky, E. C.; Bunce, N. J.; Zerner, M. C. Electronic Spectra of Cis- and Trans-Azobenzenes: Consequences of Ortho Substitution. *JACS* **1985**, *107* (21), 5884–5890. https://doi.org/10.1021/ja00307a009.

(26) Bisle, H.; Rau, H. Fluorescence of Noncyclic Azo Compounds with a Low-Lying 1(n,Π*)State. *Chem Phys Lett* **1975**, *31* (2), 264–266. https://doi.org/10.1016/0009-2614(75)85017-2.

(27) Hansen, M. J.; Lerch, M. M.; Szymanski, W.; Feringa, B. L. Direct and Versatile Synthesis of Red-Shifted Azobenzenes. *Angewandte Chemie* **2016**, *128* (43), 13712–13716. https://doi.org/10.1002/ange.201607529.

(28) Liu, Q.; Luo, X.; Wei, S.; Wang, Y.; Zhu, J.; Liu, Y.; Quan, F.; Zhang, M.; Xia, C. Palladium-Catalyzed Direct Ortho CX Bond Construction via CH Activation of Azobenzenes: Synthesis of (E)-1,2-b(2,6-Dibromo(Chloro)-Phenyl)Diazene. *Tet Lett* **2019**. https://doi.org/10.1016/j.tetlet.2019.05.056.

(29) Yin, Z.; Jiang, X.; Sun, P. Palladium-Catalyzed Direct Ortho Alkoxylation of Aromatic Azo Compounds with Alcohols. *JOC* **2013**, *78* (19), 10002–10007. https://doi.org/10.1021/jo401623j.

(30) Sailer, A.; Meiring, J. C. M.; Heise, C.; Pettersson, L. N.; Akhmanova, A.; Thorn-Seshold, J.; Thorn-Seshold, O. Pyrrole Hemithioindigo Antimitotics with Near-Quantitative Bidirectional Photoswitching Photocontrol Cellular Microtubule Dynamics with Single-Cell Precision. *Angewandte Chemie International Edition* **2021**, *n/a* (n/a). https://doi.org/10.1002/anie.202104794.

(31) Gao, L.; Meiring, J. C. M.; Varady, A.; Ruider, I. E.; Heise, C.; Wranik, M.; Velasco, C. D.; Taylor, J. A.; Terni, B.; Standfuss, J.; Cabernard, C. C.; Llobet, A.; Steinmetz, M. O.; Bausch, A. R.; Distel, M.; Thorn-Seshold, J.; Akhmanova, A.; Thorn-Seshold, O. In Vivo Photocontrol of Microtubule Dynamics and Integrity, Migration and Mitosis, by the Potent GFP-Imaging-Compatible Photoswitchable Reagents SBTubA4P and SBTub2M. *bioRxiv* **2021**. https://doi.org/10.1101/2021.03.26.437160.

(32) Iwasawa, T.; Tokunaga, M.; Obora, Y.; Tsuji, Y. Homogeneous Palladium Catalyst Suppressing Pd Black Formation in Air Oxidation of Alcohols. 2.

(33) Landry, M. L.; Crawford, J. J. LogD Contributions of Substituents Commonly Used in Medicinal Chemistry. *ACS-MedChemLett* **2020**, *11* (1), 72–76. https://doi.org/10.1021/acsmedchemlett.9b00489.

(34) Arrivault, S.; Guenther, M.; Fry, S. C.; Fuenfgeld, M. M. F. F.; Veyel, D.; Mettler-Altmann, T.; Stitt, M.; Lunn, J. E. Synthesis and Use of Stable-Isotope-Labeled Internal Standards for Quantification of Phosphorylated Metabolites by LC–MS/MS. *Analytical Chemistry* **2015**, *87* (13), 6896–6904. https://doi.org/10.1021/acs.analchem.5b01387.

(35) Urban, P.; Pritzl, S. D.; Ober, M. F.; Dirscherl, C. F.; Pernpeintner, C.; Konrad, D. B.; Frank, J. A.; Trauner, D.; Nickel, B.; Lohmueller, T. A Lipid Photoswitch Controls Fluidity in Supported Bilayer Membranes. *Langmuir* **2020**, *36* (10), 2629–2634. https://doi.org/10.1021/acs.langmuir.9b02942.

(36) Thorn-Seshold, O. Photoswitchable Cytotoxins. In *Molecular Photoswitches*; Wiley, 2022.

(37) Maier, M. S.; Hüll, K.; Reynders, M.; Matsuura, B. S.; Leippe, P.; Ko, T.; Schäffer, L.; Trauner, D. Oxidative Approach Enables Efficient Access to Cyclic Azobenzenes. *JACS* **2019**, *141* (43), 17295–17304. https://doi.org/10.1021/jacs.9b08794.

(38) Lentes, P.; Stadler, E.; Röhricht, F.; Brahms, A.; Gröbner, J.; Sönnichsen, F. D.; Gescheidt, G.; Herges, R. Nitrogen Bridged Diazocines: Photochromes Switching within the Near-Infrared Region with High Quantum Yields in Organic Solvents and in Water. *JACS* **2019**, *141* (34), 13592–13600. https://doi.org/10.1021/jacs.9b06104.

TOC graphic

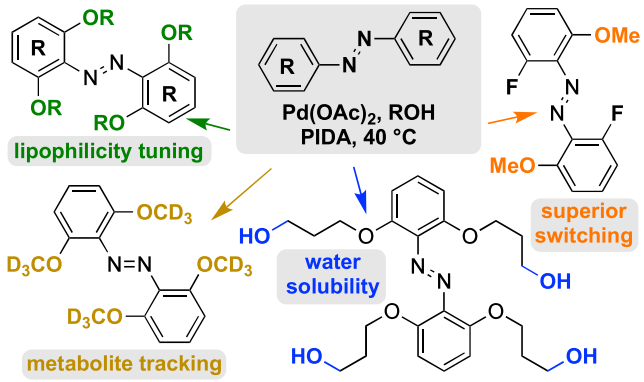

Supporting Information to:

Exhaustive catalytic *ortho*-alkoxylation of azobenzenes: flexible access to functionally diverse yellow-light-responsive photoswitches

Adrian Müller-Deku[1], Oliver Thorn-Seshold[1,*]

1: Department of Pharmacy, Ludwig-Maximilians University, Butenandtstrasse 5-13, Munich 81377, Germany.

* Correspondence to O.T.-S. (oliver.thorn-seshold@cup.lmu.de)

ORCIDs: A.M-D. 0000-0001-6050-2545; O.T.-S. 0000-0003-3981-651X

Table of Contents

Part A: Chemical Synthesis

Conventions

Abbreviations:

The following abbreviations are used: Boc – *tert*-butoxycarbonyl; brsm – based on recovered starting material; DCM: dichloromethane; DIPEA: diisopropylethylamine; DMF: dimethylformamide; DMSO: dimethylsulfoxide; EA: ethyl acetate; Hex/iHex: distilled isohexane; Me: methyl; TFA: trifluoroacetic acid; PBS – phosphate buffered saline; PIDA, phenyliodine(III) diacetate; PIFA, phenyliodine(III) bis(trifluoroacetate; wt% - percentage by weight.

Safety Hazards:

No unusual safety hazards were encountered.

Reagents and Conditions:

Unless stated otherwise, (1) all reactions and characterisations were performed with unpurified, undried, non-degassed solvents and reagents, used as obtained, under closed air atmosphere without special precautions; (2) "hexane" used for chromatography was distilled from commercial crude isohexane fraction by rotary evaporation; (3) "column" and "chromatography" refer to manual flash column chromatography on Merck silica gel Si-60 (40–63 μm) unless otherwise specified; (4) procedures and yields are unoptimised; (5) yields refer to isolated chromatographically and spectroscopically pure materials; (6) all eluent and solvent mixtures are given as volume ratios unless otherwise specified, thus "1:1 Hex:EA" indicates a 1:1 mixture (by volume) of hexanes and ethyl acetate; (7) chromatography eluent gradients e.g. "3:1 → 1:1" indicate continuous (small steps) changes of eluent composition.

Thin-layer chromatography (TLC):

TLC was run on 0.25 mm Merck silica gel plates (60, F-254), typically with Hex:EA eluents. All compounds carrying an azobenzene need no visualization on the TLC-plate but are clearly visible as colored spots (color range yellow to red). The presence of an azobenzene can be verified by exposure of the colored spot to TFA vapors, which transiently changes the color to shades of purple according to basicity. For further visualization UV light (254 nm) was used. TLC characterizations are abbreviated as $\mathbf{R}_f$ = 0.64 (UV 254 nm, EA:Hex = 1:1).

Nuclear magnetic resonance spectroscopy (NMR):

Standard NMR characterisation was by ^{1}H- and ^{13}C-NMR spectra on a Bruker Ascend 400 (400 MHz & 100 MHz for ^{1}H and ^{13}C respectively). Chemical shifts (δ) are reported in ppm calibrated to residual non-perdeuterated solvent as an internal reference[1]. Peak descriptions singlet (s), doublet (d), triplet (t), quartet (q), multiplet (m) and broad (br) are used. Apparent multiplicities (resolved by 2D experiments or determined by complete spectral assignment) are denoted by a tilde, eg. "appears as a triplet with apparent coupling constant J = 3 Hz" is denoted (~t, 3 Hz). NMR spectra are given in Part F.

High resolution mass spectrometry (HRMS):

HRMS was carried out by the Zentrale Analytik of the LMU Munich using EI or ESI ionisation in the positive mode as specified. HRMS was performed by electron impact (EI) at 70 eV with a Thermo Finnigan MAT 95 or a Jeol GCmate II spectrometer; or electrospray ionization (ESI) with a Thermo Finnigan LTQ FT Ultra Fourier Transform Ion Cyclotron resonance mass spectrometer; as specified.

.

Analytical high-performance liquid chromatography coupled to mass spectrometry (LCMS):

Analytical high-performance liquid chromatography (HPLC) was performed on an Agilent 1100SL coupled HPLC system with (a) a binary pump to deliver H_2O:MeCN eluent mixtures containing 0.1% formic acid at a 0.4 mL/min flow rate, (b) Thermo Scientific Hypersil GOLD™ C18 column (1.9 µm; 3 × 50 mm) maintained at 25°C, whereby the solvent front eluted at t_{ret} = 0.5 min, (c) an Agilent 1100 series diode array detector, (d) an Agilent LC/MSD iQ mass spectrometer. Typical run conditions were a linear gradient of H_2O:MeCN eluent composition from 90:10 through to 0:100, applied during the separation phase (first 10 min), then 0:100 for 2 min for flushing; the column was (re)equilibrated with 90:10 eluent mixture for 2 min before each run. Ion peaks from (positive/negative mode) are reported as (+/-) with units Th (m/z). Thus "LCMS(+): t_{ret} = 5.82 min, each 419 Th = $[MH]^+$" indicates LCMS under the standard run conditions with ESI ionisation giving a positive ion peaks eluting at 5.82 min retention at m/z = 419 Th, attributed as the protonated molecular ion. Unless stated otherwise, all reported peaks in the positive mode were $[MH]^+$ peaks.

Preparative high-performance liquid chromatography

Preparative high-performance liquid chromatography (prep-HPLC) was performed on an Agilent 1260 system with (a) a binary pump to deliver H_2O:MeCN eluent mixtures containing 0.1% formic acid at a 20 mL/min flow rate, (b)PrepHT C18 column (21.2 x 250 mm, 10 μM), (c) an Agilent 1260 series diode array detector. Typical run conditions were a linear gradient of H_2O:MeCN eluent composition from 90:10 through to 0:100, applied during the separation phase (first 28 min), then 0:100 for 2 min for flushing; the column was (re)equilibrated with 90:10 eluent mixture for 2 min before each run

Standard Procedures

Where Standard Procedures were used in synthesis, unless stated otherwise, the amounts of reactants/reagents employed were implicitly adjusted to maintain the same molar ratios as in the given Procedure, and no other alterations from the Standard Procedure (eg. reaction time, extraction solvent, temperature) were made, unless stated otherwise.

A: Asymmetric azobenzene preparation using Mills coupling

A flask was charged with a nitrosobenzene (1.2 eq, 2.4 mmol). Acetic acid (20 mL) was added. The aniline reaction partner (1 eq., 2 mmol) was added. The reaction mixture was stirred at

room temperature for 16 h. Upon completion water was added onto the reaction and the mixture was extracted with EA (3 x 50 mL). The combined organic phases were dried and concentrated. The crude product was purified using column chromatography (iHex:EA).

B: Pd-catalysed tetra-*ortho*-alkoxylation of an azobenzene

A flask was charged with the azobenzene (0.2 mmol, 1 eq.), $Pd(OAc)_2$ (18 mg, 0.08 mmol, 0.4 eq.) and PIDA (322 mg., 1 mmol, 5 eq.). Toluene (1 mL) and a primary alcohol (1 mL) were added. An oil bath was preheated to precisely 40 °C (avoiding overheating which can happen e.g. with air-cooled aluminium thermoblocks going through temperature fluctuations is important for yields). The flask was placed in the oil bath, equipped with a reflux condenser and the reaction was allowed to stir for 16 h. Subsequently, the solvent was removed *in vacuo*. The crude product was purified by column chromatography (iHex:EA = 7:3 → 1:1). In case of unsatisfactory purity the products were repurified using the standard preparative HPLC method.

C: Symmetrical azobenzene preparation using oxidative coupling

A flask was charged with an aniline (8 mmol, 1 eq.). Toluene (25 mL) was added. MnO_2 (2.78 g, 32 mmol, 4 eq.) was added. The flask was equipped with a reflux condenser and the reaction mixture was heated to 70 °C for 16 h. KOH as solid was added until no further precipitate formed. The precipitate was removed by filtration. Water (30 mL) was added to the filtrate and the aqueous was phase was extracted with EA (3 x 50 mL). The combined organic phases were dried, concentrated and purified by column chromatography (iHex:EA).

Screening and Optimisations

Screenings were conducted according to a standard protocol: a 4 mL reaction vial was charged with an azobenzene (36 mg, ca. 0.2 mmol, 1 eq.). All other components were added according to screening conditions specified. The vials were equipped with a condenser and heated in a preheated aluminum screening block. After the intended reaction time, 1 mL of MeCN was added onto the reaction and a 10 μL aliquot of the mixture was taken for sample preparation. The aliquot was mixed with 987 μL ACN and 13 μL of 0.1 M aqueous solution of caffeine as an internal standard. The samples were analyzed by analytical HPLC, taking the ratio of 210 nm trace integrals of the exhaustively substituted product peaks (*E+Z* isomers) over the product peak of the caffeine standard to compare reaction conditions. HPLC analysis yield estimates are used where chromatography to give isolated yields was not used.

Matching the main text, **conditions screening** (**Table S1**) focused on several parameters. Decreases in temperature led to reduction of Pd-black formation and increases in yield (**entries 1-4).** Temperatures of 20 (RT), 40, 60, 80 °C were screened with 40 °C giving the best results. Increasing catalyst loading (10 mol% to 40 mol%) increased the yield further, although not to a degree that we considered cost-effective (**entries 5-7**), which also indicates that the low yields are not only due to catalyst instability. A small set of Pd ligand additives were tested, but these hindered reaction (**entries 8-10**). A range of cosolvents to the alcohols

was investigated (**entries 11-20**), from THF to DMF. The screening showed toluene and xylene as the solvents giving the best product yields in HPLC analysis. Toluene was used for further reactions because we find it more practical to work with (easy rotavap removal). Decreasing the alcohol concentration significantly decreased the Product/Standard ratios, while increasing it led to only insignificant increase in P/S (**entries 21-26**). Changing the oxidizing agent did not identify significantly improved results compared to initial trials (**entries 27-32**). Potassium peroxosulfate and AgOAc failed to produce any product while any changes to PIDA amounts decreased the yields significantly. The addition of base, or acid, or activated 3Å molecular sieves, did not increase the P/S ratios (**entries 33-40**).

Table S1: Conditions screened for tetra-*ortho*-methoxylation of azobenzene.

entry	T [°C]	solvent	Additive/Spec. cond	Oxidant (eq.)	Cat. (mol%)	P/Stand.
			Temperature			
1	80	MeOH	pressure tube	PIDA (5)	$Pd(OAc)_2$ (10)	**6%***
2	60	MeOH	-	PIDA (5)	$Pd(OAc)_2$ (10)	**9%***
3	40	MeOH	-	PIDA (5)	$Pd(OAc)_2$ (10)	**21%***
4	RT	MeOH	-	PIDA (5)	$Pd(OAc)_2$ (10)	-
			Catalyst loading			
5	40	MeOH:PhMe 1:1	-	PIDA (5)	$Pd(OAc)_2$ (10)	**28%***
6	40	MeOH:PhMe 1:1	-	PIDA (5)	$Pd(OAc)_2$ (20)	**33%***
7	40	MeOH:PhMe 1:1	-	PIDA (5)	$Pd(OAc)_2$ (40)	**38%*** *% isolated yields
			Ligands			
8	60	MeOH:pyridine 1:1	-	PIDA (5)	$Pd(OAc)_2$ (10)	-
9	60	MeOH	pyridine 10%	PIDA (5)	$Pd(OAc)_2$ (10)	-
10	60	MeOH	2,2'-bipyridine	PIDA (5)	$Pd(OAc)_2$ (10)	-
			Solvent			
11	40	methanol:dioxane 1:1	-	PIDA (5)	$Pd(OAc)_2$ (40)	1.89
12	40	methanol:THF 1:1	-	PIDA (5)	$Pd(OAc)_2$ (40)	1.11
13	40	methanol:toluene 1:1	-	PIDA (5)	$Pd(OAc)_2$ (40)	4.20
14	40	methanol:ACN 1:1	-	PIDA (5)	$Pd(OAc)_2$ (40)	4.09
15	40	methanol:DCM 1:1	-	PIDA (5)	$Pd(OAc)_2$ (40)	2.35
16	40	methanol:DME 1:1	-	PIDA (5)	$Pd(OAc)_2$ (40)	1.05
17	40	methanol:DMF 1:1	-	PIDA (5)	$Pd(OAc)_2$ (40)	1.68
18	40	methanol:xylol 1:1	-	PIDA (5)	$Pd(OAc)_2$ (40)	4.50
19	40	methanol:DMSO 1:1	-	PIDA (5)	$Pd(OAc)_2$ (40)	-
20	40	methanol:NMP 1:1	-	PIDA (5)	$Pd(OAc)_2$ (40)	2.64
			Alcohol/Substrate concentration			
21	40	methanol:toluene 1:1	-	PIDA (5)	$Pd(OAc)_2$ (40)	2.19
22	40	methanol:toluene 4:1	-	PIDA (5)	$Pd(OAc)_2$ (40)	2.04
23	40	methanol:toluene 9:1	-	PIDA (5)	$Pd(OAc)_2$ (40)	1.53
24	40	methanol:toluene 19:1	-	PIDA (5)	$Pd(OAc)_2$ (40)	0.55
25	40	methanol:toluene 1:2	-	PIDA (5)	$Pd(OAc)_2$ (40)	2.24

26	40	methanol:toluene 1:1	dilute (0.05 M substrate)	PIDA (5)	$Pd(OAc)_2$ (40)	-
			Oxidizing agent			
27	40	methanol:toluene 1:1	-	PIDA (5)	$Pd(OAc)_2$ (40)	2.09
28	40	methanol:toluene 1:1	-	PIDA (10)	$Pd(OAc)_2$ (40)	0.98
29	40	methanol:toluene 1:1	-	PIFA (5)	$Pd(OAc)_2$ (40)	0.24
30	40	methanol:toluene 1:1	-	oxone (5)	$Pd(OAc)_2$ (40)	0.39
31	40	methanol:toluene 1:1	-	$K_2S_2O_8$ (5)	$Pd(OAc)_2$ (40)	-
32	40	methanol:toluene 1:1	-	AgOAc (5)	$Pd(OAc)_2$ (40)	-
			Additive/special conditons			
33	40	methanol:toluene 1:1	-	PIDA (5)	$Pd(OAc)_2$ (40)	2.37
34	40	methanol:toluene 1:1	PTSA	PIDA (5)	$Pd(OAc)_2$ (40)	-
35	40	methanol:toluene 1:1	$MeSO_3H$	PIDA (5)	$Pd(OAc)_2$ (40)	-
36	40	methanol:toluene 1:1	TfOH	PIDA (5)	$Pd(OAc)_2$ (40)	-
37	40	methanol:toluene 1:1	DIPEA	PIDA (5)	$Pd(OAc)_2$ (40)	0.51
38	40	methanol:toluene 1:1	NaOMe	PIDA (5)	$Pd(OAc)_2$ (40)	1.47
39	40	methanol:toluene 1:1	mol sieve 4Å	PIDA (5)	$Pd(OAc)_2$ (40)	1.83
40	40	methanol:toluene 1:1	AcOH	PIDA (5)	$Pd(OAc)_2$ (40)	0.32

Supporting Note 1: substituent patterns

Alkyl-substituted azobenzenes respond efficiently to light only up to ca. 500 nm. They are often used with two-colour photoisomerisations around 360 nm (PSS ca. 20:80 *E:Z*) and 450 nm (PSS ca. 80:20 *E:Z*). Such azobenzenes have been widely applied, with particular successes as photoresponsive lipids for membrane biophysics[1] and signaling cascades.[2]

Several azobenzene substitution pattern classes have been developed that influence the HOMO-LUMO transition energies, so tuning the PSSs that can be reached by photoswitching and therefore shifting the "best" photoisomerisation wavelengths (usually but not only defined as, those giving the most complete bulk isomerisation in each direction - see section **Photoresponse Kinetics**); as well as affecting other key properties such as the rate of spontaneous *Z*→*E* relaxation, -N=N- basicity, etc.

For example, **balanced electron rich** patterns (4,4'-bis-substitution with moderately electron donating groups such as alkoxy, anilide, or urea) are increasingly widely-used, permitting high PSSs in each direction under near-visible-light photoswitching, as well as fairly rapid *bulk* photoresponse; and they are broadly applicable in chemical biology.[3,4] **Push-pull** substituent patterns (e.g. 4-nitro-4'-amino-azobenzenes) are widely used where monodirectional visible light *E*→*Z* isomerisation is permissable in combination with rapid *Z*→*E* relaxation, as in receptor and ion channel photopharmacology.[5]

Tetra-*ortho* patterns are overviewed in the main text. Except for the small tetra-fluoro system, these feature a twisted nonplanar *E* isomer geometry due to steric repulsion between the *ortho* groups, which destabilises the *n*-orbital-like HOMO; and the lone pairs of alkoxy, thioether, or chloro *ortho* substituents provide additional repulsive destabilisation of the *E*-isomer's *n* orbital; both combining to redshift the $n\rightarrow\pi^*$ band of the *E* isomer so reducing its overlap with the $n\rightarrow\pi^*$ band of the *Z* isomer: thus giving excellent *E*→*Z* switching completeness in the range 520-600 nm by rather *E*-selective $n\rightarrow\pi^*$ transition.[6] In both isomers, the $\pi\rightarrow\pi^*$ transitions are blue shifted compared to typical azobenzenes due to π stabilisation by the inductively withdrawing *ortho* groups.[7,8] Most of these patterns drastically stabilise the *Z*-isomer against spontaneous relaxation, which can be beneficial in some settings.

The tetra-*ortho*-fluoro substitution pioneered by Hecht exploits fluorine's electron-withdrawing character to blue-shift the *Z*-isomer's $n\rightarrow\pi^*$ absorption band relative to the *E*-isomer, giving excellent *E*→*Z* isomerisation around 500 nm and *Z*→*E* isomerisation around 400 nm.[6] Tetra-*ortho*-methoxy,[9] tetra-*ortho*-thioalkyl[10], and tetra-*ortho*-chloro[11] azobenzenes were pioneered by Woolley to improve on the tetra-*ortho*-alkyl azobenzenes first reported nearly 50 years ago.[12,13] These sterically congested species red-shift the nonplanar *E*-isomer's $n\rightarrow\pi^*$ absorption band relative to the *Z*-isomer, giving excellent *E*→*Z* isomerisation around 550 nm (which is more biocompatible and penetrates more easily through biological samples), so making them particularly alluring for photopharmacology towards *in vivo* uses;[14] *Z*→*E* isomerisation is most complete around 400 nm. Tetra-*ortho*-alkoxyazobenzenes in particular feature excellent *E*→*Z* switching speed and completeness in the green at 550 nm, often maintained up to 600 nm.[6,9]

Note that polyphenol alkylation does not seem a promising route to per-*ortho*-alkoxylation: while mono-*O*-alkylation of *meta*- or *para*-azophenols is a flexible and unproblematic route for installing alkoxy groups, polyphenolic substrates are problematic to synthesise and handle, are more prone to *C*-alkylation by keto-enol tautomerism, and even mono-*O*-alkylation of *ortho*-azophenols is problematic due to azo-hydrazone tautomerism giving *N*-alkylation byproducts.

Synthetic Overview of Stepwise Modifications

For all reactions, the conditions as identified above were used (standard procedure **B**).

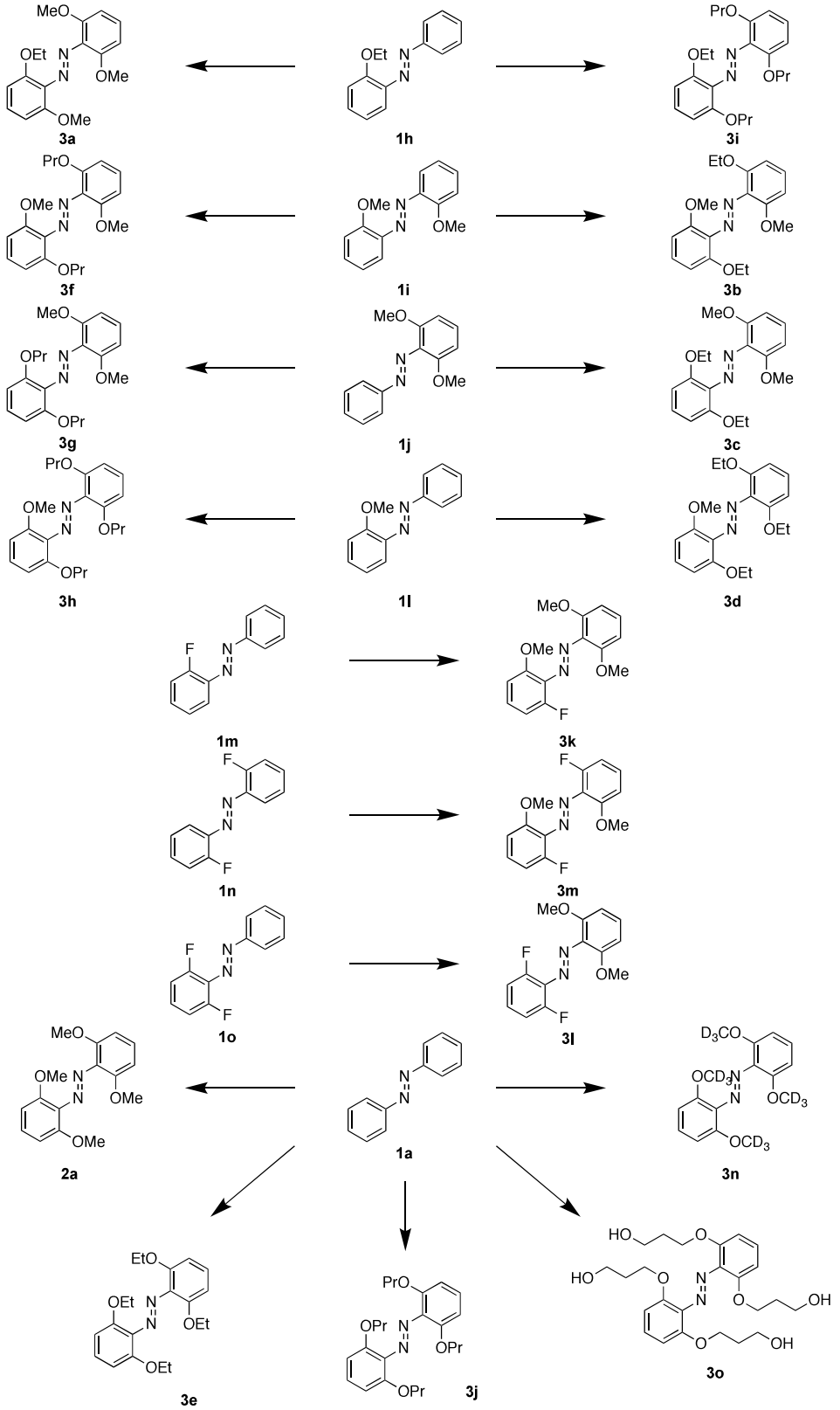

Scheme S1: overview of reactions explored in this work.

Tetra-ortho-*alkoxyazobenzenes: syntheses*

1,2-bis(2,6-dimethoxyphenyl)diazene (2a)

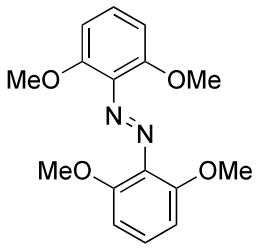

Commercially available azobenzene **1a** (36 mg, 0.2 mmol, 1.00 eq) was reacted with methanol using standard procedure B. The desired product **2a** (23 mg, 0.76 mmol, **38%**) was obtained as an orange solid; it is literature-known from a different synthesis.[15]

^{1}H NMR (400 MHz, Chloroform-*d*) δ (ppm) = 7.22 (t, *J* = 8.4 Hz, 2H), 6.67 (d, *J* = 8.4 Hz, 4H), 3.85 (s, 12H).

^{13}C NMR (101 MHz, Chloroform-*d*) δ (ppm) = 152.8, 135.0, 129.7, 105.7, 57.1.

HRMS (EI): calc. for $C_{16}H_{18}N_2O_4^+$ $[M]^+$: 302.1267; found: 302.1259.

1-(2,6-dimethoxy-4-methylphenyl)-2-(2,6-dimethoxyphenyl)diazene (2b)

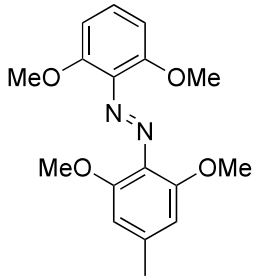

We prepared 4-methylazobenzene[16] **1b** by standard procedure A. 4-methylazobenzene (39 mg, 0.2 mmol, 1.0 eq) was then reacted with methanol using standard procedure B and the desired product **2b** (4 mg, 0.013 mmol, **6%**) was obtained as a red solid.

^{1}H NMR (400 MHz, Chloroform-*d*) δ (ppm) = 7.27 (t, *J* = 8.4 Hz, 1H), 6.77 (d, *J* = 8.5 Hz, 2H), 6.62 (s, 2H), 3.72 (s, 6H), 3.71 (s, 6H), 2.36 (s, 3H).

^{13}C NMR (101 MHz, $CDCl_3$) δ (ppm) = 151.9, 151.4, 140.2, 129.0, 106.0, 105.4, 56.1, 56.1, 21.9.

LCMS(+): t_{ret} = 6.8 min, 317 Th = $[MH]^+$.

HRMS (EI): calc. for $C_{17}H_{20}O_4N_2^+$ $[M]^+$: 316.1423; found: 316.1423.

1-(2,6-dimethoxy-3-methylphenyl)-2-(2,6-dimethoxyphenyl)diazene (2c)

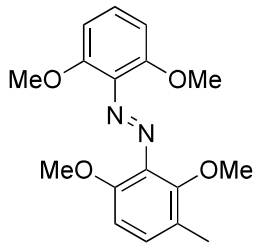

We prepared 3-methylazobenzene[17] by standard procedure A. 3-methylazobenzene (39 mg, 0.2 mmol, 1.0 eq) was then reacted with methanol using standard procedure B and the desired product **2c** (18 mg, 0.057 mmol, **28%**) was obtained as a red solid.

^{1}H NMR (400 MHz, DMSO-*d*$_6$) δ (ppm) = 7.32 (t, *J* = 8.4 Hz, 1H), 7.17 (dd, *J* = 8.6, 0.9 Hz, 1H), 6.84 (d, *J* = 8.5 Hz, 1H), 6.81 (d, *J* = 8.5 Hz, 2H), 3.75 (s, 6H), 3.73 (s, 3H), 3.56 (s, 3H), 2.20 (d, *J* = 0.8 Hz, 3H).

^{13}C NMR (101 MHz, DMSO) δ (ppm) = 151.72, 150.50, 149.16, 138.16, 133.32, 130.23, 129.87, 123.37, 108.08, 105.32, 60.79, 56.17, 56.14, 15.11.

LCMS(+): t_{ret} = 7.3 min, 317 Th = $[MH]^+$.

HRMS (EI): calc. for $C_{17}H_{20}O_4N_2^+$ $[M]^+$: 316.1423; found: 316.1420.

1-(2,6-dimethoxyphenyl)-2-(2,3,6-trimethoxyphenyl)diazene (2d)

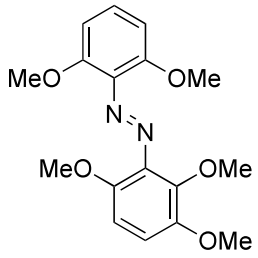

We prepared methyl 1-(3-methoxyphenyl)-2-phenyldiazene[18] **1d** by standard procedure A, and reacted 43 mg (0.2 mmol, 1.0 eq) of it with methanol using standard procedure B. The desired product **2d** (3 mg, 0.009 mmol, **5%**) was obtained as a dark red solid.

^{1}H NMR (400 MHz, Chloroform-*d*) δ (ppm) = 7.26 (t, *J* = 8.0 Hz, 6.84 (d, *J* = 9.0 Hz, 1H), 6.69 (d, *J* = 8.0 1H), 6.67 (d, *J* = 8.0 2H) 3.86 (s, 9H), 3.85 (s, 9H), 3.82 (s, 6H), 3.80 (s, 6H).

LCMS(+): t_{ret} = 7.6 min, 333 Th = $[MH]^+$.

HRMS (EI): calc. for $C_{17}H_{20}O_5N_2^+$ $[M]^+$: 332.1372; found: 332.1367.

methyl 4-((2,6-dimethoxyphenyl)diazenyl)-3,5-dimethoxybenzoate (2e)

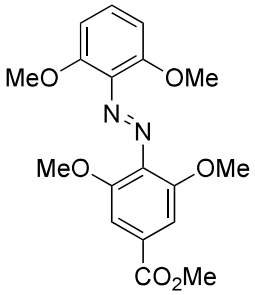

We prepared methyl 4-carboxyazobenzene[17] **1e** by standard procedure A, and reacted 48 mg (0.2 mmol, 1.0 eq) of it with methanol using standard procedure B. The desired product **2e** (13 mg, 0.036 mmol, **18%**) was obtained as a red solid.

^{1}H NMR (400 MHz, Chloroform-*d*) δ (ppm) = 7.36 (s, 2H), 7.25 (t, *J* = 8.4 Hz, 1H), 6.68 (d, *J* = 8.5 Hz, 2H), 3.94 (s, 3H), 3.89 (s, 6H), 3.86 (s, 6H).

^{13}C NMR (101 MHz, $CDCl_3$) δ (ppm) = 166.72, 152.72, 151.66, 137.76, 134.28, 130.26, 130.10, 106.63, 105.23, 56.81, 56.73, 52.48.

LCMS(+): t_{ret} = 6.5 min, 361 Th = $[MH]^+$.

HRMS (EI): calc. for $C_{19}H_{22}O_7N_2^+$ $[M]^+$: 360.1321; found: 360.1186.

1-(2,6-dimethoxyphenyl)-2-(4-fluoro-2,6-dimethoxyphenyl)diazene (2f)

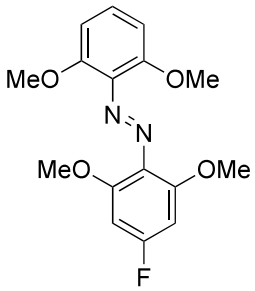

1-(4-fluorophenyl)-2-phenyldiazene[17] **1f** prepared by standard procedure A (40 mg, 0.2 mmol, 1.0 eq) was reacted with methanol using standard procedure B and the desired product **2f** (10 mg, 0.31 mmol, **16%**) was obtained as an orange solid.

^{1}H NMR (400 MHz, Chloroform-*d*) δ (ppm) = 7.23 (t, J = 8.5 Hz, 1H), 6.67 (d, J = 8.5 Hz, 2H), 6.41 (d, J = 10.7 Hz, 2H), 3.86 (s, 12H).

^{13}C NMR (101 MHz, $CDCl_3$) δ (ppm) =154.5, 153.9 (d, *J* = 12.9 Hz), 152.6, 129.5, 105.4, 105.0 (d, *J* = 6.7 Hz), 93.2 (d, *J* = 26.4 Hz), 56.9, 56.8.

LCMS(+): t_{ret} =6.6 min, 321 Th = $[MH]^+$.

HRMS (EI): calc. for $C_{16}H_{17}FO_4N_2^+$ $[M]^+$: 320.1172; found: 320.1161.

1-(4-chloro-2,6-dimethoxyphenyl)-2-(2,6-dimethoxyphenyl)diazene (2g)

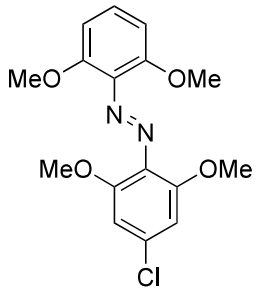

1-(4-chlorophenyl)-2-phenyldiazene[17] **1g** prepared by standard procedure A (43 mg, 0.2 mmol, 1.0 eq) was reacted with methanol using standard procedure B and the desired product **2g** (11 mg, 0.033 mmol, **16%**) was obtained as red solid.

^{1}H NMR (400 MHz, DMSO-*d*$_6$) δ (ppm) = 7.31 (t, *J* = 8.4 Hz, 1H), 6.89 (s, 2H), 6.79 (d, *J* = 8.5 Hz, 2H), 3.76 (s, 6H), 3.73 (s, 6H).

^{13}C NMR (101 MHz, $CDCl_3$) δ (ppm) = ^{13}C NMR (101 MHz, $CDCl_3$) δ 153.19, 152.89, 135.23, 130.10, 106.39, 106.12, 105.61, 105.26, 57.22, 57.06.

LCMS(+): t_{ret} = 6.8 min, 337 Th = $[MH]^+$.

HRMS (EI): calc. for $C_{16}H_{17}ClO_4N_2^+$ $[M]^+$: 336.0877; found: 336.0632.

1-(2,6-dimethoxy-4-nitrophenyl)-2-(2,6-dimethoxyphenyl)diazene (2h)

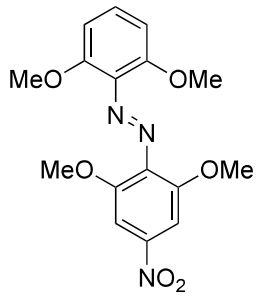

We prepared 4-nitroazobenzene[19] **1h** by standard procedure A, and reacted 45 mg (0.2 mmol, 1.0 eq) of it with methanol using standard procedure B. The desired product **2h** (16 mg, 0.046 mmol, **23%**) was obtained as a red solid.

^{1}H NMR (400 MHz, Chloroform-*d*) δ (ppm) = 7.50 (s, 2H), 7.23 (t, *J* = 8.5 Hz, 1H), 6.62 (d, *J* = 8.5 Hz, 2H), 3.84 (s, 6H), 3.80 (s, 6H).

^{13}C NMR (101 MHz, $CDCl_3$) δ (ppm) = 153.36, 152.01, 147.89, 139.22, 134.24, 131.47, 105.55, 101.38, 57.37, 57.11.

LCMS(+): t_{ret} = 6.7 min, 348 Th = $[MH]^+$.

HRMS (EI): calc. for $C_{16}H_{17}O_6N_3^+$ $[M]^+$: 347.1117; found: 347.1111.

1-(2,6-dimethoxyphenyl)-2-(2-ethoxy-6-methoxyphenyl)diazene (3a)

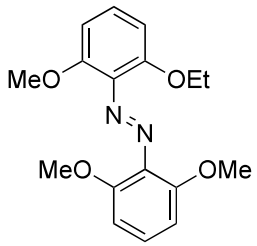

1-(2-ethoxyphenyl)-2-phenyldiazene[20] **1h** prepared by standard procedure A (45 mg, 0.2 mmol, 1.0 eq) was reacted with methanol using standard procedure B and the desired product **3a** (8 mg, 0.025 mmol, **13%**) was obtained as red solid.

^{1}H NMR (400 MHz, Chloroform-*d*) δ (ppm) = 7.20 (m, 8.3 Hz, 2H), 6.72 – 6.60 (m, 4H), 4.06 (q, *J* = 7.0 Hz, 2H), 3.85 (m, 9H), 1.37 (t, *J* = 7.0 Hz, 3H).

^{13}C NMR (101 MHz, $CDCl_3$) δ (ppm) = 152.88, 152.53, 151.12, 135.26, 134.63, 129.33, 129.08, 106.90, 105.27, 105.09, 65.25, 56.67, 56.62, 15.00.

LCMS(+): t_{ret} = 6.6 min,317 Th = $[MH]^+$.

HRMS (EI): calc. for $C_{17}H_{20}O_4N_2^+$ $[M]^+$: 316.1423; found: 316.1416.

1,2-bis(2-ethoxy-6-methoxyphenyl)diazene (3b)

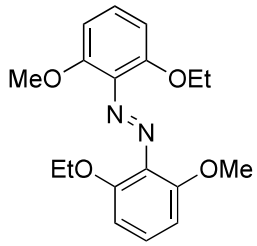

(E)-1,2-bis(2-methoxyphenyl)diazene[21] **1i** prepared by standard procedure A (48 mg, 0.2 mmol, 1.00 eq) was reacted with methanol using standard procedure B and the desired product **3b** (11 mg, 0.033 mmol, **16%**) was obtained as red solid.

^{1}H NMR (400 MHz, Chloroform-*d*) δ (ppm) 7.19 (t, *J* = 8.4 Hz, 2H), 6.66 (dd, *J* = 8.4, 2.7 Hz, 4H), 4.07 (q, *J* = 7.0 Hz, 4H), 3.85 (s, 6H), 1.36 (t, *J* = 7.0 Hz, 6H).

^{13}C NMR (101 MHz, $CDCl_3$) δ (ppm) = 153.25, 151.53, 135.56, 129.36, 107.28, 105.40, 65.60, 56.86, 15.33.

LCMS(+): tret = 6.2 min, 331 Th = $[MH]^+$.

HRMS (EI): calc. for $C_{14}H_{12}O_3N_2^+$ $[M]^+$: 330.1580; found: 330.1571.

1-(2,6-diethoxyphenyl)-2-(2,6-dimethoxyphenyl)diazene (3c)

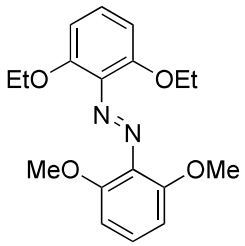

1-(2,6-dimethoxyphenyl)-2-phenyldiazene[22] **1j** prepared by standard procedure A (49 mg, 0.2 mmol, 1.0 eq) was reacted with methanol using standard procedure B and the desired product **3c** (30 mg, 0.091 mmol, **45%**) was obtained as a red solid.

^{1}H NMR (400 MHz, Chloroform-*d*) δ (ppm) = 7.23 (t, *J* = 8.4 Hz, 1H), 7.15 (t, *J* = 8.3 Hz, 1H), 6.68 (d, *J* = 8.4 Hz, 2H), 6.64 (d, *J* = 8.4 Hz, 2H), 4.06 (d, *J* = 7.0 Hz, 4H), 3.85 (s, 6H), 1.38 (t, *J* = 7.0 Hz, 6H).

^{13}C NMR (101 MHz, $CDCl_3$) δ (ppm) = 152.50, 151.40, 135.68, 134.37, 129.20, 128.64, 106.57, 105.09, 65.02, 56.39, 14.89.

LCMS(+): tret = 6.2 min, 331 Th = $[MH]^+$.

HRMS (EI): calc. for $C_{14}H_{12}O_3N_2^+$ $[M]^+$: 330.1580; found: 330.1572.

1-(2,6-diethoxyphenyl)-2-(2-ethoxy-6-methoxyphenyl)diazene (3d)

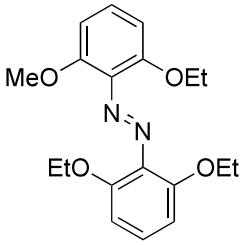

1-(2-methoxyphenyl)-2-phenyldiazene[22] **1l** prepared by standard procedure A (43 mg, 0.2 mmol, 1.0 eq) was reacted with ethanol using standard procedure B and the desired product **3d** (11 mg, 0.032 mmol, **16%**) was obtained as a red solid.

^{1}H NMR (400 MHz, Chloroform-*d*) δ (ppm) = 7.22-7.13 (m, *J* = 17.5, 8.4 Hz, 2H), 6.70 – 6.61 (m, 4H), 4.08 (dq, *J* = 8.7, 7.0 Hz, 6H), 3.84 (s, 3H), 1.35 (t, *J* = 7.0 Hz, 9H).

^{13}C NMR (101 MHz, $CDCl_3$) δ (ppm) = 152.61, 151.38, 151.31, 135.83, 135.09, 128.87, 128.56, 106.89, 106.69, 104.97, 65.17, 65.06, 56.32, 14.85, 14.84.

LCMS(+): tret = 7.2 min, 345 Th = $[MH]^+$.

HRMS (EI): calc. for $C_{19}H_{24}O_4N_2^+$ $[M]^+$: 344.1736; found: 344.1728.

1,2-bis(2,6-diethoxyphenyl)diazene (3e)

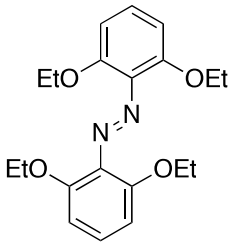

Commercially available azobenzene**1a** (36 mg, 0.2 mmol, 1.0 eq) was reacted with ethanol using standard procedure B and the desired product **3f** (8 mg, 0.022 mmol, **11%**) was obtained as a red solid.

^{1}H NMR (400 MHz, Chloroform-*d*) δ (ppm) = 7.16 (t, *J* = 8.4 Hz, 1H), 6.65 (d, *J* = 8.4 Hz, 2H), 4.08 (q, *J* = 7.0 Hz, 4H), 1.34 (t, *J* = 7.0 Hz, 7H).

^{13}C NMR (101 MHz, $CDCl_3$) δ (ppm) = 151.91, 136.38, 129.02, 107.34, 65.61, 15.31.

LCMS(+): tret = 7.4 min, 359 Th = $[MH]^+$.

HRMS (EI): calc. for $C_{20}H_{26}O_4N_2^+$ $[M]^+$: 358.1893; found: 358.1892.

1,2-bis(2-methoxy-6-propoxyphenyl)diazene (3f)

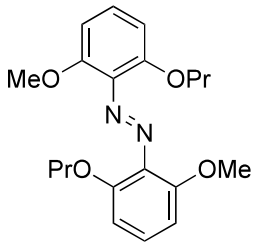

1,2-bis(2-methoxyphenyl)diazene[21] **1i** prepared by standard procedure C (49 mg, 0.2 mmol, 1.0 eq) was reacted with propanol using standard procedure B and the desired product **3f** (21 mg, 0.059 mmol, **29%**) was obtained as a red solid.

^{1}H NMR (400 MHz, Chloroform-*d*) δ (ppm) = 7.11 (t, J = 8.4 Hz, 2H), 6.57 (dd, J = 8.4, 3.1 Hz, 4H), 3.87 (t, J = 6.7 Hz, 4H), 3.75 (s, 6H), 1.67 (h, J = 7.1 Hz, 4H), 0.87 (t, J = 7.4 Hz, 6H).

^{13}C NMR (101 MHz, $CDCl_3$) δ (ppm) = 153.07, 151.14, 135.11, 128.95, 106.78, 104.83, 71.16, 56.40, 22.66, 10.49.

LCMS(+): t_{ret} = 6.9 min, 359 Th = $[MH]^+$.

HRMS (EI): calc. for $C_{20}H_{26}O_4N_2^+$ $[M]^+$: 358.1893; found: 358.1889.

1-(2,6-dimethoxyphenyl)-2-(2,6-dipropoxyphenyl)diazene (3g)

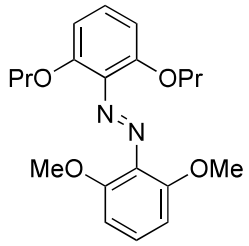

1-(2,6-dimethoxyphenyl)-2-phenyldiazene[22] **1j** prepared by standard procedure A (49 mg, 0.2 mmol, 1.0 eq) was reacted with propanol using standard procedure B and the desired product **3g** (56 mg, 0.16 mmol, **78%**) was obtained as a red solid.

^{1}H NMR (400 MHz, Chloroform-*d*) δ (ppm) = 7.23 (t, *J* = 8.5 Hz, 1H), 7.14 (t, *J* = 8.4 Hz, 1H), 6.67 (d, *J* = 8.5 Hz, 2H), 6.62 (d, *J* = 8.4 Hz, 2H), 3.95 (t, *J* = 6.6 Hz, 4H), 3.83 (s, 6H), 1.76 (h, *J* = 7.0 Hz, 4H), 0.95 (t, *J* = 7.4 Hz, 6H).

^{13}C NMR (101 MHz, $CDCl_3$) δ (ppm) = 152.98, 151.89, 136.12, 134.65, 129.64, 128.92, 106.74, 105.38, 71.35, 56.69, 23.03, 10.83.

LCMS(+): t_{ret} = 6.8 min, 359 Th = $[MH]^+$.

HRMS (EI): calc. for $C_{14}H_{12}O_3N_2^+$ $[M]^+$: 358.1853; found: 358.1888.

1-(2,6-dipropoxyphenyl)-2-(2-methoxy-6-propoxyphenyl)diazene (3h)

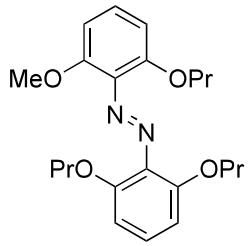

1-(2-methoxyphenyl)-2-phenyldiazene[22] **1l** prepared by standard procedure A (43 mg, 0.2 mmol, 1.0 eq) was reacted with ethanol using standard procedure B and the desired product **3i** (29 mg, 0.049 mmol, **25%**) was obtained as a red solid.

^{1}H NMR (400 MHz, Chloroform-*d*) δ (ppm) = 7.19 (t, *J* = 8.4 Hz, 1H), 7.14 (t, *J* = 8.4 Hz, 1H), 6.70 – 6.59 (m, 4H), 4.01 – 3.90 (m, 6H), 3.81 (s, 3H), 1.81 – 1.67 (m, 6H), 0.93 (t, *J* = 7.4 Hz, 9H).

^{13}C NMR (101 MHz, $CDCl_3$) δ (ppm) = 152.11, 150.96, 135.26, 134.41, 128.29, 127.88, 106.24, 105.94, 104.21, 70.61, 70.43, 55.65, 21.97, 21.94, 9.83.

LCMS(+): t_{ret} = 7.2 min, 387 Th = $[MH]^+$.

HRMS (EI): calc. for $C_{22}H_{30}O_4N_2^+$ $[M]^+$: 386.2206; found: 386.2199.

1-(2,6-dipropoxyphenyl)-2-(2-ethoxy-6-propoxyphenyl)diazene (3i)

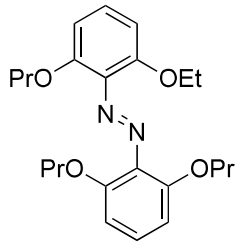

(E)-1-(2-ethoxyphenyl)-2-phenyldiazene[20] **1h** prepared by standard procedure A (45 mg, 0.2 mmol, 1.0 eq) was reacted with propanol using standard procedure B and the desired product **3k** (6 mg, 0.015 mmol, **8%**) was obtained as red solid.

^{1}H NMR (400 MHz, Chloroform-*d*) δ (ppm) = 7.15 (td, *J* = 8.4, 2.5 Hz, 2H), 6.64 (dd, *J* = 8.4, 2.2 Hz, 4H), 4.07 (q, *J* = 7.0 Hz, 2H), 3.94 (t, *J* = 6.8 Hz, 6H), 1.73 (q, *J* = 7.1 Hz, 6H), 1.32 (t, *J* = 7.0 Hz, 3H), 0.92 (td, *J* = 7.5, 1.0 Hz, 9H).

^{13}C NMR (101 MHz, $CDCl_3$) δ (ppm) = 152.05, 128.95, 128.87, 107.18, 107.10, 71.55, 71.52, 65.52, 22.95, 15.25, 10.84, 10.82.

LCMS(+): t_{ret} = 7.1 min, 401 Th = $[MH]^+$.

HRMS (ESI): calc. for $C_{23}H_{33}O_4N_2^+$ $[M+H]^+$: 401.2435; found: .401.2445.

1,2-bis(2,6-dipropoxyphenyl)diazene (3j)

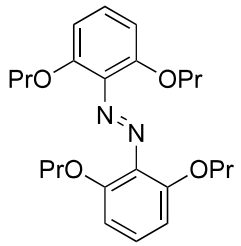

Commercially available azobenzene **1a** (36 mg, 0.2 mmol, 1.00 eq) was reacted with propanol using standard procedure B and the desired product **3j** (4 mg, 0.010 mmol, **5%**) was obtained as a red solid.

^{1}H NMR (400 MHz, Chloroform-*d*) δ (ppm) = 7.15 (t, *J* = 8.4 Hz, 2H), 6.64 (d, *J* = 8.4 Hz, 4H), 3.94 (t, *J* = 6.8 Hz, 8H), 1.72 (h, *J* = 7.2 Hz, 8H), 0.91 (t, *J* = 7.4 Hz, 12H).

^{13}C NMR (101 MHz, $CDCl_3$) δ (ppm) =152.11, 136.29, 128.88, 107.11, 71.55, 22.94, 10.83.

LCMS(+): t_{ret} = 8.1 min, 415 Th = $[MH]^+$.

HRMS (EI): calc. for $C_{14}H_{12}O_3N_2^+$ $[M]^+$: 414.2519; found: 414.2506.

1-(2,6-dimethoxyphenyl)-2-(2-fluoro-6-methoxyphenyl)diazene (3k)

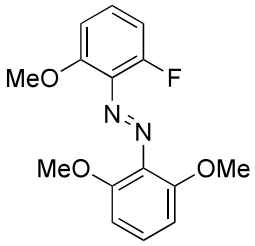

1-(2-fluorophenyl)-2-phenyldiazene prepared[23] **1m** by standard procedure A (40 mg, 0.2 mmol, 1.00 eq) was reacted with ethanol using standard procedure B and the desired product **3k** (10 mg, 0.034 mmol, **17%**) was obtained as a red solid.

^{1}H NMR (400 MHz, Chloroform-*d*) δ (ppm) = 7.28 – 7.19 (m, 2H), 6.84 – 6.76 (m, 2H), 6.67 (d, *J* = 8.4 Hz, 2H), 3.92 (s, 3H), 3.86 (s, 6H).

^{13}C NMR (101 MHz, $CDCl_3$) δ (ppm) = 7.25 – 7.19 (m, 2H), 6.84 – 6.76 (m, 2H), 6.67 (d, *J* = 8.4 Hz, 2H), 3.92 (s, 3H), 3.86 (s, 6H).

LCMS(+): t_{ret} = 6.2 min, 291 Th = $[MH]^+$.

HRMS (EI): calc. for $C_{15}H_{15}FO_3N_2^+$ $[M]^+$: 290.1067; found: 290.1060.

1,2-bis(2-fluoro-6-methoxyphenyl)diazene (3l)

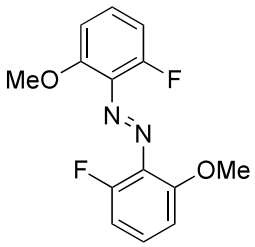

1,2-bis(2-fluorophenyl)diazene[24] **1n** (44 mg, 0.2 mmol, 1.00 eq; prepared from 1-fluoro-2-nitrosobenzene reacting with 2-fluoroaniline similar to Standard Procedure A) was reacted with ethanol using standard procedure B and the desired product **3l** (3 mg, 0.011 mmol, **5%**) was obtained as a red solid.

^{1}H NMR (400 MHz, Chloroform-*d*) δ (ppm) = 7.32 – 7.26 (m, 2H), 6.87 – 6.77 (m, 4H), 3.93 (s, 6H).

^{13}C NMR (101 MHz, $CDCl_3$) δ (ppm) = 155.18 (d, *J* = 4.3 Hz), 154.66, 152.10, 130.58 (d, *J* = 10.7 Hz), 109.22 (d, *J* = 21.0 Hz), 107.85 (d, *J* = 3.3 Hz).

LCMS(+): t_{ret} = 6.9 min, 279 Th = $[MH]^+$.

HRMS (EI): calc. for $C_{14}H_{12}F_2O_2N_2^+$ $[M]^+$: 278.0867; found: 278.0863.

1-(2,6-difluorophenyl)-2-(2,6-dimethoxyphenyl)diazene (3m)

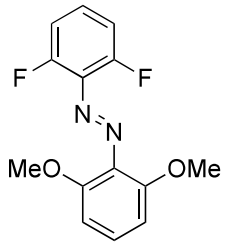

2,6-difluoroazobenzene[22] **1o** prepared by standard procedure D (44 mg, 0.2 mmol, 1.0 eq) was reacted with methanol using standard procedure B, and the desired product **3m** (6 mg, 0.022 mmol, **11%**) was obtained as a red solid, it is literature-known from a different synthesis.[15]

^{1}H NMR (400 MHz, Chloroform-*d*) δ (ppm) = 7.33 – 7.26 (m, 2H), 7.02 (t, *J* = 8.5 Hz, 2H), 6.69 (d, *J* = 8.4 Hz, 2H), 3.87 (s, 6H).

^{13}C NMR (101 MHz, $CDCl_3$) δ (ppm) = 155.04, 152.52, 151.34, 132.49, 129.49, 128.27, 128.17, 128.07, 110.99, 110.75, 103.64, 55.12.

LCMS(+): t_{ret} = 6.1 min, 279 Th = $[MH]^+$.

HRMS (EI): calc. for $C_{14}H_{12}F_2O_2N_2^+$ $[M]^+$: 278.0867; found: 278.0868.

1,2-bis(2,6-bis(methoxy-*d*$_3$)phenyl)diazene (3n)

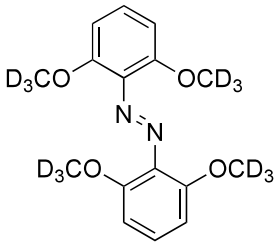

Commercially available azobenzene **1a** (36 mg, 0.2 mmol, 1.0 eq) was reacted with methanol-*d*$_4$ using standard procedure B and the desired product **3n** (15 mg, 0.050 mmol, 25**%**) was obtained as a red solid.

^{1}H NMR (400 MHz, Chloroform-*d*) δ (ppm) = 7.22 (t, *J* = 8.4 Hz, 1H), 6.66 (d, *J* = 8.5 Hz, 2H).

^{13}C NMR (101 MHz, $CDCl_3$) δ (ppm) = 152.49, 134.66, 129.41, 105.26, 55.89 (hept, *J* = 22.2 Hz).

LCMS(+): t_{ret} = 6.3 min, 315 Th = $[MH]^+$.

HRMS (EI): calc. for $C_{14}H_{12}F_2O_2N_2^+$ $[M]^+$: 314.2020; found: 314.2014.

3,3',3'',3'''-((diazene-1,2-diylbis(benzene-2,1,3-triyl))tetrakis(oxy))tetrakis(propan-1-ol) (3o)

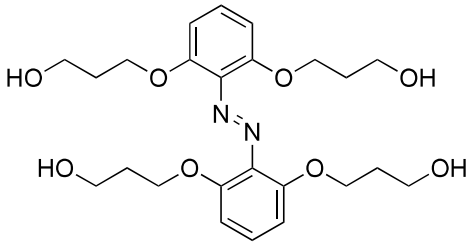

Commercially available azobenzene **1a** (36 mg, 0.2 mmol, 1.0 eq) was reacted with 1,3-propanediol using standard procedure B and the desired product **3o** (4 mg, 0.008 mmol, 4**%**) was obtained as a red solid following prep-HPLC.

^{1}H NMR (400 MHz, Methanol-d_4) δ (ppm) = 7.28 (t, J = 8.4 Hz, 2H), 6.80 (d, J = 8.4 Hz, 4H), 4.14 (t, J = 6.1 Hz, 8H), 3.65 (t, J = 6.1 Hz, 8H), 1.96 – 1.89 (m, 8H).

^{13}C NMR (101 MHz, Methanol-d_4) δ (ppm) = 153.18, 131.18, 107.43, 67.61, 59.97, 33.13.

LCMS(+): t_{ret} = 4.8 min, 479 Th = $[MH]^+$.

HRMS (EI): calc. for $C_{24}H_{34}O_8N_2^+$ $[M]^+$: 478.2315; found: 478.2333.

Potential Catalytic Cycle Mechanism

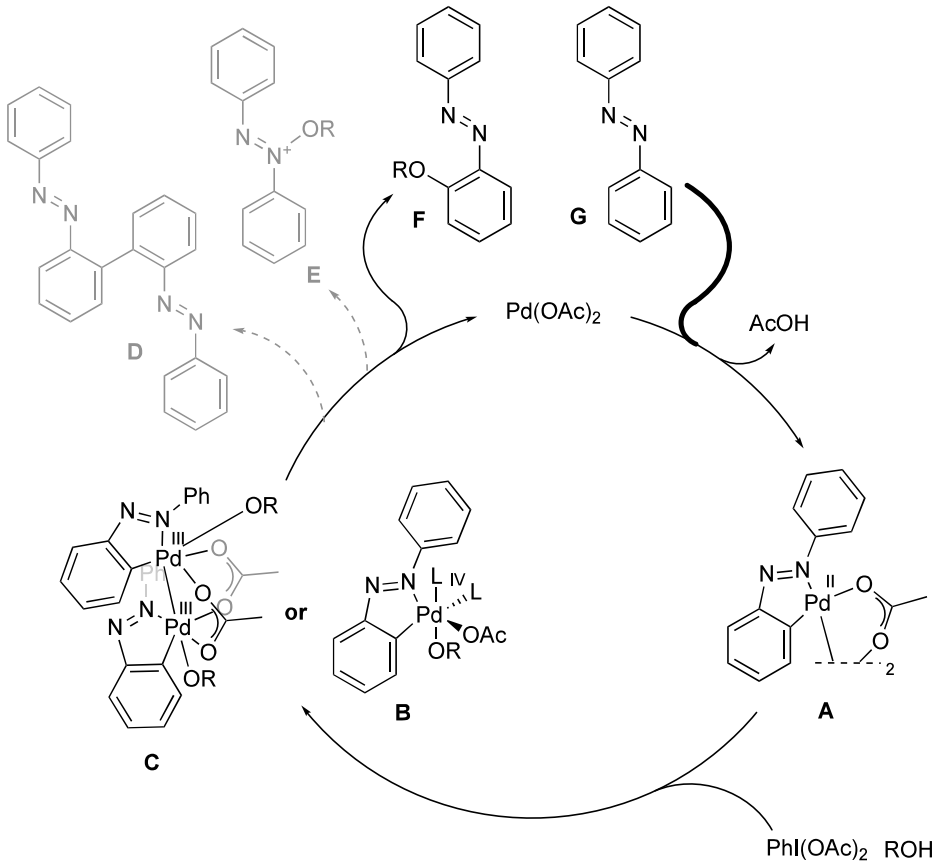

Scheme S2: Potential mechanism of each C-O bond formation cycle. Bold entry arrow for **G** into the cycle indicates that this can also be an entry for additionally substituted or alkoxylated intermediates (*en route* to per-alkoxylation)

Pd-dependent mechanism and effects: A plausible reaction mechanism for each *o*-alkoxylation step has been postulated by Sun[20]. The authors base their assumption on Wang[25,26] who described the *ortho*-acetylation of benzamides and *N*-methoxybenzamides. The $Pd(OAc)_2$ coordinates to the diazene which functions as the directing group in the subsequent CH-activation, giving the dimeric complex **A** with a 5-membered palladacycle. This reaction and the dimeric nature of the resulting complex was first reported by Cope[27] with chloride as the bridging ligand. The Pd^{II}-species **A** has been suggested to be oxidized to the Pd^{IV}-species **B** by PIDA, leading to coordination of alcohol ROH; Crabtree[28] suggested that the Pd^{IV} oxidation state is necessary for the reductive elimination forming a C-O bond, and the C-O bond-forming capabilities of Pd^{IV}-complexes were further supported by Sanford[29,30], which in our case would to an alkoxylation event. However, Ritter[31] has doubted the Pd^{IV}-oxidation state, suggesting a Pd^{II}/Pd^{III} pathway with a dimeric Pd^{III}/Pd^{III}-complex (corresponding in our case to **C**) forming by PIDA oxidation of the complex **A**, and demonstrated its higher kinetic competency in catalysis compared to complex **B**.[32] In our study, neither pathway can be excluded as contributing significantly to the reaction. Another mechanistic pathway was suggested by Sunoj[33] who found evidence for a solvent-assisted concerted metalation/deprotonation.

As a potential side-reaction, Pd^{IV}-species have been shown to be capable of not only C-O bond formation but also C-C bond formation giving **D**.[34] A coupling reaction between two C-N ligands was not observed by Sanford[29,30] yet it too is a viable side reaction, so further reaction of compound **D** cannot be excluded.

Compound **E** was observed by LCMS, with R = Me or as the azoxybenzene (R= negative charge), at retention times that are distinct from those of the *ortho*-alkoxylated desired product; although there is no literature about N-O bond forming with Pd^{IV} or Pd^{II}-complexes, therefore we do not know how the oxidation works here (though it need not be Pd-catalysed).

Substrate and Oxidant effects: We interpret the contrast of tolerated substituents in *para/meta* as indicating that electronics in the diazene, much more than at the palladated carbons, determine reaction outcomes. For example, excess oxidant may directly attack the increasingly electron-rich diazene to produce azobenzene-*N*-oxides, particularly when *para*-electron-donating groups can increase its oxidation sensitivity without the inductive and steric crowding depressions of reactivity associated to these same groups being in *ortho* (e.g. failed tetra-alkoxylation of *para*-methoxyazobenzene, but more successful reaction of the *meta* regioisomer and still more successful reaction of unsubstituted azobenzene; the role of sterics at least for the C-H insertion step is attested by the observation that trialkoxylated intermediates unsubstituted at the crowded *ortho* position were the major species recovered from *meta*-substituted azobenzene reactions).

Applications

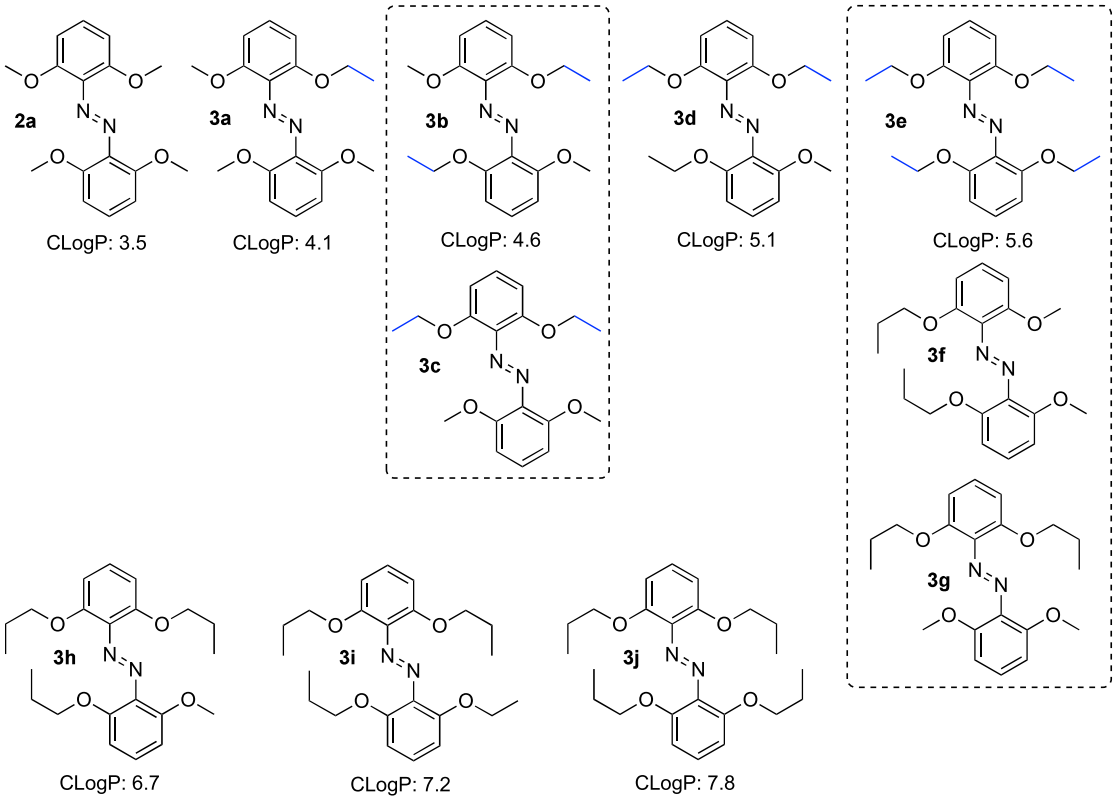

Scheme S3: Stepwise lipophilicity tuning. CLogP values calculated in ChemDraw.

Part B: Photocharacterisation

General Methods

HPLC for UV-Vis spectroscopy of separated isomers

HPLC analysis for photocharacterisation was performed on the Agilent 1100SL HPLC as described above except using an Agilent 10 Prep-C18 Scalar 250 x 4,6 mm C18 column (10 µm, 100 Å) maintained at 25°C, using the diode array detector to acquire peak spectra of separated photoswitch isomers inline over the range 200–550 nm, manually baselining across each elution peak of interest to correct for eluent composition effects.

UV-Vis spectrophotometry to monitor photoswitching and relaxation in bulk samples

Absorption spectra in cuvette ("UV-Vis") were acquired on a Varian CaryScan 60 (1 cm pathlength). For photoisomerisation measurements, Hellma microcuvettes (108-002-10-40) taking 250 μL volume to top of optical window were used with test solution such that the vertical pathlength of the isomerization light is less than 7 mm to the bottom of the cuvette, with the default test solution concentrations of 50 μM. Measurements on all photoswitches were performed by default in acetonitrile unless stated otherwise. Photoisomerisations and relaxation rate measurements were performed at room temperature unless stated otherwise.

“Star” LEDs (H2A1-models spanning 360–590 nm from Roithner Lasertechnik) or a universal LED illumination system (pE-4000, CoolLED) were used for photoisomerisations in cuvette.

PSS spectra of isolated products

UV-Vis absorption spectra of all isolated products were acquired according to general methods. “Dark” samples (DMSO stocks kept for at least 24 h at 60 °C in the dark, wrapped in aluminium foil, handled under light-excluded conditions) were illuminated sequentially at the given wavelengths (from longest to shortest) until PSS at each wavelength was reached; PSS spectra are shown at the following wavelengths (with line colours on graphs matching perceived colour): 550 nm (yellow-green), 525 nm (bright green), 490 (cyan), 470 nm (mid-blue), 435 nm (deep blue), and 405 nm (purple) (**Fig S1**).

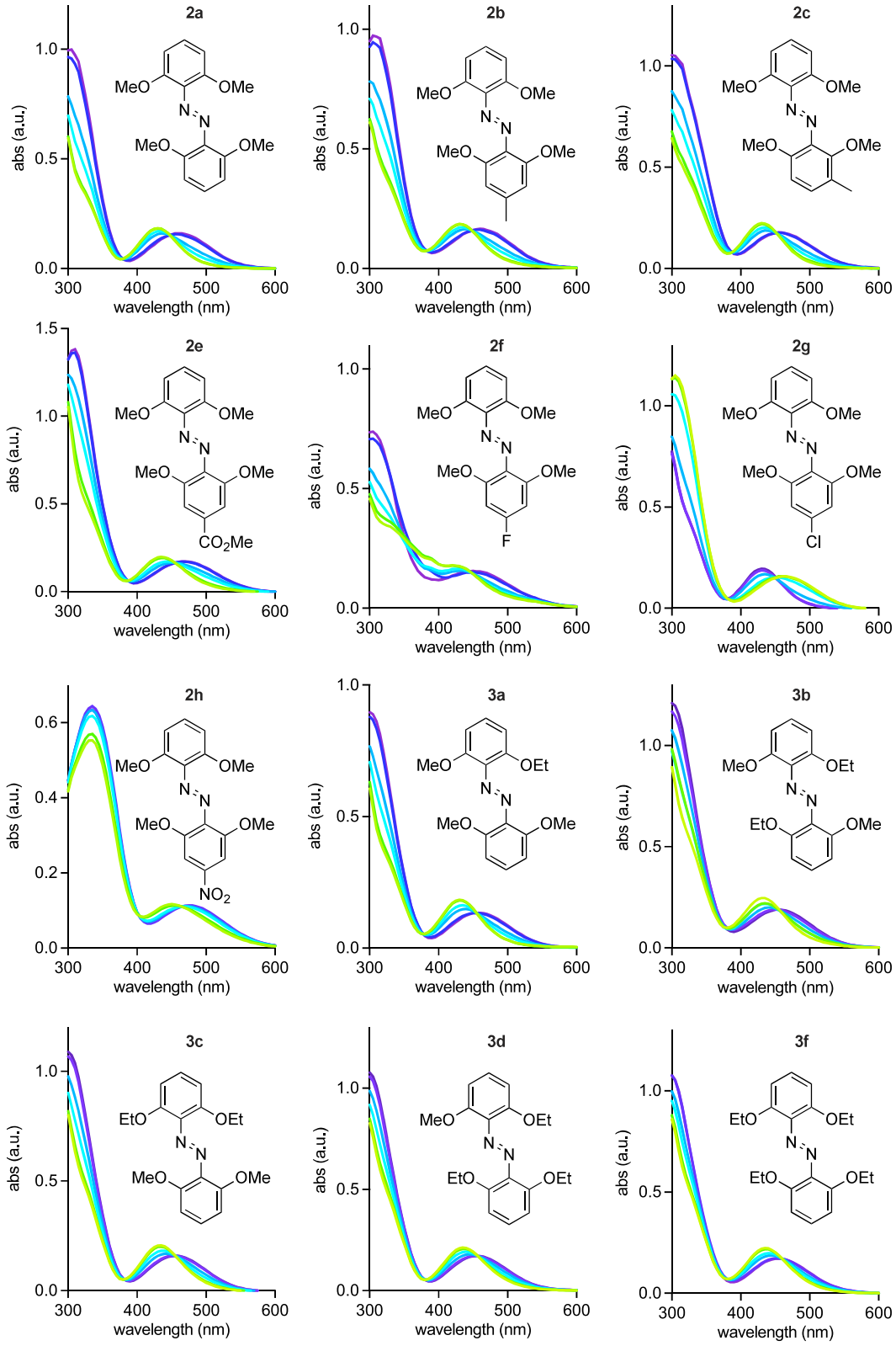

Figure S1 continues next page

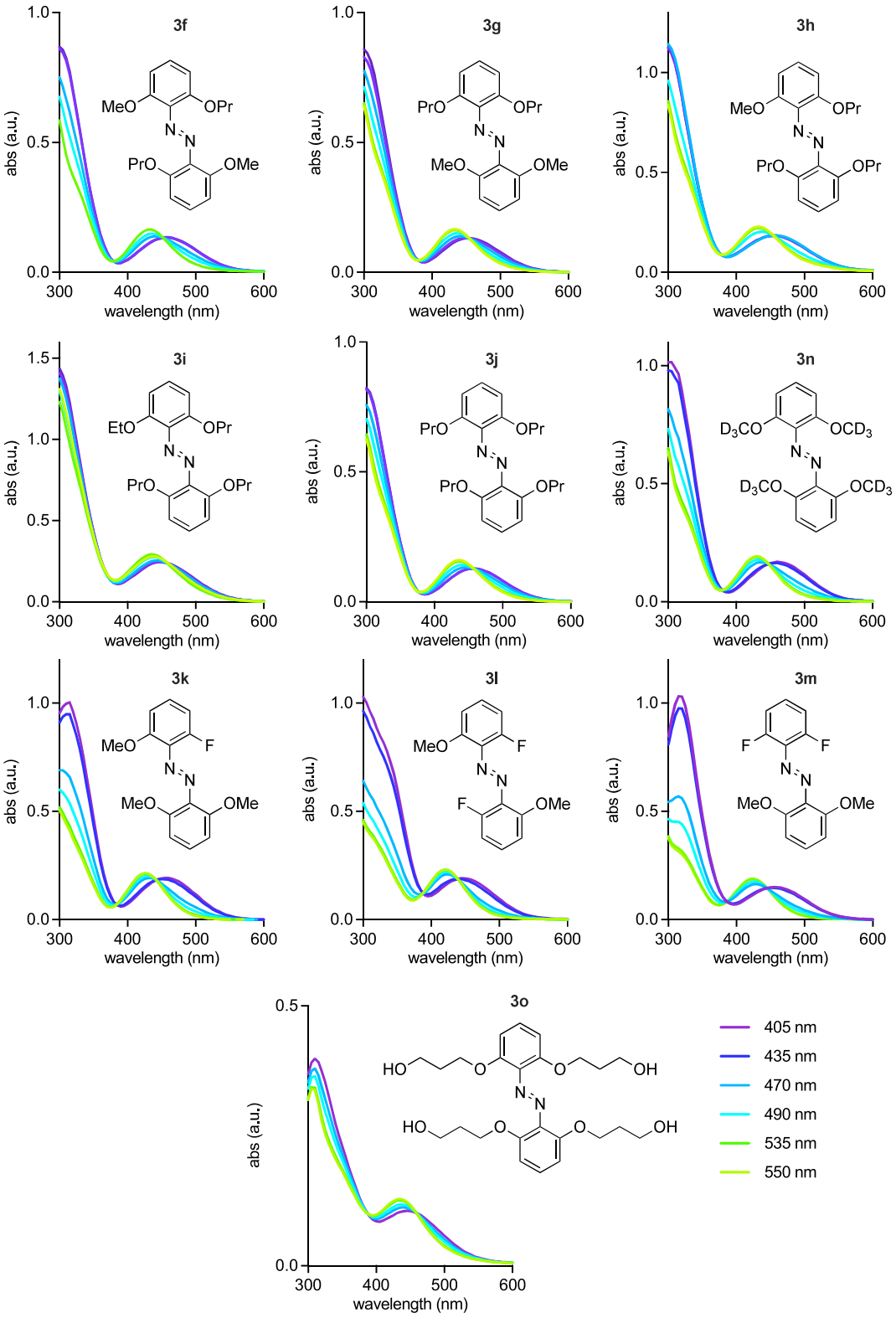

Fig S1 UV-Vis spectra at different PSS of compounds **2a-2g** and **3a-3n** at 50 μM in acetonitrile, and **3o** in water

Four compounds were investigated further due to interesting structural features, as described in the main text (**Fig 5**). Primary spectral data of selected compounds of interest is given in the **Supporting Datafile**.

Further Photocharacterisation

Thermal relaxation

Thermal relaxation was measured in acetonitrile at 50 μM in a closed cuvette over a time course of 12 h. The compounds were isomerized to a predominantly-*Z* state and then absorbance at a strongly absorbed and strongly-isomer-reporting wavelength (typically ca. 300 nm) was measured at infrequent intervals with low intensity measurement light applied for short duration (so as not to greatly photoisomerise the samples). All compounds had thermal relaxation rates that would be several orders of magnitude slower than biological processes of typical interest for addressing with photoswitches (**Fig S2a**).

Photostability

Photostability was measured by repeated switching between predominantly-*Z* and -*E* states with appropriate wavelengths (**Fig S2b**) applied from a CoolLED pE-4000 illumination system (**Fig S3**) with MicroManager v1.4.24 software[35] used for temporal control of light pulses. All measurements were conducted in acetonitrile, sealed with parafilm to stop evaporation, but under air. All measured compounds showed no photoinstability.

Pure *E* and *Z* spectra

All-*E* and all-*Z* spectra (**Fig S2c**) were obtained by inline UV-Vis during HPLC as specified in the general methods. For *E/Z* analysis, 2 μL of 5 mM photoswitch solutions in MeCN were injected. The spectra were exported from ChemStation software (vRev B.04.03-SP2) then normalized to an isosbestic point (depending on the compound, ca. 445-460 nm).

Monitoring %*Z* during isomerisations by UVVis

The degree of isomerisation indicated by a given sample's UVVis absorption at any time during photoisomerisation was determined by: (1) calibrating the absorbance at a strongly absorbed and strongly-isomer-reporting wavelength (typically ca. 300 nm) as measured in cuvette in the UVVis spectrophotometer, to *E/Z* ratios determined by HPLC; then (2) measuring UVVis spectra during bulk isomerisation/after reaching PSS, and using the calibrant series to convert from absorbance to %*Z*.

The calibration was performed by measuring samples of each compound (spanning from high-*E*- to high-*Z*- proportions) in both UVVis and HPLC.

Typically, a 1 mM stock solution in DMSO or MeCN is prepared. HPLC vials with micro inserts are charged with 50 μL of the stock solution, then irradiated with calibrant wavelengths (405-530 nm) for 3 min. 5 μL are injected into the HPLC by autosampler and the HPLC E/Z ratios are determined by integrating the inline UVVis trace at the effective isosbestic point wavelength λ_{ei} (although eluent composition changes during the run, as long as λ_{ei} is chosen such that the (*E*-peak-integral + *Z*-peak-integral) of the λ_{ei}-trace gives a constant sum at all

sample calibrant wavelengths for the same stock solution, this method is an accurate determinant of *E/Z* proportions). Immediately after injection, the remaining illuminated sample solution is diluted to 50 μM in the same solvent and UV/Vis spectrum is measured by spectrophotometer according to general methods; after the first measurement, the cuvette is irradiated again at the calibrant wavelength and remeasured; as long as no significant difference is seen, concentration-dependent effects on PSS as well as disruption of original *E/Z* ratio by roomlight/daylight exposure can be excluded (and indeed, working carefully under dark conditions, no such effects were seen in this study). Thus the HPLC isomer ratio can be assigned to any parameter of the UV-Vis spectra (absorption at a single given wavelength at a fixed concentration [e.g. 300 nm, 50 μM; **Fig S2d**]; or, which is generally more robust, the ratio of absorptions between two strongly-absorbed wavelengths that together report sensitively on *E/Z* ratio [e.g. ratio A_{500}/A_{420}]) to convert between that parameter's experimentally measured value and the sample's %*Z*. This has been done in **Fig 5c**.

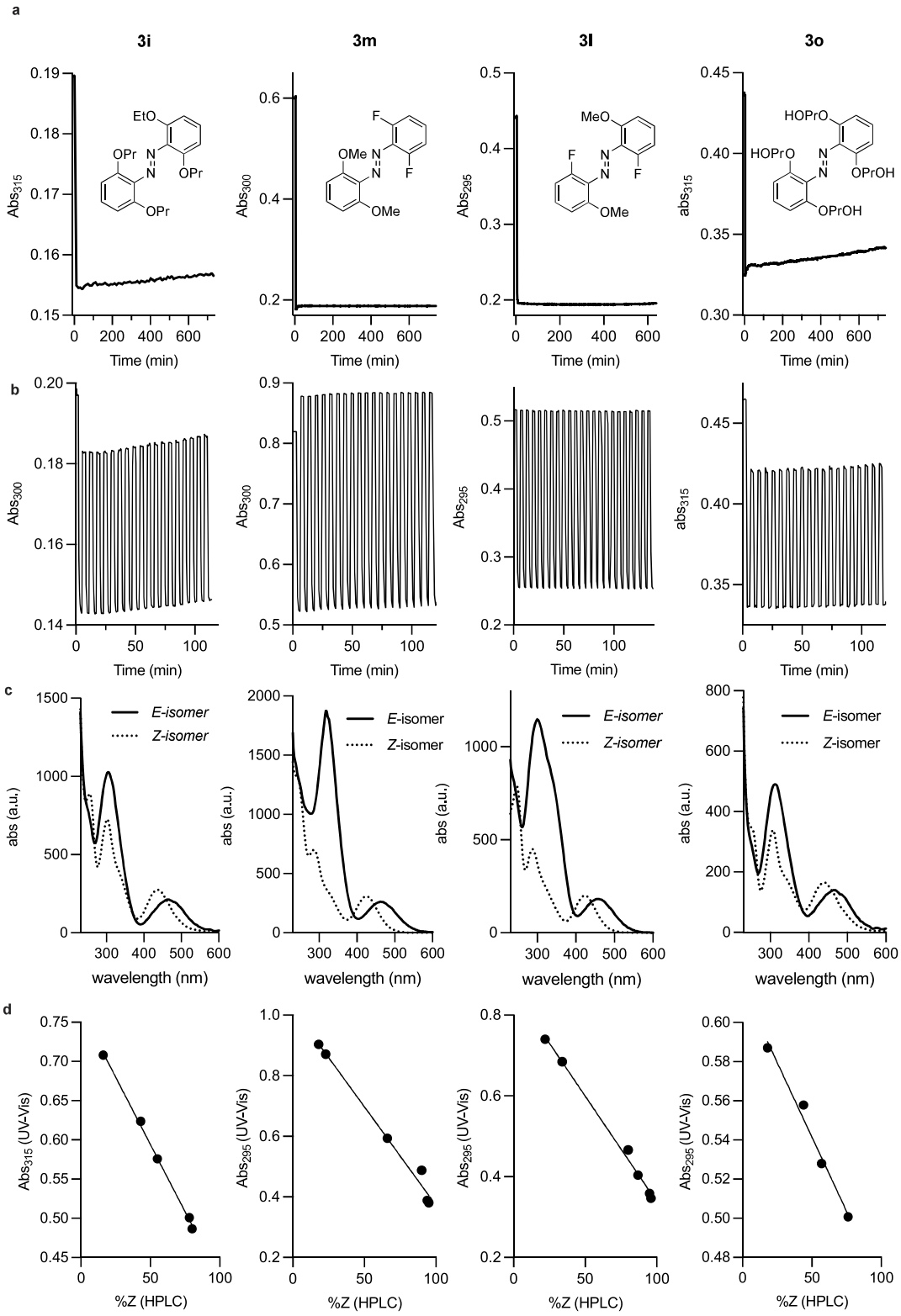

Fig S2 a) thermal relaxation of compounds **3i** and **3l** (in MeCN) and **3o** (in distilled water) at 23°C. b) Photostability to multiple switching cycles (405 nm / 525 nm cycles). c) Comparison of the UV/Vis spectra of the *Z*/*E*-isomers as acquired by inline HPLC (water:MeCN eluant). d) Sample HPLC/UVVis calibrants, used in the analysis for **Fig 5c.**

Bulk Photoresponse Kinetics

Bulk photoresponse kinetics (**Fig 5c**) are a vital parameter for practical applications of photoswitches (compare Supporting Note 1). Bulk photoresponses were measured using the same UV-Vis setup as for PSS spectra, monitoring the absorbance at the strongly-absorbed and strongly-isomer-reporting wavelength used in isomer cycling (typically ca. 300 nm). To benchmark biologically useful bulk photoswitching speeds, we used 405 nm or 435 nm light to isomerise samples to a predominantly *E*-state (note: 405 nm is the most common suitable confocal microscopy laser for this photoisomerisation direction), then photoswitched with test wavelengths to various more *Z*-rich PSSs, applying each test wavelength for at least 1 min (optionally longer until either PSS was reached or else until it was demonstrated that isomerization is possible but very slow, or else is not possible); then returned them to starting state with 405 nm or 435 nm to verify no losses or degradation (**Fig 5c**). Full LED powers at each wavelength were used (giving variable optical intensities at output according to wavelength: 13-130 mW/mm^2: see **Fig S3**) to keep experiments as short as possible.

The caveat to this LED-based experiment - which has very likely been a problem for most literature LED-based "long-wavelength photoswitching" studies - is that most azobenzenes could be slowly isomerized using the 595 nm LED – yet, nearly no significant absorption above background is observed at 595 nm in the UV-Vis spectra, except perhaps for the tetra-propoxy **3i** in organic solvent. While other interpretations are possible and some of those have been published, we instead believe that the "595 nm LED" responses we saw are not due to any atypical absorption process (such effects are thought to operate in ordered phases, but our experiments are in molecular solution), but arise simply from the quite typical broadness of the emitting LED (specifications of the pE-4000 describe a substantial emission tail intensity of the 595 nm LED; **Fig S3**) - and thus actually represent photoresponse to yellow light in the range 560-590 nm. Given that the laser lines of biological interest in this region have a spectral gap from 561 nm typically to 632 or 647 nm (i.e. what matters is response at 561 nm), and that absorption spectra are anyway modified in biological environments, we do not think it meaningful at this stage to study this wavelength range in more detail; we are satisfied simply to have shown robust yellow-light responses.

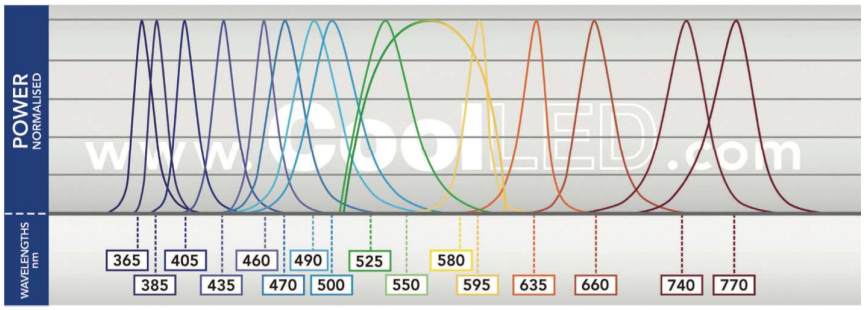

pE-4000																			
			Wavelength (nm)	365	385	405	435	460	470	490	500	525	550 / 580	595	635	660	740	770
LLG	Output diameter	3 mm	FWHM (nm)	12.54	11.38	16.08	13.02	17.61	23.26	25.19	24.72	28.32	82.79	14.61	16.72	21.42	41.12	27.75
At output	Output length (m)	1.5	Power (mW)	712.48	1931.30	935.91	344.72	1481.17	495.87	391.56	136.60	81.79	694.75	95.10	389.07	655.75	359.59	244.41
	Output NA	0.58	Intensity (mW/mm^2)	100.80	273.22	132.40	48.77	209.54	70.15	55.39	19.32	11.57	98.29	13.45	55.04	92.77	50.87	34.58

Fig S3 Emission spectra and power table of pE-4000 LEDs[36]

Supplementary Information Bibliography

(1) Urban, P.; Pritzl, S. D.; Konrad, D. B.; Frank, J. A.; Pernpeintner, C.; Roeske, C. R.; Trauner, D.; Lohmüller, T. Light-Controlled Lipid Interaction and Membrane Organization in Photolipid Bilayer Vesicles. *Langmuir* **2018**, *34* (44), 13368–13374. https://doi.org/10.1021/acs.langmuir.8b03241.

(2) Frank, J. A.; Moroni, M.; Moshourab, R.; Sumser, M.; Lewin, G. R.; Trauner, D. Photoswitchable Fatty Acids Enable Optical Control of TRPV1. *Nature Communications* **2015**, *6*, 7118. https://doi.org/10.1038/ncomms8118 https://www.nature.com/articles/ncomms8118#supplementary-information.

(3) Borowiak, M.; Nahaboo, W.; Reynders, M.; Nekolla, K.; Jalinot, P.; Hasserodt, J.; Rehberg, M.; Delattre, M.; Zahler, S.; Vollmar, A.; Trauner, D.; Thorn-Seshold, O. Photoswitchable Inhibitors of Microtubule Dynamics Optically Control Mitosis and Cell Death. *Cell* **2015**, *162* (2), 403–411. https://doi.org/10.1016/j.cell.2015.06.049.

(4) Gutzeit, V. A.; Acosta-Ruiz, A.; Munguba, H.; Häfner, S.; Landra-Willm, A.; Mathes, B.; Mony, J.; Yarotski, D.; Börjesson, K.; Liston, C.; Sandoz, G.; Levitz, J.; Broichhagen, J. A Fine-Tuned Azobenzene for Enhanced Photopharmacology in Vivo. *Cell Chemical Biology* **2021**. https://doi.org/10.1016/j.chembiol.2021.02.020.

(5) Mourot, A.; Kienzler, M. A.; Banghart, M. R.; Fehrentz, T.; Huber, F. M. E.; Stein, M.; Kramer, R. H.; Trauner, D. Tuning Photochromic Ion Channel Blockers. *ACS Chem. Neurosci.* **2011**, *2* (9), 536–543. https://doi.org/10.1021/cn200037p.

(6) Bléger, D.; Schwarz, J.; Brouwer, A. M.; Hecht, S. O-Fluoroazobenzenes as Readily Synthesized Photoswitches Offering Nearly Quantitative Two-Way Isomerization with Visible Light. *Journal of the American Chemical Society* **2012**, *134* (51), 20597–20600. https://doi.org/10.1021/ja310323y.

(7) Wegener, M.; Hansen, M. J.; Driessen, A. J. M.; Szymanski, W.; Feringa, B. L. Photocontrol of Antibacterial Activity: Shifting from UV to Red Light Activation. *J. Am. Chem. Soc.* **2017**, *139* (49), 17979–17986. https://doi.org/10.1021/jacs.7b09281.

(8) Rullo, A.; Reiner, A.; Reiter, A.; Trauner, D.; Isacoff, E. Y.; Woolley, G. A. Long Wavelength Optical Control of Glutamate Receptor Ion Channels Using a Tetra- *Ortho* -Substituted Azobenzene Derivative. *Chem. Commun.* **2014**, *50* (93), 14613–14615. https://doi.org/10.1039/C4CC06612J.

(9) Beharry, A. A.; Sadovski, O.; Woolley, G. A. Azobenzene Photoswitching without Ultraviolet Light. *Journal of the American Chemical Society* **2011**, *133* (49), 19684–19687. https://doi.org/10.1021/ja209239m.

(10) Samanta, S.; McCormick, T. M.; Schmidt, S. K.; Seferos, D. S.; Woolley, G. A. Robust Visible Light Photoswitching with Ortho-Thiol Substituted Azobenzenes. *Chem. Commun.* **2013**, *49* (87), 10314–10316. https://doi.org/10.1039/C3CC46045B.

(11) Samanta, S.; Beharry, A. A.; Sadovski, O.; McCormick, T. M.; Babalhavaeji, A.; Tropepe, V.; Woolley, G. A. Photoswitching Azo Compounds in Vivo with Red Light. *J. Am. Chem. Soc.* **2013**, *135* (26), 9777–9784. https://doi.org/10.1021/ja402220t.

(12) Forber, C. L.; Kelusky, E. C.; Bunce, N. J.; Zerner, M. C. Electronic Spectra of Cis- and Trans-Azobenzenes: Consequences of Ortho Substitution. *J. Am. Chem. Soc.* **1985**, *107* (21), 5884–5890. https://doi.org/10.1021/ja00307a009.

(13) Bisle, H.; Rau, H. Fluorescence of Noncyclic Azo Compounds with a Low-Lying 1(n,Π*)State. *Chemical Physics Letters* **1975**, *31* (2), 264–266. https://doi.org/10.1016/0009-2614(75)85017-2.

(14) Frank, J. A.; Antonini, M.-J.; Chiang, P.-H.; Canales, A.; Konrad, D. B.; Garwood, I. C.; Rajic, G.; Koehler, F.; Fink, Y.; Anikeeva, P. In Vivo Photopharmacology Enabled

by Multifunctional Fibers. *ACS Chem. Neurosci.* **2020**, *11* (22), 3802–3813. https://doi.org/10.1021/acschemneuro.0c00577.
(15) Hansen, M. J.; Lerch, M. M.; Szymanski, W.; Feringa, B. L. Direct and Versatile Synthesis of Red-Shifted Azobenzenes. *Angewandte Chemie* **2016**, *128* (43), 13712–13716. https://doi.org/10.1002/ange.201607529.
(16) Dong, R.; Liu, Y.; Zhou, Y.; Yan, D.; Zhu, X. Photo-Reversible Supramolecular Hyperbranched Polymer Based on Host–Guest Interactions. *Polym. Chem.* **2011**, *2* (12), 2771–2774. https://doi.org/10.1039/C1PY00426C.
(17) Lv, H.; Laishram, R. D.; Yang, Y.; Li, J.; Xu, D.; Zhan, Y.; Luo, Y.; Su, Z.; More, S.; Fan, B. TEMPO Catalyzed Oxidative Dehydrogenation of Hydrazobenzenes to Azobenzenes. *Org. Biomol. Chem.* **2020**, *18* (18), 3471–3474. https://doi.org/10.1039/D0OB00103A.
(18) Singh, S.; Chauhan, P.; Ravi, M.; Taneja, I.; Wahajuddin, W.; Yadav, Prem. P. A Mild CuBr–NMO Oxidative System for the Coupling of Anilines Leading to Aromatic Azo Compounds. *RSC Adv.* **2015**, *5* (76), 61876–61880. https://doi.org/10.1039/C5RA12535A.
(19) Lim, Y.-K.; Lee, K.-S.; Cho, C.-G. Novel Route to Azobenzenes via Pd-Catalyzed Coupling Reactions of Aryl Hydrazides with Aryl Halides, Followed by Direct Oxidations †. *Org. Lett.* **2003**, *5* (7), 979–982. https://doi.org/10.1021/ol027311u.
(20) Yin, Z.; Jiang, X.; Sun, P. Palladium-Catalyzed Direct Ortho Alkoxylation of Aromatic Azo Compounds with Alcohols. *The Journal of Organic Chemistry* **2013**, *78* (19), 10002–10007. https://doi.org/10.1021/jo401623j.
(21) Yan, Z.; Xie, X.; Song, Q.; Ma, F.; Sui, X.; Huo, Z.; Ma, M. Tandem Selective Reduction of Nitroarenes Catalyzed by Palladium Nanoclusters. *Green Chem.* **2020**, *22* (4), 1301–1307. https://doi.org/10.1039/C9GC03957K.
(22) Tombari, R. J.; Tuck, J. R.; Yardeny, N.; Gingrich, P. W.; Tantillo, D. J.; Olson, D. E. Calculated Oxidation Potentials Predict Reactivity in Baeyer–Mills Reactions. *Org. Biomol. Chem.* **2021**, *19* (35), 7575–7580. https://doi.org/10.1039/D1OB01450A.
(23) Kaiser, M.; Leitner, S. P.; Hirtenlehner, C.; List, M.; Gerisch, A.; Monkowius, U. Azobenzene-Functionalized N-Heterocyclic Carbenes as Photochromic Ligands in Silver(i) and Gold(i) Complexes. *Dalton Trans.* **2013**, *42* (41), 14749. https://doi.org/10.1039/c3dt51565f.
(24) Knie, C.; Utecht, M.; Zhao, F.; Kulla, H.; Kovalenko, S.; Brouwer, A. M.; Hecht, S.; Bléger, D. Ortho-Fluoroazobenzenes: Visible Light Switches with Very Long-Lived Z Isomers. *Chemistry – A European Journal* **2014**, *20* (50), 16492–16501. https://doi.org/10.1002/chem.201404649.
(25) Wang, G.-W.; Yuan, T.-T.; Wu, X.-L. Direct Ortho-Acetoxylation of Anilides via Palladium-Catalyzed Sp2 C−H Bond Oxidative Activation. *J. Org. Chem.* **2008**, *73* (12), 4717–4720. https://doi.org/10.1021/jo8003088.
(26) Wang, G.-W.; Yuan, T.-T. Palladium-Catalyzed Alkoxylation of N-Methoxybenzamides via Direct Sp2 C−H Bond Activation. *J. Org. Chem.* **2010**, *75* (2), 476–479. https://doi.org/10.1021/jo902139b.
(27) Cope, A. C.; Siekman, R. W. Formation of Covalent Bonds from Platinum or Palladium to Carbon by Direct Substitution. *J. Am. Chem. Soc.* **1965**, *87* (14), 3272–3273. https://doi.org/10.1021/ja01092a063.
(28) Yoneyama, T.; Crabtree, R. H. Pd(II) Catalyzed Acetoxylation of Arenes with Iodosyl Acetate. *Journal of Molecular Catalysis A: Chemical* **1996**, *108* (1), 35–40. https://doi.org/10.1016/1381-1169(95)00289-8.
(29) Dick, A. R.; Kampf, J. W.; Sanford, M. S. Unusually Stable Palladium(IV) Complexes: Detailed Mechanistic Investigation of C−O Bond-Forming Reductive Elimination.

Journal of the American Chemical Society **2005**, *127* (37), 12790–12791. https://doi.org/10.1021/ja0541940.
(30) Racowski, J. M.; Dick, A. R.; Sanford, M. S. Detailed Study of C−O and C−C Bond-Forming Reductive Elimination from Stable $C_2N_2O_2$−Ligated Palladium(IV) Complexes. *J. Am. Chem. Soc.* **2009**, *131* (31), 10974–10983. https://doi.org/10.1021/ja9014474.
(31) Powers, D. C.; Ritter, T. Bimetallic Pd(III) Complexes in Palladium-Catalysed Carbon–Heteroatom Bond Formation. *Nature Chem* **2009**, *1* (4), 302–309. https://doi.org/10.1038/nchem.246.
(32) Powers, D. C.; Geibel, M. A. L.; Klein, J. E. M. N.; Ritter, T. Bimetallic Palladium Catalysis: Direct Observation of Pd(III)−Pd(III) Intermediates. *J. Am. Chem. Soc.* **2009**, *131* (47), 17050–17051. https://doi.org/10.1021/ja906935c.
(33) Anand, M.; Sunoj, R. B. Palladium(II)-Catalyzed Direct Alkoxylation of Arenes: Evidence for Solvent-Assisted Concerted Metalation Deprotonation. *Organic Letters* **2011**, *13* (18), 4802–4805. https://doi.org/10.1021/ol201830r.
(34) Canty, A. J. Development of Organopalladium(IV) Chemistry: Fundamental Aspects and Systems for Studies of Mechanism in Organometallic Chemistry and Catalysis. *Acc. Chem. Res.* **1992**, *25* (2), 83–90. https://doi.org/10.1021/ar00014a005.
(35) Edelstein, A. D.; Tsuchida, M. A.; Amodaj, N.; Pinkard, H.; Vale, R. D.; Stuurman, N. Advanced Methods of Microscope Control Using MManager Software. *Journal of Biological Methods* **2014**, *1* (2), e10–e10. https://doi.org/10.14440/jbm.2014.36.
(36) PE-4000 | LED Light Sources | CoolLED LED Illumination System. *CoolLED*.

Part C: NMR Spectra

1,2-bis(2,6-dimethoxyphenyl)diazene (2a): ^{1}H-NMR

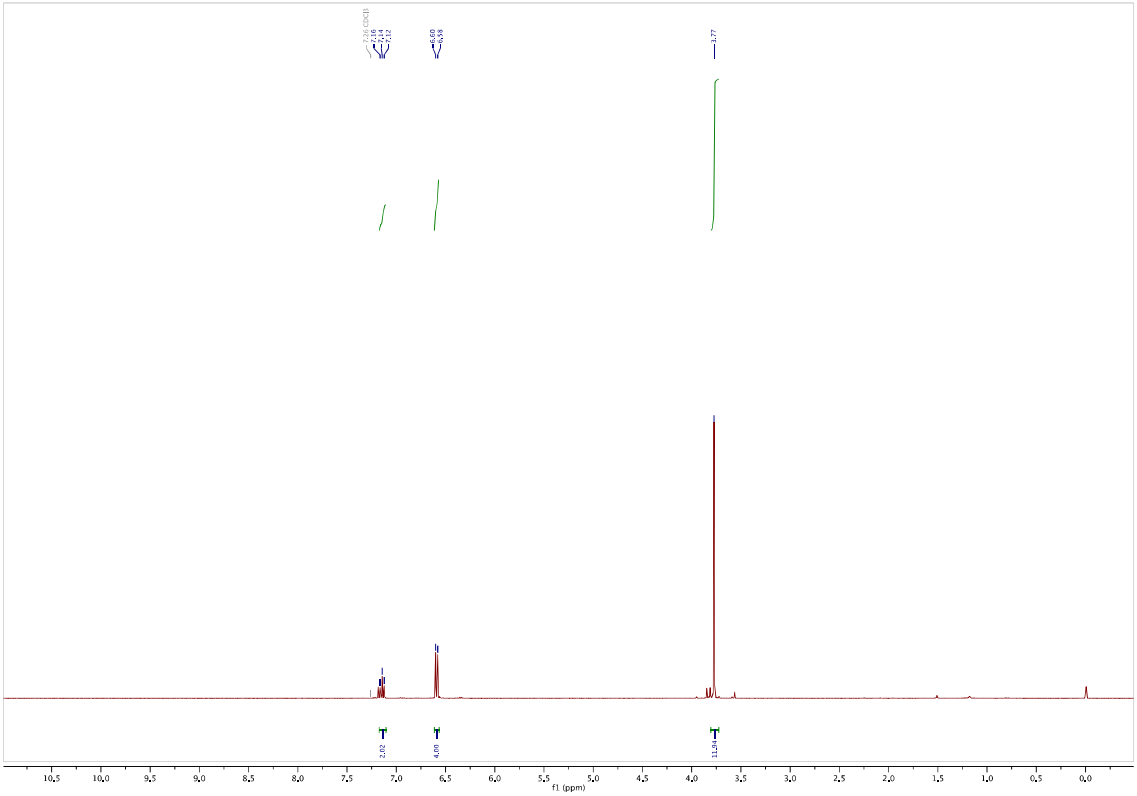

^{13}C-NMR

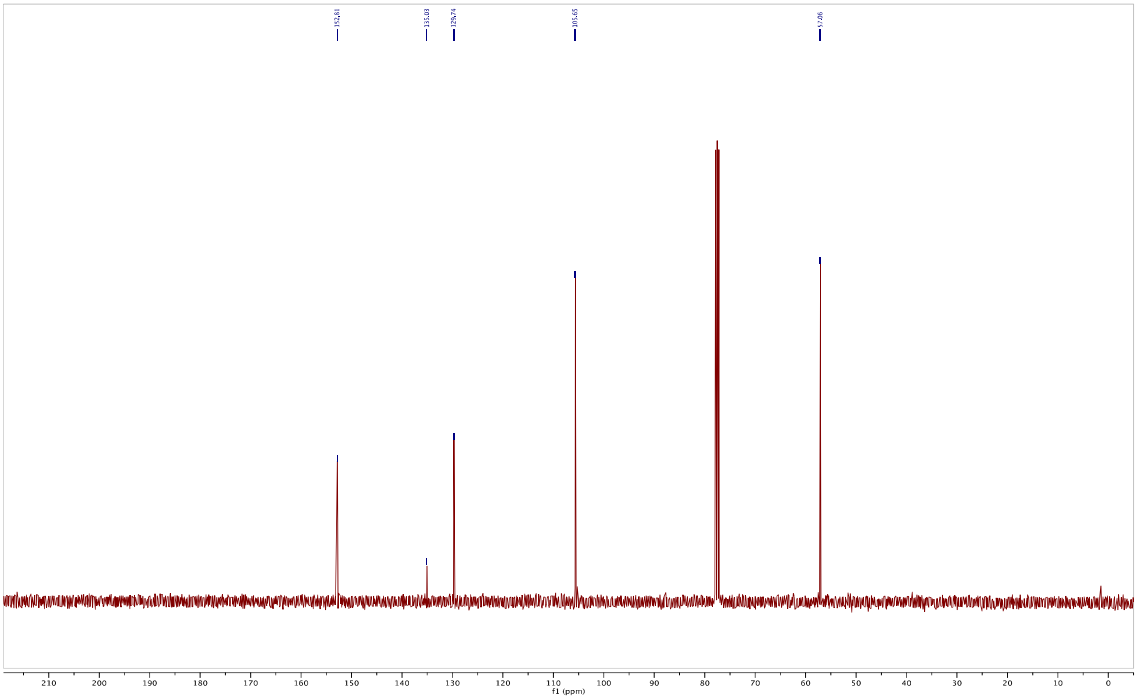

1-(2,6-dimethoxy-4-methylphenyl)-2-(2,6-dimethoxyphenyl)diazene (2b): 1H-NMR

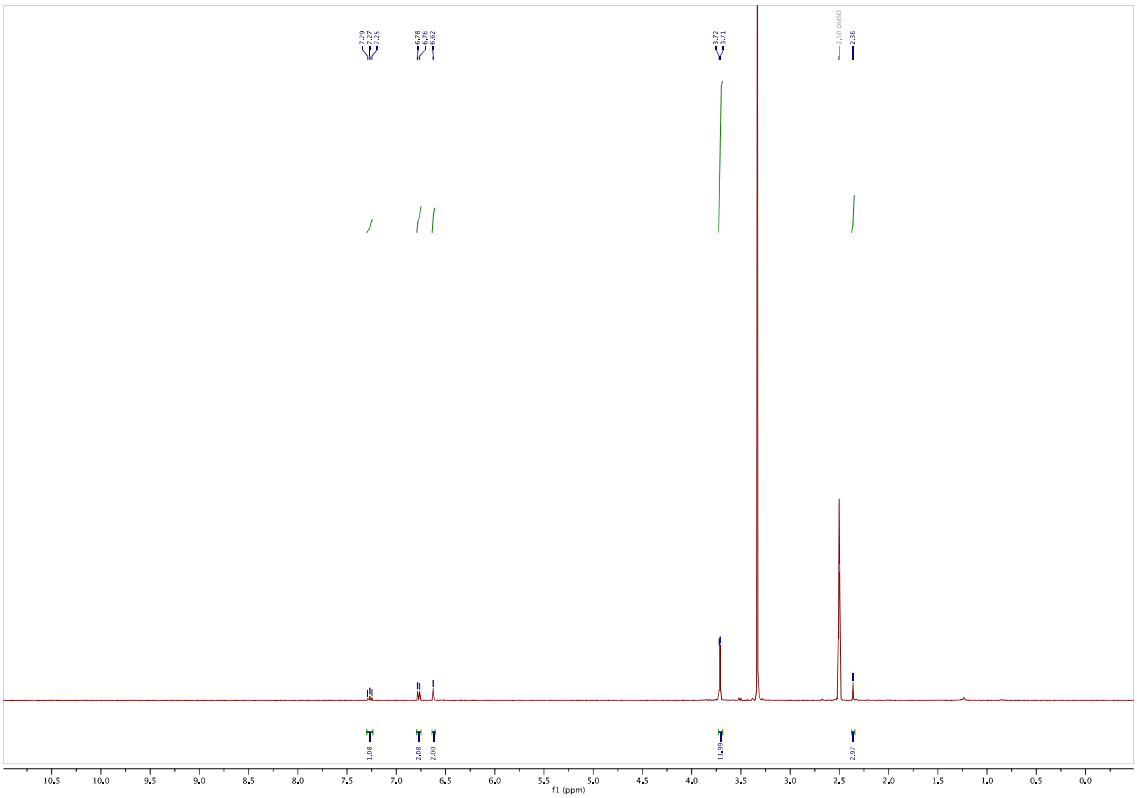

^{13}C-NMR

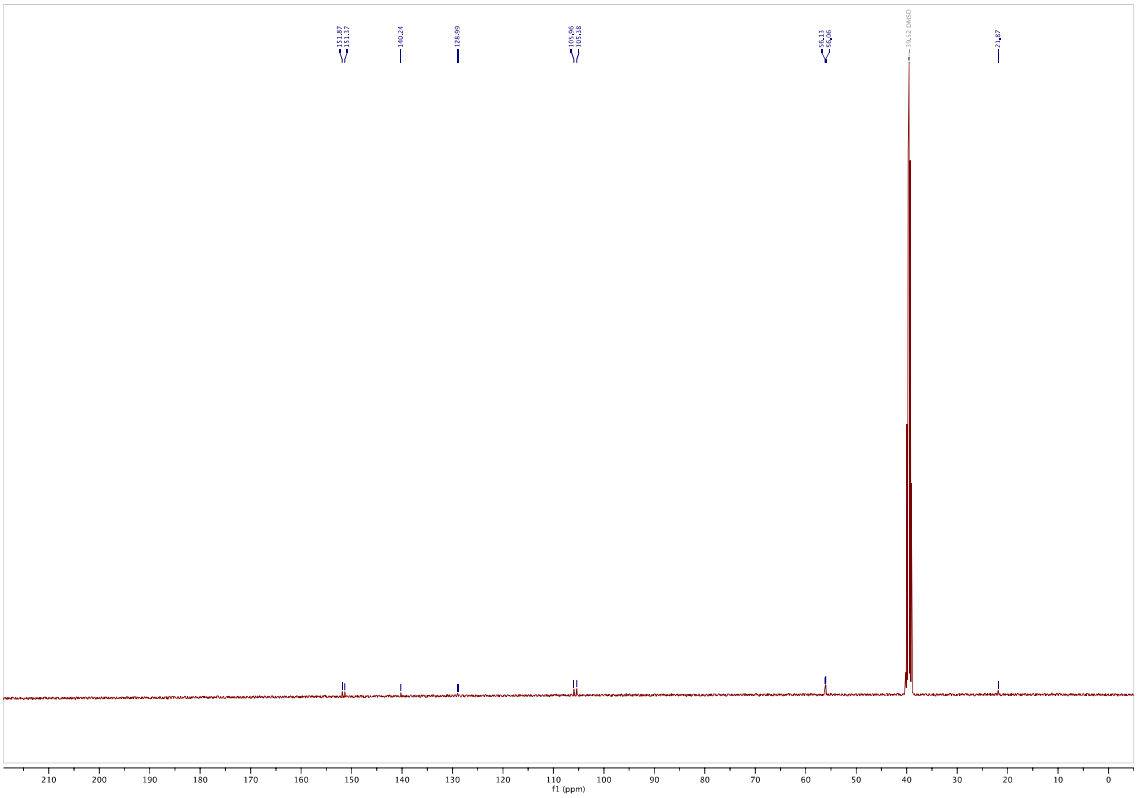

1-(2,6-dimethoxy-3-methylphenyl)-2-(2,6-dimethoxyphenyl)diazene (2c): ^{1}H-NMR

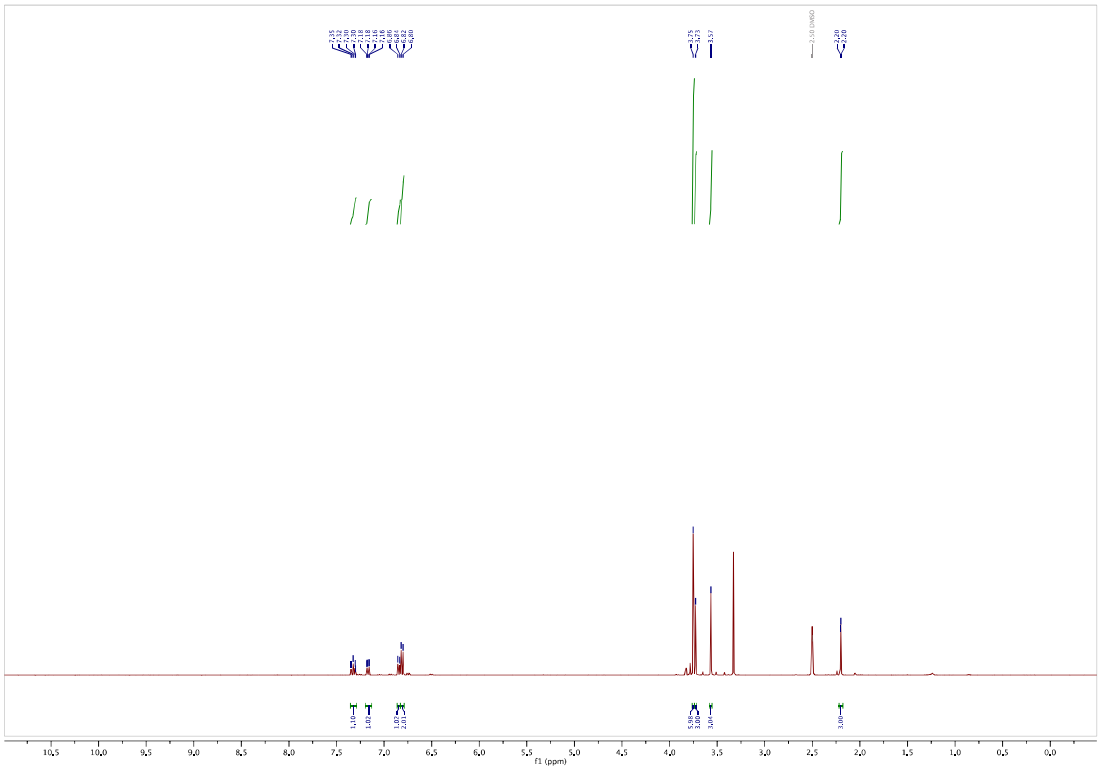

^{13}C-NMR

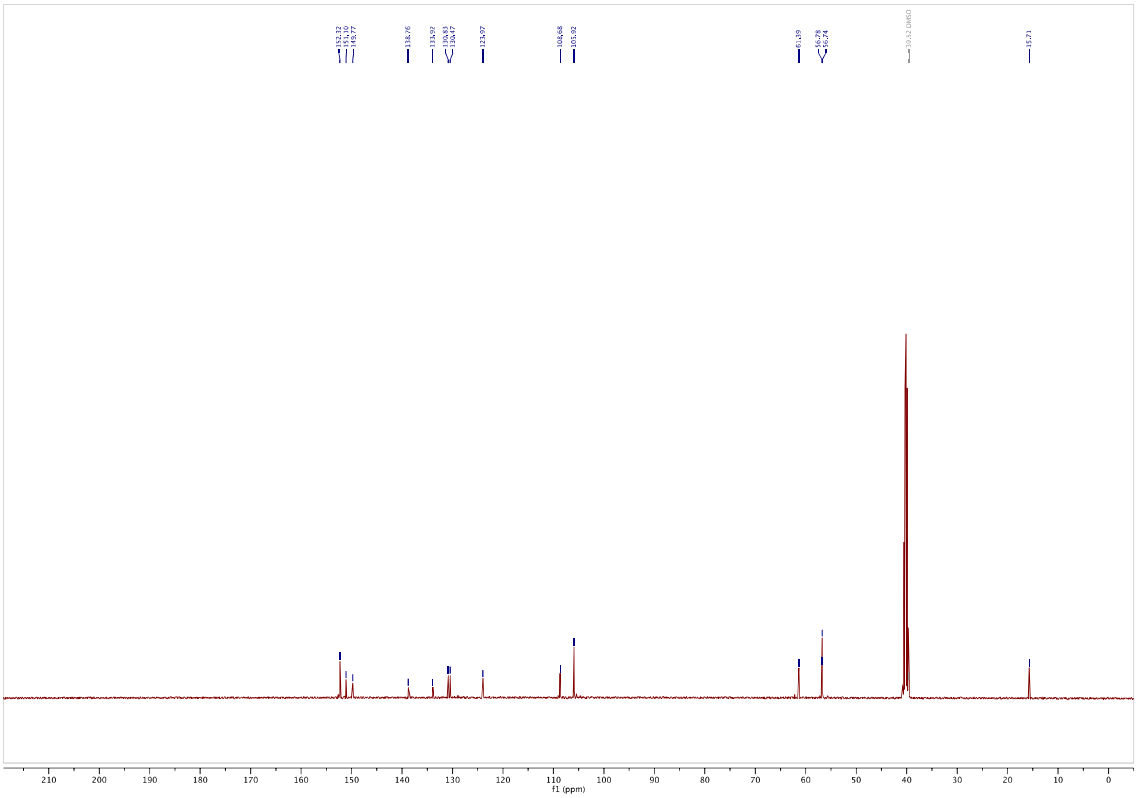

1-(2,6-dimethoxyphenyl)-2-(2,3,6-trimethoxyphenyl)diazene (2d)

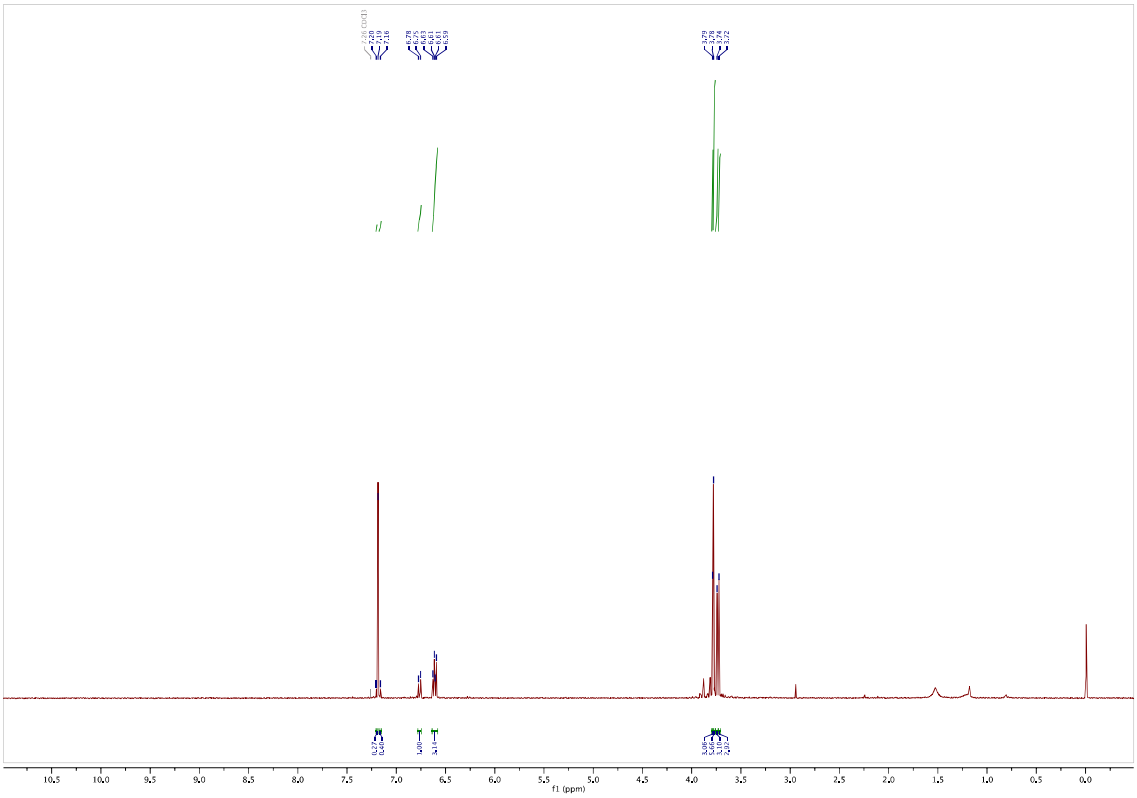

Text

methyl 4-((2,6-dimethoxyphenyl)diazenyl)-3,5-dimethoxybenzoate (2e): ^{1}H-NMR

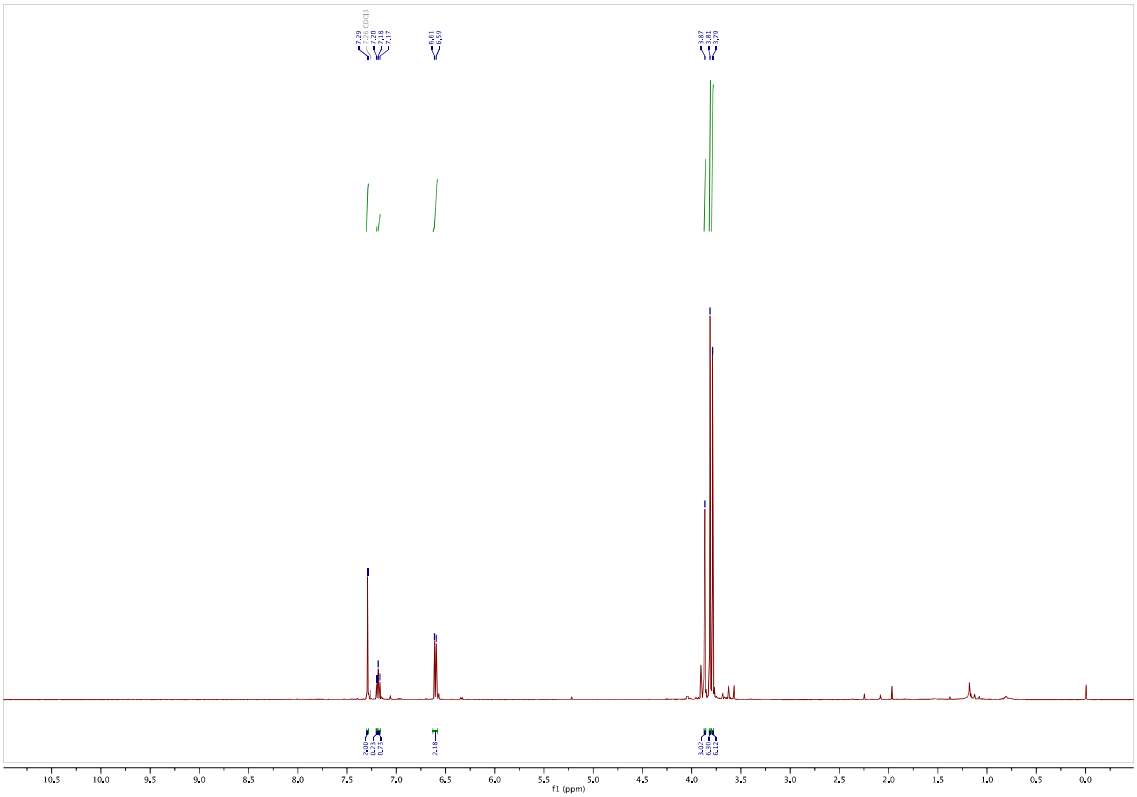

^{13}C-NMR

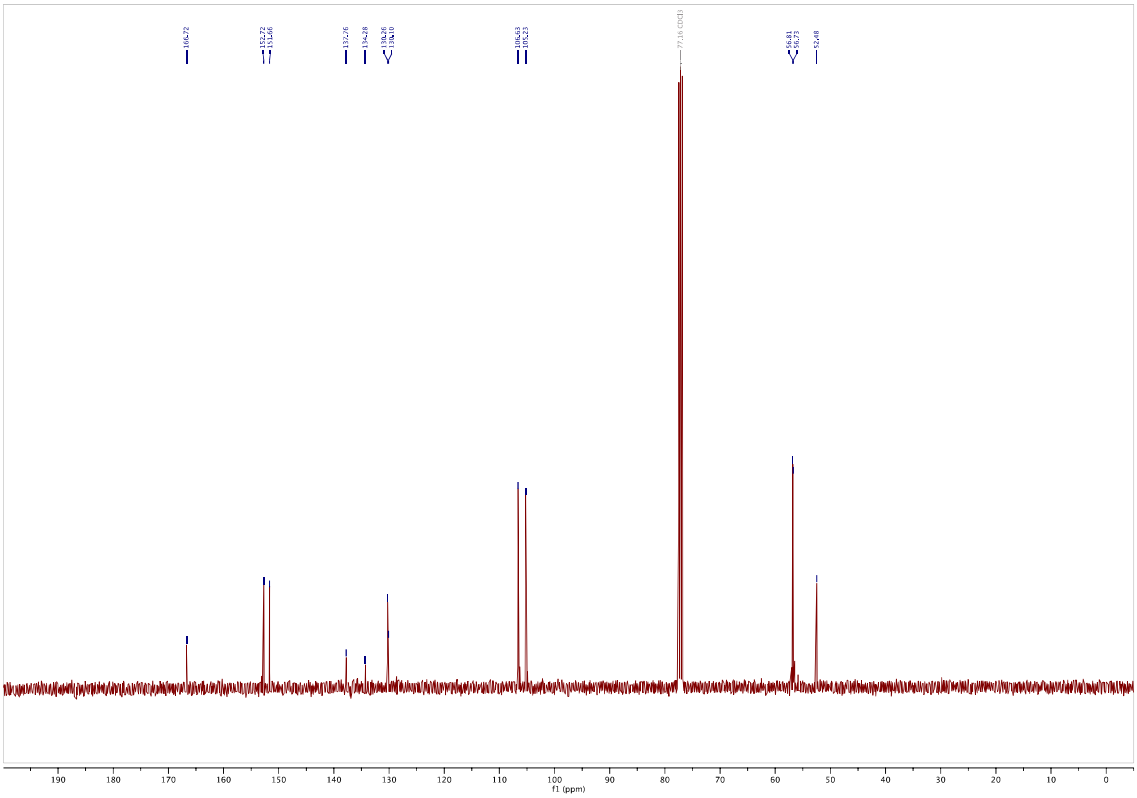

1-(2,6-dimethoxyphenyl)-2-(4-fluoro-2,6-dimethoxyphenyl)diazene (2f): 1H-NMR

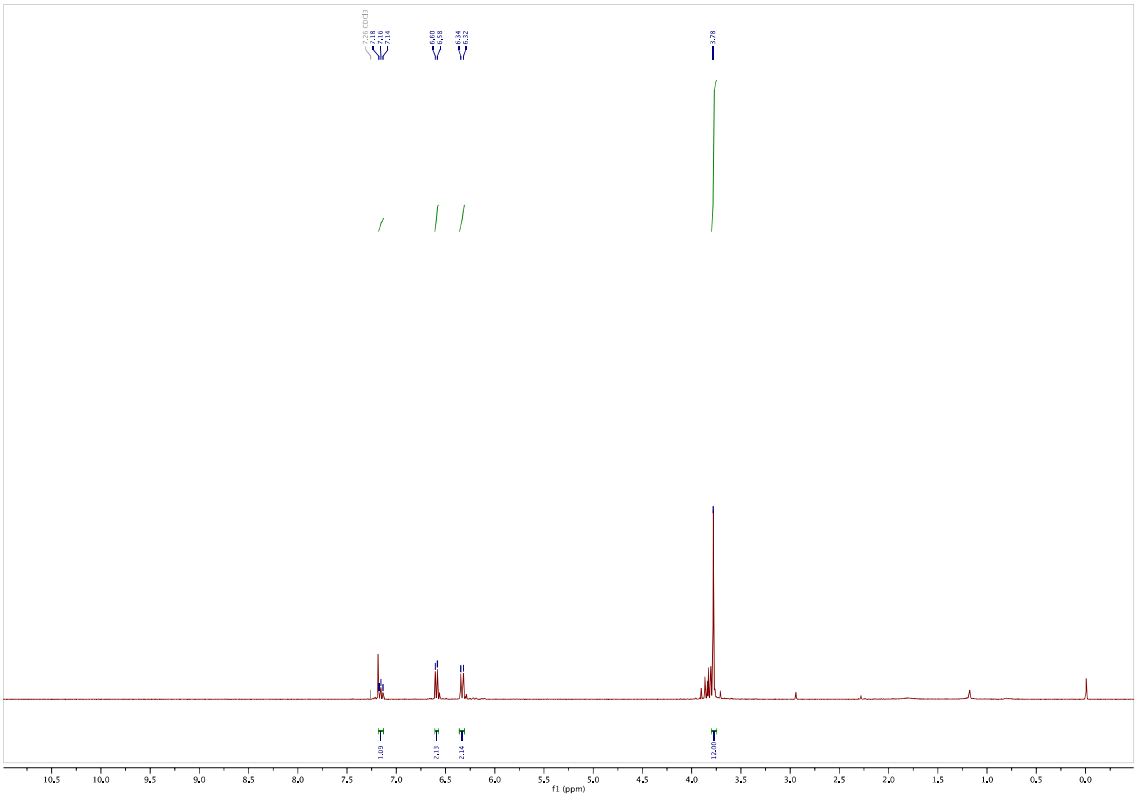

^{13}C-NMR

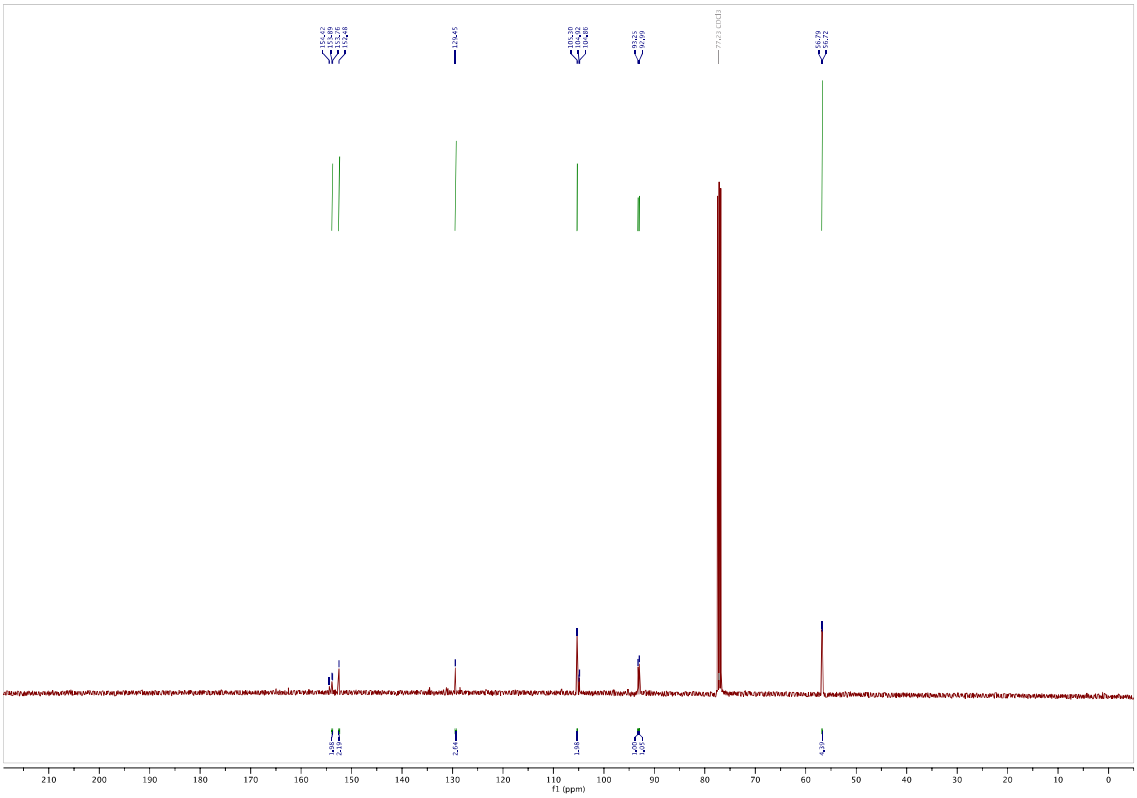

1-(4-chloro-2,6-dimethoxyphenyl)-2-(2,6-dimethoxyphenyl)diazene (2g): ^{1}H-NMR

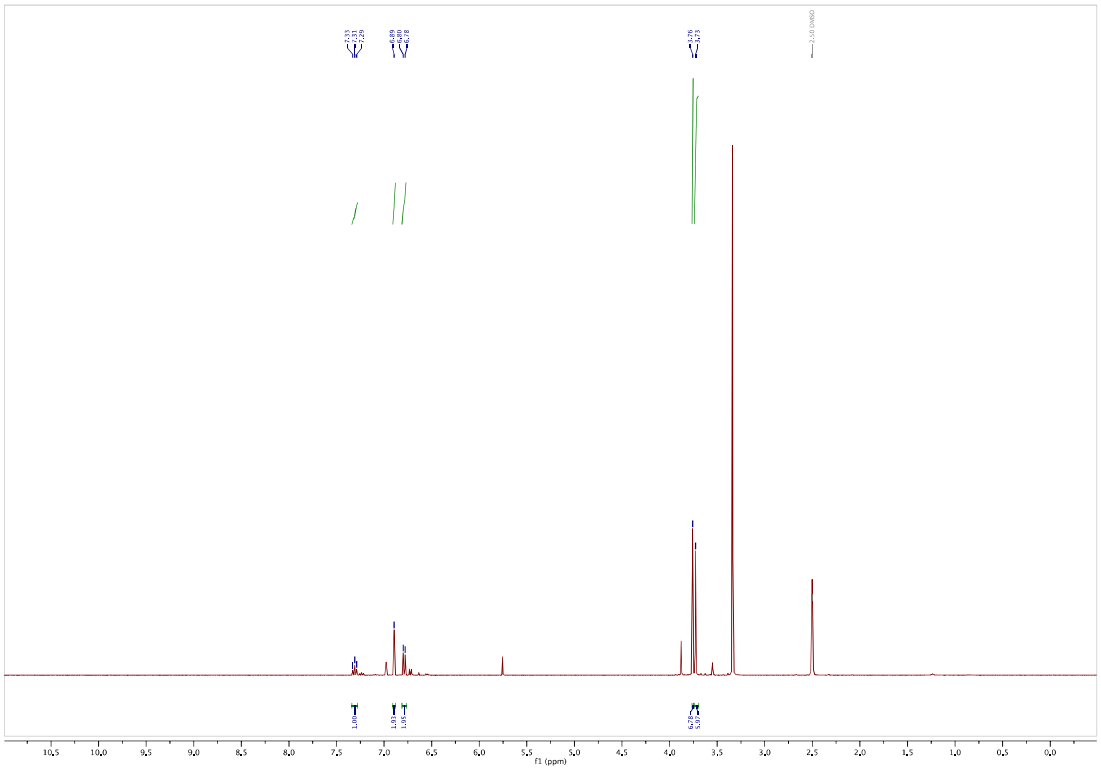

^{13}C-NMR

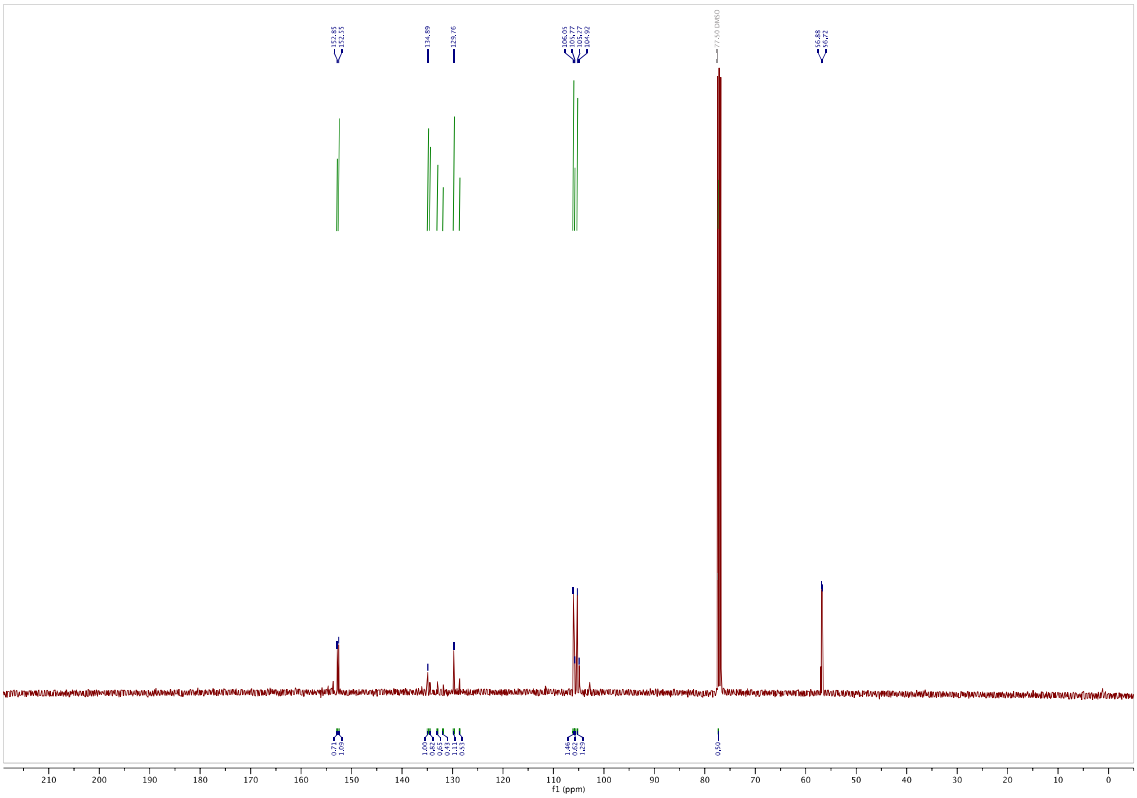

1-(2,6-dimethoxy-4-nitrophenyl)-2-(2,6-dimethoxyphenyl)diazene (2h): ^{1}H-NMR

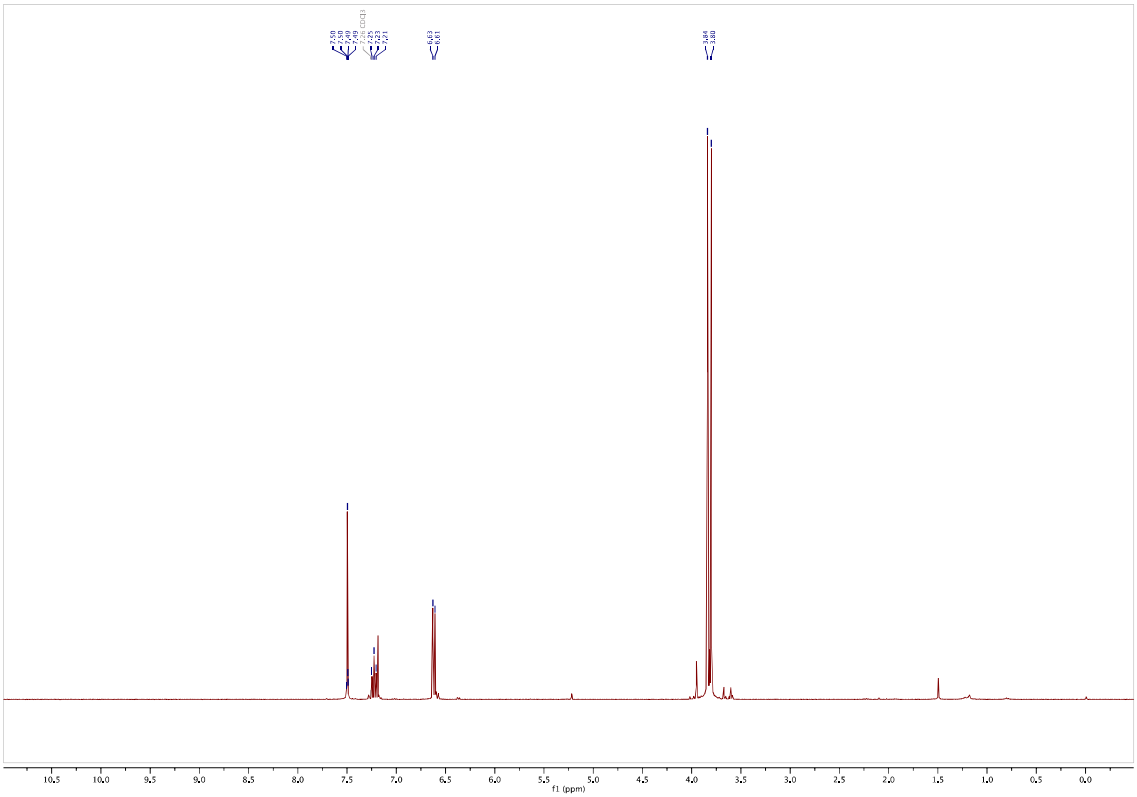

^{13}C-NMR

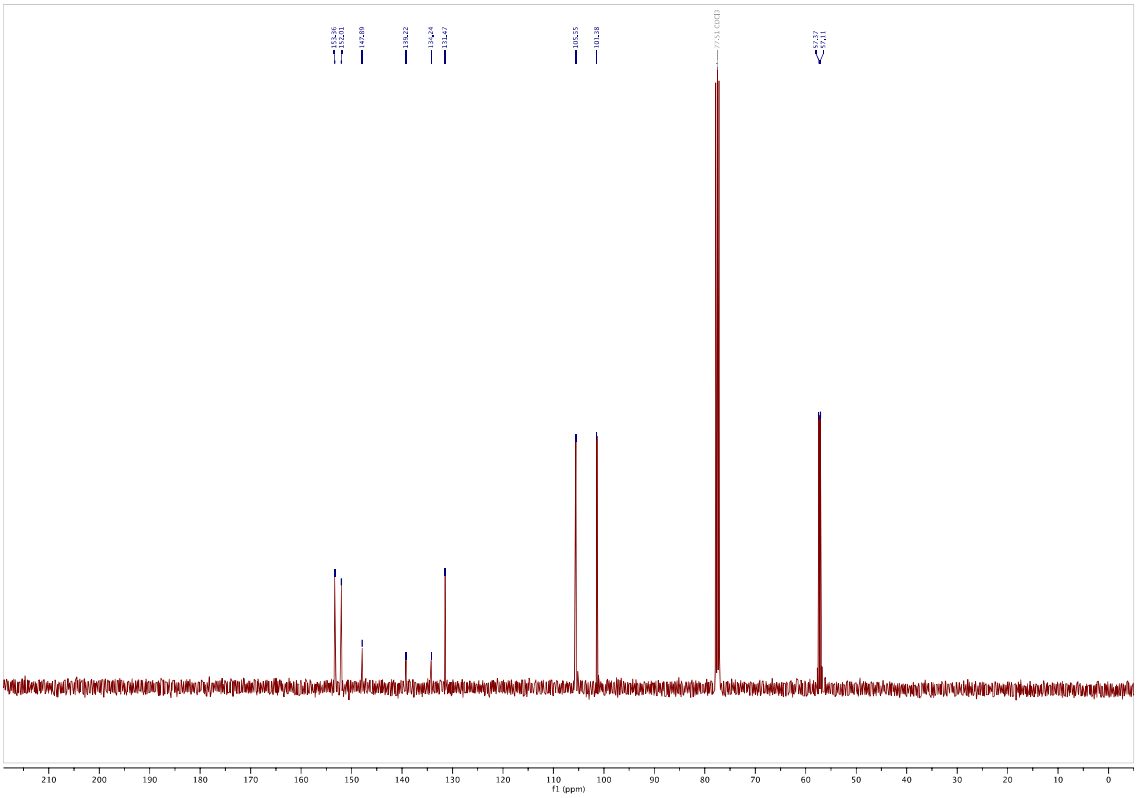

1-(2,6-dimethoxyphenyl)-2-(2-ethoxy-6-methoxyphenyl)diazene (3a): 1H-NMR

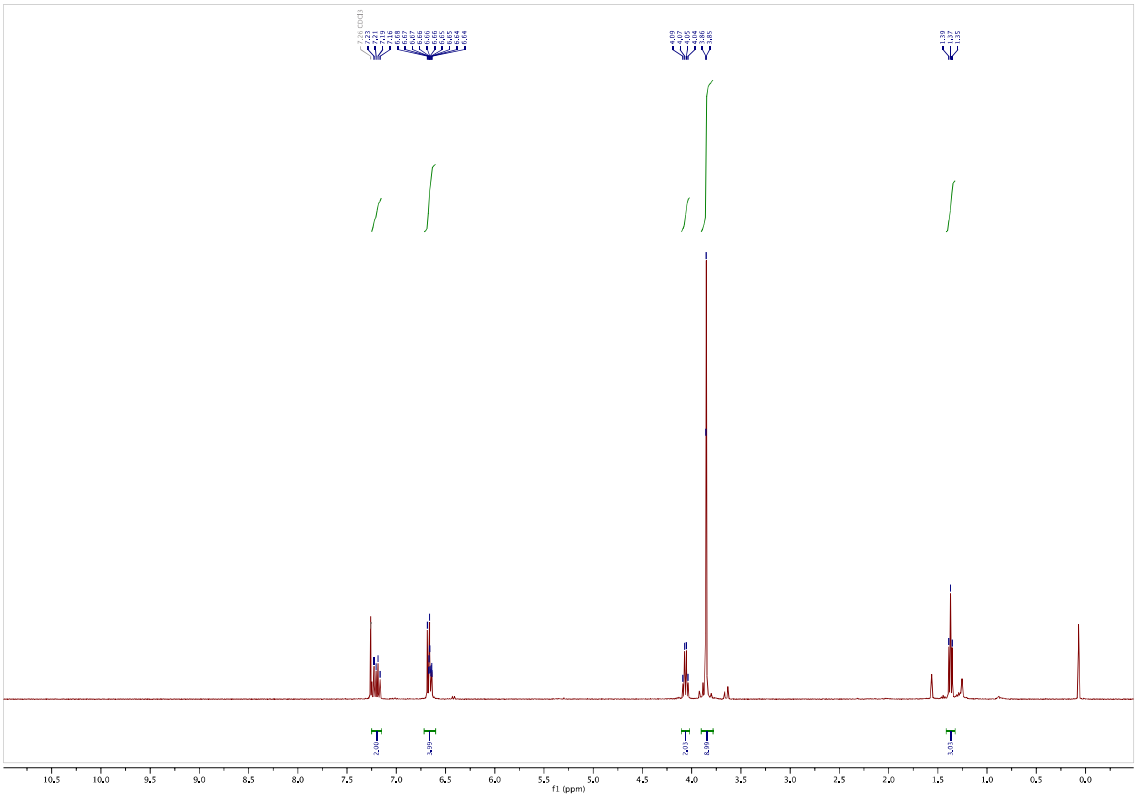

^{13}C-NMR

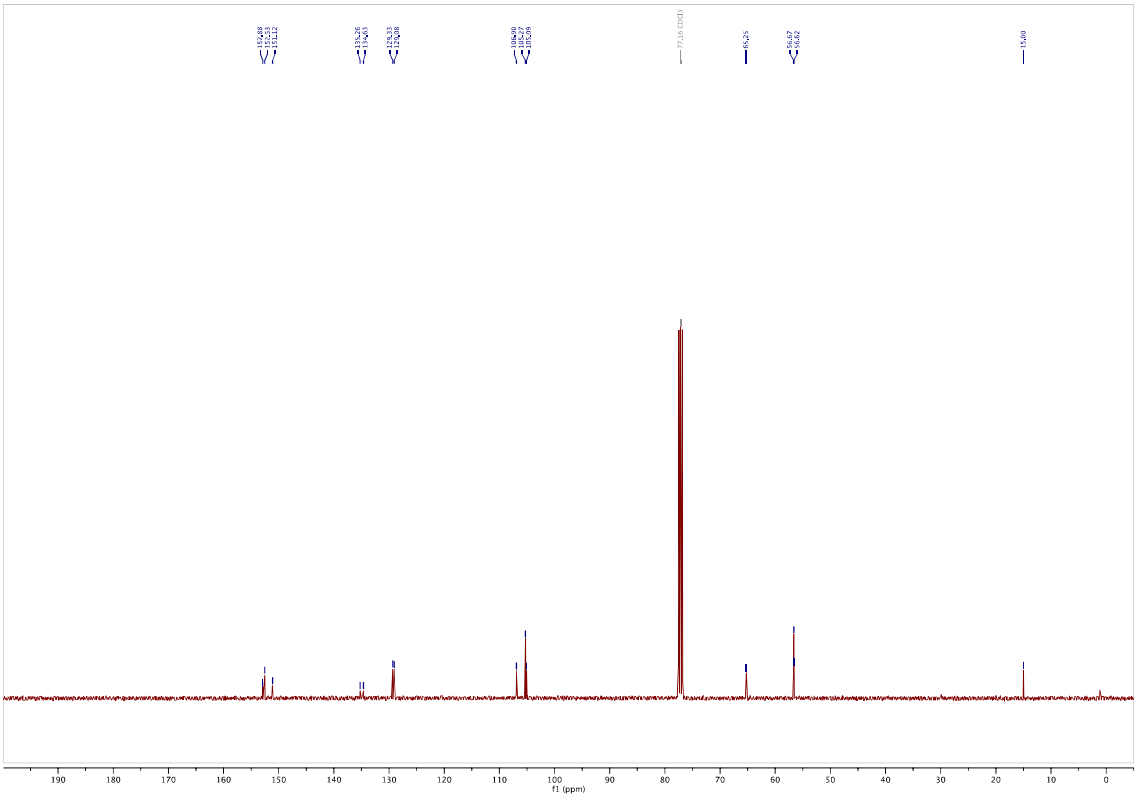

1,2-bis(2-ethoxy-6-methoxyphenyl)diazene (3b): ^{1}H-NMR

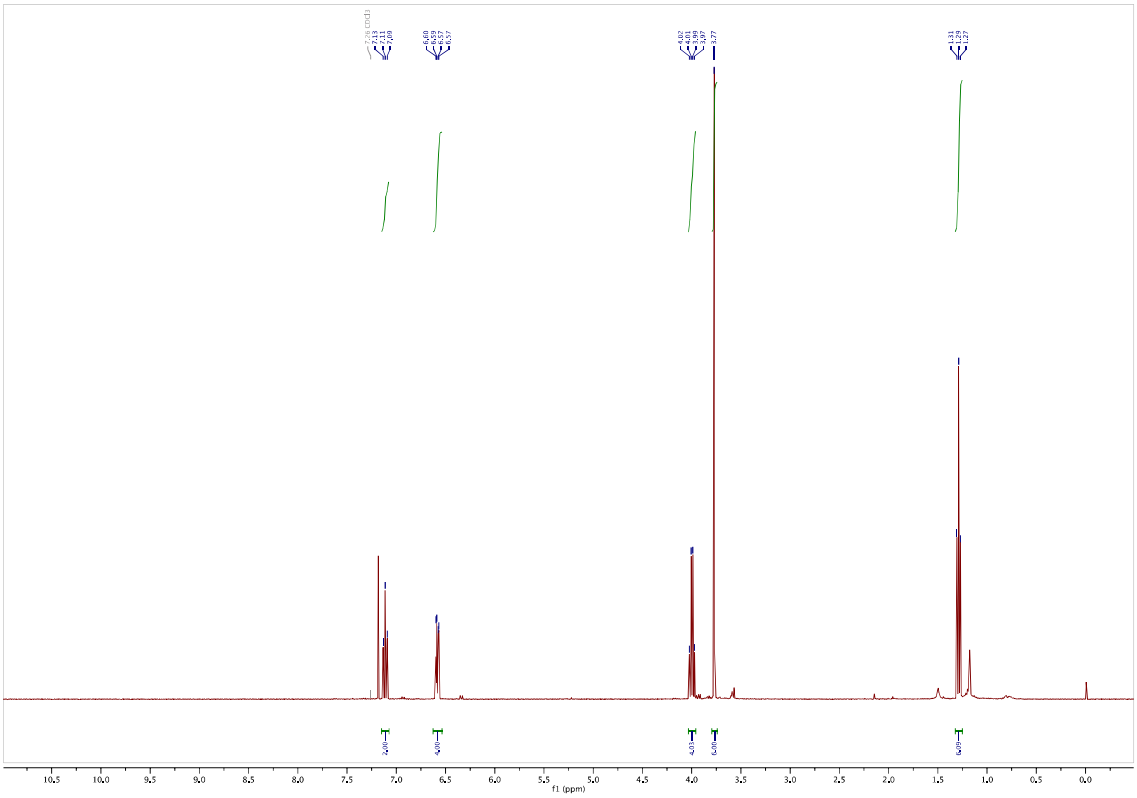

^{13}C-NMR

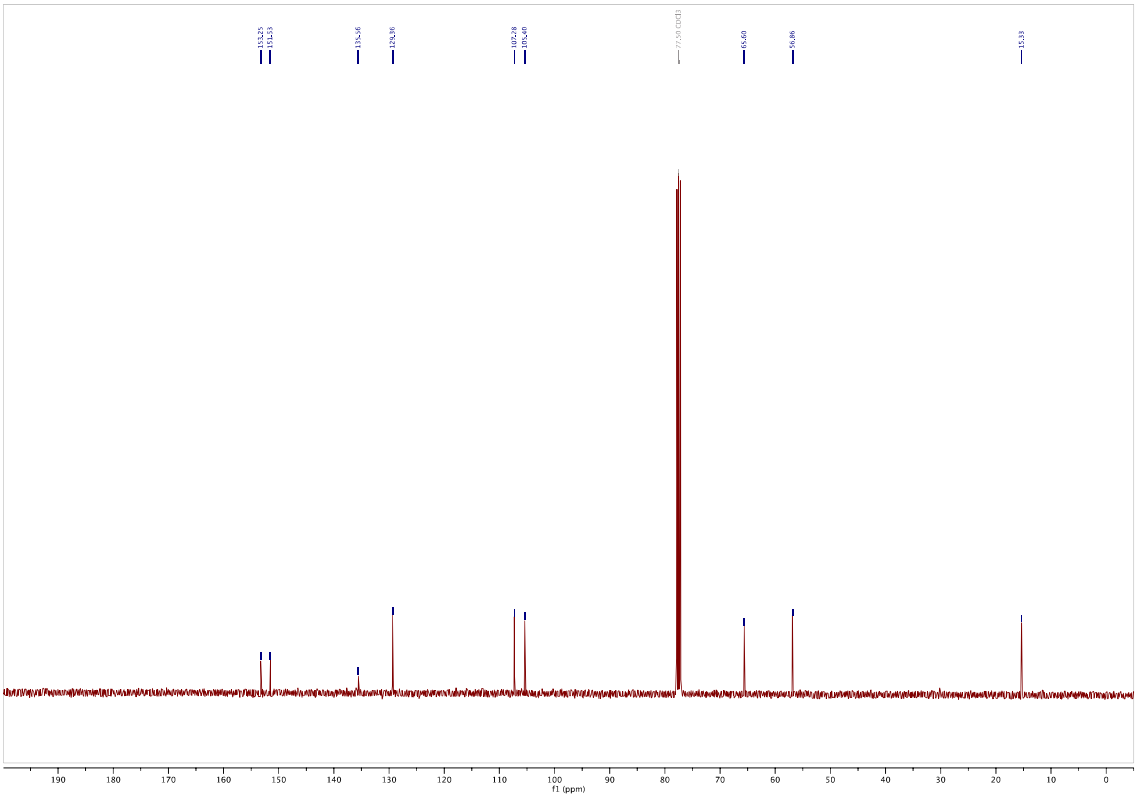

1-(2,6-diethoxyphenyl)-2-(2,6-dimethoxyphenyl)diazene (3c): ^{1}H-NMR

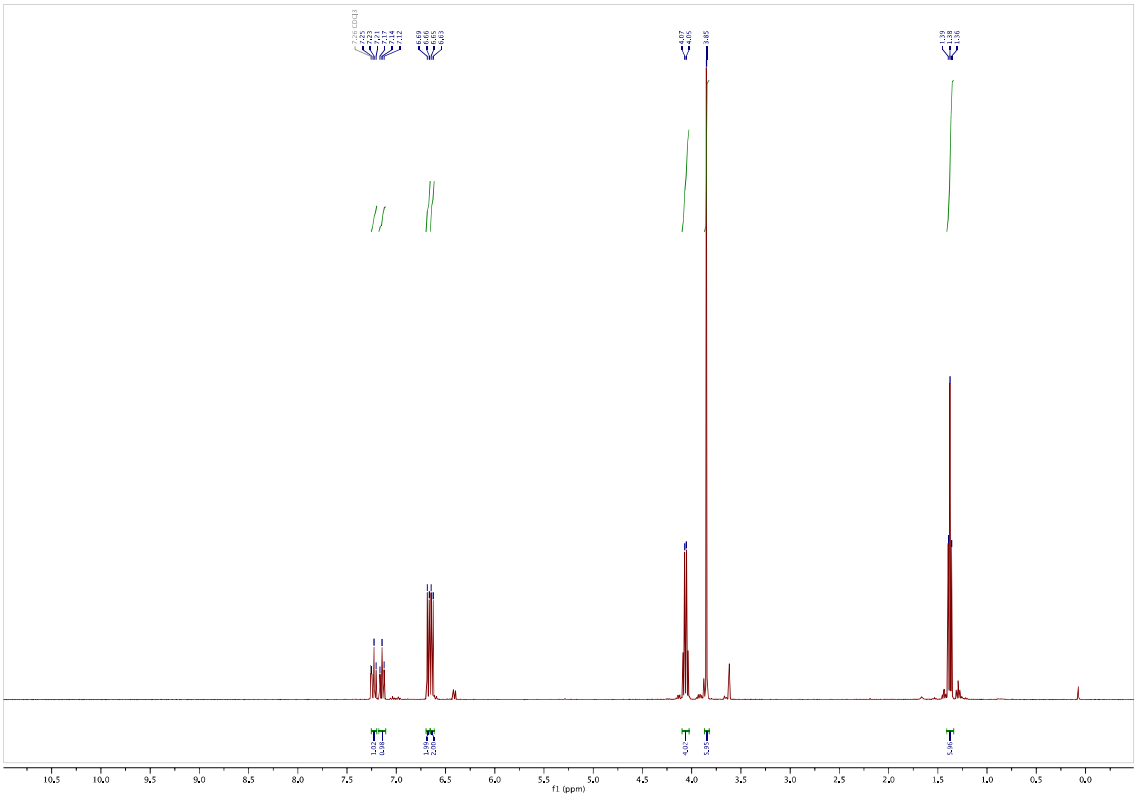

^{13}C-NMR

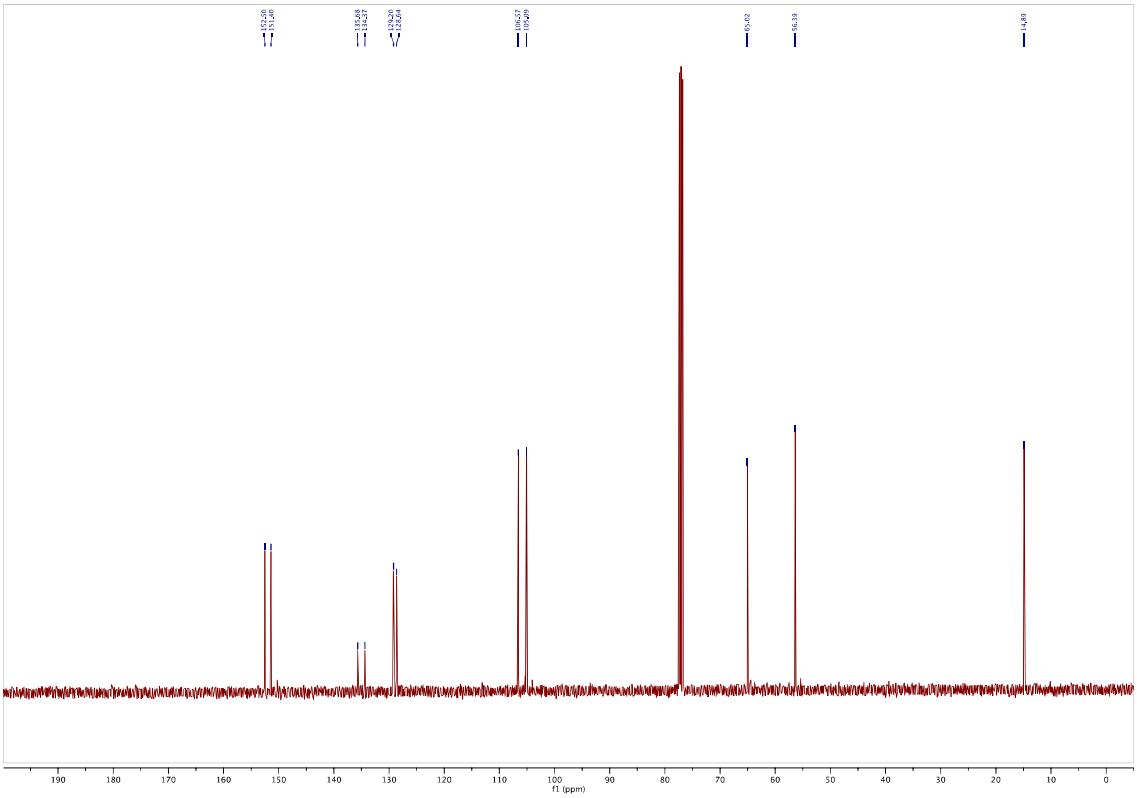

1-(2,6-diethoxyphenyl)-2-(2-ethoxy-6-methoxyphenyl)diazene (3d): ^{1}H-NMR

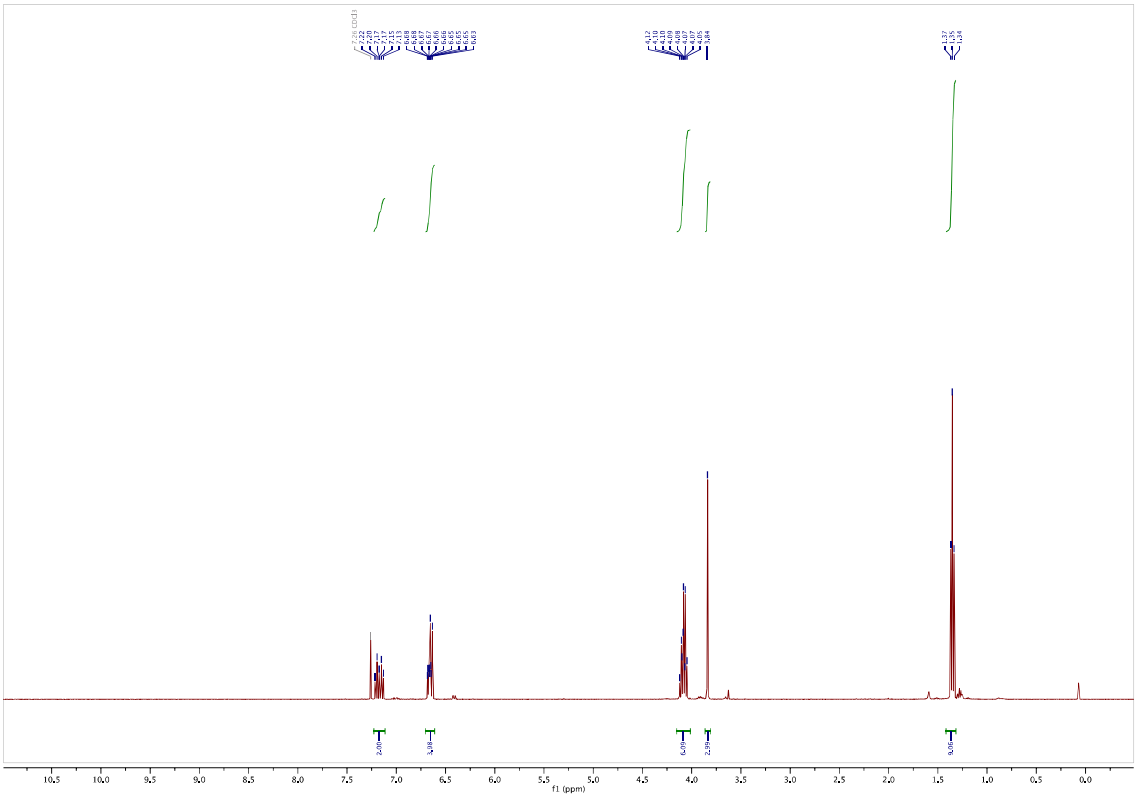

^{13}C-NMR

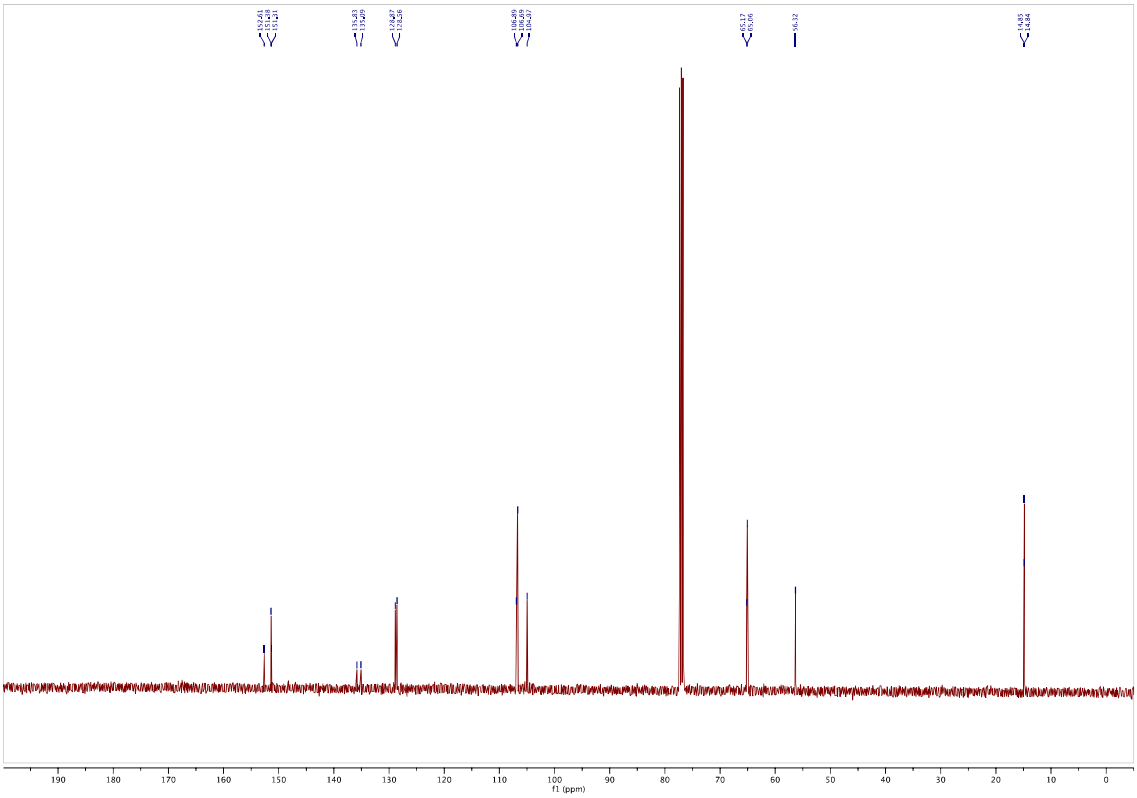

1,2-bis(2,6-diethoxyphenyl)diazene (3e): ^{1}H-NMR

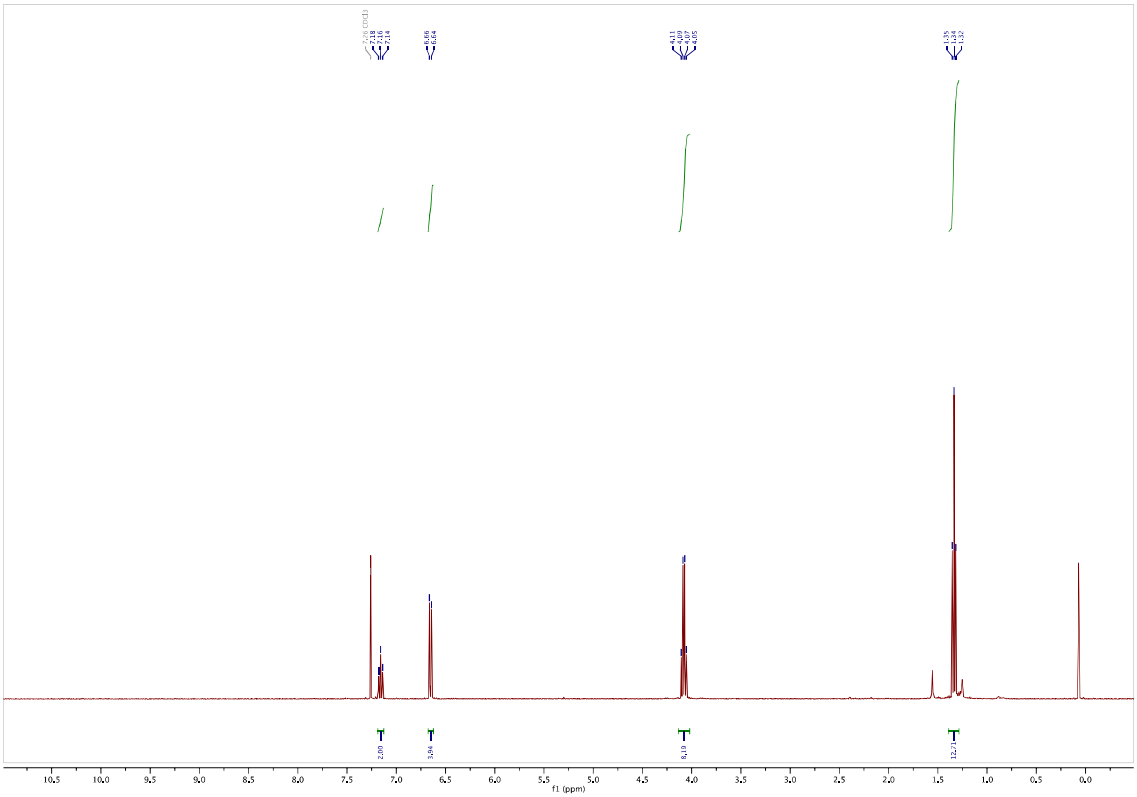

^{13}C-NMR

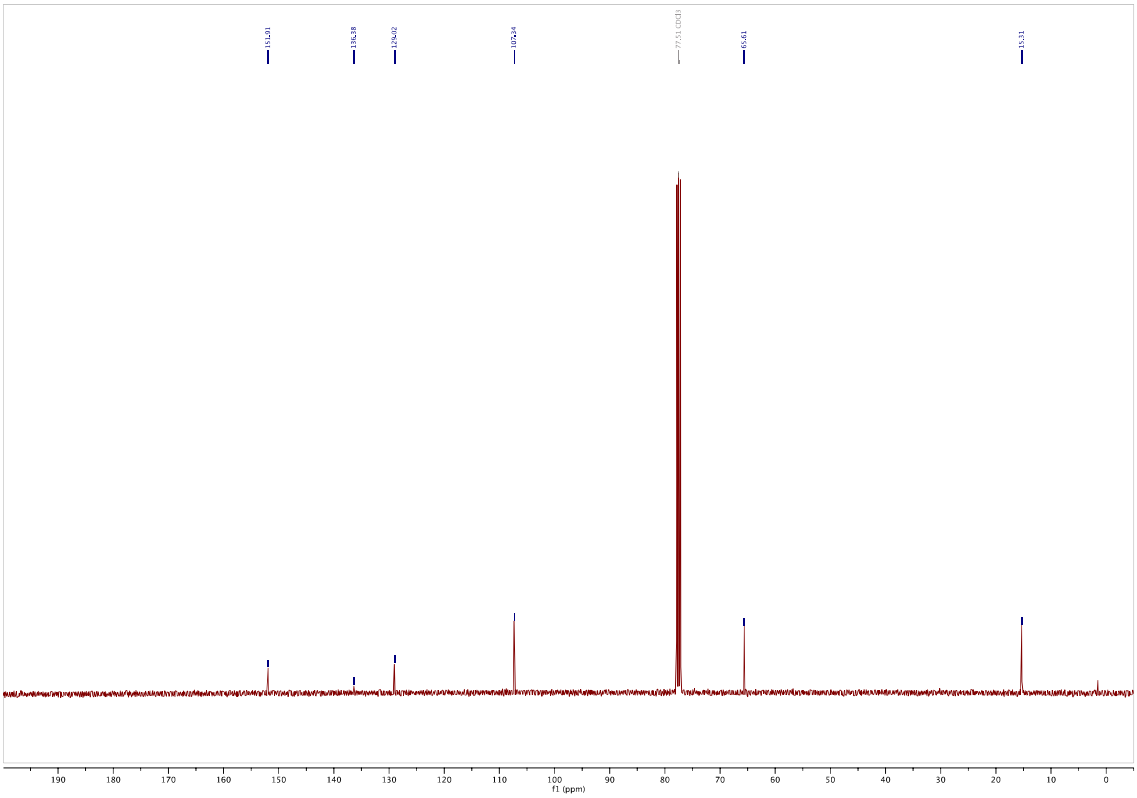

1,2-bis(2-methoxy-6-propoxyphenyl)diazene (3f): ^{1}H-NMR

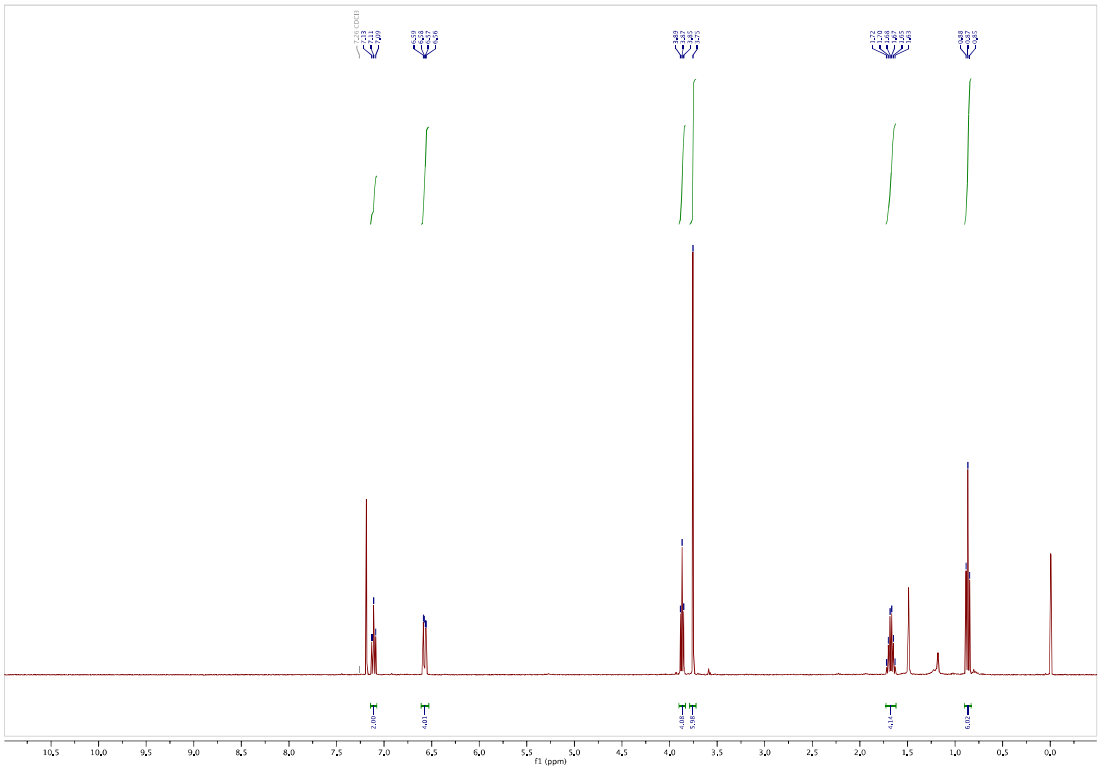

^{13}C-NMR

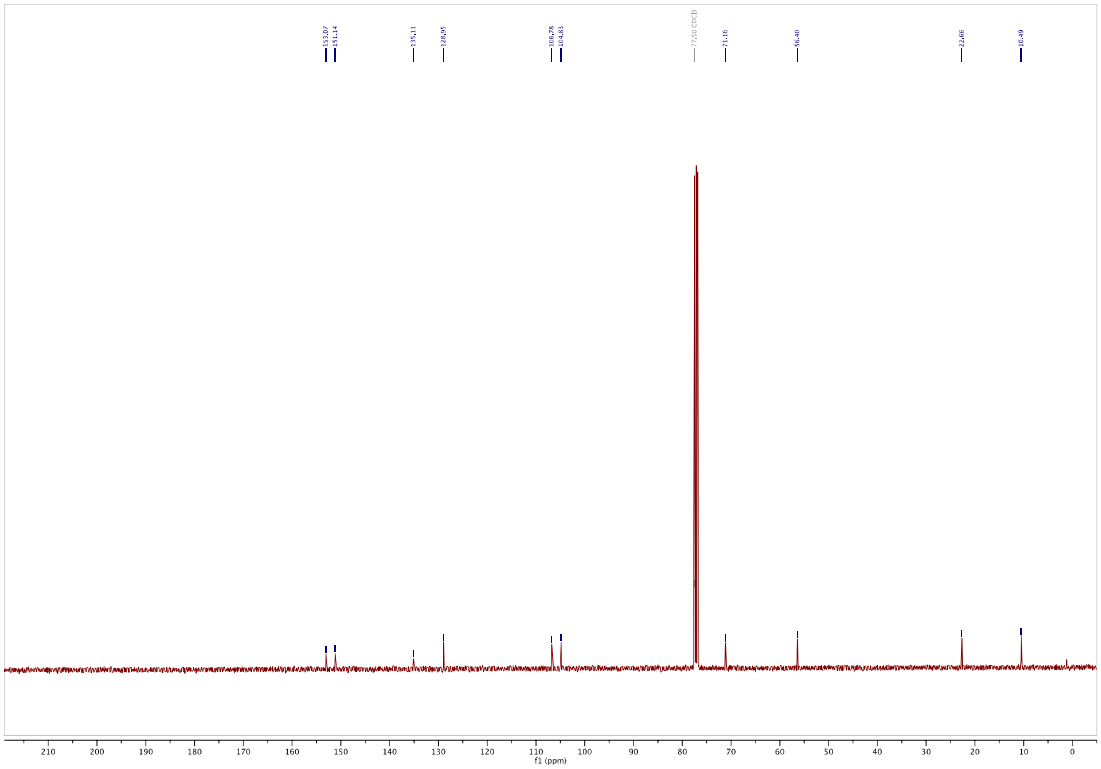

1-(2,6-dimethoxyphenyl)-2-(2,6-dipropoxyphenyl)diazene (3g): ^{1}H-NMR

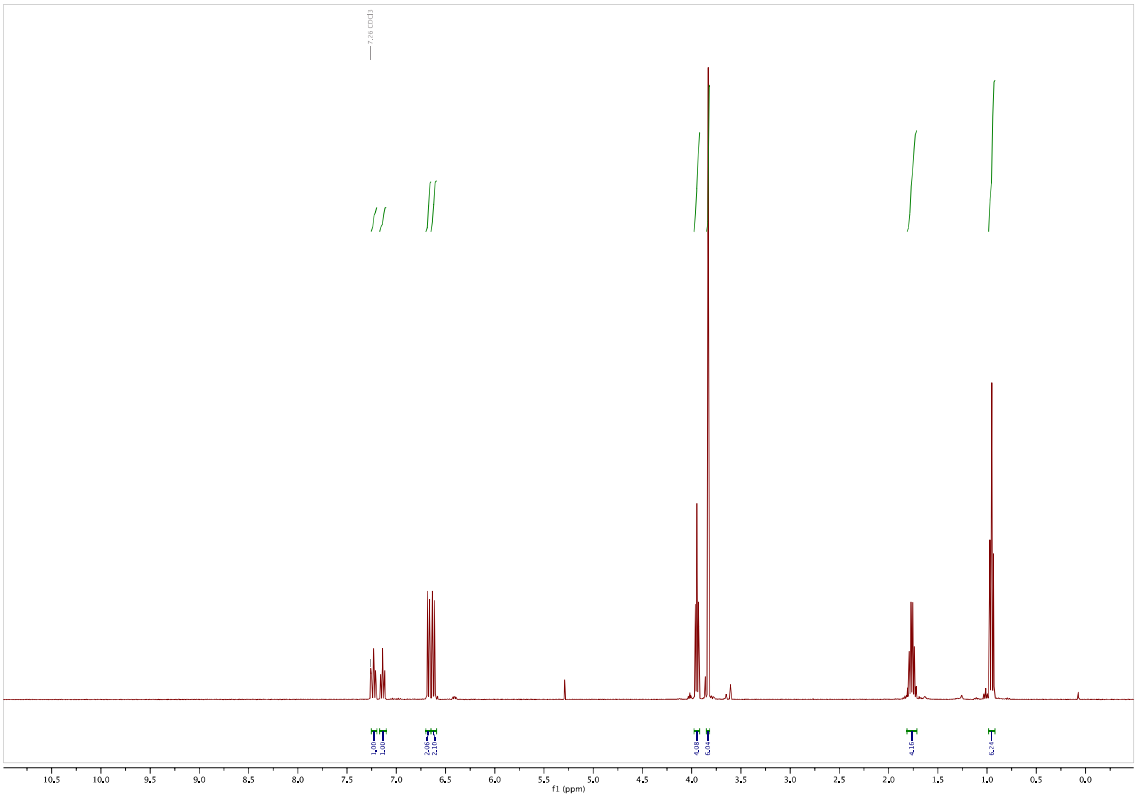

^{13}C-NMR

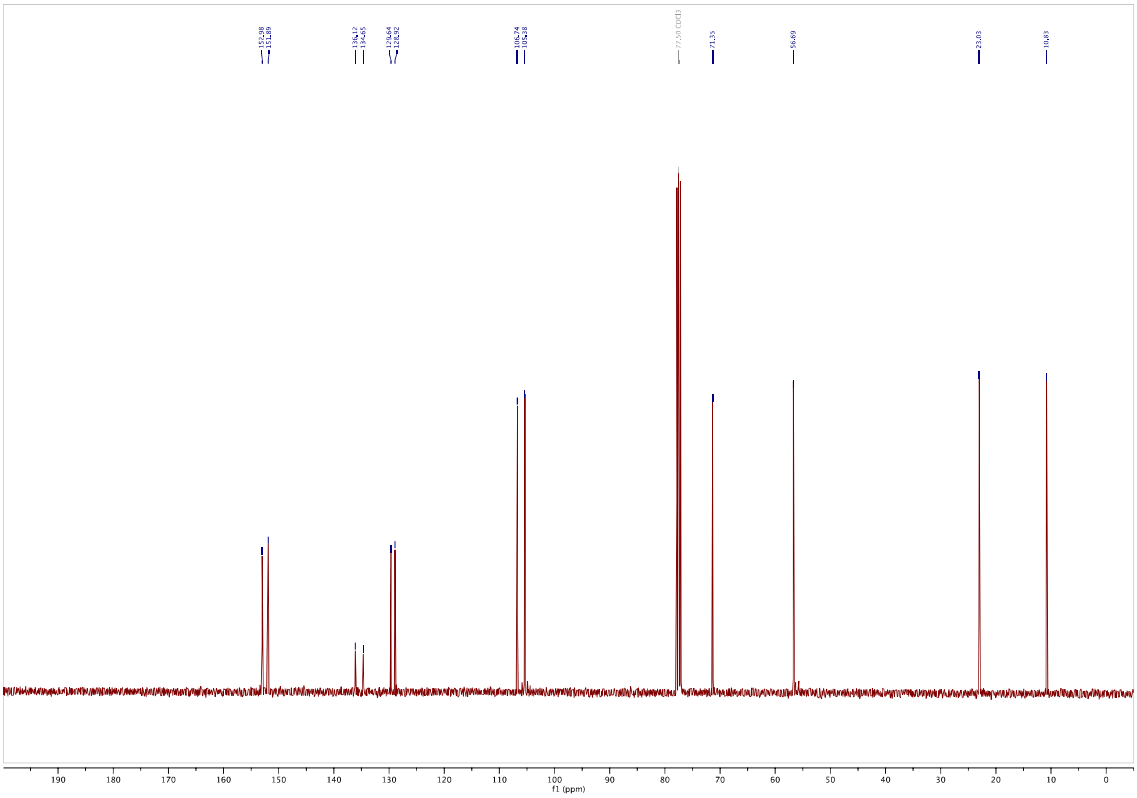

1-(2,6-dipropoxyphenyl)-2-(2-methoxy-6-propoxyphenyl)diazene (3h): ^{1}H-NMR

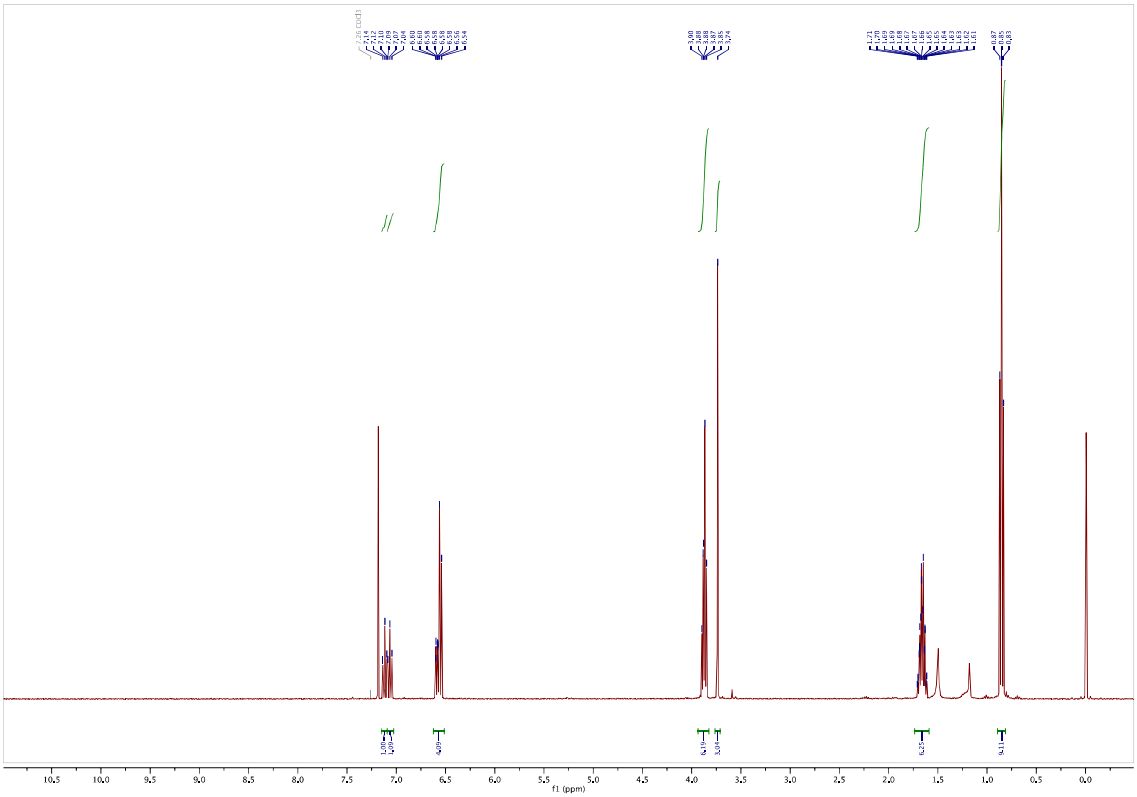

^{13}C-NMR

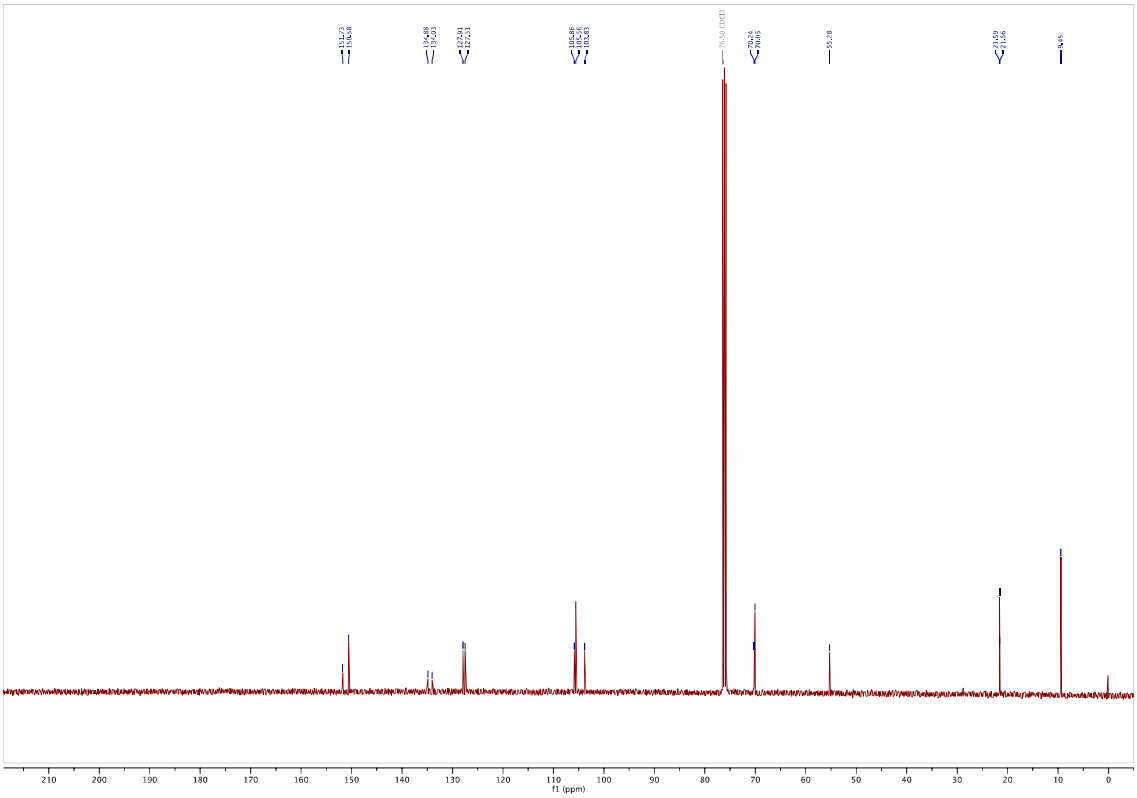

1-(2,6-dipropoxyphenyl)-2-(2-ethoxy-6-propoxyphenyl)diazene (3i): ^{1}H-NMR

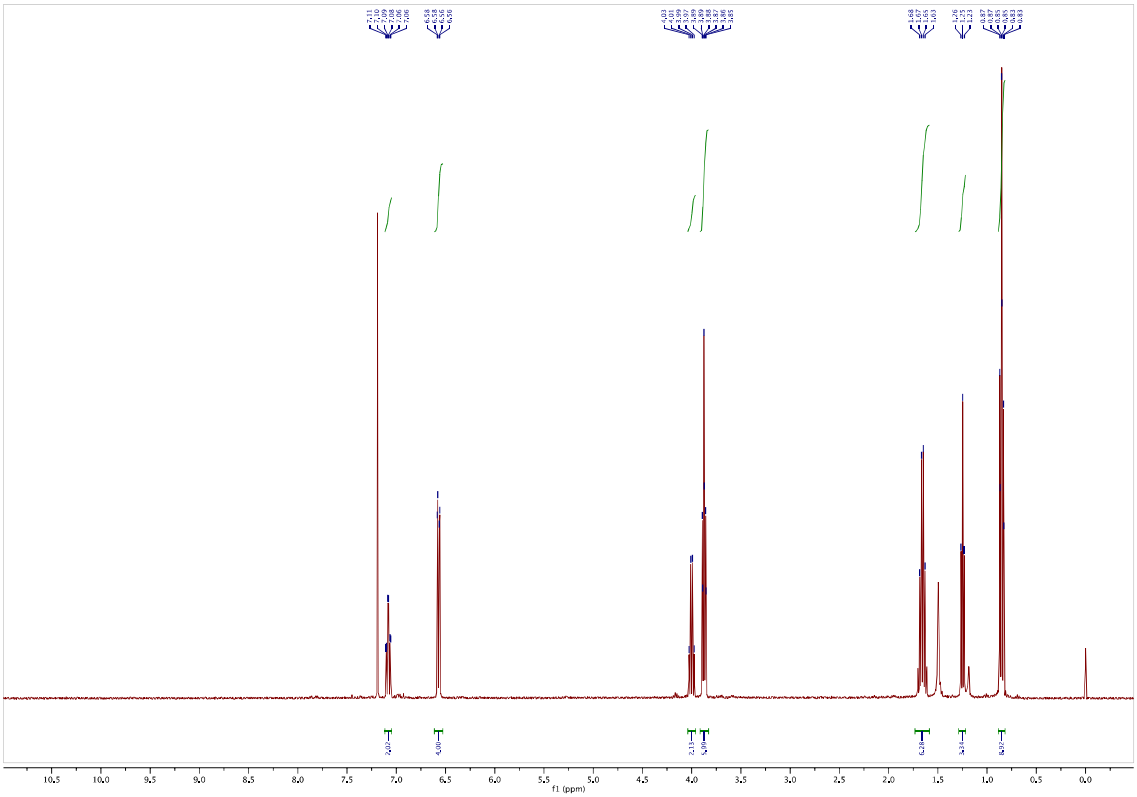

^{13}C-NMR

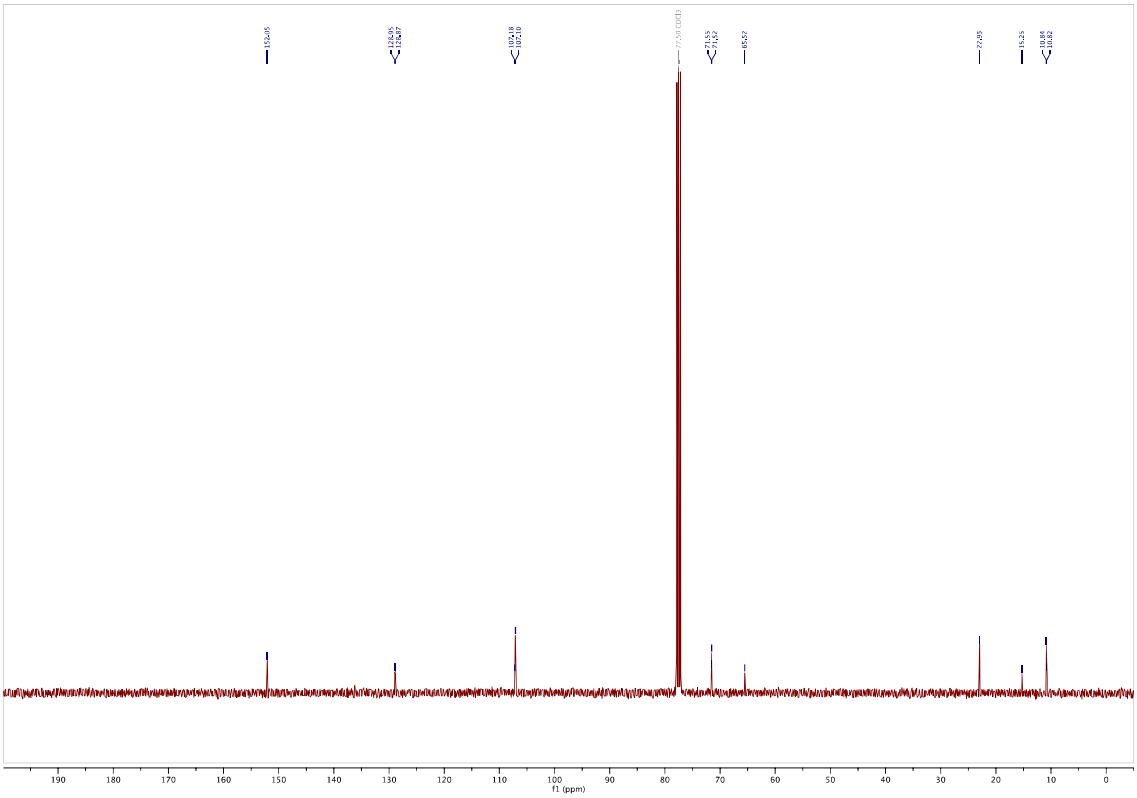

1,2-bis(2,6-dipropoxyphenyl)diazene (3j): ^{1}H-NMR

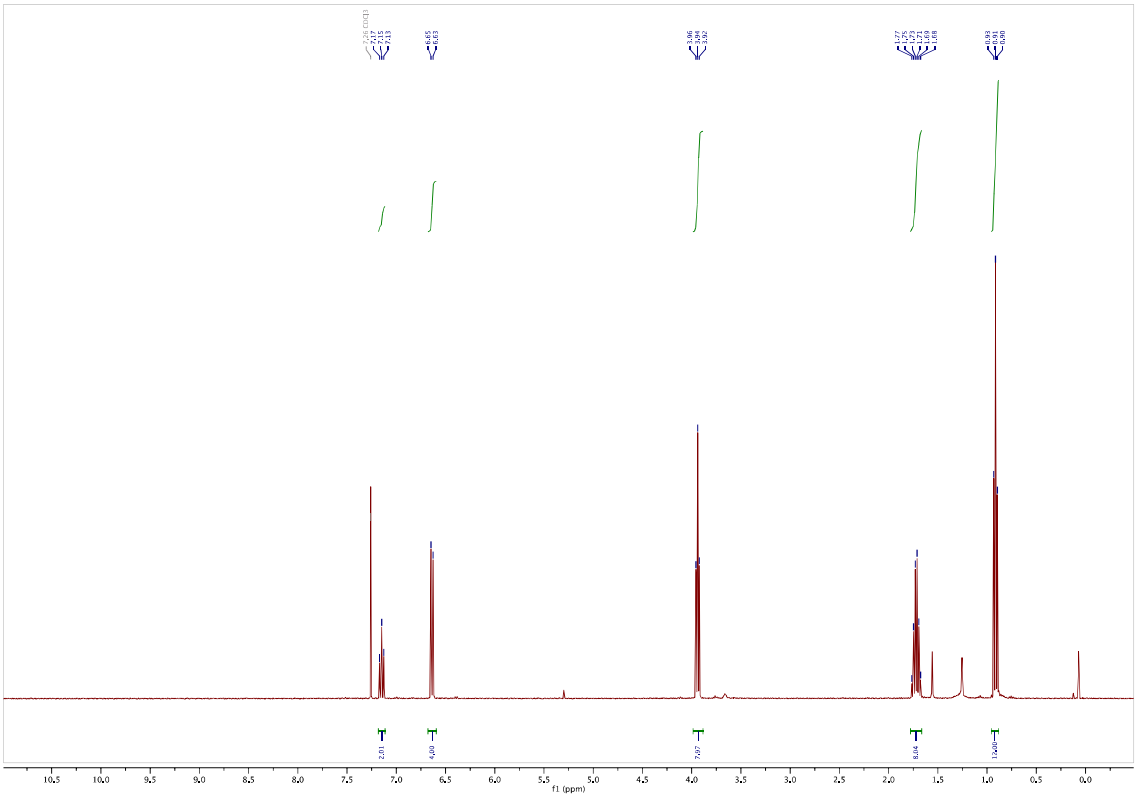

^{13}C-NMR

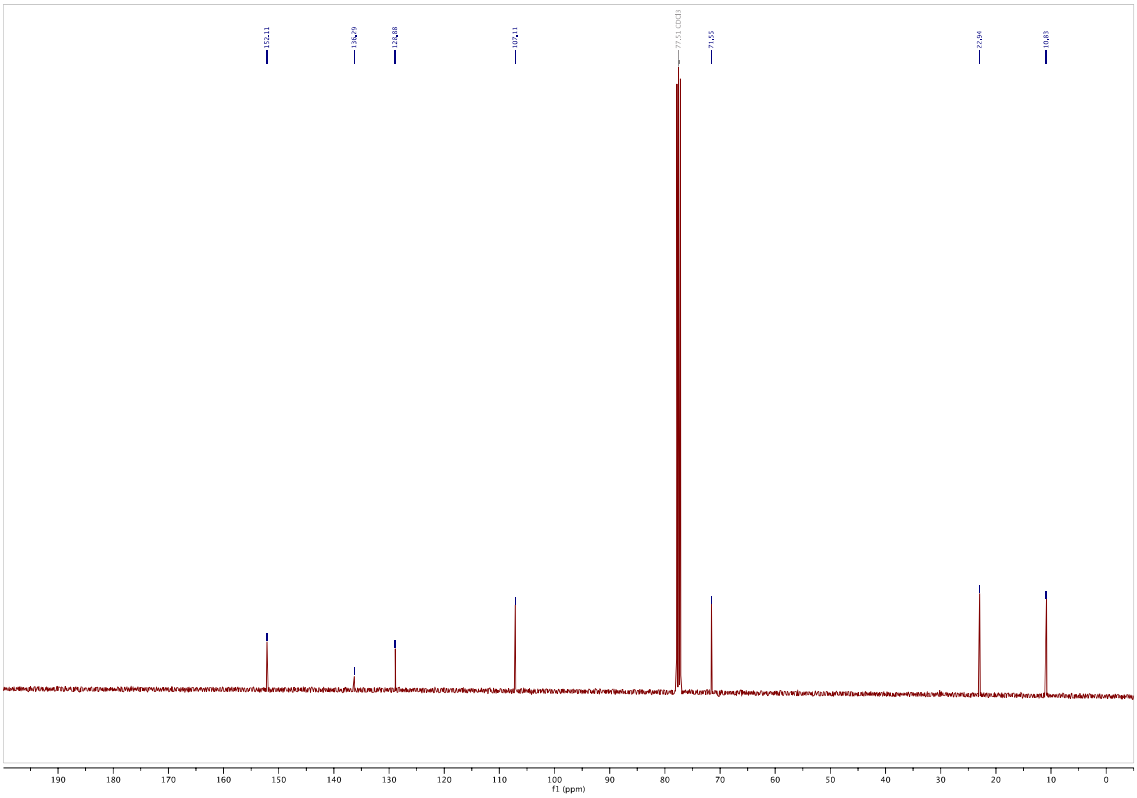

1-(2,6-dimethoxyphenyl)-2-(2-fluoro-6-methoxyphenyl)diazene (3k): ^{1}H-NMR

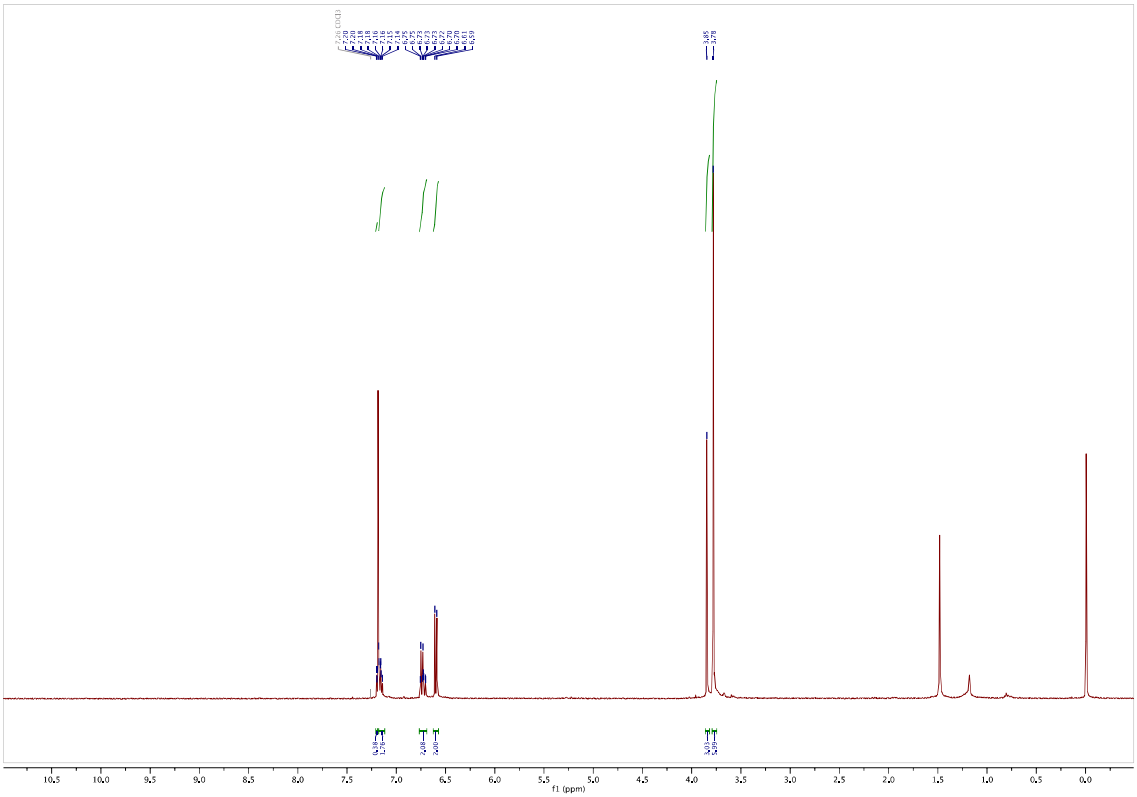

^{13}C-NMR

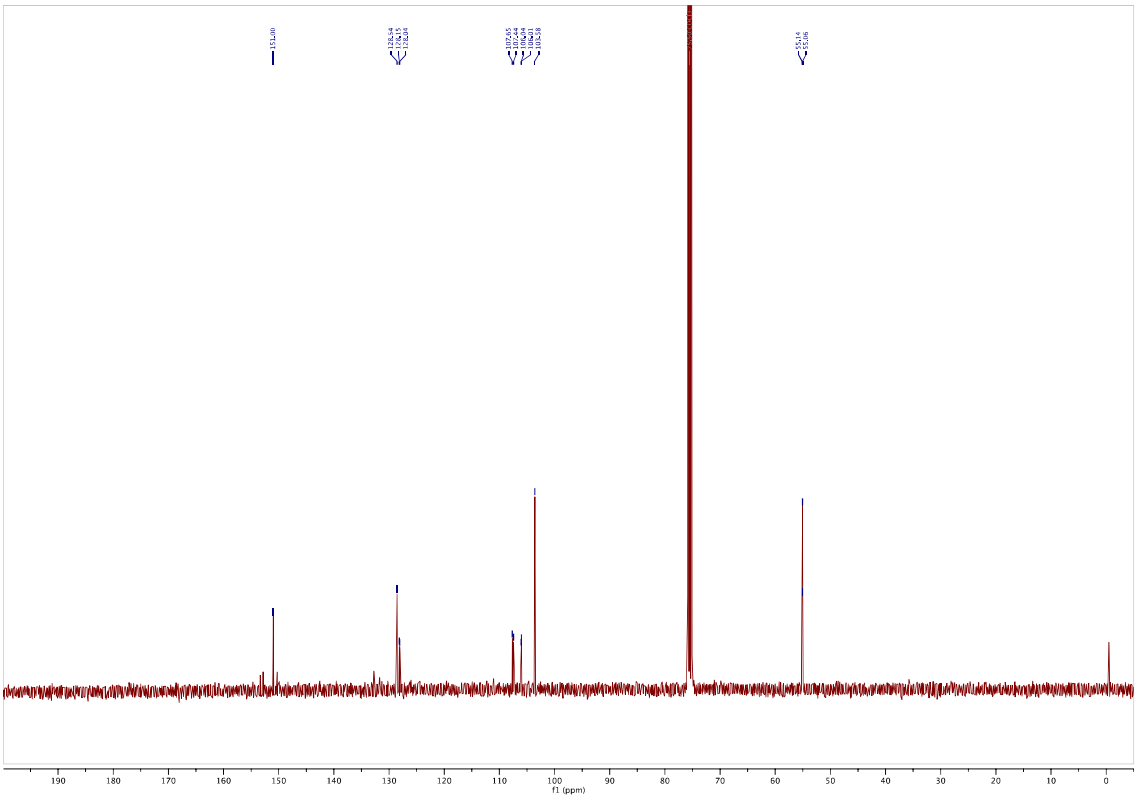

1,2-bis(2-fluoro-6-methoxyphenyl)diazene (3l): ^{1}H-NMR

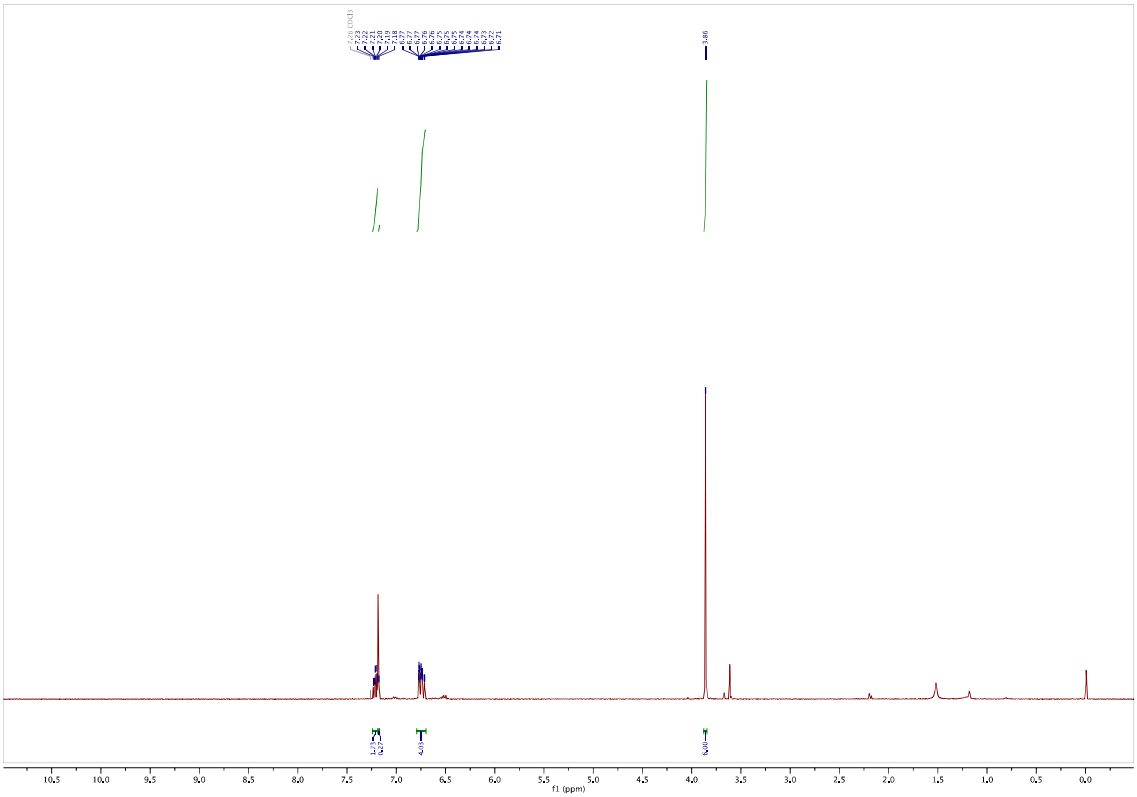

^{13}C-NMR

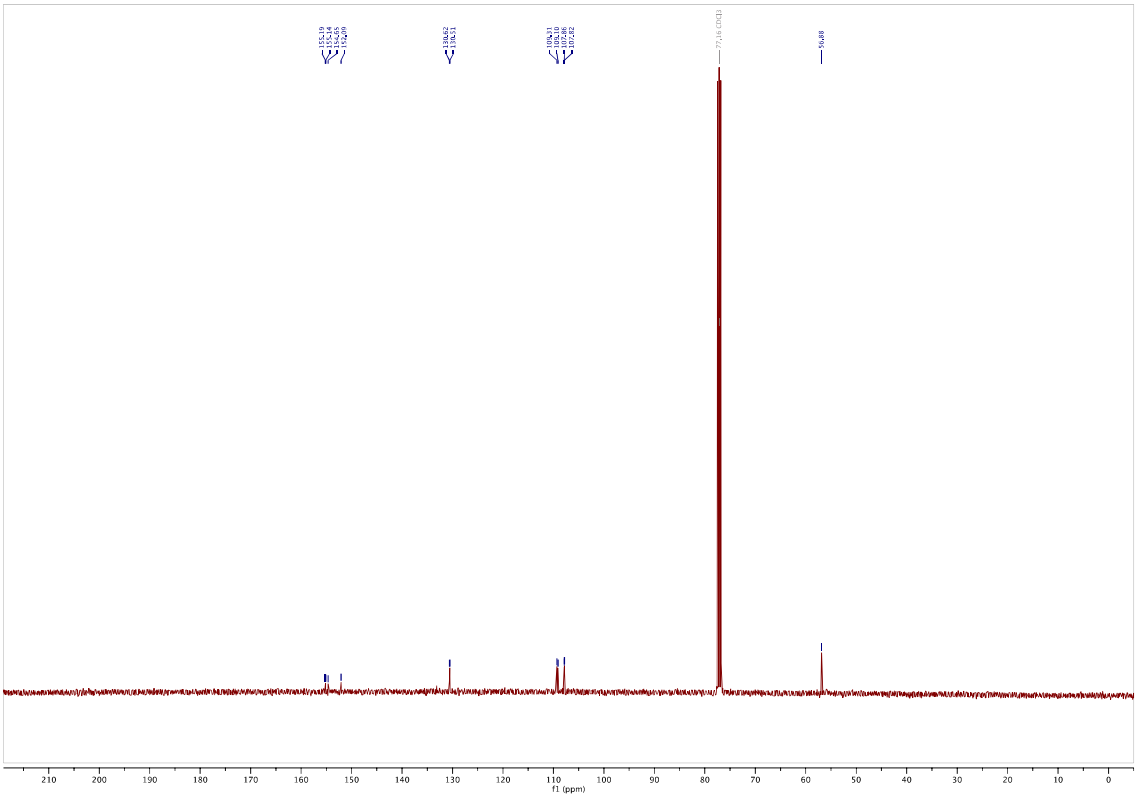

1-(2,6-difluorophenyl)-2-(2,6-dimethoxyphenyl)diazene (3m): ^{1}H-NMR

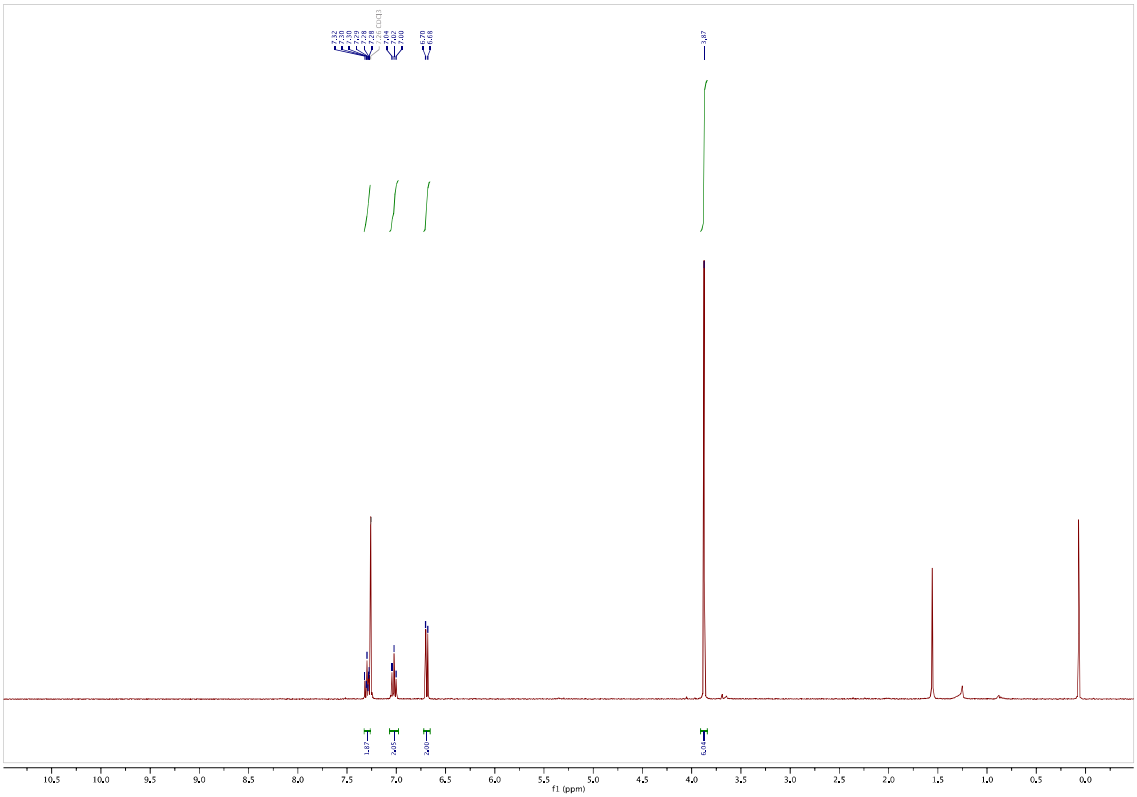

^{13}C-NMR

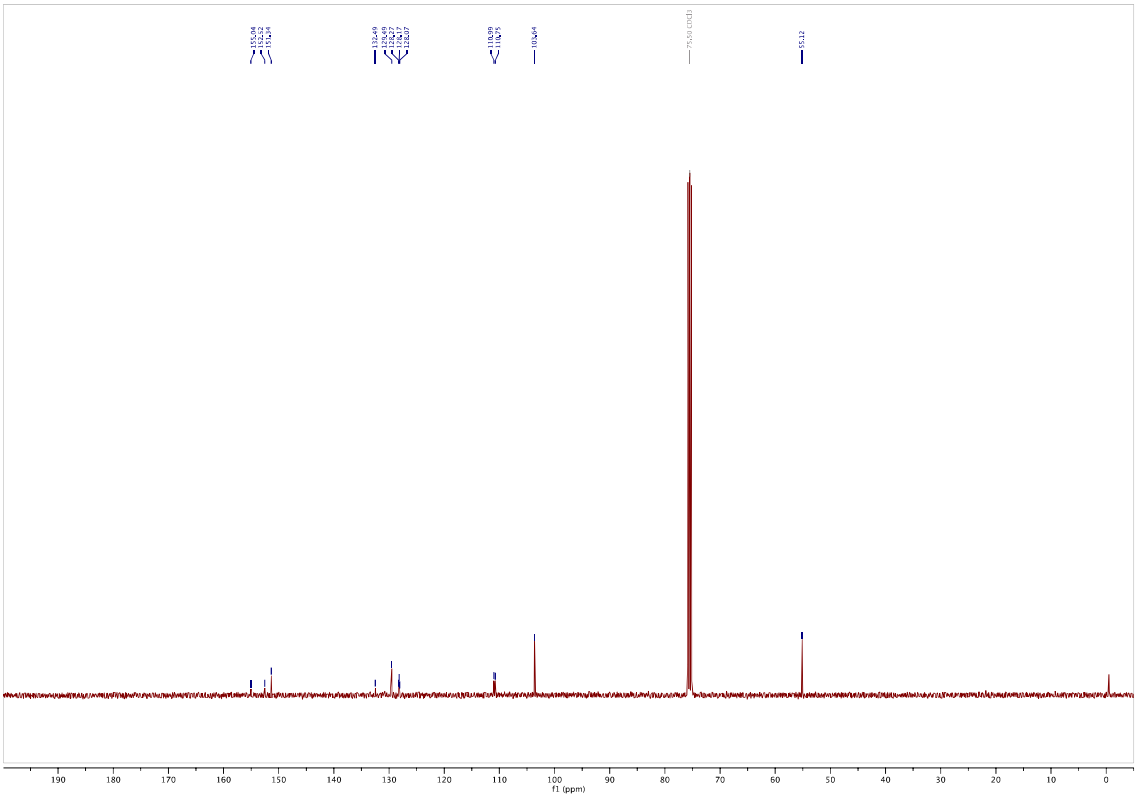

1,2-bis(2,6-bis(methoxy-d_3)phenyl)diazene (3n): ^{1}H-NMR

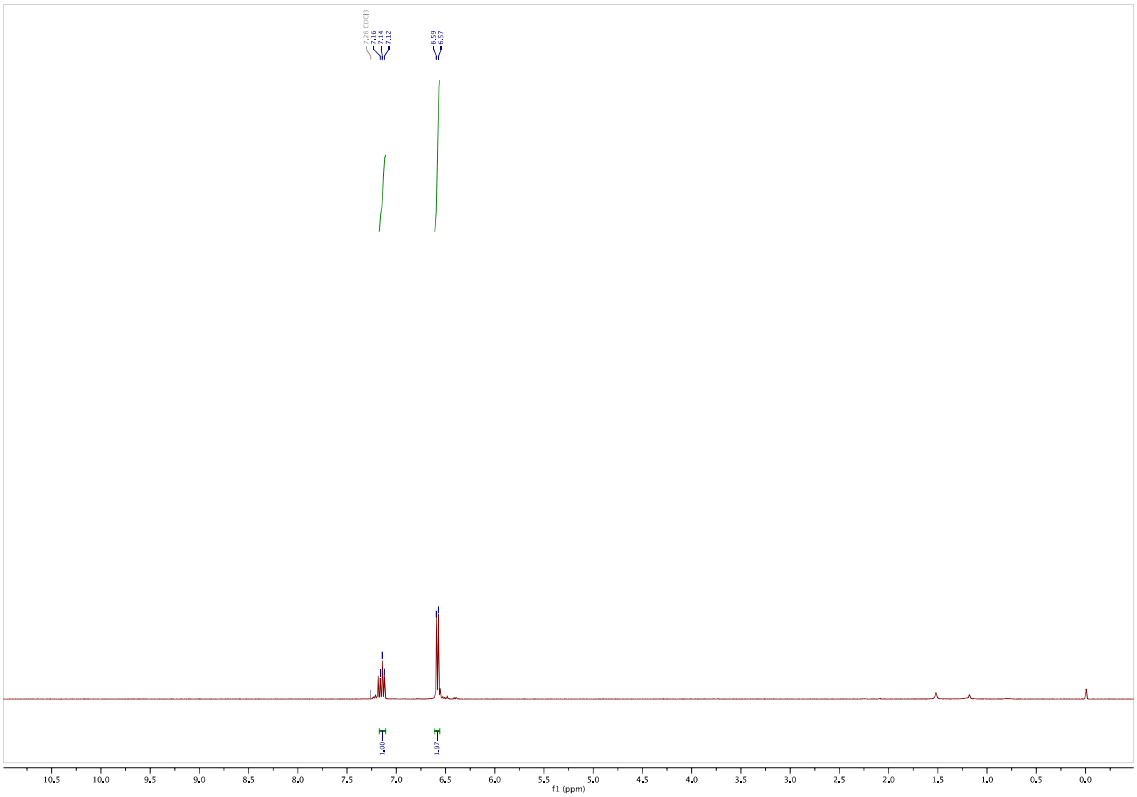

^{13}C-NMR

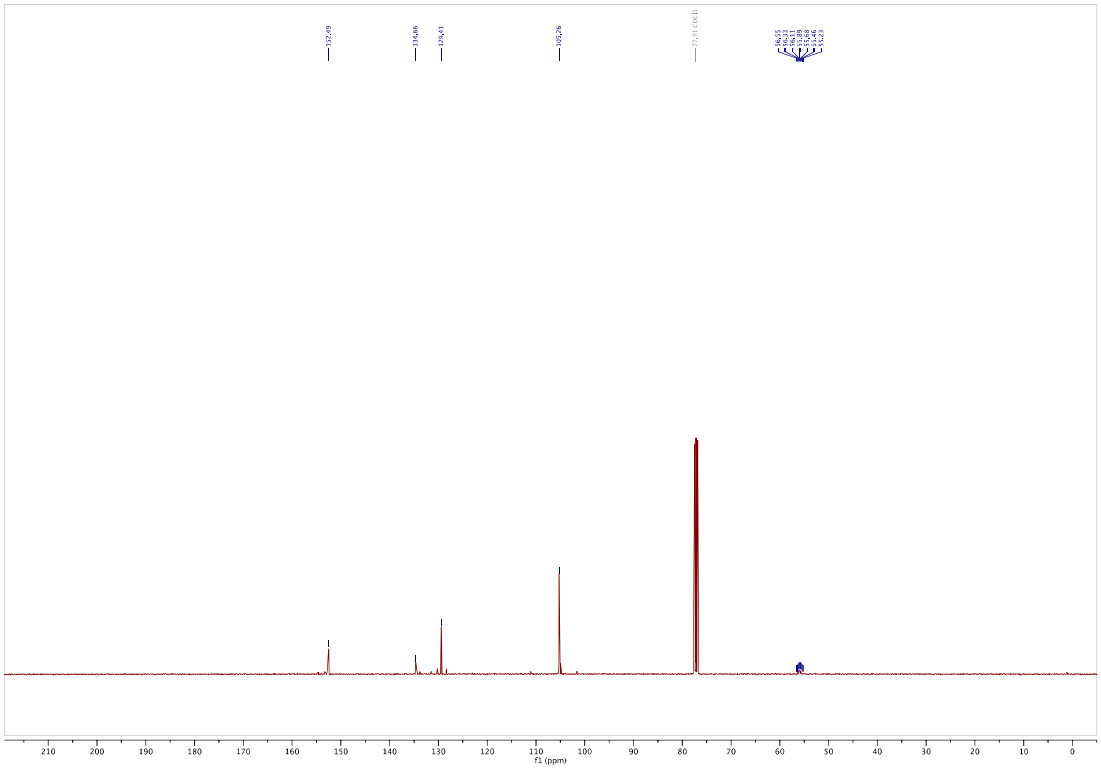

3,3',3'',3'''-((diazene-1,2-diylbis(benzene-2,1,3-triyl))tetrakis(oxy))tetrakis(propan-1-ol) (3o): ^{1}H-NMR

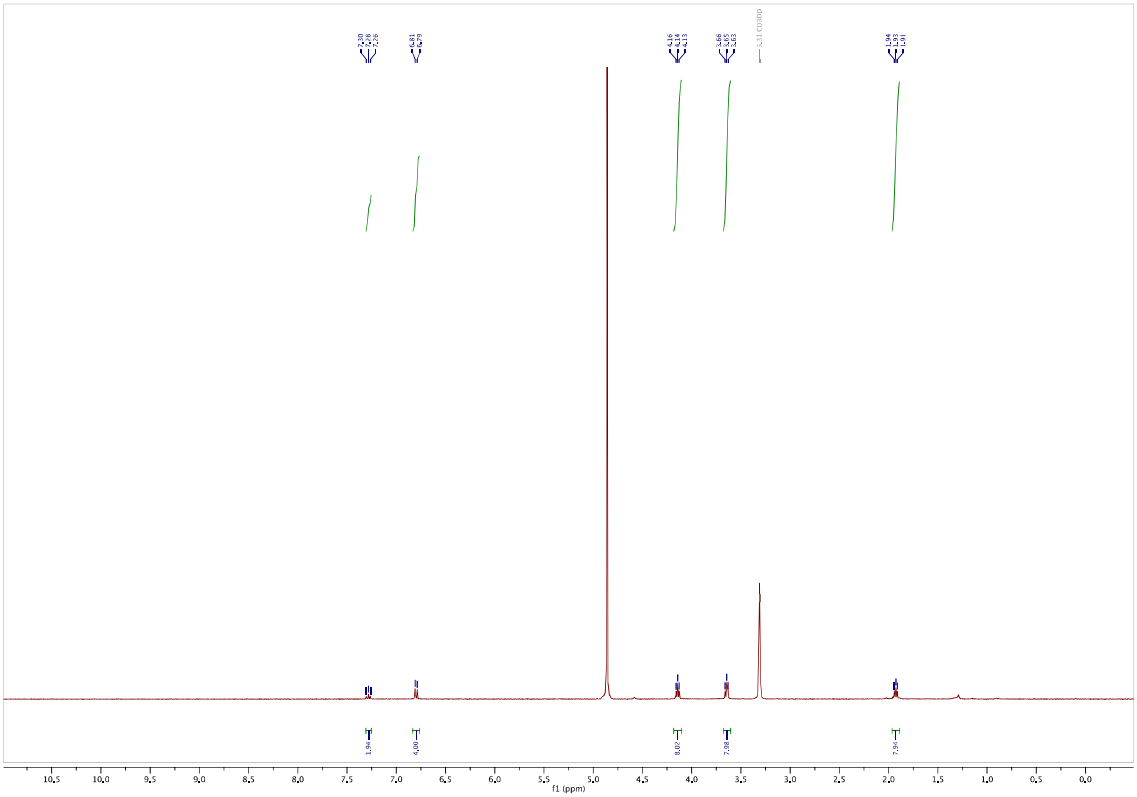

^{13}C-NMR

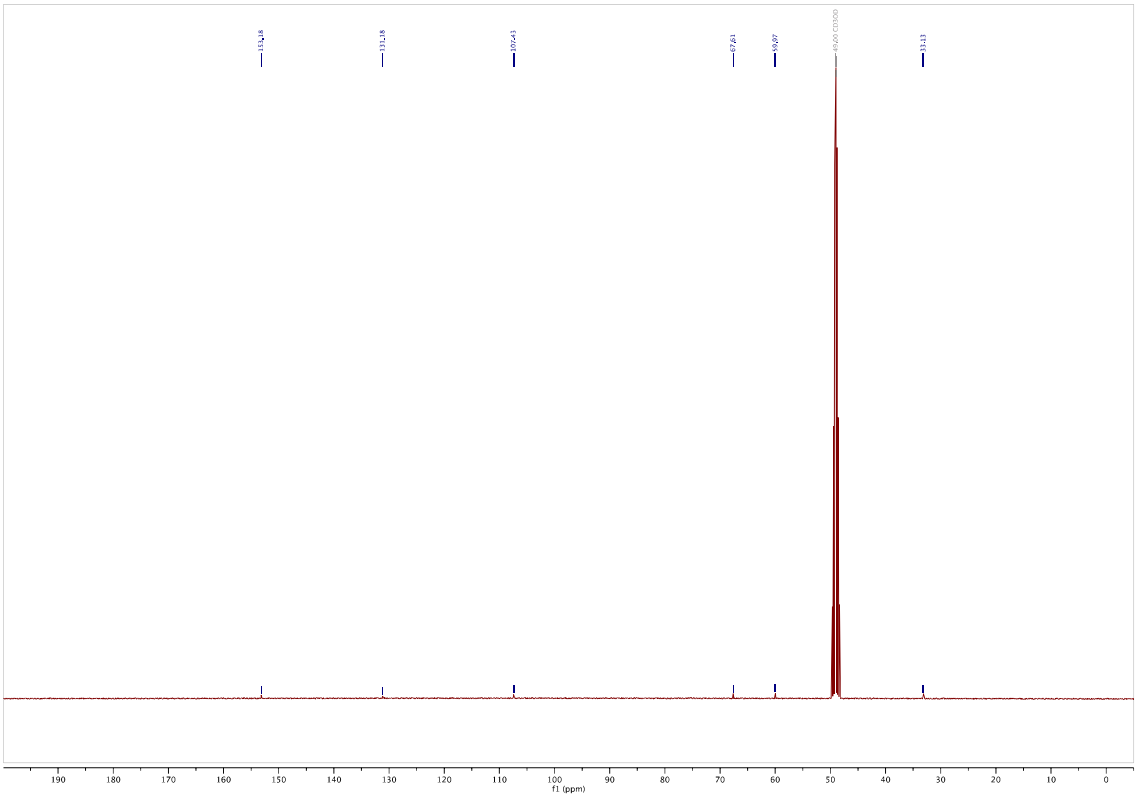
153.48
131.18
105.43
67.83
59.97
49.00 CDCl3
33.33
190
180
170
160
150
140
130
120
110
100
90
80
70
60
50
40
30
20
10
0
f1 (ppm)

7 SAXS based measurements of membrane thickness allow for the investigation of photoswitching in azolipid based small unilamellar vesicles (SUVs)

Lipid membranes are critical for life; they are the barrier for compartmentalisation, maintaining gradients and keeping interacting partners in proximity. To imitate the dynamic nature of biological lipid membranes in an artificial setting, special tools are required that can controllably vary the properties of the membrane.

A class of tool becoming extensively used for this purpose are phosphatidylcholine lipids that contain azobenzenes in their lipid tails (AzoPC). AzoPC can form unilamellar vesicles in which many of their properties can be controlled by light, with changes in properties (fluidity, membrane thickness, budding and transient pore formation) depending on the ratio of *Z* to *E*-isomer in the lipid. However, it is complex to determine the *E/Z* ratio in membranes, therefore, the actual correlation between changes in properties and the change in *Z*/*E*-ratio had, as far as we know, never been determined.

In this publication we present an indirect readout of the *Z*/*E* isomer ratio, then disclose unexpected effects uncovered with the readout. Small angle X-ray scattering (SAXS) can be used to observe the dynamic changes in membrane thickness of vesicles upon irradiation. We prepared a calibration curve correlating the SAXS membrane thickness to the %Z isomer in the membrane. For the calibration, SUVs were prepared from stocks with *Z*/*E*-isomer ratios that were in turn determined from UV/Vis and HPLC studies calibrated to optical reference materials. The measured membrane thickness linearly correlates to the ratio of isomers.

We used SAXS to observe SUVs under 365 nm illumination in deionized water, giving membrane thinning and reaching ca. 60% *Z*-isomer. When 465 nm is applied, the membrane thickness increases and 80% *E*-isomer is reached. Interestingly, if the experiment is conducted in PBS buffer, 465 nm illumination returns the membrane much nearer to 100% *E*-isomer. This difference and the values reached are contrary to isomerisations observed in dilute solution. However, it provides a greater range of control over the membrane thickness and raises a point of caution that may until now have been overlooked until now.

Then, searching for methods to increase the switching yield of AzoPC, increasing X-ray radiation dose was deposited into the sample, without any visible light present. Full *Z* to *E* isomerisation was achieved, and the isomerisation was reversible with further UV light, when 8 keV soft X-rays were applied: we assume via a mechanism initiated by radiolysis of water to give radicals. 54 keV X-rays on the other hand do not influence the medium or the membrane thickness, which uncovers new orthogonal ways to measure or control the membrane properties of AzoPC vesicles.

Research Article

Martina F. Ober, Adrian Müller-Deku, Anna Baptist, Benjamin Ajanović, Heinz Amenitsch, Oliver Thorn-Seshold and Bert Nickel*

SAXS measurements of azobenzene lipid vesicles reveal buffer-dependent photoswitching and quantitative *Z*→*E* isomerisation by X-rays

https://doi.org/10.1515/nanoph-2022-0053
Received February 3, 2022; accepted April 3, 2022;
published online April 15, 2022

Abstract: Photoresponsive materials feature properties that can be adjusted by light near-instantaneously, reversibly, and with high spatiotemporal precision. There is considerable interest in maximising the degree of photoswitching, and in measuring this degree during illumination in complex environments. We study the switching of photoresponsive lipid membranes that allow for precise and reversible manipulation of membrane shape, permeability, and fluidity. Though these macroscopic responses are clear, it is unclear how large the changes of *trans*/*cis* ratio are, and whether they can be improved. Here, we used small-angle X-ray scattering to measure the thickness of photoswitchable lipid membranes, and we correlate lipid bilayer thickness to *trans*/*cis* ratios. This reveals an unexpected dependency of photoswitching ratio upon aqueous phase composition. In buffer with ionic strength, we observe thickness variations twice as large as previously observed. Furthermore, soft X-rays can quantitatively isomerise photolipid membranes to the all-*trans* state; enabling X-ray-based membrane control. High energy X-rays do not influence the state of the photoswitches, presumably because they deposit less dose in the sample.

Keywords: azobenzene; high-energy X-ray; isomerization; lipid bilayer; photoswitch; SAXS.

***Corresponding author: Bert Nickel**, Faculty of Physics and CeNS, Ludwig-Maximilians-Universiät München, Geschwister-Scholl-Platz 1, Munich 80539, Germany, E-mail: nickel@lmu.de. https://orcid.org/0000-0002-0254-8841
Martina F. Ober, Anna Baptist and Benjamin Ajanović, Faculty of Physics and CeNS, Ludwig-Maximilians-Universiät München, Geschwister-Scholl-Platz 1, Munich 80539, Germany, E-mail: Martina.Ober@physik.lmu.de (M.F. Ober). https://orcid.org/0000-0001-7827-8027 (M.F. Ober)
Adrian Müller-Deku and Oliver Thorn-Seshold, Department of Pharmacy, Ludwig-Maximilians-Universität München, Butenandtstraße 5-13, Munich 81377, Germany, E-mail: oliver.thorn-seshold@cup.lmu.de (O. Thorn-Seshold). https://orcid.org/0000-0003-3981-651X (O. Thorn-Seshold)
Heinz Amenitsch, Institute of Inorganic Chemistry, Graz University of Technology, Stremayrgasse 9, Graz 8010, Austria, E-mail: heinz.amenitsch@elettra.eu. https://orcid.org/0000-0002-0788-1336

1 Introduction

Azobenzene photoswitches are molecular units, which can be switched between *trans* and *cis* isomer states at the single-molecule level by light. By embedding photoswitches into polymers or supramolecular assemblies containing many individual photoswitch units, materials with mechanical, electrical or optical properties that depend on the *trans*/*cis* ratio of the photoswitch population can be created: i.e., photoresponsive materials where these properties are adjustable by light [1–6]. Supramolecular assemblies can also provide further degrees of complexity, for example the populations of the two isomers may phase separate [7], or a highly ordered assembly process may select for or stabilise one of the isomer states [8].

As a photoresponsive material's properties depend on the isomer ratio, there is considerable interest in measuring and maximising the degree of switching between mostly-*trans* and mostly-*cis* populations [9]. Typically, it is not possible to perform quantitative photoisomerisations to all-*cis* or to all-*trans* azobenzene populations, due to absorption overlaps [8, 10–13]. Hence, illuminations lead to mixed photostationary state (PSS) populations, with *trans*/*cis* ratios that depend on the absorption coefficients of the two isomers and the quantum yields of their photoisomerisation. However, a rare example of quantitative switching in one direction (to all-*trans*) was pioneered by Hecht et al. using electrocatalytic pathways that transiently oxidise or reduce the azobenzenes [14–17].

Here we study the switching of photoresponsive lipid membranes assembled from azobenzene-containing

phosphatidylcholine (azo-PC), a synthetic lipid with a light-responsive azobenzene group in one of its two hydrophobic tails. Optical control of membranes constructed from pure azo-PC allows precise and reversible manipulation of many mechanical properties including membrane shape, permeability, fluidity, and domain formation, and influence membrane protein function [4, 18–21]. So far, it remains unclear how large the changes of *trans*/*cis* ratio are that cause these property changes; and whether these ratio are close to the theoretical maxima of pure states, or whether they could be substantially improved by tailored conditions and switching stimuli – with associated improvements to switching of biophysical properties [22]. This partly derives from a technical challenge: while it is straightforward to measure *trans*/*cis* ratios in molecular solutions by a variety of methods, it is not straightforward to measure them in the pure azo-PC membranes. The reason for doubt is that membranes are dense anisotropic assemblies. These give rise to a variety of optical shifts depending on the detailed nature of intermolecular interaction, which are still under investigation [19, 23]. Furthermore, it is widely demonstrated that the azobenzene photoisomerization yield is dramatically improved by embedding amphiphilic azobenzenes in the hydrophobic environment of a lipid membrane [24]. In this study, the synthetic photolipids themselves form the vesicle. Whether the azo-PC membrane's dielectric environment will yield the same protection from the aqueous phase needs to be tested by experiments. For example, ultrastructure studies based on X-ray experiments have shown photostimulated membrane thickness changes of ca. 4 Å for ca. 42 Å azo-PC membranes [4]: but it was not known if this 10% change is already maximal, nor was it known what population-level of *trans*/*cis* ratios were responsible for this change. Clearly, larger thickness changes would lead to more pronounced biophysically relevant effects.

In this work, we use orthogonal solvent measurements to relate photolipid bilayer thickness to the population-level of *trans*/*cis* ratios. Comparison of illumination in chloroform and in water reveals an unexpected sensitivity of the photoswitches inside the hydrophobic part of the lipid membrane to the aqueous buffer conditions outside. In water, we observe a smaller-than-expected photoswitching yield under low ionic strength. Furthermore, by mixing pre-switched monomers from chloroform, we show that membrane variations of minimum 8 Å are experimentally possible when photoswitching efficiency is high. In water with high ionic strength, we observe large thickness variations close to illumination in chloroform. These thickness changes are twice as large as thickness variation observed in previous vesicle photoswitching experiments [4], and much larger than the membrane thickness variations achievable within typical physiologically relevant conditions in natural lipids by change of temperature [25–28].

We also discovered that while hard X-rays do not switch the membranes under study, soft X-rays (8 keV) efficiently and *quantitatively* isomerise photolipid membranes to the all-*trans* state within seconds, which we attribute to radical redox reactions following X-ray dose deposition in the medium. This enables soft X-rays to enforce a higher degree of membrane property control than photoswitching alone can achieve, while emphasising the role of high energy X-rays as low dose probes in soft matter experiments.

2 Materials and methods

2.1 Synthesis of azo-PC and reference photoswitch FAzoM

Azo-PC was purchased from Avanti Polar Lipids, Inc. (Alabama, United States). Novel reference photoswitch FAzoM was synthesised by standard reactions (see Supporting Information).

2.2 Synthesis of azo-PC and reference photoswitches for benchmarking

In our hands, standard techniques to measure *trans*:*cis* ratios in molecular solutions (H-NMR, HPLC) were not reproducible when applied *in situ* to lipid membranes (ordered assemblies). Destructive readouts (e.g. adding cosolvents to homogenise membrane/water mixtures before HPLC measurement) were also tested but were also not reproducible, which we attributed to difficulties arising from the surfactant nature of the AzoPC. Finally, we developed a method to relate photolipid membrane *trans*/*cis* isomer ratio to the thickness determined by SAXS by using a calibration series for lipid membranes of known *trans*/*cis* composition. This series was created by mixing preconditioned all-*trans* and mostly-*cis* stocks (see below). The *trans*/*cis* ratios in the preconditioned AzoPC stocks were in turn determined by comparison of their UV–Vis spectra with that of the isoelectronic reference photoswitch FAzoM in the same conditions, since the *trans*/*cis* ratio of the apolar FAzoM can be reliably quantified by HPLC (see Supporting Information section S1 for details).

2.3 Preconditioning and mixing of azo-PC

Azo-PC was dissolved in chloroform (25 mg/mL) and stored at –20 °C until further use. Azo-PC stocks have been stored in dark for several days to reach the all-*trans* state. After illumination of molecularly-dissolved azo-PC by UV-A LED (*Roschwege Star-UV365-03-00-00*, λ = 365 nm, 9 nm FWHM, Conrad Electronic SE, Germany) the photostationary state (PSS_{UV}) has a *cis* fraction of 83%

(see Supporting Notes for further detail). To adjust the *cis* fraction in the assembly, we mix azo-PC in the all-*trans* state with azo-PCs with *cis* fraction of 83%, in appropriate proportions. After mixing, we follow the protocol for vesicle preparation. All preparation steps were made in the dark.

2.4 Small unilamellar vesicle (SUV) preparation

The Azo-PC chloroform stock solution was evaporated under a nitrogen stream and stored under vacuum for 12 h. The resulting dry lipid film was dissolved in cyclohexane, and exposed to a vacuum of 6×10^{-3} mbar at a temperature of −60 °C yielding a fluffy lipid powder. Immediately after lyophilisation, the azo-PC powder was hydrated with deionized (DI) water (Milli-Q, Reptile Bioscience Ltd., Boston, MA), or with PBS buffer (pH 7.5), or with 1× TE buffer (10 mM Tris, 1 mM EDTA, pH 8), to a final concentration of 30 mg/mL. The suspension was gently vortexed and subjected to five freeze/thaw cycles. Finally, the sample solution was extruded ca. 25 times through a polycarbonate membrane with a pore diameter of 50–80 nm using a Mini Extruder (Avanti Polar Lipids, Inc., Alabama, United States). The small vesicle size promotes unilamellar membranes [29].

2.5 UV-A/blue light illumination

For photoswitching of azo-PC membranes during SAXS, we built a dual UV-A and blue light LED setup shown in the Supporting Information section S2. For UV-A illumination, we focus a high-power LED (*Roschwege Star-UV365-03-00-00*, λ = 365 nm, 9 nm FWHM, Conrad Electronic SE, Germany) on the sample capillary. The total maximum optical power of 170 mW and a focal spot size of 4 mm^2 yield an irradiance of 4.25 W cm^{-2}. For blue light illumination, fed in by a dichroic mirror, a high-power LED (*Roschwege LSC-B*, λ = 465 nm, 18 nm FWHM, Conrad Electronic SE, Germany) was used. The blue light is focused with the same focal spot size and a total maximum optical power of 120 mW, resulting in an irradiance of 3.0 W cm^{-2}. The LEDs and the X-ray detector were remote controlled by TTL signals from an Arduino microprocessor (Reichelt electronics GmBH & Co. KG, Germany). For both LEDs, photostationary states are achieved within a few seconds and multiple switching cycles yield identical SAXS intensities.

2.6 SAXS measurements at 17.4 keV

X-ray data from azo-PC SUVs with preconditioned *trans*:*cis* ratios were recorded at a Mo-sourced small angle X-ray scattering (SAXS) setup [30]. The Mo anode delivers a beam with an energy of 17.4 keV, a beam size of 1.0 mm^2, and a flux of $2 \cdot 10^6$ cts·s^{-1} mm^{-2}. X-ray data were recorded by a Dectris Pilatus 3R Detector with 487 × 619 pixels of size 172 × 172 μm^2. All in-house SAXS measurements were performed in darkness.

2.7 SAXS measurements at 8 keV

SAXS data from azo-PC SUVs were recorded at the Austrian SAXS beamline at ELETTRA synchrotron using a beam energy of 8 keV [31] and a beam size of 0.5 × 2.0 mm^2. The sample solution was loaded in 1.5–2 mm diameter quartz glass capillaries by flow-through and placed in our UV-A/blue LED setup. A Pilatus detector from Dectris Ltd., Switzerland with 981 × 1043 pixels of size 172 × 172 μm^2 served as detector.

2.8 SAXS measurements at 54 keV

The high energy SAXS data from azo-PC SUVS were recorded at beamline P21.1 at the PETRA III ring at DESY. We measured with a beam energy and size of 54 keV and 1 × 1 mm^2, respectively. For the high energy SAXS experiments, the sample solution was first switched optically and then loaded in Kapton tubes of 40 mm in length and 2.5 mm in diameter. A Lambda detector (X-Spectrum GmbH, Germany) with 772 × 516 pixels with 55 × 55 μm^2 pixel size was used.

3 Results and discussion

Azo-PC monomers dissolved in low-dielectric chloroform are driven towards *cis*-rich photostationary state by UV-A light at 365 nm, and towards *trans*-rich state by blue light of 465 nm (Figure 1a). The absorption spectra of these mixed states, either in molecular solution or in assemblies, have been reported by us and others [4, 18, 19] and substantial differences between them have been noted [19]. Previously, we have used SAXS to determine the membrane thickness for blue or UV light photostationary states reached in lipid vesicles in DI water [4]. Here, we prepared calibration series of azo-PC vesicles of known *trans*/*cis* ratios by mixing stocks of dark-adapted all-*trans* azo-PC with 83% *cis* azo-PC (see methods and SI). We use calibrants of 0%, 10%, 19%, 39%, 58% and 83% *cis* isomers to cover the full range of ratios accessible during membrane photoswitching, with an estimated error margin of ±5% of the given value to account for mixing precision as well as *cis* fraction uncertainties in the preconditioned samples. The referencing method developed to determine the stock *cis* percentage is novel in this field. This method can prove generally useful for analysis of systems which lack reliable bulk references, i.e. which cannot be interpreted with help of UV–Vis spectra of monomer solution, see Methods and Supporting Information for details.

The SAXS measurements for these calibrant ratios are summarized in Figure 1b. The X-ray intensity distributions are typical for lipid bilayer samples [32, 33] and are stable over several hours (see Figure S3). The distributions vary strongly with the *trans*-to-*cis* ratio, e.g. the intensity dip around q = 0.05 Å^{-1} shifts consecutively to higher q-values with increasing *cis* content. This indicates that the membrane thickness decreases with increasing *cis* isomer fraction. To extract the head-to-head distances d_{HH}, we model the SAXS intensities in Figure 1b by an established lipid

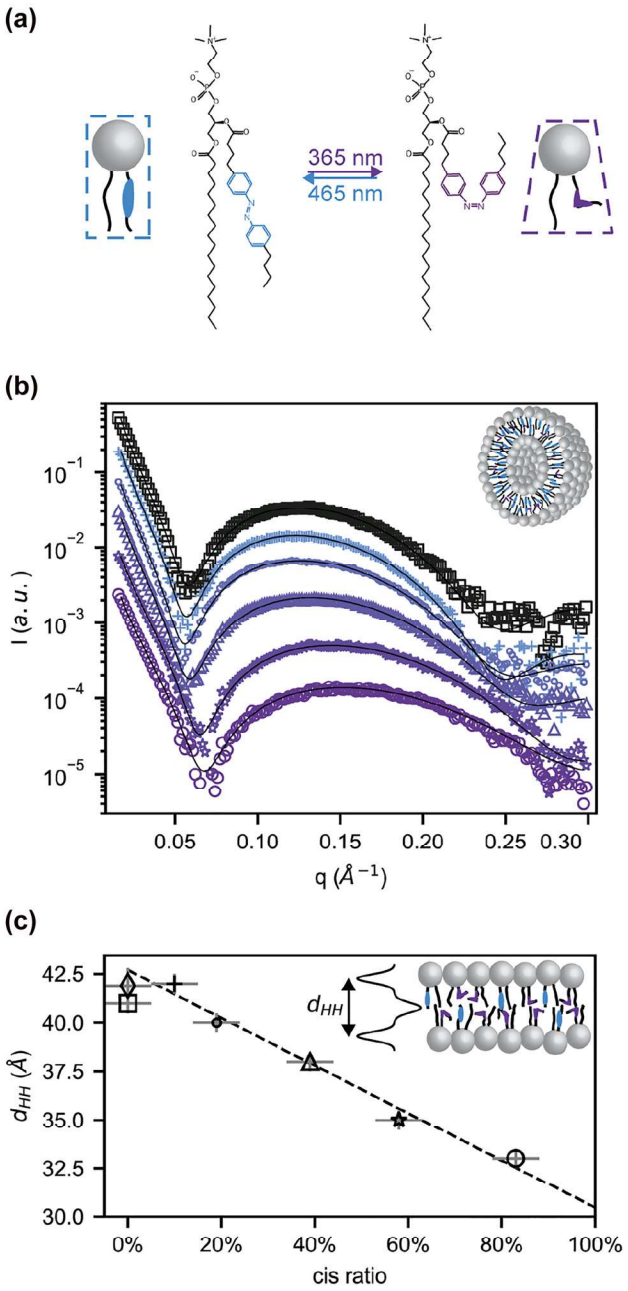

Figure 1: X-ray structural data of photoswitchable membranes.
(a) Schematic representation of the chemical structure of the azo-PC photolipids used in this study and their *trans* and *cis* configuration. (b) SAXS intensities for unilamellar azo-PC vesicles prepared from predefined *trans* to *cis* ratios: Dark-adapted state (100:0), (90:10), (81:19), (61:39), (42:58) and (17:83) are shown as squares, crosses, dots, triangles, stars, and circles. Intensities are vertically offset for clarity. (c) Head-to-head distance (d_{HH}) of azo-PC membranes as function of the percentage of azo-PCs in *cis* isomerization state are shown with the same symbols as in (b). Additionally, the mean value of d_{HH} for the dark-adapted photostationary states obtained from azo-PC SUVs in DI water (Figure 2b) is shown as diamond. The linear fit of d_{HH} in dependence of *cis* isomer percentage is indicated as dashed line. See Supporting Information (section S8) for details.

bilayer electron density profile, using the software SasView (see Supporting Information section S6) [34]. The results of this analysis are shown in Figure 1c. The dark-adapted state shows a head-to-head-distance of d_{HH} (0 ± 5% cis) = 40.9 ± 0.6 Å. The analysis reveals that the thickness of the azo-PC membrane depends almost linearly on the *trans*-to-*cis* ratio over a broad range. Increasing the percentage of *cis* azo-PC thins the membrane down to d_{HH} (83 ± 5% cis) = 33.0 ± 0.5 Å for 83% *cis*. Thus, the membrane thickness changes by 8 Å.

In the following measurements, we use this relation between membrane thickness and *cis* fraction to infer the *cis* fraction of various photostationary states in response to illumination and buffer conditions (Figure 1). Our previous photoswitching experiments have been performed on vesicles in deionized water (DI water): a common choice for lipids since DI water facilitates unilamellar membrane formation by increasing lipid vesicle stability. The maximal membrane thickness change obtained by optical switching under these conditions was only 4 to 5 Å. The new experiments with premixed lipids reported in Figure 1 now reveal that this optical control window covers only about half of the thickness change effect which could be achieved in ideal photoswitching conditions. We therefore studied two widely used buffer systems, phosphate-buffered saline

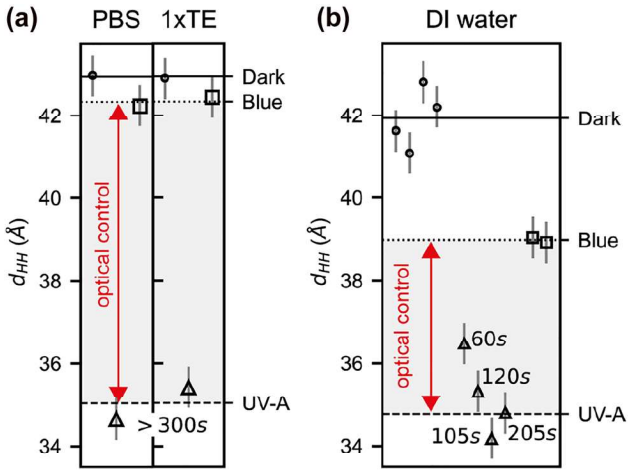

Figure 2: Switching behaviour of photomembranes in buffer and in DI water.
(a) Head-to-head distances (d_{HH}) obtained for azo-PC SUVs in PBS and 1×TE buffer. (b) d_{HH} obtained for azo-PC SUVs in DI water. The dark-adapted state, and several photostationary states induced via UV-A and blue light are labelled accordingly. Horizontal lines indicate mean values of d_{HH} for the dark-adapted, UV-A, and blue light photostationary states, shown as solid, dashed, and dotted line, respectively. The exposure time of UV-A light while approaching the photostationary state is indicated in seconds. The optical control window for the different buffer conditions is indicated by a red double-headed arrow.

(PBS), and a mixture of Tris with EDTA (1×TE), for their influence on the optical control window. The analysis of the SAXS data is condensed in Figure 2, the full data set is shown in Figures S4 and S5a.

The dark-adapted states (all-*trans*) yielded mean membrane thicknesses of d_{HH} (dark, buffers) = 42.9 ± 0.2 Å and d_{HH} (dark, deionized water) = 41.9 ± 0.9 Å (Figure 2a and b, circles, solid line). Hence, all conditions allow for the formation of dense, all-trans membranes in the dark. To photoswitch towards high *cis* contents, UV-A illumination was used until a photostationary state was achieved. Independent of the usage of buffer or not, the UV photostationary states do not reach a *cis* fraction of 83% as obtained by preconditioning monomers in chloroform. Instead, the observed membrane thicknesses of d_{HH}^{UV} = 34.8 ± 0.6 Å (see Figure 2b, dashed line and Figure S5) indicates *cis* contents around 64%. This is not unexpected, given the blue-shifting of azobenzene absorption spectra seen upon going from molecular solutions to assembled systems [19].

However, when using blue light to photoswitch from a *cis*- to a *trans*-enriched state, the outcomes depend greatly on whether the system is buffered or not. In DI water, the maximal blue light photostationary state membrane thickness is d_{HH}^{blue} = 39.0 ± 0.3 Å (Figure 2b, squares, dotted line), i.e. 30% *cis* isomer still remains. Instead, in PBS or 1× TE buffer, the membrane thickness increases to d_{HH}^{blue} = 42.3 ± 0.4 Å (Figure 2a, squares, dotted line), i.e. only 3% *cis* isomer remains. Optical control of vesicles is therefore highly efficient in these buffered aqueous solutions. Follow up experiments with NaCl solutions (see Figure S9), indicate that ionic strength rather than pH buffering is key to efficient photoswitching towards *trans*-enriched states in lipid vesicles. This effect is not observed for molecular monomers in aqueous solutions, where azobenzenes lose their ability to efficiently isomerize anyway [24]. Increasing ionic strength was reported to remove water molecules from inside the membrane promoting tighter packing of lipids [35, 36]. This should enhance the protection of the azobenzene photoswitch from water.

Next, we explored possible influence of X-ray on photostationary states. For this study, we used X-ray exposures to deposit a certain X-ray dose into the vesicle solution, i.e. a certain energy of absorbed X-rays per mass of the exposed sample [37]. The X-ray absorption drops drastically for increasing energies and in turn high X-ray energies enable low-dose SAXS experiments and vice versa (cf. Figure S7 and Note S7). Thus, the dosing experiment was conducted as follows. First, we prepared the vesicles in a high *cis* fraction by UV-A illumination. Next, we exposed the sample to a rather high X-ray energy of 54 keV for 60 s. Five such consecutive exposures yield an identical SAXS signal. There is no sign of any hard X-ray induced effects after 5 min in total, even though this experiment was performed at a high brilliance Petra III synchrotron beamline with full beam on the sample, cf. Figure 3a. This finding is in agreement with the fact that the cross section for photoabsorption is dramatically reduced for high X-ray energies.

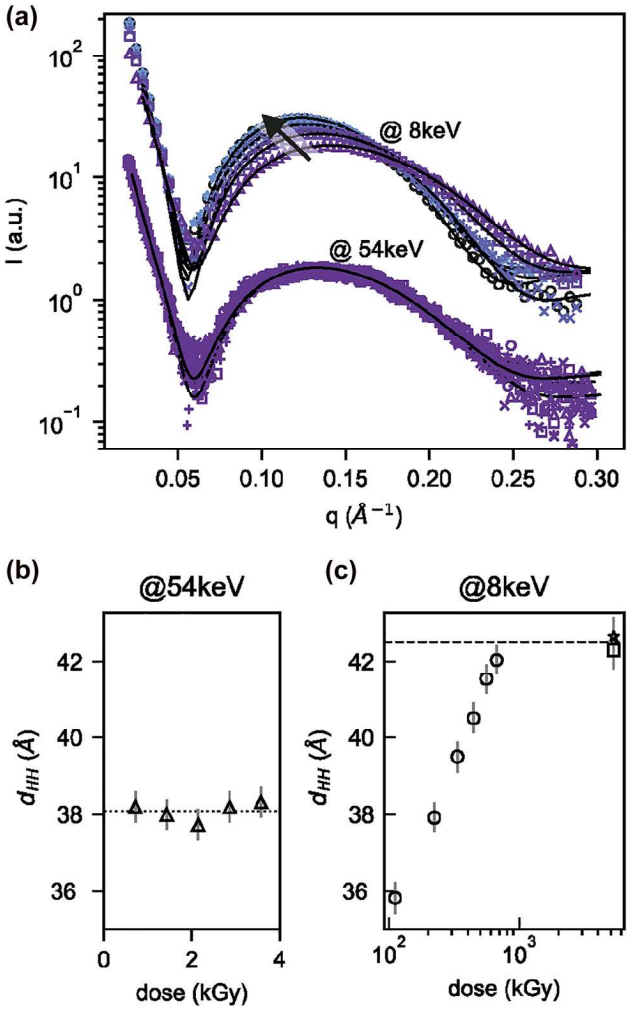

Figure 3: Catalytic switching of photomembranes induced by soft X-rays.
(a) After initial UV illumination, two different X-ray SAXS experiments are performed at 8 and 54 keV on unilamellar photolipid vesicles. Solid curves indicate modelling of the SAXS data by symmetrical bilayers. (b) Head-to-head distances (d_{HH}) obtained for azo-PC SUVs in DI water as function of X-ray dose measured at 54 keV. Dotted line indicates the mean value of d_{HH} for the stable UV-A induced PSS. (c) d_{HH} obtained for azo-PC SUVs in DI water as function of X-ray dose measured at 8 keV. Horizontal dashed line indicate the average d_{HH} after saturating 8 keV X-ray exposure.

Depositing high doses in water requires soft X-rays (discussion in the Supporting Information section S7). Such soft X-rays give rise to radiolysis of water, and oxidising and reducing radicals and reactive species [38, 39], which may provide pathways for catalytic redox-based unidirectional switching towards the thermodynamic groundstate (all-*trans*) [15]. Therefore, we tested also the change of membrane thickness during six consecutive 8 keV X-ray exposures each of 2 s (Figure 3a). After each X-ray exposure, a shift of the SAXS pattern was visible. To quantify the thickness change of the photomembrane, we modelled to extract the head-to-head distances, which increased dramatically after each soft X-ray exposure, depending on the total delivered X-ray dose. Remarkably, the final mean membrane thickness of $d_{\mathrm{HH}}^{\mathrm{xray}} = 42.5 \pm 0.3$ Å (Figure 3b, star and square datapoints at high dose, dashed line; Figure S5b) matches the thickness of the dark-adapted all-*trans* state $d_{\mathrm{HH}}^{\mathrm{dark}} = 41.9 \pm 0.9$ Å (Figure 2b, circular data points from repeated measurements, solid line). This is a direct indication of quantitative switching obtained by 8 keV X-ray exposure.

These X-ray induced changes of the isomerisation state of the azobenzene photoswitch are fully reversible and should not be mistaken as irreversible radiation damage. They can however be employed as a reversible X-ray dose readout. To demonstrate this, we plot the membrane thickness as observed by hard X-ray SAXS in response to soft X-ray exposure with dose expressed in kGray [kGy] in Figure 3b. The calculation of the dose, a routine calculation in radiation protection, is explained in the Supporting Information. Here, quantitative switching starts above 100 kGy, and saturates for an X-ray dose above 700 kGy. We propose that the measurement of azo-PC *cis* to *trans* transition for SUVs in DI water can be used to read out the effective X-ray dose in a regime of up to 700 kGy. This range may help to calibrate critical doses for biological SAXS experiments which can range from 51 kGy [40], to 400 kGy [41], to 284–7056 kGy [38].

The SAXS signal is almost independent of the X-ray energy (Figure S7, inset). Therefore, the minimum of the X-ray dose for samples with high water fraction at 36 keV (Figure S7) should be used to prevent radiation effects. Our experiments demonstrate that high quality SAXS data may be obtained even for weakly scattering biological samples.

4 Conclusions and summary

SAXS with hard X-rays provides a direct read out of the membrane bilayer thickness. We find that membrane thickness has a linear dependency of photolipid isomerization fraction. The 8 Å thickness change accessible by photoswitching in buffered solutions (20% of the membrane thickness) is massive, and apparently only possible because the membrane itself seals the azobenzene from the unfavourable polar solvent. Hydrophobic matching of membrane thickness with trans-membrane proteins is a wide research field that could benefit enormously from the large thickness change effects observed here [42]. Due to the rapid development of high power UV-A LEDs, and the availability of pulsed UV-A lasers at synchrotron sources [43], we expect that future experiments with pulsed illumination may allow rapid membrane thickness transition times of few ms and below. At these short timescales, the hydrodynamic coupling of the intercalated water to the photolipids may give rise to further interesting transient phenomena [25]. We also highlight the versatility of high energy X-rays as low-dose probes.

Acknowledgements: This work benefited from SasView software, originally developed by the DANSE project under NSF award DMR-0520547. The authors acknowledge the CERIC-ERIC Consortium for the access to experimental facilities. Portions of this research were carried out at the light source PETRA III at DESY, a member of the Helmholtz Association (HGF). We would like to thank Oleh Ivashko for assistance in using beamline P21.1 for high energy experiments.

Author contribution: MFO performed vesicle preparation, and SAXS experiments and X-ray data analysis, and wrote the manuscript; AMD performed synthesis of azo-PC and FAzoM, and spectroscopic and HPLC analyses of *cis*/*trans* isomer ratios; AB developed a protocol for photolipid SUV preparation; BA performed the SAXS experiments in NaCl solution; HA enabled the SAXS experiments at ELETTRA and provided in depth expertise on SAXS calibration and data conversion; OTS designed *cis*/*trans* ratio measurements and wrote the manuscript; BN designed the study, and joined the X-ray experiments, and wrote the manuscript.

Research funding: We acknowledge financial support by the German Research Foundation (DFG) through SFB1032 (Nanoagents) projects A07 (to B.N.) and B09 (to O.T.-S.) number 201269156, SFB TRR 152 project P24 number 239283807 to O.T.-S., Emmy Noether grant TH2231/1-1 to O.T.-S., and SPP 1926 project number 426018126 to O.T.-S.; by the Federal Ministry of Education and Research in Germany (BMBF) grant no. 05K19WMA (LUCENT) to B.N.; and by the Bavarian State Ministry of Science, Research, and Arts grant “SolarTechnologies go Hybrid (SolTech)” to B.N.

Conflict of interest statement: The authors declare no conflicts of interest regarding this article.

References

[1] Y. Yu, M. Nakano, and T. Ikeda, "Directed bending of a polymer film by light," *Nature*, vol. 425, no. 6954, p. 145, 2003.

[2] M. Hoshino, E. Uchida, Y. Norikane, et al., "Crystal melting by light: X-ray crystal structure analysis of an azo crystal showing photoinduced crystal-melt transition," *J. Am. Chem. Soc.*, vol. 136, no. 25, pp. 9158–9164, 2014.

[3] F. Reise, J. E. Warias, K. Chatterjee, et al., "Photoswitchable glycolipid mimetics: synthesis and photochromic properties of glycoazobenzene amphiphiles," *Chem. Eur J.*, vol. 24, no. 66, pp. 17497–17505, 2018.

[4] P. Urban, S. D. Pritzl, M. F. Ober, et al., "A lipid photoswitch controls fluidity in supported bilayer membranes," *Langmuir*, vol. 36, no. 10, pp. 2629–2634, 2020.

[5] A. Goulet-Hanssens, F. Eisenreich, and S. Hecht, "Enlightening materials with photoswitches," *Adv. Mater.*, vol. 32, no. 20, p. 1905966, 2020.

[6] D.-Y. Kim, T. Christoff-Tempesta, G. Lamour, X. Zuo, K.-H. Ryu, and J. H. Ortony, "Morphological transitions of a photoswitchable aramid amphiphile nanostructure," *Nano Lett.*, vol. 21, no. 7, pp. 2912–2918, 2021.

[7] R. H. Zha, G. Vantomme, J. A. Berrocal, et al., "Photoswitchable nanomaterials based on hierarchically organized Siloxane Oligomers," *Adv. Funct. Mater.*, vol. 28, no. 1, p. 1703952, 2018.

[8] Z. Wu, R. Xue, M. Xie, et al., "Self-assembly-triggered cis-to-trans conversion of azobenzene compounds," *J. Phys. Chem. Lett.*, vol. 9, no. 1, pp. 163–169, 2018.

[9] F. A. Jerca, V. V. Jerca, and R. Hoogenboom, "Advances and opportunities in the exciting world of azobenzenes," *Nat. Rev. Chem*, vol. 6, pp. 51–69, 2021.

[10] Y. Lin, X. Cheng, Y. Qiao, et al., "Creation of photo-modulated multi-state and multi-scale molecular assemblies via binary-state molecular switch," *Soft Matter*, vol. 6, no. 5, pp. 902–908, 2010.

[11] D. Bléger, J. Schwarz, A. M. Brouwer, and S. Hecht, "o-Fluoroazobenzenes as readily synthesized photoswitches offering nearly quantitative two-way isomerization with visible light," *J. Am. Chem. Soc.*, vol. 134, no. 51, pp. 20597–20600, 2012.

[12] C. Weber, T. Liebig, M. Gensler, et al., "Cooperative switching in nanofibers of azobenzene oligomers," *Sci. Rep.*, vol. 6, no. 1, p. 25605, 2016.

[13] M. Baroncini, J. Groppi, S. Corra, S. Silvi, and A. Credi, "Light-responsive (supra)molecular architectures: recent advances," *Adv. Opt. Mater.*, vol. 7, no. 16, p. 1900392, 2019.

[14] A. Goulet-Hanssens, M. Utecht, D. Mutruc, et al., "Electrocatalytic Z → E isomerization of azobenzenes," *J. Am. Chem. Soc.*, vol. 139, no. 1, pp. 335–341, 2017.

[15] A. Goulet-Hanssens, C. Rietze, E. Titov, et al., "Hole catalysis as a general mechanism for efficient and wavelength-Independent Z → E Azobenzene Isomerization," *Inside Chem.*, vol. 4, no. 7, pp. 1740–1755, 2018.

[16] J. L. Greenfield, M. A. Gerkman, R. S. L. Gibson, G. G. D. Han, and M. J. Fuchter, "Efficient electrocatalytic switching of azoheteroarenes in the condensed phases," *J. Am. Chem. Soc.*, vol. 143, no. 37, pp. 15250–15257, 2021.

[17] K. Kuntze, J. Isokuortti, A. Siiskonen, N. Durandin, T. Laaksonen, and A. Priimagi, "Azobenzene photoswitching with near-infrared light mediated by molecular oxygen," *J. Phys. Chem. B*, vol. 125, no. 45, pp. 12568–12573, 2021.

[18] C. Pernpeintner, J. A. Frank, P. Urban, et al., "Light-controlled membrane mechanics and shape transitions of photoswitchable lipid vesicles," *Langmuir*, vol. 33, no. 16, pp. 4083–4089, 2017.

[19] P. Urban, S. D. Pritzl, D. B. Konrad, et al., "Light-controlled lipid interaction and membrane organization in photolipid bilayer vesicles," *Langmuir*, vol. 34, no. 44, pp. 13368–13374, 2018.

[20] S. D. Pritzl, P. Urban, A. Prasselsperger, et al., "Photolipid bilayer permeability is controlled by transient pore formation," *Langmuir*, vol. 36, no. 45, pp. 13509–13515, 2020.

[21] M. Doroudgar, J. Morstein, J. Becker-Baldus, D. Trauner, and C. Glaubitz, "How photoswitchable lipids affect the order and dynamics of lipid bilayers and embedded proteins," *J. Am. Chem. Soc.*, vol. 143, no. 25, pp. 9515–9528, 2021.

[22] J. Pfeffermann, B. Eicher, D. Boytsov, et al., "Photoswitching of model ion channels in lipid bilayers," *J. Photochem. Photobiol. B Biol.*, vol. 224, p. 112320, 2021.

[23] S. D. Pritzl, D. B. Konrad, M. F. Ober, et al., "Optical membrane control with red light enabled by red-shifted photolipids," *Langmuir*, vol. 38, no. 1, pp. 385–393, 2021.

[24] G. M. Paternò, E. Colombo, V. Vurro, et al., "Membrane environment enables ultrafast isomerization of amphiphilic azobenzene," *Adv. Sci.*, vol. 7, no. 8, p. 1903241, 2020.

[25] G. Pabst, M. Rappolt, H. Amenitsch, S. Bernstorff, and P. Laggner, "X-ray kinematography of temperature-jump relaxation probes the elastic properties of fluid bilayers," *Langmuir*, vol. 16, no. 23, pp. 8994–9001, 2000.

[26] M. Rappolt, F. Vidal, M. Kriechbaum, et al., "Structural, dynamic and mechanical properties of POPC at low cholesterol concentration studied in pressure/temperature space," *Eur. Biophys. J.*, vol. 31, no. 8, pp. 575–585, 2002.

[27] S. Leekumjorn and A. K. Sum, "Molecular characterization of gel and liquid-crystalline structures of fully hydrated POPC and POPE bilayers," *J. Phys. Chem. B*, vol. 111, no. 21, pp. 6026–6033, 2007.

[28] N. Kucerka, M.-P. Nieh, and J. Katsaras, "Fluid phase lipid areas and bilayer thicknesses of commonly used phosphatidylcholines as a function of temperature," *Biochim. Biophys. Acta Biomembr.*, vol. 1808, no. 11, pp. 2761–2771, 2011.

[29] H. L. Scott, A. Skinkle, E. G. Kelley, M. N. Waxham, I. Levental, and F. A. Heberle, "On the mechanism of bilayer separation by extrusion, or why your LUVs are not really unilamellar," *Biophys. J.*, vol. 117, no. 8, pp. 1381–1386, 2019.

[30] L. K. Bruetzel, S. Fischer, A. Salditt, S. M. Sedlak, B. Nickel, and J. Lipfert, "A Mo-anode-based in-house source for small-angle X-ray scattering measurements of biological macromolecules," *Rev. Sci. Instrum.*, vol. 87, no. 2, 2016, Art no. 025103.

[31] H. Amenitsch, S. Bernstorff, and P. Laggner, "High-flux beamline for small-angle X-ray scattering at ELETTRA," *Rev. Sci. Instrum.*, vol. 66, no. 2, pp. 1624–1626, 1995.

[32] M. R. Brzustowicz and A. T. Brunger, "X-ray scattering from unilamellar lipid vesicles," *J. Appl. Crystallogr.*, vol. 38, no. 1, pp. 126–131, 2005.

[33] K. Komorowski, A. Salditt, Y. Xu, et al., "Vesicle adhesion and fusion studied by small-angle X-ray scattering," *Biophys. J.*, vol. 114, no. 8, pp. 1908–1920, 2018.

[34] M. Doucet, J. H. Cho, G. Alina, et al., *SasView version 4.2, Zenodo 2018*, https://doi.org/10.5281/zenodo.1412041.

[35] S. Šegota, D. Vojta, G. Pletikapić, and G. Baranović, "Ionic strength and composition govern the elasticity of biological membranes. A study of model DMPC bilayers by force- and transmission IR spectroscopy," *Chem. Phys. Lipids*, vol. 186, pp. 17–29, 2015.
[36] P. Mukhopadhyay, L. Monticelli, and D. P. Tieleman, "Molecular dynamics simulation of a palmitoyl-oleoyl phosphatidylserine bilayer with Na+ counterions and NaCl," *Biophys. J.*, vol. 86, no. 3, pp. 1601–1609, 2004.
[37] F. H. Attix, *Introduction to Radiological Physics and Radiation Dosimetry*, Weinheim, Wiley VCH, 2004.
[38] C. M. Jeffries, M. A. Graewert, D. I. Svergun, and C. E. Blanchet, "Limiting radiation damage for high-brilliance biological solution scattering: practical experience at the EMBL P12 beamline PETRAIII," *J. Synchrotron Radiat.*, vol. 22, no. 2, pp. 273–279, 2015.
[39] J. L. Dickerson and E. F. Garman, "The potential benefits of using higher X-ray energies for macromolecular crystallography," *J. Synchrotron Radiat.*, vol. 26, no. 4, pp. 922–930, 2019.
[40] J. C. Brooks-Bartlett, R. A. Batters, C. S. Bury, et al., "Development of tools to automate quantitative analysis of radiation damage in SAXS experiments," *J. Synchrotron Radiat.*, vol. 24, no. 1, pp. 63–72, 2017.
[41] S. Kuwamoto, S. Akiyama, and T. Fujisawa, "Radiation damage to a protein solution, detected by synchrotron X-ray small-angle scattering: dose-related considerations and suppression by cryoprotectants," *J. Synchrotron Radiat.*, vol. 11, no. 6, pp. 462–468, 2004.
[42] T. M. Weiss, P. C. A. van der Wel, J. A. Killian, R. E. Koeppe, and H. W. Huang, "Hydrophobic mismatch between helices and lipid bilayers," *Biophys. J.*, vol. 84, no. 1, pp. 379–385, 2003.
[43] M. Burian, B. Marmiroli, A. Radeticchio, et al., "Picosecond pump-probe X-ray scattering at the Elettra SAXS beamline," *J. Synchrotron Radiat.*, vol. 27, no. 1, pp. 51–59, 2020.

Supplementary Material: The online version of this article offers supplementary material (https://doi.org/10.1515/nanoph-2022-0053).

Supporting Information

Martina F. Ober[1], Adrian Müller-Deku[2], Anna Baptist[1], Benjamin Ajanović[1], Heinz Amenitsch[3], Oliver Thorn-Seshold[2], and Bert Nickel[1]

[1] Faculty of Physics and CeNS, Ludwig-Maximilians-University München, Geschwister-Scholl-Platz 1, 80539 Munich, Germany
[2] Department of Pharmacy, Ludwig-Maximilians-Universität München, Butenandtstraße 5-13, 81377 Munich, Germany
[3] Institute of Inorganic Chemistry, Graz University of Technology, Stremayrgasse 9, 8010 Graz, Austria

Corresponding author: *nickel@lmu.de

Content

Notes:

(1) ***trans*- (or *E*-) and *cis* (or *Z*-)** are the two isomer states of any single azo-PC molecule.

(2) On a **population** level, samples of azo-PC are denoted as e.g. "all-*trans*" or "80% *cis* " to indicate isomer ratios in the sample.

(3) **Photostationary states ("PSSs")** are equilibrium *E/Z* ratios reached under saturating illumination at given wavelengths, which depend on factors including the absorption coefficients of the *E* & *Z* isomers at that wavelength in their molecular environment, and the environment-dependent quantum yields of *E*>*Z* and *Z*>*E* photoisomerisation at that wavelength.

Therefore, the PSS at a given wavelength can be different depending on whether the photoswitch is in a molecular solution in a certain solvent (e.g. in a dilute solution in chloroform, typically < 100 μM concentration), or in a different solvent (e.g. same dilution but in methanol), or is present as a photolipid membrane.

Where PSSs are mentioned in the text, these are understood to be the PSSs established in SUVs, unless otherwise specified.

S1: Determination of the *E/Z* ratio of azo-PC by UV-Vis and HPLC

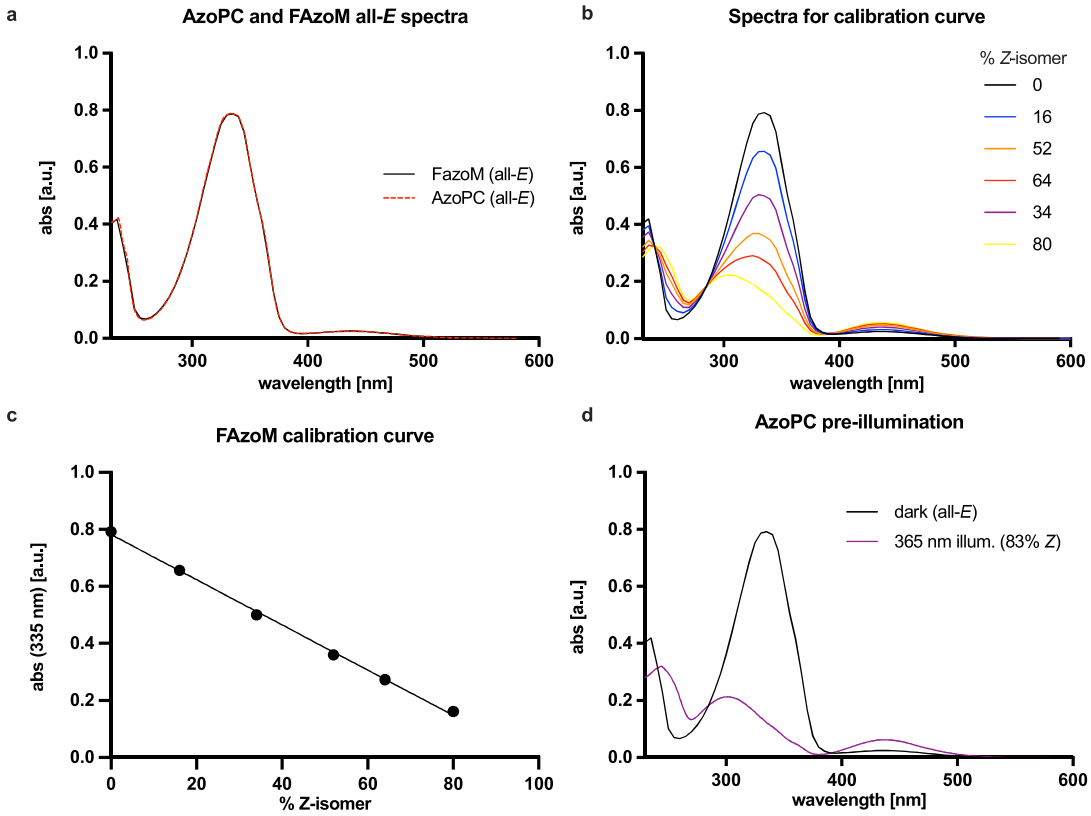

Figure S1 – UV-Vis spectroscopy (all as diluted molecular solutions, all in >99% methanol). **a.** Overlay of the UV-Vis spectra of azo-PC and of model photoswitch FAzoM, showing their equivalence when in molecular solution. **b.** UV-Vis spectra of FAzoM samples with different E/Z ratios, given as %Z (FAzoM at 19 µM). **c.** Calibration curve of absorbance at 335 nm as a function of %Z (FAzoM at 19 µM). **d.** UV-Vis measurements of azo-PC before and after 365 nm illumination (stock in chloroform was illuminated, and aliquots were diluted into methanol for UV-Vis measurement).

Our first aim was to establish a calibration curve relating photolipid membrane ("p-membrane") isomer ratio to the thickness determined by SAXS, so we could then use SAXS thickness measurements to determine the p-membrane isomer ratio in test samples during photoswitching and during X-ray administration.

We did not succeed in reproducibly calibrating and measuring *trans:cis* ratios for intact p-membranes by H-NMR, by HPLC, or by UV-Vis. Therefore, we required another method to determine p-membrane isomer composition for generating the SAXS calibration curve.

Procedure

For calibrations, we prepared SUVs from samples of azo-PC with predefined *trans:cis* ratios, which were established by mixing two chloroform solution stocks each of known isomer composition (all-*trans* and mostly-*cis*) in varying proportions. The all-*trans* stock is accessible by thermal relaxation of a solution of azo-PC (e.g. 80°C overnight in a closed vessel). A mostly-*cis* stock was accessed by saturating UVA illumination of a solution of azo-PC in chloroform. The remaining task was then to measure the %Z content in the mostly-*cis* chloroform stock, in order to know the *E/Z* ratios in the SUVs.

High-performance liquid chromatography (HPLC) of azo-PC stocks, aiming to separate *E* and *Z* isomers and quantify their relative proportions by inline detection (eg. diode array detector), also proved poorly reproducible, due to the zwitterionic surfactant nature of the compound.

However, the simpler, non-charged and non-polar compound FAzoM (Scheme S1) that contains the same chromophore as azo-PC, can be analysed quantitatively and reproducibly for *cis:trans* ratio by HPLC. Therefore, we established a calibration series of UV-Vis spectra for different *cis:trans* ratios of FAzoM that were checked by HPLC (Fig S1b-c); confirmed that spectra for FAzoM and AzoPC were essentially identical so spectra of samples of AzoPC could be mapped onto those of samples of FAzoM to determine isomer ratios (Fig S1a); and finally derived the percentage of *cis*-AzoPC in the mostly-*cis* chloroform stock by taking a UV-Vis spectrum of an aliquot of this stock diluted into methanol, and comparing it to the calibration series.

The synthesis and characterisation of the useful model compound FAzoM has, to our knowledge, not been reported before, so is provided below.

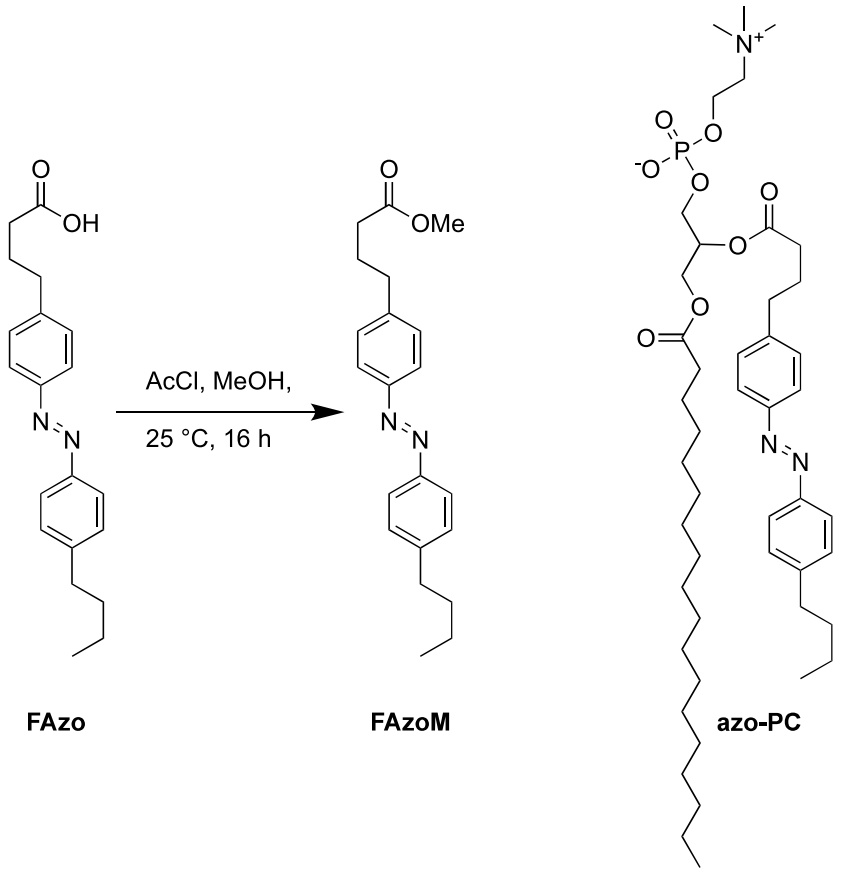

Scheme S1. FAzoM synthesis from FAzo and comparison to azo-PC structure

FAzoM (methyl (E)-4-(4-((4-butylphenyl)diazenyl)phenyl) butanoate)

A round bottom flask was charged with (*E*)-4-(4-((4-butylphenyl)diazenyl)phenyl) butanoic acid (FAzo [1]) (1 eq., 200 mg, 0.616 mmol) and 4 mL methanol was added. Acetyl chloride (1 eq., 44 µL, 48.4 mg, 0.616 mmol) was added dropwise. The flask was closed and stirred at 25 °C for 16 h. The methanol was removed by evaporation and the crude product was purified by column chromatography using 9:1 hexanes:ethyl acetate eluent. The desired product FAzoM was obtained as an orange solid (187 mg, 0.553 mmol, 90%).

^{1}H NMR (400 MHz, Chloroform-*d*) δ (ppm) = 7.84 – 7.82 (m, 4H), 7.31 (d, *J* = 8.1 Hz, 4H), 3.68 (s, 3H), 2.73 (t, *J* = 7.6 Hz, 2H), 2.69 (t, *J* = 7.6 Hz, 2H), 2.36 (t, *J* = 7.4 Hz, 2H), 2.01 (p, *J* = 7.5 Hz, 2H), 1.57 (p, *J* = 7.5 Hz, 2H), 1.39 (h, *J* = 7.4 Hz, 2H), 0.95 (t, *J* = 7.3 Hz, 3H). **^{13}C NMR** (101 MHz, $CDCl_3$) δ (ppm) = 173.9, 151.4, 151.1, 146.5, 144.6, 129.3, 129.2, 123.0, 122.9, 51.7, 35.7, 35.1, 33.6, 33.5, 26.4, 22.5, 14.1. **LCMS(+):** t_{ret} = 8.0 min, $[MH]^+$ = 339 Th. **HRMS (EI):** calc. for $C_{21}H_{26}O_2N_2^+$ $[M]^+$: 338.1994 Th; found: 338.1995 Th.

Next, it was first verified that the UV/Vis-spectra of azo-PC and FAzoM in molecular solution match well to each other (Fig S1a). After that, a 3.8 mM stock of FAzoM in chloroform was prepared; and 50 µL were transferred to several clear glass tubes. The FAzoM aliquots were irradiated for different durations with a 370 nm LED (3W H2A1-model from Roithner Lasertechnik; FWHM bandwidth ca. 20 nm) to give a series of different *E/Z* ratios (longer illumination approaches more closely the PSS at 370 nm). The FAzoM *E/Z* ratios in each tube were determined by HPLC analysis (see **Methods** below). Subsequently, the FAzoM samples were diluted with methanol to a concentration of 19 µM (i.e. >99% methanol) and UV-Vis spectra in molecular solution were measured. The spectra were normalized to the absorbance at the isosbestic point in methanol at 285 nm (Fig S1b) to correct for variations due to pipetting volumes (typically <5% correction), and the absorbance at 335 nm (maximum absorbance of the *E* isomer) was correlated to the HPLC-determined %*Z* in the sample, resulting in a linear correlation (Fig S1c):

$$A_{335} = -0.007923 \times (\%Z) + 0.7818 \quad (R^2 = 0.998)$$

Applying this calibration curve to the correspondingly diluted and normalised UV-Vis spectrum of the UV-illuminated stock of azo-PC in chloroform that we employed, we calculated its %*Z* to be 83% (Fig S1d). The thermally relaxed stock of azo-PC intended to be all-*trans* was also measured spectroscopically and confirmed to have %*Z* < 0.5%. Finally, the all-*trans* and the mostly-*cis* stocks of azo-PC were mixed in a range of proportions, before SUVs were prepared and membrane thicknesses measured by SAXS, as detailed in the following sections.

Methods: HPLC was performed on an Agilent 1100 SL coupled HPLC system with (a) a binary pump to deliver H_2O:MeCN eluent mixtures containing 0.1% formic acid at a 1 mL/min flow rate, (b) Agilent 10 Prep-C18 Scalar 250 x 4.6 mm maintained at 30°C, whereby the solvent front eluted at t_{ret} = 2.3 min, and (c) an Agilent 1100 series diode array detector (DAD). For isomer separation, a gradient from 90% to 100% MeCN over 10 min, and holding at 100% MeCN until completion, was used. Under these conditions the *Z* isomer eluted at 5.2 min and the *E*-isomer at 10.3 min. For ratio determination, the signals in the 391 nm DAD trace were integrated, since this is an isosbestic point for FAzoM in >90% MeCN. **UV-Vis** absorption spectra in cuvette were acquired on a Varian CaryScan 60 (1 cm pathlength) using Hellma precison SUPRASIL quartz cells.

S2: Custom-built UV-A/blue light pump – x-ray probe setup

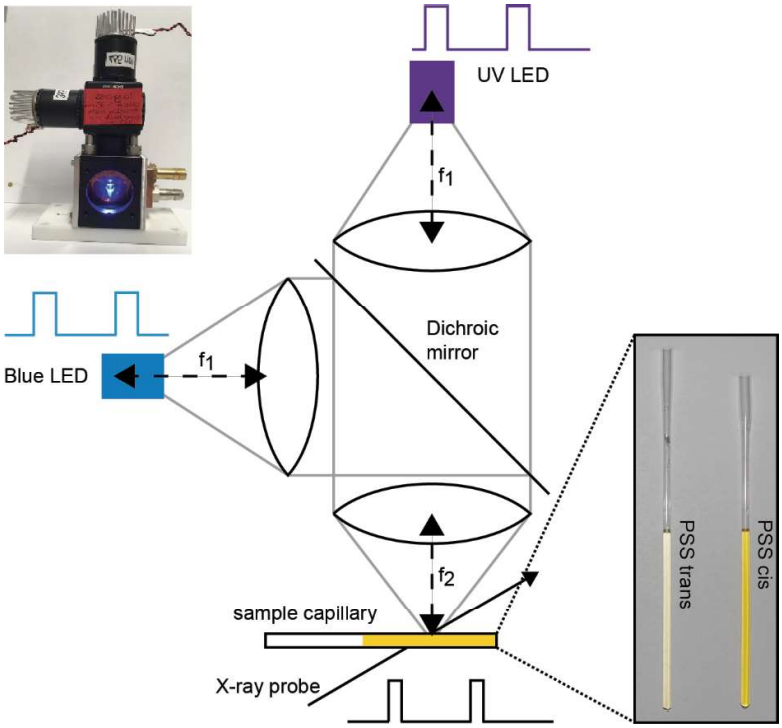

Figure S2: Schematic of our custom-built UV-A/blue light illumination setup used for illuminations during SAXS measurements. A photograph of the setup, and of two capillaries with azo-PC SUVs in the predominantly *trans* PSS at 465 nm (left) and predominantly *cis* PSS at 370 nm (right), are shown.

S3: cis-enriched azo-PC SUVs do not spontaneously isomerize to trans

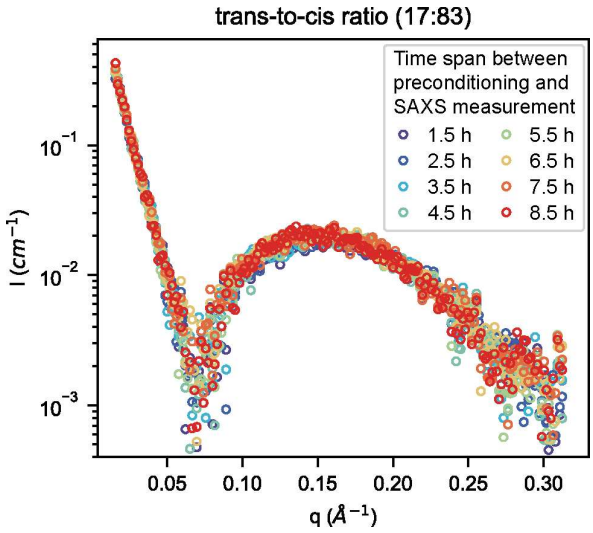

Figure S3: SAXS intensities for unilamellar azo-PC vesicles prepared with a predefined trans-to-cis ratio of (17:83) integrated over 1h with a time-lap between preconditioning and SAXS measurement as indicated in the legend.

Eight consecutive SAXS measurements of preconditioned trans-to-cis ratio of (17:83) azo-PC SUVs yield an identical SAXS signal. There is no sign of a spontaneous back reaction, i.e. cis-to-trans isomerization, over 8.5 h of monitoring after the preconditioning of the azo-PC SUVs was performed (we estimate that at least a 4% relaxation would be visible, so, we can offer an upper bound of 4% spontaneous relaxation over 8 hours, which translates to insignificant change during the active experiments). This finding is in agreement with the slow thermal relaxation rate for *Z*-para,para'-bis(alkyl)azobenzenes (days to weeks under physiological conditions) [2].

S4: Photoswitching azo-PC SUVs in PBS and in TE buffer via UV and blue light

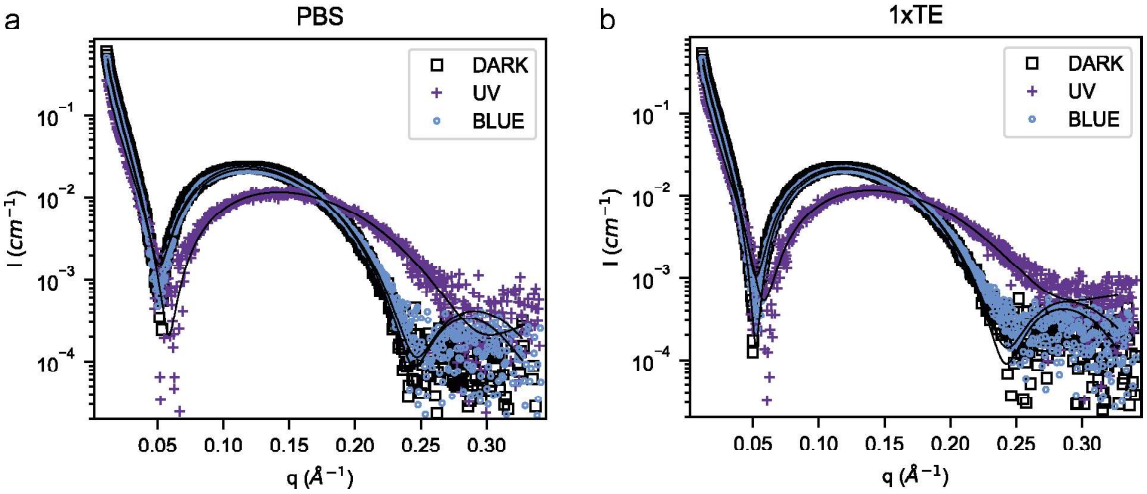

Figure S4: SAXS intensities for unilamellar azo-PC vesicles prepared in PBS buffer (a) and 1×TE buffer (b), for the dark-adapted state, and for photostationary states induced by extended UV-A or blue light illumination (each >300s) are shown as squares, crosses and circles respectively. Intensities are on an absolute scale. Note the crossing point at ca. q = 0.18, as expected for measurements with linear response in the absence of hysteresis, therefore indicating the reproducibility of these measurements.

S5: Comparison of the *Z>E* switching of azo-PC SUVs in deionized water from blue light (partial *Z>E* switching) and from x-rays (full *Z>E* switching)

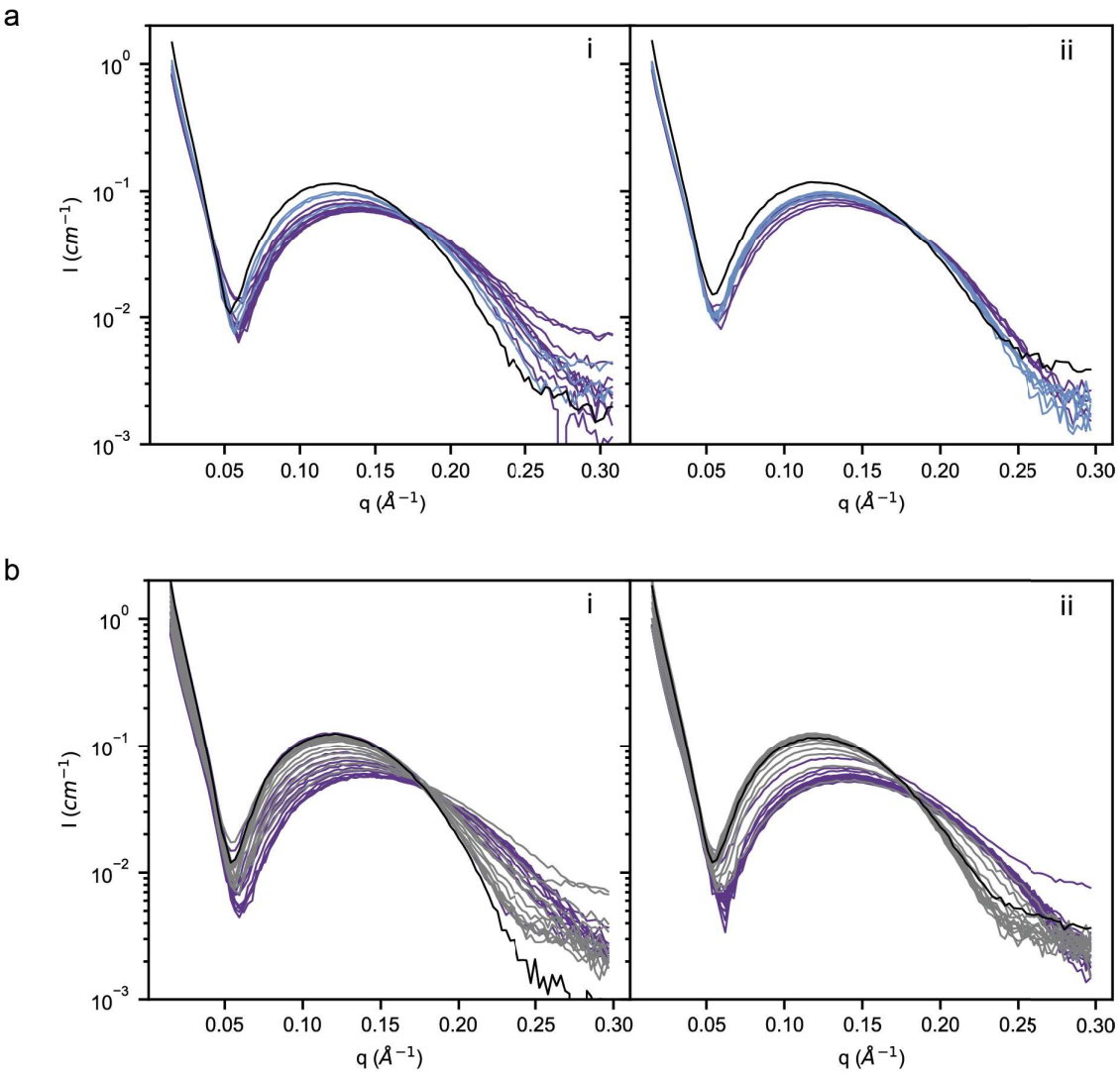

Figure S5: **Switching of photolipid membranes in DI water via blue light and via x-rays** (data related to Figures 2-3). **a(i)** In-situ SAXS measurements on azo-PC SUVs initially in the dark state (all-trans, black), then during 120 s of UV illumination (purple, increased %Z), then during 30 s of blue illumination (blue, %Z intermediate between UV and dark conditions). **a(ii)** Similar in-situ SAXS measurements on azo-PC SUVs as in **a(i)**, but using 60 s of UV illumination and 60 s of blue illumination. **b(i)** In-situ SAXS measurements on azo-PC SUVs initially in the dark state (black, all-trans) then during 105 s of UV illumination (purple) then during subsequent x-ray exposures (grey). **b(ii)** Similar in-situ SAXS measurements on azo-PC SUVs as in **b(i)**, but using 205 s of UV illumination. Note again the crossing points at ca. q = 0.18, indicating the reproducibility of these measurements (cf Fig S3). X-ray exposure and delay times are given in Table S1.

	Number of x-ray exposures	x-ray exposure time [s]	x-ray off time [s]	$t_{UV}[s]$	$t_{blue}[s]$
Fig S4a(i)	15	5	5	120	30
Fig S4a(ii)	12	5	5	60	60
Fig S4b(i)	40	5	5	205	
Fig S4b(ii)	30	5	5	105	
Fig. 3a (8keV)	20	1	19	160	

151 Table S1 Detailed timing parameters for SAXS experiments for data in Figures.

S6: Small angle X-ray scattering (SAXS) analysis

All bilayer parameters are obtained from model fits of the total scattering intensity *I(q)* to an electron density profile $\Delta\rho(z)$ composed of three Gaussians.

$$\Delta\rho(z) = \Delta\rho_H \exp\left[-\frac{(z-z_H)^2}{2\sigma_H^2}\right] + \Delta\rho_{CH} \exp\left[-\frac{(z)^2}{2\sigma_{CH}^2}\right] + \Delta\rho_H \exp\left[-\frac{(z+z_H)^2}{2\sigma_H^2}\right]$$

Here, $\Delta\rho_H$ is the scattering length contrast of the lipid head groups compared to water, i.e. $\Delta\rho(z) = \Delta\rho_H - \Delta\rho_w$. z_H is the spatial peak offset of the head centers in respect to the center of the bilayer, and σ_H is the corresponding variance of the Gaussian functions. $\Delta\rho_{CH}$ is the scattering length contrast of the lipid chains and σ_{CH} the variance of the Gaussian function describing the chain region. For the data shown in Figure 1b and Figure S5 we used a power law to account for additional background. Model fitting was achieved by running the software-internal population-based DREAM algorithm using the software package SasView (http://www.sasview.org/). The head-to-head distance uncertainty composes of purely statistical parameter errors corresponding to the 95% (two-σ) confidence interval and uncertainties reflecting the robustness of d_{HH} with respect to the fitting model, which is approximately $\pm$ 0.5 Å.

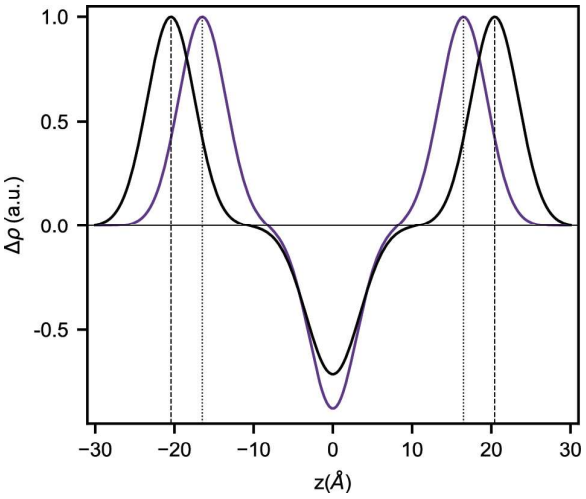

Figure S6 Exemplary electron density profiles Δρ(z) corresponding to the 0% *cis* (all-*trans,* dark state, black) and 80% *cis* (mostly-*cis*, UV-illuminated, purple) p-membranes (SAXS data in Figure 1b) as a function of distance z from the bilayer center. The bilayer thicknesses of the all-*trans*-azo-PC membrane (dashed lines) and of the 80% *cis*-azo-PC membrane (dotted lines) are highlighted.

171 Detailed fit parameters: $\Delta\rho_H = 1$ (Fixed), $\sigma_H = 3$Å (Fixed)

Data	z_H [Å]	$\Delta\rho_{CH}$[a.u.]	σ_{CH}[Å]	χ^2_{red}
Fig. 1b 0±5% cis	20.44±0.04	-0.71±0.00	3.37±0.02	1.96
Fig. 1b 10±5% cis	20.75±0.03	-1.08±0.00	2.25±0.01	2.05
Fig. 1b 19±5% cis	20.21±0.03	-0.87±0.00	2.97±0.01	3.48
Fig. 1b 39±5% cis	19.16±0.03	-0.87±0.00	3.00±0.01	3.49
Fig. 1b 58±5% cis	17.34±0.04	-0.86±0.00	3.00±0.01	1.87
Fig. 1b 83±5% cis	16.49±0.04	-0.88±0.00	3.00±0.01	1.30
Fig. 3a top I	17.91±0.09	-2.58±0.05	1.08±0.01	0.76
Fig. 3a top II	18.96±0.04	-2.53±0.06	1.06±0.01	1.64
Fig. 3a top III	19.75±0.05	-4.56±0.10	0.57±0.01	2.00
Fig. 3a top IV	20.26±0.06	-3.07±0.03	0.83±0.01	2.76
Fig. 3a top V	20.77±0.05	-1.77±0.02	1.39±0.01	3.46
Fig. 3a top VI	21.02±0.04	-4.07±0.03	0.61±0.01	2.10
Fig. 3a bottom I	19.09±0.06	-0.93±0.01	2.71±0.02	5.81
Fig. 3a bottom II	19.00±0.06	-2.45±0.02	1.02±0.01	6.10
Fig. 3a bottom III	18.86±0.06	-0.65±0.01	4.01±0.04	5.90
Fig. 3a bottom IV	19.10±0.05	-0.58±0.01	4.34±0.04	5.19
Fig. 3a bottom V	19.16±0.06	-6.05±0.02	0.41±0.01	5.02
Figure S4a dark (PBS)	21.48±0.03	-1.20±0.00	2.39±0.01	0.32
Figure S4a PSS_{UV} (PBS)	17.33±0.03	-1.01±0.00	3.14±0.01	3.89
Figure S4a PSS_{blue} (PBS)	21.11±0.01	-0.95±0.01	3.13±0.00	6.11
Figure S4b dark (1xTE)	21.45±0.04	-0.98±0.00	2.76±0.01	0.33
Figure S4b PSS_{UV} (1xTE)	17.71±0.02	-0.98±0.00	3.14±0.00	8.73
Figure S4b PSS_{blue} (1xTE)	21.22±0.04	-0.86±0.01	3.12±0.02	0.32
Figure S5a (i) dark	20.54±0.02	-0.99±0.00	2.74±0.01	2.25
Figure S5a (i) PSS_{UV}	17.66±0.01	-0.97±0.00	3.16±0.02	2.50
Figure S5a (i) PSS_{blue}	19.46±0.02	-0.95±0.00	3.13±0.02	2.43
Figure S5a (ii) dark	20.81±0.07	-0.99±0.01	2.57±0.02	0.12
Figure S5a (ii) PSS_{UV}	18.24±0.03	-0.97±0.00	3.17±0.01	0.53
Figure S5a (ii) PSS_{blue}	19.52±0.02	-0.95±0.00	3.10±0.01	0.98
Figure S5b (i) dark	21.40±0.02	-0.99±0.01	2.42±0.01	1.95

Figure S5b (i) PSS_{UV}	17.09±0.01	-0.99±0.00	3.17 ±0.01	4.20
Figure S5b (i) x-ray	21.15±0.02	-0.82±0.01	3.14 ±0.01	5.78
Figure S5b (ii) dark	21.10±0.02	-0.81±0.01	2.99±0.01	3.11
Figure S5b (ii) PSS_{UV}	17.40±0.02	-0.82±0.01	3.75±0.02	4.95
Figure S5b (ii) x-ray	21.32±0.02	-0.83±0.00	3.04±0.01	6.15
Figure S *8* dark	20.61±0.1	-0.85±0.01	3.00±0.02	1.61
Figure S *8* PSS_{UV}	18.52±0.2	-0.88±0.01	3.00±0.02	1.70
Figure S *8* PSS_{blue}	21.78±0.2	-0.82±0.01	3.00±0.03	2.28

Table S2: Parameters obtained from least-squares fitting of SAXS data of 50 nm extruded azo-PC vesicles to a symmetrical, flat bilayer model. Errors indicate the purely statistical parameter uncertainties corresponding to a two-sigma confidence interval.

S7: Higher x-ray energies for SAXS

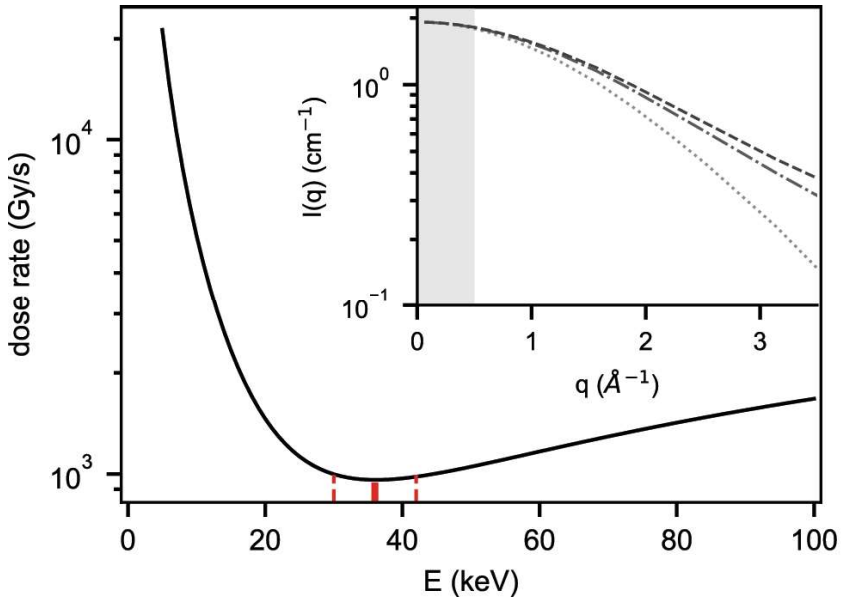

Figure S7 Energy dependent dose rate for water calculated for an optimal sample transmission of 37 % and a beam fluence of 10^{12} cts.s^{-1}.mm^{-2}. The dose rate minimum at 36 keV is highlighted in red. The inset shows the Rayleigh scattering intensity for carbon on absolute scale dependent on the scattering vector q for x-ray energies of 8 keV (dotted), 13 keV (solid), 17 keV (dashed-dotted), and 54 keV (dashed).

We stress the benefit of reducing the x-ray dose for solution-based BioSAXS experiments that using high-energy x-rays brings, as recently discussed for macromolecular crystallography by Dickerson and Garman [4]. The absorbed dose rate *D* can be calculated via the equation below [5]:

$$D = \frac{E_T}{m} = \frac{I_0 * E * t\,(1-\exp(-\mu_{ic}(E) * \lambda))}{V * \rho} = \frac{I_0 * E * t\,(1-\exp(-\mu_{ic}(E) * \lambda))}{A * \lambda * \rho} \quad (1)$$

Here, E_T/m is the transferred energy per mass, I_0 the beam intensity, E the x-ray energy, t the exposure time, μ_{ic} the incoherent contribution of the attenuation coefficient [6], i.e. the Compton and the photoelectric contribution, V the sample volume, ρ its density and λ its attenuation length; all these parameters are known and tabulated. Since the main volume fraction in SUV experiments is water, Figure S6 uses the energy dependence of the x-ray dose for water. As evident from Figure S6 the absorbed dose drastically drops for increasing energies in the regime $\mathbf{5-30\ keV}$. After a minimum of $\mathbf{36\ keV}$, the dose rate shows a mild increase for energies bigger than

195 $\mathbf{40\ keV}$. Such considerations clearly point to a favourable x-ray energy regime of
196 $\mathbf{30 - 42\ keV}$ for SAXS experiments on radiation-sensitive samples. The dose rate is
197 calculated using the mass attenuation coefficients from the NIST XCOM database [7].

198 Using higher x-ray energies does not imply per se a loss of scattering signal. In order
199 to explain this, we plot the SAXS intensity for a carbon scattering centre in dependence
200 of the scattering vector q in $[\text{Å}^{-1}]$ for three different x-ray beam
201 energies $8.0\ keV$, $17.4\ keV$, and $53.7\ keV$ as dotted line, dashed-dotted line, dashed
202 line, respectively, as inset in Figure S6 [8]. The intensity of a SAXS experiment on an
203 absolute scale in $[cm]^{-1}$ is given by the differential Rayleigh cross section $\frac{d\sigma_R}{d\Omega}$, i.e. the
204 detection probability of an elastically scattered photon per unit solid angle and the
205 number density ρ of the scatters:

206 $$I_{SAXS}(\theta) = \rho \frac{d\sigma_R}{d\Omega}$$

207 $$\frac{d\sigma_R}{d\Omega} = r_e^2 P |f(\theta)|^2$$

208 Here, the Thomson radius is denoted as r_e, $f(\theta)$ is the atomic form factor, and P the
209 polarization of the x-ray beam. From the inset of Figure S6 it is readily apparent that
210 there is almost no difference in the number of elastically scattered photons, within the
211 SAXS regime $(0 - 0.5\ \text{Å})$ for the x-ray energies discussed. The same is also true for
212 the differential Compton scattering cross section within the SAXS regime (data not
213 shown), i.e. the Compton scattering does not result in additional background signal.
214 This is maybe surprising in view of the total Compton scattering cross section, which
215 becomes larger than the photoelectric effect and the Rayleigh scattering beyond
216 28 keV. However, for SAXS we are only interested in the Compton forward scattering,
217 which remains low. In agreement with our experiments shown in Figure 2a, high energy
218 SAXS yields high quality data even for weakly scattering samples.

219

S8: Head-to-head distance of azo-PC membranes depends on the percentage of azo-PCs in *cis*-state

We obtain a linear correlation of the head-to-head distance of azo-PC membranes with the percentage of azo-PC that is in the *cis* isomer state (see Fig. 1c),

$$d_{HH} = 42.7 - 0.1226 \times (\%\text{cis})$$

by least-squares fitting of five different membrane compositions: 10%, 19%, 39%, 58% and 83% *cis* isomer. As the measured head-to-head distances d_{HH} for the dark-adapted state are not well-reproducible (Fig 1c, Fig 2b), the first data point (0% cis) was treated as an outlier and omitted during the linear fitting.

Applying this calibration curve to the measured head-to-head distances, we calculated *cis* isomer fractions as given in Table S3.

	PBS / 1xTE		Deionized water	
	d_{HH} (Å)	%cis isomer	d_{HH} (Å)	%cis isomer
dark-adapted	42.9 ± 0.2	0% ± 2%	41.9 ± 0.9	7% ± 11%
PSS_{UV}	35.0 ± 0.4	63% ± 5%	34.8 ± 0.6	64% ± 7%
PSS_{blue}	42.3 ± 0.4	3% ± 5%	39.0 ± 0.3	30% ± 4%
PSS_{x-ray}			42.5 ± 0.3	2% ± 4%

Table S3 Relevant mean head-to-head distances of azo-PC membranes obtained for various photostationary states (PSS) and their calculated percentages of cis isomer.

S9: Photoswitching azo-PC SUVs in NaCl solution via UV and blue light

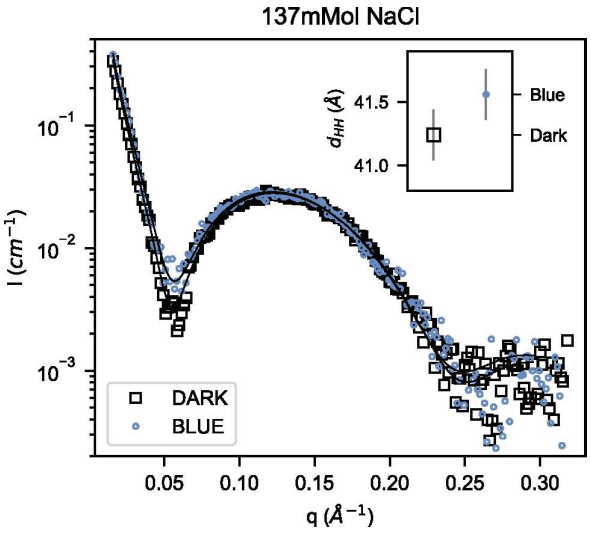

Figure S 8: SAXS intensities for unilamellar azo-PC vesicles prepared in 137 mM NaCl solution for the dark-adapted state, and the photostationary state induced by extended blue light illumination (>300s) are shown as squares and circles respectively. The Intensity of the blue photostationary state is vertically offset for clarity. Head-to-head distances (d_{HH}) obtained for azo-PC SUVs in NaCl solution are shown in the inset. The dark-adapted state, and photostationary states induced via blue light are labelled accordingly.

References:

1. Frank, J. A.; Moroni, M.; Moshourab, R.; Sumser, M.; Lewin, G. R.; Trauner, D., Photoswitchable fatty acids enable optical control of TRPV1. Nature Communications 2015, 6 (1), 7118.
2. Morstein, J.; Trauner, D., Chapter Eleven - Photopharmacological control of lipid function. In *Methods in Enzymology*, Chenoweth, D. M., Ed. Academic Press: 2020; Vol. 638, pp 219-232.
3. Komorowski, K.; Salditt, A.; Xu, Y.; Yavuz, H.; Brennich, M.; Jahn, R.; Salditt, T., Vesicle Adhesion and Fusion Studied by Small-Angle X-Ray Scattering. Biophys J 2018, 114 (8), 1908-1920.
4. Dickerson, J. L.; Garman, E. F., The potential benefits of using higher X-ray energies for macromolecular crystallography. Journal of Synchrotron Radiation 2019, 26 (4), 922-930.
5. Attix, F. H., Introduction to Radiological Physics and Radiation Dosimetry. Wiley VCH: 2004.
6. Berger, M. J., Hubbell, J.H., Seltzer, S.M., Chang, J., Coursey, J.S., Sukumar, R., Zucker, D.S., and Olsen, K., XCOM: Photon Cross Section Database (version 1.5). National Institute of Standards and Technology, Gaithersburg, MD.: 2010.
7. Berger, M. J.; Hubbell, J. H.; Seltzer, S. M.; Chang, J.; Coursey, J. S.; Sukumar, R.; Zucker, D. S.; and Olsen, K., XCOM: Photon Cross Sections Database. National Institute of Standards and Technology, Gaithersburg, MD, USA 1998.
8. Hubbell, J. H.; Veigele, W. J.; Briggs, E. A.; Brown, R. T.; Cromer, D. T.; Howerton, R. J., Atomic form factors, incoherent scattering functions, and photon scattering cross sections. Journal of Physical and Chemical Reference Data 1975, 4 (3), 471-538.

8 Other projects published or ongoing

8.1 Photoswitchable Epothilone-Based Microtubule Stabilisers Allow GFP-Imaging-Compatible, Optical Control over the Microtubule Cytoskeleton

Styrobenzothiazoles have many advantages as photoswitches. They are metabolically stable and are completely GFP orthogonal. I endeavoured to use them for photoswitching microtubule stabilisers by synthesizing **SBTax**, an analogue of **AzTax3MP.** However, it gave only limited isomer-dependency of antiproliferative activity in cells. We then changed the inhibitor scaffold to epothilone, and **STEpo** compounds that showed isomer dependent microtubule stabilization were synthesized by Li Gao who also contributed the rest of the chemical work. These **STEpo** photocontrolled MT dynamics in live cells, and our results were published in Angewandte Chemie in 2022.[103]

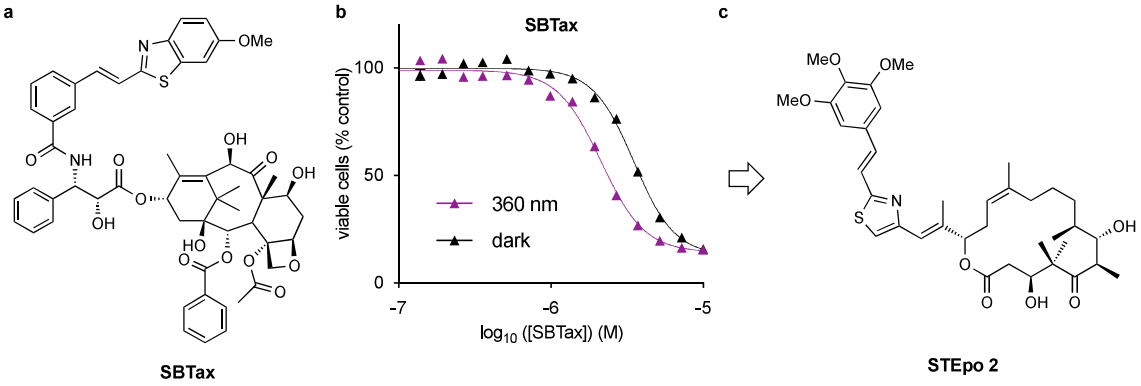

Figure 17: **(a)** The structure of **SBTax**: the core structure is that of paclitaxel, an SBT photoswitch is attached at the 3'N, similarly to **AzTax. (b)** The light-dependant antiproliferative activity of **SBTax** against HeLa cells shows a small difference in toxicity of the illuminated vs. the dark experiment. **(c)** Changing the scaffold to epothilone resulted in the **STEpo** compounds which showed improved biological applications.

8.2 Photoswitchable covalent colchicine site binders

Light can be applied with very high spatial precision; however, small molecules can move through a cell in a matter of milliseconds. This diffusion drastically limits the resolution of photocontrol over proteins with time constants on the seconds to minutes scale, and complicates applications that require subcellular precision. Covalent attachment of the photopharmaceutical to the protein of interest is a potential solution for this problem, however it often requires genetic engineering of the protein.[104]

We aimed at preparing a photoswitchable colchicine site binder that instead forms a covalent attachment to endogenous tubulin after docking (Fig 14). The colchicine binding site contains two cysteine residues, Cys239 and Cys354, that are potentially in the right position to react with an appropriate electrophile.[105] We prepared a library of compounds modelled after PST1 but carrying different electrophiles. The compounds were tested in light-dependent

antiproliferation assays, and the most promising candidates were investigated in mass spectrometry studies and crystallization experiments.

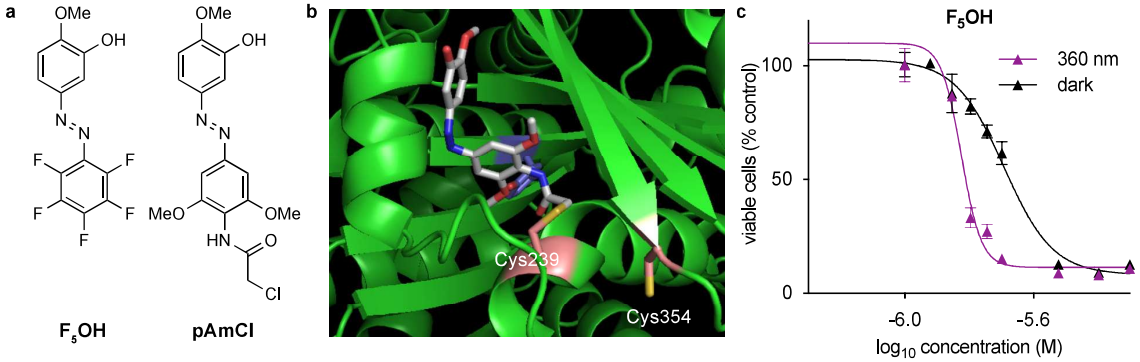

Figure 14: **(a)** PST1 derivatives with cysteine reactive sites. **F_5OH** showed tubulin-alkylating reactivity in MS studies. **pAmCl** showed partial occupancy and protein labeling in a protein co-crystallization study. **(b)** Crystal structure of **pAmCl** bound to Cys239. **(c)** Antiproliferation assay of **F_5OH** showing a difference in antiproliferative activity against HeLa cells depending on light irradiation.

For parts of this research a manuscript is in preparation, and I would like to thank all people who made contributions to this project: particularly, Rebecca Bechtel (synthesis), Dominik Lonken (mass spectrometry), Michel Steinmetz (crystallisation supervision), Tobias Weinert (crystallisation), Maximilian Wranik (crystallisation) and Marina Fütterer (bioassays).

8.3 Assisted photoswitching

Photoelectron transfer is a phenomenon often used in ion sensing probes by employing electron transfer to quench florescence.[106] We investigated photoelectron transfers within covalent conjugates of azobenzenes and fluorophores that operate primarily in the singlet manifold, as a means of accessing photoredox-based isomerisation (Fig 15). As outlined in section 2.1.5, if a fluorophore is excited, it can oxidize an azobenzene to the radical cation, lowering the bond order of the diazene, and allowing the *Z*-azobenzene to isomerize quantitatively and rapidly to the *E*-isomer. However, the redox potentials of the two reaction partners (azobenzene and fluorophore) must match for the reaction to proceed.

I did initial investigations into this project, preparing conjugates of azobenzenes with the fluorophores rhodamine and fluorescein, investigating them by UV/Vis spectroscopy, and conducting initial CV measurements. I observed isomerisation of the azobenzene when the fluorophore was excited, however I could not elucidate by what mechanism. All further research was then conducted by Benedikt Winkler, and a manuscript is now in preparation. I would like to give special thanks to Stefan Hecht and Lutz Gruber for discussions and CV.

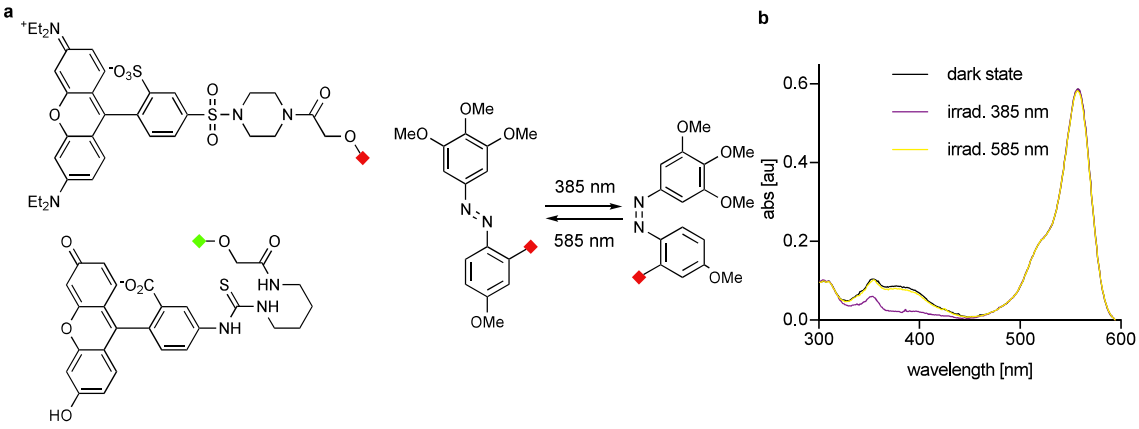

Figure 15: **(a)** Azobenzene sulforhodamine (red) and fluorescein (green) conjugates were. The azobenzene-sulforhodamine can be switched *E*→*Z* with 385 nm and *Z*→*E* with 585 nm, each with high yield. **(b)** The absorbance spectra of the azobenzene sulforhodamine conjugate at different PSS (black: all-*E*, purple: after 385 nm irradiation, yellow: after 585 nm irradiation that followed the 385 nm irradiation).

8.4 Assisted photoswitching in Lipid Vesicles

Photocontrollable SUVs are an important model system to investigate lipid membranes. However, the control over the properties of the vesicles is dependent on the isomerisation yields of the azobenzene employed. We combined the concept of assisted photoswitching (section 8.3) with photoswitchable lipids (chapter 7) to try to improve the photoswitching yield in membranes. I prepared **OxyPC**, a new derivative of AzoPC, and other lipids that have a suitable redox potential for photoredox *Z*→*E* switching, with improved *E*→*Z* direct photoswitching yield, and other improved photoproperties (Fig 16). Furthermore, I synthesized fluorophore fatty acid conjugates to anchor fluorescent photoredox catalysts in membranes. This project is still proceeding with our collaborators from the Nickel group and the Lohmüller group; I would like to thank Benedikt Winkler, Martina Ober, Jinhua Zhang, Bert Nickel and Theobald Lohmüller for their collaboration and assistance.

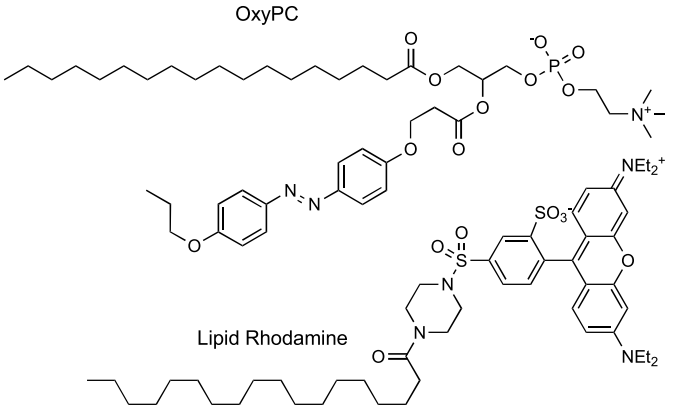

Figure 16: The chemical structure of **OxyPC**, a photoswitchable phosphatidylcholine derivative, and a lipid functionalized rhodamine derivative that localizes the fluorophore to the lipid membrane.

Conclusion & Summary

8.5 Research Summary

I have presented three research arcs working towards the improvement and use of azobenzenes as research tools for biology. Chapter 5 demonstrated that azobenzenes can be employed to control the effect of taxanes on the cytoskeleton; upon irradiation the AzTax tool compounds stabilise MTs and inhibit MT dynamics with cellular or subcellular resolution in living cells. In Chapter 6, I developed a convenient method for access to tetra-*ortho*-alkoxylated azobenzenes via CH-activation, also accessing thus far unknown azobenzene derivatives. In Chapter 7, we investigated photocontrollable SUVs based on AzoPC, discovered photoproperties that differ from those of azobenzenes in solution, and established azobenzene isomerisation based on X-rays as a new way to control membrane thickness.

8.6 Specific Conclusions

The wide range of possibilities provided by azobenzenes is reflected in my thesis that spans over different areas of research ranging from photopharmacology over C-H activation to the physics of lipid membranes. It is difficult to predict which tool of the vast toolbox of azobenzenes fits the needs of future scientists. However, azobenzenes will continue to provide unique and new utility to researchers and develop into more refined and easier to use compounds. In my thesis I have worked towards this goal.

(1) The AzTax compounds were the first photoswitchable MT stabilisers, therefore, they opened new avenues of research into the functions and dynamics of MTs. Their high spatial precision coupled with the deep knowledge that already exists about the mechanism of action of the taxol scaffold make the AzTax compounds more than a “proof of concept” tool. However, they are limited by the modest difference in bioactivity between the two isomers, which increases the need for optimisation before use.

(2) Tetra-*ortho*-substituted azobenzenes are a significant development for azobenzenes as tool compounds, due to their exceptional photoproperties. The synthetic access can be a challenge that hampers the adoption of these new and improved azobenzenes for the appropriate applications. The CH-activation approach has been used before - most importantly for tetra-*ortho*-chlorination – but Pd catalysed C-O bond formations are a special challenge since the substrate is progressively deactivated. The methodology provides thus far unknown azobenzene derivatives that have interesting physical and photochemical properties. However, the low to moderate yields, and the substrate scope that does not allow electron rich substrates, limit the utility in synthesis, and further improvements are necessary for broader application.

(3) SUVs made from azobenzene containing phosphatidylcholine derivatives (AzoPC) are an interesting model system that provides great control over the properties of the lipid membrane. The observation that azobenzenes behave differently when embedded in a lipid membrane and are surrounded by different conditions, will be of great importance when AzoPC SUVs are used to model biological systems. Being able to control the azobenzene isomerisation with X-ray radiation in a SAXS set-up is a new observation; however, it can only be applied in unique circumstances.

8.7 General Conclusion

All in all, I have been working on the key properties that make azobenzenes functional as photoswitches. I optimised the switching efficiency and the light response by synthesizing azobenzenes with exceptional band separation and complete visible light addressability or worked towards new methods that approach azobenzene isomerisation from a different direction. In application, I applied rational design ideas to the interaction between the azobenzene photoswitch and a protein of interest. In all projects we demonstrated the power, versatility and malleability of the azobenzene photoswitch. In this PhD I have contributed new tools and methods that will make azobenzenes easier to synthesize, that provide more complete control, and I have explored different applications for azobenzenes. This diverse set of applications is a further step in providing the tools that can help push the frontiers of our knowledge in biochemical research.

9 Outlook

9.1 Photoswitchtable paclitaxel based microtubule stabiliser

9.1.1 AzTax as a tool compound

We reported the first photoswitchable microtubule stabiliser and its proof-of-concept applications in live cell and neuronal hippocampal explants. I believe this microtubule stabiliser will add to the toolbox of cytoskeleton researchers and allow for new insights into microtubule dynamics and function. Much biological activity is based on the dynamic nature of microtubules, but there are also many, more permanent microtubule structures that play an important role. Especially, in neurons a large portion of the tubulin is bound in microtubules that are almost non dynamic due to special microtubule associated proteins (MAPs) and posttranslational modifications. They are often located in the axon and function as avenues of transportation.[107] With photoswitchable stabilisers it may be possible to externally control the formation of such MT structures. That could lead an increase of transport along an axon or in a certain area of a neuron. Inducing MT-dependent processes might be as valuable in research as inhibiting activity has traditionally been in the investigation of cellular processes.

9.1.2 AzTax improvement

The **AzTax3MP** give a ~6-fold difference in antiproliferative activity between the *Z*-isomer and the *E*-isomer. An ideal photoswitch would have no initial bioactivity, then maximum bioactivity upon irradiation. This behaviour is very rare due to residual binding of the less active isomer, further complicated by incomplete switching. However, it would be of interest to further tune the isomer dependent binding affinity of light controllable paclitaxel derivatives.

The AzTax compounds have been created based on an azoextension approach. An obvious change would be to change the attachment site of the azobenzene on the taxane scaffold. Ojima *et al.* published extensive SAR studies on paclitaxel and permuted all the relevant side chains that, in my analysis, could be replaced/extended with an azobenzene. The phenyl ring at C3' tolerates some attachment of residues but a strong decrease in binding affinity can be observed if the modification increases in bulkiness. In the crystal structure published by Nogales *et al.*[108] the phenyl ring seems to be oriented into the protein. It is however difficult to predict the effect of the integration of an azobenzene (Fig. 18a,b, purple). Similarly, regarding the benzoate attached to C2-OH, this position tolerates a certain degree of modification though an increased size of substituents leads to a decrease in binding affinity which is undesirable (Fig. 18a,b, yellow).[109] There is extensive research into C10 modification even though it is unclear whether it contributes to binding at all or has some other mechanism of increasing toxicity. However, in the crystal structure the C10 residue is oriented towards the M-loop that is important for binding of other Taxol site binders (Fig. 18a,b, orange) and here I particularly see potential for photoswitch attachment to provide better-performing tools (more potent and perhaps more photoswitchability of potency). It would be valuable to investigate some of these other possible sites for photoswitching, depending on the ease of synthesis.

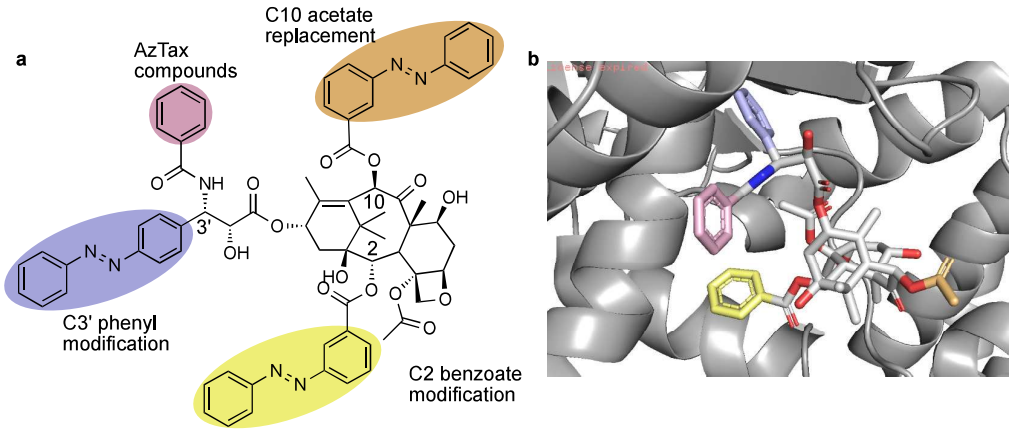

Figure 18: **(a)** Illustration of the different possible sites for attachment of an azobenzene. C3'-phenyl attachment is marked in purple, C3'-N in pink, C2 in yellow and C10 in orange. **(b)** Electron microcopy image of taxol in its binding pocket on β-tubulin (PDB: 3J6G[108]) with color coded residues corresponding to Fig 18a.

9.1.3 Other photoswitchable microtubule stabilisers

Following our publication on azobenzene based microtubule stabilisers, we explored exchanging the azobenzene in AzTax for a SBT photoswitch. SBTs have certain advantages, such as better compatibility with 488 nm laser set-ups and better metabolic stability compared to azobenzenes. However, SBTax did not deliver satisfactory results in terms of switchable bioactivity. Therefore, we switched to epothilone B as a scaffold. STEpo gave lower concentration toxicity and good ratio of lit to dark toxicity however, SBTs cannot reversibly be switched by light, so it would be of interest to prepare an azobenzene derivative of STEpo, such as "AzoEpo" (Fig 19).[103]

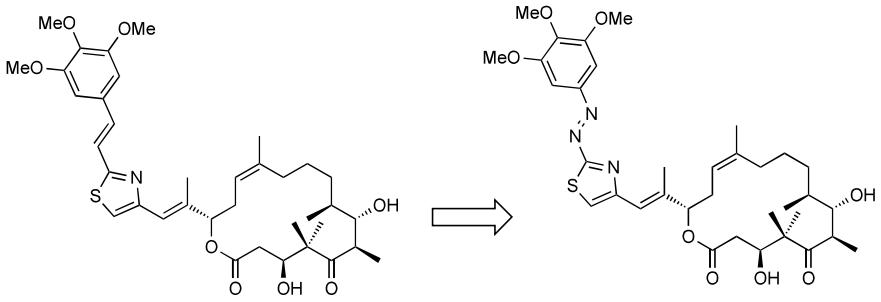

Figure 19: Azobenzene analogue of STEpo2

9.2 Tetra-ortho-alkoxylation

Palladium catalysed C-O bond forming reactions are challenging. We demonstrated that we could perform four consecutive C-O bond forming reactions via C-H activation on one molecule to yield a highly useful scope of products. The reaction has limitations, but opens the path towards remarkable molecules in a straightforward fashion. I believe that the reaction could be tuned towards finer control of the reaction products. Every electron donating substituent deactivates the compound for further reaction, therefore, it should be possible to isolate the separate intermediates. The mono-alkoxylated azobenzenes are already accessible via 80 °C and pressure tube as reaction conditions. With increased oxidant loading at 40 °C the tetra-*ortho*-alkoxylated products are obtained. Expanding the methodology to prepare other degrees of substitution in the *ortho* position would provide photochemists more options to create photoswitches tailored to their respective applications (Fig. 20).

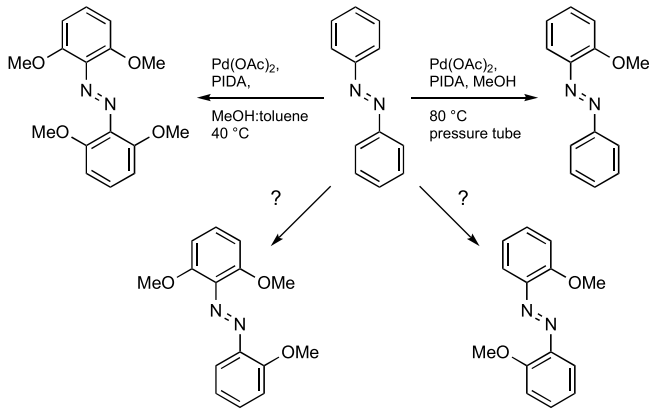

Figure 20: Total control over azobenzene *ortho*-methoxylation patterns by CH activation.

The mechanism of the C-O coupling reaction likely goes through a Pd^{II} with a C-Pd bond with chelation of the palladium by the free electron pair of the distal nitrogen in the diazene bridge. When the azobenzene is isomerised, this coordination is prevented; and coordination to the proximal free electron pair would require an unfavourable four membered ring. Thus a free coordination site on the palladium should be opened by *E*→*Z* isomerisation (Figure 21a). This may have applications in restricting the degree of substitution during synthesis; but it might also find other applications in photopharmacology. For example, cisplatin was approved by the FDA for use against testicular and ovarian cancer in 1979[110,111] and has been one of the most successful anticancer drugs. Cisplatin complexes and crosslinks DNA through the coordination sites that are vacated after chloride ligand exchange. These DNA crosslinks hinder cell division. Instead of platinum, palladium could perhaps be used, with an *E* azobenzene ligand. The palladium could then associate to DNA in monodentate fashion, but the neighbouring coordination site to form the toxic crosslink would only be freed upon isomerisation of the azobenzene (Fig. 21b). A deeper understanding of the reaction mechanism may thus lead to diverse applications even outside synthesis.

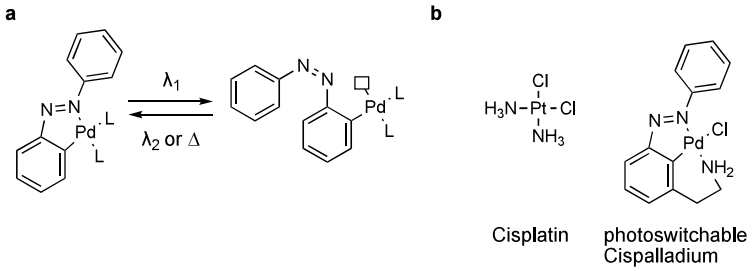

Figure 21: **(a)** photoswitching of the Pd-azobenzene complex that leads to free coordination site **(b)** structural comparison of Cisplatin with a potentially photoswitchable cispalladium DNA-binder.

9.3 Lipids

9.3.1 Different sources of electrons

Azobenzenes can be isomerised using electrons instead of light. In our experiments, we likely sourced electrons from X-ray radiolysis / ionization of water to give radicals. However, X-rays require an extensive setup and other options for the generation of electrons might be well suited for use in lipid membranes. The electron/hole triggered photoswitching induced with a fluorophore that Hecht *et al.* introduced[55] could, we believe, be transferred into lipid membranes: where the tight organisation of the membrane could benefit the propagation of oxidation/reduction. Photoredox-active fluorophores or chromophores would grant more convenient access to highly penetrating (longer wavelength) photoswitching in membranes, than soft X-rays; though lipid photoswitches would need to be engineered to the right redox potentials.

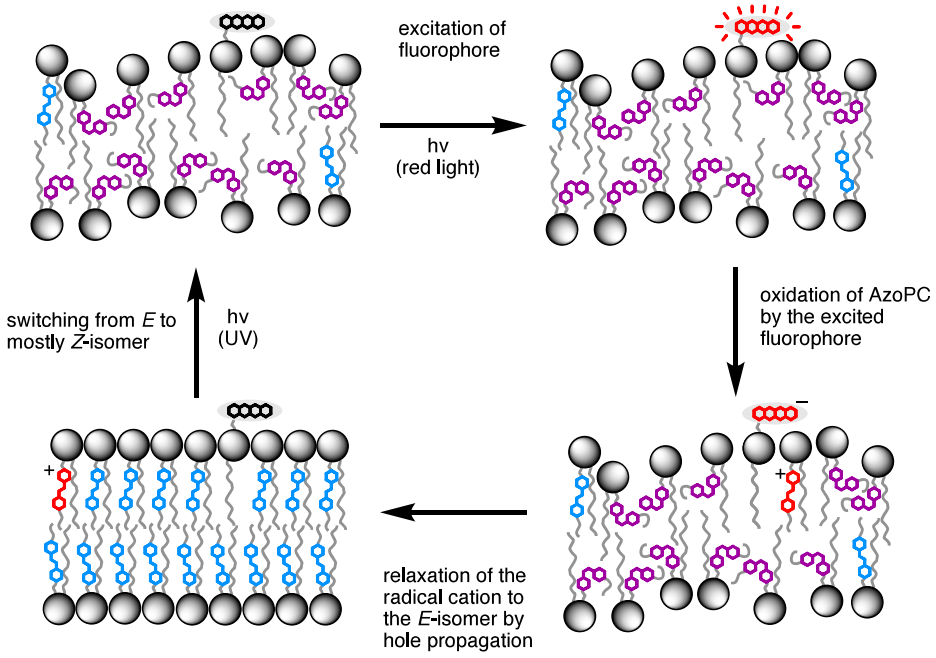

Figure 22: Schematic representation of fluorophore assisted photoswitching in lipid membranes. Predominantly *Z* membrane doped with a membrane localized fluorophore is irradiated with the appropriate wavelength for fluorophore excitation. A photoelectron transfer between fluorophore and azobenzene leads to charge separation and *Z*→*E* isomerisation. The isomerisation propagates through the membrane. The membrane can be switched to the predominantly *Z*-state by direct excitation of azobenzene.

9.3.2 Investigating mechanosensitive receptors in photocontrollable lipid membranes

The membrane environment directly impacts the function and activity of proteins.[112,113] Creating artificial membrane environments for transmembrane proteins and then controlling the functions of these proteins by changing the properties of the membranes is a long standing goal in the photolipid community. I believe AzoPC could be developed further in that direction based on the studies of its physical properties in SUVs and giant unilamellar veiscles (GUVs).

For example, Glaubitz *et al.* prepared liposomes from a 1:6 mix of AzoPC:non-photoswitchable lipid and observed the influence of photoswitching of the membrane on the diacylglycerol kinase protein (DgkA) by NMR.[114] The model system could be used to investigate mechanosensitive ion channels. Not all mechanosensitive channels react to changes in the membrane, but an example are TREK/TRAAK channels. TREK/TRAAK proteins are potassium channels that are not voltage gated and are found in the node of Ranvier.[115] They are thermo and mechanosensitive and are activated when the surrounding membrane is stretched.[116] There are some indications that AzoPC membranes could provide suitable membrane stretching upon *E*→*Z* switching, as this increases SUV size and decreases membrane thickness: so potentially triggering TREK/TRAAK channel opening. Photoswitchable lipids could thus provide new insights in the function and mechanism of mechanosensitive proteins, if control via membrane embedding were investigated.

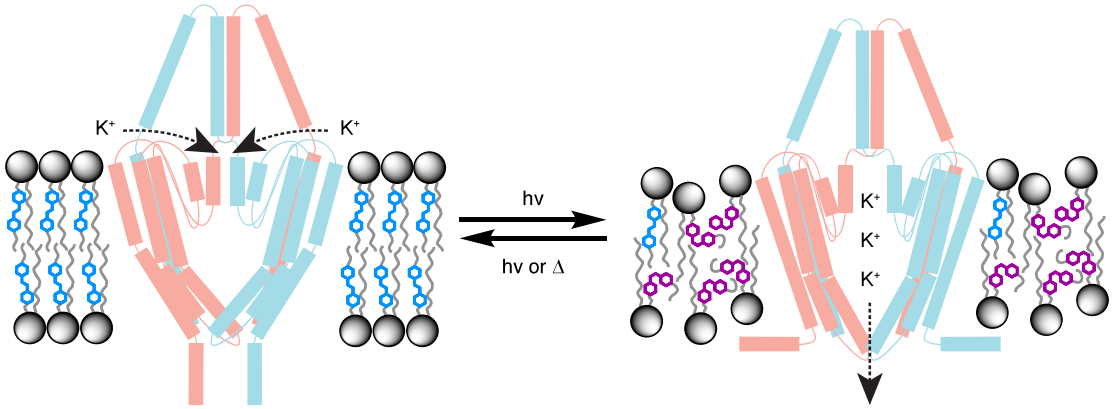

Figure 23: TREK/TRAAK channel in an AzoPC membrane. The channel is closed in an all-*E* membrane. Upon irradiation the membrane changes its properties and the channel reacts to the change in its surrounding by opening for potassium ion passage. The mechanosensing channel would be controlled by light.

10 Acknowledgements

First of all, I would like to thank my supervisor Dr. Oliver Thorn-Seshold for giving me the opportunity and all the support, knowledge and trust I needed to complete this thesis. I really enjoyed working with you and your many ideas and suggestions and I was very happy to have been part of you group.

I am very grateful to Dr. Dorian Didier who agreed to be the second reviewer of my thesis and I would also like to thank all other members of my defence committee: Prof. Dr. Ivan Huc, Prof. Dr. Lena Daumann, Prof. Dr. Franz Bracher, Prof. Dr. Philip Tinnefeld.

I want to thank Prof Dr. Klaus Wanner for his supervision and support in the first 2 year of my PhD. I would also like to thank the Wanner group and especially Janina, Heinrich and Jörg.

To the current TS group members Alex, Jan, Lukas, Ben, Markus, Philipp, Annabel, Carina, Nynke, Martin R. Thank you and you are free now! You can eat lunch with an open door at 1.30 pm and skip Denksport but in the back of your mind all of you will know: it is wrong!

Li – now I finally have my sock as well – thank you for the great time we had together from beginning to end.

Further, I would like to thank all former members of TS group, Cytoswitch and NanoCapture It was a great pleasure to work with you – Elena L, Lena, Franzi, Elena F-R, Martin M., Dominik, Evi, Yelena, Julia, Kristina, Marina, Doris, Tilmann, Petar, Bekkah, Constanze, Monique, Andrea, Carina G.

I also want to thank my collaborators, especially Martina, Joyce and Jinhua and my interns Marc, Jonas, Nurunissa, Nesrin and Anika. I am also grateful to the Lars and Claudia for measuring all my NMRs.

Last of course I would like to thank my family Linh, Lulu, Heike and Tobias.

11 Appendix

11.1 List of abbreviations

CA4	combretastatin A4
CV	cyclic voltammetry
DgkA	diacylglycerol kinase protein
DNA	desoxyribonucleic acid
DTE	dithienylethene
FACS	fluorescence activated cell sorting
FDA	Federal drug administration
GDP	guanosine diphosphate
GPCR	G-protein coupled receptor
GTP	guanosine triphosphate
GUV	giant unilamellar vesicle
HOMO	highest occupied molecular orbital
HTI	hemithioindigo
MAP	microtubule associated protein
MDA	microtubule disrupting agent
MO	molecular orbital
MSA	microtubule stabilising agent
MT	microtubule
NMR	nuclear magnetic resonance
POI	protein of interest
PRC	photoredox catalyst
PROTAC	proteolysis targeting chimera
PSS	photostationary state
SAR	structure activity relationship
SAXS	small angle X-ray scattering
SBT	styrylbenzothiazole
SPMC	spiropyran merocyanine
SUV	small unilamellar vesicle
UV	ultraviolet
VGIC	voltage gated ion channels

11.2 Bibliography

(1) Feringa, B. L. The Art of Building Small: From Molecular Switches to Motors (Nobel Lecture). *Angew. Chem. Int. Ed.* **2017**, *56* (37), 11060–11078. https://doi.org/10.1002/anie.201702979.

(2) Wensel, T. G. Chapter 51 - Molecular Biology of Vision. In *Basic Neurochemistry (Eighth Edition)*; Brady, S. T., Siegel, G. J., Albers, R. W., Price, D. L., Eds.; Academic Press: New York, 2012; pp 889–903. https://doi.org/10.1016/B978-0-12-374947-5.00051-1.

(3) Mayer, G.; Heckel, A. Biologically Active Molecules with a "Light Switch." *Angew. Chem. Int. Ed.* **2006**, *45* (30), 4900–4921. https://doi.org/10.1002/anie.200600387.

(4) Aprahamian, I. The Future of Molecular Machines. *ACS Cent. Sci.* **2020**, *6* (3), 347–358. https://doi.org/10.1021/acscentsci.0c00064.

(5) Russew, M.-M.; Hecht, S. Photoswitches: From Molecules to Materials. *Adv. Mater* **2010**, *22* (31), 3348–3360. https://doi.org/10.1002/adma.200904102.

(6) Fuchter, M. J. On the Promise of Photopharmacology Using Photoswitches: A Medicinal Chemist's Perspective. *J. Med. Chem.* **2020**, *63* (20), 11436–11447. https://doi.org/10.1021/acs.jmedchem.0c00629.

(7) Hüll, K.; Morstein, J.; Trauner, D. In Vivo Photopharmacology. *Chem. Rev.* **2018**, *118* (21), 10710–10747. https://doi.org/10.1021/acs.chemrev.8b00037.

(8) Waldeck, D. H. Photoisomerization Dynamics of Stilbenes. *Chem. Rev.* **1991**, *91* (3), 415–436. https://doi.org/10.1021/cr00003a007.

(9) Villarón, D.; Wezenberg, S. J. Stiff-Stilbene Photoswitches: From Fundamental Studies to Emergent Applications. *Angew. Chem. Int. Ed.* **2020**, *59* (32), 13192–13202. https://doi.org/10.1002/anie.202001031.

(10) *The Nobel Prize in Chemistry 2016*. NobelPrize.org. https://www.nobelprize.org/prizes/chemistry/2016/feringa/facts/ (accessed 2022-03-04).

(11) Gao, L.; Kraus, Y.; Stegner, A.; Wein, T.; Heise, C.; Brunn, L. von; Fajardo-Ruiz, E.; Thorn-Seshold, J.; Thorn-Seshold, O. Self-Reporting Styrylthiazolium Photopharmaceuticals: Mitochondrial Localisation as Well as SAR Drive Biological Activity. **2022**. https://doi.org/10.26434/chemrxiv-2022-bm5gq.

(12) Gao, L.; Meiring, J. C. M.; Kraus, Y.; Wranik, M.; Weinert, T.; Pritzl, S. D.; Bingham, R.; Ntouliou, E.; Jansen, K. I.; Olieric, N.; Standfuss, J.; Kapitein, L. C.; Lohmüller, T.; Ahlfeld, J.; Akhmanova, A.; Steinmetz, M. O.; Thorn-Seshold, O. A Robust, GFP-Orthogonal Photoswitchable Inhibitor Scaffold Extends Optical Control over the Microtubule Cytoskeleton. *Cell Chem. Biol.* **2021**, *28* (2), 228-241.e6. https://doi.org/10.1016/j.chembiol.2020.11.007.

(13) Wiedbrauk, S.; Dube, H. Hemithioindigo—an Emerging Photoswitch. *Tetrahedron Lett.* **2015**, *56* (29), 4266–4274. https://doi.org/10.1016/j.tetlet.2015.05.022.

(14) Sailer, A.; Ermer, F.; Kraus, Y.; Lutter, F. H.; Donau, C.; Bremerich, M.; Ahlfeld, J.; Thorn-Seshold, O. Hemithioindigos for Cellular Photopharmacology: Desymmetrised Molecular Switch Scaffolds Enabling Design Control over the Isomer-Dependency of Potent Antimitotic Bioactivity. *ChemBioChem* **2019**, *20* (10), 1305–1314. https://doi.org/10.1002/cbic.201800752.

(15) Sailer, A.; Ermer, F.; Kraus, Y.; Lutter, F. H.; Donau, C.; Bremerich, M.; Ahlfeld, J.; Thorn-Seshold, O. Hemithioindigos for Cellular Photopharmacology: Desymmetrised Molecular Switch Scaffolds Enabling Design Control over the Isomer-Dependency of Potent Antimitotic Bioactivity. *ChemBioChem* **2019**, *20* (10), 1305–1314. https://doi.org/10.1002/cbic.201800752.

(16) Sailer, A.; Meiring, J. C. M.; Heise, C.; Pettersson, L. N.; Akhmanova, A.; Thorn-Seshold, J.; Thorn-Seshold, O. Pyrrole Hemithioindigo Antimitotics with Near-Quantitative Bidirectional Photoswitching That Photocontrol Cellular Microtubule Dynamics with Single-Cell Precision**. *Angew. Chem. Int. Ed.* **2021**, *60* (44), 23695–23704. https://doi.org/10.1002/anie.202104794.
(17) Gerwien, A.; Mayer, P.; Dube, H. Green Light Powered Molecular State Motor Enabling Eight-Shaped Unidirectional Rotation. *Nat. Commun.* **2019**, *10* (1), 4449. https://doi.org/10.1038/s41467-019-12463-4.
(18) Aprahamian, I. Hydrazone Switches and Things in Between. *Chem. Commun.* **2017**, *53* (50), 6674–6684. https://doi.org/10.1039/C7CC02879B.
(19) Hoorens, M. W. H.; Medved', M.; Laurent, A. D.; Di Donato, M.; Fanetti, S.; Slappendel, L.; Hilbers, M.; Feringa, B. L.; Jan Buma, W.; Szymanski, W. Iminothioindoxyl as a Molecular Photoswitch with 100 Nm Band Separation in the Visible Range. *Nat. Commun.* **2019**, *10* (1), 2390. https://doi.org/10.1038/s41467-019-10251-8.
(20) Klajn, R. Spiropyran-Based Dynamic Materials. *Chem. Soc. Rev.* **2014**, *43* (1), 148–184. https://doi.org/10.1039/C3CS60181A.
(21) Regehly, M.; Garmshausen, Y.; Reuter, M.; König, N. F.; Israel, E.; Kelly, D. P.; Chou, C.-Y.; Koch, K.; Asfari, B.; Hecht, S. Xolography for Linear Volumetric 3D Printing. *Nature* **2020**, *588* (7839), 620–624. https://doi.org/10.1038/s41586-020-3029-7.
(22) Irie, M. Diarylethenes for Memories and Switches. *Chem. Rev.* **2000**, *100* (5), 1685–1716. https://doi.org/10.1021/cr980069d.
(23) Matsuda, K.; Irie, M. Diarylethene as a Photoswitching Unit. *J. Photochem. Photobiol. C: Photochem. Rev.* **2004**, *5* (2), 169–182. https://doi.org/10.1016/j.jphotochemrev.2004.07.003.
(24) Yokoyama, Y. Fulgides for Memories and Switches. *Chem. Rev.* **2000**, *100* (5), 1717–1740. https://doi.org/10.1021/cr980070c.
(25) Klaue, K.; Han, W.; Liesfeld, P.; Berger, F.; Garmshausen, Y.; Hecht, S. Donor–Acceptor Dihydropyrenes Switchable with Near-Infrared Light. *J. Am. Chem. Soc.* **2020**, *142* (27), 11857–11864. https://doi.org/10.1021/jacs.0c04219.
(26) Beharry, A. A.; Woolley, G. A. Azobenzene Photoswitches for Biomolecules. *Chem. Soc. Rev.* **2011**, *40* (8), 4422–4437. https://doi.org/10.1039/C1CS15023E.
(27) Noble, A. III. Zur Geschichte des Azobenzols und des Benzidins. *Ann. Chem. Pharm.* **1856**, *98* (2), 253–256. https://doi.org/10.1002/jlac.18560980211.
(28) Hartley, G. S. The Cis-Form of Azobenzene. *Nature* **1937**, *140* (3537), 281–281. https://doi.org/10.1038/140281a0.
(29) Hartley, G. S.; Fèvre, R. J. W. L. 119. The Dipole Moments of Cis- and Trans-Azobenzenes and of Some Related Compounds. *J. Chem. Soc.* **1939**, No. 0, 531–535. https://doi.org/10.1039/JR9390000531.
(30) Oscurato, S. L.; Salvatore, M.; Maddalena, P.; Ambrosio, A. From Nanoscopic to Macroscopic Photo-Driven Motion in Azobenzene-Containing Materials. *Nanophotonics* **2018**, *7* (8), 1387–1422. https://doi.org/10.1515/nanoph-2018-0040.
(31) Bléger, D.; Schwarz, J.; Brouwer, A. M.; Hecht, S. O-Fluoroazobenzenes as Readily Synthesized Photoswitches Offering Nearly Quantitative Two-Way Isomerization with Visible Light. *J. Am. Chem. Soc.* **2012**, *134* (51), 20597–20600. https://doi.org/10.1021/ja310323y.
(32) Griffiths, J. II. Photochemistry of Azobenzene and Its Derivatives. *Chem. Soc. Rev.* **1972**, *1* (4), 481–493. https://doi.org/10.1039/CS9720100481.

(33) Rau, H. Spectroscopic Properties of Organic Azo Compounds. *Angew. Chem. Int. Ed.* **1973**, *12* (3), 224–235. https://doi.org/10.1002/anie.197302241.
(34) Bandara, H. M. D.; Burdette, S. C. Photoisomerization in Different Classes of Azobenzene. *Chem. Soc. Rev.* **2012**, *41* (5), 1809–1825. https://doi.org/10.1039/C1CS15179G.
(35) Dokić, J.; Gothe, M.; Wirth, J.; Peters, M. V.; Schwarz, J.; Hecht, S.; Saalfrank, P. Quantum Chemical Investigation of Thermal Cis-to-Trans Isomerization of Azobenzene Derivatives: Substituent Effects, Solvent Effects, and Comparison to Experimental Data. *J. Phys. Chem. A* **2009**, *113* (24), 6763–6773. https://doi.org/10.1021/jp9021344.
(36) Rodionova, G. N.; Krutovskaya, I. V.; Tuchin, Y. G.; Rodionov, A. N.; Karpov, V. V. Electronic Spectra and Structure of Several Azo Dyes in Various States of Aggregation. *Zhurnal Prikladnoi Spektroskopii* **1981**, *34* (4), 667–672.
(37) Konrad, D. B.; Savasci, G.; Allmendinger, L.; Trauner, D.; Ochsenfeld, C.; Ali, A. M. Computational Design and Synthesis of a Deeply Red-Shifted and Bistable Azobenzene. *J. Am. Chem. Soc.* **2020**, *142* (14), 6538–6547. https://doi.org/10.1021/jacs.9b10430.
(38) Aleotti, F.; Nenov, A.; Salvigni, L.; Bonfanti, M.; El-Tahawy, M. M.; Giunchi, A.; Gentile, M.; Spallacci, C.; Ventimiglia, A.; Cirillo, G.; Montali, L.; Scurti, S.; Garavelli, M.; Conti, I. Spectral Tuning and Photoisomerization Efficiency in Push–Pull Azobenzenes: Designing Principles. *J. Phys. Chem. A* **2020**, *124* (46), 9513–9523. https://doi.org/10.1021/acs.jpca.0c08672.
(39) Siewertsen, R.; Neumann, H.; Buchheim-Stehn, B.; Herges, R.; Näther, C.; Renth, F.; Temps, F. Highly Efficient Reversible *Z*−*E* Photoisomerization of a Bridged Azobenzene with Visible Light through Resolved S_1 (Nπ*) Absorption Bands. *J. Am. Chem. Soc.* **2009**, *131* (43), 15594–15595. https://doi.org/10.1021/ja906547d.
(40) Hammerich, M.; Schütt, C.; Stähler, C.; Lentes, P.; Röhricht, F.; Höppner, R.; Herges, R. Heterodiazocines: Synthesis and Photochromic Properties, *Trans* to *Cis* Switching within the Bio-Optical Window. *J. Am. Chem. Soc.* **2016**, *138* (40), 13111–13114. https://doi.org/10.1021/jacs.6b05846.
(41) Samanta, S.; Qin, C.; Lough, A. J.; Woolley, G. A. Bidirectional Photocontrol of Peptide Conformation with a Bridged Azobenzene Derivative. *Angew. Chem. Int. Ed.* **2012**, *51* (26), 6452–6455. https://doi.org/10.1002/anie.201202383.
(42) Maier, M. S.; Hüll, K.; Reynders, M.; Matsuura, B. S.; Leippe, P.; Ko, T.; Schäffer, L.; Trauner, D. Oxidative Approach Enables Efficient Access to Cyclic Azobenzenes. *J. Am. Chem. Soc.* **2019**, *141* (43), 17295–17304. https://doi.org/10.1021/jacs.9b08794.
(43) Forber, C. L.; Kelusky, E. C.; Bunce, N. J.; Zerner, M. C. Electronic Spectra of Cis- and Trans-Azobenzenes: Consequences of Ortho Substitution. *J. Am. Chem. Soc.* **1985**, *107* (21), 5884–5890. https://doi.org/10.1021/ja00307a009.
(44) Beharry, A. A.; Sadovski, O.; Woolley, G. A. Azobenzene Photoswitching without Ultraviolet Light. *J. Am. Chem. Soc.* **2011**, *133* (49), 19684–19687. https://doi.org/10.1021/ja209239m.
(45) Bléger, D.; Hecht, S. Visible-Light-Activated Molecular Switches. *Angew. Chem. Int. Ed.* **2015**, *54* (39), 11338–11349. https://doi.org/10.1002/anie.201500628.
(46) Samanta, S.; Beharry, A. A.; Sadovski, O.; McCormick, T. M.; Babalhavaeji, A.; Tropepe, V.; Woolley, G. A. Photoswitching Azo Compounds in Vivo with Red Light. *J. Am. Chem. Soc.* **2013**, *135* (26), 9777–9784. https://doi.org/10.1021/ja402220t.
(47) Knie, C.; Utecht, M.; Zhao, F.; Kulla, H.; Kovalenko, S.; Brouwer, A. M.; Hecht, S.; Bléger, D. Ortho-Fluoroazobenzenes: Visible Light Switches with Very Long-Lived Z

Isomers. *Eur. J. Chem.* **2014**, *20* (50), 16492–16501. https://doi.org/10.1002/chem.201404649.
(48) Samanta, S.; McCormick, T. M.; Schmidt, S. K.; Seferos, D. S.; Woolley, G. A. Robust Visible Light Photoswitching with Ortho-Thiol Substituted Azobenzenes. *Chem. Commun.* **2013**, *49* (87), 10314–10316. https://doi.org/10.1039/C3CC46045B.
(49) Neta, P.; Levanon, H. Spectrophotometric Study of the Radicals Produced by the Reduction of Syn- and Anti-Azobenzene. *J. Phys. Chem.* **1977**, *81* (24), 2288–2292. https://doi.org/10.1021/j100539a018.
(50) Laviron, E.; Mugnier, Y. A Study of the Isomerization of Cis-Azobenzene Anion Radical in Dimethylformamide. *J. Electroanal. Chem.* **1978**, *93*, 69–73.
(51) Goulet-Hanssens, A.; Utecht, M.; Mutruc, D.; Titov, E.; Schwarz, J.; Grubert, L.; Bléger, D.; Saalfrank, P.; Hecht, S. Electrocatalytic Z → E Isomerization of Azobenzenes. *J. Am. Chem. Soc.* **2017**, *139* (1), 335–341. https://doi.org/10.1021/jacs.6b10822.
(52) Moreno, J.; Grubert, L.; Schwarz, J.; Bléger, D.; Hecht, S. Efficient Sensitized Z→E Photoisomerization of an Iridium(III)-Azobenzene Complex over a Wide Concentration Range. *Eur. J. Chem.* **2017**, *23* (56), 14090–14095. https://doi.org/10.1002/chem.201703376.
(53) Isokuortti, J.; Kuntze, K.; Virkki, M.; Ahmed, Z.; Vuorimaa-Laukkanen, E.; Filatov, M. A.; Turshatov, A.; Laaksonen, T.; Priimagi, A.; Durandin, N. A. Expanding Excitation Wavelengths for Azobenzene Photoswitching into the Near-Infrared Range *via* Endothermic Triplet Energy Transfer. *Chem. Sci.* **2021**, *12* (21), 7504–7509. https://doi.org/10.1039/D1SC01717A.
(54) Kuntze, K.; Isokuortti, J.; Siiskonen, A.; Durandin, N.; Laaksonen, T.; Priimagi, A. Azobenzene Photoswitching with Near-Infrared Light Mediated by Molecular Oxygen. *J. Phys. Chem. B* **2021**, *125* (45), 12568–12573. https://doi.org/10.1021/acs.jpcb.1c08012.
(55) Goulet-Hanssens, A.; Rietze, C.; Titov, E.; Abdullahu, L.; Grubert, L.; Saalfrank, P.; Hecht, S. Hole Catalysis as a General Mechanism for Efficient and Wavelength-Independent Z → E Azobenzene Isomerization. *Chem* **2018**, *4* (7), 1740–1755. https://doi.org/10.1016/j.chempr.2018.06.002.
(56) Broichhagen, J.; Frank, J. A.; Trauner, D. A Roadmap to Success in Photopharmacology. *Acc. Chem. Res.* **2015**, *48* (7), 1947–1960. https://doi.org/10.1021/acs.accounts.5b00129.
(57) Borowiak, M.; Nahaboo, W.; Reynders, M.; Nekolla, K.; Jalinot, P.; Hasserodt, J.; Rehberg, M.; Delattre, M.; Zahler, S.; Vollmar, A.; Trauner, D.; Thorn-Seshold, O. Photoswitchable Inhibitors of Microtubule Dynamics Optically Control Mitosis and Cell Death. *Cell* **2015**, *162* (2), 403–411. https://doi.org/10.1016/j.cell.2015.06.049.
(58) Borowiak, M.; Küllmer, F.; Gegenfurtner, F.; Peil, S.; Nasufovic, V.; Zahler, S.; Thorn-Seshold, O.; Trauner, D.; Arndt, H.-D. Optical Manipulation of F-Actin with Photoswitchable Small Molecules. *J. Am. Chem. Soc.* **2020**, *142* (20), 9240–9249. https://doi.org/10.1021/jacs.9b12898.
(59) Wegener, M.; Hansen, M. J.; Driessen, A. J. M.; Szymanski, W.; Feringa, B. L. Photocontrol of Antibacterial Activity: Shifting from UV to Red Light Activation. *J. Am. Chem. Soc.* **2017**, *139* (49), 17979–17986. https://doi.org/10.1021/jacs.7b09281.
(60) Urban, P.; Pritzl, S. D.; Konrad, D. B.; Frank, J. A.; Pernpeintner, C.; Roeske, C. R.; Trauner, D.; Lohmüller, T. Light-Controlled Lipid Interaction and Membrane Organization in Photolipid Bilayer Vesicles. *Langmuir* **2018**, *34* (44), 13368–13374. https://doi.org/10.1021/acs.langmuir.8b03241.

(61) Morstein, J.; Awale, M.; Reymond, J.-L.; Trauner, D. Mapping the Azolog Space Enables the Optical Control of New Biological Targets. *ACS Cent. Sci.* **2019**, *5* (4), 607–618. https://doi.org/10.1021/acscentsci.8b00881.
(62) Rodríguez-Soacha, D. A.; Fender, J.; Ramírez, Y. A.; Collado, J. A.; Muñoz, E.; Maitra, R.; Sotriffer, C.; Lorenz, K.; Decker, M. "Photo-Rimonabant": Synthesis and Biological Evaluation of Novel Photoswitchable Molecules Derived from Rimonabant Lead to a Highly Selective and Nanomolar " *Cis* -On" CB $_1$ R Antagonist. *ACS Chem. Neurosci.* **2021**, *12* (9), 1632–1647. https://doi.org/10.1021/acschemneuro.1c00086.
(63) Volgraf, M.; Gorostiza, P.; Numano, R.; Kramer, R. H.; Isacoff, E. Y.; Trauner, D. Allosteric Control of an Ionotropic Glutamate Receptor with an Optical Switch. *Nat. Chem. Biol.* **2006**, *2* (1), 47–52. https://doi.org/10.1038/nchembio756.
(64) Kienzler, M. A.; Reiner, A.; Trautman, E.; Yoo, S.; Trauner, D.; Isacoff, E. Y. A Red-Shifted, Fast-Relaxing Azobenzene Photoswitch for Visible Light Control of an Ionotropic Glutamate Receptor. *J. Am. Chem. Soc.* **2013**, *135* (47), 17683–17686. https://doi.org/10.1021/ja408104w.
(65) Reynders, M.; Matsuura, B. S.; Bérouti, M.; Simoneschi, D.; Marzio, A.; Pagano, M.; Trauner, D. PHOTACs Enable Optical Control of Protein Degradation. *Sci. Adv. 6* (8), eaay5064. https://doi.org/10.1126/sciadv.aay5064.
(66) Pfaff, P.; Samarasinghe, K. T. G.; Crews, C. M.; Carreira, E. M. Reversible Spatiotemporal Control of Induced Protein Degradation by Bistable PhotoPROTACs. *ACS Cent. Sci.* **2019**, *5* (10), 1682–1690. https://doi.org/10.1021/acscentsci.9b00713.
(67) Steinmetz, M. O.; Prota, A. E. Microtubule-Targeting Agents: Strategies To Hijack the Cytoskeleton. *Trends Cell Biol.* **2018**, *28* (10), 776–792. https://doi.org/10.1016/j.tcb.2018.05.001.
(68) Westermann, S.; Weber, K. Post-Translational Modifications Regulate Microtubule Function. *Nat. Rev. Mol. Cell Biol.* **2003**, *4* (12), 938–948. https://doi.org/10.1038/nrm1260.
(69) Gahan, P. B. Molecular Biology of the Cell (4th Edn) B. Alberts, A. Johnson, J. Lewis, K. Roberts and P. Walter (Eds), Garland Science, 1463 Pp., ISBN 0-8153-4072-9 (Paperback) (2002). *Cell Biochemistry and Function* **2005**, *23* (2), 150–150. https://doi.org/10.1002/cbf.1142.
(70) Akhmanova, A.; Steinmetz, M. O. Tracking the Ends: A Dynamic Protein Network Controls the Fate of Microtubule Tips. *Nat. Rev. Mol. Cell Biol.* **2008**, *9* (4), 309–322. https://doi.org/10.1038/nrm2369.
(71) Akhmanova, A.; Steinmetz, M. O. Control of Microtubule Organization and Dynamics: Two Ends in the Limelight. *Nat. Rev. Mol. Cell Biol.* **2015**, *16* (12), 711–726. https://doi.org/10.1038/nrm4084.
(72) Yajima, H.; Ogura, T.; Nitta, R.; Okada, Y.; Sato, C.; Hirokawa, N. Conformational Changes in Tubulin in GMPCPP and GDP-Taxol Microtubules Observed by Cryoelectron Microscopy. *J. Cell Biol.* **2012**, *198* (3), 315. https://doi.org/10.1083/jcb.201201161.
(73) Dumontet, C.; Jordan, M. A. Microtubule-Binding Agents: A Dynamic Field of Cancer Therapeutics. *Nat. Rev. Drug Discov.* **2010**, *9* (10), 790–803. https://doi.org/10.1038/nrd3253.
(74) Wani, M. C.; Taylor, H. L.; Wall, M. E.; Coggon, P.; McPhail, A. T. Plant Antitumor Agents. VI. Isolation and Structure of Taxol, a Novel Antileukemic and Antitumor Agent from Taxus Brevifolia. *J. Am. Chem. Soc.* **1971**, *93* (9), 2325–2327. https://doi.org/10.1021/ja00738a045.
(75) *The Story of Taxol | History of medicine*. Cambridge University Press. https://www.cambridge.org/de/academic/subjects/history/history-medicine/story-taxol-

nature-and-politics-pursuit-anti-cancer-drug, https://www.cambridge.org/de/academic/subjects/history/history-medicine (accessed 2022-03-14).
(76) Schiff, P. B.; Fant, J.; Horwitz, S. B. Promotion of Microtubule Assembly in Vitro by Taxol. *Nature* **1979**, *277* (5698), 665–667. https://doi.org/10.1038/277665a0.
(77) Menzin, A. W.; King, S. A.; Aikins, J. K.; Mikuta, J. J.; Rubin, S. C. Taxol (Paclitaxel) Was Approved by FDA for the Treatment of Patients with Recurrent Ovarian Cancer. *Gynecol. Oncol.* **1994**, *54* (1), 103.
(78) Elie-Caille, C.; Severin, F.; Helenius, J.; Howard, J.; Muller, D. J.; Hyman, A. A. Straight GDP-Tubulin Protofilaments Form in the Presence of Taxol. *Curr. Biol.* **2007**, *17* (20), 1765–1770. https://doi.org/10.1016/j.cub.2007.08.063.
(79) Yang, C.-P. H.; Horwitz, S. B. Taxol®: The First Microtubule Stabilizing Agent. *Int. J. Mol. Sci.* **2017**, *18* (8), 1733. https://doi.org/10.3390/ijms18081733.
(80) Lobert, S.; Vulevic, B.; Correia, J. J. Interaction of Vinca Alkaloids with Tubulin: A Comparison of Vinblastine, Vincristine, and Vinorelbine. *Biochemistry* **1996**, *35* (21), 6806–6814. https://doi.org/10.1021/bi953037i.
(81) Zieve, G. W.; Turnbull, D.; Mullins, J. M.; McIntosh, J. R. Production of Large Numbers of Mitotic Mammalian Cells by Use of the Reversible Microtubule Inhibitor Nocodazole: Nocodazole Accumulated Mitotic Cells. *Exp. Cell Res.* **1980**, *126* (2), 397–405. https://doi.org/10.1016/0014-4827(80)90279-7.
(82) Kavallaris, M. Microtubules and Resistance to Tubulin-Binding Agents. *Nat. Rev. Cancer* **2010**, *10* (3), 194–204. https://doi.org/10.1038/nrc2803.
(83) Miltenburg, N. C.; Boogerd, W. Chemotherapy-Induced Neuropathy: A Comprehensive Survey. *Cancer Treat. Rev.* **2014**, *40* (7), 872–882. https://doi.org/10.1016/j.ctrv.2014.04.004.
(84) Wühr, M.; Tan, E. S.; Parker, S. K.; Detrich, H. W.; Mitchison, T. J. A Model for Cleavage Plane Determination in Early Amphibian and Fish Embryos. *Curr. Biol.* **2010**, *20* (22), 2040–2045. https://doi.org/10.1016/j.cub.2010.10.024.
(85) Bergeijk, P. van; Adrian, M.; Hoogenraad, C. C.; Kapitein, L. C. Optogenetic Control of Organelle Transport and Positioning. *Nature* **2015**, *518* (7537), 111–114. https://doi.org/10.1038/nature14128.
(86) Zenker, J.; White, M. D.; Templin, R. M.; Parton, R. G.; Thorn-Seshold, O.; Bissiere, S.; Plachta, N. A Microtubule-Organizing Center Directing Intracellular Transport in the Early Mouse Embryo. *Science* **2017**, *357* (6354), 925–928. https://doi.org/10.1126/science.aam9335.
(87) Skwarczynski, M.; Noguchi, M.; Hirota, S.; Sohma, Y.; Kimura, T.; Hayashi, Y.; Kiso, Y. Development of First Photoresponsive Prodrug of Paclitaxel. *Bioorg. Med. Chem. Lett.* **2006**, *16* (17), 4492–4496. https://doi.org/10.1016/j.bmcl.2006.06.030.
(88) Noguchi, M.; Skwarczynski, M.; Prakash, H.; Hirota, S.; Kimura, T.; Hayashi, Y.; Kiso, Y. Development of Novel Water-Soluble Photocleavable Protective Group and Its Application for Design of Photoresponsive Paclitaxel Prodrugs. *Bioorg. Med. Chem.* **2008**, *16* (10), 5389–5397. https://doi.org/10.1016/j.bmc.2008.04.022.
(89) Gropeanu, R. A.; Baumann, H.; Ritz, S.; Mailänder, V.; Surrey, T.; del Campo, A. Phototriggerable 2′,7-Caged Paclitaxel. *PLoS ONE* **2012**, *7* (9), e43657. https://doi.org/10.1371/journal.pone.0043657.
(90) Alberts, B.; Johnson, A.; Lewis, J.; Morgan, D.; Raff, M.; Roberts, K.; Walter, P. *Molecular Biology of the Cell*, 6th ed.; Garland Science: New York, 2014.
(91) Andersen, O. S.; Koeppe, R. E. Bilayer Thickness and Membrane Protein Function: An Energetic Perspective. *Annu. Rev. Biophys. Biomol. Struct.* **2007**, *36* (1), 107–130. https://doi.org/10.1146/annurev.biophys.36.040306.132643.

(92) Goñi, F. M.; Alonso, A.; Bagatolli, L. A.; Brown, R. E.; Marsh, D.; Prieto, M.; Thewalt, J. L. Phase Diagrams of Lipid Mixtures Relevant to the Study of Membrane Rafts. *Biochimica et Biophysica Acta (BBA) - Molecular and Cell Biology of Lipids* **2008**, *1781* (11), 665–684. https://doi.org/10.1016/j.bbalip.2008.09.002.
(93) Fujiwara, H.; Yonezawa, Y. Photoelectric Response of a Black Lipid Membrane Containing an Amphiphilic Azobenzene Derivative. *Nature* **1991**, *351* (6329), 724–726. https://doi.org/10.1038/351724a0.
(94) Song, X.; Perlstein, J.; Whitten, D. G. Supramolecular Aggregates of Azobenzene Phospholipids and Related Compounds in Bilayer Assemblies and Other Microheterogeneous Media: Structure, Properties, and Photoreactivity [1]. *J. Am. Chem. Soc.* **1997**, *119* (39), 9144–9159. https://doi.org/10.1021/ja971291n.
(95) DiFrancesco, M. L.; Lodola, F.; Colombo, E.; Maragliano, L.; Paternò, G. M.; Bramini, M.; Cimò, S.; Colella, L.; Fazzi, D.; Eleftheriou, C. G.; Maya-Vetencourt, J. F.; Bertarelli, C.; Lanzani, G.; Benfenati, F. A Membrane-Targeted Photoswitch Potently Modulates Neuronal Firing. bioRxiv July 22, 2019, p 711077. https://doi.org/10.1101/711077.
(96) Chan, Y.-H. M.; Boxer, S. G. Model Membrane Systems and Their Applications. *Curr. Opi. Chem. Biol.* **2007**, *11* (6), 581–587. https://doi.org/10.1016/j.cbpa.2007.09.020.
(97) Heesemann, J. Studies on Monolayers. 1. Surface Tension and Absorption Spectroscopic Measurements of Monolayers of Surface-Active Azo and Stilbene Dyes. *J. Am. Chem. Soc.* **1980**, *102* (7), 2167–2176. https://doi.org/10.1021/ja00527a004.
(98) Hamada, T.; Sugimoto, R.; Nagasaki, T.; Takagi, M. Photochemical Control of Membrane Raft Organization. *Soft Matter* **2011**, *7* (1), 220–224. https://doi.org/10.1039/C0SM00797H.
(99) Pernpeintner, C.; Frank, J. A.; Urban, P.; Roeske, C. R.; Pritzl, S. D.; Trauner, D.; Lohmüller, T. Light-Controlled Membrane Mechanics and Shape Transitions of Photoswitchable Lipid Vesicles. *Langmuir* **2017**, *33* (16), 4083–4089. https://doi.org/10.1021/acs.langmuir.7b01020.
(100) Urban, P.; Pritzl, S. D.; Ober, M. F.; Dirscherl, C. F.; Pernpeintner, C.; Konrad, D. B.; Frank, J. A.; Trauner, D.; Nickel, B.; Lohmueller, T. A Lipid Photoswitch Controls Fluidity in Supported Bilayer Membranes. *Langmuir* **2020**, *36* (10), 2629–2634. https://doi.org/10.1021/acs.langmuir.9b02942.
(101) Pritzl, S. D.; Urban, P.; Prasselsperger, A.; Konrad, D. B.; Frank, J. A.; Trauner, D.; Lohmüller, T. Photolipid Bilayer Permeability Is Controlled by Transient Pore Formation. *Langmuir* **2020**, *36* (45), 13509–13515. https://doi.org/10.1021/acs.langmuir.0c02229.
(102) Konrad, D. B.; Frank, J. A.; Trauner, D. Synthesis of Redshifted Azobenzene Photoswitches by Late-Stage Functionalization. *Eur. J. Chem.* **2016**, *22* (13), 4364–4368. https://doi.org/10.1002/chem.201505061.
(103) Gao, L.; Meiring, J. C. M.; Heise, C.; Rai, A.; Müller-Deku, A.; Akhmanova, A.; Thorn-Seshold, J.; Thorn-Seshold, O. Photoswitchable Epothilone-Based Microtubule Stabilisers Allow GFP-Imaging-Compatible, Optical Control over the Microtubule Cytoskeleton**. *Angew. Chem. Int. Ed.* **2022**, *61* (10), e202114614. https://doi.org/10.1002/anie.202114614.
(104) Jing, C.; Cornish, V. W. Chemical Tags for Labeling Proteins Inside Living Cells. *Acc. Chem. Res.* **2011**, *44* (9), 784–792. https://doi.org/10.1021/ar200099f.
(105) Bai, R.; Covell, D. G.; Pei, X.-F.; Ewell, J. B.; Nguyen, N. Y.; Brossi, A.; Hamel, E. Mapping the Binding Site of Colchicinoids on β-Tubulin. *J. Biol. Chem.* **2000**, *275* (51), 40443–40452. https://doi.org/10.1074/jbc.M005299200.

(106) Bryan, A. J.; de Silva, A. P.; De Silva, S. A.; Rupasinghe, R. A. D. D.; Sandanayake, K. R. A. S. Photo-Induced Electron Transfer as a General Design Logic for Fluorescent Molecular Sensors for Cations. *Biosensors* **1989**, *4* (3), 169–179. https://doi.org/10.1016/0265-928X(89)80018-5.
(107) Baas, P. W.; Rao, A. N.; Matamoros, A. J.; Leo, L. Stability Properties of Neuronal Microtubules. *Cytoskeleton* **2016**, *73* (9), 442–460. https://doi.org/10.1002/cm.21286.
(108) Alushin, G. M.; Lander, G. C.; Kellogg, E. H.; Zhang, R.; Baker, D.; Nogales, E. High-Resolution Microtubule Structures Reveal the Structural Transitions in Aβ-Tubulin upon GTP Hydrolysis. *Cell* **2014**, *157* (5), 1117–1129. https://doi.org/10.1016/j.cell.2014.03.053.
(109) Ojima, I.; Das, M. Recent Advances in the Chemistry and Biology of New Generation Taxoids. *J. Nat. Prod.* **2009**, *72* (3), 554–565. https://doi.org/10.1021/np8006556.
(110) Rosenberg, B.; Van Camp, L.; Krigas, T. Inhibition of Cell Division in Escherichia Coli by Electrolysis Products from a Platinum Electrode. *Nature* **1965**, *205* (4972), 698–699. https://doi.org/10.1038/205698a0.
(111) Trzaska, S. Cisplatin. *C&EN* **2010**. https://doi.org/10.1021/cen-v083n025.p052.
(112) Battle, A. R.; Ridone, P.; Bavi, N.; Nakayama, Y.; Nikolaev, Y. A.; Martinac, B. Lipid–Protein Interactions: Lessons Learned from Stress. *Biochimica et Biophysica Acta (BBA) - Biomembranes* **2015**, *1848* (9), 1744–1756. https://doi.org/10.1016/j.bbamem.2015.04.012.
(113) Cohen, B. E. Membrane Thickness as a Key Factor Contributing to the Activation of Osmosensors and Essential Ras Signaling Pathways. *Front. Cell Dev. Biol.* **2018**, *6*.
(114) Doroudgar, M.; Morstein, J.; Becker-Baldus, J.; Trauner, D.; Glaubitz, C. How Photoswitchable Lipids Affect the Order and Dynamics of Lipid Bilayers and Embedded Proteins. *J. Am. Chem. Soc.* **2021**, *143* (25), 9515–9528. https://doi.org/10.1021/jacs.1c03524.
(115) Kanda, H.; Ling, J.; Tonomura, S.; Noguchi, K.; Matalon, S.; Gu, J. G. TREK-1 and TRAAK Are Principal K+ Channels at the Nodes of Ranvier for Rapid Action Potential Conduction on Mammalian Myelinated Afferent Nerves. *Neuron* **2019**, *104* (5), 960-971.e7. https://doi.org/10.1016/j.neuron.2019.08.042.
(116) Aryal, P.; Jarerattanachat, V.; Clausen, M. V.; Schewe, M.; McClenaghan, C.; Argent, L.; Conrad, L. J.; Dong, Y. Y.; Pike, A. C. W.; Carpenter, E. P.; Baukrowitz, T.; Sansom, M. S. P.; Tucker, S. J. Bilayer-Mediated Structural Transitions Control Mechanosensitivity of the TREK-2 K2P Channel. *Structure* **2017**, *25* (5), 708-718.e2. https://doi.org/10.1016/j.str.2017.03.006.